Fraktionierter Sedimenttransport in Flüssen:

Numerische Modelle und ihre Anwendungen

Habilitationsschrift von

Dr.-Ing. Dipl.-Math. Minh Duc Bui

Lehrstuhl für Wasserbau und Wasserwirtschaft
Ingenieurfakultät Bau Geo Umwelt
Technische Universität München

Mai 2020

DANKSAGUNG

Die vorliegende Arbeit entstand während meiner Tätigkeit als wissenschaftlicher Mitarbeiter am Lehrstuhl für Wasserbau und Wasserwirtschaft der Technischen Universität München.

Mein besonderer Dank gilt Herrn Prof. Dr. sc. techn. Peter Rutschmann für das Vertrauen, die Diskussionen und die Unterstützung, die das Gelingen dieser Arbeit ermöglicht haben.

Außerdem meinen herzlichen Dank an Herrn Prof. Dr.-Ing. Dr.h.c. mult. Franz Nestmann vom Institut für Wasser und Gewässerentwicklung des Karlsruher Instituts für Technologie und Herrn Prof. Dr. Anton Schleiss vom Laboratoire de constructions hydrauliques der EPFL für die Übernahme des Fachmentorates.

Danken möchte ich auch den Kolleginnen und Kollegen am Institut, allen voran, meinen ehemaligen Doktoranden Weiwei Yao, Keivan Kaveh und Ateeq Sadar, sowie meinen jetzigen Doktoranden Markus Reisenbüchler und Van Hieu Bui für die schöne und effektive Kooperation, Tobias Liepert und Ngoc Dung Nguyen für die computertechnische Unterstützung, Birgit Stögmüller und Sigrid Machauer für die nette Mithilfe.

Mein ganz herzlicher Dank geht an Herrn Dr. Wolfgang Zwecker für die Assistenz bei der sprachlichen Überarbeitung dieser Arbeit.

Schließlich danke ich meiner großen Familie und besondere meiner Frau Phuong sowie meinen beiden Kindern Viet und Mai. Ohne ihr Verständnis und ihre Unterstützung wäre meine Arbeit nicht in dieser Form zustande gekommen.

Inhaltsverzeichnis

ZUSAMMENFASSUNG

Um ein nachhaltiges Sedimentmanagement angesichts der Gestaltung von Flüssen, der Erhaltung von Lebensräumen und der Wiederherstellung von Flussökosystemen besser planen und ausführen zu können, sind Untersuchungen von hydromorphologischen Vorgängen in Mischsohlflüssen in den meisten wasserbaulichen und wasserwirtschaftlichen Projekten von besonderer Bedeutung. Dabei werden, neben Labor- und Felduntersuchungen, numerische Modellierungen von hydromorphologischen Vorgängen in zunehmendem Maße eingesetzt.

In dieser Arbeit wurde das Fachwissen über die herkömmlichen numerischen Modelle des fraktionierten Sedimenttransportes bereitgestellt. Die Modellkonzepte wurden ausführlich diskutiert und die unterschiedlichen Modellanwendungen anhand von Beispielen belegt. Dabei wurden die von dem Autor und seiner Forschungsgruppe durchgeführten Entwicklungen der neuen Modellansätze für nichtgleichgewichten Geschiebetransport und für Sedimenttransport in Kiessohlflüssen vorgestellt. Anwendungen von Künstlichen Neuronalen Netzen (eng.: ANN) für Sedimenttransportberechnung wurden an verschiedenen Beispielen gezeigt. Anschließend wurden die Erkenntnisse über die konzeptionellen Probleme der derzeitigen Geschiebeberechnung sowie über die praktischen Probleme der Modellverwendung formuliert und abschließend Möglichkeiten für die künftigen Forschungen aufgezeigt.

1. EINLEITUNG

Sedimente auf der Erde entstehen aus unterschiedlichen Prozessen der Verwitterung von Festgesteinen, die durch Wind, Wasser und Schwerkraft transportiert werden können. Nur ein Anteil dieser Lockergesteine wird dann in die Flüsse eingetragen. In einem Flusssystem bestehen Sedimente aus einer Mischung von Körnern unterschiedlicher Größe, Form und Eigenschaft, die für verschiedene Sohlbereiche gewisse Veränderungen aufweisen und zudem zeitlichen Schwankungen unterworfen sind. In einem Fluss wird Sediment als Geschiebe an der Gewässersohle oder als Schwebstoff in der Wassersäule transportiert. Neben weiteren Verwitterungsprozessen findet während dieses Transports eine Sohlumlagerung und vor allem auch eine Sortierung der Mischsohle statt. Der Fluss kann seine Sedimente in der Strömungsrichtung, Querrichtung und vertikaler Richtung sortieren. Die Sohlsortierung wird meistens durch den Differenztransport unterschiedlicher Sedimentgrößen bzw. –gewichten erreicht. Es handelt sich dabei um einen komplexen, mehrdimensionalen und dynamischen Prozess, der sich aus den Wechselwirkungen von Strömung und Sedimenttransport ergibt. Dadurch wird jeweils eine charakteristische Morphologie bestimmt. Zusammenfassungen differenter Arten der Flussmorphologie finden sich z.B. in Whiting (1996) und Powell (1998). Generell wird ein Fluss als Sandbettfluss bezeichnet, wenn die Mittelgröße des Sohlenmaterials in dem Sandbereich (< 2 mm) ist, ansonsten als Kiesbettfluss. In der Regel besitzen Flüssen mit Kiessohlen ein größeres Gefälle und ihr Sohlenmaterial weist eine hohe Ungleichförmigkeit auf. Während großer Hochwasserereignisse kann der Fluss seine Sedimente stark sortieren, wodurch für jeden einzelnen Fall eine charakteristische Morphologie bestimmt wird.

In vielen Kiesbettflüssen ist die Flusssohle vertikal geschichtet mit einer groben Schicht auf der Sohloberfläche. Diese grobe Deckschicht weist eine höhere Stabilität auf und kann die Erosion der darunter befindlichen Feinsedimente bei einer starken Strömung begrenzen. In der Natur ist dies vor allem bei ganzjährig wasserführenden Fließgewässern zu beobachten (Leopold et al., 1964). Einige Kiesbettflüsse zeigen jedoch keine Schichtung in der Vertikalen oder eine vertikale Sohlstruktur mit gröberen Sedimenten in der Unterschicht. Ein Beispiel für jede Art der Flusssohle ist in Abbildung $1.$ dargestellt. Der Unterschied zwischen den beiden Bildern ist, dass sich das Bild auf der linken Seite auf einen perennierenden (engl.: perennial) Fluss mit geringer Sedimentzufuhr und moderatem Hochwasser bezieht, während das Bild auf der rechten Seite einen ephemeren (engl.: emphemerial) Fluss mit hoher Sedimentzufuhr und starkem Hochwasser betrifft.

In Kiessohlflüssen mit einer geometrischen Standardabweichung der Sieblinie von $\sigma_g > 2$ findet nach Überschreiten des sog. kritischen Strömungsangriffs ein selektiver Transport des Feinkornanteils statt (Little und Mayer, 1976). Bei relativ langsamen Fließgeschwindigkeiten und vernachlässigbar kleinem Geschiebeeintrag von Oberstrom werden hier nach und nach feinkörnige Kornfraktionen aus der oberen Sedimentschicht ausgewaschen, so dass

gröberes Material zurückbleibt und sich dort allmählich akkumuliert. Gleichzeitig geht der Geschiebeaustrag aus dem betrachten Flussabschnitt trotz anhaltendem Strömungsangriff mit der Zeit auf nahezu null zurück (Koll, 2002). Weiterhin kann es zum Aufbau einer gröberen Sohlenoberfläche mit einer höheren Stabilität kommen, die einem größeren Strömungsangriff widerstehen kann und das darunter befindliche Sediment schützt. Dieser Effekt wird als Abpflasterung (engl.: Armouring oder auch Pavement) bezeichnet. Die so entstandene Sohlenoberfläche mit gröberen Kornfraktionen als das Ursprungsmaterial wird auch als stabile Deckschicht bezeichnet. Als weitere Ursache für die Akkumulation gröberen Materials an der Sedimentoberfläche wird die Auswirkung der vertikalen Sortierungsprozesse angesehen (Parker und Klingeman, 1982). Da auf größere Partikel ein höherer dispersiver Druck einwirkt, wandern diese allmählich nach oben. Es kommt somit zu einer vertikalen Sortierung der Kornfraktionen. Hierfür muss das Korngemisch jedoch vollständig in Bewegung sein. Bei der Bewegung einzelner Körner verändern sich die Lücken im Korngefüge. Entsteht eine Lücke unterhalb eines Korns, so ist es kleinen Körnern aufgrund ihrer Größe eher möglich, in die Lücke nachzurutschen und diese Lücke wieder aufzufüllen. Infolgedessen wandern in Korngemischen kleinere Kornfraktionen mit der Zeit nach unten und größere Körner werden Richtung Oberfläche gehoben (Gray et al., 2006). Bei einer weiteren Steigerung des Strömungsangriffs können alle Kornfraktionen in Bewegung mit der Strömung kommen und deshalb kann diese stabile Deckschicht zerstört werden. Bei ausreichendem Strömungsangriff und Geschiebeeintrag von Oberstrom kann sich aber ein Transportgleichgewicht und damit eine mobile Deckschicht ausbilden (Wilcock, 1997).

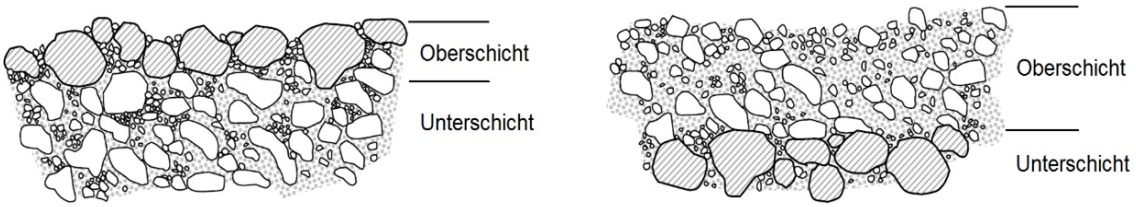

Abbildung 1 Sohlschichten in perennierenden (links) und ephemeren (rechts) Kiesbettflüssen (nach Almedeij, 2002)

Besteht die Sohle aus gröberem Material, bieten die Porenräume zwischen den Sedimenten die Voraussetzungen für die Einlagerung feiner Sedimente. In der Regel wird zu Zeiten geringen Abflusses mehr feines Material sedimentiert und auf der Flusssohle akkumuliert oder aber es dringt unter die oberste Schicht des groben Materials (Schälchli, 1993). Maßgebend für diesen Ablagerungsprozess sind die vom Abfluss transportierten Schwebstoffe und eine in die Sohle gerichtete Sickerströmung. Dadurch gelangen die Feinsedimente in Porenräume, wo sie ausfiltriert und abgelagert werden. Dieser Prozess ist unter anderem für die Kolmation von Flusssohlen von Bedeutung (Beyer und Banscher, 1975; Geldner, 1982). Im Gegenteil zur Deckschichtbildung führt die Kolmation zur einer Reduzierung des verfügbaren Porenraums, dadurch wird die Sohle verdichtet. Von besonderer Bedeutung sind dabei die feinen Schwebstoffe der Silt- und Tonfraktion, die aufgrund ihrer kohäsiven Eigenschaft die Sohle verfestigen und die Durchlässigkeit entscheidend verringern. Weiterhin kommt es zu einer hydraulischen Glättung. Die angreifende Strömung erzeugt somit eine geringere Sohl-

schubspannung, was indirekt zu einer höheren Sedimentstabilität bei gleichem Abfluss führt (Mitchner und Torfs, 1996; Venditti et al., 2010). Reine Sandablagerungen können zu einem instabilen Substrat mit einer vergleichsweise geringen Durchlässigkeitsabnahme führen.

Im Allgemeinen weisen Sandbettflüsse das Vorhandensein von Dünen als die vorherrschende Sohlenform auf. Das Verhalten der Dünen ist abhängig von den Sohlensedimenteigenschaften, z.B. in Flüssen mit feinen Sandböden tauchen die Sohlformen früher auf und wachsen höher als in Flüssen mit groben Sandböden. Generell sind die Sohlenformen nicht nur auf Sandbettflüsse begrenzt. Wenn die Strömung von ausreichender Stärke ist, können sich die Sohlformen wie Dünen und Antidünen auch in Kiesbettflüssen bilden (Dinehart, 1992). In Abhängigkeit von der Strömungsintensität kann die Korngrößenverteilung mit den Sohlformen interagieren und eine vertikale Sortierung induzieren. Wiederum können die Sohlstrukturen einen wesentlichen Einfluss auf die Strömung nehmen und folglich die Sedimenttransportkapazität bzw. die Morphologie eines Fließgewässers beeinflussen. Abbildung $2.$ zeigt exemplarisch eine solche Sohlstruktur, wobei Dünen gleichzeitig mit Sortiereffekten auftreten können, und das Sohlenmaterial relativ gröber in der Tiefe, relativ feiner in den Dünenspitzen sowie relativ gröber in den Dünenmulden und unter den Dünen ist.

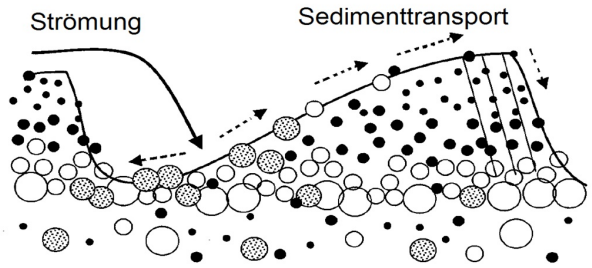

Abbildung 2 Vertikale Sortierung in Dünen (nach Blom et al., 2003)

Bei einigen Publikationen wurde darauf hingewiesen, dass der Sedimenttransport und die Sedimentablagerung in Kiesbettflüssen nicht verstanden werden kann, wenn die vertikale Sortierung nicht berücksichtigt wird (Wilcock, 1993; Wathen et al., 1995). Auch die Wichtigkeit der Sohlenform für den nichtgleichförmigen Sedimenttransport und die Kornverteilung wurde gezeigt (Ribberink, 1987).

Der Sedimenttransport, die Sohlumlagerung im Flussschlauch und der Sedimentaustausch mit den Vorländern sind natürliche Phänomene eines sich im dynamischen Gleichgewicht befindenden Fließgewässers. Jede Störung des Sedimenttransportkontinuums im Flusssystem kann eine Vielzahl von Konsequenzen zur Folge haben. Im Zuge des Hochwasserschutzes, der Kanalisierung für die Schifffahrt oder des Aufstaus für die Trinkwassergewinnung und Bewässerung sowie für die Energieerzeugung führen jedoch anthropogene Eingriffe in der Sedimentdynamik zu einer zunehmenden Beeinflussung des Flusssystems, wobei der natürliche Charakter der Flüsse bzw. ihre ökologische Vielfalt weitgehend verloren gegangen ist. Aus diesem Grund ist es sehr wichtig, ein nachhaltiges Sedimentmanagement in Bezug auf die Gestaltung von Flüssen, die Erhaltung von Lebensräumen und die Wiederherstellung von

Flussökosystemen besser zu planen. Dafür sind verschiedene Aspekte der Untersuchung des fraktionierten Sedimenttransports mit der Sohlensortierung u.a. von besonderer Bedeutung.

Sedimentdynamik und Flussmorphologie sind Gegenstand eines sehr komplizierten Fachgebietes, das unterschiedliche Fachbereiche der Naturwissenschaft umfasst, in denen seit mehreren Jahrzehnten geforscht wird. Trotz weltweit intensiver und langer Forschungsbemühungen unterliegt die mathematische Beschreibung von Prozessen des Sedimenttransports in Mischsohlflüssen aufgrund vielfältiger Einflussfaktoren noch heute erheblichen Unsicherheiten. Vor allem sind die feineren Kenntnisse über die grundlegenden Prozesse wie z.B. die Wechselwirkung zwischen Strömung, Sedimenttransport, Kornsortierung und Solveränderung immer noch nicht vollständig geklärt bzw. es sind noch einige Fragen offen. Auf dem Gebiet der Sedimentdynamik spielen experimentelle Untersuchungen und Feldstudien eine wichtige Rolle. Aus Messdaten und mit vereinfachten Annahmen wurden empirische Modellansätze für Teilprozess des Gesamtproblems entwickelt. In den letzten Jahrzehnten wurden sowohl in der Computertechnik als auch in der Strömungsmechanik, insbesondere in Bezug auf turbulente Strömungen und Strömungen von granularem Material, bedeutende Fortschritte erzielt, von denen auch die Sedimenttransportmodellierung profitierte. Dazu gehört ein höherer Kenntnisstand über die physikalischen Prozesse. Aufgrund eines verbesserten Prozessverständnisses sowie durch die Bereitstellung räumlich und zeitlich hoch aufgelöster Datensätze machte die Modellentwicklung insgesamt gesehen große Fortschritte.

In der heutigen Zeit werden numerische Simulationen immer wichtiger. Teure und zeitaufwendige Experimente können durch numerische Modelle unterstützt und im besten Fall sogar ersetzt werden. Sind die Vorgänge zu komplex, um durch Messungen ausgewertet zu werden, ermöglichen erst numerische Simulationen die nähere Beleuchtung dieser Vorgänge. Gegenüber der Laboruntersuchung hat das numerische Modell den Vorteil, dass für das Testen einer Reihe von Szenarien nur wenig Zeit erforderlich ist. Darüber hinaus können verschiedene empirische Ansätze desselben physikalischen Phänomens getestet werden. Der bedeutendste Beitrag zur Integration phänomenologischer Grundkenntnisse in die praktischen Ingenieurarbeiten ist wahrscheinlich das computergestützte mathematische Modell. Mit dem Einsatz von leistungsfähigen Datenverarbeitungsanlagen hat die Verwendung von numerischen Modellen zur Untersuchung der flussmorphologischen Fragestellungen immer mehr an Bedeutung gewonnen. Neben Labor- und Felduntersuchungen werden für die Planung und Ausführung einer Baumaßnahme in zunehmendem Maße numerische Modellierungen von hydromorphologischen Vorgängen in Flüssen eingesetzt. Die Anwendung von hydro-morphodynamischen numerischen Modellen zeigt bereits gute Ergebnisse in Bezug auf die Prognose von Entwicklungen der Flussmorphologie bzw. auch der Qualität des Gewässerlebensraums. Sie bietet somit die Möglichkeit, die Auswirkung des Sedimenttransports auf geplante wasserbauliche und wasserwirtschaftliche Projekte sowie auf deren Folgen hin zu bewerten bzw. auch durch Maßnahmen zu optimieren und damit technische, wirtschaftliche und ökologische Probleme im Betrieb zu minimieren. Die einfachere Durchführbarkeit

von umfangreichen Variantenstudien durch die Möglichkeiten der grafischen bzw. visuellen Rechnerunterstützung bei Modellerstellung und Datenauswertung machen die numerische Modellierung zu einem idealen Werkzeug in der Hand des Ingenieurs, das die Voraussetzung für ein erfolgreiches Flussregimemanagement liefern kann.

Die vorhandenen numerischen Ansätze zur Untersuchung des Sedimenttransportes können in zwei Gruppen, nämlich das Lagrange'sche und das Euler'sche Verfahren, unterteilt werden. In dem Lagrange'schen Ansatz werden Sedimentpartikeln als Punkte oder kleine Kugeln definiert, die durch die Wasserströmung transportiert werden können. Ziel dieses Verfahrens ist die Bestimmung der Felder der charakteristischen lokalen Größen für die Sedimentphase (z.B. die lokale Verteilung der Partikelanzahl, der Partikelgröße, der Partikelgeschwindigkeit usw.). Dafür verfolgt man das Bewegungsverhalten jedes Partikels im strömenden Wasser. Für jedes einzelne Teilchen muss eine Transportgleichung gelöst werden. Bei der Berechnung der Partikelbahn werden die lokalen Eigenschaften der Partikel abgespeichert. Nach der Verfolgung einer genügend großen Anzahl an Partikelbahnen werden für jedes Kontrollvolumen die statistischen Mittelwerte der Eigenschaften zur Charakterisierung der Sedimentphase bestimmt. Um statistisch zuverlässige Werte zu erhalten, ist es in der Regel erforderlich, einige tausend Partikelbahnen zu berechnen. Infolgedessen wird eine große Computerleistung oder eine längere Rechenzeit gefordert. Darüber hinaus besteht eine Sohlmischung aus Partikeln unterschiedlicher Größe, dies macht jeden Modellierungsprozess komplizierter. Obwohl diese Technik ein sehr wichtiges und nützliches Werkzeug hauptsächlich für Anwendungen in kleinem Maßstab und für die Grundforschung ist, ist sie zu rechenintensiv, um in technischen Anwendungen der Flussmorphologie eingesetzt zu werden, hierbei muss die Simulation normalerweise in einem großen Gebiet und für eine angemessen lange Zeit erhalten werden. Im Unterschied zu dem Lagrange'schen Verfahren behandelt die Euler'sche Methode Sedimente auf die gleiche Weise wie die Wasserphase. Die Sedimentphase wird stattdessen als Kontinuum beschrieben, dabei liegen die Transportgleichungen der Massenbilanz des Sediments zugrunde und das Vorhandensein von Sedimentpartikeln in Wasser wird durch eine Konzentration dargestellt. Unter dem Gesichtspunkt der Rechenzeit ist der Euler'sche Ansatz viel effizienter als der Lagrange'sche Ansatz. Des Weiteren lässt sich die Euler'sche Methode für den Sedimenttransport in Flüssen leichter auf die technische Modellierung anwenden. Im Rahmen dieser Arbeit konzentrieren wir uns deshalb auf das Euler'sche Verfahren und untersuchen nur Methoden, die üblicherweise in Modellsystemen implementiert werden, um den Sedimenttransport und die hydromorphologische Veränderung in Flüssen vorherzusagen.

Die vorliegende Habilitationsschrift hat zum Ziel, das Fachwissen über numerische Modellierung in Flüssen mit Mischsohle bereitzustellen. Die Modellkonzepte des fraktionierten Sedimenttransportes werden ausführlich diskutiert und die unterschiedlichen Modellanwendungen anhand von Beispielen belegt. Im Zusammenhang mit dieser Arbeit entstanden differente Veröffentlichungen, die von dem Autor und seiner Forschungsgruppe durchgeführt wurden.

Nach dieser Einleitung wird in Kapitel 2 auf die Grundgleichungen des hydromorphodynamischen Modells, basierend auf dem Euler'schen Ansatz, eingegangen. Dabei wird ein Überblick der Anfangs- und Randbedingungen sowie des Lösungsalgorithmus gegeben. Die von dem Autor und seiner Forschungsgruppe durchgeführten Entwicklungen von Modellen werden in Kapitel 3 vorgestellt. Es handelt sich dabei um die neuen Modellansätze für nichtgleichgewichten Geschiebetransport und Sedimenttransport in Kiessohlflüssen. Anwendungen von Künstlichen Neuronalen Netzen (eng.: ANN) für Sedimenttransportberechnung werden an verschiedenen Beispielen gezeigt. Anschließend wird in Kapitel 4 auf Beispiele des Modelleinsatz in verschiedenen wasserbau- und wasserwirtschaftlichen Projekten eingegangen. Trotz der unstrittigen Leistungsfähigkeit der modernen hydromorphologischen numerischen Modelle muss auch auf Defizite verwiesen werden. Die Arbeit schließt mit einer Schlussfolgerung aus dem Ist-Zustand und einem Ausblick über die Zukunft der numerischen Modellierung (Kapitel 5) ab.

2. HERKÖMMLICHE MODELLE

Mathematische Modelle, die den Sedimenttransport erfassen, bestimmen systematisch die Bewegung des Wasserkörpers und daraus resultierend die Bewegung des Sediments. Jeder Teilprozess kann in Form von Erhaltungsgleichungen der Masse und des Impulses ausgedrückt werden. Die diesen Prozess beschreibenden Variablen der Strömung, des Sedimenttransports und der Flusssohle bilden durch die Kopplung ein System. Solange das System im Ungleichgewicht ist, ändern sich alle diese Variablen mit der Zeit. Die Bewegung des Wasserkörpers veranlasst den Sedimenttransport. Wegen des Ungleichgewichtes verändert sich die Sohleigenschaft bzw. -höhe. Das Strömungsfeld wird wiederum durch Sohlveränderung modifiziert und damit auch der Sedimenttransport. Ein vollständiges mathematisches Modell zur Berechnung der Strömung mit Sedimenttransport wird durch ein gekoppeltes Gleichungssystem beschrieben, dessen Lösung das zeitabhängige Strömungs- und Sedimenttransportfeld sowie die Eigenschaft der Flusssohle liefert.

2.1. Strömung

Mit dem heutigen Wissensstand ist es möglich, die meisten Strömungsphänomene technischer Anwendungen mit Hilfe der Erhaltungsgleichungen für Masse, Impuls und Energie zu beschreiben, die als Navier-Stokes-Gleichungen (NSG) bekannt sind. Ableitungen dieser Gleichungen finden sich zusammen mit ihrem Gültigkeitsbereich in Lehrbüchern (z.B. Bachelor, 1967).

Sowohl aus physikalischer als auch aus mathematischer Sicht ist ein Strömungsproblem erst vollständig definiert, wenn zusätzlich zu den Erhaltungsgleichungen geeignete Anfangs- und Randbedingungen für die zu berechnenden Strömungsgrößen vorgegeben sind. I.Allg. ist die Anzahl der vorzuschreibenden Bedingungen durch die höchste Ableitung einer unabhängigen Variablen gegeben. Ihre Aufteilung in Anfangs- und Randbedingungen wird durch den Typ der partiellen Differentialgleichungen bestimmt. Elliptische partielle Differentialgleichungen verlangen Randwertprobleme, d.h. dort sind auf allen Rändern Randbedingungen vorzuschreiben. Hyperbolische und parabolische partielle Differentialgleichungen haben reelle Charakteristiken, und somit einen begrenzten Einflussbereich, für den auf einer nichtcharakteristischen Berandung Anfangsbedingungen vorgeschrieben werden (Anfangswertproblem). Ist der Einflussbereich zusätzlich durch Ränder begrenzt, müssen dort noch Randbedingungen vorgeschrieben werden (Anfangs-Randwertproblem). Die Art der Randbedingungen wird durch das zu lösende physikalische Problem festgelegt.

Die allgemeingültigen NSG mit Start- und Randbedingungen beschreiben sowohl laminare als auch turbulente Strömungen. Der Übergang von der einen Strömungsform zur anderen

wird durch die Reynolds-Zahl Re charakterisiert, die i.Allg. definiert ist als:

$$Re = \frac{UL}{\nu} \tag{2.1.1}$$

mit U als charakteristischer Geschwindigkeit, L als charakteristischer Länge und ν als kinematische Viskosität. Diese dimensionslose Kennzahl beschreibt das Verhältnis von Trägheits- zu Zähigkeitskräften. Für Gerinneströmung basiert sie auf dem hydraulischen Radius und der mittleren Geschwindigkeit. Der Übergang von der einen Strömungsform zur anderen wird durch eine kritische Reynolds-Zahl Re_{cr} gekennzeichnet. Unterhalb einer kritischen Reynolds-Zahl Re_{cr}, die bekanntermaßen für eine Gerinneströmung bei 590 (Uhlmann, 2000) liegt, dominieren die viskosen Kräfte, diese Strömung wird als laminar bezeichnet. Nimmt die Reynolds-Zahl größere Werte an und wird der Einfluss der Trägheitskräfte stärker, so bezeichnet man den Charakter der Strömung als turbulent.

Für die Flussströmung können wir annehmen, dass das Wasser von konstanter Dichte bzw. konstanter molekularer Viskosität ist. Zusätzlich beschränken wir die Volumenkräfte auf die Erdanziehungskraft, die durch das Produkt aus Masse und Erdbeschleunigung gegeben ist. In diesem Fall kann das System der NSG durch das Weglassen der Energieerhaltung vereinfacht werden. Das System der NSG für die Flussströmung ist ein gekoppeltes, nichtlineares, partielles Differentialgleichungssystem vom gemischt parabolisch-elliptischem Typ. Die Frage nach der Existenz einer eindeutigen Lösung der NSG unter sehr allgemeinen Bedingungen ist bisher nicht abschließend geklärt (Galdi, 1994; Temam, 1995). Im Rahmen der hier besprochenen Bedingungen können wir jedoch die Existenz einer solchen Lösung voraussetzen und von der Diskussion dieses Aspektes absehen. Da es bis heute noch keine allgemeine analytische Lösung gibt, muss ein numerisches Verfahren zur Lösung der NSG eingesetzt werden. Hierbei werden der zu berechnende Raum und die simulierende Zeit in geeigneter Weise für das verwendete numerische Verfahren diskretisiert.

Direkte Numerische Simulation (DNS) bezeichnet Verfahren, bei denen das numerische Gitter so fein ist, dass auch die kleinsten Schwankungen der Strömung in Raum und Zeit durch das Diskretisierungsverfahren aufgelöst und damit berechnet werden können. Da turbulente Strömungen sich aus Wirbelstrukturen verschiedener Größenordnungen zusammensetzen und stochastisches Verhalten aufweisen, ergibt sich eine Abschätzung der Knotenanzahl N_R für die dreidimensionale räumliche Diskretisierung für die DNS:

$$N_R \sim Re^{\frac{9}{4}} \tag{2.1.2}$$

Neben der räumlichen Diskretisierung muss der Zeitschritt proportional zum Ortsschritt kleiner werden. Demzufolge kann eine Zeitschrittanzahl N_Z für die zeitliche Diskretisierung abgeschätzt werden (Williams, 1985; Gill, 1995):

$$N_Z \sim Re^{\frac{1}{2}} \tag{2.1.3}$$

Die optimale Komplexität eines Algorithmus, der in jedem Zeitschritt verwendet wird, ist linear mit der Zahl der Gitterpunkte, deshalb steigt für turbulente Strömungen der numerische Aufwand mit $Re^{11/4}$. Aus diesem Grund wird die DNS vorwiegend zur Grundlagenforschung eingesetzt. Neben der DNS gibt es die Methode der Turbulenzmodellierung, die mithilfe von Annahmen eine gröbere Diskretisierung und somit die Berechnung der Turbulenzströmung mit den heutigen Ressourcen an Computerkapazitäten ermöglicht.

2.1.1. Statistische Turbulenzmodelle

Bei der statistischen Betrachtung der Turbulenz auf der Grundlage der Reynolds gemittelten Navier Stokes Gleichungen (RANS – Verkürzung vom Terminus „Reynolds Averaged Navier Stokes“) werden alle zeitlichen Schwankungen durch den Mittelungsprozess entfernt, jedoch die Fluktuationen erscheinen in ihrem Mittel noch in den Gleichungen. Für diese Terme wird ein Modell eingeführt, ein sogenanntes statistisches Turbulenzmodell. Mit dem Grundgedanken, dass als Ergebnis einer Strömungsberechnung meist nur der zeitliche Mittelwert der gesuchten Größe von Interesse ist, wird eine beliebige momentane Strömungsgröße f in einen zeitlichen Mittelwert $\overline{f}$ und die dazugehörige Schwankungsgröße f' aufgeteilt:

$$f = \overline{f} + f' \tag{2.1.4}$$

Diese Aufspaltung wurde bereits 1895 von Reynolds vorgeschlagen. Dem entsprechend spricht man auch von der Reynolds-Mittelung. Turbulente Strömungen weisen häufig stochastisch stationären Charakter auf, wodurch die statistische Mittelung in der Zeit folgendermaßen durchgeführt werden kann:

$$\overline{f(t)} = \frac{1}{T_t} \int_{t-\frac{T_t}{2}}^{t+\frac{T_t}{2}} f(\tau) d\tau \tag{2.1.5}$$

wobei die Integrationszeit T_t als groß gegenüber der charakteristischen Zeitskala der größten Wirbel betrachtet werden kann, jedoch als klein gegenüber der Zeitskala der mittleren Strömung (Rodi, 1993). Werden die Erhaltungsgleichungen für eine Flussströmung zeitlich gemittelt, ergibt sich das RANS Gleichungssystem:

- Maßerhaltung

$$\frac{\partial \overline{u}}{\partial x} + \frac{\partial \overline{v}}{\partial y} + \frac{\partial \overline{w}}{\partial z} = 0 \tag{2.1.6}$$

- Impulserhaltung in x-Richtung

$$\begin{aligned} &\frac{\partial \overline{u}}{\partial t} + \overline{u}\frac{\partial \overline{u}}{\partial x} + \overline{v}\frac{\partial \overline{u}}{\partial y} + \overline{w}\frac{\partial \overline{u}}{\partial z} \\ &= -\frac{1}{\rho}\frac{\partial \overline{p}}{\partial x} + \nu\left(\frac{\partial^2 \overline{u}}{\partial x^2} + \frac{\partial^2 \overline{u}}{\partial y^2} + \frac{\partial^2 \overline{u}}{\partial z^2}\right) - \left(\frac{\partial \overline{u'u'}}{\partial x} + \frac{\partial \overline{u'v'}}{\partial y} + \frac{\partial \overline{u'w'}}{\partial z}\right) \end{aligned} \tag{2.1.7}$$

- Impulserhaltung in y-Richtung

$$\begin{aligned}&\frac{\partial \overline{v}}{\partial t} + \overline{u}\frac{\partial \overline{v}}{\partial x} + \overline{v}\frac{\partial \overline{v}}{\partial y} + \overline{w}\frac{\partial \overline{v}}{\partial z} \\ &= -\frac{1}{\rho}\frac{\partial \overline{p}}{\partial y} + \nu(\frac{\partial^2 \overline{v}}{\partial x^2} + \frac{\partial^2 \overline{v}}{\partial y^2} + \frac{\partial^2 \overline{v}}{\partial z^2}) - (\frac{\partial \overline{v'u'}}{\partial x} + \frac{\partial \overline{v'v'}}{\partial y} + \frac{\partial \overline{v'w'}}{\partial z})\end{aligned} \tag{2.1.8}$$

- Impulserhaltung in z-Richtung

$$\begin{aligned}&\frac{\partial \overline{w}}{\partial t} + \overline{u}\frac{\partial \overline{w}}{\partial x} + \overline{v}\frac{\partial \overline{w}}{\partial y} + \overline{w}\frac{\partial \overline{w}}{\partial z} \\ &= -\frac{1}{\rho}\frac{\partial \overline{p}}{\partial z} + \nu(\frac{\partial^2 \overline{w}}{\partial x^2} + \frac{\partial^2 \overline{w}}{\partial y^2} + \frac{\partial^2 \overline{w}}{\partial z^2}) - (\frac{\partial \overline{w'u'}}{\partial x} + \frac{\partial \overline{w'v'}}{\partial y} + \frac{\partial \overline{w'w'}}{\partial z}) - g\end{aligned} \tag{2.1.9}$$

wobei die Dichte des Wassers mit ρ und der physikalische Druck mit p bezeichnet werden. In diesen Gleichungen steht t für die Zeit. x und y sind die horizontalen Raumkoordinate. z ist in der vertikalen Richtung. g bezeichnet die Erdbeschleunigung.

Die Struktur des RANS Gleichungssystems ist identisch mit dem der momentanen Werte. Durch die Mittelung treten lediglich die zusätzlichen Unbekannten auf, die entsprechend als Reynolds-Spannungstensor $\mathcal{R}$ bezeichnet werden.

$$\mathcal{R} = \left[\overline{u_i' u_j'}\right] = \frac{1}{\rho}\left[\overline{\tau_{ij}}\right] \tag{2.1.10}$$

Die Indizes i und j variieren zwischen 1 und 3, für u_i gilt die Geschwindigkeitskomponente in x_i-Richtung. Hier bezeichnen die Abkürzungen $(x_i; i = 1, 2, 3)$ die Richtungen (x, y, z) und für $(u_i; i = 1, 2, 3)$ gelten die Geschwindigkeitskomponenten (u, v, w).

Die Terme in Gleichung $(2.1.9)$ resultieren aus den konvektiven Anteilen der Erhaltungsgleichungen. Der Reynoldsspannungstensor $\mathcal{R}$ bildet eine Matrix aus neun Korrelationstermen, die bezüglich der Hauptdiagonalen symmetrisch sind. Sechs unbekannte Korrelationsterme verbleiben somit. In dieser Korrelation der Schwankungswerte liegt die Information, die durch die zeitliche Mittelung den momentanen Werten entzogen wurde.

Das Gleichungssystem $(2.1.6)-(2.1.9)$ ist nicht geschlossen, da der Reynolds-Spannungstensor $\mathcal{R}$ bestimmt werden muss. Dies wird allgemein als Schließungsproblematik der Turbulenz bezeichnet. Um dieses Problem zu lösen, werden statistische Turbulenzmodelle nämlich Wirbelviskositäts und Reynolds-Spannungsmodelle verwendet.

Bei den Reynolds-Spannungsmodellen wird ein exaktes Transportgleichungssystem für den unbekannten Reynolds-Spannungstensor aus den NSG abgeleitet. In diesem Gleichungssystem treten aber unbekannte Korrelationsterme höherer Ordnung auf, für die wiederum exakten Erhaltungsgleichungen aufgestellt werden können. Diese Vorgehensweise lässt sich beliebig fortsetzen und führt zu unbekannten Termen immer höherer Ordnung. Um das Pro-

blem endgültig zu lösen, sind geeignete empirische Vorgaben notwendig.

Bei Wirbelviskositätsmodellen ist das von Boussinesq in 1877 eingeführte Prinzip von entscheidender Bedeutung (Rodi, 1993). Darin wird die Annahme getätigt, dass sich die turbulenten Reynold-Spannungen, in Analogie zu den viskosen Spannungen, proportional den Geschwindigkeitsgradienten oder der Scherrate bestimmen lassen. Hierfür wird eine turbulente Viskosität oder Wirbelviskosität ν_t eingeführt, die jedoch im Gegensatz zu ihrem viskosen Analogon keine Stoffgröße sondern eine im Strömungsfeld Veränderliche ist und von der Turbulenzstruktur abhängt. Der Wirbelviskositätsansatz kann folgendermaßen formuliert werden:

$$\frac{1}{\rho}\overline{\tau_{ij}} = -\nu_t \left(\frac{\partial \overline{u_i'}}{\partial x_j} + \frac{\partial \overline{u_j'}}{\partial x_i} \right) + \frac{2}{3}\delta_{ij}k \;\; ; \quad k = \frac{1}{2}\overline{u_i' u_j'} \tag{2.1.11}$$

wobei das Kronecker-Delta mit δ_{ij} und die turbulente kinetische Energie mit k bezeichnet werden. Unter Verwendung des Wirbelviskositätsansatzes zur Modellierung des Reynold-Spannungstensors $\mathcal{R}$ ergibt sich die turbulente Viskosität ν_t als weitere Unbekannte. Zur Modellierung der turbulenten Viskosität ν_t gibt es verschiedene Ansätze, die nach der Anzahl der zusätzlich gelösten Transportgleichungen unterteilt werden können. Bei Null-, Ein- und Zweigleichungsmodellen werden die Korrelationen zweiter Ordnung über ein charakteristisches turbulentes Längenmaß L und Zeitmaß T_t mit bekannten Größen des Hauptströmungsfeldes algebraisch verknüpft. Diese Modelle werden auch als Momentenmodelle erster Ordnung bezeichnet (Rodi, 1993).

Neben den Wirbelviskositätsmodellen, die auf der Annahme von Boussinesq beruhen und damit nur lineare Terme zur Berechnung des Reynolds-Spannungstensors berücksichtigen, gibt es auch nichtlineare Wirbelviskositätsmodelle. Wie der Name schon verdeutlicht, verwenden diese Turbulenzmodelle auch Terme höherer Ordnung. Da derartige Modelle in dieser Arbeit nicht für Berechnungen benutzt wurden, sei an dieser Stelle auf Bauer (1998) verwiesen, der in seiner Dissertation einen guten Überblick dieser nichtlinearen Turbulenzmodelle bietet.

2.1.2. Large Eddy Simulation

Eine andere Systematik liegt der Large Eddy Simulation (LES) zugrunde, bei der die NSG in einem ersten Schritt tiefpassgefiltert werden. Somit ergibt sich ein Gleichungssystem mit weniger Freiheitsgraden, was eine gröbere Diskretisierung als bei der DNS zulässt. Aufgrund der Wechselwirkung zwischen den numerisch aufgelösten turbulenten Skalen und den kleineren durch das Gitter nicht mehr auflösbaren Skalen (Feinstruktur) treten die sog. Feinstrukturspannungen $\overline{\overline{\mathcal{T}}}$ auf, die mit einem sog. Feinstrukturmodell (subgrid scale model) modelliert werden müssen.

$$\overline{\overline{\mathcal{T}}} = \frac{1}{\rho}\left[\overline{\overline{\tau_{ij}}}\right] \tag{2.1.12}$$

In der letzten Zeit gibt es verschiede Ansätze, in denen der Energiekaskadenprozess den wesentlichen Ansatzpunkt zur Feinstrukturmodellierung liefert. Bei dem Energiekaskadenprozess wird Energie von den großen zu den kleinen Skalen transferiert und dort dissipiert. Es

gibt aber auch einen rückwärtigen, inversen Energietransfer (back scatter) von den kleinen zu den großen Skalen. Eine wesentliche Aufgabe eines Feinstrukturmodells ist, die durch diesen Energietransfer den kleinen Skalen zugeführte Energie zu dissipieren, damit sie sich nicht an den kleineren noch aufgelösten Skalen in unphysikalischer Weise akkumuliert, was dann zu einer unphysikalischen Beeinflussung der größeren Skalen führen kann. Wirbelviskositätsmodelle sind geeignet, der Strömung die Energie auf den kleineren Skalen zu entziehen. Ein dominierender inverser Energietransfer, bei dem der aufgelösten Strömung Energie aus den nicht aufgelösten Skalen zugeführt wird, lässt sich mit Wirbelviskositätsmodellen nicht modellieren. Diese sind nämlich unter der Voraussetzung einer positiven Wirbelviskosität immer dissipativ. Durch eine negative Wirbelviskosität würde sich zwar ein inverser Energietransfer ergeben, jedoch führt dies zu Instabilitäten in der Simulation. Zur Modellierung des inversen Energietransfers sind stochastische Modelle, die mittels einer Zufallskraft die Strömung anregen, besser geeignet (Hinterberger, 2004). Eine umfassende und detaillierte Übersicht zur Feinstrukturmodellierung mit diversen Ansätze gibt Rodi et al. (2013) u.a.

Bei der LES wird überwiegend ein sehr einfaches statistisches Turbulenzmodell verwendet. Der Grund dafür ist, dass die turbulente Feinstruktur weniger anisotrop und von den Randbedingungen des Problems unabhängiger ist als die turbulente Grobstruktur. Auf dieser Annahme der Isotropie der kleinen Skalen beruhen die statistischen Modelle. Eines der gebräuchlichsten Modelle beim LES-Verfahren ist das Smagorinsky Modell. Dieses robuste und relativ einfache Wirbelviskositätsmodell basiert auf der Annahme eines lokalen Gleichgewichts zwischen Produktion und viskoser Dissipation der Feinstruktur-Turbulenzenergie. Mit dem aufgelösten Geschwindigkeitsfeld $\overline{\overline{u_i}}$ und der Tiefpassfilterweite Δ gilt für die Wirbelviskosität bzw. die Feinstrukturspannungen:

$$\overline{\overline{\tau_{ij}}} = -\nu_t \left(\frac{\partial \overline{\overline{u_i'}}}{\partial x_j} + \frac{\partial \overline{\overline{u_j'}}}{\partial x_i} \right) \quad ; \quad \nu_t = \left(C_s \Delta f(z^+)\right) \sqrt{\left(\frac{\partial \overline{\overline{u_i'}}}{\partial x_j} + \frac{\partial \overline{\overline{u_j'}}}{\partial x_i} \right) \frac{\partial \overline{\overline{u_i'}}}{\partial x_j}} \tag{2.1.13}$$

Hierbei ist C_s eine nach Smagorinsky benannte Modellkonstante, die an das jeweilige Strömungsproblem angepasst werden muss. Für Gerinneströmungen hat sich C_s zwischen 0.065 und 0.1 bewährt (Rodi et al., 2013). Durch eine Dämpfungsfunktion $f(z^+)$ nach van Driest wird in Wandnähe die Abnahme der turbulenten Viskosität berücksichtigt (Moin & Kim, 1982):

$$f(z^+) = \sqrt[\frac{3}{2}]{1 - e^{\frac{-z^+}{A^+}}} \tag{2.1.14}$$

Hierbei ist A^+ eine empirische Konstante $(A^+ = 25)$, z^+ der dimensionslose Wandabstand. Die Dämpfungsfunktion hat nur in Wandnähe einen Einfluss auf das Längenmaß und ist daher nur bei Simulationen notwendig, bei denen die Wandgrenzschicht nicht mit einer Wandfunktion überbrückt, sondern durch das Gitter aufgelöst wird.

Grundlage für die Trennung in berechnete und modellierte Anteile der LES ist eine räumliche und damit auch zeitliche Filterung. Das für LES benötigte Gitter kann wegen des Wegfalls der kleinskaligen Anteile grober sein als für DNS. Es ist aber immer noch eine dreidimen-

sionale, instationäre Rechnung auf einem relativ feinen Gitter durchzuführen. Die wesentliche Schwierigkeit bei diesem Ansatz ist das innige Ineinandergreifen von mathematischer, physikalischer und numerischer Modellierung sowie Aspekte der Implementierung und des High–Performance Computing. Bei DNS und LES muss sich der Zeitschritt an den nicht nur räumlich, sondern auch zeitlich aufzulösenden Wirbelstrukturen orientieren. Er ist daher i.Allg. proportional der Gitterschrittweite, sodass bei den feinen bzw. extrem feinen Gittern entsprechend kleine Zeitschritte entstehen. Sollen mit Hilfe von DNS oder LES statistische Mittelwerte gebildet werden, ist die Simulation über einen entsprechend langen Zeitraum durchzuführen. Im Vergleich zu DNS ist LES deutlich weniger rechenintensiv jedoch für die meisten Strömungen in Flüssen noch zu aufwendig. Bei einer RANS-Modellierung ist dagegen die Reihenfolge von Diskretisierung und Mittelung umgekehrt. Hier werden Gleichungen für die Mittelwerte diskretisiert, so dass die nachträgliche Mittelung entfällt und die Berechnung eher den Charakter eines Iterationsverfahrens besitzt (Fröhlich, 2006).

2.1.3. Flachwassergleichungen

Der durch die Komplexität des 3D NS bzw. RANS Gleichungssystems bedingte extreme Lösungsaufwand erfordert die Ableitung approximativer Gleichungen. Für die weiteren Vereinfachungen wird angenommen, dass die charakteristische Skalenlänge und Skalengeschwindigkeit in vertikaler Richtung (Wassertiefe und Vertikalgeschwindigkeit w) viel kleiner als in horizontaler Richtung (Flussbreite- und Horizontalgeschwindigkeit u und v) sind. Durch asymptotische Betrachtung reduziert sich die Impulserhaltung in z-Richtung auf:

$$\frac{\partial \overline{p}}{\partial z} + \rho g = 0 \tag{2.1.15}$$

Integration der Gleichung $(2.1.15)$ über die Wassertiefe ergibt:

$$\overline{p}(z) = p_0 + \int_z^{z_b+h} \rho g dz = p_0 + \rho g \left(z_b + h - z\right) \tag{2.1.16}$$

p_0 bezeichnet den atmosphärischen Druck, h die Wassertiefe, z_b die Sohlenhöhe und $z_s = z_b + h$ die Höhe der Wasseroberfläche. Die Gleichung $(2.1.16)$ besagt, dass diese Vereinfachung gleichbedeutend mit der Annahme hydrostatischer Druckverteilung ist. Mit der Ableitung des Druckes in horizontaler Richtungen x und y und der Vernachlässigung von atmosphärischen Druckschwankungen ergibt sich daraus:

$$\frac{\partial \overline{p}}{\partial x} = \rho g \left(\frac{\partial z_b}{\partial x} + \frac{\partial h}{\partial x}\right) \tag{2.1.17}$$

$$\frac{\partial \overline{p}}{\partial y} = \rho g \left(\frac{\partial z_b}{\partial y} + \frac{\partial h}{\partial y}\right) \tag{2.1.18}$$

Die aus dem RANS System mit der Vernachlässigung von molekularer Viskosität resultierenden Gleichungen nehmen die folgende Form an und können als 3D Fachwassergleichungen

bezeichnet werden:

$$\frac{\partial \overline{u}}{\partial x} + \frac{\partial \overline{v}}{\partial y} + \frac{\partial \overline{w}}{\partial z} = 0 \tag{2.1.19}$$

$$\frac{\partial \overline{u}}{\partial t} + \overline{u}\frac{\partial \overline{u}}{\partial x} + \overline{v}\frac{\partial \overline{u}}{\partial y} + \overline{w}\frac{\partial \overline{u}}{\partial z} = -g\left(\frac{\partial z_b}{\partial x} + \frac{\partial h}{\partial x}\right) + \frac{1}{\rho}\left(\frac{\partial \overline{\tau}_{xx}}{\partial x} + \frac{\partial \overline{\tau}_{xy}}{\partial y} + \frac{\partial \overline{\tau}_{xz}}{\partial z}\right) \tag{2.1.20}$$

$$\frac{\partial \overline{v}}{\partial t} + \overline{u}\frac{\partial \overline{v}}{\partial x} + \overline{v}\frac{\partial \overline{v}}{\partial y} + \overline{w}\frac{\partial \overline{v}}{\partial z} = -g\left(\frac{\partial z_b}{\partial y} + \frac{\partial h}{\partial y}\right) + \frac{1}{\rho}\left(\frac{\partial \overline{\tau}_{yx}}{\partial x} + \frac{\partial \overline{\tau}_{yy}}{\partial y} + \frac{\partial \overline{\tau}_{yz}}{\partial z}\right) \tag{2.1.21}$$

$$\frac{\partial \overline{p}}{\partial z} + \rho g = 0 \tag{2.1.22}$$

Für die Lösung von Differentialgleichungen $(2.1.19) - (2.1.22)$ werden Randbedingungen benötigt. Allgemeine Randbedingungen werden in Abschnitt 2.4 thematisiert. Dennoch werden hier die speziellen Aspekte an der Sohle und der freien Wasseroberfläche behandelt, da sie für die Ableitung der 2D Flachwassergleichungen bedeutend sind.

Unter Vernachlässigung der Windkräfte, welche die Schubspannungen an der freien Oberfläche verschwinden lassen, lautet die kinematische Randbedingung an der Wasserfläche:

$$\overline{w}_s = \frac{\partial z_s}{\partial t} + \overline{u}_s\frac{\partial z_s}{\partial x} + \overline{v}_s\frac{\partial z_s}{\partial y} \tag{2.1.23}$$

Analog ergibt sich die kinematische Randbedingung an der Sohle:

$$\overline{w}_b = \frac{\partial z_b}{\partial t} + \overline{u}_b\frac{\partial z_b}{\partial x} + \overline{v}_b\frac{\partial z_b}{\partial y} \tag{2.1.24}$$

Mit den Indizes s und b wird die Lage der jeweiligen Größe an der freien Oberfläche, respektive an der Sohle, beschrieben.

2D Flachwassergleichungen

Durch Integration der 3D Flachwassergleichungen über die Fließtiefe entstehen die sogenannten 2D Flachwassergleichungen. Ohne ausführliche Herleitung, die in z.B. Flokstra (1977) oder Beffa (1994) zu finden ist, ergeben sich die tiefengemittelten Flachwassergleichungen unter Zuhilfenahme der kinematischen Randbedingungen und des Integrationssatz von Leibniz:

$$\frac{\partial h}{\partial t} + \frac{\partial (hU)}{\partial x} + \frac{\partial (hV)}{\partial y} = 0 \tag{2.1.25}$$

$$\begin{aligned}&\frac{\partial (hU)}{\partial t} + \frac{\partial (hUU)}{\partial x} + \frac{\partial (hUV)}{\partial y} = \\ &-gh\frac{\partial z_s}{\partial x} + \frac{1}{\rho}\left(\frac{\partial (hT_{xx})}{\partial x} + \frac{\partial (hT_{xy})}{\partial y}\right) + \frac{1}{\rho}\left(\frac{\partial (hD_{xx})}{\partial x} + \frac{\partial (hD_{xy})}{\partial y}\right) - \frac{1}{\rho}\tau_{bx}\end{aligned} \tag{2.1.26}$$

$$\frac{\partial(hV)}{\partial t} + \frac{\partial\left(hUV\right)}{\partial x} + \frac{\partial\left(hVV\right)}{\partial y} = \\ -gh\frac{\partial z_s}{\partial y} + \frac{1}{\rho}\left(\frac{\partial\left(hT_{yx}\right)}{\partial x} + \frac{\partial\left(hT_{yy}\right)}{\partial y}\right) + \frac{1}{\rho}\left(\frac{\partial\left(hD_{xy}\right)}{\partial x} + \frac{\partial\left(hD_{yy}\right)}{\partial y}\right) - \frac{1}{\rho}\tau_{by} \tag{2.1.27}$$

wobei U und V die tiefengemittelte Geschwindigkeit bezeichnen. T_{xx}, T_{xy}, T_{yx}, und T_{yy} sind die tiefengemittelten Schubspannungen. τ_{bx} und τ_{by} sind die Sohlschubspanungskomponente. Für jede Größe f kann folgende Mittelung F über die Wassertiefe definiert werden:

$$F = \frac{1}{h}\int_{z_b}^{z_s} f(z)dz \tag{2.1.28}$$

D_{xx}, D_{xy}, D_{yx}, und D_{yy} präsentieren den dispersiven Impulstransport aufgrund vertikaler Ungleichförmigkeit der Geschwindigkeit:

$$D_{xx} = \frac{\rho}{h}\int_{z_b}^{z_s}(\overline{u} - U)^2 dz \\ D_{xy} = D_{yx} = \frac{\rho}{h}\int_{z_b}^{z_s}(\overline{u} - U)(\overline{v} - V)dz \\ D_{yy} = \frac{\rho}{h}\int_{z_b}^{z_s}(\overline{v} - V)^2 dz \tag{2.1.29}$$

Die durch die Reynolds- und Tiefenmittelung entstandenen Terme müssen jedoch durch Modellannahmen in Abhängigkeit der mittleren Strömungsgrößen ausgedrückt werden, damit das System der 2D Flachwassergleichungen geschlossen lösbar wird. Die Methoden zur Bestimmung dieser Terme werden in den folgenden Abschnitt vorgestellt.

Sohlschubspannungsmodelle

Der Spannungsanteil, der die an der Sohle wirkende Scherkraft darstellt, wird als Sohlschubspannung bzw. Wandschubspannung bezeichnet und ist der Widerstand der Sohle gegen die Strömung. Die Sohlschubspannung beeinflusst durch ihre Reibung zwischen Sohle (bzw. Wand) und Wasserkörper maßgeblich die Turbulenz und kann für den Sedimenttransport eine wichtige Größe spielen. Messungen haben einen eindeutigen Zusammenhang zwischen der Sohlschubspannung und der mittleren Strömungsgeschwindigkeit im Quadrat ergeben. Definiert man einen Sohlreibungsbeiwert c_f kann die Sohlschubspannung wie folgt beschrieben werden:

$$\vec{\tau_b} = (\tau_{bx}, \tau_{by}) \;\; ; \quad \tau_{bx} = \rho c_f U_{res} U \;\; ; \quad \tau_{by} = \rho c_f U_{res} V \tag{2.1.30}$$

Wobei die resultierende Geschwindigkeit $U_{res} = \sqrt{U^2 + V^2}$ ist. Für die Schubspannungs-

geschwindigkeit u_* ergibt sich:

$$u_* = \sqrt{c_f} U_{res} \tag{2.1.31}$$

Der Reibungskoeffizient c_f stellt das Verhältnis zwischen dem Quadrat der Schubspannungsgeschwindigkeit und dem Quadrat der mittleren Fließgeschwindigkeit dar. Es gibt nun verschiedene Modelle, diesen Koeffizienten darzustellen.

Für glatte Sohlen lässt er sich mittels der von Schlichting & Gersten (2006) angegebenen Beziehung bestimmen:

$$c_f = 0.027 \left(\frac{\nu}{h U_{res}} \right)^{\frac{1}{4}} \tag{2.1.32}$$

Für rauhe Sohlen kann die Gauckler-Manning-Strickler Beziehung verwendet werden:

$$c_f = \frac{g}{k_{st}^2 R^{\frac{1}{3}}} \tag{2.1.33}$$

Dabei ist R der hydraulische Radius. Der Strickler-Rauheitsbeiwert k_{st} kann durch die umfangreichen Tabellenwerke z.B. von Chow (1959) oder Henderson (1966) bestimmt werden. Unter der Annahme, dass die Breite des betrachteten Flussabschnittes sehr viel grösser ist als die Fließtiefe und somit die Sohlreibung gegenüber der Seitenwandreibung überwiegt, kann der hydraulische Radius gleich der Fließtiefe h gesetzt werden.

Im Verhältnis zum Chezy-Wiederstandsbeiwert c_z ergibt sich für den Reibungskoeffizienten:

$$c_f = \frac{g}{c_z^2} \tag{2.1.34}$$

Der Wert von c_z muss als eine Funktion des hydraulischen Radius und der Sohlrauheit angesehen werden. Es sind vielfach Gleichungen vorgeschlagen worden, die den Sachverhalt genauer wiedergeben sollen. Dabei besteht jedoch für die Bestimmung des Beiwertes immer die Schwierigkeit, die gerade vorliegende Sohlrauheit richtig einzuschätzen. Für breite Flüsse mit natürlicher Sohle und steinigem Geschiebe kann nach Strickler (Prandtl, 1965)

$$c_z = 21.1 \left(\frac{h}{k_s} \right)^{\frac{1}{6}} \tag{2.1.35}$$

gesetzt werden. Durch eine logarithmische Funktion des hydraulischen Radius und der äquivalenten Rauheit kann nach Van Rijn (1987) der Chezy-Wiederstandsbeiwert ebenfalls berechnet werden:

$$c_z = 18 \log \left(\frac{h}{k_s} \right) \tag{2.1.36}$$

Dabei ist die equivalente Sohlrauheit k_s bei beweglicher Sohle in gewissem Maße von der Wassertiefe, dem mittleren Korndurchmesser, der Sohlform und dem Sohlgefälle abhängig. Diese effektive Sohlrauheit entspricht etwa der halben Transportkörperhöhe. Liegen keine Transportkörper vor (ebene Sohle), empfiehlt van Rijn (1984) dann mit $k_s \approx 3d_{90}$ zu arbeiten.

Tiefengemittelte Turbulenzmodelle

Zur Bestimmung der in den Impulsgleichungen $(2.1.26)$ und $(2.1.27)$ auftretenden tiefengemittelten Turbulenzschubspannungen T_{ij} können verschiedene Modelle verwendet werden. Die meisten Modelle basieren auf dem Wirbelviskositätskonzept, bei dem die turbulenten Schubspannungen zu den Gradienten der charakteristischen Geschwindigkeiten in Beziehung gesetzt werden.

$k-\epsilon$ *Modell*

Eine tiefengemittelte Version des Standard $k-\epsilon$ hat schon eine breite Anwendung in vielen Gebieten des Ingenieurwesens gefunden. Das Modell basiert auf dem Wirbelviskositätskonzept, bei dem die turbulenten Schubspannungen zu den Gradienten der tiefengemittelten Geschwindigkeiten in Beziehung gesetzt werden. Diese Beziehungen lauten wie folgt (Rodi, 1993):

$$\frac{1}{\rho}T_{ij} = -\overline{\nu_t}\left(\frac{\partial U_i}{\partial x_j} + \frac{\partial U_j}{\partial x_i}\right) + \frac{2}{3}\delta_{ij}\overline{k} \tag{2.1.37}$$

Die Abkürzungen x_i bezeichnen die Richtungen x, y und für U_i gilt U und V . Die Indizes i und j variieren zwischen 1 und 2.

Ähnlich wie im 3D Standard $k-\epsilon$ Modell, wurde hier angenommen, dass der lokale, tiefengemittelte Zustand der Turbulenz durch zwei Parameter, die turbulente kinetische Energie und die Dissipationsrate der turbulenten kinetischen Energie, charakterisiert werden kann. Für die turbulente Viskosität ergibt sich dann:

$$\overline{\nu_t} = c_\mu \frac{\overline{k}^2}{\overline{\epsilon}} \tag{2.1.38}$$

Hierbei ist c_μ eine empirische Konstante. Die Turbulenzparameter $\overline{k}$ und $\overline{\epsilon}$ werden in jedem Punkt eines Strömungsgebiets durch Lösen folgender halbempirischer Transportgleichungen bestimmt:

$$\frac{\partial \overline{k}}{\partial t} + U_i\frac{\partial \overline{k}}{\partial x_i} = \frac{\partial}{\partial x_i}\left(\frac{\overline{\nu_t}}{\sigma_k}\frac{\partial \overline{k}}{\partial x_i}\right) + \overline{G} + \overline{P}_k - \overline{\epsilon} \tag{2.1.39}$$

$$\frac{\partial \overline{\epsilon}}{\partial t} + U_i\frac{\partial \overline{\epsilon}}{\partial x_i} = \frac{\partial}{\partial x_i}\left(\frac{\overline{\nu_t}}{\sigma_\epsilon}\frac{\partial \overline{\epsilon}}{\partial x_i}\right) + c_{\epsilon 1}\frac{\overline{\epsilon}}{\overline{k}}\overline{G} + \overline{P}_\epsilon - c_{\epsilon 2}\frac{\overline{\epsilon}^2}{\overline{k}} \tag{2.1.40}$$

Mit $\overline{G}$ wird die Produktionsrate der turbulenten kinetischen Energie infolge der horizontalen Geschwindigkeitsgradienten bezeichnet:

$$\overline{G} = \overline{\nu_t}\left(\frac{\partial U_i}{\partial x_j} + \frac{\partial U_j}{\partial x_i}\right)\frac{\partial U_i}{\partial x_j} \tag{2.1.41}$$

Es sei hier erwähnt, dass $\overline{k}$, $\overline{\epsilon}$ und $\overline{\nu_t}$ keine tiefengemittelten Werte im engeren Sinne sind. Die Gleichungen $(2.1.39)$ und $(2.1.40)$ können nur dann als tiefengemittelte Version der ursprünglich dreidimensionalen Ausgangsgleichungen des Standard $k-\epsilon$ Modells angese-

hen werden, wenn man annimmt, dass alle Terme, die aus der Ungleichförmigkeit vertikaler Verteilungen resultieren, durch die sekundären Quell- bzw. Senkenterme $\overline{P_k}$ repräsentiert werden. Der Hauptanteil dieser Terme entsteht aus dem nicht zu vernachlässigenden Geschwindigkeitsgradienten nahe der Sohle, welche mit den dort vorliegenden turbulenten Scherspannungen Turbulenz produzieren. Diese zusätzlichen Produktionsterme sind stark abhängig von der Sohlrauheit. Es ist daher sinnvoll, sie über die Sohlschubspannung τ_b bzw. die Schubspannungsgeschwindigkeit u_* zu modellieren:

$$\begin{aligned} \overline{P_k} &= \frac{1}{c_f^{\frac{1}{2}}} \frac{u_*^3}{h} \\ \overline{P_\epsilon} &= c_{\epsilon\Gamma} \frac{c_{\epsilon 2}}{c_f^{\frac{3}{4}}} c_\mu^{\frac{1}{2}} \frac{u_*^4}{h^2} \end{aligned} \tag{2.1.42}$$

Die zusätzliche Konstante $c_{\epsilon\Gamma}$ basiert auf empirischer Information über die turbulenten Austauschgrößen in Gerinnen und kann folgendermaßen bestimmt werden:

$$c_{\epsilon\Gamma} = \left(\frac{1}{e_* \sigma_t} \right)^{\frac{1}{2}} \quad ; \quad e_* = \frac{\Gamma}{u_* h} \quad ; \quad \Gamma = \frac{\overline{\nu_t}}{\sigma_t} \tag{2.1.43}$$

Dabei werden σ_t und Γ als die turbulente Schmidtzahl und die turbulente Diffusivität bezeichnet. e_* ist die dimensionslose Diffusivität. In den meisten Anwendungsfällen wurde die Schmidtzahl meist konstant zu 0.5 gesetzt. Wie Messungen von Arnold et al. (1989) belegen, kann σ_t in querschnitts- und rauheitsgegliederten Gewässern bis auf 1.0 ansteigen. Ebenso ungeklärt ist die Größe der dimensionslosen Diffusivität. Messungen in Laborgerinnen und in der Natur belegen einen Wertbereich von 0.075 < e_* < 0.9. In rechteckigen Laborgerinnen kann man für e_* einen Wert von 0.15 annehmen (Rodi, 1993). Das ASCE-Task-Committee (1988) schlägt für natürliche Fließgewässer die Verwendung von e_* = 0.6 und σ_t = 0.5 vor. Es sollte hier erwähnt werden, dass e_* in Wirklichkeit stark variieren kann und nicht davon auszugehen ist, dass der Wert von e_* = 0.6 in allen Fällen gute Ergebnisse liefert. Mit anderen Worten hängt der e_* - Wert vom jeweiligen Problem ab, deshalb muss dieser strenggenommen an jede Strömungssituation angepasst werden (Bui, 1998).

Elder Modell

Basierend auf dem Konzept der sog. „Reynolds Analogy“ sowie unter Annahme einer logarithmischen Verteilung der vertikalen Geschwindigkeit und einer linearen Verteilung der Schubspannung hat Elder (1959) eine parabolische Verteilung für die turbulente Viskosität hergeleitet:

$$\nu_t = u_* \kappa z \left(1 - \frac{z}{h} \right) \tag{2.1.44}$$

Durch Integration dieser Gleichungen über die Fließtiefe ergibt sich näherungsweise für die tiefengemittelte Viskosität:

$$\overline{\nu_t} = \frac{u_* \kappa h}{6} \tag{2.1.45}$$

Basierend auf dem Wirbelviskositätskonzept können die tiefengemittelten Turbulenzschubspannungen Tij mit der Gleichung $(2.1.37)$ definiert werden. Da das Elder Modell nicht den Transport von Turbulenz mit der Strömung berücksichtigt, wird der Einfluss von Scherschichten nur unzureichend erfasst.

Modellierung der Dispersionsterme

Die mathematisch exakte Integration in vertikaler Richtung führt auf tiefengemittelte Gleichungen, die zusätzliche von vertikalen Ungleichförmigkeiten der Geschwindigkeit stammende Dispersionsterme beinhalten. Diese Terme sind nur dort zum Vernachlässigen klein, wo sehr gleichförmige vertikale Geschwindigkeitsprofile vorliegen. Die physikalische Bedeutung der Dispersionsglieder ist derjenigen der turbulenten Schubspannungen ähnlich (Pavlovic, 1981). In den tiefengemittelten Modellen, die auf der Annahme von gleichförmiger vertikaler Verteilung der behandelten Größen basieren, werden die Dispersionsglieder i.Allg. vernachlässigt. Unter Umständen weichen die lokalen Geschwindigkeitswerte jedoch so stark vom tiefengemittelten Wert ab, dass die dispersiven Terme berücksichtigt werden sollten. Dies gilt besonders für Strömungsvorgänge mit ausgeprägter Sekundärbewegung und vertikale Rezirkulationszonen hinter Bauwerken oder über- und umströmten Bauwerken.

Flokstra (1977) hat einen Ansatz zur Erfassung der Dispersionsterme in einer 180^0- Krümmung vorgeschlagen:

$$\begin{aligned} D_{xx} &= \rho\left(\alpha_0 U^2 - 2\alpha_1 UV + \alpha_2 V^2\right) \\ D_{xy} &= D_{yx} = \rho\left(\alpha_1 U^2 + (\alpha_0 - \alpha_2)UV - \alpha_1 V^2\right) \\ D_{yy} &= \rho\left(\alpha_2 U^2 + 2\alpha_1 UV + \alpha_0 V^2\right) \end{aligned} \tag{2.1.46}$$

Die α_i-Werte berechnen sich zu

$$\alpha_0 = 0.02 \;\; ; \quad \alpha_1 = 0.34\frac{h}{r} \;\; ; \quad \alpha_2 = 7.20\left(\frac{h}{r}\right)^2 \tag{2.1.47}$$

mit r - Krümmungsradius der mittleren Stromlinie.

Zur Modellierung der Dispersionsterme haben Jin & Steffler (1993) ein sogenanntes Moment-of-Momentum Verfahren entwickelt. Im Modell wurde ein Ansatz für die vertikale Geschwindigkeitsverteilung eingesetzt, die von der tiefengemittelten Geschwindigkeit, Schubspannungsgeschwindigkeit und Sekundärströmung an der Wasseroberfläche abhängt. Mit dieser Annahme haben sie die Momente der beiden horizontalen Impulsgleichungen hergeleitet und dann beide über die Fließtiefe integriert. Jedoch berichtete Bui (1998) über die Erfahrungen mit verschiedenen Ansätzen zur Erfassung der Dispersionsterme für starke Krümmungen. Es zeigt sich, dass trotz der Modellkomplexität die Verwendung des Moment-of-Momentum Verfahrens die Ergebnisse i.Allg. nicht nennenswert verbessert.

Eine weitere Methode zur Modellierung der Dispersionsterme ist der Ansatz nach Elder

(1959), der aus theoretischen Überlegungen und experimentellen Messungen in einer Kanalströmung die Dispersion in lateraler $\overline{D_x}$ und transversaler $\overline{D_y}$ Strömungsrichtung in Abhängigkeit der Wassertiefe und der Schubspannungsgeschwindigkeit beschreibt:

$$\overline{D_x} = a_x u_* h \;\; ; \quad \overline{D_y} = a_y u_* h \tag{2.1.48}$$

Für die dimensionslosen Dispersionskoeffizienten a_x und a_y gibt Elder in lateraler Richtung Werte für a_x im Bereich 5.9 – 6.3 und in transversaler Richtung für a_y = 0.23 an. Die Dispersionsterme werden dann folgenmaßen definiert:

$$\begin{aligned} D_{xx} &= \rho\overline{D_x}\frac{\partial U}{\partial x} \;\; ; \quad D_{xy} = \rho\overline{D_y}\frac{\partial U}{\partial y} \\ D_{yx} &= \rho\overline{D_x}\frac{\partial V}{\partial x} \;\; ; \quad D_{yy} = \rho\overline{D_y}\frac{\partial V}{\partial y} \end{aligned} \tag{2.1.49}$$

Bei einem Verzicht auf die direkte Modellierung der Dispersionsterme, kann sie auch in den Diffusionstermen berücksichtigt werden. Eine übliche Strategie ist die entsprechende Erhöhung der Wirbelviskosität. Bei Verwendung der tiefengemittelten Version des $k-\epsilon$ Modells lässt sich dies über die Wirbelviskosität durch die Kalibrierung der im sekundären Produktionsterm enthaltenen dimensionslosen Diffusivität e_* erreichen. Wegen der Proportionalität zwischen $\overline{\nu_t}$ und e_* ist es angebracht, Bereiche intensiver Sekundärströmung mit einer erhöhten Diffusivität zu kalibrieren. Zur Simulation von Strömungsvorgängen in stark gekrümmten Laborgerinnen wurden die verschiedenen e_* Werte mit einem Maximum von 5.8 von Bui (1998) verwendet. Die berechneten Fließgeschwindigkeiten haben dann eine gute Übereinstimmung mit den experimentellen Daten gezeigt. Es sollte hier nochmals betont werden, dass der e_* Wert vom jeweiligen Problem abhängt und bei der Modellverwendung an jede Strömungssituation angepasst werden muss.

2.2. Sedimenttransport

2.2.1. Mehrschichtansatz

Bestehen Sohlen fließender Gewässer aus beweglichen Sedimenten, so wird dieses Bettmaterial bei ausreichend großer Strömungsgeschwindigkeit mobilisiert und transportiert. In Zusammenhang mit Vorgängen im Wasserköper und an der Flusssohle wird der Bodensatz erodiert und gelangt in sohlnahe Bewegung (als Geschiebetransport) oder in Suspension (als Schwebstofftransport). Obwohl in der Natur zwischen beiden Transportarten keine scharfe Grenze bestehen, hat Van Rijn (1987) eine für die mathematische Simulierung notwendig Trennung der Schichten vorgeschlagen: Wenn die Sohlteilchen unter den Strömungsbedingungen über eine definierte Sprunghöhe hüpfen, definiert er sie als Schwebstofftransport, während die Teilchen mit kleinerer Sprunghöhe als Geschiebetransport definiert werden. Die Abbildung 3 zeigt schematisch die Schichtenverteilung in einer vertikalen Säule eines alluvialen Gerinnes in einem numerischen mathematischen Modell. Dabei werden drei Bereiche unterschieden. Die oberste Schicht (1) enthält die Wasser-Schwebstoffmischung. In der mitt-

leren Schicht (2) wird das Geschiebe transportiert. Zudem findet hier der Austausch zwischen dem Geschiebe, dem suspendierten Feststoff und dem darunterliegenden Sediment statt. Die Bodenschicht (3) kann sich aus mehreren Lagen mit unterschiedlichen Kornverteilungen zusammensetzen.

Nach Van Rijn (1987) entspricht die mittlere Sprunghöhe für eine näherungsweise ebene Bodenfläche grob dem Dreifachen des mittleren Korndurchmessers. Bei Berücksichtigung des Sohlformeinflusses wird die mittlere Sprunghöhe als halbe Sohlformhöhe definiert.

Das natürliche Sohlmaterial mit ausgeprägter Kornverteilung erfährt auf seinem Weg stromabwärts eine Sortierung, in dem z.B. in Aufweitungsstrecken oder Bereichen mit kleinerem Sohlengefälle gröberes Material abgelagert wird, welches infolge der reduzierten Schleppkraft nicht mehr transportiert werden kann. Dieser Effekt kann mit einem herkömmlichen uniformen Geschiebemodell, welches nur einen mittleren bzw. charakteristischen Korndurchmesser beinhaltet, natürlich nicht simuliert werden. Dazu bedarf es der Einführung eines fraktionierten Transportmodelles, wobei das Sohlenmaterial in Klassen verschiedener Korngrößen unterteilt wird. Der Transport pro Kornfraktion wird dann mit den empirischen Konzepten beschrieben, die für den uniformen Sedimenttransport entwickelt wurden. Der Gesamttransport ergibt sich durch anschließendes gewichtetes Aufsummieren für die Werte einzelner Fraktionen.

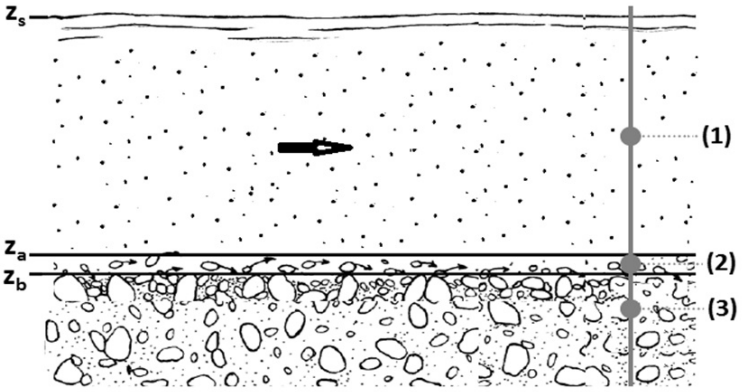

Abbildung 3 Das idealisierte physikalische System für Mehrschichtansatz für ein Kontrollvolumen der Wassersäule; (1)-Schwebstofftransportschicht; (2)-Geschiebetransportschicht; (3)-Bodenschicht

2.2.2. Zuordnung der Transportart

Übersteigt die Sohlschubspannung einen kritischen Wert, wird das Material erodiert und als Geschiebetransport oder als Schwebstofftransport transportiert. In Suspension wird es solange weiter transportiert, bis es in ein Gebiet kommt, in dem die lokalen Strömungsbedingungen das Sediment nicht weiter transportieren können und es sich wieder ablagert. Aufgrund von theoretischen und experimentellen Untersuchungen hat Van Rijn (1984) ein Verhältnis

von Geschiebe- zu Schwebstofftransport graphisch dargestellt, das in Form der folgenden Gleichung weiterentwickelt werden kann:

$$\gamma_k = \frac{q_{sk}}{q_{bk} + q_{sk}} = \begin{cases} 1 & \text{wenn} \quad \frac{u_*}{w_{sk}} \geq 10 \\ 0.28466 + 0.31066 \ln\left(\frac{u_*}{w_{sk}}\right) & \text{wenn} \quad 0.4 < \frac{u_*}{w_{sk}} < 10 \\ 0 & \text{wenn} \quad \frac{u_*}{w_{sk}} \leq 0.4 \end{cases} \tag{2.2.1}$$

wobei γ_k den Parameter zur Zuordnung der Transportart für jede Fraktion k darstellt und w_{sk} die mittlere Sinkgeschwindigkeit der Fraktion k ist. Die Aufteilung zwischen Geschiebe- q_{bk} und Schwebstofftransport q_{sk} basiert auf dem Verhältnis von Schubspannungs- zu Sinkgeschwindigkeit. Wird das Verhältnis größer als 10, wird die entsprechende Kornklasse vollständig in suspendierter Form transportiert und der Parameter γ_k, mit dem die Zuweisung zur Transportart gesteuert wird, wird zu eins. Bei einem Verhältnis nicht größer als 0.4 werden alle Partikel der Kornfraktion als Geschiebe transportiert.

2.2.3. Geschiebetransport

Der Geschiebetransport ist der dominierende Mechanismus zur Steuerung der Morphodynamik des Flussbetts. Die grundlegende Aufgabenstellung bei der Simulation des Geschiebetransports ist eine eindeutige Beziehung zwischen den hydraulischen und sedimentologischen Parametern und dem Geschiebefluss zu finden. Im Labor gelingt dies in gewissen Grenzen der Gefällevariation, falls Normalabflussverhältnisse vorliegen und die Zugabe des Kornmaterials gerade der Transportkapazität entspricht. D.h. der Geschiebetransport findet in einem Gleichgewichtzustand statt. In natürlichen Gerinnen mit einer Mischsohle scheint dies kaum möglich. Die Verhältnisse werden dominiert durch die Interaktion zwischen der Wasserströmung und der Sohle bzw. Geometrie in Bezug auf Sohlrauheit, Sortiereffekte, Deckschichtbildung und Veränderung der Geometrie und hängen damit stark von der Vorgeschichte ab. Dabei können auch Sekundäreffekte wie Lagerungsdichte, örtliche Exposition, Verfügbarkeit des Materials und die Konzentration des suspendierten Materials eine wichtige Rolle spielen. Um diesen komplexen Transportmechanismus des Geschiebes wenigstens qualitativ richtig zu beschreiben, kann angenommen werden, dass die herkömmlichen Geschiebetriebformeln in einem räumlich und zeitlich begrenzten Rahmen gültig sind. Der so bestimmte Geschiebefluss wird dann mit Korrekturparametern modifiziert oder/und mit zusätzlichen Ansätzen modelliert, um die anderen Effekten zu erfassen.

Geschiebetransportrate

Ansätze zur Berechnung der Geschieberate sind global in zwei Gruppen zu unterteilen, nämlich stochastische und deterministische Modelle. Es hängt davon ab, wie die effektive Sohlschubspannung bestimmt wird. In deterministischen Modellen wird angenommen, dass die Geschiebetransportrate mit einer Funktion der Strömungs- und Sedimentparametern explizit beschrieben werden kann. In stochastischen Modellen kommt der Charakter des Geschiebetransportes in einer Wahrscheinlichkeitsverteilung der auf der Sohle wirkenden Schubspan-

nungen zum Ausdruck, um vor allem den Effekt von turbulenten Bewegungen dicht oberhalb der Sohle auszudrücken.

Im Allgemeinen können deterministische Geschiebetransportfunktionen in der folgenden dimensionslosen Form ausgedrückt werden:

$$\Phi_b = \frac{q_b}{d\sqrt{g\left(s_s - 1\right)d}} \tag{2.2.2}$$

wobei Φ_b - die von Einstein (1950) eingeführte, dimensionslose Geschiebetransportrate; q_b – die spezifische Geschieberate pro Meter Flussbreite; d – der charakteristische Korndurchmesser; s_s – die relative Dichte des Sediments zu Wasser.

In der Literatur findet man eine große Auswahl an Geschiebevorhersagemodellen. Jede Formel wurde mit einem spezifischen Ziel entwickelt und hat ihren eigenen Anwendungsbereich. Einige Formeln wurden für die Beschreibung des Transports von grobem Sohlenmaterial entwickelt, andere für feines Sohlenmaterial. Manche Formeln dürfen nur im Falle von uniformem Sohlenmaterial gebraucht werden, andere wurden speziell für gradiertes Sohlenmaterial entwickelt. Es ist noch unbekannt, welche Geschiebeformel unter welchen Umständen die beste Leistung erbringt. Bei der Wahl einer Geschiebefunktion muss darum kritisch auf das Anwendungsgebiet dieser Formeln und die daran gekoppelte Rauheitsformulierung geachtet werden.

Unter der Bedingung, dass die Sohle zu 100% aus verschieden Fraktionen besteht, kann die gesamte Geschiebetransportrate q_b als Summe aller Transportraten q_{bk} je Fraktion angegeben werden. Diese fraktionelle Geschiebetransportrate kann mit einer geeigneten empirischen Geschiebeformel berechnet werden, die für den uniformen Sedimenttransport entwickelt wurde.

In einer Mischsohle ist jedoch die Mobilität je Fraktion unterschiedlich. Die großen Körner sind übermäßig dem Strömungsangriff ausgesetzt. Die kleinen Körner sind im Strömungsschatten der großen Körner. Deshalb wird ihre Transportkapazität verringert. Zur Berücksichtigung dieser Effekte führt man in dem Modell den sog. Hiding-Exposure Faktor oder die Ausgleichfunktion ξ_k ein. Dadurch wird der kritische Shields-Parameter (die dimensionslose Schubspannung) oder die Geschiebefracht q_bk für jede Fraktion k modifiziert.

Unter der Annahme, dass Sedimentparameter in der Regel auf einen charakteristischen Korndurchmesser reduziert und Strömungsparameter durch die Sohlschubspannung τ_b ersetzt werden können, nehmen die meisten Geschiebeformeln die folgende Form an:

$$q_{bk} = F\left(\tau_b, \tau_{ck}, \xi_k, d_k\right) \tag{2.2.3}$$

wobei τ_{ck} - die sog. kritische Sohlschubspannung; d_k – der charakteristische Korndurchmesser der Fraktion k.

Geschiebetransportrichtung

In der Tat wird bei der experimentalen Bestimmung der Geschiebetransportrate angenommen, dass die Richtung des Geschiebetransports und der Sohlschubspannung gleich ist. Das heißt, der Vektor der Geschiebetransportrate ist dreidimensional. Allgemein wird jedoch angenommen, dass die Richtung des Geschiebetransports von der mittleren Strömung in Bodennähe und der Sohlneigung abhängt und es sich bei der Sedimenttransportrate um einen horizontalen Vektor handelt. Zur Bestimmung der kartesischen Komponenten des Geschiebetransports in s - Hauptströmungsrichtung q_{bs} und n - Querrichtung q_{bn} auf der horizontalen Koordinate ergibt sich:

$$\begin{aligned} q_{bs} &= \cos(\alpha) q_b \;\; ; \quad q_{bn} = \sin(\alpha) q_b \\ \alpha &= \delta + \Delta_\beta \;\; ; \quad \tan(\delta) = \frac{\overline{u}_{bn}}{\overline{u}_{bs}} \end{aligned} \tag{2.2.4}$$

Wobei α der Winkel zwischen Geschiebetransportrichtung und s – Richtung, $(\overline{u}_{bn}, \overline{u}_{bs})$ die mittlere Geschwindigkeit in der Geschiebeschicht, δ der Winkel zwischen der Richtung von der Strömung in Bodennähe und s-Richtung, und Δ_β die Winkeländerung infolge Sohlneigung sind.

Bei Verwendung eines 2D tiefengemittelten Modells für Krümmungen können die Geschwindigkeiten in Bodennähe aus Ansätzen über vertikale Geschwindigkeitsverteilungen berechnet werden. Auf den folgenden Potenzansatz für die Geschwindigkeitskomponente in Hauptströmungsrichtung $\overline{u}_s(z)$ kann zurückgegriffen werden (Odgaard & Bergs, 1988):

$$\overline{u}_s(z) = U_s \frac{m+1}{m} \left(\frac{z - z_b}{h} \right)^{\frac{1}{m}} \quad ; \quad m = \frac{\kappa U_s}{u_*} \tag{2.2.5}$$

Für die Geschwindigkeitskomponente in Querrichtung $\overline{u}_n(z)$ wird die folgende Gleichung eingesetzt:

$$\overline{u}_n(z) = U_n + \frac{2m+1}{\kappa^2 m} \frac{h}{r} U_s \left(\frac{z - z_b}{h} - \frac{1}{2} \right) \tag{2.2.6}$$

Wobei U_s und U_n die tiefgemittelten Geschwindigkeitskomponenten in s - Hauptströmungsrichtung und n - Querrichtung sind.

Eine andere Methode zur Bestimmung des Winkels α bei Verwendung eines 2D tiefengemittelten Modells ist, dass sich dieser Winkel aus dem Winkel der tiefengemittelten Hauptströmungsrichtung δ, der Winkeländerung infolge Sohlneigung Δ_β und der Winkelabweichung infolge Sekundärströmung Δ_ψ summiert:

$$\alpha = \delta + \Delta_\beta + \Delta_\psi \;\; ; \quad \tan(\delta) = \frac{U_n}{U_s} \tag{2.2.7}$$

In der Praxis quantifiziert man zumeist nicht direkt die Größe des Winkels Δ_β und Δ_ψ sondern nur ihren Einfluss auf die Geschiebetransportrichtung und den -betrag (Bui, 1998).

Geschiebetransport über eine geneigte Sohle

Die Auswertung des Geschiebetransports auf einer beliebig geneigten Sohle ist einer der wichtigsten Aspekte in jedem morphodynamischen Modell, das die Sohlentwicklung betrachtet: wenn die Sohle in Längs- und Querrichtung gekippt wird, spielt die Schwerkraft eine wichtige Rolle bei der Partikeldynamik und dem Geschiebetransport. Die meisten Geschiebetransportformeln wurden für eine nahezu horizontale Sohle abgeleitet (Sohlneigung kleiner als 10^{-3}). Experimentelle Daten in geneigten Kanälen zeigen aber eine starke Zunahme der Geschieberaten an der Sohle. Die Sohlneigung kann die lokale Strömungsgeschwindigkeit nahe der Sohle beeinflussen und die Schwellenwertbedingung für den Bewegungsbeginn ändern. Sie kann auch die Partikelgeschwindigkeit verändern, sobald das Sediment in Bewegung ist. Dies betrifft im numerischen morphologischen Modell eine Modifikation der kritischen Sohlschubspannung, des Betrages und der Richtung der Transportrate, aber auch eine Berücksichtigung der bodenmechanischen Wirkungen wie ein plötzliches Rutschen des Bodens, wenn ein kritischer Sohlneigungswinkel überschritten wird. Dafür sind zusätzliche Ansätze nötig (Bui, 1998).

Ein wichtiger diesen Ansätzen zugrundliegender geometrischer Parameter, der von der Sedimentbeschaffenheit abhängt, ist der Winkel der inneren Reibung ϕ_k für jede Kornfraktion k. Die effektive kritische Sohlschubspannung τ_{ck}^{slp}, die den Bewegungsbeginn dieser Kornfraktion definiert, kann basierend auf einem modifizierten Ansatz von Schoklitsch bestimmt werden:

$$\tau_{ck}^{slp} = \alpha_\tau^{slp} \tau_{ck} \;\; ; \quad \alpha_\tau^{slp} = \frac{\sin\left(\phi_k \pm \beta_s\right)}{\sin \phi_k} \cos\beta_n \left(1 - \frac{\tan^2 \beta_n}{\tan^2 \phi_k}\right) \tag{2.2.8}$$

Wobei β_s und β_n die Sohlneigung in s- und n-Richtung sind. Das Vorzeichen $(+)$ ist für ansteigende und $(-)$ für abfallende Sohle. Ausgangspunkt für die Herleitung der Gleichung $(2.2.8)$ ist das Gleichgewicht zwischen mobilisierenden und stabilisierenden Kräften an einem an der Sohle liegenden Sedimentpartikel (Van Rijn, 1993).

Analog zur Modifikation der kritischen Sohlschubspannung kann auch die Geschiebetransportrate verändert werden. Auf Grundlage der Arbeit von Bagnold (1956) und Van Rijn (1993) kann eine Beziehung zwischen der Geschieberate auf einem geneigten Bett q_{bk}^{slp} und auf einem horizontalen Bett q_{bk} abgeleitet werden, die lautet:

$$q_{bk}^{slp} = \alpha_q^{slp} q_{bk} \;\; ; \quad \alpha_q^{slp} = \frac{\tan^2 \phi_k}{\cos\beta_s \left(\tan\phi_k \pm \tan\beta_s\right) \cos\beta_n \left(\tan\phi_k \pm \tan\beta_n\right)} \tag{2.2.9}$$

Ähnlich wie oben gilt das Vorzeichen $(+)$ für ansteigende Sohle und $(-)$ für abfallende Sohle. Nach Van Rijn (1993) kann der Einfluss der Sohlneigung in n-Richtung auf die Richtung des Geschiebetransports über die folgende Beziehung berücksichtigt werden:

$$\tan\alpha = c_\alpha \tan\delta \left(\frac{\theta_{ck}}{\theta_k}\right)^{0.5} \tan\beta_n \tag{2.2.10}$$

wobei θ die dimensionlose Sohlschubspannung nach Shield ist. Die Konstante c_α hängt von dem Verhältnis zwischen Korngröße und Wassertiefe ab. Für feine Sedimente wird $c_\alpha = 1.5$ verwendet.

Geschiebetransport über eine feste Sohle

In allen Geschiebeformeln hat man angenommen, dass die Sedimenttransportrate der Fähigkeit der Strömung zum Sedimenttransport entspricht. Es gibt aber die Situation, wo nicht hinreichend Sediment an der Sohle vorhanden ist. In diesem Fall ist die Sedimenttransportrate immer kleiner als die Transportkapazität der Strömung. Um die tatsächlich bewegte Sedimenttransportrate q_{bk}^{sld} zu berechnen, kann das von Struiksma (1999) vorgeschlagene Konzept verwendet werden:

$$q_{bk}^{sld} = \alpha_q^{sld} q_{bk} \;\; ; \quad \alpha_q^{sld} = \frac{z_b - z_f}{E_a}\left(2 - \frac{z_b - z_f}{E_a}\right) \tag{2.2.11}$$

wobei $E_a = z_b - z_c$ die unverminderte Dicke der Aktivschicht ist (s. Abb. 4). Solche ungesättigten Transportbedingungen treten auf, wenn die Höhe einer unerodierbaren Schicht z_f größer als die Höhe der Grundfläche der unverminderten Aktivschicht z_c ist (Eine ausführliche Definition der Aktivschicht ist im Abschnitt 2.3.2 zu finden). Um die Kontinuität des Geschiebetransports zu bewahren, soll in Sohlbereichen z.B. (A) und (B) in Abbildung 4, Beginn und Ende der Sedimentmangelbedingung, das Modell für den ungleichgewichten Sedimenttransport verwendet werden (s. Abschnitt 3.1).

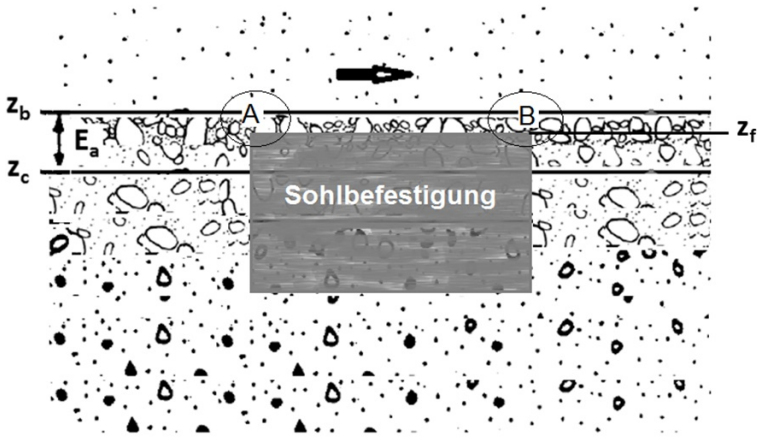

Abbildung 4 Modellkonzept für eine unerodierbare Schicht

Aktuelle Geschieberate

Als weitere Modifikation wird die theoretische effektive Transportrate für die Kornklasse k mit dem Parameter zur Zuordnung der Transportart $(1 - \gamma k)$ multipliziert (s. Gl. $(2.2.1)$), damit der Anteil der Partikel, die in Suspension geraten, abgezogen wird. Der Grund hierfür beruht auf der Tatsache, dass die Transportformeln unter Verhältnissen hergeleitet werden, bei

denen der Geschiebetransport dominiert. In einem natürlichen Gerinne können Strömungsbelastung und Korngröße über einen großen Bereich variieren, sodass die meisten Partikel sowohl als Geschiebe wie auch in suspendierter Form transportiert werden können.

$$q_{bk}^{act} = (1 - \gamma_k) \left(q_{bk}^{slp} + q_{bk}^{sld} \right) \tag{2.2.12}$$

wobei q_{bk}^{act} die aktuelle Geschieberate von der Kornklasse k ist.

2.2.4. Schwebstofftransport

Das suspendierte Sediment wird im Kontinuum alleine durch seine Konzentration beschrieben. Hierbei wird der Sedimentpartikel als passiver Skalar betrachtet. Dies bedeutet, dass eine Wechselwirkung der Partikel auf die Strömung nicht modelliert wird. Bei der Eulers-Betrachtungsebene wird der Schwebstofftransport über die Konzentrationsverteilung mit Hilfe der Konvektions-Diffusions-Gleichung beschrieben:

$$\frac{\partial c_k}{\partial t} + \frac{\partial}{\partial x_i} \left[(u_i - w_{sk}\delta_{i3})\, c_k - \frac{\nu}{\sigma} \frac{\partial c_k}{\partial x_i} \right] = 0 \tag{2.2.13}$$

wobei c_k die Volumenkonzentration von der Kornklasse k ist. Die Schmidtzahl σ stellt das Verhältnis zwischen der Diffusivität des Sediments und der kinematischen Viskosität des Wassers ν dar.

An der freien Oberfläche z_s findet kein Stoffaustausch statt und es gilt die Randbedingung:

$$w_{sk} c_k|_{z=z_s} - \frac{\nu}{\sigma} \frac{\partial c_k}{\partial z}|_{z=z_s} = 0 \tag{2.2.14}$$

Direkt an der Referenzfläche z_a, d.h. an der Grenzfläche zwischen Geschiebe- und Schwebstofftransport, wird der Vertikalgradient der Konzentration mit Hilfe der Erosionsrate S_{Ek} und Sedimentationsrate S_{Dk} bestimmt. Es gilt:

$$w_{sk} c_k|_{z=z_a} - \frac{\nu}{\sigma} \frac{\partial c_k}{\partial z}|_{z=z_a} = S_{Dk} - S_{Ek} \tag{2.2.15}$$

wobei diese Raten mit einer Einheit in Volumen pro Einheitsfläche und Zeit $(m^3/s/m^2)$ dargestellt werden.

Wendet man die Reynolds-Mittelung oder Feinstrukturfilterung auf die Konzentrationsgleichung $(2.2.13)$ an, erhält man die folgenden Gleichungen:

$$\frac{\partial \overline{c}_k}{\partial t} + \frac{\partial}{\partial x_i} \left[(\overline{u}_i - w_{sk}\delta_{i3})\, \overline{c}_k - \frac{\nu}{\sigma} \frac{\partial \overline{c}_k}{\partial x_i} + \overline{\chi}_i \right] = 0 \tag{2.2.16}$$

$$\frac{\partial \overline{\overline{c}}_k}{\partial t} + \frac{\partial}{\partial x_i} \left[(\overline{\overline{u}}_i - w_{sk}\delta_{i3})\, \overline{\overline{c}}_k - \frac{\nu}{\sigma} \frac{\partial \overline{\overline{c}}_k}{\partial x_i} + \overline{\overline{\chi}}_i \right] = 0 \tag{2.2.17}$$

wobei

$$\overline{\chi}_i = \overline{u_i c_k} - \overline{u}_i \overline{c}_k \;\; ; \quad \overline{\overline{\chi}}_i = \overline{\overline{u_i c_k}} - \overline{\overline{u}}_i \overline{\overline{c}}_k \tag{2.2.18}$$

die turbulenten Flüsse der Konzentration darstellen. Dazu nehmen wir $w_{sk} = \overline{w}_{sk} = \overline{\overline{w}}_{sk}$ an. Die turbulenten Flüsse können mit dem Wirbelviskositätskonzept modelliert werden:

$$\overline{\chi}_i = -\frac{\nu_t}{\sigma_t} \frac{\partial \overline{c}_k}{\partial x_i} \;\; ; \quad \overline{\overline{\chi}}_i = -\frac{\nu_t}{\sigma_t} \frac{\partial \overline{\overline{c}}_k}{\partial x_i} \tag{2.2.19}$$

wobei ν_t die turbulente Viskosität und σ_t die turbulente Schmidtzahl ist. Die Schwebstofftransportrate q_{sk} von der Kornfraktion k ergibt sich durch Integration von Schwebstoffflüssen zwischen der Referenzfläche z_a und der freien Oberfläche z_s:

$$q_{sik} = \int_{z_a}^{z_s} \left(u_i c_k + \frac{\nu}{\sigma} \frac{\partial c_k}{\partial x_i} \right) dz \tag{2.2.20}$$

womit $q_{sik} (i = 1, 2)$ die kartesischen horizontalen Komponente des fraktionierten Schwebstofftransports in x_i - Richtungen sind. Dabei kommt es im Wesentlichen auf das Produkt $u_i c_k$ an. Wendet man die Reynolds-Mittelung oder Feinstrukturfilterung auf die Konzentrationsgleichung $(2.2.13)$ an, ergibt sich:

$$q_{sik} \approx \int_{z_a}^{z_s} \left(\overline{u}_i \overline{c}_k \right) dz \;\; ; \quad q_{sik} \approx \int_{z_a}^{z_s} \left(\overline{\overline{u}}_i \overline{\overline{c}}_k \right) dz \tag{2.2.21}$$

Sedimentationsrate

Wird eine kritische Strömungsgeschwindigkeit unterschritten, wird der Partikel nicht mehr in Suspension weitertransportiert und lagert sich ab (Deposition bzw. Sedimentation). Mit Hilfe der Eulerschen Betrachtungsebene ist es möglich, die Konzentrationsverteilung im Strömungsgebiet und somit auch die Konzentration in Sohlnähe zu berechnen. Die Sedimentationsrate S_{Dk} wird als der abwärts advektive Fluss durch die Sinkgeschwindigkeit w_{sk}, wie folgt, bestimmt:

$$S_{Dk} = w_{sk} c_{ak} \tag{2.2.22}$$

wobei c_{ak} die aktuelle Volumenkonzentration von der Kornfraktion k an der Referenzfläche z_a darstellt.

Erosionsrate

Zur Bestimmung der Erosionsrate existieren diverse empirische Ansätze, die auf dem Partikelaufnahmekonzept (sediment-pick-up concept) basieren. Der erste Ansatz von Einstein (1950) ist stochastischer Natur. Er geht davon aus, dass nicht die mittlere Wandschubspannung die Partikel in Bewegung setzt, sondern turbulente Fluktuationen. Entsprechend ist die mittlere Wandschubspannung nicht Bestandteil seiner Gleichung. Einstein stellt sich den Se-

dimenttransport als Zusammensetzung von Einzelsprüngen der Partikel vor. Wird durch eine kurzfristige turbulente Fluktuation die Gewichtskraft eines Partikels aufgrund der dadurch entstehenden Liftkraft überwunden, setzt sich dieser Partikel in Bewegung und übt einen Sprung aus. Den Zeitanteil, für den diese Bedingung erfüllt ist, definiert Einstein als Erosionswahrscheinlichkeit.

Unter der Berücksichtigung, dass die Menge der einzutragenden Partikel von deren Verfügbarkeit in der Austauschschicht begrenzt ist, kann die Erosionsrate durch Modifikation des Konzeptes von Einstein wie folgt bestimmt werden:

$$S_{Ek} = \beta_k \alpha_E \left(\frac{\rho_s - \rho}{\rho} g d_k \right)^{0.5} P_E \tag{2.2.23}$$

wobei β_k der Volumenanteil der Kornfraktion k in der obersten Bodenschicht. α_E stellt eine Konstante dar, die mit Hilfe experimenteller Daten bestimmt wird. P_E beschreibt die Wahrscheinlichkeit, dass ein Partikel in einem bestimmten Zeitintervall erodiert wird.

Hingegen leitet Yalin (1985) seinen Ansatz zur Bestimmung der Erosionsrate aus mittleren Strömungsgrößen her. Er benutzt die kritische dimensionlose Sohlschubspannung von Shields. Wird diese überschritten, werden Partikel erodiert und führen einen Sprung aus. Die Anzahl der erodierten Partikel steigt mit der Sohlschubspannungsgeschwindigkeit. Die Erosionsrate der Kornfraktion k kann dann folgendermaßen berechnet werden:

$$S_{Ek} = \begin{cases} \beta_k \alpha_Y u_* & \text{wenn} \quad \theta_k \geq \theta_{ck} \\ 0 & \text{wenn} \quad \theta_k < \theta_{ck} \end{cases} \tag{2.2.24}$$

wobei die Konstante α_Y auch mit Hilfe experimenteller Daten bestimmt wird.

Van Rijn (1984) hat im Delft Hydraulic Laboratory mehrere Experimente mit verschiedenen Korndurchmessern des Sandes und Strömungsbedingungen durchgeführt, um die Erosionsrate empirisch zu bestimmen. Aus den Versuchen wird die Sedimentaufnahmerate wie folgt bestimmt:

$$S_{Ek} = \frac{M_k}{\rho_s A \Delta t} \tag{2.2.25}$$

wobei M_k die Masse, A die bewegungsmögliche Oberfläche und Δt die Messperiode darstellen. Bei den Auswertungen der Versuche wird analog zu der Arbeit von Einstein (1950) die dimensionslose Erosionsrate ϕ_{Pk} verwendet, die wie folgt definiert ist:

$$\phi_{Pk} = \frac{S_{Ek}}{\left(\frac{\rho_s - \rho}{\rho} g d_k \right)^{0.5}} \tag{2.2.26}$$

Nach Auswertung der Messdaten erhält man für die Erosionsrate eine sog. Pick-up Funktion, die für die Kornfraktion k berechnet wird:

$$\phi_{Pk} = 0.0003 \beta_k \left(D_k^* \right)^{0.3} \left(T_k^* \right)^{1.5} \tag{2.2.27}$$

wobei

$$D_k^* = d_k \left[\frac{g\left(\rho_s - \rho\right)}{\rho \nu^2} \right]^{\frac{1}{3}} \quad ; \quad T_k^* = \frac{\theta_k - \theta_{ck}}{\theta_k} \tag{2.2.28}$$

Yalin (1985) und van Rijn (1987) nehmen bei ihren Berechnungen an, dass die Anzahl der erodierten Partikel mit steigender Sohlschubspannungsgeschwindigkeit zunimmt. Diese Annahme ist jedoch stark simplifiziert. Alan & Kennedy (s. Yalin, 1985) beweisen mit ihren Versuchen, dass die Strömung in Sohlnähe beim Erreichen einer bestimmten Sohlschubspannungsgeschwindigkeit „voll gesättigt“ ist und die Erosionsrate gegen einen bestimmten Wert konvergiert und nicht mehr ansteigt. Diesen Beobachtungen wird nur der Ansatz von Einstein gerecht.

Der Sedimenteintrag wird durch die sohlnahe Turbulenz induziert, damit die Erosionsrate als vertikaler Diffusionsfluss dargestellt kann werden:

$$S_{Ek} = -\frac{\nu_t}{\sigma_t} \frac{\partial \overline{c}_k}{\partial z} |_{z=z_a} \tag{2.2.29}$$

oder

$$S_{Ek} = -\frac{\nu_t}{\sigma_t} \frac{\partial \overline{\overline{c}}_k}{\partial z} |_{z=z_a} \tag{2.2.30}$$

Da sowohl die turbulente Diffusivität als auch der sohlennahe Konzentrationsgradient schwierig zu bestimmen sind, haben viele Forscher z.B. Celik & Rodi (1988), Spasojevic & Holly (1994), Bui (1998) und Wu et al. (2000) vorgeschlagen, die Erosionsrate mit Hilfe von empirischen Beziehungen analog zu der Sedimentationsrate anzusetzen. Berücksichtigt man noch, dass die Menge der einzutragenden Partikel von deren Verfügbarkeit in der Aktivschicht begrenzt ist, ergibt sich

$$S_{Ek} = \beta_k w_{sk} c_{ek} \tag{2.2.31}$$

wobei c_{ek} die gleichgewichte Volumenkonzentration von der Kornfraktion k an der Referenzfläche z_a ist.

Berücksichtigt man weiterhin, dass die Menge der einzutragenden Partikel von deren Verfügbarkeit in der Aktivschicht begrenzt ist, wird die theoretische Erosionsrate mit dem Faktor α_q^{sld} (s. Gl. $(2.2.11)$) multipliziert:

$$S_{Ek}^{sld} = \alpha_q^{sld} S_{Ek} \tag{2.2.32}$$

Unter Berücksichtigung des Anteils der Partikel, die auch als Geschiebe transportieren (s. Gl. $(2.2.12)$), wird die aktuelle Erosionsrate SEk,actual von der Kornfraktion k wie folgt berechnet.

$$S_{Ek}^{act} = \gamma_k S_{Ek} \tag{2.2.33}$$

Referenzhöhe und gleichgewichte Referenzkonzentration

Eine Angabe für die gleichgewichte Konzentration c_{ek} in einem Referenzniveau z_a kann z. B. durch eine Messung gewonnen werden. I.Allg. kann man aber nicht auf Beobachtungsdaten

zurückgreifen, sondern muss sich stattdessen mit einer Schätzung von c_{ek} zufriedengeben. Für z_a gibt es in der Literatur verschiedene Vorschläge. Entweder wird von einer Proportionalität zur Wassertiefe oder zur Korngröße ausgegangen.

Einstein (1950) hat $z_a = 2d_{35}$ für die Referenzhöhe verwendet und c_{ek} aus der Geschiebetransportrate ermittelt, wobei die gemittelte Partikelgeschwindigkeit proportional zur transportwirksamen Schubspannungsgeschwindigkeit ist. Mit der Unterstützung der Grenzschichttheorie hat er in einer Schätzung der Partikelgeschwindigkeit den Zusammenhang hergeleitet. In dimensionsloser Form folgt die sog. Einstein-Referenzkonzentration:

$$c_{ek} = 0.043 \frac{\Phi_{bk}}{\sqrt{\theta_k^*}} \tag{2.2.34}$$

wobei θ_k^* der effektive Shields-Parameter ist.

Durch Bezug der Partikelgeschwindigkeit auf die ganze Schubspannungsgeschwindigkeit kann eine Modifizierung des ursprünglichen Einstein-Konzepts für die Berechnung der Referenzkonzentration hergeleitet werden (Zanke, 2013):

$$c_{ek} = \frac{\Phi_{bk}}{2\alpha_{cek}\sqrt{\theta_k^*}} \tag{2.2.35}$$

wobei α_{cek} als Einstein-Faktor bezeichnet wird. Für den Einstein-Faktor in der Verallgemeinerung die Gleichung $(2.2.35)$ ist die Aussage der originalen Gleichung $(2.2.34)$ gleichbedeutend mit

$$\alpha_{cek} = 11.63\sqrt{\mu_b} \tag{2.2.36}$$

wobei mit μ_b der Reduktionsfaktor für die transportwirksame Sohlschubspannung gemeint ist. Wird jedoch bei der Schwebstofftransportberechnung die gesamte Sohlschubspannung verwendet, wächst dem Einstein-Faktor die Aufgabe zu, das solchermaßen modifizierte Einstein-Modell an die realen Gegebenheiten anzupassen. Daher ist der α_{cek} -Wert in der folgenden Gleichung $(2.2.37)$ keine Konstante sondern von den Strömungs- und Sedimentparametern abhängig. Auf einem Vorschlag von Zanke (2013) folgend kann der Einstein-Faktor in Abhängigkeiten von $d_m/h, D_{*k}$ und θ_k bestimmt werden:

$$\alpha_{cek} = \frac{16.84\theta_k}{D_k^*\sqrt{\frac{d_m}{h}}} \tag{2.2.37}$$

Um die Sohlformeffekte zu berücksichtigen, hat Van Rijn (1984) eine Gleichung für die gleichgewichte Referenzkonzentration vorgeschlagen, dabei wird als Bezugsabstand für die Referenzkonzentration eine Bezugshöhe $z_a = z_b + k_s$ über dem Nullniveau der Sohle gewählt. k_s stellt die äquivalente Sohlrauheit dar. Als Van Rijn-Referenzkonzentration ergibt sich die folgende Gleichung:

$$c_{ek} = \frac{0.015 d_k \left(T_k^*\right)^{1.5}}{k_s \left(D_k^*\right)^3} \tag{2.2.38}$$

Tiefengemittelte Modelle

Analog zu dem Strömungsmodell entsteht die 2D Konvektions-Diffusions-Gleichung durch Integration der 3D Gleichung über die Schwebstofftransportschicht unter Zuhilfenahme der Randbedingungen $(2.2.14)$ und $(2.2.15)$ und des Integrationssatz von Leibniz. Ohne ausführliche Herleitung, die in z.B. Höttges (1992) zu finden ist, ergibt sich angenähert die tiefengemittelte Konvektion-Diffusion-Gleichung für die Schwebstoffkonzentration:

$$\frac{\partial (hC_k)}{\partial t} + \frac{\partial}{\partial x_i} \left[h \left(U_i C_k - D_{ki} \right) \right] = S_{Ek} - S_{Dk} \tag{2.2.39}$$

wobei der Index i zwischen 1 und 2 variiert und C_k die tiefengemittelte Volumenkonzentration von der Kornklasse k ist. Die von vertikalen Ungleichförmigkeiten der Geschwindigkeit und der Konzentration stammende Dispersionsterme D_{ki} können wie folgt modelliert werden:

$$D_{ki} = \frac{1}{h} \int_{z_b}^{z_s} \left[\left(u_i - U_i \right) \left(c_k - C_k \right) \right] dz = \frac{\overline{\nu_t}}{\sigma_t} \frac{\partial C_k}{\partial x_i} \tag{2.2.40}$$

wobei $\overline{\nu_t}$ die tiefengemittelte turbulente Viskosität ist.

Zur Bestimmung der Sedimentationsrate muss die Konzentration an der Referenzfläche c_{ak} aus der tiefengemittelten Konzentration C_k ermittelt werden. Dem Vorschlag von Bui (1998) folgend wird ein Koeffizient α_{cak} eingesetzt:

$$\alpha_{cak} = \frac{c_{ak}}{C_k} \tag{2.2.41}$$

der mit Hilfe der bekannten vertikalen Konzentrationsverteilung (Rouse-Profile) bei Gleichgewicht abgeschätzt werden kann:

$$\alpha_{cak} = \frac{z_s - z_a}{\int_{z_b}^{z_s} \left[\frac{(z_s - z) z_a}{z (z_s - z_a)} \right]^{\frac{w_{sk}}{\kappa u_*}} dz} \tag{2.2.42}$$

In natürlichen Gerinnen befinden sich im Allgemeinen keine Gleichgewichtsbedingungen. Lin (1984) hat deshalb eine empirische Beziehung vorgeschlagen, wobei die Nichtstationarität und Ungleichmäßigkeit der Strömungs- bzw. Schwebstoffverteilungen berücksichtigt wurden:

$$c_{ak} = \left[3.25 + 0.55 \ln \frac{w_{sk}}{\kappa u_*} \right] C_k \tag{2.2.43}$$

2.3. Sohlveränderung

Werden über ein Kontrollvolumen die ein- und ausgetragenen Sedimente bilanziert, lassen sich Erosionen und Sedimentationen bzw. Veränderungen der Kornverteilung quantifizieren. Durch Änderungen in der Sohlenlage und in der Kornzusammensetzung ändern sich auch die

Strömungen. Die veränderten Strömungen führen wiederum zu einer Umformung der Sohle. Im Sohlmaterial können unterschiedliche Fraktionen von feinem Material wie Schlamm, Sand bis zu grobem Material wie Kies oder Stein vorhanden sein. Unter der Bedingung, dass die Sohle zu 100% aus diesen Fraktionen besteht, kann die Sohlveränderung als Summe aller Änderungsraten je Fraktion angegeben werden.

$$\frac{\partial z_b}{\partial t} = \sum_{k=1}^{K} \frac{\partial z_{bk}}{\partial t} \tag{2.3.1}$$

wobei $\frac{\partial z_{bk}}{\partial t}$ der zeitliche Sohlveränderungsanteil der einzelnen Kornklassen k im Kontrollvolumen der Aktivschicht und K die Anzahl der Kornfraktionen darstellen.

2.3.1. Sohlveränderungsanteil für jede Kornfraktion

Es wird angenommen, dass der Geschiebetransport als kontinuierlicher Prozess und die Sohlveränderung als direkte Konsequenz der Massenveränderung beschrieben werden kann. Außerdem wird angenommen, dass alle Partikel einer bestimmten Kornklasse - unabhängig von ihrer Position in der Transportschicht eines Kontrollvolumen - gleich verfügbar sind. Die einfachste Überlegung zur Aufstellung einer Massenbilanz für den Sedimenttransport ist, dass in jeder Kontrollwassersäule die zeitliche Veränderung der Sohlhöhe gleich der Summe der räumlichen Veränderungen der Ein- und Austräge der Sedimentflüsse über die Seitenflächen der Wassersäule ist. Betracht man im Modell sowohl Schwebstoff- als auch Geschiebetransport und unter der weiteren Annahme der konstanten Sedimentkonzentration in der Geschiebetransportschicht, folgt eine Massenbilanzgleichung, die eine Modifikation der ursprünglichen Exner - Gleichung darstellt:

$$(1 - p_b)\,\frac{\partial z_{bk}}{\partial t} = -\left[\frac{\partial\left(q_{bsk} + q_{ssk}\right)}{\partial s} + \frac{\partial\left(q_{bnk} + q_{snk}\right)}{\partial n}\right] + S_{Lk} \tag{2.3.2}$$

Mit dem Quellterm SLk kann eine lokale Sedimentzugabe oder -entnahme spezifiziert werden. Werden über ein Kontrollvolumen in der Geschiebetransportschicht die eingetragenen und ausgetragenen Sedimente bilanziert, kann die zeitliche Änderung der volumetrischen Anteile der einzelnen Kornklassen k im Kontrollvolumen auch mit der folgenden Gleichung quantifiziert werden:

$$(1 - p_b)\,\frac{\partial z_{bk}}{\partial t} = -\left(\frac{\partial q_{bsk}}{\partial s} + \frac{\partial q_{bnk}}{\partial n}\right) + \left(S_{Dk} - S_{Ek}\right) + S_{Lk} \tag{2.3.3}$$

Wie in den herkömmlichen morphologischen Modellen, gilt für die beiden Gleichungen die Annahme, dass die Dichte des Sedimentes bzw. die Bodenporosität p_b konstant ist.

2.3.2. Kornsortierungskonzept

Durch Änderungen in der Sohlenlage kann sich die Kornzusammensetzung in der Bodenschicht verändern. Die Interaktion zwischen fraktioniertem Sedimenttransport, Sohlverände-

rungen und vertikaler Sortierung wird in numerischen Modellen meist durch sogenannte Sedimentkontinuitätsmodelle beschrieben.

Das sog. Einschichtmodell wurde zuerst von Hirano (1971) zur numerischen Simulation dieser Interaktion des fraktionierten Sedimenttransports entwickelt. Dabei wird die Sohle in eine aktive Schicht oder Transportschicht mit konstanter Dicke und eine unbewegliche Unterschicht schematisiert. Beide Schichten haben eine bestimmte Kornzusammensetzung. Außerdem tritt zwischen der Aktivschicht und der Unterschicht ein vertikaler Sedimentfluss nur bei einer Veränderung der Sohlenhöhe im Laufe der Zeit (also im Fall einer Erosion oder Deposition) auf. Die Untersuchungen z.B. von Ribberink (1987) und Armanini (1995) haben ergeben, dass dies keine Bedingung für den vertikalen Austausch von Sedimenten sein muss. Als Hauptgründe für die Entwicklung eines Zweischichtkonzeptes hat Ribberink (1987) folgendes angegeben:

- Das Laborexperiment zeigt die Existenz einer Austauschschicht zwischen der Transportschicht und dem in der Unterschicht liegenden Sediment, welches nicht durch die Strömung angegriffen wird.
- Im Fall einer Erosion, kombiniert mit einer sich nicht bewegenden Schicht aus feinerem Sediment als das transportierte Material, erhält das Einschichtmodell einen elliptischen mathematischen Charakter, dessen numerische Lösung instabil wird.
- Eine Simulation für den Nichtgleichgewichtzustand führt zu keinen befriedigenden Ergebnissen. Vor allem erfordern instationäre Fließvorgänge und Unregelmäßigkeiten der Sohle (Riffel und Dünen) ein Zweischichtkonzept.

Um diese Effekte zu berücksichtigen, wurde von Ribberink zwischen der Aktivschicht und Unterschicht eine zusätzliche Schicht platziert. Sein Zweischichtmodell wurde nur für zwei Kornfraktionen (feine und grobe) entwickelt.

Armanini (1995) wies auf das Defizit des Schichtenansatzes hin. Die diskrete Teilung der Sohle in Schichten sei eine zu starke Vereinfachung der tatsächlichen Transportprozesse. Er benutzte ein Kontinuum-Modell für die Sohle, wobei der vertikale Kornaustausch innerhalb der Sohle als Diffusionsprozess beschrieben wird. Das Modell lieferte jedoch nicht übereinstimmende Ergebnisse mit einigen Laboruntersuchungen.

Eine andere Entwicklung ist die Rahmenarbeit von Parker et al. (2000). Diese geht von der Kontinuität des Sediments ohne Unterschied in den einzelnen Bodenschichten aus. Die zugrundeliegende Idee war, dass die Erosionswahrscheinlichkeit eines Korns von der Sohlenhöhe abhängt. Es besteht ein Zusammenhang zwischen der Schwankung der Sohlenhöhe und dem Geschiebetransport. Darin sind zwar die Kontinuitätsgleichungen angegeben, jedoch bleiben die Wahrscheinlichkeitsverteilungen der Sohlzusammensetzung ungelöst. Dieser Mangel wurde von Blom (2008) und Blom et al. (2008) beseitigt. Dabei wurde ein neues Sedimentkontinuitätsmodell für die vertikale Sortierung entwickelt, das speziell auf Bedingun-

gen ausgerichtet ist, in denen Dünen dominieren. In dem Modell werden die Dünenhöhe und -länge mit einer Wahrscheinlichkeitsverteilungsfunktion bestimmt. Die Änderung der Sedimentmasse erfolgt durch die Deposition- und Erosionsrate jeder Kornfraktion. Dabei werden drei Typen von Deposition und Erosion bzw. vier Typen von Zeitskalen nämlich die Zeitskala der Dünenmigration, die Zeitskala zur Adaption der Dünendimension, die Zeitskala der vertikalen Sortierung und die Zeitskala der größeren flussmorphologischen Änderungen unterschieden. Das Modell ist aber für praktische Anwendungen sehr kompliziert und zeitaufwendig.

Basierend auf den Modellkonzepten von Holly & Odgaard (1992) und Ribberink (1987) haben Bui & Rutschmann (2010) Mehrschichtmodelle für den gemischten Boden entwickelt, die auch die Simulation der Wechselwirkung zwischen Geschiebe- und Schwebstofftransport in unterschiedlichen Fließgewässertypen allgemein ermöglichen. Hierbei kann der Untergrund in eine große Anzahl von Bodenschichten aufgeteilt werden, die jeweils eine andere Zusammensetzung haben können (Abb. 5). Auf diese Weise kann man die vertikale Schichtung des Bodens berücksichtigen und bei Erosion oder Sedimentation gehen keine Information verloren. Im Hinblick auf die alten Modelle mit nur einer großen Unterschicht ist dies eine wichtige Verbesserung.

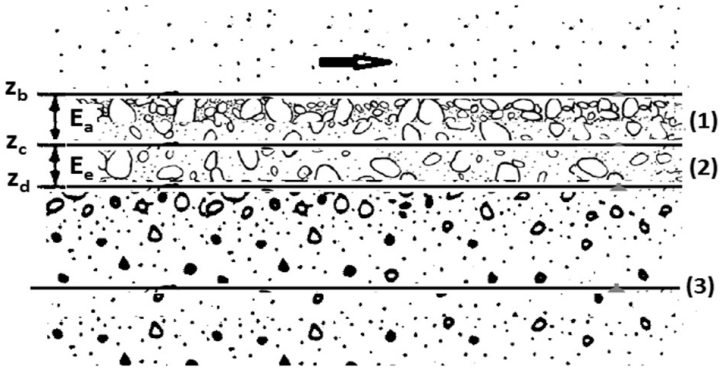

Abbildung 5 Das idealisierte physikalische System für Mehrschichtansatz für eine Sedimentsäule des Flussbettes; (1)-Aktivschicht; (2)-Austauschschicht; (3)-Unterschichten; E_a- Aktivschichtdicke; E_e-Austauschschichtdicke

Kornsortierung in der Aktivschicht

Die zeitliche Änderung der volumetrischen Anteile der einzelnen Kornklassen in einem Kontrollvolumen der Aktivschicht entspricht dem Nettofluss des Geschiebes über die Seitenflächen des Elementarvolumens sowie den Feststoffflüssen über deren Deck- bzw. Grundfläche, die in den Quelltermen ausgedrückt werden. Unter der Annahme, dass die Sedimentdichte bzw. die Bodenporosität konstant ist, kann die Massenerhaltungsgleichung für jede Kornfraktion k wie folgt angesetzt werden:

$$(1-p_b)\frac{\partial(\beta_k E_a)}{\partial t} = -\left(\frac{\partial q_{bsk}}{\partial s} + \frac{\partial q_{bnk}}{\partial n}\right) + \alpha_{DEk}(S_{Dk} - S_{Ek}) + S_{Fk} + S_{Lk} \qquad (2.3.4)$$

Mit der Konstante $0 \leq \alpha_{DEk} \leq 1$ kann das Modell den vertikalen Sedimentaustausch zwischen der Aktiv- und Austauschschicht bzw. ihre neue Kornsortierung berücksichtigen, ohne dass sich die Sohlhöhe im Laufe der Zeit verändert. Außerdem kann sich die Höhe der Grundfläche der Aktivschicht z_c mit jeder Änderung der Sohlenoberfläche verschieben. Verlagert sich die Grundfläche nach unten, wird das Material der Unterschicht, das i.Allg. aus einer anderen Kornverteilung besteht, Teil der Austauschschicht. Dieser Materialfluss kann mit dem Quellterm S_{Fk} wie folgt beschrieben werden.

$$S_{Fk} = -(1-p_b)\frac{\partial(\beta_k^* z_c)}{\partial t} = -(1-p_b)\frac{\partial}{\partial t}\left[\beta_k^*(z_b - E_a)\right] \tag{2.3.5}$$

wobei β_k^* der Volumenanteil der Kornfraktion k an der Grenzfläche z_c ist.

$$\beta_k^* = \begin{cases} \beta_k & \text{wenn} \quad \frac{\partial z_b}{\partial t} \geq 0 \\ \beta_{ek} & \text{wenn} \quad \frac{\partial z_b}{\partial t} < 0 \end{cases} \tag{2.3.6}$$

wobei β_{ek} der Volumenanteil der Kornfraktion k in der Austauschschicht ist.

Im Übrigen repräsentiert der Ausdruck $(1-p_b)E_a$ das Volumen pro Einheitsfläche aller Sedimentpartikel in der Aktivschicht. β_k bezeichnet das Verhältnis des Sedimentvolumens der Fraktion k zum Gesamtvolumen aller Feststoffe in der Aktivschicht und drückt somit die Veränderung der Sohlenoberfläche bezüglich der Anteile der verschiedenen Korngrößen aus.

Kornsortierung in der Austauschschicht

Da die Deckfläche der Austauschschicht mit der Grundfläche der Aktivschicht identisch ist, muss die Kornverteilung in der Austauschschicht numerisch angepasst werden, wenn sich die Schichtgrenze bewegt oder der Austausch zwischen Geschiebe- und Schwebstofftransport stattfindet. Analog zu der Aktivschicht kann eine Maßerhaltungsgleichung für das Kontrollvolumen der Austauschschicht beschrieben werden:

$$(1-p_b)\frac{\partial(\beta_{ek}E_e)}{\partial t} = -(1-\alpha_{DEk})(S_{Dk} - S_{Ek}) - S_{Fk} + S_{Fek} + S_{Lek} \tag{2.3.7}$$

wobei S_{Lek} die Änderungsrate der Kornfraktion k in der Austauschschicht infolge einer lokalen Sedimentzugabe oder -entnahme darstellt. Mit dem Quellterm S_{Fek} kann der Einfluss der Bewegung ihre Grundfläche z_d berücksichtigt werden.

$$S_{Fek} = -(1-p_b)\frac{\partial(\beta_{ek}^* z_d)}{\partial t} = -(1-p_b)\frac{\partial}{\partial t}\left[\beta_{ek}^*(z_c - E_e)\right] \tag{2.3.8}$$

wobei β_{ek}^* der Volumenanteil der Kornfraktion k an der Grenzfläche z_d ist.

$$\beta_{ek}^* = \begin{cases} \beta_{ek} & \text{wenn} \quad \frac{\partial z_c}{\partial t} \geq 0 \\ \beta_{fk} & \text{wenn} \quad \frac{\partial z_c}{\partial t} < 0 \end{cases} \tag{2.3.9}$$

wobei β_{fk} der Volumenanteil der Kornfraktion k in der ersten Unterschicht ist.

Kornsortierung in den Unterschichten

Unter der Annahme, dass sich alle Sedimentpartikel in den Unterschichten nicht bewegen und damit keine physikalischen Sedimentflüsse stattfinden, können sich die Kornverteilungen in diesen nicht aktiven Schichten infolge der Höheveränderung der definierten Grenzflächen verändern. Die Maßerhaltung für jede Kornfraktion k in der ersten Unterschicht kann wie folgt beschrieben werden:

$$(1-p_b)\frac{\partial\left(\beta_{fk}E_f\right)}{\partial t} = -S_{Fek} + S_{Ffk} + S_{Lfk} \tag{2.3.10}$$

wobei E_f die Dicke der ersten Unterschicht und S_{Lfk} die Änderungsrate der Kornfraktion k in der ersten Unterschicht infolge einer lokalen Sedimentzugabe oder -entnahme darstellen. Mit dem Quellterm S_{Ffk} kann der Einfluss der Bewegung ihrer Grundfläche z_e berücksichtigt werden.

$$S_{Ffk} = -(1-p_b)\frac{\partial\left(\beta^*_{fk}z_e\right)}{\partial t} = -(1-p_b)\frac{\partial}{\partial t}\left[\beta^*_{fk}\left(z_d - E_f\right)\right] \tag{2.3.11}$$

wobei β^*_{fk} der Volumenanteil der Kornfraktion k an der Grenzfläche z_e ist.

$$\beta^*_{fk} = \begin{cases} \beta_{fk} & \text{wenn} \quad \frac{\partial z_d}{\partial t} \geq 0 \\ \beta_{gk} & \text{wenn} \quad \frac{\partial z_d}{\partial t} < 0 \end{cases} \tag{2.3.12}$$

wobei β_{gk} der Volumenanteil der Kornfraktion k in der zweiten Unterschicht ist.

Analog kann man die Kornsortierungsgleichung für die anderen Unterschichten erhalten. Die Voraussetzung für die Wahl der Dicke dieser Unterschichten ist, dass das Feststoffmaterial der einzelnen Schicht durch eine uniforme Kornverteilung repräsentiert werden kann. Man postuliert also einen schichtartigen Aufbau des Untergrundes, der oft auch für natürliche Verhältnisse charakteristisch ist.

Dicke der Aktivschicht

Es wird angenommen, dass die Dicke der Aktivschicht der Tiefe entspricht, bis zu der die Sohle durch den Geschiebetransport gestört wird. Mit dieser Dicke Ea wird das Kontrollvolumen definiert, für das die Massenbilanz der einzelnen Kornklassen formuliert wird. Je nachdem, ob sich die Sohle im Erosionszustand oder in Auflandung befindet, wird die Dicke unterschiedlich bestimmt. Die Aktivschichtdicke ist ein empirischer Parameter, der von den Strömungsbedingungen, dem Sohlmaterial, sowie der Sohlverformung abhängt (Bui & Rutschmann, 2010).

Im Erosionszustand werden die Partikel an der Oberfläche der Sohle mit jenen der unmittelbar darunterliegenden Schicht durchmischt. Die Dicke der Aktivschicht wird so gewählt, dass angenommen werden darf, das Feststoffgemisch sei über die Tiefe des Kontrollvolumens homogen verteilt. Befindet sich das Gerinne in einem Auflandungszustand, wird die Sohle kaum durchmischt und das Sohlmaterial unmittelbar unter der zuletzt abgelagerten Schicht beeinflusst die Strömung nicht mehr. Das entsprechende Material müsste also aus der Aktivschicht entfernt und der darunterliegenden Schicht zugeschlagen werden. Um das Modellieren der Schichten und das Aktualisieren der Zusammensetzung einfach zu halten, wird das abgelagerte Material der Aktivschicht zugeschlagen und mit dem darin befindlichen Material voll durchmischt.

Für die Dicke der Aktivschicht gibt es in der Literatur sehr unterschiedliche Annahmen. Die meisten Ansätze für die Bestimmung der Aktivschichtdicke beziehen sich auf einen charakteristischen Korndurchmesser der Sohle. Die Aktivschichtdicke kann als Vielfaches dieser Korndurchmesser der Aktivschicht berechnet werden (Einstein, 1950; Park & Jain, 1987; Parker, 1991; Vogel et al., 1992; Armanini, 1995).

Bennet & Nordin (1977) haben vorgeschlagen, dass die Aktivschichtdicke als Funktion der Erosionsrate angesetzt wird:

$$E_a = \alpha_{Ea} \Delta z_b \tag{2.3.13}$$

wobei der Wert von Δz_b dem im aktuellen Zeitschritt erodieren Material entspricht und α_{Ea} der Proportionalitätsfaktor ist. Der Proportionalitätsfaktor wurde aufgrund von Literaturangaben zu $\alpha_{Ea} = 20$ angesetzt. Im Auflandungsfall wird zur Bestimmung der Aktivschichtdicke zum Zeitpunkt $t^{(n+1)}$ die Sohländerung zur Schichtdicke zum bekannten Zeitpunkt t^n addiert.

Da die Transportrate mit zunehmender Größe der Körner abnimmt, akkumulieren sich die gröberen Partikel an der Oberfläche der Sohle. Dieser Abpflasterungseffekt bewirkt, dass die Erosionsrate abnimmt, weil die feineren Partikel unter der Deckschicht vor Erosion geschützt sind. Strebt die Erosionsrate gegen Null oder der Sedimenttransport zu einem Gleichgewichtzustand, wird Ea nach diesem Ansatz auch zu Null. Um dies zu verhindern, haben Borah et al. (1982) folgenden Ansatz vorgeschlagen:

$$E_a = \frac{d_L}{(1 - p_b) \sum_{k=L}^{K} \beta_k} \tag{2.3.14}$$

wobei d_L der Durchmesser der kleinsten Kornfraktion ist, die nicht mehr transportiert werden kann. Darüber hinaus gilt, je grösser L ist, desto gröber das Korn. Die Aktivschichtdicke ist nach diesem Konzept proportional zur durch die Schubspannung ausgeübten Belastung an der Sohle und zur Dicke der bewegten Sedimentschicht. Bei geringen Sohlschubspannungen ist der Durchmesser der ersten unbeweglichen Sedimentklasse d_L und somit auch die Aktivschichtdicke klein. Dieser Ansatz berücksichtigt somit sowohl die effektiv wirkende als auch die zum Bewegungsbeginn notwendige Sohlschubspannung.

Gemäß dem Vorschlag von Armanini & Di Silvio (1988) wird die Aktivschichtdicke als halbe Höhe der Sohlform dynamisch berechnet. Ribberink (1997) setzt zur Untersuchung des mit der Bewegung von Dünen verbundenen Sedimenttransportes die Dicke der aktiven Schicht als die halbe Dünenhöhe an. Die Bestimmung der Sohlformhöhe kann dabei nach Van Rijn (2007) erfolgen.

Neben den o.g. Ansätzen, existieren andere Methoden, wobei die Aktivschichtdicke als eine Funktion der Sohlschubspannung und eines charakteristischen Korndurchmessers der Sohle angegeben wird (z.B. Wilcock et al., 1996; Wilcock, 1997; Wong et al., 2007).

Nach De Vries (2002) und Recking et al. (2008) können diese Formulierungen durchaus als Näherungen der natürlichen Prozesse gesehen werden. Diese Dicke nimmt mit zunehmender Belastung bis zu einem bestimmten Grenzwert zu, der nach Wilcock et al. (1996) bei $1.7d_{90}$ oder nach De Vries (2002) im Bereich zwischen $2d_{90}$ und $2.2d_{90}$ liegt. In Flüssen mit Dünen als maßgebende Bettform kann die Aktivschichtdicke durch die Höhe der größten Sohlenform, die nach Ribberink (1997) als 1.5-mal der mittleren Dünenhöhe bestimmt wird, begrenzt werden.

Es ist wichtig zu betonen, dass je kleiner der in numerischen Modellen ausgewählte Wert E_a ist, desto besser kann die simulierte Schichtung des Bodens aufgelöst werden. Ist E_a grösser als die eigentliche Schichtstärke, wird die Kornverteilung gleichsam über die Tiefe verschmiert. Damit kann unter Umständen der zeitliche Verlauf einer späteren Erosion verfälscht werden. Da die Festlegungen von E_a meist auf konzeptionellen Überlegungen beruhen und kaum durch ausführlich empirischen Untersuchungen belegt sind, ist es nötig, die Sensitivität der Aktivschichtdicke in numerischen Modellen zu untersuchen (Bui et al., 2009).

2.4. Anfangs- und Randbedingungen

Ähnlich den Integrationskonstanten für gewöhnliche Differentialgleichung fallen Funktionen bei der Integration partieller Differentialgleichung an. Eine geschlossene Lösung erhält man nur sofern diese durch zusätzliche Bedingungen bestimmbar werden. Hierbei unterscheidet man zwischen Anfangs- und Randbedingungen. Anfangsbedingungen sind Vorschriften an den Wert der zu berechnenden Feldgrößen im Ausgangszustand. Randbedingungen sind Vorschriften an den Wert dieser Variablen oder ihrer Ableitung auf dem Bereichsrand.

Die Anfangs- und Randbedingungen definieren das physikalische Problem, welches durch Lösung der Erhaltungsgleichungen bestimmt werden soll. Die Anzahl der vorzuschreibenden Bedingungen ist durch die höchste Ableitung einer unabhängigen Variablen gegeben. Ihre Aufteilung in Anfangs- und Randbedingungen wird durch den Typ der partiellen Differentialgleichungen bestimmt. Elliptische partielle Differentialgleichungen führen auf Randwertprobleme, d.h. dort sind auf allen Rändern Randbedingungen vorzuschreiben. Hyperbolische und parabolische partielle Differentialgleichungen haben reelle Charakteristiken, und somit

einen begrenzten Einflussbereich, für den auf einer nichtcharakteristischen Berandung Anfangsbedingungen vorgeschrieben werden (Anfangswertproblem). Ist der Einflussbereich zusätzlich durch Ränder begrenzt, müssen dort noch Randbedingungen vorgeschrieben werden (Anfangs-Randwertproblem).

Welche Anfangsbedingungen vorgegeben werden, beeinflusst im stationären Fall lediglich die Konvergenz, da die Lösung zeitunabhängig ist und somit die Anfangsbedingungen keinen Einfluss auf der Ausgangssituation haben. Im instationären Fall ist jedoch das Ergebnis von der gegebenen Anfangssituation abhängig.

Die Art der Randbedingungen wird durch das zu lösende physikalische Problem festgelegt. Folgende Randbedingungen sind namentlich bekannt:

- Dirichletbedingung: Der Wert der Unbekannten ist entlang des Bereichsrandes vorgegeben.
- Neumannbedingung: Die normale Ableitung der Unbekannten entlang des Randes ist vorgegeben.
- Cauchybedingung: Hiermit sind Kombinationen von Dirichlet- und Neumannbedingung gemeint.

In der hydromorphologischen Berechnung sind diese Randbedingungen den charakteristischen Berandungen zuzuordnen. Sie sind: feste Wände, Sohle, Wasseroberfläche sowie Ein- und Ausströmrand. Eine weitere Art der Ränder sind die Land-Wasser Ränder. Sie entstehen z.B. durch Trockenfallen bzw. Benetzen der einzelnen Kontrollvolumen im Berechnungsgebiet.

Wichtigste Voraussetzung für die Lösung des Problems ist die Formulierung eines sachgemäßen Problems, d.h. kleine Änderungen der Anfangs- oder Randwerte von $O(\epsilon)$ dürfen auch nur kleine Änderung der Lösung von $O(\epsilon)$ bewirken.

2.4.1. Randbedingungen

Feste Wände

Auf vertikalen festen Oberflächen gilt die sogenannte Haftbedingung nach Stokes, bei der alle Komponenten der Fließgeschwindigkeit identisch Null sind. Bei Anwendung dieser Randbedingung ist eine extrem feine, räumliche Auflösung im Bereich der Grenzschicht erforderlich, um die hier auftretenden steilen Geschwindigkeitsgradienten ausreichend genau berechnen zu können. Eine Simulation des Strömungsfeldes in der Grenzschicht bedeutet einen hohen rechnerischen Aufwand, dessen Ergebnis für die gesuchten Aussagen über das Hauptströmungsfeld von untergeordneter Bedeutung ist. Daher wird auf eine solche Simulation des wandnahen Bereichs verzichtet. Im Allgemeinen kann die Wirkung der wandnahen Strö-

mung durch den Ansatz von Randbedingungen in Form von Schubspannungen simuliert werden. Diese werden aus Wandgesetzen ermittelt, die sich durch den Wandabstand, die lokale Fließgeschwindigkeit und die Wandschubspannung beschreiben lassen. Bedingung für die Anwendung der Wandgesetze ist, dass die Randknoten des Berechnungsnetzes im Gültigkeitsbereich des logarithmischen Wandgesetzes liegen. Die Impulsgleichungen und die Transportgleichung für Turbulenzgröße bedürfen an diesen Rändern eine gesonderte numerische Behandlung. Eine andere Möglichkeit ergibt sich durch die Annahme einer Undurchlässigkeitsbedingung. Hierbei wird eine Strömung senkrecht zur Wand unterbunden. Oftmals wird der Druckgradient orthogonal zur Wand zu Null gesetzt.

Für den Schwebstofftransport wird angenommen, dass es keinen Schwebstoffffluss durch die Wand gibt und somit der Konzentrationsgradient zur Wand null ist. Für den Geschiebetransport und die Sohlveränderung nehmen wir im Modell an, dass der Geschiebetransport an diesen Rändern im Gleichgewicht ist und sich daher die Sohlhöhe bzw. Kornverteilung nicht ändert.

Einströmrand

Am Einströmrand werden die Fließgeschwindigkeiten wie auch die turbulenten Größen als Dirichletbedingung spezifiziert. Die Geschwindigkeitsverteilung über den Querschnitt kann, sofern keine Messwerte dafür vorliegen, näherungsweise der Verteilung der Wassertiefen im Querschnitt angepasst werden. Die Werte von Turbulenzgrößen werden in der Regel vereinfachend aus der Betrachtung des mittleren Strömungsgebietes mit gleichförmigem Abfluss bestimmt.

Für den Sedimenttransport und die Sohländerung werden hierbei die Dirichletbedingungen ausgewählt. D.h., die Werte der Schwebstoffkonzentration und der Geschiebefracht sowie der Sohlhöhen und der Kornverteilung, die von der jeweiligen Strömungssituation abhängen, werden vorgegeben.

Ausströmrand

Am Ausströmrand muss der Druck bzw. Wasserspiegel als Dirichletbedingung spezifiziert werden. Für die verbleibenden Strömungs- und Sedimenttransportgrößen werden hierbei Neumannbedingungen eingesetzt. Mit der Annahme, dass für diesen Rand annähernd gleichförmige Strömungs- bzw. Transportverhältnisse gelten, werden die Gradienten dieser Variablen in Randnormalenrichtung zu Null gesetzt. Im numerischen Modell werden die Werte der Geschwindigkeit, der Turbulenzgrößen, der Schwebstoffkonzentration und Geschiebefracht sowie der Sohländerung am Ausströmrand aus benachbarten Werten im Innern des Strömungsgebietes extrapoliert.

Wasseroberfläche

Die Position der freien Oberfläche ist nur zum Anfangszeitpunkt bekannt. Ihre Position zu späteren Zeitpunkten muss als Teil der Lösung bestimmt werden. Um dies zu erreichen, müssen das Raumerhaltungsgesetz und die Randbedingungen an diesem Rand verwendet werden. Die freie Oberfläche ist eine Grenze zwischen Wasser und Luft. Wenn ein Phasenwechsel an der freien Oberfläche vernachlässigt werden kann, gelten dort die folgenden Randbedingungen:

- Die kinematische Randbedingung: Sie verlangt, dass die freie Oberfläche eine scharfe Grenze zwischen dem Wasser und der Luft ohne Durchfluss ist. Dies bedeutet, dass die Komponente der Wassergeschwindigkeit in Richtung der Normalen zur freien Oberfläche gleich der Geschwindigkeit ist, mit der sich die freie Oberfläche in diese Richtung bewegt.
- Die dynamische Randbedingung: Sie verlangt, dass die Kräfte, die auf das Wasser an der freien Oberfläche wirken, im Gleichgewicht sind. Dies bedeutet, dass die normalen Kräfte auf jeder Seite der freien Oberfläche den gleichen Betrag, aber entgegengesetzte Richtungen haben, während die tangentialen Kräfte gleichen Betrag und Richtung haben. Die Implementierung dieser Randbedingungen ist nicht so einfach. Wäre die Lage der freien Oberfläche bekannt, gäbe es kein Problem. Der Massenfluss könnte dann für die Kontrollvolumenseiten, die in der freien Oberfläche liegen, gleich null gesetzt werden, und man könnte grundsätzlich die Kräfte, die auf die Kontrollvolumenseite von außen wirken, berechnen. Das Problem besteht darin, dass weder die Form noch die Lage der freien Oberfläche normalerweise im Voraus bekannt sind – sie müssen als Teil der Lösung erst bestimmt werden. Man kann deshalb nur eine der Randbedingungen an der freien Oberfläche direkt implementieren. Die andere muss zur Lokalisierung der freien Oberfläche verwendet werden. Dies muss iterativ erfolgen, was die Komplexität der Aufgabe erheblich steigert.

Unter Verwendung der kinematischen Randbedingung verbietet die freie Beweglichkeit der Wasseroberfläche die Spezifikation der vertikalen Fließgeschwindigkeit in der vertikalen Richtung als Dirichletbedingung. Daher wird der Zusammenhang der drei Komponenten der Fließgeschwindigkeit durch eine kinematische Randbedingung (Gl. $(2.1.23)$) beschrieben, die in Kombination mit der tiefenintegrierten Kontinuitätsbedingung (Gl. $(2.1.25)$) verwendet wird. An diesem Rand wird angenommen, dass kein Stoffaustausch stattfindet. Für den Schwebstofftransport gilt die Gleichung $(2.1.23)$.

Für die verbleibenden Strömungsgrößen werden Neumannbedingungen mit Nullgradienten in der vertikalen Richtung eingesetzt. Wenn Luftdruckschwankungen vernachlässigt werden können, dann ist der Wasserspiegel eine isobare Fläche und der Druck p kann dort zu Null gewählt werden.

Wasser-Land Ränder

Ein Wasser-Land Rand beschreibt die Grenze zwischen dem Strömungsgebiet und dem umliegenden trockenen Vorland, dem potentiellen Überschwemmungsgebiet. In Flachwassergebieten wie Flüssen, Seen und Küstengewässern befindet sich dieser Rand an der Grenze zu dem Ufer, wo die Wasser- und Bodenhöhe gleich sind. Im Allgemeinen variiert die Wassertiefe stetig mit oftmals hohen Gradienten am Rand. Wenn ein numerisches Gitternetz zur Modellierung des Strömungsgebietes verwendet wird, muss der Rand diskret in Abhängigkeit der Gitterlage abgebildet werden. Daher kann die Sohlhöhe nicht mehr stetig variieren und der Rand muss als eine vertikale Wand dargestellt werden.

In einigen Fällen werden diese Ränder im Voraus definiert. Für andere Fälle hängen sie vom Wasserstand im Gebiet ab, der den Uferverlauf markiert. Ein beweglicher Rand dient im Modell dazu, Strömungen zu simulieren, die eine starke Abhängigkeit der Uferlinien vom Wasserstand besitzen. Eine einfache Methode, diese beweglichen Ränder in der Berechnung zu erfassen, bietet das Prinzip der gefrorenen Zellen. Dabei wird ein Kontrollvolumen, wenn die Fließtiefe unter einen vorher definierten Wert fällt, als trocken angesehen und aus dem aktuellen Strömungsgebiet entfernt. Die Dynamik des Strömungsgebietes führt hingegen auch dazu, dass die Trockenzellen den Status ändern. Steigt der Wasserstand, wird das Strömungsgebiet durch Überflutung neuer Teilflächen vergrößert. Daher muss die Berandung angepasst werden (Bui, 1998).

An diesen Rändern wird oftmals eine Undurchlässigkeitsbedingung angenommen. Außerdem kann für die turbulente Strömung in der Regel eine Wandfunktion eingesetzt werden.

Flusssohle

Analog zur Wasseroberfläche ergibt sich die kinematische Randbedingung $(2.1.23)$ an der Referenzfläche z_a. Als Neumann-Randbedingungen werden hierbei Nullgradienten in der vertikalen Richtung für den Druck und die horizontalen Geschwindigkeiten verwendet. Für Schwebstoffkonzentration gelten die Gleichungen $(2.2.15)$ und $(2.2.22)$. Mit diesen Gleichungen ergibt sich eine Neumannbedingung für die Schwebstoffkonzentration an der Referenzfläche.

Direkt an der Sohle zb gilt die hydrostatische Verteilung für den Druck und die Haftbedingung für die Strömung.

2.4.2. Anfangsbedingungen

Die Anfangsbedingungen sind durch den Systemzustand zu Beginn einer Simulation gekennzeichnet, und zwar sowohl im Wasserkörper (z.B. Strömungs- und Sedimenttransportgröße) als auch im Flussbett (z.B. Sohlenhöhe und Kornverteilung).

Eine konsistente Anfangsbedingung für das Strömungsfeld resultiert aus der Forderung nach Kontinuität. Im einfachsten Fall können die Strömungsgeschwindigkeiten zu Null gesetzt und der Wasserspiegel mit einem konstanten Wert initialisiert werden. Mit anderen Worten wird zu Beginn der Simulation angenommen, dass das Wasser vollständig in Ruhe und ohne Sedimenttransport ist. Eine andere Möglichkeit zur Initialisierung bietet ein bekannter stationärer Strömungszustand, der die Prognose eines stationären Strömungsproblems oder der stationäre Zustand einer gemessenen Strömungssituation sein kann. In diesem Fall wird für den Sedimenttransport Gleichgewicht angenommen.

2.5. Lösungsalgorithmus für das gesamte Modellsystem

In der Realität beeinflussen sich die physikalischen Prozesse der Strömung und des Sedimenttransportes gegenseitig, da sie direkt miteinander gekoppelt sind. In der mathematischen Beschreibung sind die einzelnen Gleichungen über gemeinsame Variablen verknüpft. Je nach Art und Weise, wie die numerische Lösung dieses Gleichungssystems erfolgt, werden gekoppelte und entkoppelte Modelle unterschieden.

Bei einem gekoppelten Modell werden alle Gleichungen immer numerisch zusammengelöst. Daraus resultieren in jedem Zeitschritt neue Strömungs- und Sedimenttransportgrößen sowie eine neue Sohlenhöhe und eine neue Sohlzusammensetzung. Aufgrund ihrer Komplexität und des hohen numerischen Aufwands werden gekoppelte Modelle zur Bestimmung der Strömungs- und Sedimenttransportgrößen in Flüssen sehr selten verwendet.

Bei einem entkoppelten Modell werden in jedem Zeitschritt die Differentialgleichungen für die Strömung und für den Sedimenttransport sowie für die Sohlveränderung nach einander numerisch gelöst. Dabei werden meistens zwei Vereinfachungen für die Berechnung der Flussmorphologie eingeführt. Mit der Annahme kleiner Konzentrationen kann der Einfluss des Schwebstoffs auf die Strömung vernachlässigt werden. Die zweite Annahme ist die „Quasi-Stationär-Bedingung“: die Strömungs- und Sedimenttransportberechnung sowie die Berechnung der Sohlveränderung kann in einem Zeitschritt getrennt behandelt werden. D.h. während der Strömungsberechnung gilt die Flusssohle als ein unveränderlicher Parameter und während der Berechnung der Sohlveränderung ist das Strömungsfeld unverändert. Die Kopplung zwischen den Modellvariablen wird durch zeitliche Iterationen erreicht, wobei eine Korrektur der Strömungsgrößen und wiederum einschließend der Sohleigenschaften für den folgenden Zeitschritt erfolgt. Die Modellstruktur für eine solche numerische Simulation kann gemäß Abbildung 6 dargestellt werden. Das Gesamtmodell besteht aus drei Modulen. Das Hydrodynamikmodul berechnet die Strömungsgeschwindigkeiten sowie die Sohlschubspannungen und die Wassertiefen. Das Sedimenttransportmodul dient der Berechnung der Transportrate und der Austauschrate zwischen Geschiebe- und Schwebstofftransport. Basierend auf dem Sedimenttransport wird abschließend die Höhe- bzw. Eigenschaftsänderung der Flusssohle im Sohlveränderungsmodul berechnet .

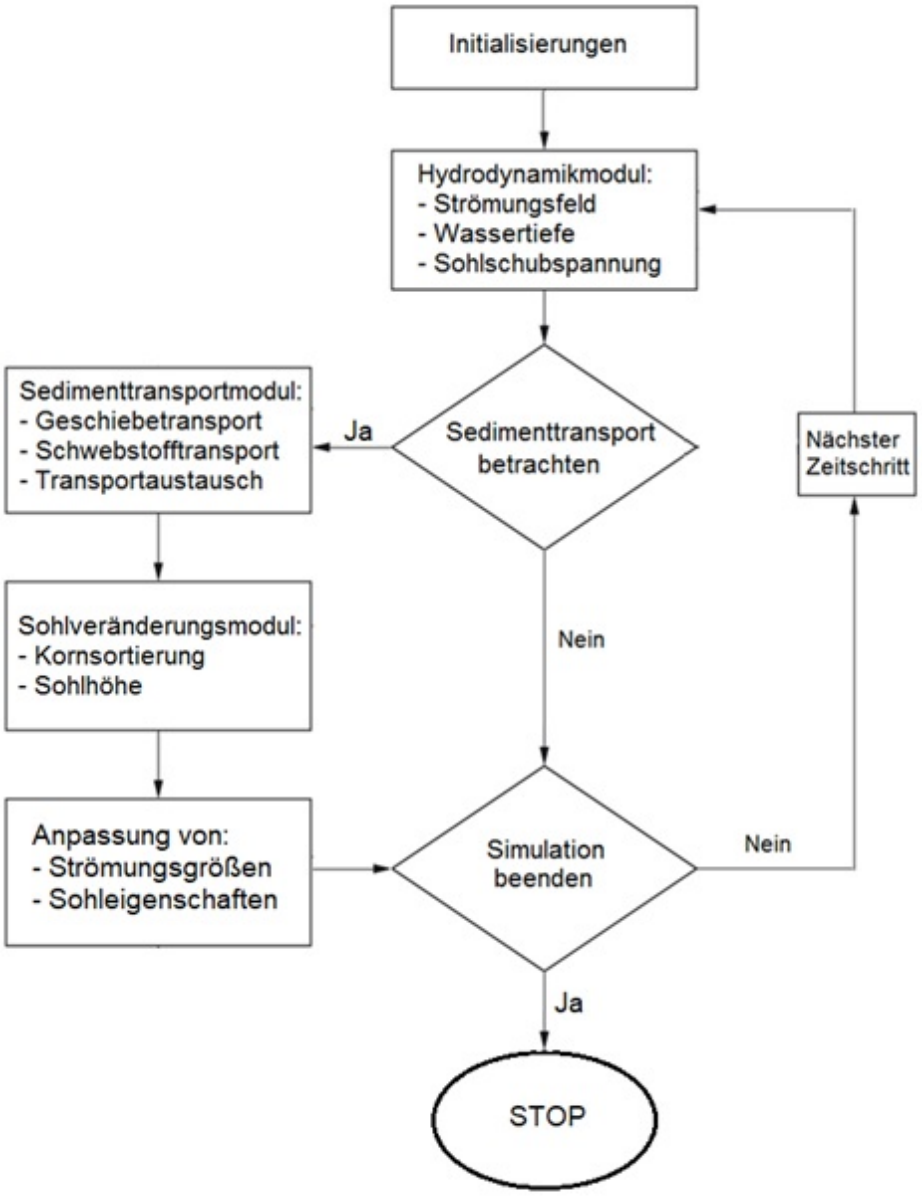

Abbildung 6 Flussdiagramm für ein entkoppeltes Lösungsverfahren

Dieses Vorgehen ist zulässig, wenn innerhalb eines betrachteten Zeitschrittes die Auswirkungen der Sedimentvariablen auf die Strömungsgrößen klein sind. Die Länge des Zeitschrittes wird durch die charakteristischen Geschwindigkeiten, mit der sich Störungen im Berechnungsgebiet ausbreiten, begrenzt. Da sich Änderungen der Strömungsvariablen um Größenordnungen schneller ausbreiten als jene der Sedimentvariablen, kann im Allgemeinen ein größerer Zeitschritt für die morphologische Berechnung ausgewählt werden.

Des Weiteren wird, um die Strömungs- und Transportprozesse in den numerischen Modellen zu beschreiben, das betrachtete Untersuchungsgebiet in einzelne Rechenzellen (Kontrollvolumen) unterteilt. Die Größe der gesuchten Variablen (Geschwindigkeit bzw. Sohlschub-

spannung, Druck bzw. Wasserstand, Konzentration der Schwebstoffe, Sohlhöhenveränderung etc.) in jedem Kontrollvolumen ergibt sich dann, indem alle Massen- und Impulsflüsse bilanziert werden. Bei der Formulierung dieser Erhaltungsgleichungen werden zusätzliche, sekundäre Unbekannte (z.B. Geschiebetrieb, Austauschrate zwischen Transportschichten, Ungleichgewichts-anpassungslänge etc.) eingeführt. Damit die Gleichungen gelöst werden können, müssen diese sekundären Unbekannten durch empirische Schließbedingungen beschrieben werden.

3. WEITERENTWICKLUNG VON MODELLEN

In Abschnitt 2.2 wurde gezeigt, dass die Strömungs- und Sedimenttransportphänomene mit einem gekoppelten System aus nichtlinearen partiellen Differentialgleichungen mit Anfangs- und Randbedingungen beschrieben werden können. Die morphologischen Gleichungen enthalten einige empirische Modelle, die meistens auf relativ einfachen Annahmen basieren. Da die Zuverlässigkeit der hydro-morphologischen Modellierung und Vorhersage stark von diesen Ansätzen abhängig ist, ist eine Modellverbesserung nötigt. Dieses Kapitel liefert Beiträge zur weiteren Entwicklung der Modelle.

3.1. Geschiebetransport bei Ungleichgewicht

Die meisten klassischen deterministischen Geschiebetransportansätze wurden auf der Grundlage des Gleichgewichtskonzepts entwickelt. Die Formeln wurden für stationäre, gleichförmige Abflussverhältnisse mit der Annahme, dass die tatsächliche örtliche Geschiebetransportrate der lokalen Geschiebetransportkapazität der Wasserströmung entspricht, abgeleitet. Unter diesen Bedingungen ist die Menge des oben zugeführten Sediments gleich groß wie die, die am Ausstromrand heraustransportiert wird. Ein Gleichgewichtszustand, bei dem vollkommen stationäre und gleichförmige Verhältnisse herrschen, existiert aber in der Natur nur in den seltensten Fällen. Es gibt jedoch solche Strömungssituationen, wo die Instationärität der Strömung sowie die Inhomogenität der Strömungs- und Sohlstruktur die Zeit- und Raumverzögerung zwischen Sedimenttransport und Wasserströmung verursachen können. Da kein Gleichgewichtssedimenttransport in diesen Strömungssituationen existiert, kann die Anwendung der Gleichgewichtsformeln zu unrealistischen Rechenergebnissen der Sohlverformung und des Strömungsfelds führen (Bui et al., 2004, 2006).

Im Folgenden wird ein am Lehrstuhl entwickelten Modell für nichtgleichgewichten fraktionierten Sedimenttransport vorgestellt.

- M.D. Bui, P. Rutschmann (2010): "Numerical modelling of non-equilibrium graded sediment transport in a curved open channel". Computers & Geosciences. Elsevier.

Computers & Geosciences 36 (2010) 792–800

Contents lists available at ScienceDirect

Computers & Geosciences

journal homepage: www.elsevier.com/locate/cageo

Numerical modelling of non-equilibrium graded sediment transport in a curved open channel

Minh Duc Bui [a,*], Peter Rutschmann [b,1]

[a] Institute of Hydraulic and Water Resources Engineering, Technische Universität München, D–82432 Obernach / Walchensee, Germany
[b] Institute of Hydraulic and Water Resources Engineering, Technische Universität München, Arcisstrasse 21, D–80333 München, Germany

ARTICLE INFO

Article history:
Received 15 March 2009
Received in revised form
23 November 2009
Accepted 2 December 2009

Keywords:
Alluvial channel
Graded sediment transport
Numerical model

ABSTRACT

The computer code FAST3D has been developed to calculate flow and sediment transport in open channels. In the code, the flow field is calculated by solving the full Reynolds-averaged Navier–Stokes equations with k–ε turbulence model; the bed-load transport is simulated with a non-equilibrium model containing an important parameter, the so-called non-equilibrium adaptation length, which characterizes the distance for sediment to adjust from a non-equilibrium state to an equilibrium state; the bed deformation is obtained from an overall mass-balance equation for sediment transport. The governing equations are solved numerically with a finite volume method on an adaptive, non-staggered grid. The former model assumed uniform bed material. In order to take into account the influence of grain-size distribution of the bed-surface on the evolution of the bed topography and consequently also on the flow field, a sediment transport module has been presently developed by the authors at the Institute of Hydraulic and Water Resources Engineering, Technische Universität München, Germany, for fractional sediment transport using a multiple layer model. This paper presents the numerical results for sediment sorting and the bed deformation in a curved alluvial channel under unsteady-flow conditions according to Yen and Lee (1995). The calculations were compared with data from laboratory measurements. Further, the sensitivity of the simulated results to the non-equilibrium adaptation length is investigated.

1. Introduction

Most of the existing bed-load models employ an empirical relation for the equilibrium transport rate, which corresponds to the transport capacity of the flow; i.e., the bed-material load discharge is equal to the sediment transport capacity of the flow. Further, sediment transport equations are equilibrium relationships based upon laboratory and field data collected under uniform flow conditions in shallow water bodies. However, for alluvial flow conditions, in which the sediment load is unable to adapt instantaneously to sharp spatial or temporal variations in the flow and the spatial-delay and/or time-delay between sediment transport and water flows are considerable, an equilibrium sediment transport does not exist and a non-equilibrium transport occurs. Thus, using equilibrium bed-load models for these flow situations may lead to unrealistic morphological predictions. It was found that the traditional equilibrium transport models need to be improved in order to take into account the non-equilibrium features of sediment transport. Tsubaki and Saito (1967) appear to be the first investigators who have applied the non-equilibrium concept to sediment transport. More details on this concept, which is used and analysed in this paper, can be found in Phillips and Sutherland (1989).

Further, an important assumption in the existing uniform sediment transport models is the uniformity of the bed material, where the sediment mixture is characterised by a single grain-size and this grain size is constant in space and in time. Applying this model to graded sediment transport may not always be adequate to simulate sediment behaviour correctly. The transport rate of the coarse size-fractions may be different from the transport rate of the fine size-fractions: depending on the hydraulic and sediment boundary conditions some particle sizes may be eroded, while others may be deposited or may be immovable. Consequently the total transport rates of all grain sizes and the bed deformation rate may differ. The pioneering research on the fractional transport rate of non-uniform sediment is attributed to Einstein (1950). After that, several investigators proposed different methods to calculate the fractional transport rate of non-uniform bed load. An overview of different approaches for graded sediment can be obtained from Van der Scheer et al. (2001). In the numerical models these equations combining with the so called multi-layer methods can be used to compute the size composition of non-uniform bed material (see Wu, 2007).

* Corresponding author. Tel: +49 8858 920350; fax: +49 8858 920333.
E-mail addresses: m.bui@bv.tum.de (M.D. Bui), p.rutschmann@bv.tum.de (P. Rutschmann).
[1] Tel.: +49 89 28923160; fax: +49 89 28923172.

0098-3004/$ - see front matter © 2010 Elsevier Ltd. All rights reserved.
doi:10.1016/j.cageo.2009.12.003

For many engineering applications 1D and 2D hydro-morphological numerical models are commonly used and adequate. Flows in channel bends and near channel training structures usually exhibit complex 3D features that significantly affect sediment transport and morphological evolution processes. For realistically predicting sediment transport in these flow situations, only a 3D model should be used.

The computer code FAST3D has been firstly developed at the Institute for Hydromechanics, University of Karlsruhe, Germany, to calculate flow and sediment transport in open channels. In the code, the flow field is calculated by solving the full Reynolds-averaged Navier–Stokes equations with k–ε turbulence model and the bed-load transport is simulated with a non-equilibrium model, for which the concept based on the stochastic bed-load description of Einstein is applied. By this concept, the rate of sediment exchange between bed and flow is assumed proportional to the difference between the actual instantaneous sediment load and the equilibrium sediment load, and related to the so-called non-equilibrium adaptation length, which characterizes the distance for sediment to adjust from a non-equilibrium state to an equilibrium state. The governing equations are solved numerically with a finite-volume method on an adaptive, non-staggered grid. The former model assumed uniform bed material (see Bui and Rodi, 2006). For graded sediment, a sediment transport module has been presently developed at the Institute of Hydraulic and Water Resources Engineering, Technische Universität München, Germany, using a multiple-layer model with the so-called size-fraction method, in which, the bed is divided into an active layer and several substrate layers and the bed material is divided into a number of size-fractions, each characterised by a certain diameter and by a volume percentage of occurrence in the bed material. As a result of computing sediment transport by size fraction and sediment exchange between the active-layer and the active-stratum one, the grain sorting process can be approached. The model can take the influence of sediment size distribution on the bed development and consequently also the flow field for account.

In the present paper, the computer model FAST3D is validated comparing the sediment sorting and the bed deformation in a curved alluvial channel under unsteady flow conditions. This experiment has been carried out in the Hydraulic Research Laboratory of the National Taiwan University (see Yen and Lee, 1995). The experimental results have shown that the morphological processes in this channel bend were essentially affected by unsteadiness of flow. Thus, grain-sorting and bed deformation were likely to be affected by non-equilibrium sediment transport. A series of numerical experiments is carried out and the calculated results are compared with data from the laboratory measurements, in order to validate the developed model and to analyse the effects of the non-equilibrium bed load on the modelling of morphological processes in the channel.

2. Model system

The model system FAST3D consists of an unsteady hydrodynamic module, a sediment-transport module and a bed-deformation module. The numerical model is uncoupled. In the computer code, these modules communicate through a quasi-steady morphodynamic time-stepping mechanism: during the flow computation the bed level is assumed constant and during the computation of the bed level the flow and sediment transport quantities are assumed invariant to the bed level changes. The modules are linked together at the programming level.

2.1. Hydrodynamic module

For calculating the flow field, we assume that the flow is not influenced by the presence of sediments. This assumption is valid in most cases, where the concentration of suspended sediment is small and the bed-load layer thin. However, the sediments may have an indirect effect on the flow in that they may form ripples and dunes and hence roughness elements that change the boundary conditions at the bed. This will be accounted for through the bed boundary conditions. With the above assumptions, the flow field is determined by the Reynolds-averaged continuity and Navier–Stokes' equations for incompressible fluid in a Cartesian coordinate system x_i ($x_1=x$, $x_2=y$, $x_3=z$), which can be written in common tensor notation form as follows:

$$\frac{\partial u_i}{\partial x_i}=0 \tag{1}$$

$$\frac{\partial u_j}{\partial t}+\frac{\partial (u_i u_j)}{\partial x_i}=-\frac{1}{\rho_w}\frac{\partial p}{\partial x_j}+\frac{1}{\rho_w}\frac{\partial \tau_{ij}}{\partial x_i}+F_j \tag{2}$$

where t is time; u_j ($j=1, 2, 3$) are the velocity components; F_j is the gravity force per unit volume; ρ_w is fluid density; and p is pressure. The turbulent stresses τ_{ij} are calculated with the k–ε turbulence model (Rodi, 1993), which employs the eddy viscosity relation

$$\tau_{ij}=\rho_w \nu_t\left(\frac{\partial u_i}{\partial x_j}+\frac{\partial u_j}{\partial x_i}\right)-\frac{2}{3}\delta_{ij}k \quad \text{with} \quad \nu_t=c_\mu\frac{k^2}{\varepsilon} \tag{3}$$

where δ_{ij} is the Kronecker symbol with $j=3$ indicating the vertical direction; the turbulent kinetic energy k and its dissipation rate ε determining the eddy viscosity ν_t are obtained from the following model equations:

$$\frac{\partial k}{\partial t}+\frac{\partial (u_j k)}{\partial x_j}=\frac{\partial}{\partial x_j}\left(\frac{\nu_t}{\sigma_k}\frac{\partial k}{\partial x_j}\right)+G-\varepsilon \tag{4}$$

$$\frac{\partial \varepsilon}{\partial t}+\frac{\partial (u_j \varepsilon)}{\partial x_j}=\frac{\partial}{\partial x_j}\left(\frac{\nu_t}{\sigma_\varepsilon}\frac{\partial \varepsilon}{\partial x_j}\right)+(c_{\varepsilon 1}G-c_{\varepsilon 2}\varepsilon)\frac{\varepsilon}{k} \tag{5}$$

$$G=\nu_t\left(\frac{\partial u_i}{\partial x_j}+\frac{\partial u_j}{\partial x_i}\right)\frac{\partial u_i}{\partial x_j} \tag{6}$$

Here G is the production of k. The standard values of the model coefficients are used: $c_\mu=0.09$, $c_{\varepsilon 1}=1.44$, $c_{\varepsilon 1}=1.92$, $\sigma_k=1.0$, and $\sigma_\varepsilon=1.3$.

The water surface elevation is calculated from a 2D Poisson equation for the surface height as described in detail in Wu et al. (2000).

2.2. Sediment-transport module

In the sediment transport module the so-called size-fraction method has been used, where the bed material is divided into a number of size-fractions, each characterised by a certain diameter and by a volume percentage of occurrence in the bed material (probability β_j). For graded bed material the sediment-transport rates depend on the bed-material composition, which itself depends on the history of erosion and deposition rates.

Changes in the bed composition are not only restricted to a layer, that is to the material exposed to the flow, but that a finer sub-layer also forms under the coarser surface layer. To reproduce these features, multi-layer models have been proposed. In the multi-layer model the bed is divided into an active layer and several substrate layers (see Fig. 1). The active layer and the first substrate layer (active stratum) constitute the so-called mixing layer. Sediment particles are continuously exchanged between flow and the active layer. Sediment particles are exchanged

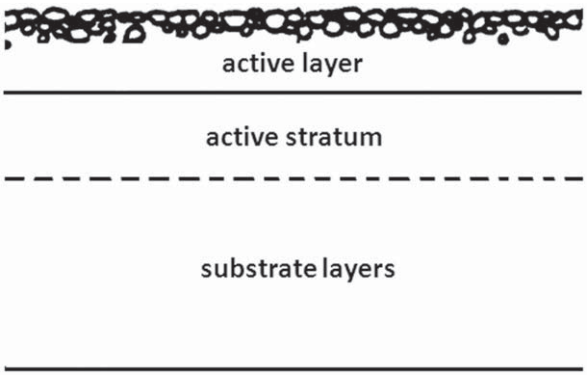

Fig. 1. Multiple-layer approximation of graded sediment transport.

between active layer and substrate when the bed scours or fills. As erosion occurs, entrainment of sediment particles from the active layer and its ensuing downward displacement causes particles from substrate layers to be mixed with those in the active layer. On the contrary, deposition of sediment particles on the bed leads to an upward displacement of the active layer and the initiation of new substrate layers.

In principle, the bed topography in a channel is related to the transport of both bed load and suspended load. In case of coarse-material bed, the influence of suspended load is relatively minor, whereas the bed load plays a major role. In the present study only the bed load is considered.

The total bed load rate, Q_b for graded sediment is computed using the formula

$$Q_b = \sum_{j=1}^{N} Q_{b,j} \tag{7}$$

where N=number of size classes; and $Q_{b,j}$=capacity for each size fraction. In the code $Q_{b,j}$ for a particular fraction of graded sediment is computed by using the well-known bed load functions with some modifications accounting for the so-called non-equilibrium, gravity and hiding/exposure effects.

2.2.1. Non-equilibrium bed load

Based upon the stochastic bed-load description of Einstein (1950); Tsubaki and Saito (1967) appear to be the first investigators who have applied the non-equilibrium concept to sediment transport (see Phillips and Sutherland, 1989). The rate of sediment exchange between bed and flow was assumed proportional to the difference between the actual instantaneous sediment load and the equilibrium sediment load, and related to the so-called non-equilibrium adaptation length, which characterizes the distance for sediment to adjust from a non-equilibrium state to an equilibrium state. Several investigators have already used this concept for non-equilibrium sediment transport modelling but have assigned significantly differing values for the adaptation length parameter and different bases for choosing these values (see Armanini and Di Silvio, 1988; Thuc, 1991; Wu, et al., 2004). Employing this concept and extending the one-dimensional non-equilibrium bed-load transport equation of Thuc (1991) to two dimensions yields

$$\frac{\partial \alpha_{bs} Q_{b,j}}{\partial s} + \frac{\partial \alpha_{bn} Q_{b,j}}{\partial n} = -\frac{1}{L_s}(Q_{b,j} - Q_{e,j}) \tag{8}$$

where α_{bs} ,α_{bn} are direction cosines determining the components of the bed-load transport $Q_{b,j}$ in the s and n direction, respectively; s is the main-flow direction along the longitudinal grid lines and the cross-flow direction n is perpendicular to this. This is the mass-balance equation for bed-load sediment transport in which all non-equilibrium effects are expressed through the model on the right hand side, assuming the effects to be proportional to the difference between non-equilibrium bed-load $Q_{b,j}$ and equilibrium bed-load $Q_{e,j}$ and related to the non-equilibrium adaptation-length L_s. Both $Q_{e,j}$ and L_s are determined from empirical formulae.

Generally, the non-equilibrium adaptation length L_s is related to the dimensions of sediment movements, bed forms, and channel geometry. In Bell and Sutherland's (1983) experiment of channel degradation due to clear water, the sediment transport was significantly influenced by the scouring hole of the bed that developed with time, advancing downstream from the inlet. They proposed that the adaptation length is related to the magnitude of the scouring hole and in turn is a function of time. If there are only ripples on the bed, which usually occur in experimental cases, the non-equilibrium adaptation length for bed load may take the value of the average saltation step length of particles or the length of ripples. Phillips and Sutherland (1989) proposed another equation for the average saltation step length

$$L_s = \alpha_p(\theta_j - \theta_{cr})d_{50,j} \tag{9}$$

where α_p=constant (as suggested by these authors, in the present paper the value of α_p=4000 was chosen). The average saltation step length of particles L_s can also be calculated from an empirical formula of van Rijn (1987)

$$\begin{aligned} &L_s = 3d_{50,j}D_*^{0.6}T^{0.9};\ D_* = d_{50,j}\left[\frac{(\rho_s-\rho_w)g}{\rho_w \nu^2}\right]^{1/3} \\ &T = \frac{(U'_*)^2-(U_{*cr})^2}{(U_{*cr})^2};\ U'_* = \frac{Ug^{1/2}}{C'};\ C' = 18\log\left(\frac{12h}{3d_{90,j}}\right) \end{aligned} \tag{10}$$

where $d_{50,j}$, $d_{90,j}$=fractional grain sizes; g=gravitational acceleration ; ν=kinematic molecular viscosity and ρ_s=density of sediment. If sand dunes are the dominant bed form, L_s may be taken as the length of sand dunes. Based on a large number of reliable flume and field data, Van Rijn (1987) has proposed the following expression for the bed-form length:

$$L_s = 7.3h \tag{11}$$

where h=water depth. Eq. (11) indicates that the dune length is related only to the mean flow depth. This has also been reported by Yalin (1972).

As mentioned above, different researchers have applied rather different values for the non-equilibrium adaptation length L_s. Thuc (1991); Bui (1998); Wu et al. (2000) used the length of sand ripples on the bed as the value of the non-equilibrium adaptation length. Rahuel et al. (1989) and Fang (2000) adopted much larger values for L_s, such as the numerical mesh size or twice that size. Wu et al. (2004) chose the length of sand dunes as the value for the non-equilibrium adaptation length. One reason for the disparity is that L_s is closely related to the dimensions of the studied sediment movements, bed forms, and channel geometry, which are usually markedly different in laboratory and field situations. In laboratory experiments, sediment transport processes occur at small scales with small bed-forms such as sand saltation with ripples and dunes, while in natural streams, sediment transport processes occur usually at larger scales and with longer periods. Another reason for the adoption of different values is that L_s is an important parameter for numerical stability. In this paper the Eqs. (9), (10) and (11) are used to test the effect of the non-equilibrium adaptation length L_s on the simulated results.

2.2.2. Hiding/exposure effect

In the processes of graded sediment movement, the coarser particles on the bed have a higher chance of exposure to the flow.

The situation is reversed for the fine particles on the bed due to the fact that they are more likely sheltered by coarse particles. This effect is called hiding/exposure effect. These effects result in a smaller critical bed shear stress for larger grains and a higher critical bed shear stress for smaller grains. Until now, most of the studies on graded sediment transport are based on introducing some kind of correction factors to account for this hiding/exposure effect and use these factors to modify the existing formulas of uniform sediment transport. Mostly they are based on experimental results. The hiding/exposure factors not only correct the critical bed shear stress but may take also some other effects of gradation into account. In this paper the hiding/exposure factor (ξ_j) is computed by using the following function proposed by Karim and Kennedy, Holly et al. and others (see Holly and Odgaard, 1992):

$$Q_{e,j}^{(1)} = \beta_j \xi_j Q_{e,j}^{(0)}; \quad \xi_j = \left(\frac{d_{m,j}}{d_M}\right)^{\alpha}; \quad \alpha = 0 \div 1 \tag{12}$$

in which d_M=mean grain size of the active layer; $d_{m,j}$=mean grain size of j-fraction; $Q_{e,j}^{(0)}$=equilibrium bed-load rate with hiding/exposure effect.

For the calculation of the bed-shear driven resultant bed-load $Q_{e,j}^{(0)}$ various well-known empirical transport formulae e. g. van Rijn, Meyer-Peter Müller, Shields, Kalinske Frijlink, Fukuoka can be used (see Bui, 1998). In this paper the formula of Meyer-Peter Mueller (1948) is applied

$$Q_{e,j}^{(0)} = 8\left[\left(\frac{C}{C_{90,j}}\right)^{3/2}\theta_j - \theta_{cr}\right]^{3/2}\left(\frac{\rho_s}{\rho_w} g d_{m,j}^3\right)^{-1/2}; \quad \theta_{cr} = 0.047 \tag{13}$$

in which C=Chézy friction coefficient; $C_{90,j}$=grain related Chézy value; θ_j=fractional Shields parameter; θ_{cr}=critical Shields value.

2.2.3. Gravity effect

Accounting for the down-slope gravitational effect on the magnitude of the transport by the multiplication factor in brackets in Eq. (14) there follows for the equilibrium bed-load transport in the main-flow direction:

$$Q_{es,j} = Q_{e,j}^{(1)}\left(\cos\delta - \beta_1 \frac{\partial z_b}{\partial s}\right) \tag{14}$$

The equilibrium bed-load transport in the cross-stream direction, Q_{en} , is calculated from a relation developed at Delft Hydraulics (see Sekine et al., 1992):

$$Q_{en,j} = Q_{e,j}^{(1)}\left(\sin\delta - \frac{(\rho_s - \rho_w) g d_{m,j}}{\beta_2 U_*^2 \rho_w}\frac{\partial z_b}{\partial n}\right) \tag{15}$$

in which β_1, β_2=dimensionless coefficients of order one (a value of 1 was chosen in all calculations); U^*=bed shear velocity; and δ=angle between the direction of bed shear stress and main-flow direction. The first term on the right-hand sides of Eqs. (14) and (15) is due to the bed-shear stress and the second term expresses the effect of gravity on particles on sloped beds. $Q_{e,j}$ is composed of its components $Q_{es,j}$ and Q_{en} by $Q_{e,j}=(Q_{es,j}^2+Q_{en,j}^2)^{1/2}$. Assuming that the direction of non-equilibrium bed-load coincides with the direction of equilibrium bed load, the direction cosines in Eq. (8) are then calculated from $\alpha_{bs}=Q_{es,j}/Q_{e,j}$ and $\alpha_{bn}=Q_{en,j}/Q_{e,j}$.

2.3. Bed-deformation module

In this module the bed-level change due to the j-th fraction of sediment ($\partial Z_{b,j}/\partial t$) is calculated from the mass-balance equation

$$(1-P)\frac{\partial Z_{b,j}}{\partial t} + \nabla \vec{Q}_{b,j} = 0 \tag{16}$$

where P=porosity of the bed material; and $\vec{Q}_{b,i}$=fractional bed load flux. The total bed deformation ($\partial Z_b/\partial t$) is then determined by

$$\frac{\partial Z_b}{\partial t} = \sum_{j=1}^{N}\frac{\partial Z_{b,j}}{\partial t} \tag{17}$$

The key concept of multiple-layer modelling is that of a mixing layer, where the flow picks up the sediment to be transported and receives the sediment that the flow is unable to transport. The active-layer can be reduced into finite elemental volumes of thickness E_m. The mass conservation for a size class j of particles in the active-layer volume is then

$$(1-P)\frac{\partial(\beta_j E_m)}{\partial t} + \nabla \vec{Q}_{b,j} - S_{F,j} = 0 \tag{18}$$

where $S_{F,j}$=active-layer floor source term, which represents the exchange of sediment particles between the active-layer and the active-stratum control volumes due to active-layer floor movement.

The mass of a particular size class j in the active-stratum control volume may change only due to active-layer movement, i.e. due to exchange of material between the active-layer and active-stratum. This is expressed by a mass conservation equation for a particular size class in the active-stratum control volume

$$(1-P)\frac{\partial[\beta_{s,j}(Z_b - E_m)]}{\partial t} + S_{F,j} = 0 \tag{19}$$

where $\beta_{s,j}$=active-stratum size fraction j; Z_b=bed elevation; (Z_b-E_m)=active-layer floor elevation, i.e. active-stratum ceiling.

The active-layer floor source term $S_{F,j}$, again specific to the size class j, can be expressed using Eq. (19). When the active-layer floor descends, then

$$S_{F,j} \approx (P-1)\beta_{s,j}\frac{\partial(Z_b - E_m)}{\partial t} \tag{20}$$

gives the mass of the size class j, formerly comprising size fraction $\beta_{s,j}$ of the active-stratum control volume, which becomes part of the active-layer elemental volume. When the active-layer floor rises, then

$$S_{F,j} \approx (P-1)\beta_{sj}\frac{\partial(Z_b - E_m)}{\partial t} \tag{21}$$

gives the mass of the size class j, formerly comprising size fraction β_j of the active-layer elemental volume, which becomes part of the active-stratum control volume.

The active-layer thickness E_m is evaluated by an appropriate empirical concept of the depth of bed material which supplies material for bed load transport and suspended-sediment entrainment. Usually the active-layer thickness is related to the flow and sediment conditions, as well as the instantaneous bed deformation. Researchers have considered the active-layer thickness to be a function of dune height or water depth, e.g. Armanini and Di Silvio (1988); Rahuel et al. (1989); Langendoen and Simon (2000) or grain size, eg. Borah et al. (1982); Van Niekerk et al. (1992); Cui et al. (1996), or model time scale, e.g. Rahuel et al. (1989); Langendoen and Simon (2000). Throughout the last decades many new formulas to calculate the active-layer thickness have been proposed. However, all formulas were derived in a different way and a definition of the active-layer thickness based on physical processes in this layer has not been given yet. In the FAST3D model, the active layer thickness is assumed to be either constant or maximal value of the bed deformation at the current time step and the mean grain size of the active layer.

2.4. Numerical solution procedure

The equations for the mean flow (1–2) and the turbulence model (4–5) given above in Cartesian coordinates are transformed to generalized curvilinear coordinates, but the velocity components u_i remain in the Cartesian coordinate system. The transformed equations can be written in conservative form in generalized curvilinear coordinates as follows:

$$J\frac{\partial \phi}{\partial t}+\frac{\partial}{\partial y_i}(C_i\phi+D_{i\phi})=JS_\phi;\quad i=1,2,3 \tag{22}$$

The Jacobean J describes the transformation between the general coordinate system y_i and the Cartesian system x_i. For the different dependent variables ϕ , the terms C_i and $D_{i\phi}$ relate to convection and diffusion, respectively. S_ϕ is the source term for the variable ϕ. The detailed expressions for these terms can be found in Zhu (1992).

The equations for non-equilibrium bed load (8) and bed change (16) are written in 2D curvilinear coordinates and have the same form as Eq. (22) with $i=1, 2$. (see Bui, 1998).

The above equations are solved numerically with a special version of the computer code FAST3D for free surface flow and sediment transport. In this code, the equations are discretized in the computational domain using the finite-volume technique with a curvilinear non-orthogonal grid and a non-staggered variable arrangement. The second-order bounded HLPA differencing scheme is employed in treating the convective and diffusive fluxes (Zhu, 1992). In order to avoid checkerboard splitting for the cell-centered arrangement, the momentum interpolation technique of Rhie and Chow (see Zhu, 1992) is used for evaluating cell-face variables from centered quantities. The strongly implicit procedure of Stone is applied for solving the system of algebraic difference equations. More details on the numerical solution procedure can be obtained from Zhu (1992); Wu et al. (2000), and Bui (1998).

3. Calculation results

Experiments were conducted in the Hydraulic Research Laboratory of the National Taiwan University to study bed topography and transverse sediment sorting in an alluvial channel bend under unsteady-flow conditions with non-uniform sediment, Yen and Lee (1995). The 180° channel bend had a rectangular cross-section with a radius of 4.0 m and a width of 1.0 m. The bend was connected to a stilling basin, an upstream straight reach of 11.5 m, a downstream straight reach of the same length, and a sediment settling tank. A layer of sand mixture around 20 cm thick, with median grain size of $d_{50}=1$ mm and initial standard deviation of sediment size gradation of $\sigma_0=2.5$ was placed on the bed at the start of the experiment. Sand mixture was sorted into eight sizes with different average size-fractions showed in Table 1, then used to compose a desired size gradation (see Fig. 2). The initial bed was flat with a slope of 0.2%. The water depth was controlled by a weir at the downstream end to produce roughly uniform flow along the bend with a base flow-discharge of 0.02 m^3/s and a base flow depth (h_0) of 5.44 cm. After this initial phase the flow was run at the several discharges with different unsteadiness characteristics. No sediment was supplied from upstream. Measurements of bed elevation were made at the end of the experiment.

Table 1
Representative size classes of initial bed material.

Size class	1	2	3	4	5	6	7	8
Grain size d_j (mm)	8.52	4.76	3.36	2.00	1.19	0.84	0.42	0.25
Fraction (%)	5.0	5.0	14.0	18.0	18.0	25.0	10.0	5.0

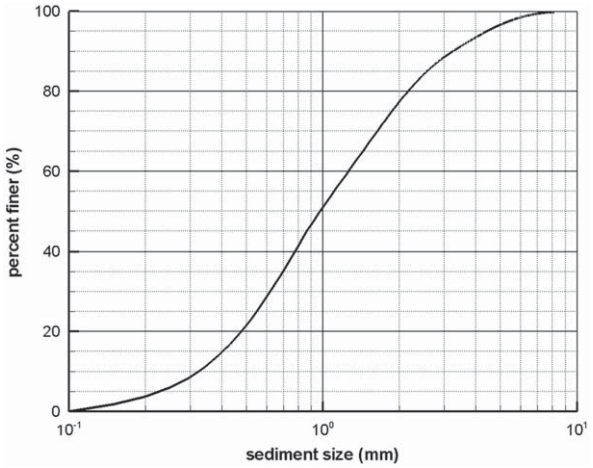

Fig. 2. Initial sediment size gradation curve.

The experimental results have shown that the morphological processes were essentially affected by unsteadiness of flow. Thus, grain-sorting and bed deformation were likely to be affected by non-equilibrium sediment transport.

A numerical grid system of 154 grid points in the longitudinal direction, 23 grid points in the transverse direction and 9 points in the water-depth direction was used. For the simulations in the numerical model the procedure of the flume experiment mentioned above was adapted, i.e. the sediment transport simulation started after reaching steady and nearly uniform flow conditions at the base flow-discharge of 0.02 m^3/s. The development of the flow, grain-sorting and bed form was calculated for two hydrographs with different unsteadiness characteristics (see Fig. 3).

Indeed, the computer model FAST2D with graded sediment transport module was applied in an earlier study (see Bui and Rutschmann, 2005) to calculate the bed deformation in this curved channel under the flow condition with moderate unsteadiness characteristic (Exp.4). In this application, the secondary flow transport effects were taken into account by adjusting the dimensionless diffusivity coefficient in the depth-averaged version of the k–ε turbulence model. A quasi-3D flow approach assuming a logarithmic velocity distribution was used to simulate the effect of secondary flows due to channel curvature on bed-load transport. Analysing the calculated results showed that the hiding/exposure factor and the active layer thickness can be used as parameters for model calibration. By adjusting the two above mentioned parameters in the graded sediment model the following selection of parameters was obtained: hiding/exposure factor formula (Eq. (12)) with $\alpha=0.5$ and active layer thickness E_m with constant value of 2.5 cm. In general the agreement between the measurements and the predicted results was found to be satisfactory. These values of the two above mentioned parameters are used again in the following 3D computations.

For the present study the fully three-dimensional model FAST3D with standard wall-function is used to calculate the resultant shear stress at the side walls. For calculation of the shear stress at the channel bed, the standard wall-function with the roughness function proposed by Cebeci and Bradshaw (1977) is applied (see Wu et al., 2000). This roughness function contains the roughness Reynolds number, which in turn is related to the equivalent roughness height (or resistance coefficient) of the channel bed. The equivalent roughness height k_s quantifies the

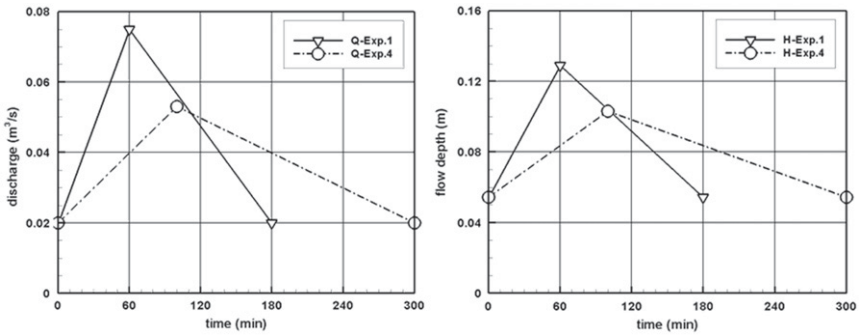

Fig. 3. Hydrograph of experiments.

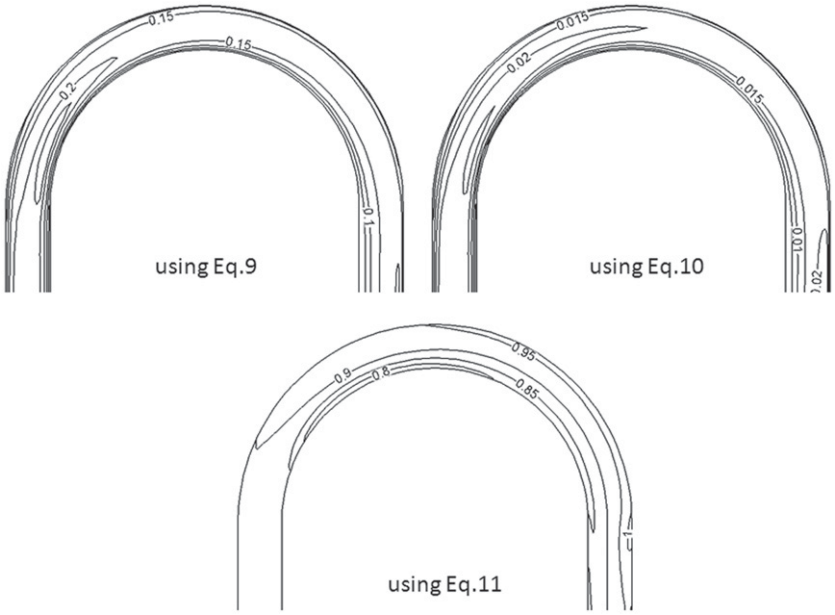

Fig. 4. Computed distribution of non-equilibrium adaptation length at peak of hydrograph of Exp.1.

influence of roughness elements such as bed materials and bed forms. For smooth beds, $k_s=0$. For flat beds in laboratory experiments, k_s is usually set to the median diameter d_{50} of the bed material because there is only sand-grain roughness on the bed. For flat beds in real rivers, k_s should theoretically also be about d_{50}, but in practice usually somewhat higher values are adopted (e.g., $3d_{90}$ by van Rijn, 1987). The hydraulic roughness of a movable bed surface with bed forms should be caused by grain roughness and by form roughness.

In the model, we used the bed roughness to calibrate the flow model. The qualitative observations in the laboratory have shown that at the base flow discharge 0.02 m^3/s no sediment transport occurred and the flow was roughly uniform along the bend. The calculations were made first for this base flow discharge. The values of the equivalent roughness height k_s of a flat bed were adjusted in order to get good agreement between the numerical results and qualitative observations. Here the value $k_s=3.5d_M$ was selected. In the following morphological calculations a modification of the linear approach proposed by van Rijn (1987) is used for specifying the resistance coefficient, where the equivalent roughness height is the sum of grain roughness and bed-form roughness. The equilibrium grain roughness is related to the d_M of the bed material and has the selected value. The mean grain size of the bed material is estimated in each time step. Following Van Rijn (1987), the dimensions and the equivalent roughness of bed forms in the dune and plane bed regimes are expressed by simple functions of the resulting dune-height and dune-length, which can be calculated from empirical expressions of a dimensionless transport stage parameter and a particle parameter.

Further, a series of calculations was carried out using different approaches of non-equilibrium adaptation length. Fig. 4 presents the calculated distributions of non-equilibrium adaptation length L_s due to various prescription methods in the channel at the peak of hydrograph ($T=60$ min) for the case with strong unsteadiness characteristics (Exp.1). The numbers on the contour lines indicate L_s values in m. It can be seen, rather different values for L_s result from the different methods. Assuming L_s to take on a value of the average saltation step length of particles, the maximum values of $L_s=0.23$ m and $L_s=0.03$ m are obtained with Eqs. (9) and (10) respectively in the domain with maximal bed shear stress (between sections 30° and 40°). Assuming the non-equilibrium adaptation length to take on the length of bed-forms (Eq. (11)), the maximum value is $L_s=1.01$ m in the area with maximal water depth.

Fig. 5 shows the calculated distributions of the bed deformation along the channel at the end of Exp.1 ($T=180$ min). The numbers on the contour lines indicate ratios of final bed change ΔZ_b to initial base flow depth h_0. It was found that in the case of omitting the non-equilibrium approach (Eq. (8)), numerous ripples form on the bed in the area between sections 70° and 105° and in the area at the exit from the bend. This calculated bed form is not qualitatively similar to that observed in

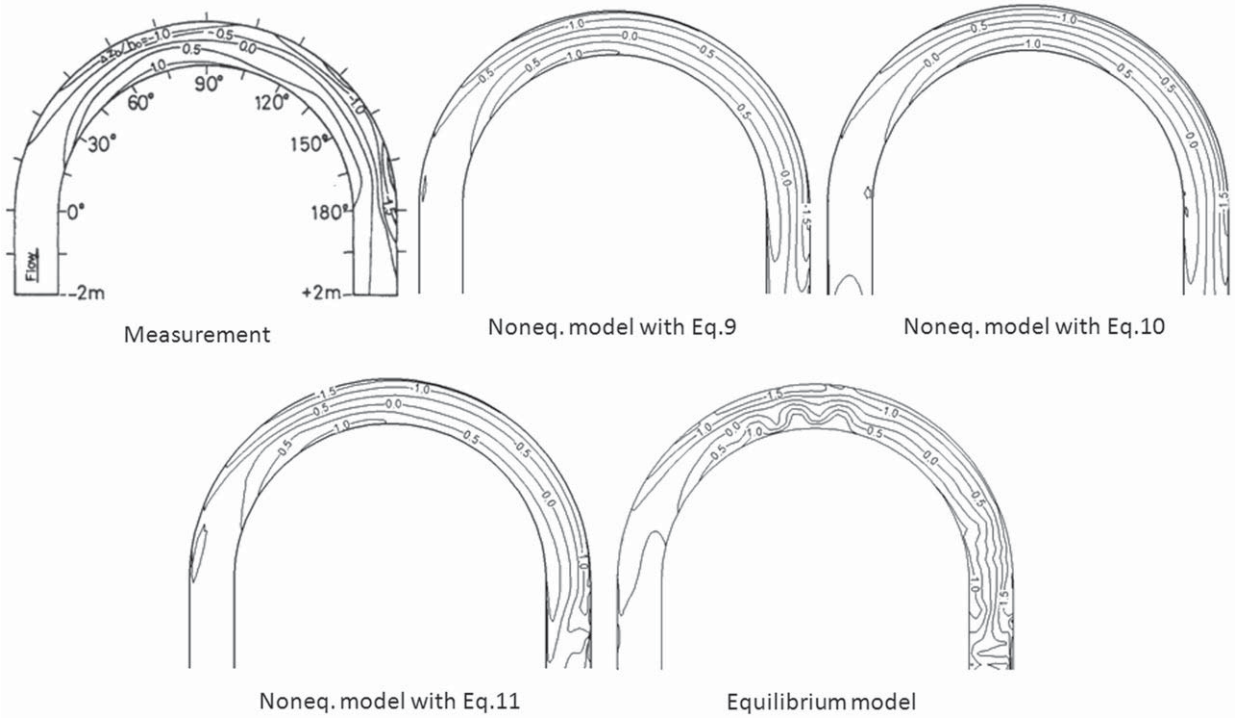

Fig. 5. Computed and measured contours of bed deformation at end of Exp.1.

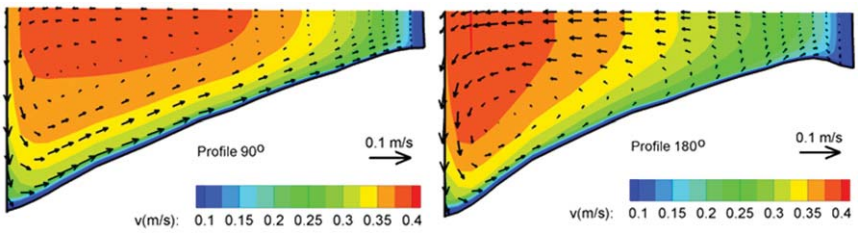

Fig. 6. Predicted contours of streamwise velocity and vectors of secondary flow at profiles 90° and 180° at end of Exp.1.

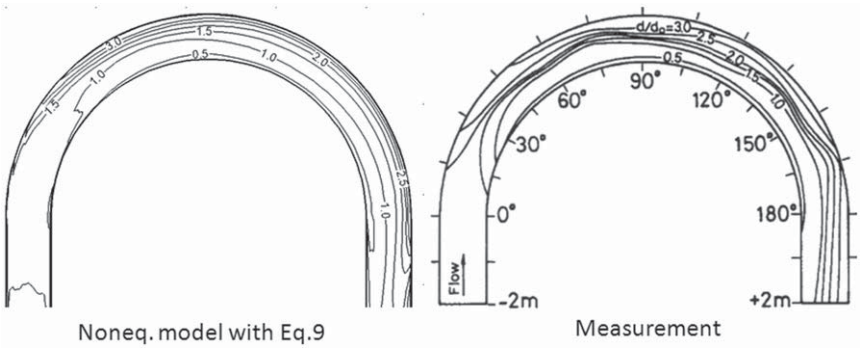

Fig. 7. Predicted and measured contours of median grain size at end of Exp.1.

the laboratory at the end of the experiment. Further, this bed form caused an amplification of the resulting errors in the computed velocity field, bed load rate, and bed elevation, which could lead to divergence of the computations, thus indicating some interrelation between modelling and numerical effects. Using the non-equilibrium approach (Eq. (8)) with different formula for adaptation length L_s, qualitatively better results were obtained. In this case, the most conspicuous features of the bed topography in the fluvial curved channel bend were achieved. They are the point bar along the inner bank and the accompanying relatively deep scour hole along the outer bank. With the non-equilibrium adaptation length formula proposed by Phillips and Sutherland (Eq. (9)), the calculated results agree best with the measurements, so that the further calculations were carried out only with this formula.

In curved channels, the secondary currents are produced from the lateral gradients in pressure and bed form. Further, there will be some interaction or coupling of these two mechanisms. Fig. 6

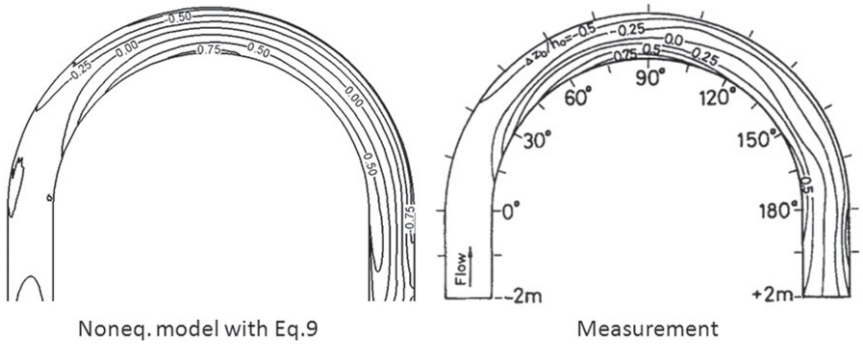

Fig. 8. Predicted and measured contours of bed deformation at end of Exp.4.

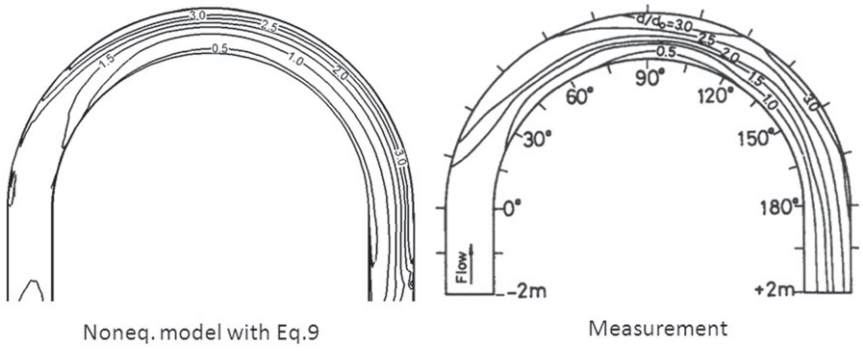

Fig. 9. Predicted and measured contours of median grain size at end of Exp.4.

shows the predicted contours of streamwise velocity and the calculated vectors of secondary flow at the end of Exp.1 at the sections 90° and 180°, where maximum deposition and maximum scour occur. The secondary flow and high longitudinal velocity in the outer-bank region results in maximum scour depth and intensive transverse grain sorting in this area. In the inner-bank region the water velocity is lower. However, due to the secondary flow finer particles are transported from the outer-bank region to the inner-bank one. Consequently, the high proportion of finer particles is found in the inner-bank region.

Fig. 7 shows the distribution of the measured and calculated mean grain size at the end of Exp.1. The numbers on the contour lines indicate ratios of final to initial mean grain size. As can be seen, the values of this ratio increase from inner bank towards outer bank. The model shows qualitatively good agreement between the calculated distribution of grain sorting and measurements.

Using the above calibrated model parameters, further calculations were carried out for the other flow condition with moderate unsteadiness characteristic (Exp.4). Figs. 8 and 9 show the distribution of the measured and calculated bed deformation and mean grain size at the end of the experiment ($T=300$ min). As can be seen again, the model shows qualitatively good agreement between the calculated results and measurements.

4. Conclusions

The FAST3D computer code using a finite volume method with boundary-fitted grids to calculate flow and sediment transport in alluvial channels was developed for fractional sediment transport. A multiple layer model was used to simulate bed composition changes. The influence of grain-size distribution on the bed-load, the bed development and consequently also the flow field was taken into account. The model was applied to calculate the sediment sorting and the bed deformation in curved alluvial channels under unsteady flow conditions.

The predictions have been compared with data from the laboratory measurements and prototype observations of Yen and Lee (1995). Analysing the calculated results showed that omitting the non-equilibrium approach, the model could not produce good results for the case with strong unsteadiness characteristics. The model results depend on the modelling of the non-equilibrium term and hence, on the value of the non-equilibrium adaptation length. Using the non-equilibrium approach the main features of grain-sorting and bed change were generally well reproduced. With the non-equilibrium adaptation-length formula proposed by Phillips and Sutherland, who relate L_s to the saltation step length of the sediment particles, the calculated results agreed best with the measurements. As for further test cases, the model should be validated by applications to other laboratories and real river flow situations with graded sediment bed material.

Acknowledgements

The authors would like to express their gratitude to Prof. W. Rodi at the Institute for Hydromechanics, University of Karlsruhe, Germany, for placing the FAST3D code at our disposal.

References

Armanini, A., Di Silvio, G., 1988. A one-dimensional model for the transport of a sediment mixture in non-equilibrium conditions. Journal of Hydraulic Research 26 (3), 275–292.

Borah, D.K., Alonso, C.V., Prasad, S.N., 1982. Routing graded sediments in streams: Formulations. Journal of the Hydraulics Division, ASCE 108 (12), 1486–1505.

Bell, R.G., Sutherland, A.J., 1983. Nonequilibrium bedload transport by steady flows. Journal of Hydraulic Engineering, ASCE 109 (3), 353–367.
Bui, M.D., 1998. Calculation of flow and sediment transport in rivers by means of a depth averaged numerical method. Ph.D. Dissertation, Institute for Hydromechanics, University of Karlsruhe, 187pp, (in German).
Bui, M.D., Rodi, W., 2006. 3D model for calculation of nonequilibrium sediment transport in rivers. Report No. 828, Institute for Hydromechanics, University of Karlsruhe, 47pp (in German).
Bui, M.D., Rutschmann, P., 2005. Validation of a numerical model for graded sediment transport in open channels. In: Proceedings of the XXXI International Association of Hydraulic Engineering and Research Congress, Seoul, pp. 1580–1592.
Cui, Y., Parker, G., Paola, C., 1996. Numerical simulation of agradation and downstream fining. Journal of Hydraulic Research 34 (2), 185–204.
Einstein, H.A., 1950. The bed load function for sediment transportation in open channel flow. US Department of Agriculture, Washington, D.C., Technical Bulletin No. 1026, 71pp.
Fang, H.W., 2000. Three-dimensional calculations of flow and bed load transport in the Elbe River. Report No. 763, Institute for Hydromechanics, University of Karlsruhe, 32pp.
Holly, F.M., Odgaard, A.J., 1992. Sediment transport modelling in the upper Rhine River, assessment of modelling opportunities. Limited distribution report, Iowa institute of hydraulic research, University of Iowa, 42pp.
Langendoen, E.J., Simon, A., 2000. Stream channel evolution of Little Salt Creek and North Branch west Papillion Creek, eastern Nebraska. Report, US Department of Agriculture, Agricultural Research Service, National Sedimentation Laboratory, Oxford, MS, 55pp.
Meyer-Peter, E., Mueller, R., 1948. Formula for bed-load transport. In: Proceedings of the International Association for Hydraulic Research, Stockholm, pp. 39–64.
Phillips, B.C., Sutherland, A.J., 1989. Spatial lag effects in bed load sediment transport. Journal of Hydraulic Research 27 (1), 115–133.
Rahuel, J.L., Holly, F.M., Chollet, J.P., Belleudy, P.J., Yang, G., 1989. Modelling of riverbed evolution for bed load sediment mixtures. Journal of Hydraulic Engineering 115 (11), 1521–1542.
Rodi, W., 1993. Turbulence Models and their Applications in Hydraulics, IAHR Monograph 3rd Edition Balkema, Rotterdam, pp. 116.
Thuc, T., 1991. Two-dimensional morphological computations near hydraulic structures, Ph.D. Dissertation. Asian Institute of Technology, Bangkok, Thailand, pp. 218.
Tsubaki, T., Saito, T., 1967. Regime criteria for sand waves in erodible bed channels. Kyushu University, Faculty of Engineering, Annuals 40, 741–748 (in Japanese).
Van der Scheer, P., Blom, A., Ribberink, J.S., 2001. Transport formulas for graded sediment. Research report 2001R-003/MICS-022, Civil Engineering and Management, University of Twente, The Netherlands, 84pp.
Van Niekerk, A., Vogel, K., Slingerland, R.L., Bridge, J.S., 1992. Routing of heterogeneous sediments over movable bed: model development. Journal of Hydraulic Engineering 118 (2), 246–262.
Van Rijn, L.C., 1987. Mathematical modelling of morphological processes in the case of suspended sediment transport. Doctoral dissertation, Faculty of Civil Engineering, Delft University of technology, The Netherlands, 260pp.
Wu, W., 2007. Computational River Dynamics. Taylor & Francis, London, pp. 494.
Wu, W., Rodi, W., Wenka, T., 2000. 3D numerical modeling of flow and sediment transport in open channels. Journal of Hydraulic Engineering ASCE 126 (1), 4–15.
Wu, W., Vieira, D.A., Wang, S.S.Y., 2004. One-dimensional numerical model for non-uniform sediment transport under unsteady flows in channel networks. Journal of Hydraulic Engineering, ASCE 130 (9), 914–923.
Yalin, M.S., 1972. Mechanics of Sediment Transport.. Pergamon, New York, pp. 298.
Yen, C.L., Lee, K.T., 1995. Bed topography and sediment sorting in channel bend with unsteady flow. Journal of Hydraulic Engineering, ASCE 121 (8), 591–599.
Zhu, J., 1992. An Introduction and Guide to the Computer Program FAST3D. Report No. 691, Institute for Hydromechanics, University of Karlsruhe, Germany, 27pp.

3.2. Anwendung von Künstlichen Neuronalen Netzen

Künstliche Neuronale Netze (englisch Artificial Neural Networks - ANN) sind mathematische Modelle, die sich an Grundprinzipien der Arbeitsweise eines biologischen Gehirns anlehnen. Im Allgemeinen besteht ein ANN aus einer Vielzahl einfach aufgebauter und komplex miteinander verknüpfter Verarbeitungseinheiten (Neuronen oder Knoten), die über gewichtete Verbindungen Informationen (Signale) miteinander austauschen. Die Stärke eines Signals ist vom Gewicht der Verbindung abhängig. An jeden Knoten werden Signale durch bestimmte mathematische Operationen verarbeitet und über eine Vernetzung an andere Neuronen weitergeleitet. Die Berechnungsvorschriften sind bei jedem Netztypen anders definiert. In der Regel wird der am Neuron eingehende Wert mit relativ einfachen, stetig differenzierbaren Funktionen (z.B. Sigmoid-Funktion) in einen Ausgabewert umgewandelt. Die eigentliche Leistungsfähigkeit der ANN entsteht durch die parallele Anwendung dieser Funktionen an vielen Knoten, die in Schichten zusammengefasst werden. Alle Schichten und deren Vernetzung untereinander werden schließlich zu einer Netzwerk-Architektur zusammengefasst. Die Gewichte aller Verbindungen werden in einer Trainings- oder Lernphase ermittelt.

Im Gegensatz zu den meisten herkömmlichen empirischen Methoden, bei denen Vorkenntnisse über die Art der Beziehungen zwischen den Daten erforderlich sind, lernen die ANN-Methoden anhand der ihnen vorgestellten Datenbeispiele, um die subtilen funktionalen Beziehungen zwischen den Daten selbst zu erfassen, auch wenn die zugrundeliegenden Zusammenhänge unbekannt sind oder die physikalische Bedeutung schwer zu erklären ist. Darüber hinaus hat ANN eine hohe Toleranz gegenüber Datenmusterfehlern nachgewiesen. Im Allgemeinen sind ANN-Modelle in der Lage, nichtlineare Input-Output-Zusammenhänge in komplexen Systemen abzubilden. Diese Eigenschaften machen die Verwendung von ANN in der jüngeren Zeit auf verschiedensten Gebieten auch für Sedimenttransportvorhersagen sehr vielversprechend. Nagy et al. (2002) berechneten zwar die Schwebstofffracht. Die Methode ist jedoch auch für Geschiebefracht anwendbar.

Es gibt weitere Variationen des ANN-Ansatzes. Jain (2008) verwendete ein zusammengesetztes Neuronales Netz (Compound Neural Network - CNN) für die Sedimentberechnung. Das CNN setzte sich aus mehreren ANN zusammen und lieferte bessere Ergebnisse als ein einzelnes ANN. Azamathulla et al. (2009) verwendeten ein adaptives Neuro Fuzzy Inferenzsystem (Adaptive Neuro-Fuzzy Interference System – ANFIS) für die Geschiebeberechnung in einem Flussnetzwerk in Malaysia.

Bei diesem Abschnitt handelt es sich um die am Lehrstuhl entwickelten ANN-Ansätze für die Sedimenttransportberechnung, die als eine Alternative zu den herkömmlichen Modellen zu verwenden sind.

3.2.1. ANN als Prädiktor

Im Folgenden sind vier wissenschaftliche Arbeiten zusammengefasst:

1. M.D. Bui, K. Kaveh, P. Penz, P. Rutschmann (2015a): “Contraction scour estimation using data driven methods”. Journal of Applied Water Engineering and Research. Taylor & Francis.
2. M.D. Bui, D. Huber, K. Kaveh, A.M.F. da Silva, P. Rutschmann (2016): “Application of artificial neural networks for river regime”. River Flow. Taylor & Francis.
3. K. Kaveh, M.D. Bui, P. Rutschmann (2017): “A comparative study of three different learning algorithms applied to ANFIS for predicting daily suspended sediment concentration”. International Journal of Sediment Research. Elsevier.
4. S. Ateeq-Ur-Rehman, M.D. Bui, P. Rutschmann (2018): “Variability and Trend Detection in the Sediment Load of the Upper Indus River”. Water. MDPI.

Das Paper [1] stellt ein ANN Modell und ein ANFIS Modell vor, mit denen die Gleichgewichtstiefe des Kontraktionskolkes genau abgeschätzt werden kann. Die entwickelten Netzwerke wurden unter Verwendung des Datensatzes trainiert, der von verschiedenen Autoren für lange Einengungstrecken unter Bedingungen mit klarem Wasser durchgeführt wurde. Die Wichtigkeit der einzelnen Eingabeparameter wurde mit einer Sensitivitätsanalyse überprüft. Dies ergab, dass das Kontraktionsverhältnis der empfindlichste Parameter ist, gefolgt von der Auswirkung der Bildung von Abpflasterungschichten für nichtuniforme Sedimente. Die berechneten Ergebnisse zeigen, dass die entwickelten Netzwerke die maximale gleichgewichte Kolktiefe signifikant besser abschätzen als gängige Methoden.

Auf der Grundlage 509 beobachteter Datensätze wurden Variationen von Feedforward Multilayer Perceptron (MLP) Netzen in Bezug auf Trainingsalgorithmus und Transferfunktionen, sowie verschiedene Netzarchitekturen im Paper [2] getestet. Ein MLP Modell zur Vorhersage der Charakteristiken des Flussregimes wurde entwickelt. Die MLP-Leistung wurde mit der thermodynamischen Entropietheorie und der Stabilitätstheorie verglichen. Eine Verbesserung der Ergebnisse des MLP-Modells wurde durch die Aufteilung der Eingangsgrößen in Sand- und Kiesbettmaterialien sowie verschiedene Abflussgruppen erreicht.

Die Abschätzung der Sedimentfracht spielt eine entscheidende Rolle bei den Randbedingungen in numerischen Sedimenttransportmodellen. Es ist sehr schwierig, diese Sedimentfracht in einem Untersuchungsgebiet mit einer starken Hysterese-Erscheinung und einem überproportionalen räumlich-zeitlichen Trend zwischen Wasserabfluss und Schwebstoffrate genau abzuschätzen. In Studie [4] wurde die Schwebstofftransportrate in einer solchen Stauhaltung anhand von dem mit Diskrete Wavelet-Transformation kombinierten ANN Modell (WA-ANN) ermittelt. Ein Vergleich der berechneten Resultate mit Messungen ergab, dass das WA-ANN Modell die guten Ergebnisse für die außergewöhnlichen Ereignisse lieferte und die

Lücke zwischen den intermittierenden Messungen der suspendierten Sedimentkonzentration (SSC) füllte. Außerdem wurde die zeitliche Veränderung der Sedimenttransportraten sowie des Wasserabflusses mithilfe von drei nichtparametrischen Trendtesten analysiert. Paper [3] stellt ein ANFIS Modell für die Sedimentfracht vor, das mit drei verschiedenen Lernprozessen getestet und entwickelt wurde. Es wurde gezeigt, dass die ANFIS-Ansätze gute Ergebnisse liefern konnten.

Journal of Applied Water Engineering and Research, 2015
http://dx.doi.org/10.1080/23249676.2015.1051141

Contraction scour estimation using data-driven methods

Minh Duc Bui*, Keivan Kaveh, Petr Penz and Peter Rutschmann

Institute of Hydraulic and Water Resources Engineering, Technische Universität München, Arcisstrasse 21, München D-80333, Germany

(*Received 13 August 2014; accepted 29 April 2015*)

The paper presents an artificial neural network (ANN) and an adaptive neuro-fuzzy inference system (ANFIS), which could accurately estimate the maximum equilibrium depth of the contraction scour. The developed networks have been trained using the data set conducted by different investigators for long contractions under clear-water conditions. The designed multilayer perceptron (MLP) ANN includes one hidden layer and seven nodes within that layer. Its hidden neurons use a hyperbolic tangent sigmoidal transfer function. The ANN model was implemented using the MATLAB software package. The importance of the individual input parameters was tested with a sensitivity analysis. This revealed the contraction ratio to be by far the most sensitive parameter, followed by the effect of armor layer formation for nonuniform sediments. For the designed MLP–ANN network, the training was based on the Levenberg–Marquardt back-propagation algorithm in batch mode. The designed ANFIS was the zero-order Takagi–Sugeno model with four bell-shaped membership functions for each input and applied the Levenberg–Marquardt algorithm for network training. The ANFIS model was implemented using a FORTRAN-based computer code. The calculated results show that the selected networks estimate the equilibrium maximum scour depth under clear-water conditions within the range of the used data set significantly better than other conventional methods.

Keywords: artificial neural network; adaptive neuro-fuzzy inference system; contraction scour; sediment transport

Introduction

Flow constriction appears where the overall width of a channel segment is significantly reduced. In accordance with the law of continuity, the mean stream velocity normal to the channel cross section speeds up to maintain the flow rate. As a result, the bottom shear stress increases. As soon as the bottom shear stress is higher than the so-called critical shear stress, the contraction scour starts to develop into depth by bed material transport. With increasing erosion, the flow cross section becomes larger and the bottom shear stress declines until equilibrium conditions are reached. At this equilibrium scour depth, the quantity of bed material being transported into the contracted reach is equivalent to that being transported out of the contracted reach. Flow constrictions can be either man-made or natural. Natural factors include, for example, stone outcrops, ice formations or jams, and debris accumulations. Streams may as well be simply contracted in a natural geologic way. Anthropogenic features among others are bridge openings, bridge abutments, roadway approach embankments, or cross-drainage works. Also cofferdams that partially enclose the river for construction or maintenance works are a type of channel contractions. Since scour-induced damage leads to decrease or even loss of the structure functionality, scour is one of the major threats to riverine hydraulic structures. A sufficient understanding of the phenomenon and an adequate analysis on scour for every object placed on or adjacent to a riverbed as well as for all types of stabilization projects is very important.

The contraction scour profile identifies two separate scour depths: the maximum contraction scour depth, which immediately occurs downstream of the contraction and the mean scour depth that occurs further downstream. Two different conditions for contraction scour can be identified, namely clear-water and live-bed scour, which are differentiated according to whether the approaching flow (in the uncontracted channel part) is already transporting a significant amount of bed material or not. Clear-water conditions describe the case in which only an insignificant amount of sediment is transported by the approaching flow. Depending on the ratio of the length of contraction to the approaching channel width, channel contractions are designated as long or short. According to Dey and Raikar (2005) a contraction is called long when this ratio is not less than one. Over a period of several decades numerous investigations have been carried out. A number of analytical models have been proposed to compute these characteristic parameters of the constriction scour. Straub (1934) presented a one-dimensional model theory of the equilibrium scour depth for live-bed conditions. He applied the Du Boys sediment

*Corresponding author. Email: bui@tum.de

transport formula and the Manning equation. Laursen (1960) adopted Straub's approach and used his own total sediment transport formula instead. This equation is valid for the live-bed case and makes it possible to differ between suspended- and bed-load transport modes. Three years later, again under the assumption of a long contraction, Laursen (1963) developed an equation for equilibrium contraction scour under clear-water conditions. Following the scheme proposed by Laursen (1960), most analytical models essentially adopt the same framework, that is, the local flow constriction was conceptualized as a cross-sectional variation. Different flume tests were conducted to develop and validate the equations for contraction scours. Komura (1966) obtained a live-bed and clear-water contraction scour equation by applying dimensional analysis to his experimental results on long contractions. The effect of armoring in the contracted section was integrated by the parameter of the geometric standard deviation. Hence, for its high values (heterogeneous bed materials) the influence on the scour depth was considered. Assuming that the sediment transport rate is proportional to the excess shear stress, Gill (1981) generalized Straub's live-bed contraction scour formula. Lim and Cheng (1998) derived a formula for live-bed long contraction scour depths similar to Gill (1981). The comparison with various sets of laboratory data for long contractions showed that their proposed equation, in spite of its simplicity, is acceptable for practical purposes (Lim & Cheng 1998) under live-bed as well as under clear-water conditions. Further, Richardson and David (2001) have developed the equations which are used in HEC-18 for scour calculation with homogenous cohesionless bed materials. Briaud et al. (2005) performed clear-water long contraction scour experiments in flumes with fine bed materials. It was also reported in the literature that the scour depth is not influenced by the contraction length for the case ratios of contraction length to contracted width greater than one quarter. Also, an influence of the transition angle between approaching flow and narrowed part could be denied based on their results. Dey and Raikar (2005) conducted a set of flume experiments in a long contraction under clear-water conditions. Their formula accounts for the maximum scour depth for sand and gravel beds with various geometric standard deviations. A significant effect of sediment gradation for nonuniform bed material on the scour depth due to armoring was observed. All the contraction scour equations were simply based on uniform flow using open channel theories. The increased turbulence within the contracted channel was neglected as one of the assumptions. The critical velocity initiating the scour was proposed by different authors for a certain flume condition, but no critical velocity equation covering the most general cases exits. Furthermore, the difference between them was the use of variant types of empirical sediment transport formulas. Hence, all empirical analytical relations are of limited generality.

Field data on contraction scour are rare. Furthermore, a comparison with contraction scour formulas is difficult. One reason is that the conditions in the field are much more complex than the controlled circumstances in the laboratory or the assumptions made for derivations. Another problem is the quality of the measured field data itself; for example, the field measurements on scour depth were mostly made after a flood event. In this case, the information about the hydraulic parameters for the relevant contraction scour depth often was unknown and the time of scour data collection could not overlap with the occurrence of the maximum scour depth. In addition, it is complicated to segregate the contraction scour share from all related components that contribute to the total scour depth of the particular field. Wagner et al. (2006) compared contraction scour estimations from several empirical analytical equations with field data. In most cases these formulas overestimated the measured scour depths, whereby cases of underestimation also occurred. They concluded that – for contraction scour computation – a better balance of simple idealized laboratory conditions to complex field conditions is necessary.

In the last decades, numerical models have been used to study scour phenomena. To facilitate the design of in-stream structures, many empirical analytical formulas have been used with 1D, 2D, and even 3D flow models to predict the maximum scour depth of the structures. To simulate the details of the erosion process due to flow contraction, especially under turbulent flow conditions, multidimensional morphodynamical models have been developed. Briaud et al. (2005) have developed an analytical model for calculating contraction scour in flumes with cohesive bed material, named SRICOS. They also applied a 3D morphodynamical model, in which equilibrium conditions for transport of very fine cohesive sediment were assumed, to test and validate their proposed scour formulas. Applying the semi-empirical non-equilibrium approach for sediment transport in the computer system FAST-3D (Bui & Rodi 2008), the main features of contraction scour have been well reproduced, in particular the development of scour and water surface elevation as well as of the flow.

Despite many years of research in contraction scour, no empirical formula exists that is generally applicable to all circumstances. In many cases, unreasonable contraction scour depths are predicted and the results of the different formulae often vary strongly. The reasons are rooted in the complexity of contraction scour and in the limitations of the most traditional empirical and statistical methods, which require prior knowledge about the nature of the relationships among the data. In the recent past, the method of artificial neural networks (ANNs) provided many promising results in the fields of civil and hydraulic engineering. These networks are a form of artificial intelligence which attempts to mimic the function of the human brain and nervous system at a sub-symbolic level. Scour processes

are very complex and not well understood. For most traditional scour models, the lack of physical understanding is usually supplemented by either simplifying the problem or incorporating several assumptions into the models. In contrast, ANNs are a data-driven approach in which the model can be trained on input–output data pairs to determine the structure and parameters of the model without any prior knowledge about the nature of the relationships among the data. In this case, there is no need to either simplify the problem or incorporate any assumptions. Moreover, ANNs can always be updated to obtain better results by presenting new training examples as new data become available. These attributes make the utilization of ANNs for contraction scour predictions very promising.

The adaptive neuro-fuzzy inference system (ANFIS) is a hybrid scheme that uses the learning capability of the ANN to derive the fuzzy if–then rules with appropriate membership functions worked out from the training pairs, which in turn leads to the inference (Jang & Sun 1997). The difference between the common ANN and the ANFIS is that while the former captures the underlying dependency in the form of the trained connection weights, the latter does so by establishing fuzzy language rules. The treatment of data nonlinearities in this way has been recently found to be useful in fields like hydrology, fluvial hydraulics, etc. (Bateni et al. 2007; Kisi et al. 2012).

In the present study an optimal ANN and an optimal ANFIS are developed, which are able to predict adequately the maximal equilibrium contraction scour depths for a wide range of circumstances, including the formation of armor layers on the channel bed.

Model approaches

ANN model

ANN is a broad term covering a large variety of network architectures, the most common of which is a multilayer perceptron (MLP). An ANN model consists of a number of artificial neurons variously known as processing elements or nodes. For MLP networks, neurons are arranged in layers: an input layer, an output layer, and one or more intermediate or hidden layers. The net is formed by these layers of neurons and each neuron in a specific layer is connected to neurons in other layers via weighted connections. Neurons are defined as mathematical expressions that filter the signal through the net. From the connected neurons in the previous layer, an individual neuron receives its weighted inputs which are usually summed along with a bias unit. The bias unit is used to scale the input to a useful range in order to improve the convergence properties of the neural network. The result of this combined summation is passed through a transfer function so as to produce the output of the neuron. This output is then passed through weighted connections to neurons in the next layer, where the process is repeated. The weight vectors connecting the different nodes of the network are found by the so-called error back-propagation method. During training the values of these parameters are varied so that the ANN output becomes similar to the measured output on a known data set (Haykin 1999; Bhattacharya et al. 2007). A trained response is achieved by changing the connections' weights in the network according to an error minimization criterion. A validation process can be used during training in order to prevent overfitting. Once the network has been trained to simulate the best response to input data, the configuration of the network is fixed and a test process is conducted to evaluate the performance of the ANN as a predictive tool. According to Shahin et al. (2002), the structure and process for node j of a MLP ANN model are illustrated in Figure 1. More details about ANN approaches with these methods can be found in Penz (2013).

ANFIS model

The fuzzy inference system (FIS) consists of linguistic or semi-linguistic rules linking the membership functions of the input variables to the membership function of the output variable. The fuzzy process models can be initialized by expert knowledge in the form of fuzzy rules and can

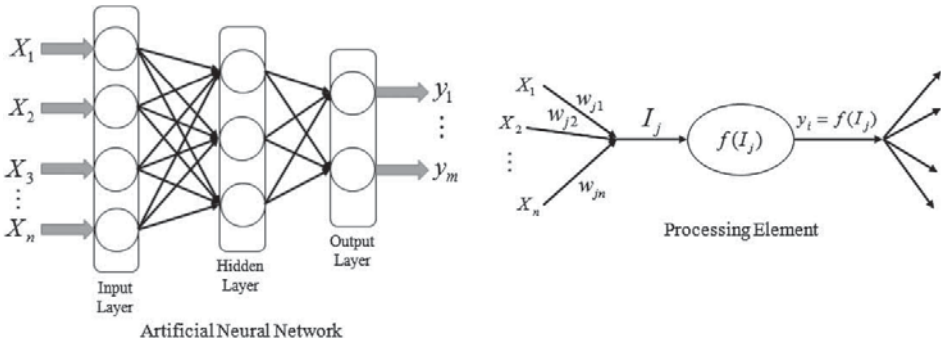

Figure 1. Typical structure and operation of an ANN ($I_j =$ level of node j; $w_{ji} =$ connection weight between nodes j and i; $x_i =$ input from node i; $y_j =$ output of node j; and $f\ (I_j) =$ transfer function).

be adapted by the use of process data. Basically, a FIS is composed of five functional blocks (Jang, 1993):

- Block 1: A rule base containing a number of fuzzy rules, each rule with the so-called premise (IF) and consequent (THEN) parts;
- Block 2: A crisp database (where objects are described in terms of precise attribute values) which defines the membership functions of the fuzzy sets used in the fuzzy rules;
- Block 3: A decision-making unit which performs the inference operations on the rules;
- Block 4: A fuzzification inference which transforms the crisp inputs into degree of match with linguistic values; and
- Block 5: A defuzzification interface which transforms the fuzzy results of the inference into a crisp output.

Normally, the rules of a FIS are designed a priori and the parameters of the membership functions are adapted in the learning process from input/output data sets. Based on the differences between the specification of the consequent part and the defuzzification schemes, several types of FIS have been proposed. Among them the Sugeno FIS (Takagi & Sugeno 1985) is the most common one, which will be used also in this study. Further, there is no systematic way to determine what type and shape of membership functions of premise variables have the best performance in a defined FIS. An efficient way of doing this is using an ANN model trained by input/output data. This approach is called ANFIS. Hence, ANFIS are fuzzy models put in the framework of adaptive systems to facilitate learning and adaptation. Such systems can be trained without the need for expert knowledge usually required to design the standard FIS.

A basic ANFIS introduced by Jang (1993) is illustrated in Figure 2. An ANFIS is a network structure consisting of a number of nodes connected through directional links. Each node is characterized by a node function with fixed or adjustable parameters.

The learning or training phase of a neural network is a process to determine parameter values to sufficiently fit the training data. The basic learning rule is the well-known back-propagation method, which seeks to minimize some measure of error, usually the sum of squared differences between network's outputs and desired outputs (Kaya et al. 2002). Depending on the types of inference operations upon fuzzy rules, most FISs can be classified into two types: Mamdani system and Takagi–Sugeno (TS) system. The TS system is more compact and computationally efficient, being output crisp, while avoiding the time-consuming and mathematically intractable defuzzification operation. It is by far the most popular candidate for sample-data-based fuzzy modeling and lends itself to the use of adaptive techniques (Takagi and Sugeno 1985). In a first-order TS system for two inputs, a typical rule set with four fuzzy rules and four membership functions can be expressed as follows:

- Rule 1: If x_1 is A_{11} and x_2 is A_{21}, then $f_1 = p_1\ x_1 + q_1\ x_2 + r_1$,
- Rule 2: If x_1 is A_{11} and x_2 is A_{22}, then $f_2 = p_2\ x_1 + q_2\ x_2 + r_2$,

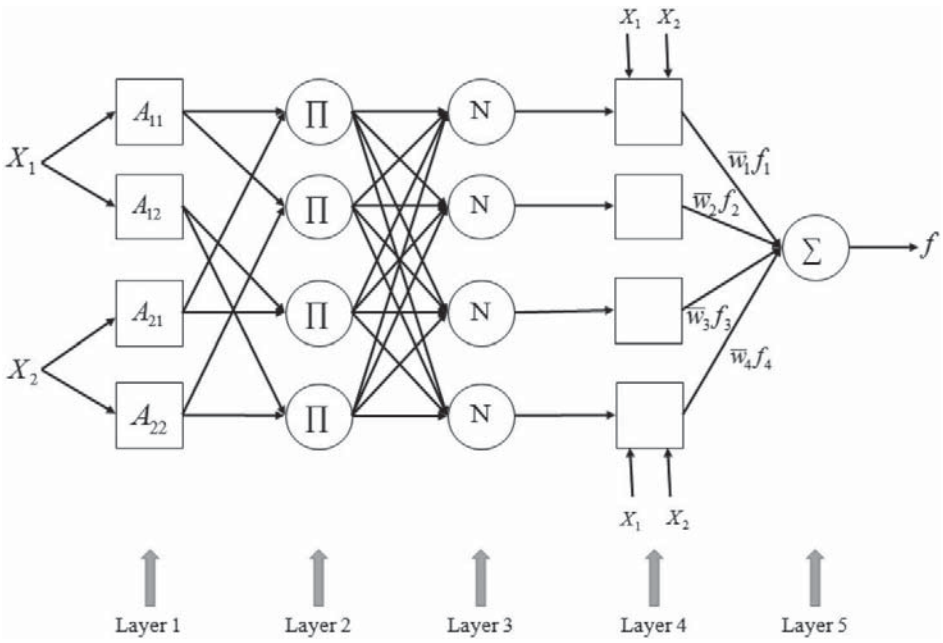

Figure 2. ANFIS architecture Sugeno's fuzzy model for two inputs with four rules.

- Rule 3: If x_1 is A_{12} and x_2 is A_{21}, then $f_3 = p_3\ x_1 + q_3\ x_2 + r_3$,
- Rule 4: If x_1 is A_{12} and x_2 is A_{22}, then $f_4 = p_4\ x_1 + q_4\ x_2 + r_4$,

where x_1 and x_2 are inputs; f_j ($j = 1$–4) are output levels. For a zero-order TS model, the output level f_j is a constant ($p_j = q_j = 0$; $j = 1$–4). ANFIS contain five layers with the following processes:

Layer 1: Each node in this layer produces membership grades of an input variable. The output of the j-th node in layer l is denoted as O_j^1. Assuming a generalized bell-shaped function as the membership function, the output O_j^1 can be computed as

$$O_j^1 = \begin{cases} \mu_j(x_1) = \dfrac{1}{1 + ((x_1 - c_j)/a_j)^{2N_j}} & j = 1, 2, \\ \mu_j(x_2) = \dfrac{1}{1 + ((x_2 - c_j)/a_j)^{2N_j}} & j = 3, 4, \end{cases} \tag{1}$$

where $\{a_j, c_j, N_j\}$ are adaptable variables known as premise parameters. The outputs of this layer are the membership values of the premise part.

Layer 2: Every node in this layer multiplies the incoming signals as (Π):

$$\begin{aligned} O_1^2 &= w_1 = \mu_1(x_1) \times \mu_3(x_2), \\ O_2^2 &= w_2 = \mu_1(x_1) \times \mu_4(x_2), \\ O_3^2 &= w_3 = \mu_2(x_1) \times \mu_3(x_2), \\ O_4^2 &= w_4 = \mu_2(x_1) \times \mu_4(x_2). \end{aligned} \tag{2}$$

Layer 3: The j-th node of this layer calculates the normalized firing strengths as (N):

$$O_j^3 = \bar{w}_j = \frac{w_j}{\sum_{i=1}^{4} w_i}, \quad j = 1 - 4. \tag{3}$$

Layer 4: Node j in this layer calculates the contribution of the j-th rule toward the model output, with the following node function:

$$O_j^4 = \bar{w}_j f_j = \bar{w}_j (p_j x_1 + q_j x_2 + r_j), \quad j = 1 - 4, \tag{4}$$

where $\bar{w}_j$ is the output of layer 3 and $\{p_j, q_j, r_j\}$ are the parameters set. Parameters of this layer are referred to as consequent.

Layer 5: The single node in this layer calculates the overall output of the ANFIS as ($\sum$):

$$O_1^5 = \sum_{i=1}^{4} \bar{w}_i f_i = f\,. \tag{5}$$

More details about the ANFIS approach can be found in Jang and Sun (1997).

Model setup

Model inputs

In the context of rivers and sediment transport, armoring describes a process by which an erosion-resistant surface layer is formed. This occurs on a river bed or a scour hole when forces of the flowing water remove finer particles and leave relatively large particles behind. The coarser bed material builds up a natural riprap-like armor layer over a heterogeneous mixture of sediment with a wide range of diameter. This armoring limits further scour development for a particular flow rate. In some cases, the formed armor layer can be destroyed again by higher levels of shear stress, leading to further development of the scour until a new armor layer is formed or the maximum scour is reached. Whether an armor layer is formed or not depends on the values of the geometric standard deviation (σ_g) of bed materials. According to Gessler (1971), armoring will arise for $\sigma_g > 2$. Later Raudkivi and Ettema (1982) reported that the bed material will not armor for values of $\sigma_g < 1.5$.

We consider an alluvial open channel with rectangular cross sections and along contraction, which means the ratio of the length of the contraction to the width of the approaching flow is larger than one. Figure 3 shows the schematic of the rectangular contraction (Dey & Raikar 2005). The physical parameters influencing the equilibrium scour depth d_s (m) in a long contraction are the approaching flow velocity v_1 (m/s), the approaching flow depth h_1 (m), the density of water ρ (kg/m^3), the density of sediment ρ_s (kg/m^3), the acceleration of gravity g (m/s^2), the kinematic viscosity of water ν (m^2/s), the median sediment particle size d_m (m), the approaching channel width b_1 (m), contracted channel width b_2 (m), and geometric standard deviation of the grain-sized distribution σ_g ($-$) (Dey & Raikar 2005).

The independent variables g, ρ, and ρ_s are presented as one combined parameter Δg. By using the Buckingham theorem for the dimensional analysis with repeating variables approaching flow velocity v_1 and width b_1, we can rewrite the relation between the 10 physical variables of the dimensional contraction scour form into the

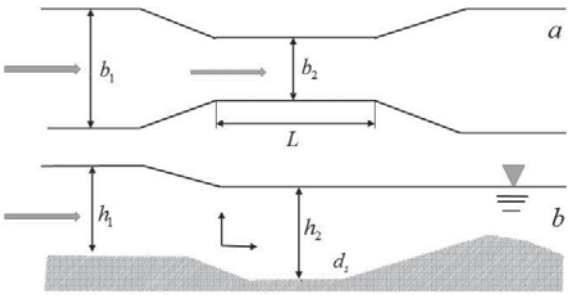

Figure 3. Schematic of a long rectangular channel contraction at equilibrium scour conditions (a – top view; b – side view).

nondimensional functional relation with only six dimensionless variables:

$$\overline{d_s} = \frac{d_s}{b_1} \quad \overline{d} = \frac{d_m}{b_1} \quad \overline{h} = \frac{h_1}{b_1} \quad \overline{b} = \frac{b_2}{b_1} \quad \overline{Fr} = \frac{v_1}{\sqrt{\Delta g d_m}}$$

$$\Delta g = \left(\frac{\rho_s - \rho}{\rho}\right) g, \quad \overline{d_s} = F(\overline{d}, \overline{Fr}, \overline{h}, \overline{b}, \sigma_g). \tag{6}$$

The channel opening ratio $\overline{b}$ shows the influence of geometric contraction on the degree of contraction scour. $\overline{d}$ represents the impact of sediment size on scour depth. $\overline{h}$ refers to the importance of approaching flow depth in scour depth. σ_g indicates the role of sediment gradation in scour depth and accounts also for armoring in well-graded sediments. The densimetric Froude number $\overline{Fr}$ considers the effect of the mobility of submerged sediment particles on scour depth. These five parameters are considered as model inputs. The dimensionless equilibrium scour depth is considered as the only output parameter. More details about the derivation of relationship (6) can be found in Dey and Raikar (2005).

Data collection

Dey and Raikar (2005) have studied long contraction scour in a rectangular tilting flume in the Hydraulic and Water Resources Engineering Laboratory, Indian Institute of Technology. The channel was 12 m long, 0.6 m wide, and 0.7 m deep with a uniform contraction length of 1 m. The approaching channel width b_1 remains over the whole experiment constant (0.6 m), whereas the contracted channel width b_2 has four different values (0.24, 0.30, 0.36, and 0.42 m). The experimental data were differentiated according to the sediment type: sand or gravel. An overall number of 131 samples with relevant parameters for contraction scour were provided; of those, 95 samples were for gravel. In order to achieve a fully developed turbulent flow, the flume inlet was located 6 m away from the contraction entrance. After a slow initial filling of the flume, the tests ran until the equilibrium scour depth was reached. Equilibrium is attained when the time-averaged transport of bed materials into the scour hole equals that which is removed from it. During all experiments, the average approaching flow velocities were kept at certain values, so that clear-water conditions were guaranteed for all conducted tests.

In the present paper, the experimental data conducted by Dey and Raikar (2005) and the data of other investigators (Komura 1966; Gill 1981; Webby 1984; Lim 1993) are used. The whole data set consists of 182 samples with the relevant parameters for contraction scour. In Table 1 the ranges of the different parameters are listed. They also represent the applicable domain of the data-driven models. Additionally, since the geometric standard deviation has a range between 1.0 and 3.60, in some cases an armor layer could be formed during the scouring event. The data set has been divided randomly into three subsets, whereby the biggest amount of data (70%) is added randomly to the training subset. The remaining data set samples are used for testing (15%) and validating the networks (15%). The training subset is used to design the weights. The validation subset is used to test the accuracy of training while training is ongoing. After each epoch, the validation subset acts as a barometer for determining when the accuracy of the MLP is at an acceptable level. After the network is considered optimally trained, the test subset is used to verify its performance.

To achieve a better performance and faster training of the network, all data were normalized. The range after the data preprocessing is chosen to be between minus one ($ra_{min} = -1$) and one ($ra_{max} = 1$). To ensure this, formula (7) is utilized. For a simpler and more understandable comparison of the computed outputs with the targets, a postprocessing is included as well. Here the outputs and targets are denormalized again, thus set back to the ranges before preprocessing. For this purpose, formula (8) is applied.

$$x_{pr} = \frac{(ra_{max} - ra_{min})(x - x_{min})}{(x_{max} - x_{min})} + ra_{min}, \tag{7}$$

$$x_{po} = \frac{(x_{pr} - ra_{min})(x_{max} - x_{min})}{(ra_{max} - ra_{min})} + x_{min}, \tag{8}$$

where x_{pr} is the preprocessed variable, x_{po} the postprocessed variable, x the original variable, and (ra_{min}, ra_{max}) is the range.

Designed networks

For many problems of hydraulic engineering, a MLP feed-forward ANN is considered as an effective tool which is also applied in the present paper. These MLP networks often have one or more hidden layers of sigmoid neurons followed by an output layer of linear neurons or nodes. The reason for this is that multiple layers of neurons with nonlinear activation functions allow the network to learn nonlinear relationships between input and output vectors. This type of configuration does not constrain the output result to a fixed range of values, which grants the network

Table 1. Range of parameters.

Limit	d_m (mm)	v_1 (m/s)	h_1 (m)	b_1 (m)	b_2 (m)	σ_g	$\overline{Fr}$	d_s (m)
Lower	0.350	0.1932	0.0240	0.400	0.100	1.00	1.1434	0.0100
Upper	14.25	0.9290	0.1366	1.586	0.524	3.60	3.2882	0.1626

the freedom to represent any possible outcome. Learning or training algorithms decide how the weights in configured ANN architectures are adjusted in order to minimize the output errors in a particular data set. This is measured by the generalization ability of the input–output mapping computed by the ANN. At present, there are numerous learning algorithms available for different network configurations and applications. Miscellaneous training algorithms can propose different equations which modify some of the weights of processing elements in response to input and output values. One of the most widely used algorithms for training a MLP is the Levenberg–Marquardt algorithm with the mean squared error (MSE) being used as an error function. The MSE computes the similarity of the prediction compared to actual values. This tool is efficient at assessing undesirably large differences. The Levenberg–Marquardt algorithm is employed in the scope of this work. Besides, an early stopping algorithm and the Nguyen–Widrow initialization for weights were utilized. More details about ANN approaches with these methods can be found in Penz (2013).

Conventional evaluations of the model prediction based on the correlation coefficient (R), the coefficient of determination (R^2), the mean absolute error (MAE), the sum of the square error (SSE), and the root mean square error (RMSE) have been critically reviewed by Legates and McCabe (1999). They indicated that the correlation coefficient R alone is unsuitable for model evaluation and proposed that a perfect evaluation of model performance should contain at least one 'goodness-of-fit' or relative error measure and at least one absolute error measure. The R parameter clarifies the relation between observed and predicted values and RMSE evaluates the residual between observed and predicted contraction scour. In this paper, performances of models are evaluated resorting to R, MAE, and RMSE. In brief, the models' predictions are optimal if R is found to be close to one, and MAE and RMSE are close to zero.

Since the appropriate number of hidden layers and dependant nodes for the models is not known, a trial-and-error method was used to find the best network's configuration. An optimal architecture was determined by varying the number of hidden layers and neurons, and based upon minimizing the difference among the neural network predicted values and the desired outputs. The training of the neural network models was stopped when either the acceptable level of error was achieved or the number of iterations exceeded a prescribed value. The neural network model configuration that minimized the MAE and RMSE and optimized the R was selected as the optimum and the whole analysis was repeated several times. The ANN architecture was modified by changing the number of hidden layers and its neurons, of the initial weights, as well as the type of input and output functions. Each modification was tested with one hundred trials, which served as the basis for performance assessment of mean values. In order to compare these mean values, different modified architectures were evaluated. After extensive trial-and-error processes, an optimal ANN for maximum equilibrium contraction scour modeling under clear-water conditions was found with the simplest multilayer feed-forward network with one hidden layer performing clearly better than the alternatives. Further, for this single hidden layer MLP, the optimal number of neurons was determined to be seven. The weight function was set as multiplication, whereas the net input function was chosen according to trial and error. A combination of the hyperbolic tangent sigmoid function in the hidden neurons with the linear transfer function for the output neuron was determined as the best alternative.

Applying the designed ANN model, the values of the weights and biases have been specified after a successful learning process. They represent the stored knowledge of the ANN for contraction scour depth modeling. The best designed network utilizes all 50 defined parameters, which are separated in one input weight matrix $\mathrm{IW}_{1,1}$, one hidden layer weight matrix $\mathrm{LW}_{2,1}$, one bias vector b_1, and one bias value b_2 with the following values:

$$\mathrm{IW}^{1,1} = \begin{bmatrix} -61.7540 & 0.7590 & 16.0804 & -2.2736 & -1.3754 \\ -36.1590 & -1.9702 & -18.4141 & 3.2689 & 3.0961 \\ 12.5222 & -0.0331 & -14.5885 & 8.0144 & -0.2061 \\ 112.9620 & 1.4127 & 2.7952 & -5.7359 & -1.0236 \\ -26.4800 & 0.0029 & 13.6386 & 8.1508 & -0.0300 \\ 128.5200 & -1.6282 & 8.8843 & -0.1999 & 0.2204 \\ -65.1840 & -1.1853 & -12.4488 & -0.9877 & -0.6407 \end{bmatrix},$$

$$\mathrm{LW}^{2,1} = \begin{bmatrix} 0.0276 & -0.0258 & -0.0726 & 0.0241 \\ -0.0312 & 0.2775 & -0.0295 \end{bmatrix},$$

$$\vec{b}^{\,1} = \begin{bmatrix} 2.1017 \\ 1.7659 \\ -0.0878 \\ 0.1017 \\ -7.2220 \\ 4.7620 \\ 3.9530 \end{bmatrix},$$

$$b^2 = [-0.1876]. \tag{9}$$

Using the designed network, we received the following equation for the normalized equilibrium scour depth $(\overline{d_\mathrm{s}})_\mathrm{pr}$:

$$(\overline{d_\mathrm{s}})_\mathrm{pr} = \mathrm{LW}^{2,1} \times \mathrm{tansig}\left(\mathrm{IW}^{1,1} \times \begin{bmatrix} \overline{d} \\ \overline{Fr} \\ \overline{h} \\ \overline{b} \\ \sigma_g \end{bmatrix}_\mathrm{pr} + \vec{b}^{\,1} \right) + b^2. \tag{10}$$

The dimensionless value of the scour depth $\overline{d_\mathrm{s}}$ can be then calculated using Equation (8). Based on this value and the approaching channel width b_1, we can define the absolute scour depth d_s.

For the ANFIS model, the same dimensionless inputs and output as well as the data sets are applied. A two-step process is used for faster training and to adjust the network parameters. Applying a hybrid learning procedure, in

the first step, the premise parameters are kept unchanged, and the information is propagated forward in the network to layer 4, where a least-squares estimator identifies the consequent parameters. In the second step, the backward pass, the chosen parameters are held fixed while the error is propagated. In MATLAB, the method of either back-propagation or a combination of least-squares estimation and back-propagation could be applied for estimating and modifying membership function parameters. Different ANFIS models were established to estimate maximum equilibrium contraction scour. Each model had different numbers of membership functions. The triangle, Gaussian, and generalized bell functions were applied to each model. After an extensive trial-and-error search for various networks, an optimal ANFIS model has been found, which is the zero-order TS model having four bell-shaped membership functions for each input. The training method is based on the Levenberg–Marquardt algorithm with a combination coefficient of 10^{-4}. More detailed description of the learning algorithms and design process for the chosen ANFIS can be found in Bui et al. (forthcoming 2014).

Results and discussion

Although there are different parameters (input variables) that affect the contraction scour, only some are of primary significance. In order to determine the effect of each individual variable, a sensitivity analysis was done. For this purpose, the ANN structure with the best validation performance was used. Table 2 provides a comparison between different ANN models having one of the independent variables removed in each case. It can be seen that the contraction ratio has the most effects on the contraction scour. This is in accordance with the contraction scour formula of Lim and Cheng (1998) who proposed that the equilibrium scour depth is only a function of the ratio of contracted to uncontracted channel width. Another sensitive parameter, the standard deviation of the size distribution of the bed materials, outstood. On the contrary, the median sediment particle size seems to have the least influence on the equilibrium scour depth.

To ensure physical plausibility of the designed ANN model, a sensitivity analysis was carried out, where the contraction ratio and the standard deviation of the size distribution of the bed materials in the test data set were altered and the effect on the modeled scour depth was assessed. The following four scenarios were considered:

- Scenario 1: Contraction ratio increased by 15%, other inputs unchanged;
- Scenario 2: Contraction ratio decreased by 15%, other inputs unchanged;
- Scenario 3: Standard deviation of bed materials increased by 15%, other inputs unchanged; and
- Scenario 4: Standard deviation of bed materials decreased by 15%, other inputs unchanged.

Table 2. Sensitivity analysis of input variables.

	Omission of variable				
	d_m/b_1	$\overline{Fr}$	h_1/b_1	σ_g	b_2/b_1
R	0.958	0.955	0.939	0.906	0.581
RMSE (m)	0.017	0.018	0.019	0.024	0.046
MAE (m)	0.012	0.013	0.014	0.016	0.037

Figure 4 shows the response curves for the effect on the scour depth of changing the contraction ratio ($\overline{b}$) by -15% and $+15\%$ and of changing the standard deviation of the bed materials (σ_g) in the same percentage range (other input variables were unchanged). As expected, by increasing the contraction ratio, the long contraction reduces its equilibrium scour depth, and decreasing the standard deviation of the bed materials increases the equilibrium scour depth. The nonlinearity of the response curves also provides further information; for example, the sensitivity of the equilibrium scour depth to the contraction ratio is much greater than that to the standard deviation of the bed materials. The results of the sensitivity analysis ensured physical plausibility of the designed ANN model.

The curve in Figure 5 shows the MLP's response for a continuous variation of contraction ratios $\overline{b}$ in the range of the whole data (between 0.4 and 0.7). In this case, mean values for the remaining parameters were used: $\overline{d} = 0.0126$ $\overline{h} = 0.171$ $\sigma_g = 2.3$ $\overline{Fr} = 2.2158$. The calculated results repeatedly confirmed the physical plausibility of the designed MLP model: by decreasing the contraction ratio, the long contraction increases the equilibrium scour depth.

Further, it should be emphasized again that the aforementioned empirical equations have been developed principally based on the simplified one-dimensional theory of Straub (1934) and the limited experimental data. Laursen (1963) assumed that the shear stress in the contracted section has reached its critical value at the end of the scouring process in a long contraction under clear-water scour condition. Using Manning's equation for the approach flow and contracted flow combined with the continuity equation, he obtained the clear-water contraction scour formula. Modifying this concept, Richardson and Davis (2001) proposed the clear-water contraction scour equations for homogeneous bed materials where the scour depth depends on the flow discharge, the contraction width, the upstream water depth, and the effective mean bed material size. Komura (1966) emphasized the influence of armoring on live-bed scour depth by arguing that the ratio of the sediment sizes in the approach flow section and contracted section influences the contraction scour depth for large values of the ratio of channel widths and the geometric standard deviation of sediment size distribution.

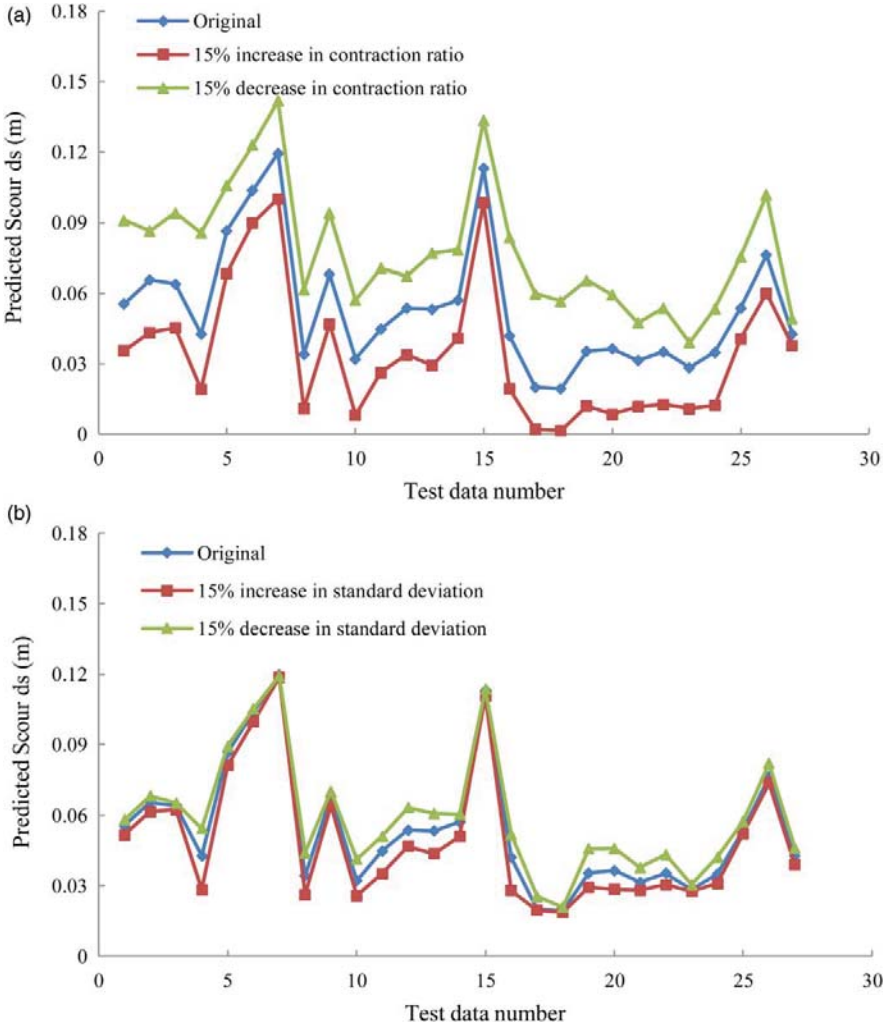

Figure 4. Response curves for the effect of the contraction ratio (a) and the standard deviation of the size distribution of the bed materials (b) on the modeled contraction scour depth.

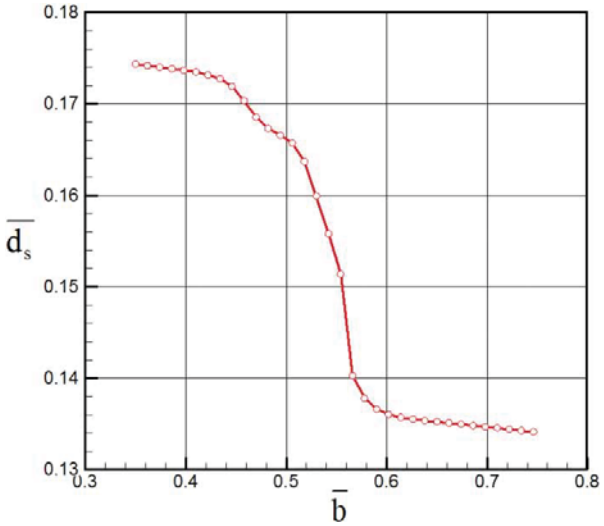

Figure 5. Response of the designed MLP for a continuous variation of contraction ratios.

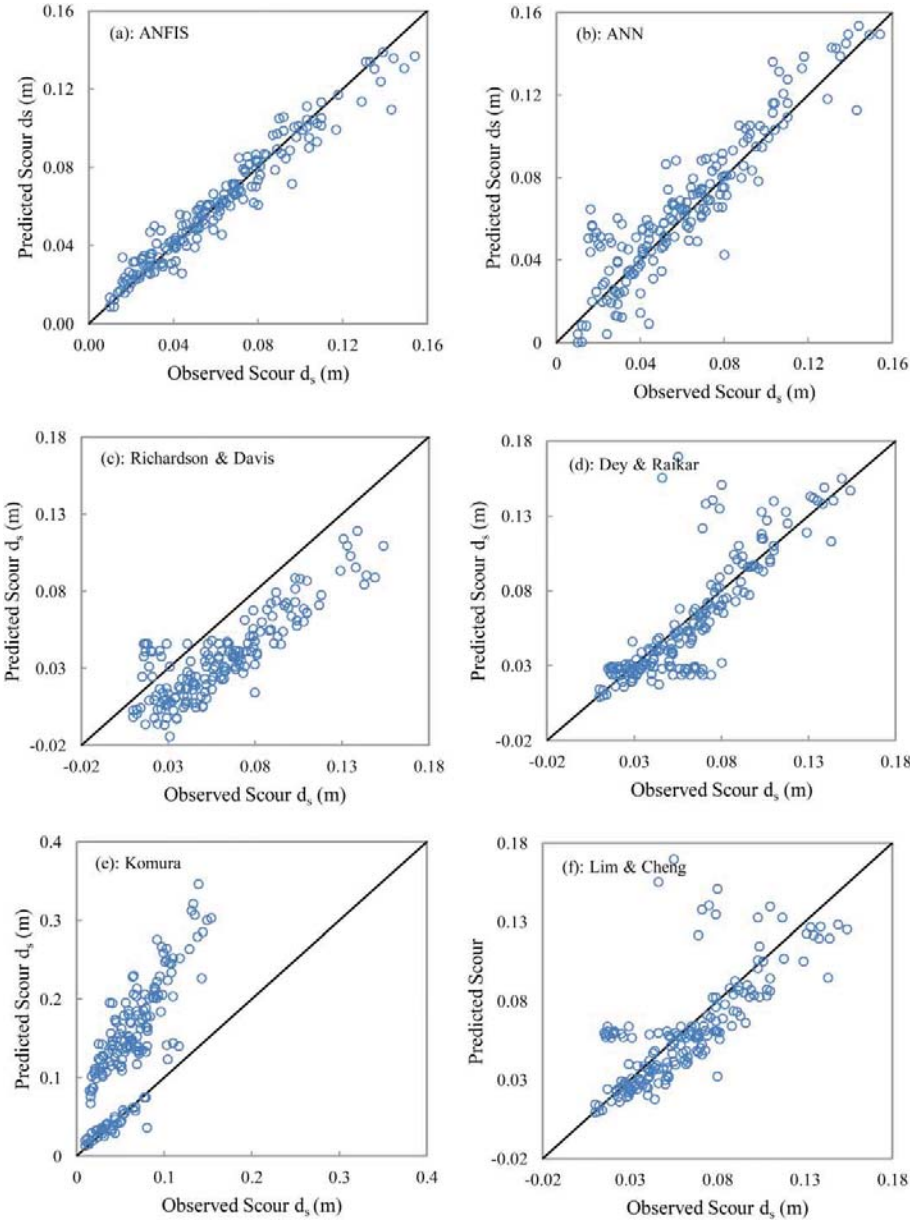

Figure 6. Comparison of the equilibrium scour depths computed using different methods with the experimental data for the whole data set.

He applied dimensional analysis to a series of laboratory experiments on live-bed and clear-water contraction scour in a long contraction and proposed a formula based on his experimental results in which dimensionless scour depth depends on the approach flow Froude number, the ratio of channel widths, and geometric standard deviation of sediment size distribution. Lim and Cheng (1998) derived a long contraction scour formula for live-bed scour along the same lines as that of Gill (1981) using a simple bed-load formula by assuming that sediment transport rate is proportional to excess shear stress. Eventually, they showed that the only solution of the equation was one in which the contraction scour depth depends on the ratio of channel widths alone. In the work of Dey and Raikar (2005), a detailed parametric investigation on scour depth in long contractions for uniform and nonuniform sediments under clear-water scour has been carried out. These own experimental data and the data conducted by other authors have been used to determine a new equation of maximum equilibrium clear-water scour depth. They defined that the characteristic parameters affecting the maximum equilibrium nondimensional scour depth (scour depth – approaching flow depth ratio) are excess approaching flow Froude number, sediment size – approaching flow depth ratio, and channel width ratio. Their results showed a significant effect of sediment with a minimum value of scour

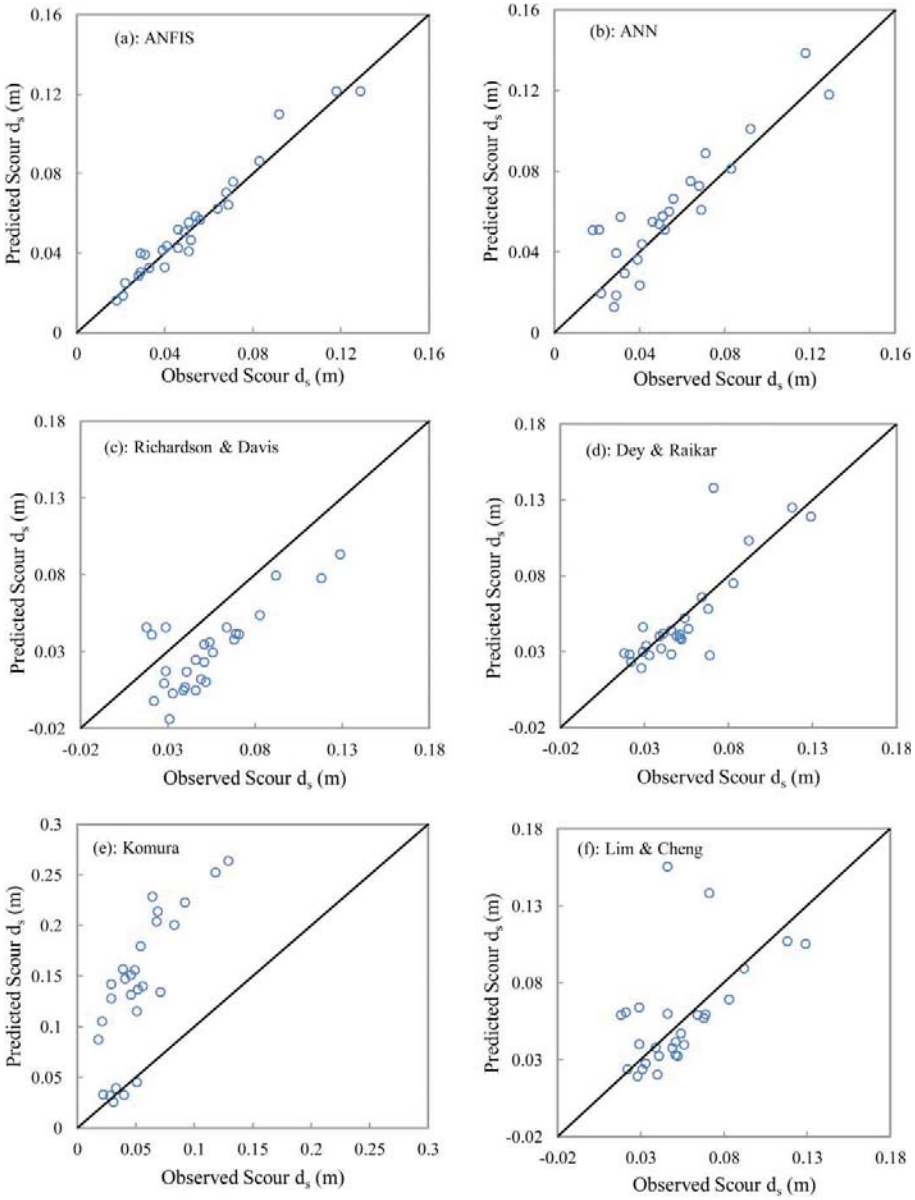

Figure 7. Comparison of the equilibrium scour depths computed using different methods with the experimental data for the test data set.

depth due to armoring given as 25% of the value for uniform sediment. From the aforementioned studies, it is revealed that apart from the work conducted by Dey and Raikar (2005) a detailed investigation describing the effects of various parameters on scour depth in long contractions is inadequate. Also, little attention is paid to study the scour depth in long contractions with nonuniform sediment.

Mohammad and Al-Saffar (2010) applied a MLP–ANN model with six inputs including the median particle diameter, the approaching flow velocity, ratio of the approaching flow velocity to the critical velocity for sediments, the approaching flow depth, the approaching channel width, and the contracted channel width. The output is the equilibrium scour depth. However, the effect of sediment gradation has not been considered in their model. It is not clear whether only uniform sediment data have been used for the development of their model. Their designed MLP model then consists of one hidden layer with 10 neurons. Logistic activation functions are applied for hidden and output layers. Since the information about the designed ANN model as well as about the final equation for scour depth is not given sufficiently in their paper, comparing the performance of their model to that of our model is not possible.

To evaluate the performance of the new data-driven methods in predicting equilibrium scour depth, a comparison between the new models and four of the existing

Table 3. Performance indices of various approaches for the whole data set.

	ANFIS	ANN	Dey and Raikar	Richardson and Davis	Komura	Lim and Cheng
R	0.976	0.965	0.836	0.853	0.790	0.748
RMSE (m)	0.013	0.015	0.035	0.054	0.170	0.048
MAE (m)	0.005	0.006	0.013	0.028	0.084	0.016

Table 4. Performance indices of various methods for the testing data set.

	ANFIS	ANN	Dey and Raikar	Richardson and Davis	Komura	Lim and Cheng
R	0.982	0.966	0.838	0.770	0.784	0.552
RMSE (m)	0.006	0.009	0.017	0.029	0.098	0.030
MAE (m)	0.004	0.007	0.011	0.027	0.085	0.020

formulae, which have been proposed by Komura (1966), Lim and Cheng (1998), Richardson and Davis (2001), and Dey and Raikar (2005), was undertaken using the same 182 cases' observed data set. For this purpose, observed equilibrium scour depth values are plotted against the predicted one. Figure 6 and Table 3 illustrate the correlation for the different contraction scour formulae and the chosen networks with the statistical performance indices between predicted and observed data. Comparing Figure 6(e) with 6(f) and looking at Table 3 again confirm the statement of Legates and McCabe (1999) that the correlation coefficient R alone is unsuitable for model evaluation. It can be seen that the formula of Komura (1966) provided a better correlation coefficient $R = 0.788$, but a worse RMSE $= 0.170$ (m). The corresponding correlation plot in Figure 6(e) shows a principal overestimation up to 200% of the Komura scour formula, whereas for small contraction scour depths the formula underestimates. The correlation plotted for the formula developed by Richardson and Davis (2001) is shown in Figure 6(c). It is apparent that of all the compared equation, it is the most underestimating. Almost all points in the plot lay below the line of perfect agreement in combination with a RMSE value (RMSE $= 0.054$ (m)). Despite its simplicity that the scour depth is only dependent on the contraction ratio of the channel, the formula of Lim and Cheng (1998) has the lower RMSE $= 0.048$ (m). From the corresponding correlation plot in Figure 6(f), again the tendency for underestimating is evident. Furthermore, some outliers can be identified, which result perhaps from neglecting a variable that would represent armoring for nonuniform sediments. Comparing all existing formulae based on the statistical values R, MAE, and RMSE shows that the formula of Dey and Raikar (2005) shows a better performance. Comparing the performance qualities of the contraction scour formulas with those of the chosen ANN and ANFIS reveals that the recommended networks have the highest R and lowest RMSE values. The new models offer improved predictions of scour depth. Applying the whole data set for the best existing method (Dey & Raikar 2005), the RMSE was 0.035 (m), compared to the RMSE of 0.008 (m) for the new ANFIS model. Corresponding values of the correlation coefficient (R) are 0.836 and 0.976.

Figure 7 and Table 4 present a graphical and statistical comparison between different methods based on the test data. Again, it is clear that ANFIS and ANN models provide better predictions than conventional methods.

Conclusion

An ANN and an ANFIS for predicting the equilibrium contraction scour depth have been developed using the data set conducted by different previous investigators for clear-water contraction scours. The optimal ANN model is based on a feed-forward MLP network with one hidden layer and seven hidden neurons using a hyperbolic tangent sigmoidal transfer function. The designed network applies the learning algorithm proposed by Levenberg–Marquardt in batch mode. The optimal ANFIS model is a zero-order TS model having four bell-shaped membership functions for each input with a training method based on the Levenberg–Marquardt algorithm.

The dimensionless equilibrium scour depth is represented by five dimensionless parameters considering the influence of geometric contraction, sediment grain size, approaching flow depth, sediment gradation, and sediment mobility on the degree of contraction scour. The importance of the individual input parameters was tested in a sensitivity analysis, which demonstrated that the contraction ratio is by far the most sensitive parameter for the contraction scour prediction, followed by the geometric standard deviation and the effect of armor layer formation for nonuniform sediment.

The predicted results demonstrate the capacity of the new approaches for the estimation of contraction scour. They indicate that using suitable ANN and ANFIS networks for the scour modeling can lead to higher prediction accuracy than using other existing methods. The errors of the ANFIS model are less than those of the ANN model. However, it is too complicated to obtain a general

ANFIS-based equation for scour depth which may be useful for engineers working in practice.

ANN and ANFIS techniques have some disadvantages. Their ability is limited when the input values in the prediction phase are far from the domain of the training data set. This means that a new input variable not used in the training phase cannot be introduced into the model in the prediction phase. Another disadvantage of ANN and ANFIS models is that their structure is difficult to determine, which can be usually done by a trial-and-error approach. Moreover, by increasing the number of input variables, fuzzy logic algorithms – especially for establishing the rule base – become very much more complicated than ANNs.

Despite the disadvantages mentioned above, the results of the present study demonstrate the simple and effective usage, as well as potential, of the new methods over the traditional ones for predicting contraction scour depths. These simple networks with the appropriate training are able to accurately estimate the scour depth in a given range for the minimum and maximum data used in network training and validation process. Still, an improvement of these networks may be achieved by feeding the networks with new measurements and also by updating the networks for time-dependent contraction scour depth.

Disclosure statement

No potential conflict of interest was reported by the authors.

Notes on contributors

Dr. Minh Duc Bui is currently lecturer and researcher coordinator at the Institute of Hydraulic and Water Resources Engineering in the Technische Universität München (TUM), Munich. He graduated with diploma degree in mathematics from Hanoi University in 1983. He got the doctoral degree in engineering in the University of Karksruhe in 1998.

Keivan Kaveh MSc., studied civil engineering and obtained a master's degree in the School of Civil Engineering, Faculty of Engineering, Semnan University, Iran, in 2011. Since 2013, he is Ph.D. student at the Institute of Hydraulic and Water Resources Engineering, TUM, Munich.

Petr Penz, MSc., studied environmental engineering and obtained a master's degree in TUM, Munich, in 2013. Presently he works at the Bavarian State Ministry for Environment and Consumer Protection, Munich.

Prof. Dr. Peter Rutschmann studied civil engineering with diploma and hold PhD degree at ETH Zurich, in 1979. He was full professor at the Institute for Hydraulic Engineering of the University of Innsbruck (2002–2007). Since 2007, he is full professor and director of the Institute of Hydraulic and Water Resources Engineering, TUM, Munich.

References

Bateni SM, Borghei SM, Jeng DS. 2007. Neural network and neuro-fuzzy assessment for scour depth around bridge piers. Eng Appl Artif Intel. 20:401–414.

Bhattacharya B, Price RK, Solomatine DP. 2007. Machine learning approach to modeling sediment transport. J Hydraul Eng. 133(4):440–450.

Briaud JL, Chen HC, Li Y, Nurtjahyo P, Wang J. 2005. SRICOS-EFA method for contraction scour in fine-grained soils. J Geotech Geoenviron, ASCE. 131:1283–1294.

Bui MD, Kaveh K, Rutschmann P. Forthcoming 2014. Performance analysis of different learning algorithms in an adaptive neuro fuzzy inference system for contraction scour prediction. Int J Sediment Res.

Bui MD, Rodi W. 2008. Numerical simulation of contraction scour in an open laboratory channel. J Hydraul Eng. 134(4):367–377.

Dey S, Raikar RV. 2005. Scour in long contractions. J Hydraul Eng. 131(12):1036–1049.

Gessler J. 1971. Critical shear stress for sediment mixtures. Proceedings of the 14th Congress of International Association for Hydraulic Research, Vol. 3, C1_1-C1_8.

Gill MA. 1981. Bed erosion in rectangular long contraction. J Hydraul Div, ASCE. 107(3):273–284.

Haykin S. 1999. *Neural networks: A comprehensive foundation*. Englewood Cliffs, NJ: Prentice-Hall.

Jang JSR. 1993. Adaptive network based fuzzy inference system: adaptive-network-based fuzzy inference system. IEEE Trans Syst Man Cybern B. 23(3):665–685.

Jang JSR, Sun CT. 1997. *Neuro-fuzzy and soft computing: a computational approach to learning and machine intelligence*. Englewood Cliffs, NJ: Prentice-Hall.

Kaya MD, Hasiloglu AS, Yesilyurt H. 2002. To estimate the design of functional sizes of chairs and desks on the basis of ISO 5970 using adaptive neuro-fuzzy inference system. FSSCIMIE'02, May 29–31.

Kisi O, Dailr AH, Cimen M, Shiri J. 2012. Suspended sediment modeling using genetic programming and soft computing techniques. J Hydrol. 450–451:48–58.

Komura S. 1966. Equilibrium depth of scour in long constrictions. J Hydraul Div, ASCE. 92(5):17–38.

Laursen EM. 1960. Scour at bridge crossings. J Hydraul Eng, ASCE. 86(2):1–54.

Laursen EM. 1963. An analysis of relief bridge scour. J Hydraul Div, ASCE. 89(3):93–118.

Legates DR, McCabe GJJ. 1999. Evaluating the use of "goodness-of-fit" measures in hydrologic and hydroclimatic model validation. Water Resour Res. 35(1):233–241.

Lim SY. 1993. Clear water scour in long contractions. Proc Inst Civil Eng Water Maritime Eng. 101(6):93–98.

Lim SY, Cheng NS. 1998. Scouring in long contractions. J Irrig Drain Eng. 124(5):258–261.

Mohammad JR, Al-Saffar MSA. 2010. Estimation of scour in long contractions using artificial neural networks. J Duhok Univ. 13(1) (Pure and Engineering Sciences): 102–108.

Penz P. 2013. Contraction scour modelling using artificial neural networks [MSc. thesis]. Munich: Technische Universität München.

Raudkivi A, Ettema R. 1982. Stability of armor layers in rivers. J Hydraul Div, ASCE. 108(9):1047–1057.

Richardson EV, Davis SR. 2001. Evaluating scour at bridges. Hydraulic Engineering Circular No. 18. Washington, DC: Federal Highway Administration.

Shahin MA, Maier HR, Jaksa MB. 2002. Predicting settlement of shallow foundations using neural networks. J Geotech Geoenviron Eng, ASCE. 128(9):785–793.

Straub LG. 1934. Effect of channel contraction works upon regimen of movable bed streams. Trans Am Geophys Union. 15(2):454–463.

Takagi T, Sugeno M. 1985. Fuzzy identification of systems and its applications to modeling and control. IEEE Trans Syst Man Cybern. 15:116–132.

Wagner CR, Mueller DS, Parola AC, Hagerty DJ, Benedict ST. 2006. Scour at contracted bridges: Transportation Research Board, National Cooperative Highway Research Program Document 83 (Project 24–14), 299p. Available from: http://onlinepubs.trb.org/onlinepubs/nchrp/nchrp_w83.pdf.

Webby MG. 1984. General scour at contraction. RRU Bulletin 73, National Roads Board, Bridge Design and Research.

Application of artificial neural networks for river regime

M.D. Bui[1], D. Huber[1], K. Kaveh[1], A.M.F. da Silva[2], P. Rutschmann[1]
[1]*Institute of Hydraulic and Water Resources Engineering, Technical University of Munich, Germany*
[2]*Department of Civil Engineering, Queen's University, Kingston, Ontario, Canada*

ABSTRACT: Predicting the geometric characteristics of a regime channel is of utmost importance in the context of river engineering and management, as regime channels require minimum protection and minimum expenses for their maintenance. There are numerous empirical and analytical methods to predict these geometric characteristics. This paper develops and tests an artificial neural network (ANN) as a model to forecast the river regime characteristics. ANN performance is compared against the Thermodynamic Entropy Theory of Yalin and da Silva (2001) and the Stability Theory of Julien and Wargadalam (1995). An improvement in the results of the ANN model has been achieved by distinguishing the input variables into sand and gravel bed materials as well as different discharge groups.

1 INTRODUCTION

An alluvial stream does not accept any channel form provided for it by humans or nature. Instead, it creates a channel of "its own", the so-called stable or regime channel – which, under ideal conditions, does not vary with time. The regime channel can be characterized by three geometric characteristics: the channel width (B), depth (h), and slope (S). A channel at regime state requires minimum protection, and therefore, minimum expenses for its maintenance (Yalin and da Silva, 2001). Since one goal of river engineering is to create streams as stable as possible, knowledge of the regime channel is of utmost importance for the planning, design and management of river works (Singh, 2003). Presently, many empirical methods to predict the regime channel geometric characteristics are available; however, all of them have limitations and restricted ranges of application.

On the other hand, in recent years the methods of artificial neural networks (ANNs) have become increasingly popular in a number of fields including hydraulics. In contrast to most traditional empirical methods, which need prior knowledge about the nature of the relationships among the data, these data driven systems learn from data examples presented to them in order to capture the subtle functional relationships among the data, even if the underlying relationships are unknown or the physical meaning is difficult to explain. Furthermore, these methods do not need to be introduced with an explicit form of the regarded task and additionally have proven to have a high tolerance against data sample errors. These attributes make the utilization of ANN for the calculation of river regime very promising.

The objective of this paper is to introduce an optimal ANN for the determination of regime channel characteristics. The regime channels are assumed to be of the "R-type", as defined by Yalin and da Silva (2001), and thus determined by the bankfull discharge (henceforth denoted by Q) and the grain size D. Use is made of an extensive database, comprised of streams covering a wide range of conditions, including different bed materials and water discharges. The method is assessed by comparing its results with those obtained from the Thermodynamic Entropy Theory of Yalin and da Silva (2001) and the Stability Theory of Julien and Wargadalam (1995).

2 METHODOLOGY

2.1 *Conventional approaches*

The regime theory is based on field experience: an alluvial river is declared to function in regime or stable conditions after a sufficiently long period of observation. In these conditions, the river can transport a certain amount of water and sediment. There are two approaches for the determination of regime channels: empirical and analytical.

The conventional empirical approach relies exclusively on field data. It attempts to establish relationships between the dependent morphological variables and the independent variables of discharge, sediment type and sediment load, strictly by revealing correlations between independent and dependent variables, without any consideration of the underlying physics. Such empirical regime equations are limited in their application and should not be extrapolated beyond the conditions of their database (Davidson and Hey, 2011).

The analytical approach provides a set of reasonable scientific equations and boundary conditions, simultaneously solved to get the desired regime channel

characteristics. The rational equations describe flow and sediment transport processes, or, in the case of extremal hypotheses, express the belief that a stream adjusts its geometry so as to enable the minimization (or maximization) of some energy-related quantity (Bettess and White 1987, Yalin and da Siva 2001). These equations link the morphology to the boundary conditions and explain how the stable state is maintained. Unfortunately, an equation determining the regime width is mostly not available, indicating that there are more unknowns than equations. One way of overcoming this difficulty is to predict channel width by using an empirical equation and then determine mean depth, slope, and velocity by using continuity, flow resistance, and bed-material transport equations (Copeland et al., 2001). In a review of various extremal hypotheses, Bettess and White (1987) compared predicted widths and slopes with associated empirical equations. They concluded that an arbitrary selection of sediment and friction relationships combined with an extremal hypothesis may not necessarily provide satisfactory results.

Julien and Wargadalam (1995) used the concepts of resistance, sediment transport, continuity, and secondary flow to develop a semi-analytical approach. The governing equations were approximated for five hydraulic geometry parameters, namely, channel width, average flow depth, mean flow velocity, channel slope, and Shields parameter, which were written in final forms as power functions of three independent variables: water discharge, median grain size, and either channel friction slope or Shields parameter.

Yalin and da Silva (2001) adopted thermodynamic basis for regime theory. They treated an alluvial stream as an isolated uniform system and explained the meaning of regime channels and the regime channel formation criterion on the basis of the first and second laws of thermodynamics as well as Gibbs' equation. The idea behind this approach is that a channel tends to acquire a regime state when one of the characteristics, being energy-related, trends to be minimal. Thus, the regime flow width, depth and slope can be derived by solving a resistance equation, an equation for the regime width, and the minimum Froude-criterion based on the thermodynamic entropy theory.

A review on various hypotheses that have been proposed for deriving hydraulic geometry relations in river regime theory can be found e.g. in the paper of Singh (2003).

2.2 *ANN approach*

ANN is a simulation method that is inspired by biological nerve system. In practical terms, ANNs are essentially very simple computer programs that can automatically find non-linear relationships in data without any predefined model from knowledge. There are several types of neural networks, which are able to perform various tasks. One of the most popular is the feedforward multi-layer perceptron (MLP) and the only type used in this work.

In a standard MLP, neurons (or nodes) are arranged in layers: an input layer, an output layer and one or more hidden layers. The net is formed by these layers of neurons, and each neuron in a specific layer is connected to neurons in other layers via weighted connections. In a feedforward network there are only weight connections in the forward direction and propagation of the signal is unidirectional without feedback cycles between nodes. Neurons are defined as mathematical expressions that filter the signal through the net. From the connected neurons in the previous layer, an individual neuron receives its weighted inputs, which are usually summed along with a bias unit. The bias unit is used to scale the input to a useful range in order to improve the convergence properties of the training process. The result of this combined summation is passed through a transfer function so as to produce the output of the neuron. This output is then passed through weighted connections to neurons in the next layer, where the process is repeated. MLP networks often have one or more hidden layers of sigmoid neurons followed by an output layer of linear neurons or nodes. The reason for this is that multiple layers of neurons with nonlinear activation functions allow the network to learn nonlinear relationships between input and output vectors.

According to Shahin et al. (2002), the structure and process for neuron *j* of a MLP model with one hidden layer can be illustrated in Figure 1. Input information X_i coming into the model through special, non-processing input nodes *i* is fed to a number of hidden nodes *j*. Each hidden node *j* performs a twofold function: first, it computes a signal I_j from all incoming information using the relation:

$$I_j = \sum_i w_{ji} X_i - b_j \tag{1}$$

where b_j is a threshold value, which is different for each node. Second, it transforms this signal using a non-linear activation function *f*. Any function can act as the activation function but for gradient descent learning methods it must be continuously differentiable. Two popular sigmoidal shaped activation functions are the logistic (logsig)

$$f(I_j) = \frac{1}{1+e^{-I_j}} \tag{2}$$

and the hyperbolic tangent (tansig)

$$f(I_j) = \frac{e^{I_j} - e^{-I_j}}{e^{I_j} + e^{-I_j}} \tag{3}$$

The outgoing signal Z_j is then fed to the subsequent layer of nodes (which can be another hidden layer or an output layer) and transformed in the same way as described above for input nodes.

The transformation of the input variables array X into the corresponding output variables array Y can be expressed synthetically as follows:

$$Y = F\left(X, W, b, f, K, N_k\right) \tag{4}$$

where the weights W, threshold b, type of the activation function f, number of hidden layers K, and number of hidden nodes N_k for each hidden layer k will be defined by a training process.

Training (or learning) is the search for a set of weights and biases that best match the inputs onto the output for the patterns in the historical database. A trained response is achieved by changing the connection weights and biases in the network according to an error minimization criterion. In other words, learning algorithms decide how the weights in configured ANN architectures are adjusted in order to minimize the output errors in a particular data set. A validation process can be used during training in order to prevent overfitting.

Once the network has been trained to simulate the best response to input data, the configuration of the network is fixed and a test process is conducted to evaluate the performance of the MLP network as a predictive tool. At present, there are numerous learning algorithms available for different network configurations and applications. One of the most widely used algorithms for training a MLP is the Levenberg–Marquardt algorithm with the mean squared error (MSE) being used as an error function. MSE computes the similarity of the prediction compared to actual values. This tool is efficient at assessing undesirably large differences.

Consider the MLP network shown in Figure 1. The running of the network training can be viewed as finding a set of weights that minimized the error (ε_i) for all samples in the training set (L). If the performances function is a sum of squares of the errors as:

$$E(W) = \frac{1}{2}\sum_{i=1}^{mL}\left(d_i - y_i\right)^2 = \frac{1}{2}\sum_{i=1}^{mL}\varepsilon_i^2 \tag{5}$$

where m is the number of output layer neurons, y_i is the network output, and d_i is the desired output. When training with the Levenberg-Marquardt algorithm, the changing of weights ΔW can be computed as follows

$$\Delta(W) = -\left[J_k^T J_k + \mu_k I\right]^{-1} J_k^T \varepsilon_k \tag{6}$$

where J is the Jacobian matrix, I is the identify matrix, $\boldsymbol{\mu}$ is the Marquardt parameter which is to be updated using the decay rate β according to the outcome. Depending on the magnitude of β, the method transits smoothly between two extremes: the Gauss-Newton method (when $\beta \to 0$) and gradient descent method (when $\beta \to \infty$). Usually, the Gauss-Newton method is more efficient but less stable and the gradient descent method more stable but less efficient. By properly setting the value of β, the Levenberg-Marquardt method can be efficient as well as stable. Normally, the damping factor β is adjusted at each iteration. If reduction of the error function E is rapid, a smaller value can be used, bringing the algorithm closer to the Gauss–Newton algorithm, whereas if an iteration gives insufficient reduction in the residual, β can be increased, giving a step closer to the gradient descent direction. A detailed description of this algorithm can be found in Jang and Mizutani (1996).

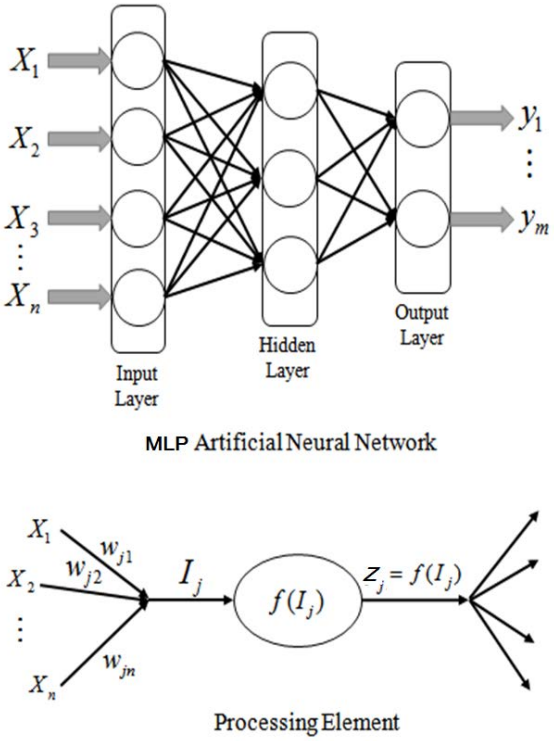

Figure 1. Typical structure and operation of an ANN model with one hidden layer (Ij = activation level of node j; w_{ji} = connection weight between nodes j and i; X_i = input from node i; Z_j = output of node j; and $f(I_j)$ = activation or transfer function).

In the present work, the Levenberg–Marquardt algorithm is also employed for its speed and effectiveness. Besides, an early stopping algorithm with the Nguyen–Widrow initialization for weights are utilized.

2.3 *ANN model setup for river regime*

Based on 509 observations, we design multilayer perceptron (MLP) artificial neural networks for studying river regime. The observed data have been collected by different authors (s. Huber, 2014).

The ranges of the different parameters are listed in Table 1. They also represent the applicable domain of the ANN models. The data set has been divided randomly into three subsets, whereby the largest amount of data (70%) is added randomly to the training subset. The remaining data set samples are used for testing (15%) and validating the networks (15%).

The training subset is used to design the weights. The validation subset is used to test the accuracy of training while training is ongoing. After each epoch, the validation subset acts as a barometer for determining when the accuracy of the MLP is at an acceptable level. After the network is considered optimally trained, the test subset is used to verify its performance. To achieve a better performance and faster training of the network, all data were normalized. The range after the data pre-processing is chosen to be between minus one and one.

Due to the different behavior of sand- and gravel-bed channels regarding the grain size a distinction is necessary. The sand-grain-size is denoted by D_1 and the gravel-grain-size by D_2. Further, as shown in Table 1, the difference between maximum and minimum water discharge as well as the variation of its observation accuracy is very large. Therefore, in order to design the optimal ANN model, we divide the dataset into two different groups concerning the value of water discharge, namely group-1 consisting of the data with water discharge less than 2 m^3/s (Q_1) and group-2 with the rest of the dataset (Q_2).

Table 1. Range of parameters

Limit	h(m)	B(m)	S(-)	D(m)	Q(m^3/s)
lower	0.018	0.3475	35×10^{-6}	55×10^{-6}	0.0037
upper	20.12	1381.40	0.06	0.1758	42468.9

In the systems, the common input variables are the discharge (Q_1, Q_2) and median grain size (D_1, D_2), the output variables are the channel width (B), depth (h) and slope (S).

The network architectures are optimized by analyzing the capability and accuracy of numerous model architectures. To evaluate the prediction qualities of the designed networks, a comparative study is carried out for these models by evaluating several statistical parameters that describe the errors associated with the model in terms of statistical measures of goodness-of-fit between the observed and estimated geometric parameters. Performances of models are evaluated resorting to the correlation coefficient (R), and the root mean square error (RMSE). R expresses the degree of similarity between predicted and actual values, with R values close to 1 indicating predicted and actual values as very similar. RMSE computes the square error of the prediction compared to actual values and computes the square root of the summation value. The RMSE is thus the average distance of a data point from the fitted line measured along a vertical line. This tool is efficient at assessing undesirably large differences. Low RMSE values indicate high confidence in model-predicted values. In brief, the model predictions are optimal if R is found to be close to one, and RMSE are close to zero.

3 MODEL RESULTS

Since the appropriate number of hidden layers and dependent nodes as well as the appropriate activation functions for the model is not known, a trial-and-error method was used to find the best network's configuration. An optimal architecture was determined by varying the number of hidden layers and neurons, and based upon minimizing the difference among the neural network predicted values and the desired outputs. The training of the neural network models was stopped when either the acceptable level of error was achieved or the number of iterations exceeded a prescribed value. The neural network model configuration that minimized the RMSE and optimized R was selected as the optimum and the whole analysis was repeated several times. The ANN architecture was modified by changing the number of hidden layers and its neurons, of the initial weights, as well as the type of input and output functions. Each modification was tested with one hundred trials, which served as the basis for performance assessment of mean values. In order to compare these mean values, different modified architectures were evaluated.

After extensive trial-and-error processes, an optimal ANN for all geometric parameters was found with the simplest multilayer feed-forward network containing only one hidden layer. For regime slope the network with four hidden neurons and log-sigmoid transfer function performs better than the alternatives. The networks using hyperbolic tangent transfer function with three and five hidden neurons were selected respectively for regime flow width and depth. The values of the weights and biases have been specified after a successful learning and validating process. They represent the stored knowledge of the ANN for river regime characteristics modeling, which are separated and defined in one input weight matrix IW, one hidden-layer weight matrix LW, one bias vector b and one bias value c for each geometric characteristic. The values of these vectors and matrices can be found in Table 2. Finally, we received the following equations:

- for regime flow width

$$B = LW^{B} \times \text{tansig}\left(IW^{B} \times \begin{bmatrix} Q_1 \\ Q_2 \\ D_1 \\ D_2 \end{bmatrix} + \vec{b}^{B} \right) + c^{B}$$

- for regime flow depth

$$h = LW^h \times \text{tansig}\left(IW^h \times \begin{bmatrix} Q_1 \\ Q_2 \\ D_1 \\ D_2 \\ B \end{bmatrix} + \vec{b}^h \right) + c^h$$

- for regime slope

$$S = LW^S \times \text{logsig}\left(IW^S \times \begin{bmatrix} Q_1 \\ Q_2 \\ D_1 \\ D_2 \\ B \\ h \end{bmatrix} + \vec{b}^S \right) + c^S$$

To evaluate the performance of the ANN method in predicting river regime, a comparison between the new model and two of the existing approaches, namely those by Yalin and da Silva (2001), and Julien and Wargadalam (1995), was undertaken using the same observed data set. For this purpose, observed geometric parameter values are plotted against the predicted ones. Figures 2-4 and Table 3 illustrate the correlation for the different methods and the chosen ANN with the statistical performance indices between predicted and observed data.

These plots contain the points ranging from fine sand to gravel and for the whole discharge range. It can be seen in Figure 2 (results of the ANN model) that almost all points in the plot lie near the line of perfect agreement.

Comparing two existing approaches based on the statistical values R and RMSE shows that the formulae of Yalin and da Silva (2001) performs better. Comparing the performance qualities of the channel regime formulas with those of the chosen ANN reveals that the recommended network has the highest R and lowest RMSE values. The new model offers improved predictions of regime flow width, regime flow depth and regime slope. Applying the whole data set for the best existing method (Yalin and da Silva, 2001), the RMSE values were 37.9 (m) for regime flow width, 1.2 (m) for regime flow depth and 0.0053 for regime slope, compared to the RMSE of 17.7 (m), 0.3 (m) and 0.0019 for the new ANN model. Corresponding values of the correlation coefficient (R) are (0.935, 0.897, 0.866) and (0.990, 0.970, 0.929). It is clear that ANN model provides better predictions than the two conventional methods under consideration.

Table 2. Values of weight matrices and biases

1. Width

IW^B			
2.6327	1.4804	2.0225	0.8001
-1.0993	0.3084	-0.3891	-11.2784
-1.8314	0.4307	-0.6335	1.2994

b^B
-5.2570
-0.9797
-0.8232

LW^B		
0.9812	-1.3047	0.7187

c^B
0.4983

2. Depth

IW^h				
-0.4594	-3.5012	-0.9682	-4.1823	-14.9311
0.0933	4.8028	0.1385	-0.6239	4.4082
-0.4844	3.4161	-0.5985	7.2029	1.1162
1.8294	-2.8268	-5.5373	5.9407	-0.9678
1.7722	2.1540	-0.7601	-1.4467	0.6633

b^h
-1.5036
1.1708
1.1566
-0.7627
1.6919

LW^h				
-3.6283	-2.4068	1.7721	0.2590	-2.3036

c^h
-0.4131

3. Slope

IW^S					
11.6941	-10.0254	12.8639	3.9292	-2.2914	1.6707
4.7240	0.7294	4.7956	1.9810	-4.4402	1.2225
42.8973	-0.4062	-3.9882	-8.7085	21.3059	75.8515
-3.3486	5.6306	5.3187	5.7861	8.0982	-10.8346

LW^S			
-0.7132	2.3945	-0.8971	-6.9980

b^S
-9.9386
-5.4758
0.5517
-10.5947

c^S
0.8905

Table 3. Performance indices of various methods for the testing data set

		B[m]	h[m]	S[-]
ANN	**RMSE**	17.7	0.3	0.0019
	R	0.990	0.970	0.929
Yalin & da Silva	**RMSE**	37.9	1.2	0.0053
	R	0.935	0.897	0.866
Julien & Wargadalam	**RMSE**	37.2	2.5	0.0050
	R	0.930	0.886	0.842

4 REMARKS

An alternative method to the conventional approaches to predicting river regime is introduced in this study. The method is based on multilayer perceptron feedforward ANN. The observation data of others were used as training, validating and testing sets in order to obtain the regime characteristics functions of the relevant parameters. Explicit neural networks formulation have been developed using sigmoidal shaped activation functions and optimal weights obtained from a training process.

The new ANN model is found to be capable of predicting channel regime characteristics in a range given for the minimum and maximum data used in network training and validation process. The estimations by the ANN model were clearly better than those of two conventional approaches, with lower error RMSE and higher correlation coefficient R.

An ANN is sometimes described as the ultimate black box modeling approach, which represents the physical phenomena through a series of weights and response functions. However, if the architecture is simple enough, it is possible to extract analytical equations that represent the ANN process. These equations may provide some insight into the important parameters governing the channel regime. The analytical equations obtained by the ANN can also easily be applied for estimating the regime characteristics in other hydro-morphological conditions.

REFERENCES

Chang H. (1998): "Fluvial Processes in River Engineering", John Wiley and Sons, New York.

Copeland, R. R., McComas, D. N., Thorne, C. R., Soar, P. J., and Jonas, M. M. (2001). "Hydraulic design of stream restoration projects", Coastal and Hydraulics Laboratory, U.S. Army Engineer Research and Development Center, Vicksburg, MS.

Bettess, R., and White, W. R. (1987): "Extremal hypotheses applied to river regime", in: Sediment transport in gravel-bed rivers, Wiley, Chichester, UK, 767–789.

Davidson, S. and Hey, R. (2011): "Regime equations for natural meandering cobble- and gravel-bed rivers", Journal of Hydraulic Engineering, 137(9), 894-910.

Huber, D. (2014): "Data Driven Approaches to Predicting the Morphology of Alluvial Rivers", MSc. Thesis, Technische Universität München.

Jang, J.S.R., Mizutani, E. (1996). Levenberg-Marquardt method for ANFIS learning. In: Fuzzy Information Processing Society. NAFIPS. Biennial Conference of the North American. Proc. IEEE, pp. 87-91.

Julien, P. Y. and Wargadalam, J. (1995): "Alluvial channel geometry: Theory and application", Journal of Hydraulic Engineering, 121(4), 312–325.

Shahin, M. A., Maier, H. R., and Jaksa, M. B. (2002): "Predicting settlement of shallow foundations using neural networks", Journal of Geotechnical & Geoenvironmental Engineering, ASCE, 128(9), 785-793.

Singh, V. P. (2003): "On the theories of hydraulic geometry", Int. J. Sediment Res., 18(3), 196-218.

White W. R., Bettess R. and Paris E. (1982): "Analytical Approach to River Regime", Journal of the Hydraulic Division, ASCE, 108(10), 1179-1193.

Yalin, M.S., and da Silva, A.M.F. (2001): Fluvial Processes. IAHR Monograph, Delft, the Netherlands.

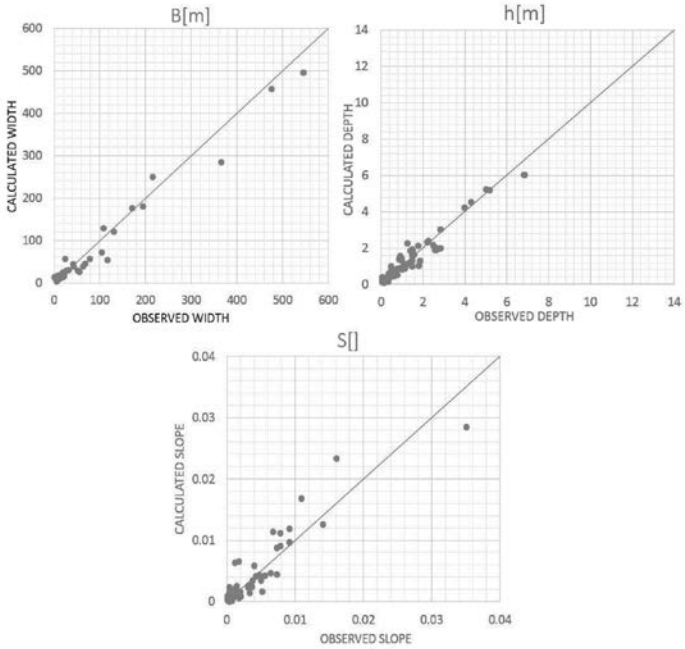

Figure 2. Comparison of the geometric characteristics computed using ANN method with the experimental data for the testing data set.

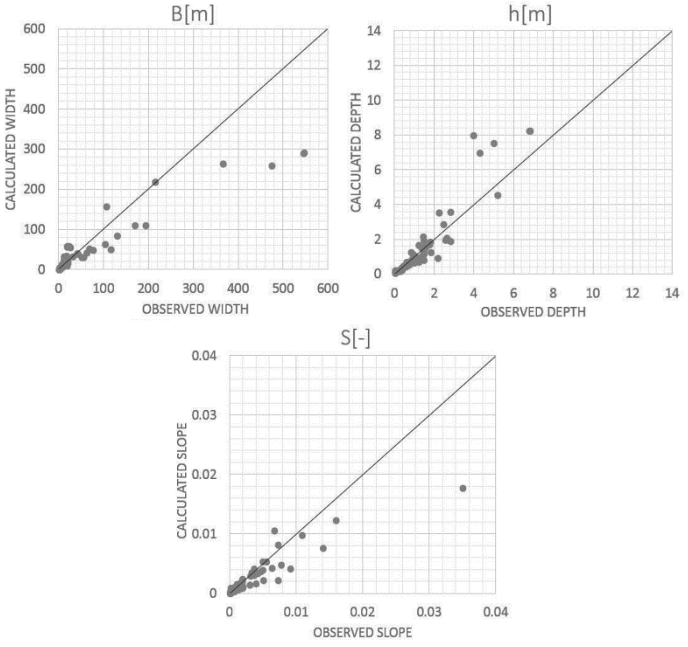

Figure 3. Comparison of the geometric characteristics computed using the method of Yalin and da Silva (2001) with the experimental data for the testing data set.

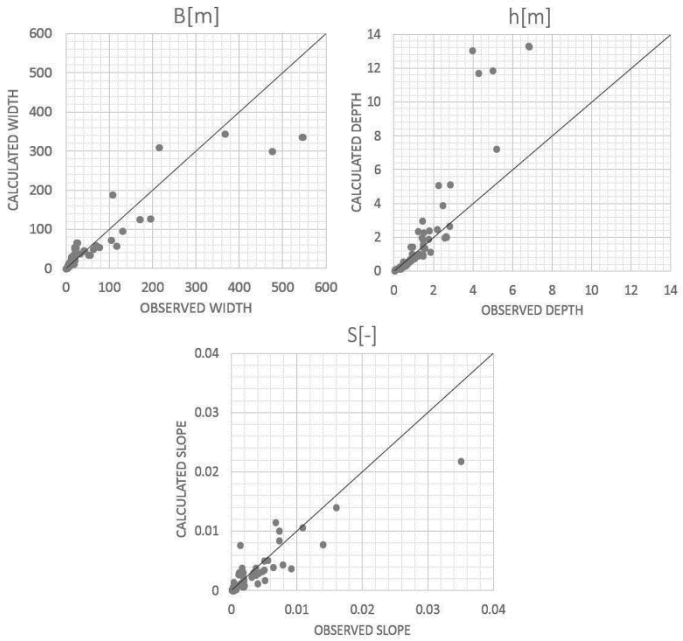

Figure 4. Comparison of the geometric characteristics computed using the method of Julien and Wargadalam (1995) with the experimental data for the testing data set.

International Journal of Sediment Research 32 (2017) 340–350

Contents lists available at ScienceDirect

International Journal of Sediment Research

journal homepage: www.elsevier.com/locate/ijsrc

Original Research

A comparative study of three different learning algorithms applied to ANFIS for predicting daily suspended sediment concentration

Keivan Kaveh *, Minh Duc Bui, Peter Rutschmann

Department of hydraulic and water resource engineering/School of civil engineering, Technische Universität München (TUM), Munich, Germany

ARTICLE INFO

Article history:
Received 17 June 2014
Received in revised form
24 October 2016
Accepted 10 March 2017
Available online 3 April 2017

Keywords:
Fuzzy Inference System
Hybrid learning rule
Levenberg-Marquardt algorithm
Schuylkill river
Suspended sediments

ABSTRACT

The modeling and prediction of suspended sediment in a river are key elements in global water recourses and environment policy and management. In the present study, an Adaptive Neuro-Fuzzy Inference System model trained with the Levenberg-Marquardt learning algorithm is considered for time series modeling of suspended sediment concentration in a river. The model is trained and validated using daily river discharge and suspended sediment concentration data from the Schuylkill River in the United States. The results of the proposed method are evaluated and compared with similar networks trained with the common Hybrid and Back-Propagation algorithms, which are widely used in the literature for prediction of suspended sediment concentration. Obtained results demonstrate that models trained with the Hybrid and Levenberg-Marquardt algorithms are comparable in terms of prediction accuracy. However, the networks trained with the Levenberg-Marquardt algorithm perform better than those trained with the Hybrid approach.

1. Introduction

The need for accurate modeling of suspended sediment has rapidly grown during recent decades in water resources and environmental engineering. Suspended load refers to the sediment that is lifted by the upward components of turbulent currents and remains in suspension for an appreciable length of time. In recent decades, numerous studies have been done on the modeling of sediment transport processes. However, due to the large number of difficulties to measure parameters involved in this phenomenon, the theoretical governing equations may not be of much advantage in gaining knowledge on the overall process. Studies have been done to reduce the complexities of the problem in terms of developing practical techniques that do not require dwell on algorithms and/or theory. Among such techniques, classical time series models, such as Multiple Linear Regression (MLR: an approach for modeling the relation between a scalar dependent variable and one or more explanatory variables) and Auto Regressive Integrated Moving Average (ARIMA), are widely used for hydrological time series forecasting (Salas, 1980). However, these models are basically linear models assuming that data are stationary, and these models have a limited ability to capture nonlinearities in hydrological and environmental data. In recent years, the use of artificial intelligence approaches is increasing due to their capability. Artificial Neural Networks (ANN) has been successfully applied in a number of diverse fields including water resources. Nagy et al. (2002) developed an ANN model to estimate Suspended Sediment Concentration (SSC) in rivers, achieved by training the ANN model to extrapolate several stream data collected from reliable sources. The network was set up using several parameters, such as Froude number, stream width ratio, mobility number, and Reynolds number, as the input pattern and the SSC as the output pattern. Raghuwanshi et al. (2006) proposed an ANN model for runoff and sediment yield modeling in the Nagwan watershed in India. A five-year data set was used for training and a two-year data set was considered for testing the model. Linear regression based daily and weekly runoff and sediment yield prediction models were also developed using the previously mentioned data set and were tested using the testing data set. The ANN model performed better than the linear regression model in predicting both runoff and sediment yield on daily and weekly simulation scales. Zhu et al. (2007) proposed an ANN model for simulating the monthly suspended sediment flux in the Longchuanjiang River in China, whereby suspended sediment flux was related to the average rainfall, temperature, rainfall intensity, and flow discharge. Results illustrated that the ANN model is capable of simulating monthly suspended sediment flux with fairly good

* Corresponding author.
E-mail addresses: Keivan.kaveh@tum.de (K. Kaveh), bui@tum.de (M. Duc Bui), p.rutschmann@tum.de (P. Rutschmann).

http://dx.doi.org/10.1016/j.ijsrc.2017.03.007
1001-6279/

Nomenclature

x_{in}	rescaled value of variable (dimensionless)
x_i	original value of variable (dimensionless)
$x_{i\ min}$	minimum of variable i (dimensionless)
$x_{i\ max}$	maximum of variable i (dimensionless)
Q_t	river discharge at time t ($m^3\ s^{-1}$)
SSC_t	suspended sediment concentration at time t ($mg\ L^{-1}$)
O_i^1	output of the ith node in the first layer of the ANFIS model (dimensionless)
x	input to node i (dimensionless)
a_i, c_i, N_i	adaptable variables known as premise parameters (dimensionless)
O_i^2	output of the ith node in the second layer of the ANFIS model (dimensionless)
w_i	Multiplication of the incoming signals (dimensionless)
O_i^3	output of the ith node in the third layer of the ANFIS model (dimensionless)
$\overline{w}_i$	normalized firing strengths (dimensionless)
O_i^4	output of the ith node in the fourth layer of the ANFIS model (dimensionless)
p_i, q_i, r_i	consequence parameters (dimensionless)
O_1^5	ANFIS output (dimensionless)
$\mu(x)$	membership function (dimensionless)
f_i	first-order Sugeno's system function (dimensionless)
$\mathbf{z}$	input vector (dimensionless)
$\boldsymbol{\theta}$	parameter vector (dimensionless)
y	model's (scalar) output (dimensionless)
t_p	target vector (dimensionless)
$E(\boldsymbol{\theta})$	objective function (dimensionless)
E_{max}	maximum acceptable error
$\Delta\mathbf{y}$	error vector (dimensionless)
A	Jacobean matrix (dimensionless)
I	identity matrix (dimensionless)
λ	combination coefficient (dimensionless)
R^2	coefficient of determination (dimensionless)
RMSE	root mean square error (dimensionless)
MAE	mean absolute error (dimensionless)
MAPE	mean absolute percentage error
NDEI	non-dimensional error index
$SSC_{(measured)}$	measured suspended sediment concentration ($mg\ L^{-1}$)
$SSC_{(predicted)}$	predicted suspended sediment concentration using the ANFIS model ($mg\ L^{-1}$)
n	number of data points (dimensionless)
SSL	suspended sediment load (ton)

accuracy considering proper variables and their correlation to the previous month on the suspended sediment flux.

In spite of the suitable flexibility of ANN in modeling hydrologic time series, sometimes if may be difficult to train an ANN when signal fluctuations are highly non-stationary and the physical hydrologic process operates under a large range of scales varying from one day to several decades. In such an uncertain situation, the Fuzzy Inference System (FIS) may be applied in the estimation of uncertainties in the real situations. Developing Hybrids of an ANN and a FIS is a current research focus, which can make use of the advantages of both ANN and FIS, these Hybrids are called Neuro-Fuzzy (NF) systems. NF systems are capable of capturing the benefits of both these techniques in a single framework and have been applied to a number of problems in water resources and environmental engineering, including ecological status simulation in surface waters (Ocampo-Duque et al., 2007), as well as river flow modeling (Zounemat-Kermani & Teshnehlab, 2008). There are few studies of the application of fuzzy logic and NF algorithms in prediction of sediment transport. Kisi et al. (2009) studied the accuracy of an adaptive neuro-fuzzy computing technique for monthly suspended sediment prediction at the Kuylus and Salur Koprusu stations in the Kizilirmak Basin in Turkey. The results of their study illustrated that the NF algorithm provided better performance than the ANN and Sediment Rating Curve (SRC) models. Rajaee et al. (2009) studied ANN, NF, MLR, and SRC models for daily simulation of SSC for two hydrometry stations. The models were trained using daily river discharge and SSC data for the Little Black River and Salt River gauging stations in the USA. Comparison of the models' results indicated that the NF model has more ability in predicting SSC in comparison to other methods.

Several papers have been published that use the Levenberg-Marquardt algorithm to train an ANN for SSC prediction (Kisi, 2004; Rajaee et al., 2009). However, to the knowledge of the authors, no work has been reported in the literature that applies the Levenberg-Marquardt (LM) learning algorithm (Jang & Mizutani, 1996) to an Adaptive Neuro-Fuzzy Inference System (ANFIS) model for prediction of daily SSC. Therefore, the main objective of this paper is to investigate capability and accuracy of ANFIS model trained with the LM algorithm in SSC estimation. Since the MATLAB program supports only the common Hybrid and Back-Propagation algorithms for ANFIS, a computer program system written in the FORTRAN language has been developed for the LM algorithm.

2. Data and methods

Data obtained from the Schuylkill River gauging station at Manayunk, Philadelphia, PA (Station No: 01473800, Basin Area = 4740 km^2, Latitude: 40° 01'41" N and Longitude: 075° 13'44" W) operated by the U.S. Geological Survey (USGS), was used to train and test all the models developed in this study. For this station, daily time series of river discharge (Q_t) and suspended sediment concentration (SSC_t) were downloaded from the web server of the USGS (http://co.water.usgs.gov/sediment/seddatabase.cfm).

Three subsets of the data -for training, validation and testing- are required to build the model. To achieve this, the data from January 1, 1949 to December 31, 1953 (83% of total data) were used for training and validation, and the data from January 1, 1954 to December 31, 1954 (17% of total data) were used as the testing set. Fig. 1 shows the time series of data related to daily flow discharge and suspended sediment concentration. The statistical analysis for training, validation, testing, and all data is listed in Table 1 which includes the minimum, maximum, mean, standard deviation (S_d), skewness coefficient (C_s), and autocorrelations from 1 day lag to 3 day lag (R_1, R_2, and R_3). It should be noted that data driven methods (e.g., ANN or ANFIS) perform best when they do not extrapolate beyond the range of data used for model training and the extreme values of the available data must be included in the training set. It can be seen from Table 1 that the extreme values of Q and SSC are in the range of the training set. Skewness coefficients are low for all data sets. This is appropriate for modeling, because a high skewness coefficient has a considerable negative effect on model performance (Altun et al., 2007). At this river station, flow discharge (Q) is highly autocorrelated while the autocorrelation coefficient for SSC is lower. In general, this table shows relatively similar statistical characteristics between the data sets, especially the validation and testing sets in terms of autocorrelation coefficients.

The correlation coefficients between observed suspended sediment concentration and river discharge time series are calculated in order to choose suitable input patterns for ANFIS models. The results are listed in Table 2. It is obvious that SSC_t has relatively higher linear correlations with Q_t, Q_{t-1}, Q_{t-2}, SSC_{t-1}, and SSC_{t-2}. The original data sets consist of different variables with different physical meanings and units, and, thus, their ranges are highly variable. To ensure that each variable is treated equally in a model and to eliminate their dimensions, all variables are preprocessed by scaling them between 0 and 1. The following simple linear mapping of the variables is most commonly used for this purpose. Input and output variables for the present study are rescaled using this formula.

$$x_{in} = \frac{x_i - x_{i\ \min}}{x_{i\ \max} - x_{i\ \min}} \quad (1)$$

where x_{in} is the rescaled value of variable i, x_i is the original value, and $x_{i\ \min}$ and $x_{i\ \max}$ are the minimum and maximum of variable i, respectively.

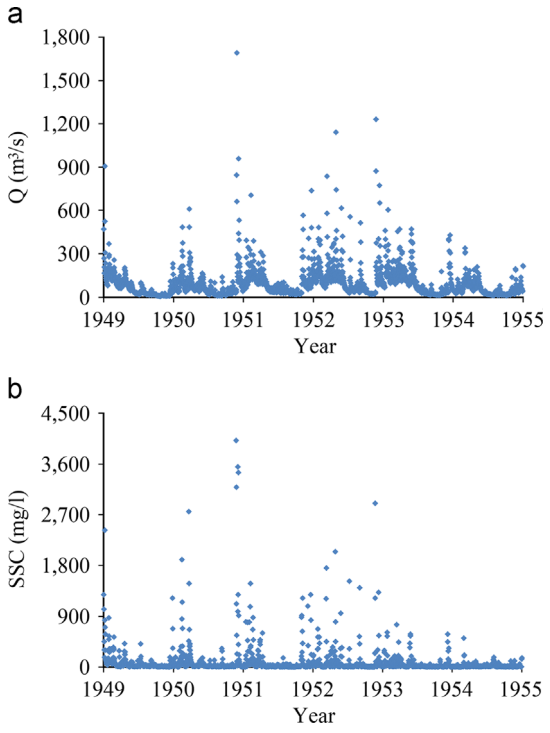

Fig. 1. River discharge and SSC time series.

2.1. Adaptive neuro-fuzzy inference system

A basic ANFIS introduced by Jang (1993) is illustrated in Fig. 2. An ANFIS is a network structure consisting of a number of nodes connected through directional links. Each node is characterized by a node function with fixed or adjustable parameters.

The learning or training phase of a neural network is a process to determine parameter values to sufficiently fit the training data. The basic learning rule is the well-known, Back-Propagation algorithm which seeks to minimize some measure of error, usually sum of squared differences between network's outputs and desired outputs, i.e. the Sum of Squared Errors, SSE (Kaya et al., 2002). Depending on the types of inference operations upon if–then rules, most fuzzy inference systems can be classified into three types: Mamdani's system, Sugeno's system, and Tsukamoto's system. Mamdani's system is the most commonly used, while Sugeno's system is more compact and computationally efficient. The output from Sugeno's system is crisp, so, without the time consuming and mathematically intractable defuzzification operation, it is by far the most popular candidate for sample-data based fuzzy modeling, and it lends itself to the use of adaptive techniques (Takagi & Sugeno, 1985). In a first-order Sugeno system, a typical rule set with two fuzzy IF/THEN rules can be expressed as (Sayed et al., 2003):

$$\text{Rule } 1: \text{ If } x \text{ is } A_1 \text{ and } y \text{ is } B_1, \text{ then } f_1 = p_1 x + q_1 y + r_1 \quad (2)$$

Table 1
Statistical analysis for training, validation, testing, and all data sets.

Statistical parameters	Training set		Validation set		Testing set		All data	
	Q (m^3/s)	SSC (mg/L)	Q (m^3/s)	SSC (mg/L)	Q (m^3/s)	SSC (mg/L)	Q (m^3/s)	SSC (mg/L)
Min	5.38	1	14.5	3	9.85	2	5.38	1
Max	1690	4010	603	750	337	508	1690	4010
Mean	95.964	92.444	107.378	43.994	52.312	21.454	90.622	72.555
S_d	120.878	292.742	100.893	94.448	47.733	37.126	110.084	244.290
C_s	4.847	7.569	1.623	4.557	2.362	7.695	4.656	8.949
R_1	0.733	0.535	0.836	0.522	0.841	0.570	0.758	0.542
R_2	0.474	0.236	0.676	0.214	0.678	0.366	0.522	0.247
R_3	0.376	0.196	0.624	0.213	0.576	0.167	0.433	0.208

Table 2
The correlation coefficients between observed SSC_t and Q_t for all data.

Parameter	Q_t	Q_{t-1}	Q_{t-2}	Q_{t-3}	Q_{t-4}	SSC_{t-1}	SSC_{t-2}	SSC_{t-3}	SSC_{t-4}	SSC_t
Q_t	1	0.7578	0.5224	0.4334	0.3852	0.6081	0.3355	0.2507	0.2150	0.7929
Q_{t-1}		1	0.7577	0.5229	0.4336	0.7930	0.6082	0.3357	0.2510	0.4373
Q_{t-2}			1	0.7584	0.5235	0.4375	0.7932	0.6082	0.3364	0.2219
Q_{t-3}				1	0.7584	0.2225	0.4382	0.7929	0.6081	0.1721
Q_{t-4}					1	0.1732	0.2243	0.4416	0.7941	0.1134
SSC_{t-1}						1	0.5375	0.2452	0.2082	0.5372
SSC_{t-2}							1	0.5381	0.2472	0.2443
SSC_{t-3}								1	0.5420	0.2072
SSC_{t-4}									1	0.1322
SSC_t										1

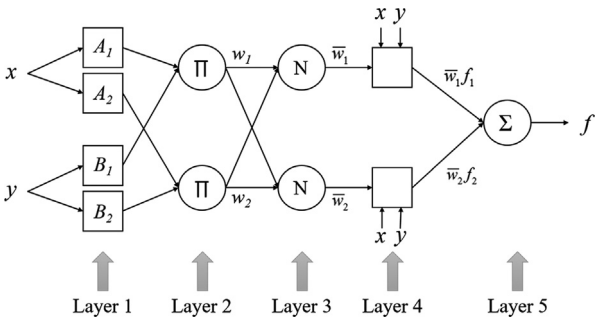

Fig. 2. ANFIS architecture Sugeno fuzzy model for two inputs with two rules.

$$\text{Rule } 2: \text{ If } x \text{ is } A_2 \text{ and } y \text{ is } B_2, \text{ then } f_2 = p_2x + q_2y + r_2 \tag{3}$$

Layer 1. Each node in this layer produces membership grades of an input variable. The output of the ith node in layer l is denoted as O_i^1. Assuming a generalized bell function as the membership function, the output O_i^1 can be computed as:

$$O_i^1 = \mu_{Ai}(x) = \frac{1}{1+\left((x-c_i)/a_i\right)^{2N_i}} = \begin{cases} \mu_{Ai}(x); & i=1,2 \\ \mu_{Bi-2}(x); & i=3,4 \end{cases} \tag{4}$$

where x is input to node i and $\{a_i, c_i, N_i\}$ are adaptable variables known as premise parameters. The outputs of this layer are the membership values of the premise part.

Layer 2. Every node in this layer multiplies the incoming signals:

$$O_i^2 = w_i = \mu_{Ai}(x) \times \mu_{Bi}(y), \qquad i = 1,\ 2 \tag{5}$$

Layer 3. The ith node of this layer calculates the normalized firing strengths as:

$$O_i^3 = \overline{w}_i = \frac{w_i}{w_1 + w_2}, \qquad i = 1,\ 2 \tag{6}$$

Layer 4. Node i in this layer calculates the contribution of the ith rule towards the model output, with the following node function:

$$O_i^4 = \overline{w}_i f_i = \overline{w}_i (p_i x + q_i y + r_i) \tag{7}$$

where $\overline{w}$ is the output of layer 3, and $\{p_i, q_i, r_i\}$ are the parameter set. Parameters of this layer are referred to as consequence parameters.

Layer 5. The single node in this layer calculates the overall output of the ANFIS as (Jang & Sun, 1995):

$$O_1^5 = \sum_i \overline{w}_i f_i = \frac{\sum_i w_i f_i}{\sum_i w_i} \tag{8}$$

2.2. Learning algorithms

As the MATLAB toolbox provides a graphical user interface for ANFIS models trained with the Hybrid and Back-Propagation (BP) algorithms, these models have been widely used by researchers in the field of water resources and environmental engineering. Therefore, the current paper analyzes the application of the Levenberg-Marquardt (LM) algorithm as an alternative learning algorithm for ANFIS applied to hydrological issues. To achieve this aim, the FORTRAN programming language is used to build an ANFIS model which uses the LM learning rule. The following sections clarify the LM algorithm and training process, which are applied to adjust the premise and consequence parameters of ANFIS networks.

2.2.1. Levenberg-Marquardt algorithm

According to Jang and Mizutani (1996), ANFIS is a network architecture that allows systematic calculations of gradient vectors (derivatives of output error with respect to modifiable parameters), so the analysis is not limited to Back-Propagation or Hybrid learning algorithms only. In fact, any gradient-based techniques in nonlinear regression and optimization can be applied, such as the Gauss-Newton method, the Levenberg-Marquardt algorithm, and the extended Kalman filter algorithm.

A nonlinear neuro-fuzzy model can be generally expressed as:

$$y = f(\mathbf{z}, \boldsymbol{\theta}) \tag{9}$$

where $\mathbf{z}$ is the input vector, $\boldsymbol{\theta} = [\theta_1, \ldots, \theta_n]$ is the parameter vector, and y is the model's (scalar) output. Given a set of training data $\{(\mathbf{z}_p; t_p), p = 1, \ldots, m\}$, a squared error measure takes the form:

$$E(\boldsymbol{\theta}) = \sum_{p=1}^{m} \left[t_p - f(\mathbf{z}_p, \boldsymbol{\theta})\right]^2 \tag{10}$$

which is the objective function to be minimized. Before introducing the Levenberg-Marquardt algorithm for minimizing Eq. (10), the closely related the Gauss-Newton method is reviewed. The Gauss-Newton method, also known as the linearization method, uses a Taylor series expansion to obtain a linear model that approximates the original nonlinear model and then applies the ordinary least-squares method to estimate the parameters. Specifically, let the current parameters be denoted by $\boldsymbol{\theta}^k$; then the nonlinear model in Eq. (9) can be expanded in a Taylor series around $\boldsymbol{\theta} = \boldsymbol{\theta}^k$ and only the linear terms are retained:

$$y = f(\mathbf{z}, \boldsymbol{\theta}^k) + \sum_{i=1}^{n} \left(\frac{\partial f(\mathbf{z}, \boldsymbol{\theta})}{\partial \theta_i}\Big|_{\boldsymbol{\theta} = \boldsymbol{\theta}^k} \right) (\theta_i - \theta_i^k) \tag{11}$$

Inspection of Eq. (11) reveals that translated output $y - f(\mathbf{z}, \boldsymbol{\theta}^k)$ is linear function of the translated parameters, $\theta_i - \theta_i^k$. Therefore, a better estimator, $\boldsymbol{\theta}^{k+1}$, can be obtained by means of the well-known pseudo-inverse formula:

$$\boldsymbol{\theta}^{k+1} = \boldsymbol{\theta}^k + \left(\mathbf{A}^T\mathbf{A}\right)^{-1}\mathbf{A}^T\Delta\mathbf{y} = \boldsymbol{\theta}^k + \Delta\boldsymbol{\theta} \tag{12}$$

where $\Delta\mathbf{y}$ is the error vector of which the pth element is equal to $t_p - f\left(\mathbf{z}_p, \boldsymbol{\theta}^k\right)$, $\Delta\boldsymbol{\theta}$ is $\left(A^TA\right)^{-1}A^T\Delta\mathbf{y}$, and the element at row p and column j of matrix $\mathbf{A}$ is $\frac{\partial f(\mathbf{z}_p, \boldsymbol{\theta})}{\partial \theta_j}\Big|_{\boldsymbol{\theta} = \boldsymbol{\theta}^k}$.

A potential problem with the Gauss-Newton method is that $\left(\mathbf{A}^T\mathbf{A}\right)^{-1}$ might not always exist, rendering this method practically unusable. Such a situation is handled by the Levenberg-Marquardt procedure, which defines $\Delta\boldsymbol{\theta}$ as follows:

$$\Delta\boldsymbol{\theta} = (\mathbf{A}^T\mathbf{A} + \lambda\mathbf{I})^{-1}\mathbf{A}^T\Delta\mathbf{y} \tag{13}$$

Where $\mathbf{I}$, is the identity matrix and λ is usually small positive constant. Depending on the magnitude of λ, the algorithm transits smoothly between two extremes: the Gauss-Newton method ($\lambda \to 0$) and gradient descent method ($\lambda \to \infty$). Usually the Gauss-Newton method is more efficient but less stable; the gradient descent method is more stable but less efficient. By properly setting the value of λ, the Levenberg-Marquardt algorithm can be efficient as well as stable.

2.2.2. Training process design

Fig. 3 shows the flowchart of the ANFIS program used for this paper. As can be seen, three sub sets of data are generated to build the model. The first one is the training set, used to update the adjustable parameters. With the update rule of the Levenberg–Marquardt algorithm (Eq. (13)) and the computation of matrix $\mathbf{A}$, the next step is to organize the training process. The aim of the training (learning) process is to achieve the best possible

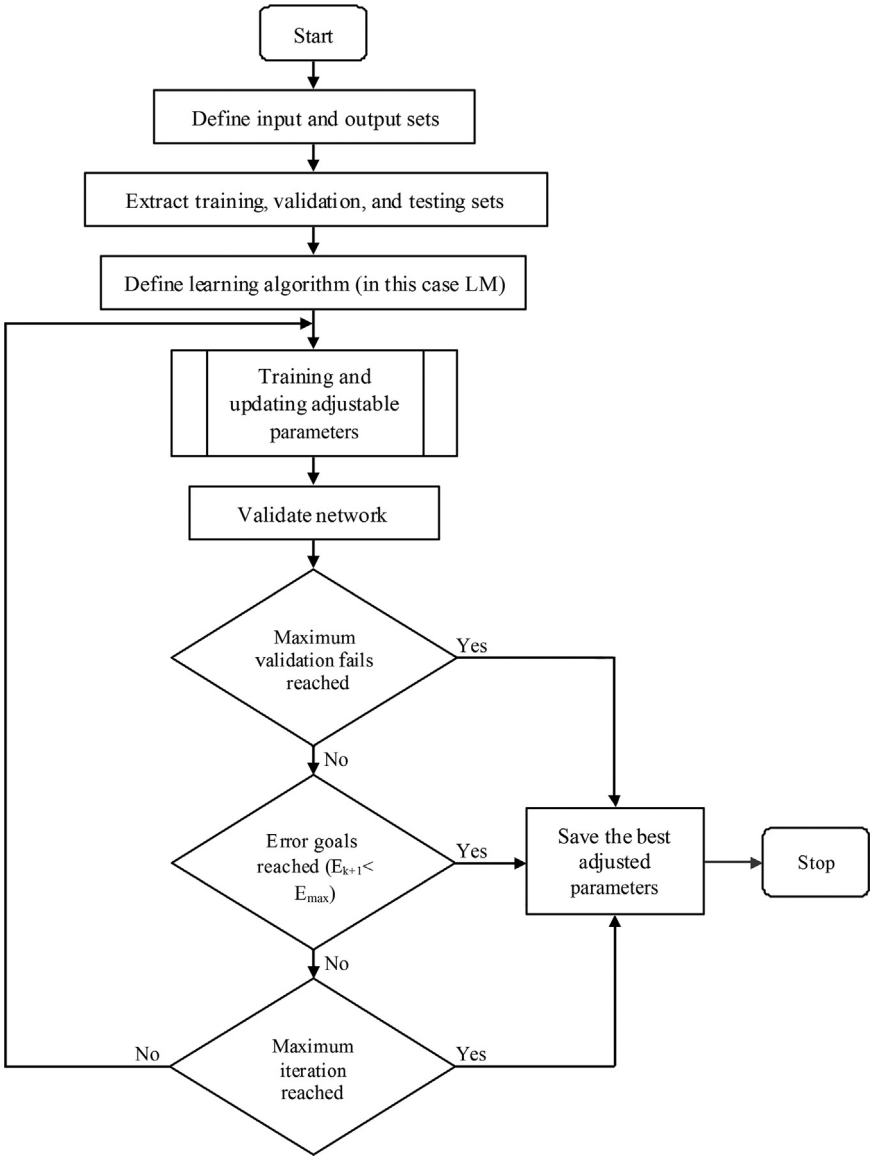

Fig. 3. Flowchart of ANFIS program.

performance of the ANFIS network by adjusting the premise and consequence parameters. The diagram of the training subroutine is shown in Fig. 4. As can be observed from this diagram, if the error reduces, which means it is smaller than the error for the previous iteration, this result implies that the quadratic approximation of the total error function is working and the combination coefficient, λ, could be reduced to decrease the influence of the gradient descent part (ready to speed up). On the other hand, if the error increases, which means it's greater than the error for the previous iteration, this result shows that it's necessary to follow the gradient more closely to look for a proper curvature for quadratic approximation and the combination coefficient λ is increased. The training process using the Levenberg–Marquardt algorithm could be designed as follows:

Step 1: With the initial parameters, evaluate the total error (*SSE*).
Step 2: Update the parameters as directed by Eq. (13).
Step 3: With the new parameters, evaluate the total error (*SSE*).
Step 4: If the current total error increased as a result of the update, then retract the step and increase combination

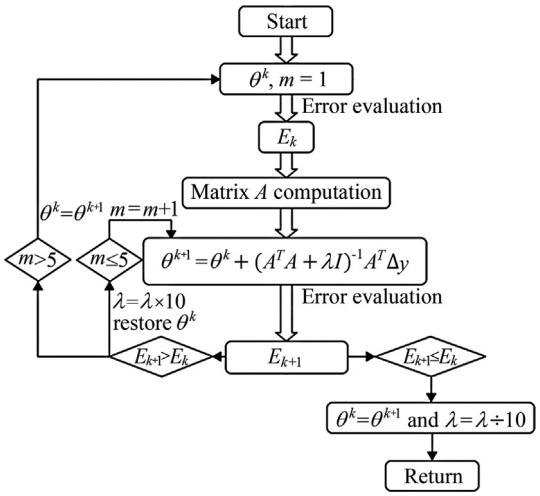

Fig. 4. Diagram for training using Levenberg–Marquardt algorithm: E_{k+1} is the current total error, and E_k is the previous total error.

coefficient, λ, by a factor of 10 or by some other factor. Then go to step 2 and try parameter update again.
Step 5: If the current total error decreased as a result of the update, then accept the step and decrease the combination coefficient, λ, by a factor of 10 or by the same factor as step 4.
Step 6: Go to step 2, with the new parameters until the current total error is smaller than the required value (E_{max}).

During the training process the error of the validation set is monitored and normally decreases during the initial phase of training. In contrast, the error of the validation set increases when the network begins to over-fit the data. At the minimum of the validation set error the premise and consequence parameters of the ANFIS are selected and saved. The last subset is used to test the developed ANFIS. Besides the stopping criteria (called early stopping criteria), several other conditions to stop the training are implemented. In this paper, the maximum number of epochs is set to 1000, while the minimum performance goal (or maximum accepted error, E_{max}) is set to zero. The maximum combination coefficient, λ, of the Levenberg-Marquardt algorithm is set to 1×10^{10}. The training stops when one of these values is reached.

2.3. Model application

2.3.1. Model evaluation

The correlation coefficient (R) alone is unsuitable for evaluation of model prediction (e.g., Legates & McCabe, 1999). Legates and McCabe (1999) proposed that a perfect evaluation of the model performance should include at least one goodness-of-fit or relative error measure (e.g., coefficient of determination: R^2) and at least one absolute error measure (e.g. root mean square error: RMSE or mean absolute error: MAE). In this paper, the ANFIS models' performances are evaluated based on the values of R^2, RMSE, and MAE which are computed utilizing the following equations:

$$R^2 = 1 - \frac{\sum_{i=1}^{n} \left(SSC_{i(measured)} - SSC_{i(predicted)}\right)^2}{\sum_{i=1}^{n} \left(SSC_{i(measured)} - SSC_{i(mean)}\right)^2} \tag{14}$$

$$RMSE = \sqrt{\frac{1}{n}\sum_{i=1}^{n} \left(SSC_{i(measured)} - SSC_{i(predicted)}\right)^2} \tag{15}$$

$$MAE = \frac{1}{n}\sum_{i=1}^{n} \left|SSC_{i(measured)} - SSC_{i(predicted)}\right| \tag{16}$$

In which $SSC_{(measured)}$ is measured suspended sediment concentration, $SSC_{(predicted)}$ is predicted suspended sediment concentration using the ANFIS model, $SSC_{(mean)}$ is the mean of the measured suspended sediment concentrations, and n is number of data points. The R^2 expresses degree of similarity between predicted and actual values and measures how well considered independent variables account for the variance of the measured dependent variable. Higher values correlate with greater model predictive capability, with R^2 values close to 1 indicating predicted and actual values as very similar. The RMSE computes the square error of the prediction compared to actual values and computes the square root of the summation value. The RMSE is, thus, the average distance of a data point from the fitted line measured along a vertical line. In contrast to the RMSE, the mean absolute error, MAE, is a quantity used to measure how close predictions are to the measured outputs. The MAE computes average

Table 3
Performance of the algorithms for SSC estimation in the Schuylkill River, at Manayunk, Philadelphia, PA.

Input combination	ANFIS-Hybrid			ANFIS-BP			ANFIS-LM		
	R^2	RMSE	MAE	R^2	RMSE	MAE	R^2	RMSE	MAE
		Test data							
1	0.5981	27.900	17.446	0.5759	43.167	35.264	0.6917	25.955	11.859
2	0.6603	38.133	14.575	0.5788	44.908	34.690	0.7513	21.467	10.938
3	0.3530	36.555	20.925	0.2934	53.810	45.841	0.3415	36.488	22.004
4	0.3273	41.945	25.271	0.2515	58.159	46.255	0.3103	47.709	24.826
5	0.7186	41.407	16.146	0.5814	44.416	34.634	0.7510	32.685	14.713
6	0.5975	26.639	17.211	0.5776	42.776	34.387	0.6400	33.691	24.041
	Validation data								
1	0.6243	25.123	16.523	0.6419	41.541	32.645	0.7213	23.185	11.078
2	0.9187	17.328	12.868	0.6848	39.578	30.085	0.9107	14.842	9.1580
3	0.3041	39.813	23.715	0.2984	54.012	47.132	0.3534	35.861	22.176
4	0.4251	34.675	20.312	0.2816	57.182	44.274	0.3864	48.193	26.826
5	0.8827	33.198	14.185	0.5756	43.437	34.032	0.8845	27.345	13.864
6	0.8075	24.689	16.197	0.5798	45.781	36.842	0.8108	28.345	21.175
	Training data								
1	0.6908	228.559	56.588	0.7326	157.622	70.566	0.7821	115.741	63.342
2	0.9686	51.368	19.488	0.7559	145.136	60.743	0.9856	46.873	16.524
3	0.3449	234.617	69.068	0.3275	238.986	89.222	0.3404	221.891	64.573
4	0.4482	215.326	63.871	0.3483	235.733	86.945	0.4298	218.452	62.124
5	0.9626	56.044	22.023	0.7608	143.865	60.506	0.9804	47.548	18.371
6	0.8532	111.060	39.824	0.7634	143.173	60.010	0.9088	102.745	31.985
	All data								
1	0.6797	202.440	55.565	0.6773	155.591	72.846	0.7512	112.032	60.347
2	0.9459	60.787	20.576	0.7091	136.008	60.822	0.9768	57.428	18.486
3	0.3540	195.307	56.704	0.3339	200.456	78.355	0.3519	201.435	61.072
4	0.4361	181.988	55.507	0.3433	198.428	77.196	0.3966	198.468	57.841
5	0.9385	60.5830	22.986	0.7154	132.900	59.999	0.9623	58.887	19.103
6	0.8335	99.5159	36.903	0.7239	131.043	59.089	0.8756	90.961	29.941

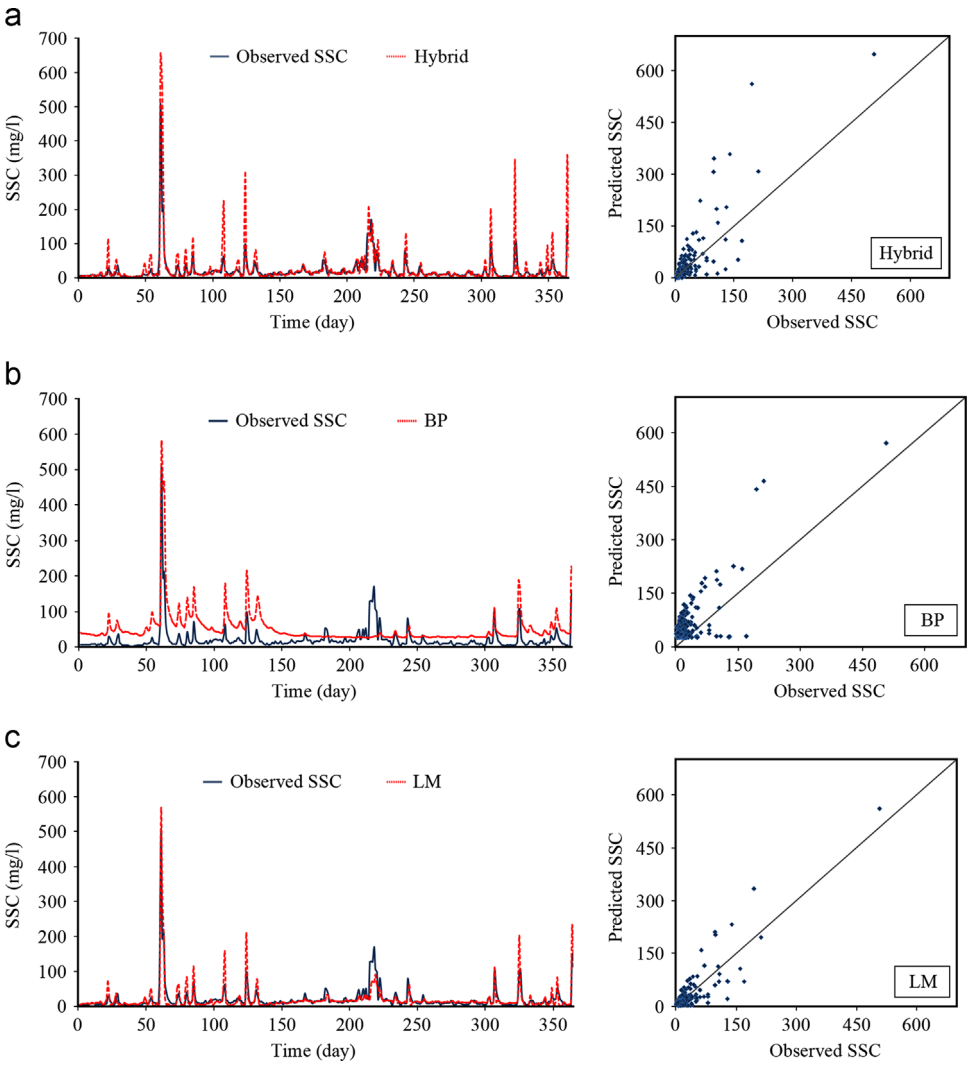

Fig. 5. SSC predicted by ANFIS models with the combination 2.

magnitude of error between predicted and actual values with no distinction between error direction. Low RMSE and MAE values indicate high confidence in the model-predicted values.

For better comparing the performance of different learning algorithms, the present study additionally used two statistical indexes. The first index, mean absolute percentage error (MAPE) can be defined as follows:

$$MAPE = \frac{1}{n}\sum_{i=1}^{n}\frac{\left|SSC_{i(measured)} - SSC_{i(predicted)}\right|}{\left|SSC_{i(measured)}\right|} \times 100\% \quad (17)$$

The MAPE is a statistical measure of predictive accuracy expressed as a percentage. The MAPE is useful for evaluating the performance of predictive models due to its relative values. MAPE effectively reflects relative differences between models because it is unaffected by the size or unit of actual and predicted values. To measure the generalization capability of the different learning rules, the non-dimensional error index (NDEI) is used as the second index, which can be defined as the RMSE divided by standard deviation of the target series (Jang, 1993).

2.3.2. Application of ANFIS models

ANN and NF models are applied as effective approaches to handle nonlinear and noisy data, especially in situations where the relations among physical processes are not fully understood. They are also particularly well suited for modeling complex systems on real time basis (Rajaee et al., 2009). The aim of this research is to investigate the efficiency of the ANFIS model trained with the LM learning algorithm for predicting SSC one day ahead. With respect to the statistical analysis presented in Table 2, the following combinations that include different numbers of input values (Q and SSC) were considered to predict the unique SSC value in one day ahead at time t. Since the variables at times $t-3$ and $t-4$ show lower correlation, these variables are ignored in the following combinations:

Combination 1: Q_t, SSC_{t-1}
Combination 2: Q_t, Q_{t-1}, Q_{t-2}, SSC_{t-1}, SSC_{t-2}
Combination 3: Q_{t-1}, SSC_{t-1}
Combination 4: Q_{t-1}, Q_{t-2}, SSC_{t-1}, SSC_{t-2}
Combination 5: Q_t, Q_{t-1}, SSC_{t-1}, SSC_{t-2}
Combination 6: Q_t, SSC_{t-1}, SSC_{t-2}

The applied ANFIS models use a fuzzy inference model of Sugeno type (Jang et al., 1997), in which the membership function parameters are tuned to fit a given input-output set by optimization algorithms. In the ANFIS model each rule contains several

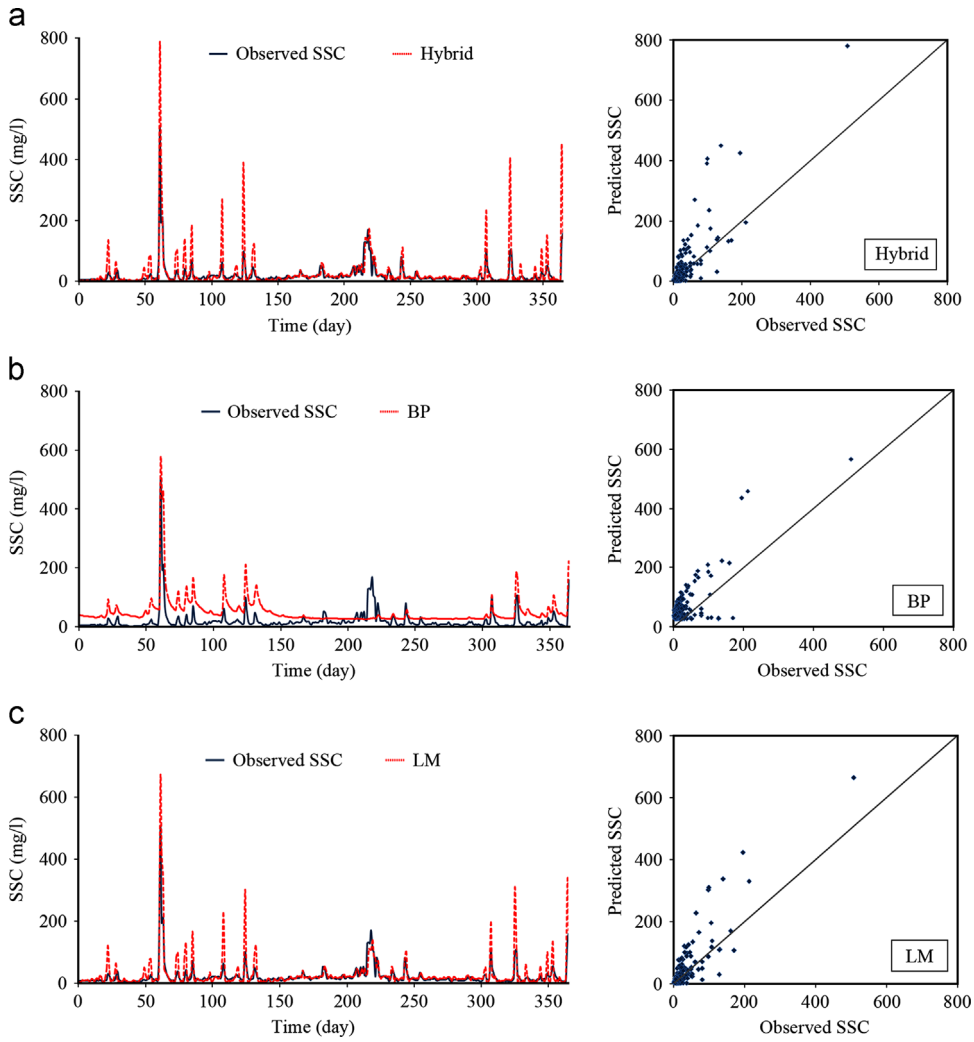

Fig. 6. SSC predicted by ANFIS models with the combination 5.

parameters of membership functions (MFs) and each variable may have several values (in terms of rules). For example, if each variable has two rules and each rule includes three parameters, then there are $[n\ (\text{variables}) \times 2\ (\text{rules}) \times 3\ (\text{parameters})] = 6n$ parameters for the determination in layer 1 (see Fig. 2). The ANFIS model trains these MFs according to the training data set. In layer 2, these rules generate 2^n neurons, and furthermore, there are $2^n \times (n+1)$ parameters undetermined within the defuzzification process in layer 4. Choosing the number of MFs for each input reflects the complexity of ANFIS model for selecting parameters. In this paper, three different ANFIS models are considered for predicting SSC values in the river. In all these models, three Gaussian membership functions for each input are found to provide the best model performance. The differences between the models lie in their training algorithms, namely the common Hybrid, Back-Propagation, and Levenberg-Marquardt algorithms.

3. Results and discussion

The three different learning algorithms previously mentioned were applied for prediction of suspended sediment load. The ANFIS networks were trained for six different input combinations defined in the Section 2.3.2. The results of the model performance are listed in Table 3. In the testing phase, the LM algorithm yields better performance than the Hybrid algorithm for several combinations, while for some others the Hybrid algorithm performs better. However, for all combinations, the Hybrid and LM learning algorithms have better performance in comparison to the BP algorithm. According to Table 3, in the Schuylkill River, the ANFIS model trained with the LM algorithm provides the best efficiency using combination 2 with the highest value of $R^2 = 0.7513$ and the lowest RMSE = 25.955 mg/l and MAE = 11.859 mg/l. For ANFIS model trained with the Hybrid algorithm the results are a little more complex, from R^2, RMSE, and MAE viewpoints, it shows the best performance for combinations 5, 6, and 2, respectively. Using the LM algorithm, the values of R^2, RMSE, and MAE vary in the ranges of 0.3103 to 0.7513, 21.467 to 47.709 mg/l, and 10.938 to 24.826 mg/l, respectively; while they are in the ranges of 0.3273 to 0.7186, 26.639 to 41.945 mg/l, and 14.575 to 25.271 mg/l, respectively, using the Hybrid algorithm. In the training phase, except for only one combination, all RMSE values for the LM algorithm are lower than those for the Hybrid and BP algorithms. Similar to the testing phase, the LM algorithm provides better R^2 values for 4 combinations. It can be said that ANFIS models trained with the Hybrid and LM algorithms are comparable in terms of the prediction accuracy. However, in general, the networks trained with the LM algorithm perform better than those trained by the Hybrid algorithm.

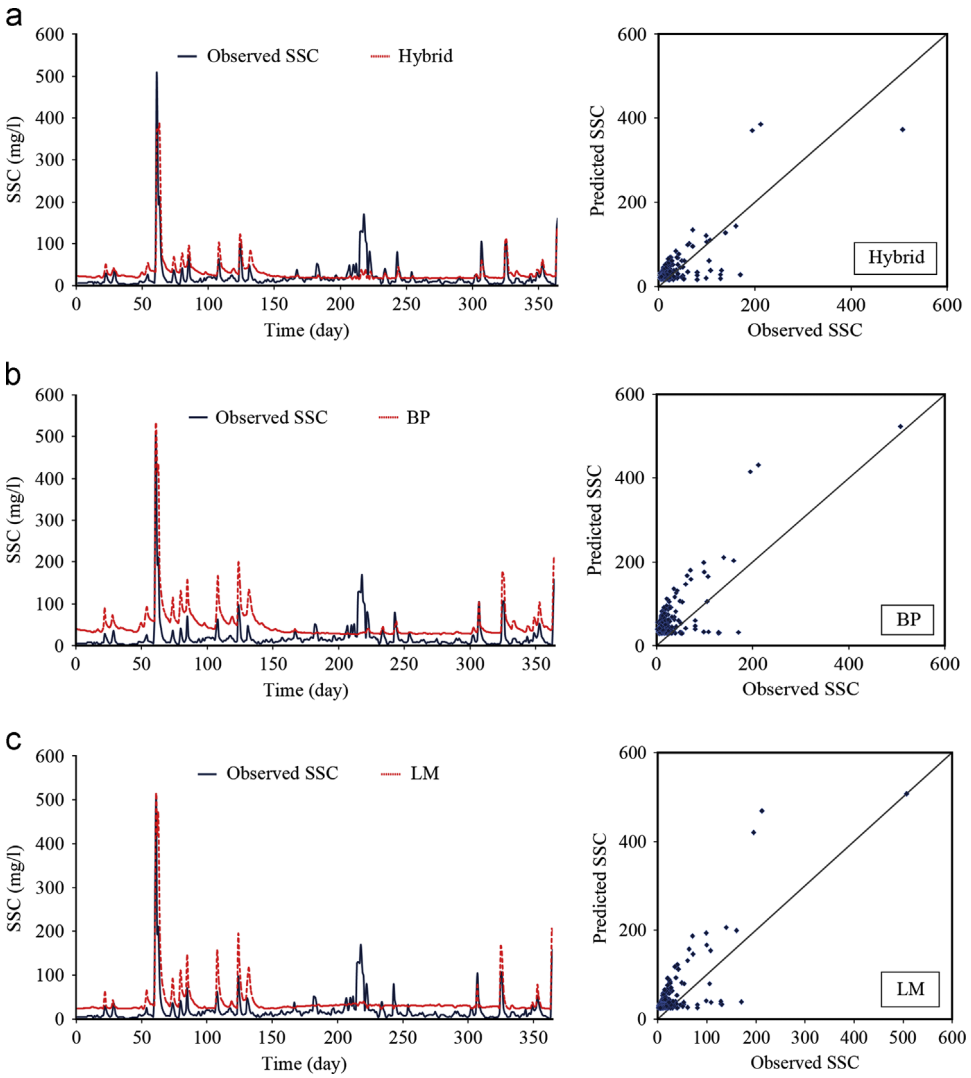

Fig. 7. SSC predicted by ANFIS models with the combination 6.

The temporal variations of the observed and predicted SSC using all three training algorithms for the combinations 2, 5, and 6 are shown in Figs. 5–7, respectively. Moreover, the predicted SSC are plotted against observed SSC in these figures. As can be seen, ANFIS models trained with the LM and Hybrid algorithms yield better results for SSC prediction than those trained by the BP algorithm. It is also obvious that the BP algorithm is almost always over-predicting measured values, except for a short interval. The critical result of the LM and Hybrid algorithms is that they consistently overestimated the SSC peaks. However, the LM algorithm shows better agreement with the observed time series at the peaks than the other algorithms. The predicted magnitudes of low, medium, and high SSC using the LM algorithm are closer to the observed values in comparison to other algorithms. On the other hand, the results of ANFIS models trained by the LM algorithm are closer to 45° straight line in the scatter plots compared with those of the other algorithms.

Fig. 8 shows the performance indexes MAPE and generalization capability (NDEI) of the networks trained with different learning algorithms and input combinations. As can be observed, the LM algorithm performs better than the Hybrid algorithm for input combinations 1, 2, and 5 while the Hybrid algorithm provides a lower MAPE value for the other input combinations. In general, it can be said that the LM algorithm is a more stable learning rule in comparison to the Hybrid and BP algorithms. According to Fig. 8 (b), by applying the LM learning rule, the lowest NDEI value was obtained for input combination 2. Except for combination 4 where Hybrid algorithm shows a slightly better result, the LM learning rule performs better for the other combinations in term of generalization capability.

Further, the cumulative suspended sediment load (SSL) was predicted using the developed ANFIS models. The results are shown in Fig. 9 for combinations 2, 5, and 6 and for the best result of each algorithm (the Hybrid algorithm with combination 5; the BP algorithm with combination 6; and the LM algorithm with combination 2). The best results for each algorithm were selected based for the comparison between the predicted maximum SSL and measurements and the chosen statistical performance indexes.

As is obvious from this Fig. 9, models trained with the BP algorithm overestimated the cumulative SSL in all cases. Applying combination 2, as expected, the model trained by the LM algorithm has the best performance. Unlike combination 2, the

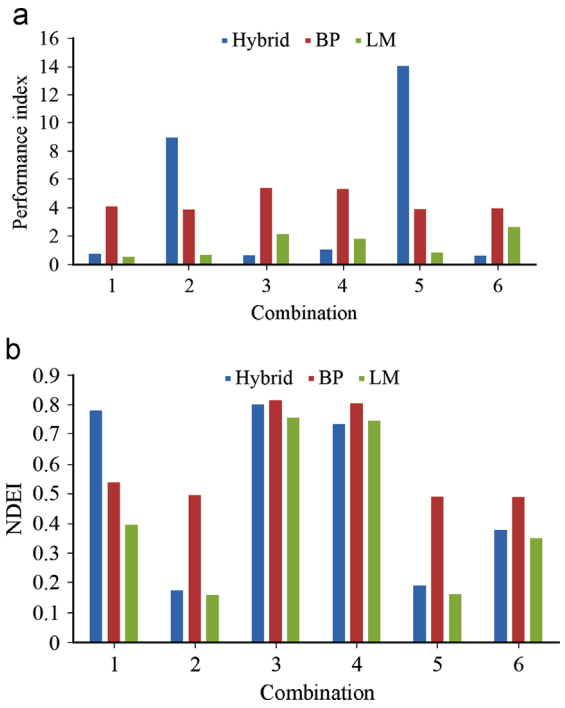

Fig. 8. (a) Performance index MPAE and (b) generalization capacity for different learning rules and input combinations.

Hybrid algorithm shows better performance than the LM algorithm for combination 6. For combination 5, the results of the Hybrid and LM algorithms are comparable while they also overestimate the SSL values. In Fig. 9(d) the measured cumulative SSL values are compared with the results of different ANFIS algorithms with the best combination for each model. The measured cumulative SSL in the verification period is 66,616.69 t. The ANFIS models trained with the Hybrid, BP, and LM algorithms overestimate SSL values by 30,726.75, 82,366.88, and 7,494.97 t, respectively. However, the LM algorithms gives better performance when compared to other algorithms. It can be concluded that, ANFIS model trained with the LM algorithm is more efficient in prediction of the cumulative SSL.

4. Conclusions

An attempt was made in this paper to investigate the use of the LM learning algorithm in ANFIS for predicting the daily suspended sediment concentration for the Schuylkill River in the United States. To achieve this aim, the FORTRAN programming language was utilized to construct ANFIS models using the LM algorithm, and MATLAB toolbox was used to build ANFIS models based on the Hybrid and BP learning algorithms. Comparisons of the predicted results indicated that the models trained with the LM algorithm had greater ability for predicting the SSC in comparison with the other algorithms. To recognize the best algorithm between the LM, Hybrid, and BP, evaluations of the performance indexes and the generalization capability of the network were presented. The results show that the LM learning rule could improve the performance and generalization of ANFIS model. It was also found that the ANFIS model, which used the LM algorithm as the learning rule, had the best accuracy when predicting the cumulative suspended sediment load. The ANFIS models trained with LM algorithm showed an improvement in the coefficient of determination, R^2, the root mean square error, RMSE, and the mean absolute error, MAE, values compared to the Hybrid model from (0.7186, 26.639, and 14.575, respectively) to (0.7513, 21.467, and 10.938, respectively), respectively. Finally, it can be said that the LM learning algorithm can be used as an alternative to the Hybrid and BP algorithms in ANFIS models for the prediction of the daily suspended sediment concentration.

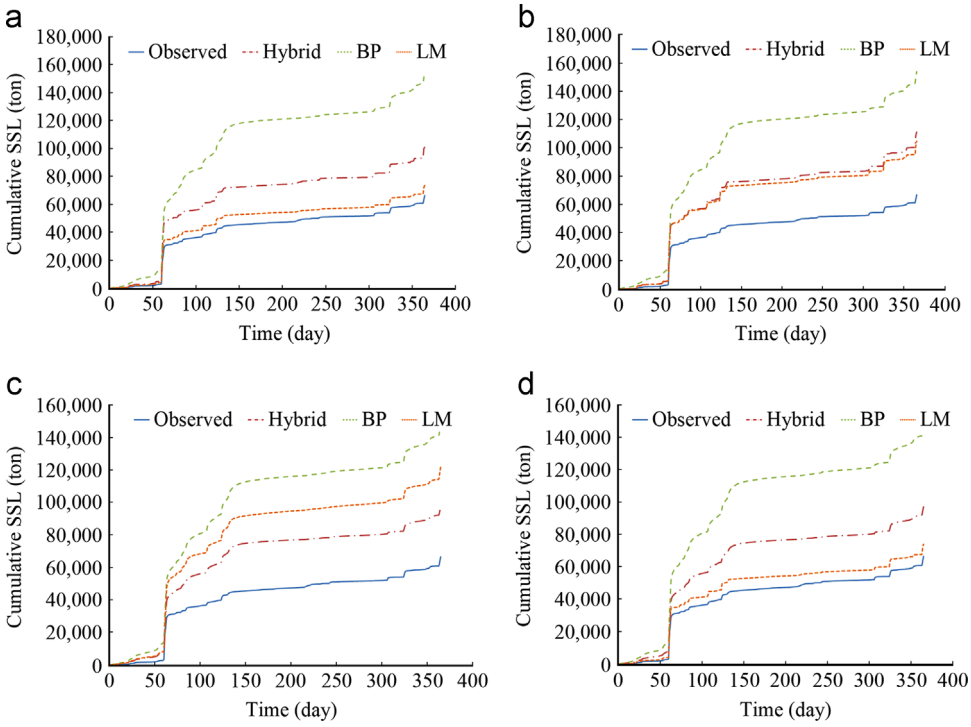

Fig. 9. Observed and estimated cumulative SSL for: (a) combination 2, (b) combination 5, (c) combination 6, and (d) the best combination for each method.

References

Altun, H., Bilgil, A., & Fidan, B. C. (2007). Treatment of multi-dimensional data to enhance neural network estimators in regression problems. *Expert Systems with Applications*, *32*(2), 599–605.

Jang, J. S. (1993). ANFIS: Adaptive-network-based fuzzy inference system. *IEEE Transactions on Systems, Man, and Cybernetics*, *23*(3), 665–685.

Jang, J. S., & Sun, C. T. (1995). Neuro-fuzzy modeling and control. *Proceedings of the IEEE*, *83*(3), 378–406.

Jang, J.S.R., & Mizutani, E. (1996, June). Levenberg-Marquardt method for ANFIS learning. In Fuzzy Information Processing Society. In *IEEE NAFIPS, biennial conference of the North American* (pp. 87–91).

Jang, J.S.R., Sun, C.T., & Mizutani, E. (1997). *Neuro-fuzzy and soft computing, a computational approach to learning and machine intelligence*.

Kaya, M. D., Hasiloglu, A. S., & Yesilyurt, H. (2002). To estimate the design of functional sizes of chairs and desks on the basis of ISO 5970 using adaptive neuro-fuzzy inference system. *Fssc ıme*, *2*, 29–31.

Kisi, Ö. (2004). Multi-layer perceptrons with Levenberg-Marquardt training algorithm for suspended sediment concentration prediction and estimation. *Hydrological Sciences Journal*, *49*, 6.

Kisi, O., Haktanir, T., Ardiclioglu, M., Ozturk, O., Yalcin, E., & Uludag, S. (2009). Adaptive neuro-fuzzy computing technique for suspended sediment estimation. *Advances in Engineering Software*, *40*(6), 438–444.

Legates, D. R., & McCabe, G. J. (1999). Evaluating the use of "goodness-of-fit" measures in hydrologic and hydroclimatic model validation. *Water Resources Research*, *35*(1), 233–241.

Nagy, H. M., Watanabe, K. A. N. D., & Hirano, M. (2002). Prediction of sediment load concentration in rivers using artificial neural network model. *Journal of Hydraulic Engineering*, *128*(6), 588–595.

Ocampo-Duque, W., Schuhmacher, M., & Domingo, J. L. (2007). A neural-fuzzy approach to classify the ecological status in surface waters. *Environmental Pollution*, *148*(2), 634–641.

Raghuwanshi, N. S., Singh, R., & Reddy, L. S. (2006). Runoff and sediment yield modeling using artificial neural networks: Upper Siwane River, India. *Journal of Hydrologic Engineering*, *11*(1), 71–79.

Rajaee, T., Mirbagheri, S. A., Zounemat-Kermani, M., & Nourani, V. (2009). Daily suspended sediment concentration simulation using ANN and neuro-fuzzy models. *Science of the Total Environment*, *407*(17), 4916–4927.

Salas, J. D. (1980). Applied modeling of hydrologic time series. *Water Resources Publication*.

Sayed, T., Tavakolie, A., & Razavi, A. (2003). Comparison of adaptive network based fuzzy inference systems and B-spline neuro-fuzzy mode choice models. *Journal of Computing in Civil Engineering*, *17*(2), 123–130.

Takagi, T., & Sugeno, M. (1985). Fuzzy identification of systems and its applications to modeling and control. *IEEE Transactions on Systems, Man, and Cybernetics*, *1*, 116–132.

Zhu, Y. M., Lu, X. X., & Zhou, Y. (2007). Suspended sediment flux modeling with artificial neural network: An example of the Longchuanjiang River in the Upper Yangtze Catchment, China. *Geomorphology*, *84*(1), 111–125.

Zounemat-Kermani, M., & Teshnehlab, M. (2008). Using adaptive neuro-fuzzy inference system for hydrological time series prediction. *Applied Soft Computing*, *8*(2), 928–936.

water

MDPI

Article

Variability and Trend Detection in the Sediment Load of the Upper Indus River

Sardar Ateeq-Ur-Rehman *, Minh Duc Bui and Peter Rutschmann

Chair of Hydraulic and Water Resources Engineering, Technical University of Munich, Arcisstr. 21, D-80333 Munich, Germany; bui@tum.de (M.D.B.); p.rutschmann@tum.de (P.R.)

* Correspondence: sardar.ateeq@tum.de; Tel.: +49-89-289-27161; Fax: +49-89-289-23172

Received: 14 November 2017; Accepted: 21 December 2017; Published: 25 December 2017

Abstract: Water reservoirs planned or constructed to meet the burgeoning energy and irrigation demands in Pakistan face a significant loss of storage capacity due to heavy sediment load from the upper Indus basin (UIB). Given their importance and the huge investment, assessments of current UIB sediment load and possible future changes are crucial for informed decisions on planning of optimal dams' operation and ensuring their prolonged lifespan. In this regard, the daily suspended sediment loads (SSLs) and their changes are analyzed for the meltwater-dominated zone up to the Partab Bridge and the whole UIB up to Besham Qila, which is additionally influenced by monsoonal rainfall. The gaps between intermittent suspended sediment concentration (SSC) samples are filled by wavelet neural networks (WA-ANNs) using discharges for each site. The temporal dynamics of SSLs and discharges are analyzed using a suite of three non-parametric trend tests while the slope is identified using Sen's slope estimator. We found disproportional spatio-temporal trends between SSLs and discharges caused primarily by intra-annual shifts in flows, which can lead to increased trap efficiency in planned reservoirs, especially upstream of Besham Qila. Moreover, a discernible increase in SSLs recorded at Partab Bridge during summer is being deposited downstream in the river channel. This is due to a decrease in river transport capacity in the monsoonal zone. These findings will not only help to identify these morphological problems, but also accurately anticipate the spatio-temporal changes in the sediment budget of the upper Indus River. Our results will help improve reservoir operational rules and sediment management strategies for existing and 30,000-MW planned dams in the UIB.

Keywords: sediment pattern; sediment load trend; sediment transport estimation; upper Indus River; wavelet neural network; Mann–Kendall test; Sen's slop test; April sediment load

1. Introduction

Estimation of the suspended sediment loads (SSLs) is important in the design and operation of water structures and in the planning of sediment management (yield reduction, routing and removal) to preserve their live storage capacities [1–5]. The temporal variations and changes in SSLs are also an important indicator of the effectiveness of existing watershed management practices or tectonic and land-sliding activities in the catchment area. Being a water stressed country amongst the top ten most climate-affected countries [6,7], Pakistan has a total water storage capacity of only 30 days (equal to 10% of the annual available water), which has been depleting due to heavy sedimentation transported through the Indus River system from the young Hindukush-Karakoram-Himalaya (HKH) ranges [8]. For example, amongst three big reservoirs, the Tarbela dam has lost 35% of its storage capacity since 1974 due to trapping of approximately 8 km^3 of sediment in the reservoir ponding area [9]. The Warsak dam constructed on Kabul River has filled with 60 Mt of SSL annually in the 30 years after its construction, and no structural or non-structural remedies can reverse its depleting storage

capacity [10]. Mangla dam, the second largest Pakistani water storing facility, had an initial storage of 7.1 billion m^3 (BCM), which was reduced to 5.6 BCM in 2005 due to sedimentation. In 2009, an additional 9 m rise of the dam increased the storage to 9.1 BCM, which cost one billion USD over five years. However, the rise created technical problems such as an increase of seepage through the dam embankment in addition to the displacement of 45,000 people living in the vicinity of the dam [11]. In view of the transboundary nature of the source of water, such a decrease in water storage capacity in Pakistan exacerbates the instability and geopolitical tensions of the region [12]. Hence, the assessment of prevalent sediment patterns and their projected changes are vital for the optimization of sediment management processes to ensure the water and food security in the country and to regulate the transboundary water availability pressures.

Although there are many studies assessing the climate-induced adverse impacts on the UIB river flow patterns [13–19], few have investigated the impact of flow pattern changes on the sediment load capacity [20,21]. Furthermore, the studies conducted in this regard differ widely in their suggested estimates. For instance, the SSL to Tarbela Dam (the country's largest) or at the immediately upstream Besham Qila discharge gauge is reported to range from 200 Mt $year^{-1}$–675 Mt $year^{-1}$ over the past 50 years (Table 1). Such uncertainty leads to poor design quality of the operating rules for existing dams and those under construction. Moreover, the studies have generally estimated the SSL by using empirically-developed sediment rating curves (SRCs), whose accuracy is limited as they oversimplify the relationship between the suspended sediment concentration (SSC) samples and the observed discharges [22–24].

Table 1. Estimates published on the suspended sediment load (SSL) of the upper Indus River.

Suspended Sediment Yield (Mt $year^{-1}$)	Estimated by
480	[25]
400	[26]
475	[27]
200	[28] reported by [29]
675	[30]
300	[31]
200	[32]
197 *	[33]
138 **	[33]
200	[2]

Note: * Besham Qila; ** Partab Bridge.

The accuracy of SRCs is also limited since it does not model the complex sediment transport processes related to hysteresis phenomena and marked hydrological variations within the UIB, such as: (a) the fluvial erosion and transport processes, which interact with other sediment-producing processes; (b) temporary sediment storage in the main river channel [34]; (c) aggradation and degradation phases of landslides [35]; (d) on average, 5–10 high flow waves of an average 10–12-day duration during the monsoon period; (e) different transit times of discharge and sediment and their different lag times from several sources to the gauge stations. Given that SRCs are employed in the estimation process, there may be a marked compromise in the design quality of reservoir sedimentation prevention measures, as apparent from the current sedimentation rate of the Tarbela and Mangla dams. Since the assessment of the SSL patterns is important for the management of water-related structures, watershed management practices and the sediment budget of the Indus, it is necessary to detect the temporal changes in sediment transport, which are influenced by the river discharge responses and hysteresis phenomena, requiring frequent discharge and SSC observations.

As opposed to the discharge time-series typically available on a daily resolution, the SSCs are intermittently sampled, which can affect the trend outcome needed to reconstruct the non-observed days. However, to deal with the non-linear nature of the time series, the wavelet transform coupled artificial neural networks (WA-ANNs) outperform SRCs, since they are able to model theoretically

any kind of relationship between the dependent and independent variables without having to know their physical relationship [36–41]. The wavelet transform decomposes the data time series up-to J levels in the time, space and frequency domains and reveals the information from a given data scenario [42]. The temporal scale of the decomposition provides information on temporary storage, aggradation and degradation phases, high flow waves and transit time of the sediment load in the detail coefficients. Given these details, i.e., the detail coefficients along with the approximation coefficient, ANN precisely models the hysteresis phenomena. WA-ANNs have been used successfully over the last decade for reconstructing the missing data by adjusting the hysteresis phenomena in sediment load processes [43–46].

In assessing temporal dynamics of SSLs and discharges, non-parametric tests are assumed to be more robust as compared to their parametric counterparts, in view of the fact that the sediment load data are not normally distributed, owing to the highly nonlinear nature of the sediment transport processes. However, several non-parametric tests may also result in distinct estimates, which requires employing a suite of successful non-parametric methods and then quantifying their associated uncertainty to build more confidence in the results.

Analyzing discharges and SSCs at two different sites over the past 50 years, this study for the first time shows how changes in the flow patterns are affecting the sediment transport capacity of the UIB for the meltwater-dominated zone (up to Partab Bridge site) and for the whole UIB (up to Besham Qila), which is additionally influenced by the summer monsoonal rainfall regime. The gaps between intermittently sampled SSCs are filled using the wavelet transforms coupled with the artificial neural networks (WA-ANNs). The temporal discharge and SSL dynamics are robustly assessed using a suite of three widely-used non-parametric approaches, including: (1) the innovative trend analysis (ITA), which can analyze the trends in low, medium and high annual SSLs without requiring any assumptions, such as serial correlation, non-normality, sample numbers and others [47]; (2) the Mann–Kendall (MK) and the seasonal Kendall (SK) tests together with Sen's slope method; the MK test detects a trend in a time series without requiring normally-distributed input data [48,49]; Sen's slope method estimates its true slope, while SK analyzes annual trends by removing the seasonal cycles in a time series; (3) a change point detection test, which reveals the changing tendency in the SSL series on monthly and annual scales [50,51]; (4) mean monthly variations, which detect monthly changes based on differences from the (a) first and last decades and (b) monthly regression equations of the analyzed records.

2. Study Area and Data Description

With a total length of 2880 km and a drainage area of 912,000 km^2, the Indus River is one of the largest in south Asia. It starts from China and then travels through India and across the whole of Pakistan, finally draining into the Arabian Sea. The drainage of the Indus River is divided into upper and lower parts, typically at the Besham Qila discharge gauge or around 65 km downstream at, so far, its only reservoir, Tarbela, which is one of the largest earth-filled dams in the world (Figure 1). The Besham Qila site located at an elevation of 580 masl drains the mostly high-altitude area of 165,515 km^2, 12% of which is covered with the Hindukush-Karakoram-Himalaya (HKH) glaciers and permanent ice, while the seasonal snow cover varies between 3 and 67% [18,52,53]. Mean annual discharge of the UIB at Besham Qila is 2405 m^3/s, which constitutes roughly half of the annual surface water availability in Pakistan [18,53]. More than 70–80% of such discharge is generated from the melting of snow and glaciers, making the Indus River amongst the most melt-water-dependent rivers in the world [12].

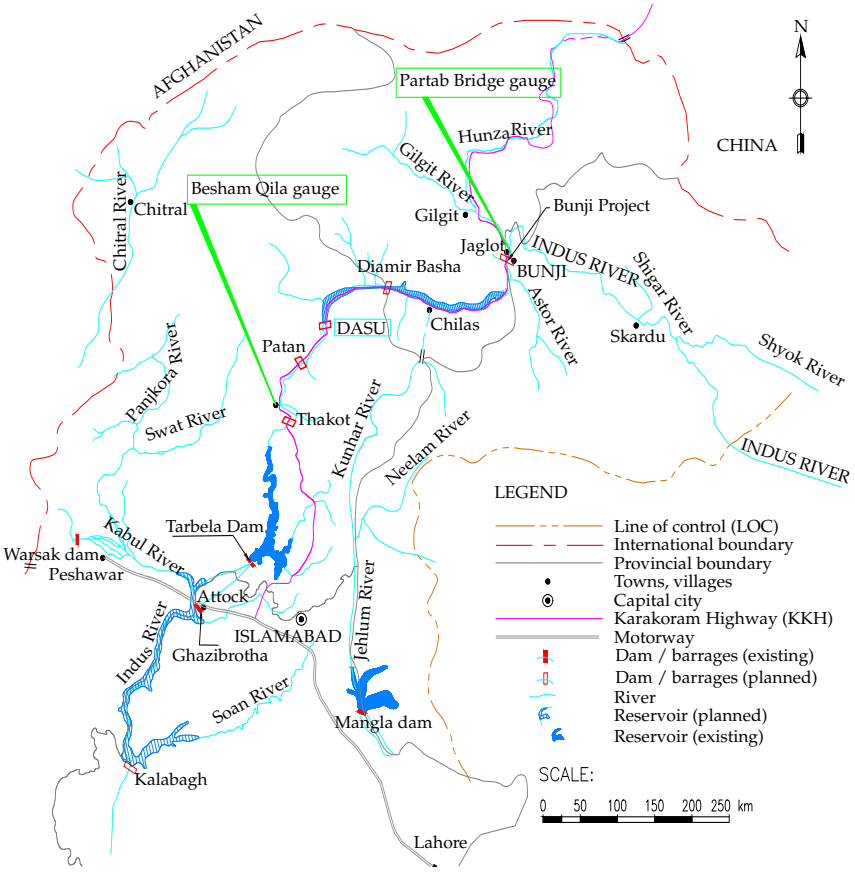

Figure 1. Locations of study gauges in the study area. Modified from [2].

The second study site at Partab Bridge is located at an elevation of 1250 masl about 300 km upstream of Besham Qila, draining around 95% of the cryospheric region and contributing around 75% of the Besham Qila flows. The rest of the Besham Qila flows are mostly received from the monsoonal rainfall from July–September. This 300-km river reach, Partab Bridge to Besham Qila, has gained in importance due to the many planned hydraulic structures. For example, the tenders for three major hydropower projects, Bunji 7100 MW (190 m high), Bhasha dam 4500 MW (272 m) and Dasu 5400 MW (242 m), have been completed for construction located downstream of the Partab Bridge gauge [54]. In addition, the river reach contains huge sediment deposits due to landslides and tectonic activities.

Since both gauges feature large drainage areas, overall variations in their discharges and SSCs are not as abrupt as in the small catchments, but such variations are still large (Table 2), indicating the occurrence of frequent hydrological events within the UIB. For instance, 1973, 1988 and 1994 were the exceptional flow years at Besham Qila with a total volume of 98.95, 95.31 and 94.88 billion m^3 (BCM), respectively (Figure 2). The year with the highest peak flow was 1984 with a volume of 89.33 BCM. In contrast, only a 61.54 BCM flow volume was observed in 1982, distinguishing it as an extremely low flow year. For Partab Bridge, the exceptional flow years were 1973, 1994 and 1990 with a total volume of 76.5, 69.7 and 69.6 BCM, respectively. On the other hand, 1965 and 1982, with a volume of 42.16 and 46.8 BCM, respectively, were the extremely low flow years. Based on flow patterns, the UIB can be classified into a low flow cycle of 1974–1977 (dry period) and a high flow cycle of 1988–1992 (wet period) with their annual average volume being 71 and 85 BCM, respectively. In drought years, with wet winter and dry summer, the share of glacier melt increases, maintaining the water supply to the Indus River [12].

Table 2. Hydrological and sedimentological characteristics at the Besham Qila and the Partab Bridge gauges.

Parameter	Besham Qila		Partab Bridge	
	Q (m^3/s)	SSC (ppm)	Q (m^3/s)	SSC (ppm)
Duration	1969–08 (daily)	1969–08 (samples)	1962–08 (daily)	1962–08 (samples)
Max discharge	13,910	3770 (at Q_{max})	9599	5780 (at Q_{max})
Min discharge	325	132 (at Q_{min})	168	221 (at Q_{min})
Max sediment	12,401	8660	1101	25,040
Min sediment	456	1	1200	1
Mean sediment	-	1071	-	1947
SD of sediment	-	1456	-	2847
Mean discharge	3000	-	2231	-
SD of discharge	2923	-	2191	-
$Q_{-10,000}$ at Dasu damsite [2]	21,218	-	-	-
Q_{-100} at Dasu damsite [2]	15,078	-	-	-

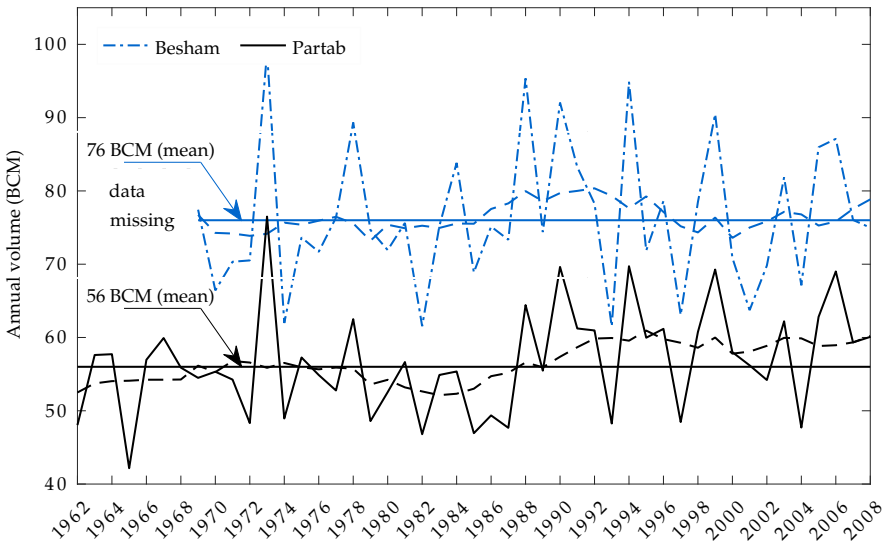

Figure 2. Hydrograph showing actual and smoothed flows with 10-year moving average (dashed lines) in billion m^3 (BCM).

The specific suspended sediment load (SSL) from the drainage area of the Indus at Besham Qila is estimated to be 1197 Mt km^{-2} $year^{-1}$, more than 90% of which reaches the Partab Bridge and Besham Qila during the high flow period that spans May–September. Such a heavy sediment load is mainly due to glacial bedrock erosion from a large number of small, but steep catchments that directly discharge into the Indus [55]. Generally, the peak SSL correlates well with the peak discharge with a short time lag, particularly for Besham Qila during the monsoon season when discharge varies significantly within a short span of a few days, accompanied by an immediate and large increase in the sediment concentration [56]. The SSC average grain size distribution for the UIB is about 45.7% sand, 39.9% silt and 14.4% clay [2].

The daily discharges and the discontinuous suspended sediment concentration (SSC) samples were collected for Partab Bridge over the period 1962–2008 and for Besham Qila over the period 1969–2008. Following the U.S. Geological Survey (USGS) guidelines, discharges at these gauges are measured using AAcurrent meter, while the SSC samples are taken once a week in winter and twice a week in summer, depending on the availability of labor and sampling feasibility [57–59]. The total SSC samples within the collection periods on record were 3213 and 2117, representing around 22% and 14% of the daily time series for the Besham Qila and the Partab Bridge sites respectively. Due to low sampling frequency at Partab Bridge, we decided to use all available data samples. The long

length of these samples improves the learning of the WA-ANN model, which in turn leads to better reconstruction of missing SSLs. The outliers in sediment data samples were excluded by examining the general behavior of the river and river catchment. More details on data collection, data quality and period of records for the Indus River can be found in [33].

3. Methods

We analyze how changes in the flow patterns are affecting the sediment transport capacity of the UIB specifically for the meltwater-dominated zone (up to the Partab Bridge site) and for the whole UIB (up to the Besham Qila), which is additionally influenced by the summer monsoonal rainfall regime. In order to do this, we analyze the observed discharges and SSCs over the past 50 years. Since the SSCs are intermittently sampled and thus represent only a fraction of the daily discharge series of the study gauges, we reconstructed the SSCs for the non-observed days using the wavelet transforms coupled with the artificial neural networks (WA-ANNs). We then employ three non-parametric statistical approaches to analyze the monthly-to-annual scale temporal dynamics of the reconstructed SSLs and observed discharges. These methods include: (1) innovative trend analysis; (2) Mann–Kendall (and seasonal-Kendall) trend test and Sen's slope method; (3) the Pettitt change point test. We also analyzed temporal dynamics by performing decadal and regressional comparisons.

3.1. Wavelet Neural Network

Artificial neural networks are widely used in hydrology and water resources studies for data optimization, reconstruction of missing sediment load and prediction of sediment load trends. The ANN architecture acts as an information processing system containing several non-linear and interconnected elements in the form of layers connected via weights. The multi-layer perceptron (MLP) is a typical ANN, which consists of a number of nodes that are organized according to a particular arrangement. The layers process the information from the input layer to the hidden layer and further the hidden layer to the output layer for the generation of results. Generally, the hidden layers contain non-linear transfer functions to process the non-linear or linear information in order to build a relation between input and output variables. The output layer normally contains a linear transfer function to produce the output outside of the range of -1–1. Moreover, the hidden layers can also vary from single to multiple layers using different numbers of neurons. The size of a hidden layer and neurons within the hidden layer also affect the model performance. Less neurons in the hidden layer may affect the learning process, while more neurons in the hidden layer or the number of hidden layers restrict the efficiency in terms of computational time. The increase of neurons may also cause a network over fitting problem. The work in [60] suggested that the neurons for optimal generalization should be in the range from $\sqrt{2n} + m$ to the value $2n + 1$, where n and m represent the number of input and output nodes, respectively.

Wavelet transform (WT) decomposes signals into successive wavelet components corresponding to a time-domain signal within a frequency range. The original signal can be represented in terms of a wavelet expansion that utilizes the coefficients of the wavelet functions. Several wavelets can be constructed from a function Ψ known as a "mother wavelet", which is confined in a finite interval. That is, WT decomposes a given signal into frequency bands and then analyses them in time. WT are broadly classified into continuous wavelet transform (CWT) and discrete wavelet transform (DWT). CWT is defined as the sum over all time of the signal to be analyzed multiplied by the scaled and shifted versions of the transforming function Ψ. The CWT of a signal $f(t)$ is defined as follows:

$$W_{a,b} = \frac{1}{\sqrt{a}} \int_{-\infty}^{\infty} f(t) \Psi^* \left(\frac{t-b}{a} \right) dt \quad (1)$$

where '*' denotes the complex conjugate. CWT searches for correlations between the signal and wavelet function. This calculation is done at different scales of a and locally around the time of b. The result is a wavelet coefficient $W_{a,b}$ contour map. However, computing the wavelet coefficients at every possible scale (resolution level) necessitates a large amount of data and computation time. DWT analyzes a given signal with different resolutions for different frequency ranges. This is done by decomposing the signal into coarse approximation and detail coefficients. For this, the scaling and wavelet functions are employed. Choosing the scales a and the positions b based on the powers of two (dyadic scales and positions), DWT for a discrete time series f_i becomes:

$$W_{m,n} = 2^{-\frac{m}{2}} \sum_{i=0}^{N-1} f_i \Psi^* \left(2^{-m} i - n\right) \tag{2}$$

where i is integer time steps ($i = 0, 1, 2, ..., N-1$ and $N = 2^M$); m and n are integers that control, respectively, the scale and time; $W_{m,n}$ is the wavelet coefficient for the scale factor $a = 2^m$ and the time factor $b = 2^m n$. The original signal can be reconstructed using the inverse discrete wavelet transform as follows:

$$f_i = A_{M,i} + \sum_{m=1}^{M} \sum_{n=0}^{(2^{M-m}-1)} W_{m,n} 2^{\frac{m}{2}} \Psi \left(2^{-m} i - n\right) \tag{3}$$

or in a simple form as:

$$f_i = A_{M,i} + \sum_{m=1}^{M} D_{m,i} \tag{4}$$

where $A_{M,i}$ is called an approximation sub-signal at level M and $D_{m,i}$ are detail sub-signals at levels $m = 1, 2, ..., M$. The approximation coefficient $A_{M,i}$ represents the high scale low frequency component of the signal, while the detail coefficients $D_{m,i}$ represent the low scale high frequency component of the signal.

There is a variety of mother wavelets such as the Haar wavelet, Daubechies wavelet, Coiflet wavelet and biorthogonal wavelet. Normally, the Daubechies wavelet, which also belongs to the Haar wavelet, has been performing better in sediment transport processes due to its ability to detect time localization information. Time localization information is useful in handling the seasonality and hysteresis phenomenon in flow discharge and sediment load processes. The Coiflet wavelet is more symmetrical than the Daubechies wavelet. Similarly, the biorthogonal wavelet has the property of a linear phase, which is needed for signal reconstruction [61]. The selection of an appropriate mother wavelet depends on the type of application and data characteristics.

Before applying an ANN, the input discharge time series are decomposed using pre-selected wavelets. After data decomposition, a portion of the signal associated with certain frequency bands need to be eliminated if there is a poor correlation between the decomposed signal and the observation data. Only the decomposed signals that have significant correlation with the observation signal are used in the forecast model. Furthermore, on decomposed signals, the permutation of the *logsig*, *tansig*, *radbas* and *purelin* transfer functions was tested for the hidden and output layers. The Levenberg–Marquardt algorithm was used to train the networks due to its simplicity. The neurons in the hidden layer were selected based on the criteria described by [60]. The stopping criteria of the models was a maximum of 1000 epochs. The final networks were saved for later use to reconstruct the missing SSCs in the daily time series. Due to the different data time series at both gauges, we developed two different WA-ANN models. Figure 3 shows the methodology of coupling WT with ANN for forecasting SSC in the study area.

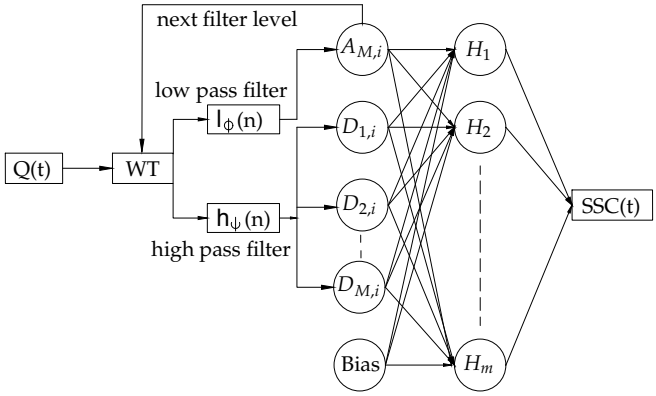

Figure 3. Schematic diagram of a wavelet transform coupled to an artificial neural network (WA-ANN). SSC, suspended sediment concentration.

The performance of the model was assessed employing the correlation coefficient (R), root mean square error (RMSE), mean absolute error (MAE) and the Nash–Sutcliffe efficiency (NSE). The correlation coefficient indicates a perfect fit at 1 and otherwise at 0. Similarly, RMSE and MAE indicate the best model performance when close to 0. The NSE ranges from $-\infty$–1, where 1 represents a perfect match and 0 indicates that the model is no better than simply representing the mean value. The simulated results are normally considered 'good' when the NSE is higher than 0.75 and 'satisfactory' when it lies between 0.36 and 0.75 [62].

3.2. Trend Analyses

3.2.1. Innovative Trend Test

The innovative trend analysis (ITA) [47] divides a time series into two halves, where the latter half is plotted against the first, after being sorted in ascending order. Given both halves are identical to each other, the plot shows a scatter of points along a 1:1 (45°) line on the Cartesian plane. The scatter of points falling above (below) the 1:1 line indicates a monotonically-increasing (decreasing) trend. ITA does not require pre-whitening, a specific sample size, a serial correlation structure of the time series or a normal probability distribution. ITA can easily identify the variations and trends in the lower, medium or higher hydrological processes [63,64]

3.2.2. Mann–Kendall Test

The Mann–Kendall (MK; [65,66]) test can detect a trend in a time series without being affected by the outliers. With the use of normal approximation, the MK test statistic S is calculated as follows:

$$S = \sum_{i=1}^{n-1} \sum_{j=i+1}^{n} sgn(X_j - X_i) \tag{5}$$

where X_i and X_j are the adjacent data values, S is the sum of positive or negative signs, n is the number of observations and:

$$sgn(X_j - X_i) = \begin{cases} +1 & (X_j - X_i) > 0 \\ 0 \quad if & (X_j - X_i) = 0 \\ -1 & (X_j - X_i) < 0 \end{cases} \tag{6}$$

The two important parameters of the MK test are the significance level and the slope. The former indicates the strength, while the latter indicates the magnitude and direction of a trend. If there are many tied data values, then the method specified for the number of data values greater than 40 is

used ([66], as reported by [67]). The variance of S (Equation (7)) takes into account these ties, where q is the number of tied groups and t_p is the number of data in the p group.

$$VAR(S) = \frac{1}{18}\left[n(n-1)(2n+5) - \sum_{p=1}^{q} t_p(t_p-1)(2t_p+5)\right] \tag{7}$$

After calculating S and its variance, an MK statistic Z is computed using Equation (8). A positive value of Z indicates an upward tend, whereas its negative value indicates a downward trend. If there is no detectable trend, then the MK statistic Z has a standard normal distribution.

$$Z = \begin{cases} \frac{S-1}{\sqrt{VAR(S)}} & S > 0 \\ 0 \quad if & S = 0 \\ \frac{S+1}{\sqrt{VAR(S)}} & S < 0 \end{cases} \tag{8}$$

To detect the season-wise monotonic trends, a slightly modified version of the MK test, namely seasonal Kendall (SK), is used, which runs the original MK test on each season (k) separately, where k can refer to any period of time within a year (e.g., months or four quarters of a year). The overall S statistic is then computed by adding each SK statistic (S_k) for m number of seasons, and the statistical significance of the trend can be assessed using the outcome of Equations (10) and (11) in Equation (8).

$$S_k = \sum_{i=1}^{n_k-1} \sum_{j=i+1}^{n_k} sgn(X_{k,j} - X_{k,i}) \tag{9}$$

$$S = \sum_{i=k}^{m} S_k \tag{10}$$

and:

$$VAR(S) = \sum_{k=1}^{m} VAR(S_k) \tag{11}$$

Based on sets of Monte Carlo simulations, [68] show that the presence of a positive serial correlation increases the variance of the distribution of S and thus increases the possibility of rejecting the null hypothesis of no trend; the same was also found by [69]. By contrast, negative serial correlation diminishes the variance of the distribution and results in underestimation of the significant trend detection probability. To limit the influence of serial correlation, we applied a correction factor, described by [70] in Equation (8), as follows;

$$Z^* = \frac{Z}{\sqrt{\eta^k}} \tag{12}$$

$$\eta^k = \begin{cases} 1 + \frac{m}{2} \sum_{i=1}^{m-1} (m-j)\rho_j & \text{for } j > 1 \\ 1 + 2\frac{\rho_1^{m+1} - m\rho_1^2 + (m-1)\rho_1}{m(\rho_1-1)^2} & \text{for } j = 1 \end{cases} \tag{13}$$

Normally, the population serial correlation coefficient ρ_j is replaced with the sample serial correlation coefficient r_j;

$$r_j = \frac{\frac{1}{m-j} \sum_{i=1}^{m-j} (X_i - \bar{X})(X_{i+j} - \bar{X})}{\frac{1}{m} \sum_{i=1}^{m} (X_i - \bar{X})^2} \qquad \text{where } j = 2, 3, ..., m-1. \tag{14}$$

$$\bar{X} = \frac{1}{m}\sum_{i=1}^{m} X_i \tag{15}$$

The correction factor η^k shrinks (expands) the MK statistics in the presence of positive (negative) serial correlation.

An estimate of trend magnitude, which is closely related to the MK test procedure, is known as Sen's slope estimator [71]. The slope estimates of N_k pairs of data of the k-season are first computed by:

$$P_{k,l} = \frac{X_{k,j} - X_{k,i}}{j - i} \tag{16}$$

for all $1 \leq i \leq j \leq n_k$ and $1 \leq l \leq N_k$. The median of these $P_{k,l}$ values is Sen's slope estimator P_k:

$$P_k = \begin{cases} P_{k,\left(\frac{N_k+1}{2}\right)} & \text{if } N_k \text{ is odd} \\ \frac{1}{2}\left[P_{k,\left(\frac{N_k}{2}\right)} + P_{k,\left(\frac{N_k}{2}+1\right)}\right] & \text{if } N_k \text{ is even} \end{cases} \tag{17}$$

Finally, P_k is tested by a two-sided test at the $(1-\alpha) \times 100\%$ confidence interval, and the true slope can be obtained. More details about the Mann–Kendall and Sen's slope tests can be found in [67,72].

3.2.3. Change Point Detection

We used the Pettitt test [50] to detect the qualitative and quantitative changes in SSL and discharge series. The Pettitt change point test is non-parametric and based on a version of the Man-n-Whitney statistics $U_{j,n}$ as follows:

$$U_{j,n} = U_{j-1,n} + \sum_{i=1}^{n} sgn(X_j - X_i) \qquad \text{where } j = 2, 3, \ldots, n \tag{18}$$

whereas X_i and X_j are the adjacent data values, n is the number of observations and sgn can be quantified using Equation (6). The statistics K_j and corresponding significance testing are given by:

$$K_{j,n} = Max|U_{j,n}| \text{ where } 1 \leq j \leq n \tag{19}$$

and:

$$p \cong 2exp\left[\frac{-6(K_{j,n})^2}{(n^3 + n^2)}\right] \tag{20}$$

If $p \leq 0.05$, a significant change point exist.

3.2.4. Decadal Analyses and Linear Regressions

Similar to the innovative trend method of [47], we divided the suspended sediment load (SSL) and discharge data into two time series of one decade each. The first time series consists of the initial decade of the dataset, and the second time series consists of the last decade of the dataset. To determine the mean annual and mean monthly changes, we compared the SSL and discharge shares of pre-selected spatial resolution for both gauges.

At the upper Indus River, the effect of high discharge events is influential; they transport a considerable amount of SSL [55]. Therefore, we also explored the mean monthly changes in most effective discharges during the initial and last decades of the datasets. The work in [73] defined the most effective discharge as the midpoint of the range of flows, which over a certain period can transport a considerable proportion of the SSL. The effective discharge can be computed using

sediment transport formulae and regional flow duration curves. In the present study, we used the effective discharge (Q/Q_{avg}) of 2.0-times the average discharge (Q_{avg}) for Besham Qila and 5.0-times the average discharge (Q_{avg}) for the Partab Bridge gauge as per the classifications formulated by [56].

To obtain the linear changes in each month during past 50 years, we developed linear regression equations of the reconstructed SSLs and observed discharges. Using these equations, we also quantitatively and qualitatively analyzed the changes.

4. Results

To analyze the trends in suspended sediment loads (SSLs) of the upper Indus River, we reconstructed the missing SSC data using wavelet neural networks (WA-ANNs) and then estimated corresponding SSLs using measured discharges, i.e., SSC × Q. The reconstructed daily data series in the form of monthly and annual SSLs were used in four different trend analysis techniques, namely: (1) innovative trend test; (2) Mann–Kendall and Sen slope tests; (3) Pettitt change point test; (4) decadal analyses and linear regressions. The study findings are described below.

4.1. Reconstruction of Daily Sediment Load Time Series

Based on several preliminary simulations for both gauges, we eventually trained both networks using 70% of the data for the training, 15% for testing and 15% for validation on a random basis. In a similar way, we also decomposed Q_t, Q_{t-1}, Q_{t-2}, for Besham Qila and Q_t, Q_{t-1} for Partab Bridge up to seven levels using the Daubechies (db1) wavelet. The best performing WA-ANN architectures reconstructed SSLs with a correlation coefficient R = 0.92 for both sites (Table 3). The RMSE and MAE for Partab Bridge were approximately two times more than Besham Qila; likewise, the standard deviation (SD) and mean in the actual SSC samples (Table 2). This difference shows the complexity in the transport process in the glacier influence zone of the upper Indus River at the Partab Bridge gauge. The NSE, which is used to analyze the model performance, was 0.85 for both stations. Therefore, we consider the WA-ANNs reconstructed suspended sediment load (SSL) series good as the NSE is higher than 0.75 [39,62,74]. In addition, both WA-ANN models reconstructed SSLs with a cumulative difference of ±1% with the measurements. Thus, according to another comparison criterion, the models that led to an error between ±10% and ±15% are considered as accurate models [37]. A comparison between the mass of suspended sediment sampled daily and computed results using WA-ANN models is also shown in Figure S1 of the Supplementary Material.

The reconstructed results showed a higher mean annual SSL of 171 Mt for Partab Bridge compared to 160 Mt at the downstream Besham Qila site (Figure 4). Moreover, the annual SSLs appear to have been rising at Partab Bridge since 1993 and causing the 10-year moving average to increase. In contrast, the annual SSLs have been decreasing at Besham Qila since 1993 (Figure 4). The similar changes in SSLs are also shown in linear and quadratic trends for both gauges (Figure 5). The statistical parameters of linear and quadratic line fittings are shown in Table S1 (supplementary part).

Table 3. Statistics of the best performing WA-ANN architectures for the Besham Qila and the Partab Bridge sites.

Location	Neurons	Transfer Function		R	RMSE (ton/day)	MAE (ton/day)	NSE
		First	Output				
Besham Qila	24	*tansig*	*purelin*	0.92	3.94×10^5	1.75×10^5	0.85
Partab Bridge	30	*logsig*	*tansig*	0.92	6.12×10^5	2.87×10^5	0.85

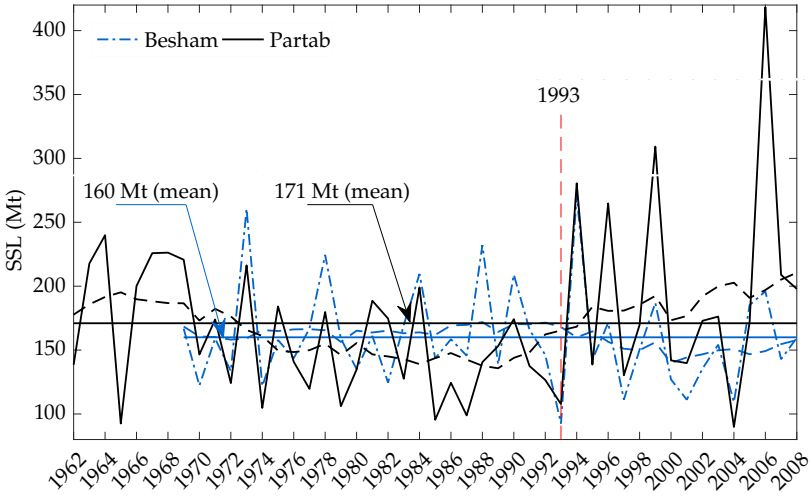

Figure 4. WA-ANN reconstructed annual suspended sediment loads (SSLs) for Besham Qila and Partab Bridge gauge stations showing an increase after 1993 at Partab Bridge (the dashed lines represent the 10-year moving average).

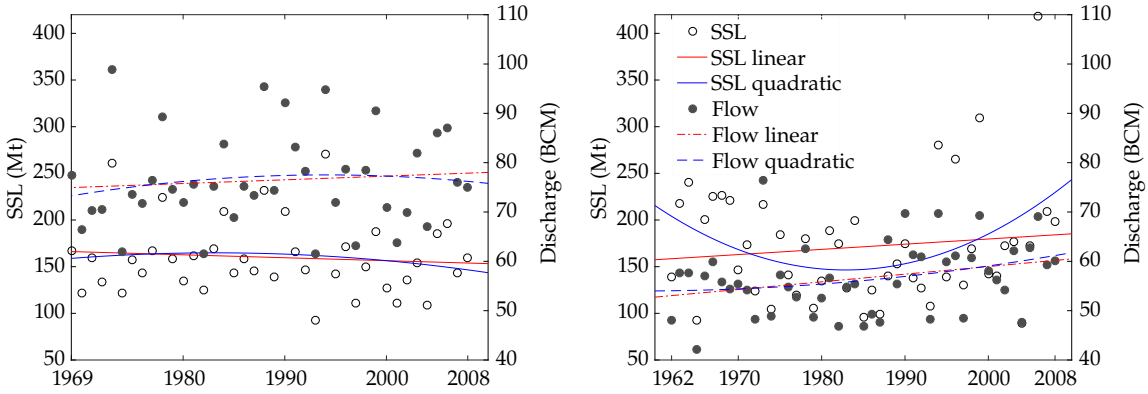

(a) Besham Qila (b) Partab Bridge

Figure 5. Linear and quadratic annual trends of reconstructed SSLs and observed discharges (legends for (**b**) also apply for (**a**)).

4.2. Innovative Trend Test for Annual Loads

The innovative trend test (ITA) shows a decreasing trend in low annual SSLs at Besham Qila against an increasing trend in high annual SSLs at the Partab Bridge site (Figure 6a,b). The frequencies have been increasing at both gauge sites. On the other hand, the overall annual flows at Partab Bridge show an increasing trend, while there are diverse trends at Besham Qila, where, apart from medium annual flows, the low and high flows have no discernible trend (Figure 6a,b). Contrary to Besham Qila, the increase in flows has also been causing an increase in SSLs at Partab Bridge. However, in the absence of hydraulic structures, urbanization or industrialization along the upper Indus River or within the UIB, this increase in annual SSLs noticed at the Partab Bridge did not appear at the downstream gauge, i.e., Besham Qila (Figure 6).

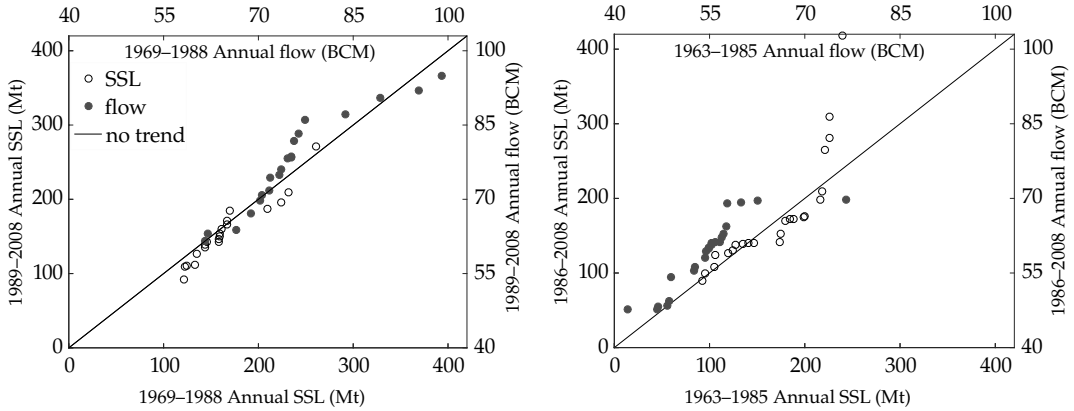

Figure 6. Results of innovative trend test showing a decreasing trend in low and high annual SSLs and flows at the Besham Qila and an increasing trend in high annual SSLs at Partab Bridge, along with an increase in all flows (legends for (**a**) also apply for (**b**)).

4.3. MK Test for Annual and Monthly Loads

The MK trend analyses show that the annual SSLs at Besham Qila have been decreasing at a rate of 0.634 Mt year^{-1} (Table 4). Calculating according to the same rate, this indicates a maximum decrease of 34 Mt from the estimate made by [28] (reported by [29]) for the Tarbela dam in 1982 (Table 1). Due to a negative slope of 0.634 Mt year^{-1}, it is possible that the estimates published in 1970s and 1980s show higher sediment loads compared to our estimate (160 Mt year^{-1}) at Besham Qila. In contrast to the results of the MK test, the seasonal Kendall (SK) test showed an annual statistically-significant increasing trend at the Besham Qila (Z = 3.2) and Partab Bridge (Z = 4.1) gauges. This contrast in both tests results arises due to the addition of each season's trend in the SK test (Equations (10) and (11)). In addition, the results of the SK test are similar either using seasons as four quarters of a year (December–February, March–May, June–August and September–November) or each month as a season.

The monthly SSLs show a significant increasing trend in the winter months (November–February) at Besham Qila with a cumulative magnitude of 0.004 Mt year^{-1}. This is a slight cumulative magnitude, which is unbalanced by the decreasing trend of -0.24 Mt year^{-1} alone in August (Table 4). Surprisingly, sandwiching increasing trends, April at Besham Qila shows a declining trend only in SSLs. The monthly SSLs at Partab Bridge, in contrast to Besham Qila, show a declining trend of 0.33 Mt year^{-1} only in August. This trend is balanced by 0.36 Mt year^{-1} rise in June and September (Table 4). Despite the diversified trends at both gauges, May showed a statistically increasing and August a statistically decreasing trend, whereas in summer, only August at Besham Qila and June, August and September at Partab Bridge show any trends. However, their contribution (33% and 83%) is still higher than the magnitudes of the trends in the remaining months of the year. In summer (July–September), the mean SSL recorded at Partab Bridge is 141 Mt year^{-1}, while during the same period or even until October, only 125 Mt passed through the Besham Qila gauge; this apparently indicates a durable deposition of SSLs between both gauges in summer.

Table 4. Mann–Kendall's (MK) annual and monthly SSL and discharge trends for the Besham Qila and the Partab Bridge sites. The minus symbol for the MK statistics indicates a downward trend, whereas the (-) symbol without numbers means no trend.

Period	SSL			Discharge		
	MK Statistic *	Sen's Slope (Mt year^{-1})	Average SSL (Mt year^{-1})	MK Statistic *	Sen's Slope (BCM y^{-1})	Average Flow (BCM y^{-1})
Besham Qila						
Annual	−1.21	−0.6345	160	-	-	76.41
January	2.74	0.0011	0.16	5.60	0.0081	1.25
February	2.76	0.0016	0.12	4.71	0.0068	1.08
March	1.08	0.0020	0.22	2.39	0.0061	1.40
April	−1.14	−0.00280	0.48	-	-	2.25
May	2.66	0.0769	4.61	2.60	0.0471	5.98
June	-	-	28.04	-	-	13.21
July	-	-	61.55	-	-	19.69
August	−1.00	−0.2414	53.80	-	-	17.53
September	-	-	9.90	-	-	7.77
October	-	-	0.74	1.55	0.0067	3.01
November	2.16	0.0013	0.22	3.51	0.0075	1.80
December	1.05	0.0004	0.15	3.71	0.0071	1.44
Partab Bridge						
Annual	-	-	171	1.77	0.1299	56.62
January	3.81	0.0007	0.07	2.11	0.0018	0.94
February	-	-	0.08	-	-	0.77
March	-	-	0.12	-	-	0.83
April	1.01	0.0009	0.25	2.81	0.0045	1.08
May	3.41	0.0476	3.09	4.64	0.0506	3.37
June	1.39	0.2308	25.25	1.55	0.0380	9.32
July	-	-	64.14	1.00	0.0299	15.08
August	−1.26	−0.3333	65.59	−1.02	−0.0274	14.15
September	1.86	0.1304	12.20	0.95	0.0181	6.26
October	2.90	0.0041	0.33	2.85	0.0100	2.33
November	3.33	0.0008	0.09	3.50	0.0060	1.38
December	2.59	0.0003	0.06	2.65	0.0034	1.10

Note: * Significant trend at 95% significance level (critical value = 1.96).

4.4. Change Point Detection Test

The test results show discernible change points in the monthly SSLs after 1982, whereas no change point was detected in annual SSLs at both gauges (Figure 7). Therefore, it might be possible that the peaks in annual SSLs recorded after 1993 at Partab Bridge gauge in Figure 4 in the absence of an increase in corresponding discharges may have been caused by degradation of landslides, which may have previously blocked the sediments [35]. On the other hand, the interventions of landslides are marginal for river flow due to a mean discharge of about 2600 m^3/s. Thus, the change points in monthly discharges are similar at both gauge stations (Table 5). As the Besham Qila site is located in a monsoon rainfall and snowmelt zone, no change in annual flows indicates a decrease in contribution from these sources (Table 5).

Interestingly, the magnitude of the increasing trend in SSLs over May at Partab Bridge was higher than Besham Qila's SSLs, which makes their mean loads approximately the same after 1997 (Figure 7). After 1997, there was no detectable increase in either parameter at either gauge station. Furthermore, September showed a significant increase of 60% no earlier than 1982, which is the highest magnitude or in the change in SSLs of the analyzed record. Compared to a noticeable increase in SSLs at Partab Bridge, surprisingly, the increasing loads are not being received at the downstream gauge (Figure 7).

Table 5. Significant change points in river flows determined using the Pettitt test.

Period	Annual	January	February	March	April	May	October	November	December
Besham Qila	-	1987	1987	1986	-	1997	1985	1986	1985
Partab Bridge	1987	1986	1987	1987	1987	1987	1985	1986	1985

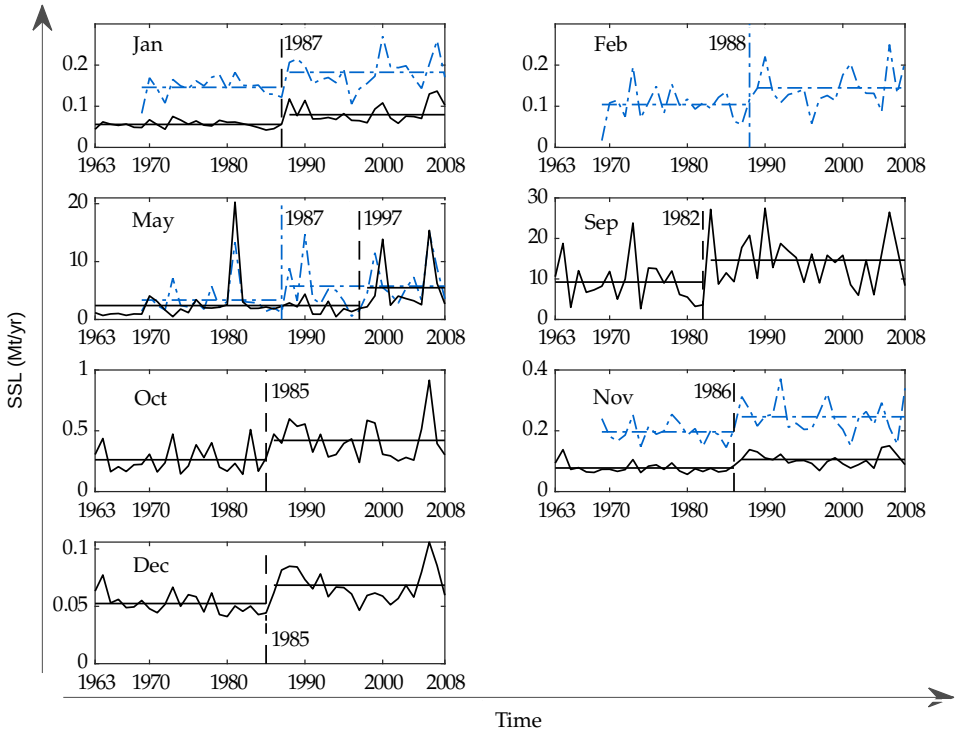

Figure 7. Significant change points in monthly SSLs determined using Pettitt test; black denotes Partab Bridge, and blue denotes Besham Qila.

4.5. Decadal Analyses and Linear Regressions

The decadal analyses only show decreasing trends in SSLs during peak summer (June and July) at Besham Qila and only over August at Partab Bridge (Figures 8ab, S2 and S3 (Supplementary Material)). The directions of changes in monthly SSLs are similar to their corresponding discharges except for July at Partab Bridge and August at Besham Qila. It might be possible that the high SSLs recorded in July at Partab Bridge have been causing the SSLs in the following month of August at the downstream gauge to increase, as shown in Figure 8. Similar deviations can be seen in effective discharges, where the SSL transport capacity of the river has been decreasing in summer (June, August and September) at Besham Qila and only over August at Partab Bridge (Figure 9).

The linear regressions also showed identical directions in the changes of the monthly SSLs and their corresponding discharges, except for April at Besham Qila (Table 6), where SSLs are decreasing against the increase in discharges. Nevertheless, there is a certain sensitive linear correlation between mean monthly SSLs and their corresponding discharges for the months in the effective discharges zone, depicted in Figure 10, where the axes represent the change in mean monthly discharges and SSLs (since 1969 and 1962) determined by linear regression equations (Figures S2 and S3 in the Supplementary Material). As can be seen from Figure 10, the change in SSLs is sensitive to the change in discharges, where a 1% change in discharges, on average, can cause a change of 3% in SSLs in the study area. However, compared to Besham Qila, the transport capacity of the river is more sensitive to the discharge change at Partab Bridge, where, for example, an 11% change in mean monthly discharges caused a 65% change in corresponding SSLs over September (Table 6). This may

be due to the location of the major source of eroded sediments in the Karakoram parts of the basin that contributes SSLs disproportionate to its drainage area at Partab Bridge [59]. On the other hand, the river slope is mild from Partab Bridge to Besham Qila, which causes substantial sediment storage of the incoming SSLs, particularly in summer.

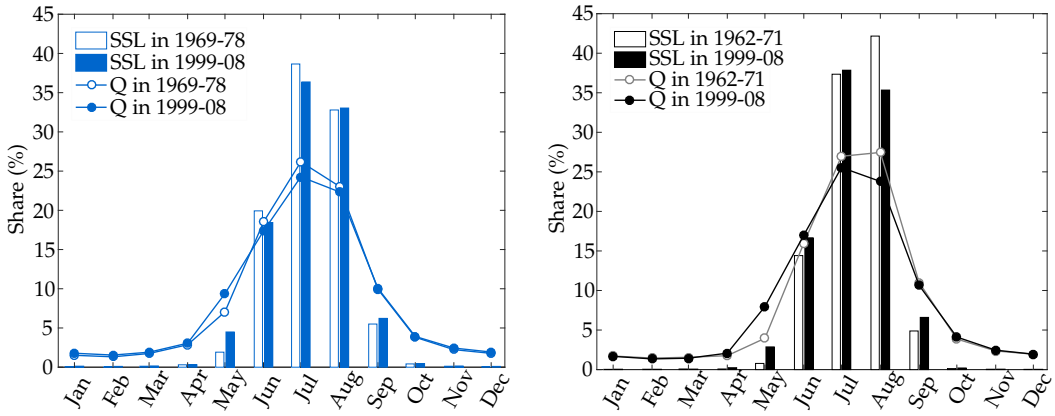

(a) Besham Qila (b) Partab Bridge

Figure 8. Monthly share of SSL and flow volume in the first and last decade of the analyzed record.

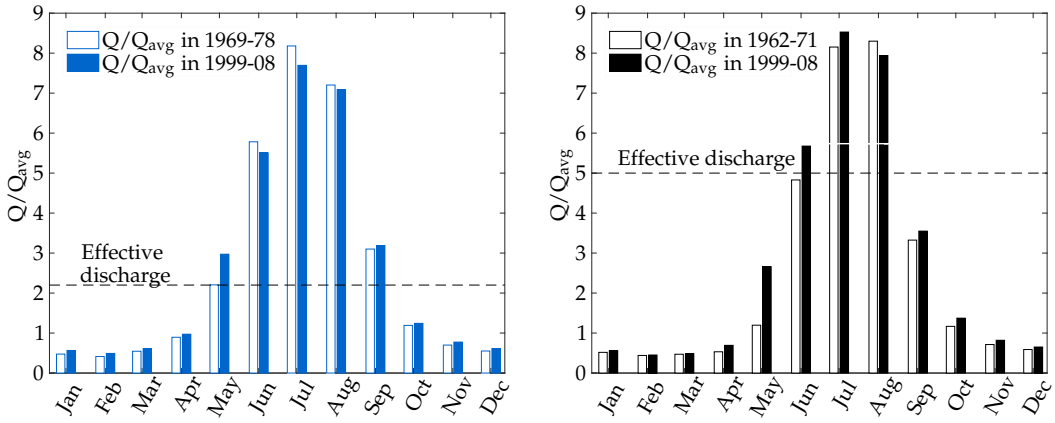

(a) Besham Qila (b) Partab Bridge

Figure 9. Monthly Q/Q_{avg} in first and last decade of the analyzed record following the monthly decadal trend of SSLs.

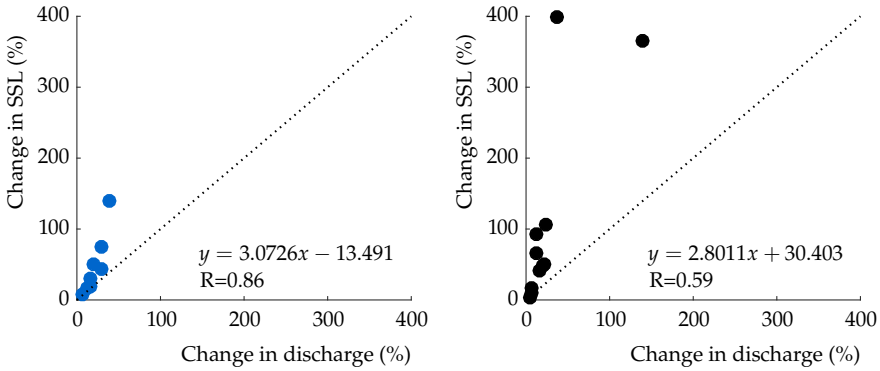

(a) Besham Qila (b) Partab Bridge

Figure 10. Linear regression of mean monthly changes in SSLs versus changes in discharges.

Table 6. Mean monthly linear variations in SSLs and discharges (flows) at both gauges (each month's regression plots are presented in Figures S2 and S3 in the Supplementary Material).

Period	Besham Qila *		Partab Bridge **	
	SSL (%)	Flow (%)	SSL (%)	Flow (%)
Annual	−7.40	3.90	13.50	16.00
January	44.64	29.49	93.56	12.85
February	77.58	29.8	10.27	6.28
March	59.43	20.8	3.36	5.01
April	-8.11	7.29	398.18	36.32
May	141.22	38.75	365.07	138.87
June	−13.41	−3.7	48.72	20.54
July	−9.04	−1.45	17.86	7.37
August	−12.79	−3.12	−8.16	−4.07
September	8.02	6.63	65.73	11.68
October	16.77	11.52	107.15	24.27
November	29.48	16.47	50.99	20.88
December	19.43	15.17	40.68	15.8

Note: * From 1969–2008; ** from 1962–2008.

To gain an overall qualitative overview of the trends, we compared the results in Table 7. The comparison reveals that SSLs have been increasing in May and decreasing in August in the study area. Apart from that, they have been monotonically increasing during winter months from November–February and also March and May. Although the annual SSLs at both gauge sites showed minor trends, they are statistically insignificant (Table 7).

Table 7. Qualitative comparison of the trends in SSLs using different methods (blue triangles imply an upward trend, whereas red triangles imply a downward trend; a "-" represents statistically insignificant/no trend). ITA, innovative trend analysis.

Period	Besham Qila					Partab Bridge				
	ITA	MK	C.P *	D.C **	Regression	ITA	MK	C.P *	D.C **	Regression
Annual	▼	▼	-	▼	▼	▲	-	-	▲	▲
January	▲	▲	▲	▲	▲	▲	▲	▲	▲	▲
February	▲	▲	▲	▲	▲	▲	-	-	▲	▲
March	▲	▲	-	▲	▲	▲	-	-	▲	▲
April	▼	▼	-	▲	▼	▲	▲	-	▲	▲
May	▲	▲	▲	▲	▲	▲	▲	▲	▲	▲
June	▼	-	-	▼	▼	▲	▲	-	▲	▲
July	▼	-	-	▼	▼	▲	-	-	▲	▲
August	▼	▼	-	▲	▼	▼	▼	-	▼	▼
September	▲	-	-	▲	▲	▲	▲	▲	▲	▲
October	▲	-	-	▲	▲	▲	▲	▲	▲	▲
November	▲	▲	▲	▲	▲	▲	▲	▲	▲	▲
December	▲	▲	-	▲	▲	▲	▲	▲	▲	▲

Note: * Change point detection test; ** decadal comparison.

5. Discussion

The WA-ANN models with a decomposition level of 7 (256 days) and a lag time of two and one day for Besham Qila and Partab Bridge, respectively, can precisely find the missing suspended sediment load for a given circumstance of hydrological data of the study area. Our findings show that the variation in flow patterns have been causing a significantly increasing trend in suspended sediment loads (SSLs) in May and a significantly decreasing trend in August at both Besham Qila and Partab Bridge gauges in the upper Indus River (Table 7). Contrary to the increase in high frequencies in low annual SSLs and river flows at Besham Qila (which is additionally influenced by monsoon rainfall), the frequencies in high SSLs and river flows are increasing at the Partab Bridge

gauge, which is located just downstream of high elevation glacierized areas of the Karakoram and Himalayas (Figures 1 and 6). Even in the absence of hydraulic structures between both gauges, the high SSLs recorded at Partab Bridge during summer are not being transported to the downstream gauge. Furthermore, the mean monthly linear variations show that an average 1% change in monthly flows can cause a 3% change in SSLs (Figure 10). However, the sediment transport capacity of the river is more sensitive to discharge change from May–August at Besham Qila and in September at Partab Bridge.

The sediment transport processes at the upper Indus River are influenced by hysteresis phenomenon and alternative cycles of dray and wet seasons. Applying simple relationship between water discharge and sediment concentration in the modeling process cannot adjust and model these impact factors. Therefore, a temporal resolution of approximately one year with a lag time of one day in the glacier-influenced zone and two days in the rainfall-influenced zone can reduce the variations in sediment load reconstruction. The reconstruction variations, in particular, increase when for example in conventional methods (sediment rating curves and ANN), temporary sediment storage in the main river channel and different transit times of discharges and sediment from their sources to the gauges are not included. Therefore, the quality of hydraulic design and sediment load trends based on poor sediment load estimation ultimately can affect the accuracy of subsequent studies and the efficiency of the overall hydraulic structure and associated benefits.

Partab Bridge gauge is located just downstream of the snow-fed and glacial melt zone of the upper Indus River. Therefore, the results indicate two types of patterns at Partab Bridge: (1) snowmelt- and (2) glacial melt-dependent SSLs. The former (snowmelt dependent) SSLs have been shifting to the spring months (April, May and June) due to an increase in early snowmelts at low altitudes [15,17,75]. Particularly in May, the significant increasing effect of early snowmelt has increased the SSL from 3.3 Mt year^{-1}–5.6 Mt year^{-1}, over the last 50 years (Figure 7). The effect of early snowmelt has also been noticed by [53], where they determined a 50 million m^3 increasing rate in May's flow at Partab Bridge. Interestingly, in comparison to Besham Qila (47 million m^3), the rate of increase in flow (50 million m^3) is higher at Partab Bridge and vice versa in SSLs (Tables 4 and 6). However, this increasing trend in flows extraordinarily increased SSLs at Partab Bridge, where after 1993, SSLs are identical to those of Besham Qila. The identical loads at both gauges point out either no increase in SSLs at Besham Qila's catchment or deposition downstream of Partab Bridge.

On the other hand, retrieval of glacial size depreciates the SSLs in August due to less water availability [14,19,56,76]; the SSLs have decreased to 34% (from 43%) over the past 50 years. It seems that glacial melt has shifted to July and September (Table 4). Although the increasing trend in both months is similar (Table 6), September's flow has remarkably increased the SSL from 9 Mt–15 Mt (similar to regressions where increase is 65%) at Partab Bridge (Figure 7). This significant increasing trend may be caused by the small increase in most effective discharge. It also shows the degree of sensitivity where only an 11% change in discharge caused a 66% change in SSL (Table 6). Furthermore, the remarkable increase in SSLs in September may reduce the reservoirs' life by increasing trap efficiency, where according to existing operation rules, the dams are normally filled to the maximum conservation level as late as 31 of August, such as at Tarbela dam.

Contrary to monotonically-increasing trends in SSL at Partab Bridge (except August), the Besham Qila gauge, located in the snow and rain-fed zone, has diversified mean monthly trends from winter to spring (Table 7). The rise in spring' SSLs at Besham Qila might be due to early snowmelt as at Partab Bridge [53]. However, the most surprising trend outcome is the decrease in SSLs during April in contrast to the increase in discharges revealed by regressions (Table 6). In the MK test, April's SSLs also showed a decreasing trend, despite an increasing trends in proceeding and immediately succeeding months (Table 4). In April, half of the flow volume recorded at Besham Qila comes from Partab Bridge [77]; however, corresponding to a 36% linear mean monthly increase at Partab Bridge (Table 6), the increase in flow at Besham Qila is only 7%. Therefore, the corresponding increase in SSLs recorded at Partab Bridge during April may be deposited (due to less

SSL transport capacity of the river) between Besham Qila and Partab Bridge, causing high SSLs during the succeeding month (May) at Besham Qila, when the river flows show a significant increasing trend at both gauges. Over August, on the contrary, the declining trend in SSLs at Besham Qila is statistically insignificant and seems to be associated with the decrease in the contribution of SSLs (Table 4) and flow volume (from which 84% of flow comes) from Partab Bridge.

As can be seen in Figure 2, over the past 40 years, at Besham Qila, the average annual volume of water was about 76 billion m^3 (BCMs), while the same average was 56 BCMs at Partab Bridge. That means the catchment at Partab Bridge (denoted by Zone 1) contributes 74.2% of the annual flow volume at Besham Qila. The remaining 25.8% in annual flow volume is contributed from the catchment between Partab Bridge and Besham Qila (denoted by Zone 2). The flow volume in Zone 2 is mostly generated from rainfall and snowmelt [17]. The linear trend from 1969–2008 in Figure 5 shows an increase in flow volume at Besham Qila of around 3.90% (denoted by ΔQ), while the same increase at Partab Bridge is around 13.50% (denoted by ΔQ_1). The variation of water availability in the area between Partab Bridge and Besham Qila (denoted by ΔQ_2) can be approximated using the following mass balance equation:

$$100 \times \Delta Q = 74.2 \times \Delta Q_1 + 25.8 \times \Delta Q_2 \quad (21)$$

From this equation, we obtain the variation in flow in Zone 2 $\Delta Q_2 = -38\%$. As Zone 2 is influenced by rainfall and snowmelt, it seems that the negative variation is attributable to trends of these parameter. These parameters (snowmelt and rainfall) have further been causing a decrease in water availability (between both gauges) required to transport the increased SSLs coming from Partab Bridge. Thus, the annual SSL trends at Besham Qila have shown a decreasing tendency since 1969 (Figure 5). Similar results have also been noted by [12], where the decrease in rainfall in the study area has been buffered by the increase in glacier melts. Additionally, the rise in glacier melt or precipitation over the western region of the upper Indus Basin noted by [16] might have been the cause of the 60% increase in SSLs during September at Partab Bridge. However, this increase has not been received at the downstream gauge, possibly due to a statistically insignificant increase in discharge downstream of the same gauge till Besham Qila (Table 4).

In the future at the upper Indus River, the overall increase in flow volume is expected to reach 7–12% [15]. This increase will mostly increase the flow share for the pre and post summer months, which will not be enough (it will be less than the most effective discharges) to transport an additional sediment load. Consequently, the annual SSLs will remain the same or will decrease slightly at Besham Qila. Therefore, in keeping with the current trends, the published sediment load estimates indicate an ongoing decline at Besham Qila (Table 1), since 1970 to the present. Regardless of the increase or decrease in the flow volume, the researchers agree on the shift in flow patterns at the upper Indus River [14,33,78]. Since there are neither hydraulic structures at the upper Indus River/basin, nor land use changes that might have affected the situation, in contrast to [79,80] studies for the East or Thames River, the temporal changes in SSLs can only be due to climate change factors. In addition, the statistically-significant monthly SSL trends contradict the previous reservoir sedimentation studies, which simply used the past SSCs without modification to the future predictions, particularly for the hydraulic structures planned upstream of Besham Qila [2,3,29,81]. Thus, using modified boundary conditions for reservoir sedimentation studies in the presence of trends can improve the overall quality of hydraulic designs and reservoirs' lives in the study area.

Nevertheless, the variations in SSLs, overall, may have serious implications for water storage, as well as the management of peak supply, peak demand and dam safety, which will require certain changes in the existing reservoirs' operational rules. These changes may include the use of additional (increased) water for power generation during low flows (winter months) and for irrigation or flushing operations in May when more water is available. Flushing in May when crops are at a mature stage and do not require irrigation will also provide the opportunity to re-fill the reservoirs in the succeeding high flow months (June–July). Although the overall flow volume at Besham Qila has been

increasing slightly, the flow contribution of the catchment between Partab Bridge and Besham Qila (Zone 2) has been decreasing and causing substantial sediment deposition and an overall decrease in the SSLs received at Besham Qila. Despite the fact that we did not include the impact of landslides on sediment deposition, the current findings are of crucial importance for 143 existing or planned dams and other construction projects in the upper Indus River, especially upstream of the Partab Bridge, which has a glacier-fed catchment and is sensitive to change in river discharges.

6. Conclusions

Reconstructed suspended sediment load (SSL) time series using wavelet neural networks (WA-ANNs) along with the innovative trend test, the Mann–Kendall test, Sen's slope estimator, the change point detection test and linear regressions have shown a shifting trend from the summer (June, July and August) to the spring and winter months due to a change in water availability at the upper Indus River over the past 50 years. The spatio-temporal trends between discharges and SSLs are disproportionate. This disproportional behavior and the significant trends strongly disconfirm the hypothesis that future inflows and SSLs are similar to the previous ones for reservoir sedimentation studies for the upper Indus River. In addition, the SSLs recorded at Partab Bridge are depositing in the river channel between both gauges. This deposition process has led to a long-term decrease in SSLs, in contrast to a long-term increase in flow volume at the Tarbela dam. For future water and food security along the Indus River command area, it is necessary to estimate the impact of long-term SSL variations on the existing and planned water storage capacities of the reservoirs. Moreover, the impact of planned construction activities along the upper Indus River, which contains enormous sediment deposits, should be evaluated.

Supplementary Materials: The following are available online at www.mdpi.com/2073-4441/10/1/16/s1. Figure S1: Comparison between the mass of suspended sediment sampled daily and computed results using WA-ANN models., (legends for (S1b) also apply for (S1a)); Figure S2: Mean monthly linear and quadratic trends in SSLs and discharges at Besham Qila site from 1969–2008; Figure S3: Mean monthly linear and quadratic trends in SSLs and discharges at Partab Bridge site from 1962–2008. Table S1: Statistical parameters of annual linear and quadratic trends of reconstructed SSLs and observed discharges for the Besham Qila and the Partab Bridge sites. Note: Q_s is annual SSL in Mt, Q is annual flow volume in BCM for Besham Qila $(1969 \leq y \leq 2008)$ and Partab Bridge $(1962 \leq y \leq 2008)$.

Acknowledgments: The German Academic Exchange Service (DAAD) and Higher Education Commission (HEC) of Pakistan jointly financed this work. The Surface Water Hydrology Project (SWHP) of WAPDAprovided the data. The German Research Foundation (DFG) and the Technical University of Munich (TUM) supported this work in the framework of the Open Access Publishing Program. We greatly appreciate their help. The first author is also thankful to Mr. Rohit Kumar, DNZEMunich, for his helpful discussions.

Author Contributions: Sardar Ateeq-Ur-Rehman designed the study, processed and analyzed the data, interpreted the results and wrote the paper. Minh Duc Bui and Peter Rutschmann contributed to the model development stage with theoretical considerations and practical guidance, assisted in the interpretations and integration of the results and helped in preparation of this paper with proof reading and corrections.

Conflicts of Interest: The authors declare no conflict of interests.

References

1. Bui, M.D.; Rutschmann, P. Numerical investigation of hydro-morphological changes due to training works in the Salzach River. In *Proceedings of River Flow 2012*; Munoz, R.E.M., Ed.; CRC Press: London, UK, 2012; Volume 1, pp. 589–594, ISBN 978-0-41-562129-8.
2. Dasu Hydropower Consultants. *Detailed Engineering Design Report, Part A, Engineering Design*; Report; Water and Power Development Authority: Lahore, Pakistan, 2013.
3. Petkovsek, G.; Roca, M. Impact of reservoir operation on sediment deposition. In *Proceedings of ICE Water Management*; Hamilton, W.A.H., Ed.; ICE Publishing: London, UK, 2014; Volume 167, pp. 577–584, ISBN 1741-7589.

4. Guerrero, M.; Rüther, N.; Haun, S.; Baranya, S. A combined use of acoustic and optical devices to investigate suspended sediment in rivers. *Adv. Water Resour.* **2017**, *102*, 1–12, doi:10.1016/j.advwatres.2017.01.008.
5. Chamoun, S.; De Cesare, G.; Schleiss, A.J. Venting of turbidity currents approaching a rectangular opening on a horizontal bed. *J. Hydraul. Res.* **2017**, 1–15, doi:10.1080/00221686.2017.1289266.
6. Babur, M.; Babel, M.; Shrestha, S.; Kawasaki, A.; Tripathi, N. Assessment of climate change impact on reservoir inflows using multi climate-models under RCPs—The case of Mangla Dam in Pakistan. *Water* **2016**, *8*, 389, doi:10.3390/w8090389.
7. Kreft, S.; David Eckstein, I.M. *Global Climate Risk Index 2017 Who Suffers Most From Extreme Weather Events? Weather-Related Loss Events in 2015 and 1996 to 2015*; Germanwatch Nord-Sued Initiative e.V.: Bonn, Germany, 2016; ISBN 978-3-943704-49-5.
8. Qiu, J. Stressed Indus River threatens Pakistan's water supplies. *Nature* **2016**, *534*, 600–601, doi:10.1038/534600a.
9. Khan, N.M.; Tingsanchali, T. Optimization and simulation of reservoir operation with sediment evacuation: A case study of the Tarbela Dam, Pakistan. *Hydrol. Process.* **2009**, *23*, 730–747, doi:10.1002/hyp.7173.
10. King, R.; Stevens, M. Sediment management at Warsak, Pakistan. *Int. J. Hydropower Dams* **2001**, *8*, 61–68.
11. Ackers, J.; Hieatt, M.; Molyneux, J.D. Mangla reservoir, Pakistan—Approaching 50 years of service. *Dams Reserv.* **2016**, *26*, 68–83, doi:10.1680/jdare.16.00036.
12. Pritchard, H.D. Asia's glaciers are a regionally important buffer against drought. *Nature* **2017**, *545*, 169–174, doi:10.1038/nature22062.
13. Immerzeel, W.W.; Van Beek, L.P.; Bierkens, M.F. Climate change will affect the Asian water towers. *Science* **2010**, *328*, 1382–1385, doi:10.1126/science.1183188.
14. Gardelle, J.; Berthier, E.; Arnaud, Y. Slight mass gain of Karakoram glaciers in the early twenty-first century. *Nat. Geosci.* **2012**, *5*, 322–325, doi:10.1038/NGEO1450.
15. Lutz, A.F.; Immerzeel, W.W.; Shrestha, A.B.; Bierkens, M.F.P. Consistent increase in High Asia's runoff due to increasing glacier melt and precipitation. *Nat. Clim. Chang.* **2014**, *4*, 587–592, doi:10.1038/nclimate2237.
16. Böhner, J.; Lucarini, V. Prevailing climatic trends and runoff response from Hindukush-Karakoram-Himalaya, upper Indus Basin. *Earth Syst. Dynam.* **2015**, doi:10.5194/esd-8-337-2015.
17. Lutz, A.F.; Immerzeel, W.; Kraaijenbrink, P.; Shrestha, A.B.; Bierkens, M.F. Climate change impacts on the upper Indus hydrology: Sources, shifts and extremes. *PLoS ONE* **2016**, *11*, e0165630, doi:10.1371/journal.pone.0165630.
18. Ul Hasson, S.; Pascale, S.; Lucarini, V.; Böhner, J. Seasonal cycle of precipitation over major river basins in South and Southeast Asia: A review of the CMIP5 climate models data for present climate and future climate projections. *Atmos. Res.* **2016**, *180*, 42–63, doi:10.1016/j.atmosres.2016.05.008.
19. Forsythe, N.; Fowler, H.J.; Li, X.F.; Blenkinsop, S.; Pritchard, D. Karakoram temperature and glacial melt driven by regional atmospheric circulation variability. *Nat. Clim. Chang.* **2017**, doi:10.1038/nclimate3361.
20. Azim, F.; Shakir, A.S.; Kanwal, A. Impact of climate change on sediment yield for Naran watershed, Pakistan. *Int. J. Sediment. Res.* **2016**, *31*, 212–219, doi:10.1016/j.ijsrc.2015.08.002.
21. Yasarer, L.M.; Sturm, B.S. Potential impacts of climate change on reservoir services and management approaches. *Lake Reserv. Manag.* **2016**, *32*, 13–26, doi:10.1080/10402381.2015.1107665.
22. Graf, W.H. *Hydraulics of Sediment Transport*; Water Resources Publication: Littleton, CO, USA, 1984; ISBN 978-0-91-833456-5.
23. McBean, E.A.; Al-Nassri, S. Uncertainty in suspended sediment transport curves. *J. Hydraul. Eng.* **1988**, *114*, 63–74, doi:10.1061/(ASCE)0733-9429(1988)114:1(63).
24. Morris, G.L.; Fan, J. *Reservoir Sedimentation Handbook: Design and Management of Dams, Reservoirs, and Watersheds for Sustainable Use*; McGraw Hill Professional: New York, NY, USA, 1998; ISBN 978-0-07-043302-1.
25. Holeman, J.N. The sediment yield of major rivers of the world. *Water Resour. Res.* **1968**, *4*, 737–747, doi:10.1029/WR004i004p00737.
26. Peshawar University. *The Sediment Load and Measurements for Their Control in Rivers of West Pakistan*; Report; Department of Water Resources: Peshawar, Pakistan, 1970.
27. Meybeck, M. Total mineral dissolved transport by world major rivers/Transport en sels dissous des plus grands fleuves mondiaux. *Hydrol. Sci. J.* **1976**, *21*, 265–284, doi:10.1080/02626667609491631.

28. Lowe, J.; Fox, I. Sedimentation in Tarbela Reservoir. In *Commission Internationale des Grandes Barrages*; Quatorzieme Congres des Grands Barrages: Rio de Janeiro, Brazil, 1982.
29. Roca, M. Tarbela Dam in Pakistan. Case study of reservoir sedimentation. In *Proceedings of River Flow*; Munoz, R.E.M., Ed.; CRC Press: London, UK, 2012; ISBN 978-0-415-62129-8.
30. Milliman, J.; Quraishee, G.; Beg, M. Sediment discharge from the Indus River to the ocean: Past, present and future. In *Marine Geology and Oceanography of Arabian Sea and Coastal Pakistan*; Haq, B.U., Milliman, J.D., Eds.; Van Nostrand Reinhold/Scientific and Academic Editions: New York, NY, USA, 1984; p. 382, ISBN 978-0-44-223216-0.
31. Summerfield, M.A.; Hulton, N.J. Natural controls of fluvial denudation rates in major world drainage basins. *J. Geophys. Res. Solid Earth* **1994**, *99*, 13871–13883, doi:10.1029/94jb00715.
32. Collins, D. *Hydrology of Glacierised Basins in the Karakoram: Report on Snow and Ice Hydrology Project in Pakistan with Overseas Development Administration, UK [ODA] and Water and Power Development Authority, Pakistan [WAPDA]*; Report; University of Manchester: Manchester, UK, 1994.
33. Ali, K.F. Construction of Sediment Budgets in Large Scale Drainage Basins: The Case of the Upper Indus River. Ph.D. Thesis, Department of Geography and Planning, University of Saskatchewan, Saskatoon, SK, Canada, 2009.
34. Bogen, J. The hysteresis effect of sediment transport systems. *Norsk Geografisk Tidsskrift* **1980**, doi:10.1080/00291958008545338.
35. Hewitt, K. Gifts and perils of landslides. *Am. Sci.* **2010**, *98*, 410–419.
36. Jain, S.K. Development of integrated sediment rating curves using ANNs. *J. Hydraul. Eng.* **2001**, *127*, 30–37, doi:doi:10.1061/(ASCE)0733-9429(2001)127:1(30).
37. Rajaee, T.; Mirbagheri, S.A.; Zounemat-Kermani, M.; Nourani, V. Daily suspended sediment concentration simulation using ANN and neuro-fuzzy models. *Sci. Total Environ.* **2009**, *407*, 4916–4927, doi:10.1016/j.scitotenv.2009.05.016.
38. Ulke, A.; Tayfur, G.; Ozkul, S. Predicting suspended sediment loads and missing data for Gediz River, Turkey. *J. Hydrol. Eng.* **2009**, *14*, 954–965, doi:10.1061/(ASCE)HE.1943-5584.0000060.
39. Rajaee, T.; Nourani, V.; Zounemat-Kermani, M.; Kisi, O. River suspended sediment load prediction: Application of ANN and wavelet conjunction model. *J. Hydrol. Eng.* **2010**, *16*, 613–627, doi:10.1061/(ASCE)HE.1943-5584.0000347.
40. Tfwala, S.S.; Wang, Y.M. Estimating sediment discharge using sediment rating curves and artificial neural networks in the Shiwen River, Taiwan. *Water* **2016**, *8*, 53, doi:10.3390/w8020053.
41. Ulke, A.; Tayfur, G.; Ozkul, S. Investigating a suitable empirical model and performing regional analysis for the suspended sediment load prediction in major rivers of the Aegean Region, Turkey. *Water Resour. Manag.* **2016**, 1–26, doi:10.1007/s11269-016-1357-z.
42. Shoaib, M.; Shamseldin, A.Y.; Melville, B.W.; Khan, M.M. A comparison between wavelet based static and dynamic neural network approaches for runoff prediction. *J. Hydrol.* **2016**, *535*, 211–225, doi:10.1016/j.jhydrol.2016.01.076.
43. Partal, T.; Cigizoglu, H.K. Estimation and forecasting of daily suspended sediment data using wavelet–neural networks. *J. Hydrol.* **2008**, *358*, 317–331, doi:10.1016/j.jhydrol.2008.06.013.
44. Adamowski, K.; Prokoph, A.; Adamowski, J. Development of a new method of wavelet aided trend detection and estimation. *Hydrol. Process.* **2009**, *23*, 2686–2696, doi:10.1002/hyp.7260.
45. Jothiprakash, V.; Garg, V. Reservoir sedimentation estimation using artificial neural network. *J. Hydrol. Eng.* **2009**, *14*, 1035–1040, doi:doi:10.1061/(ASCE)HE.1943-5584.0000075.
46. Partal, T.; Cigizoglu, H.K. Prediction of daily precipitation using wavelet—Neural networks. *Hydrol. Sci. J.* **2009**, *54*, 234–246, doi:10.1623/hysj.54.2.234.
47. Şen, Z. Innovative trend analysis methodology. *J. Hydrol. Eng.* **2011**, *17*, 1042–1046, doi:10.1061/(ASCE)HE.1943-5584.0000556.
48. Zhang, Q.; Xu, C.Y.; Becker, S.; Jiang, T. Sediment and runoff changes in the Yangtze River basin during past 50 years. *J. Hydrol.* **2006**, *331*, 511–523, doi:10.1016/j.jhydrol.2006.05.036.
49. Shi, H.; Hu, C.; Wang, Y.; Liu, C.; Li, H. Analyses of trends and causes for variations in runoff and sediment load of the Yellow River. *Int. J. Sediment. Res.* **2016**, *32*, 171–179, doi:10.1016/j.ijsrc.2016.09.002.
50. Pettitt, A.N. A non-parametric approach to the change-point problem. *J. R. Stat. Soc. C Appl. Stat.* **1979**, *28*, 126–135, doi:10.2307/2346729.

51. Sun, L.; Yan, M.; Cai, Q.; Fang, H. Suspended sediment dynamics at different time scales in the Loushui River, south-central China. *CATENA* **2016**, *136*, 152–161, doi:10.1016/j.catena.2015.02.014.
52. Hasson, S.; Lucarini, V.; Khan, M.R.; Petitta, M.; Bolch, T.; Gioli, G. Early 21st century snow cover state over the western river basins of the Indus River system. *Hydrol. Earth Syst. Sci.* **2014**, *18*, 4077–4100, doi:10.5194/hess-18-4077-2014.
53. Hasson, S.; Böhner, J.; Lucarini, V. Prevailing climatic trends and runoff response from Hindukush–Karakoram–Himalaya, upper Indus Basin. *Earth Syst. Dynam.* **2017**, *8*, 337–355, doi:10.5194/esd-8-337-2017.
54. The International Journal on Hydropower & Dams. *World Atlas & Industry Guide*; Aqua Media International Ltd.: Wallington, UK, 2017; pp. 183–186.
55. Munir, S. Role of Sediment Transport in Operation and Maintenance of Supply and Demand Based Irrigation Canals: Application to Machai Maira Branch Canals. Ph.D. Thesis, Institute for Water Education, UNESCO-IHE, Delf, The Netherlands, 2011.
56. Ali, K.F.; De Boer, D.H. Spatial patterns and variation of suspended sediment yield in the upper Indus River basin, northern Pakistan. *J. Hydrol.* **2007**, *334*, 368–387, doi:10.1016/j.jhydrol.2006.10.013.
57. Rantz, S. *Measurement and Computation of Stream Flow. Vol. 1. Measurement of Stage and Discharge; Vol. 2. Computation of Discharge*; US Geological Survey Water Supply Paper; United States Geological Survey: Reston, VA, USA, 1982; Volume 2175.
58. Edwards, T.K.; Glysson, G.D.; Guy, H.P.; U.S. Geological Survey. *Field Methods for Measurement of Fluvial Sediment*, rev. ed.; Techniques of Water-Resources Investigations of the United States Geological Survey, U.S. Geological Survey; Information Services: Reston, VA, USA; Denver, CO, USA, 1999; p. 89, ISBN 978-0-607-89738-8.
59. Ali, K.F.; De Boer, D.H. Spatially distributed erosion and sediment yield modeling in the upper Indus River basin. *Water Resour. Res.* **2010**, *46*, doi:10.1029/2009WR008762.
60. Fletcher, D.; Goss, E. Forecasting with neural networks: An application using bankruptcy data. *Inf. Manag.* **1993**, *24*, 159–167, doi:10.1016/0378-7206(93)90064-Z.
61. Railean, I.; Moga, S.; Borda, M.; Stolojescu, C.L. A wavelet based prediction method for time series. In *Stochastic Modeling Techniques and Data Analysis (SMTDA2010)*; Janssen, J., Ed.; ASMDA International: Chania, Greece, 2010.
62. Moriasi, D.N.; Arnold, J.G.; Van Liew, M.W.; Bingner, R.L.; Harmel, R.D.; Veith, T.L. Model evaluation guidelines for systematic quantification of accuracy in watershed simulations. *Trans. ASABE* **2007**, *50*, 885–900.
63. Şen, Z. Trend identification simulation and application. *J. Hydrol. Eng.* **2013**, *19*, 635–642, doi:10.1061/(ASCE)HE.1943-5584.0000811.
64. Kisi, O. An innovative method for trend analysis of monthly pan evaporations. *J. Hydrol.* **2015**, *527*, 1123–1129, doi:10.1016/j.jhydrol.2015.08.051.
65. Mann, H. Nonparametric tests against trend. *Econmetrica* **1945**, *13*, 245–259, doi:10.2307/1907187.
66. Kendall, M.G. *Rank Correlation Methods*, 4th ed.; Charles Griffin: London, UK, 1975; ISBN 978-0-85-264199-6.
67. Gilbert, R.O. *Statistical Methods for Environmental Pollution Monitoring*; John Wiley & Sons: Hoboken, NJ, USA, 1987; ISBN 978-0-47-128878-7.
68. Yue, S.; Pilon, P.; Phinney, B.; Cavadias, G. The influence of autocorrelation on the ability to detect trend in hydrological series. *Hydrol. Process.* **2002**, *16*, 1807–1829, doi:10.1002/hyp.1095.
69. Von Storch, H. Misuses of statistical analysis in climate research. In *Analysis of Climate Variability*; Springer: Berlin, Germany, 1999; pp. 11–26.
70. Yue, S.; Wang, C.Y. Regional streamflow trend detection with consideration of both temporal and spatial correlation. *Int. J. Climatol.* **2002**, *22*, 933–946, doi:10.1002/joc.781.
71. Sen, P.K. Estimates of the regression coefficient based on Kendall's tau. *J. Am. Stat. Assoc.* **1968**, *63*, 1379–1389, doi:10.1080/01621459.1968.10480934.
72. Gibbons, R.D.; Bhaumik, D.; Aryal, S. *Statistical Methods for Groundwater Monitoring*, 2nd ed.; Statistics in Practice; Wiley: Hoboken, NJ, USA, 2009; p. 374, ISBN 978-0-47-016496-9(cloth).
73. Pickup, G. Adjustment of stream-channel shape to hydrologic regime. *J. Hydrol.* **1976**, *30*, 365–373, doi:10.1016/0022-1694(76)90119-0.

74. Hassan, M.; Shamim, M.A.; Sikandar, A.; Mehmood, I.; Ahmed, I.; Ashiq, S.Z.; Khitab, A. Development of sediment load estimation models by using artificial neural networking techniques. *Environ. Monit. Assess.* **2015**, *187*, 1–13, doi:10.1007/s10661-015-4866-y.
75. Khattak, M.S.; Babel, M.; Sharif, M. Hydro-meteorological trends in the upper Indus River basin in Pakistan. *Clim. Res.* **2011**, *46*, 103–119, doi:10.3354/cr00957.
76. Mukhopadhyay, B.; Khan, A. A reevaluation of the snowmelt and glacial melt in river flows within Upper Indus Basin and its significance in a changing climate. *J. Hydrol.* **2015**, *527*, 119–132, doi:10.1016/j.jhydrol.2015.04.045.
77. Mukhopadhyay, B.; Khan, A. A quantitative assessment of the genetic sources of the hydrologic flow regimes in Upper Indus Basin and its significance in a changing climate. *J. Hydrol.* **2014**, *509*, 549–572, doi:10.1016/j.jhydrol.2013.11.059.
78. Laghari, A.; Vanham, D.; Rauch, W. The Indus basin in the framework of current and future water resources management. *Hydrol. Earth. Syst. Sci.* **2012**, *16*, 1063–1083, doi:10.5194/hess-16-1063-2012.
79. Zhang, W.; Wu, Y.; Wang, W.G.; Xing, W.Q. Characterizing the seasonal changing patterns of hydrological variables in the East River, Southern China. *J. Hydrol. Eng.* **2016**, *21*, 1–7, doi:10.1061/(ASCE)HE.1943-5584.0001445.
80. Bussi, G.; Dadson, S.J.; Bowes, M.J.; Whitehead, P.G. Seasonal and interannual changes in sediment transport identified through sediment rating curves. *J. Hydrol. Eng.* **2016**, *22*, 1–8, doi:10.1061/(ASCE)HE.1943-5584.0001466.
81. Bunji Consultants Joint Venture. *Bunji Hydropower Project, Design Report, Volume 2B Sedimentation*; Report; Water and Power Development Authority: Lahore, Pakistan, 2010.

3.2.2. Neukonzept des hydromorphologischen Modellsystems

Einer der schwächsten Punkte hydromorphologischer Modelle ist die Verwendung empirischer Formeln zur Berechnung der Sedimenttransportraten. In vielen Fällen werden unzufriedene morphologische Veränderungen vorhergesagt und die Ergebnisse der verschiedenen Formeln variieren häufig stark. Die Gründe liegen in der Komplexität der Wechselwirkung zwischen Strömung und Sedimenttransport und in den Einschränkungen der bei diesen Methoden angewandten nichtlinearen Regression. Im Folgenden sind zwei wissenschaftliche Arbeiten zusammengefasst:

1. M.D. Bui, K. Kaveh, P. Rutschmann (2015b): “Integrating artificial neural networks into hydromorphological model for fluvial channels”. Proceedings of the 36th IAHR World Congress. The Hague, The Netherlands.

2. K. Kaveh, M.D. Bui, P. Rutschmann (2019): “Integration of Artificial Neural Networks into TELEMAC-MASCARET system, new concepts for hydromorphodynamic modeling”. Advances in Engineering Software. Elsevier.

Im Paper [1] wurde ein optimales ANN-Modell entwickelt, das in ein hydromorphologisches Modellsystem integriert ist und die morphologischen Änderungen in einem geraden alluvialen Kanal bei gleichmäßiger Strömung angemessen vorhersagen kann. Eine analytische Näherung, die auf der Sedimentkonservierung basiert, wurde angewendet, um Daten zu generieren, die zum Trainieren und Testen verschiedener ANN-Modelle verwendet werden. Durch Auswertung der berechneten Ergebnisse wurden die entsprechenden Parameter für eine optimale Netzwerkstruktur für die Simulation von Sohländerung bestimmt. Die berechneten Ergebnisse zeigen, dass für die betrachtete Fallstudie und auch für die Vorhersage langfristiger Zeitreihen ANN Modelle eine gute Leistung erbringen können. Darüber hinaus kann ein gut trainiertes ANN-Modell in die hydromorphologischen Modellsysteme integriert werden und wie herkömmliche numerische Operatoren funktionieren. Weitere Entwicklung des Modellkonzepts wurde im Paper [2] präsentiert, in dem ANN-Modelle in das TELMAC-MASCARET System integriert wurden. Die Fähigkeit und Genauigkeit zahlreicher ANN-Modelle wurden analysiert, die mit unterschiedlichen Strukturen entworfen und mit unterschiedlichen Lernregeln trainiert wurden.

E-proceedings of the 36th IAHR World Congress
28 June – 3 July, 2015, The Hague, the Netherlands

Integrating artificial neural networks into hydromorphological model for fluvial channels

MINH DUC BUI [1], KEIVAN KAVEH [2] & PETER RUTSCHMANN [3]

[1] Research Coordinator, Institute of Hydraulic and Water Resources Engineering, TUM, München, Germany, bui@tum.de

(2) PhD Student, Institute of Hydraulic and Water Resources Engineering, TUM, München, Germany, keivan.kaveh@tum.de

(3) Professor, Institute of Hydraulic and Water Resources Engineering, TUM, München, Germany, p.rutschmann@tum.de

ABSTRACT

One of the weakest points of hydromorphological models is to use empirical formulae for calculating sediment transport rates, which are of limited generality. In many cases, unreasonable morphological changes are predicted and the results of the different formulae often vary strongly. The reasons are assumed in the complexity of the interaction between flow and sediment transport and in limitations of the nonlinear regression applied in these methods. In contrast to most traditional empirical methods, which need prior knowledge about the nature of the relationships among the data, the methods of artificial neural networks (ANN) learn from data examples presented to them in order to capture the subtle functional relationships among the data even if the underlying relationships are unknown or the physical meaning is difficult to explain. Additionally ANN has proven a high tolerance against data sample errors. These attributes make the utilization of ANN for sediment transport predictions very promising. In this paper an optimal ANN model has been selected, which is integrated into a hydromorphological model system and could adequately predict the morphological changes in a straight alluvial channel under steady flow discharge. For this purpose the capability and accuracy of numerous ANN models designed with different structures and trained with different learning rules has been analyzed. To evaluate the prediction qualities of the designed networks, a comparative study has been carried out for these models by evaluating several statistical parameters that describe the errors associated with the model in terms of statistical measures of goodness-of-fit between the estimated bed change and analytical approximation.

Keywords: Artificial Neural Network, Sediment transport, Hydromorphological modeling

1. INTRODUCTION

The transport of sediment as bed load is an important process that occurs in rivers, estuaries, and coastal regions. In many situations, this process and the resulting morphological changes of the bed can have a detrimental impact on the infrastructure and environment. Clearly, the processes of sediment transport and morphological evolution of the bed are determined by the properties of the fluid flow, which in turn are affected by the changes in the morphology of the bed that they induce. Thus, the motion of the fluid and the motion of the bed form an interdependent two-phase phenomenon that must be analyzed using a model system made up of two distinct but interdependent model components: (1) a hydrodynamic component defining the evolution of the flow; and (2) sediment transport/morphological component defining the evolution of the bed. Such a modeling system is often referred to as a hydromorphological model. The conventional method for performing morphodynamic simulations in rivers is to decouple the hydrodynamic and the morphodynamic systems. The decoupling approach is based on the rationale that the channel bed reacts at a much slower timescale than the flow. At implementation level, these modules communicate through a quasi-steady morphodynamic time-stepping mechanism: during flow computation, the bed level is assumed to be constant and during computation of the bed level, the flow and sediment transport quantities are assumed invariant to the bed level changes. The modules are linked together at the programming level.

In the conventional hydromorphological models the bed level changes are governed by the equation for conservation of sediment mass (Exner's equation). Neglecting the suspended load, this equation can be written in a 1D case as follows:

$$\frac{\partial z_b}{\partial t} = -\frac{1}{1-p}\frac{\partial q_b}{\partial x} \qquad [1]$$

Where z_b is the bed elevation (defined positive upward relative to a fixed datum) at each horizontal position x and time t; p is the bed porosity, q_b is the volumetric sediment transport rate per unit width. The bed load transport rate q_b is a complex function of various hydrodynamic quantities such as currents and water depth as well as quantities associated with sediment properties such as sediment density and grain size. Many empirical functions are available to calculate bed load transport. Most of the formulae available in the literature have been developed based on the analysis of laboratory and

field data using statistical methods such as the regression method, and there are drastic differences between them. No uniformly valid formulation for q_b exists at present. Yet, we are still unable to select the most accurate for a particular problem and the accuracy of computational sediment transport models remains a challenging question.

The artificial neural networks (ANN) are a form of artificial intelligence, which attempts to mimic the function of the human brain and nervous system at a sub-symbolic level. ANN learn from data examples presented to them in order to capture the subtle functional relationships within the data. The majority of hydromorphological processes are highly nonlinear in nature and, in many cases, modeling these variables with conventional models may be limited by a poor understanding of the complex interactions that are involved in the process. In such cases, ANN are often viewed as an appealing alternative, as they have the ability to extract a nonlinear relationship from data without requiring an in depth knowledge of the physics occurring within the system.

The main objective of the present study is, therefore, to develop an ANN model to predict the morphological changes in a straight alluvial channels under steady flow discharge and uniform bed material, where the bed level changes are calculated directly from the defined flow without calculation of the bed load. The prediction qualities of the designed network are studied by evaluating several statistical parameters that describe the errors associated with the model in terms of statistical measures of goodness-of-fit between the estimated bed change and analytical solution.

2. CONVENTIONAL NUMERICAL METHODS

Numerical morphological models involve coupling between a hydrodynamic model, which provides a description of the flow field leading to a specification of local sediment transport rates, and an equation for bed level change, which expresses the conservative balance of sediment volume and its continual redistribution with time. Eq. 1 can be re-written in the following form:

$$\frac{\partial z_b}{\partial t} + C(z_b)\frac{\partial z_b}{\partial x} = 0 \qquad [2]$$

where $C(z_b)$ is the phase speed of bed form, expressed as

$$C(z_b) = \frac{1}{1-p}\frac{\partial q_b}{\partial z_b} \qquad [3]$$

Because the flow field and the resulting transport rate is a nonlinear function of the bed level, the sediment conservation equation is physically a nonlinear conservation equation for the bed level. Mathematically the most interesting feature of such equations is that they admit shock waves in their solution, discontinuities in the solution that can form even from smooth initial data. Several decades of research effort has been devoted to the development of numerical solution techniques for obtaining accurate and stable simulations of shock behavior.

Many state-of-art morphological models use classical lower order Lax-Wendroff or modified Lax-Wendroff schemes for morphology which are not very stable for long time sediment transport processes simulation. Filtering or artificial diffusion are often added to achieve stability. In Hudson et al. (2005) and Long et al. (2008) several schemes using the artificial-viscosity and filtering processes as well as the so called shock capturing techniques were discussed for simulating bed level change with different accuracy and stability behaviors. Use of these schemes requires an estimate of phase speed $C(z_b)$, which is needed for approximating the flux functions and appreciating the numerical stability condition. In many instances, it is not very easy to estimate this parameter (e.g. when the bed level gradient approaches zero or changes its sign). Overestimation of $C(z_b)$ could overly smooth the solution, while underestimation of $C(z_b)$ may make the scheme unstable.

3. ANN APPROACH

Artificial neural network is a broad term covering a large variety of network architectures, the most common being a multilayer perceptron (MLP). The parameters to be found by training are the weight vectors connecting the different nodes of the input, hidden, and output layers of the network by the so-called error-back-propagation method. During training the values of the parameters (weights) are varied so that the ANN output becomes similar to the measured output on a known data set.

An ANN model consists of a number of artificial neurons variously known as processing elements or nodes. For multilayer networks, neurons are arranged in layers: an input layer, an output layer and one or more intermediate or hidden layers. The net is formed by these layers of neurons, and each neuron in a specific layer is connected to neurons in other layers via weighted connections. Neurons are defined as mathematical expressions that filter the signal through the net. From the connected neurons in the previous layer, an individual neuron receives its weighted inputs which are usually summed along with a bias unit. The bias unit is used to scale the input to a useful range in order to improve the convergence properties of the network. The result of this combined summation is passed through a transfer function so as to produce the output of the neuron. This output is then passed through weighted connections to neurons in the next layer, where the process is repeated. A trained response is achieved by changing the connections' weights in the network according to an error minimization criterion. A validation process can be used during training in order to prevent overfitting. Once the

network has been trained to simulate the best response to input data, the configuration of the network is fixed and a test process is conducted to evaluate the performance of the ANN as a predictive tool. According to Shahin et al. (2002), the structure and process for node *j* of an ANN model can be illustrated in Figure 1. More details about ANN approaches with these methods can be found in Penz (2013).

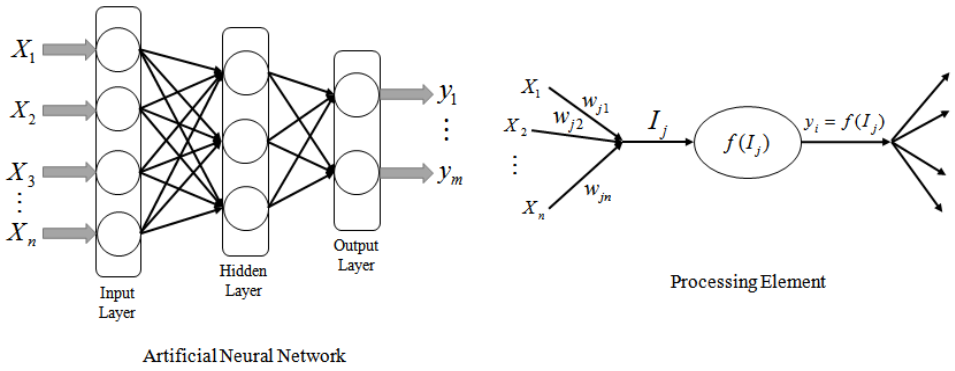

Figure 1. Typical structure and operation of an ANN model (I_j = activation level of node j; w_{ji} = connection weight between nodes j and i; x_i = input from node i; y_j = output of node j; and $f(I_j)$ = transfer function).

4. MODEL SETUP

We consider a straight channel with a length of 1000 m and a finite amplitude perturbation of the bed level near the center of the domain as illustrated in Figure 2. This case can represent a sand dune in a river flow. We assume that the bed elevation zb is very small in comparison to the water free surface level z_s and the bed form movement is only due to bed load. Assuming a steady flow discharge throughout the channel with a rigid lid H0 = z_s = const, we have

$$H \approx H_0 - z_b \quad \text{and} \quad U \approx \frac{q}{H} \qquad [4]$$

where *H* is the water depth, *U* is the mean flow velocity, and *q* is the constant fluid volume flux per unit width.

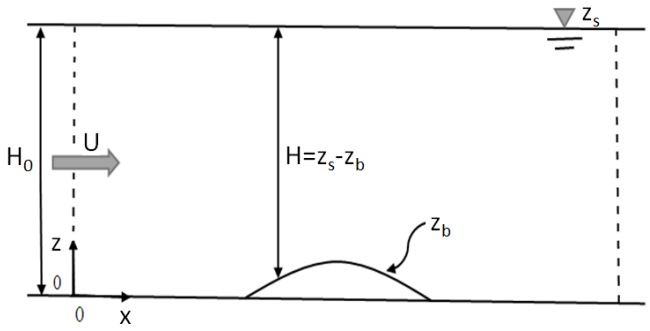

Figure 2. Bathymetry and coordinate system for the test case

4.1 Analytical approximation

Assuming that transport rate q_b is a power function of current speed *U* (Grass, 1981; van Rijn, 1993), we have

$$q_b = AU^m \qquad [5]$$

where *A* is a given function and *m* is a given positive constant both of which are specific to the particular sediment transport formula. Note that *A* is typically a function of the mean flow velocity *U*, the total height of the water column *H*, and a number of constants that are based on sediment properties (e.g. sediment type and grain size) and data fitting procedures. The constant *m* is typically in the range of $1 \le m \le 3$. The phase speed of bed form $C(z_b)$ can be now expressed as

$$C(z_b) = \frac{mAq^m}{(1-p)(H_0 - z_b)^{m+1}} \quad [6]$$

The initial condition $z_b(x_0, 0)$ is specified as follows with α =1 (m):

$$z_b(x_0,0) = \begin{cases} \alpha \sin^2\left[\frac{\pi(x_0 - 300)}{200}\right] & \text{if } 300 \le x_0 \le 500 \text{ (m)} \\ 0 & \text{otherwise} \end{cases} \quad [7]$$

Further, Eq. [2] may be solved approximately by the method of characteristics, which gives the result that z_b will remain constant along characteristics given by

$$\frac{dx}{dt} = C(z_b(x_0,0)) = \frac{mAq^m}{(1-p)(H_0 - z_b(x_0,0))^{m+1}} \quad [8]$$

Further, since z_b is constant along each characteristic, then dx/dt is constant and each characteristic is a straight line in $\{x, t\}$ with slope given by $C(z_b(x_0, 0))$ at its intersection with the x axis. Substituting the initial bathymetry into Eq. [8] and integrating gives,

$$x = x_0 + \frac{mAq^m t}{(1-p)} \begin{cases} \left(H_0 - \alpha \sin^2\left(\frac{\pi(x_0 - 300)}{200}\right)\right)^{-(m+1)} & \text{if } 300 \le x_0 \le 500 \text{ (m)} \\ H_0^{-(m+1)} & \text{otherwise} \end{cases} \quad [9]$$

which cannot be re-written in terms of x_0. Hence, the approximate solution of z_b is:

$$z_b(x,t) = \begin{cases} \alpha \sin^2\left(\frac{\pi(x_0 - 300)}{200}\right) & \text{if } 300 \le x_0 \le 500 \text{ (m)} \\ 0 & \text{otherwise} \end{cases} \quad [10]$$

where the value of x is determined by substituting values of x_0 and t into Eq. [9].

4.2 Data selection for ANN

The Eqs. [4], [9] and [10] with 0 ≤ t ≤ 60000 (s) and 250 ≤ x ≤ 550 (m) are used to generate the data for ANN model. The following quantities are specified according to similar settings in Hudson et al. (2005): m = 3, p = 0.4, H_0 =10 (m), A = 0.001 (s^2/m), and α = 1 (m). Grid spacing is chosen to be Δx = 2 (m). For all of the schemes discussed in Hudson et al. (2005) and Long et al. (2008) a very small time step was chosen to satisfy stability conditions (e.g. Δt = 0.1 (s)), however for the ANN model, we use a large time step Δt = 300 (s). To generate the data set, U has to be evaluated using Eq. [4] at all alternate grid points i at time level n (denoted by U_i^n). Then, z_b has to be similarly evaluated using Eqs. [9] and [10] at the same grid points and time level (denoted by z_{bi}^n). Once complete, the process is then repeated at time level ($n+1$) and so on.

Finally, we have a data set of 30350 patterns, which are then divided randomly into three subsets, whereby the biggest amount of data (70 %) is added randomly to the training subset. The remaining data set samples are used for validating (15%) and testing the networks (15%). The training subset is used to design the weights. The validation subset is used additionally to monitor the accuracy of training, while training is ongoing. After each epoch, the validation subset acts as a barometer for determining when the accuracy of the multilayer perceptron is at an acceptable level. After the network is considered optimally trained, the test subset is used to verify its performance.

5. DESIGN OF ANN MODEL

5.1 Model inputs

Based on different numerical schemes used in Hudson et al. (2005) and Long et al. (2008) for calculation of morphological change in alluvial channels, the following combinations including different parameters at the time step n are considered as inputs of ANN models to predict the bed level change at the grid point i and at one time step ahead $z_{bi}^{(n+1)}$:

Combination C1: $z_{bi}^n, z_{b(i-1)}^n, U_i^n, U_{(i-1)}^n$

Combination C2: $z_{bi}^n, z_{b(i+1)}^n, z_{b(i-1)}^n, U_i^n$

Combination C3: $z_{bi}^n, U_{(i+1)}^n, U_{(i-1)}^n, U_i^n$

Combination C4: $z_{bi}^n, z_{b(i+1)}^n, U_{(i+1)}^n, U_i^n$

Combination C5: $z_{bi}^n, z_{b(i-1)}^n, U_{(i+1)}^n, U_i^n$

Combination C6: $z_{bi}^n, z_{b(i-1)}^n, z_{b(i+1)}^n, U_{(i+1)}^n, U_i^n$

Combination C7: $z_{bi}^n, z_{b(i-1)}^n, z_{b(i+1)}^n, U_{(i+1)}^n, U_{(i-1)}^n$

Combination C8: $z_{bi}^n, z_{b(i-1)}^n, z_{b(i+1)}^n, U_i^n, U_{(i+1)}^n, U_{(i-1)}^n$

5.2 Model development

There is no especial rule for ANN model development. By using Kolmogorov's theorem, Marques (2001) and Hornik (1989) provided there are enough neurons in the hidden layer, only one hidden layer should be sufficient to ensure that the structure has the properties of a "universal approximator" for a number of particular problems. Further, Marques (2001), the number of neurons in the hidden layer would most likely be *2N + 1* where N is the number of neurons in the input layer. If there are too few hidden units, there will be both a high training error and generalization error due to underfitting and high statistical bias. Correspondingly, too many hidden units result in a low training error but still in a high generalization error due to overfitting and high variance. It is completely well known that MLP-ANN consist if units arranged in layers. Each layer is composed of nodes and in the fully connected network considered here, each node connects to every node in subsequent layers. During the learning phase, the network learns by adjusting the weights so as to be able to predict the correct class output of the input signals.

In this paper, estimation of bed level change is based on a MLP-ANN model with one hidden layer. It is necessary to mention that the performance of ANN model is significantly related to the number of hidden layer nodes. Trial and error approach has been employed to choose the appropriate number of nodes in the hidden layer. For the first tests, the log-sigmoid transfer function has been used for hidden layer and the linear function for the output one. Further, the inputs combination C1 and the Levenberg-Marquardt learning rule have been applied. After each training process, predicted values have been compared with the analytical approximation ones. Statistical indicators such as, correlation coefficient (R), root mean square error (RMSE) and mean absolute error (MAE) have been used to evaluate performance of the ANN models.

Based on performance indices of the ANN models, which is given in Tab. 1 for the testing data set, it can be seen that increasing the hidden neuron numbers from 10 to 14, the performance of the ANN model becomes worse. Further, there is no significant accuracy differences between models trained with 10 and 15 hidden neurons. For simplicity and decreasing the run time, this ANN configuration with teen hidden neurons is used for the next parts.

Table 1. Calculated performance indices for different number of hidden nodes

Number of hidden nodes	R	RMSE	MAE
1	0.998441596	0.021352948	0.017702165
2	0.999916956	0.004870364	0.003702761
3	0.999944596	0.003975855	0.003166062
4	0.999993485	0.001366139	0.000887091
5	0.999995027	0.001195344	0.000724811
6	0.999991556	0.001554957	0.000862329
7	0.999996922	0.000935250	0.000474243
8	0.999998215	0.000712984	0.000349783
9	0.999994961	0.001193281	0.000847712
10	0.999998217	0.000715299	0.000302255
11	0.999993837	0.001330159	0.000730059
12	0.999993191	0.001395253	0.000720088
13	0.999983820	0.002164461	0.001049258
14	0.999995347	0.001157230	0.000527408
15	0.999998600	0.000627993	0.000307361

Further tests have been carried out for different transfer functions used in the hidden layer and output one. As it can be seen in Tab. 2, applying the log-sigmoid transfer function for hidden layer and the linear function for the output one, we have the best performance of the ANN model.

It is well known that the Levenberg-Marquardt back-propagation generally is one of the fastest learning algorithms chosen. However, its convergence speed is not necessarily linked to the optimal performance behavior. Hence, the ANN configuration mentioned above is used to test against different training methods. Table 3 presents the statistical performances of ten different learning rules, where the quasi-Newton back-propagation is denoted by BFG; Resilient back-propagation by RP; Gradient descent with adaptive learning rate back-propagation by GDA; Gradient descent with momentum back-propagation by GDM; Gradient descent with momentum and adaptive learning rate back-propagation by GDX; Gradient descent back-propagation by GD; One-step secant back-propagation by OSS; Conjugate gradient back-

propagation with Fletcher-Reeves updates by CGF; Levenberg-Marquardt back-propagation by LM; and Conjugate gradient back-propagation with Powell-Beale restarts CGB. Based on the calculated performance indices, it is obvious that the LM training method is best suitable for this study case.

Table 2. Performance criteria for different transfer functions

Hidden layer	Output layer	R	RMSE	MAE
logsig	logsig	0.999986154	0.002064160	0.001556513
tansig	tansig	0.999998217	0.000715299	0.000302255
logsig	tansig	0.999994071	0.001309201	0.000629762
tansig	logsig	0.999918606	0.004906810	0.004298090
radbas	logsig	0.999982679	0.002309312	0.00190598
logsig	radbas	0.999958384	0.003600103	0.002800004
radbas	tansig	0.999986789	0.001949762	0.001211715
tansig	radbas	0.999976341	0.002695672	0.002108262
radbas	radbas	0.999995727	0.001134885	0.000877396
logsig	purelin	0.999999999	1.37587E-05	9.13265E-06
tansig	purelin	0.999999877	0.000185895	0.000127205
radbas	purelin	0.999999999	1.82015E-05	1.49397E-05

Table 3. Calculated performance indices for different learning algorithms

	BFG	RP	GDA	GDM	GDX	GD	OSS	CGF	LM	CGB
R	0.99999	0.99998	0.99058	0.99006	0.99644	0.99035	0.99995	0.99857	0.99999	0.99996
RMSE	0.00059	0.00246	0.05130	0.05276	0.03202	0.05169	0.00359	0.01997	1.3E-05	0.00311
MAE	0.00046	0.00181	0.04317	0.03638	0.02242	0.03940	0.00285	0.01459	9.1E-06	0.00238

Table 4. Calculated performance indices for different inputs combinations

Combination	R	RMSE	MAE
C1	0.999999999	1.37587E-05	9.13265E-06
C2	0.999999976	9.11042E-05	6.97687E-05
C3	0.999999556	0.000352664	0.000281516
C4	0.999999975	8.40489E-05	6.22015E-05
C5	0.999999710	0.000286002	0.000208044
C6	0.999999995	3.71712E-05	2.62146E-05
C7	0.999999945	0.00012373	9.37268E-05
C8	0.999999864	0.000195382	0.000160089

According to Table 4, the designed ANN model with the inputs combination C1 provides the best performance. As it can be seen from Eq. [6], the phase speed of bed form is always positive. Hence, in this study case the morphological change at the point *i* depend mostly on the bed level and water velocity at this point and at the upstream neighbor point (*i-1*).

6. RESULTS AND DISCUSSION

Applying this designed ANN model, the values of the weights and biases have been specified after a successful learning and validating process. They represent the stored knowledge of the ANN for bed level change modeling, which are separated in one input weight matrix $IW^{1,1}$, one hidden-layer weight matrix $LW^{2,1}$, one bias vector b^1 and one bias value b^2 with the following values:

$$IW^{1,1} = \begin{bmatrix} 5.8720 & -6.2430 & 26.1509 & 34.6502 \\ 4.4199 & 5.1539 & -45.8799 & -46.2625 \\ -4.6946 & 6.2918 & 43.7671 & -27.4119 \\ 5.5531 & 0.0688 & 51.5353 & -54.2679 \\ 2.5215 & 5.7512 & 29.1313 & -65.7119 \\ -5.5153 & -4.7864 & 33.8444 & 42.4838 \\ -6.4566 & -2.6638 & 56.3371 & 45.2583 \\ 1.0147 & 8.6364 & -20.8286 & -35.2006 \\ 6.4408 & 4.4430 & 19.5797 & 56.1871 \\ 5.5915 & 5.4314 & -342711 & -48.4119 \end{bmatrix}; \quad \vec{b}^1 = \begin{bmatrix} -69.1472 \\ 88.7288 \\ -14.0323 \\ -2.0066 \\ 34.0812 \\ -76.1308 \\ -103.4181 \\ 56.2286 \\ -80.3684 \\ 86.0117 \end{bmatrix}; \quad b^2 = \begin{bmatrix} -0.22516 \end{bmatrix} \quad [11]$$

$$LW^{2,1} = \begin{bmatrix} 0.176690 & -0.419430 & -0.068665 & 0.071825 & 0.197520 & -1.445500 & 0.601230 & -0.180750 & -0.000003 & 1.134200 \end{bmatrix}$$

Using the designed network, we received the following equation for the bed level change:

$$z_{bi}^{(n+1)} = LW^{2,1} \times \text{logsig}\left(IW^{1,1} \times \begin{bmatrix} z_{bi}^{n} \\ z_{b(i-1)}^{n} \\ U_{i}^{n} \\ U_{(i-1)}^{n} \end{bmatrix} + \vec{b}^{1} \right) + b^{2} \quad [12]$$

Since the characteristic time scale of bed-evolution and bed load transport processes is normally much greater than that of fluid flow, it can be assumed that changes in the bed elevation during one computational time step do not significantly influence the flow field. This assumption leads to the computationally attractive possibility of coupling flow and sediment computations in an iterative manner. Hereby, the flow and sediment-transport modules communicate through a quasi-steady morphodynamic time-stepping mechanism: during the flow computation, the bed level is assumed constant and during the computation of the bed level the flow and sediment transport are assumed invariant to the bed level changes. Based on this coupling concept, the main calculation procedure implemented in this study is shown in Figure 3.

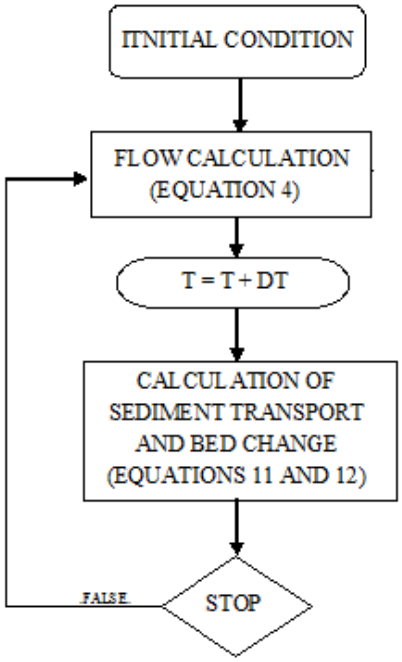

Figure 3. Flow chart of the coupling system

Now we analyze the capability of the designed ANN model for prediction of bed level changes in the new coupling model. First, the initial values (at time t = 0) are defined at every grid point i. The bed levels at one time step ahead t = 5 (min) are calculated using the ANN-based Eqs. [11] and [12]. The water velocities at this time step are updated using Eq. [4]. This procedure is repeated until the last time step is reached. Table 5 presents the statistical performances indices of the model based on a comparison between the predicted bed levels and analytical approximation at different time steps. The results indicate that the designed ANN performs well the morphological change in the channel with high values of *R* as well as small values of *RMSE* and *MAE*.

Further, it should be noted that many time series problems involve the task of predicting a sequence of future values using the values observed in the past. A typical approach to solve this problem is to construct a single model from historical values of the time series and then applies the model step-by-step to predict its future states. This approach is known as multi stage prediction. As it uses the predicted values from the past, multi stage prediction could be susceptible to the error accumulation problem, i.e. errors committed in the past are propagated into future predictions. The same error problem can be found also in the conventional numerical models for morphodynamics.

Figure 4 is a plot of the bed level calculated by analytical approximation and prediction of the designed ANN model at after 1000 and 2000 minutes. The fit is extremely good and it is rather difficult to discern one graph from the other at any time t ≤ 1500 minutes.

Table 5. Statistical performance of the designed ANN model at different times

	500 min	**1000 min**	**1500 min**	**2000 min**
R	0.999974058	0.999975566	0.999865582	0.999066096
RMSE	0.003169166	0.004032175	0.007504624	0.016973207
MAE	0.002571133	0.003245455	0.006233827	0.012875298

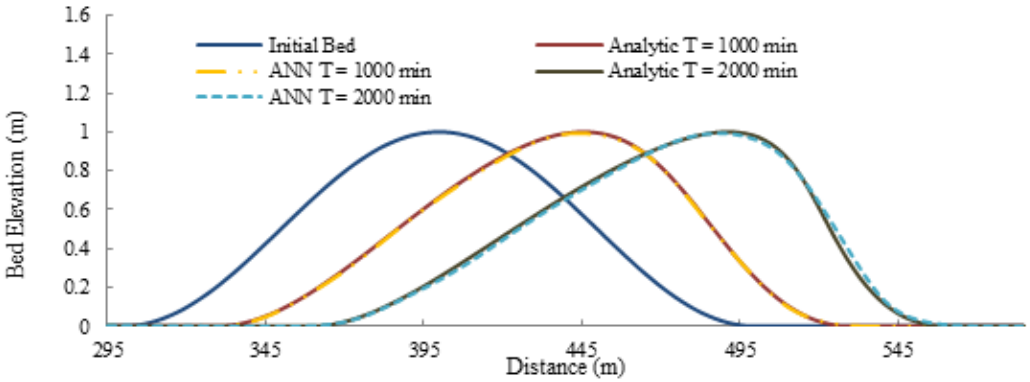

Figure 4. Bed elevation after 1000 and 2000 minutes

7. CONCLUSIONS

An analytical approximation based on the equation of conservation of sediment has been applied to generate data used for training and testing different ANN models. By evaluating the calculated results, the related parameters for an optimal network structure has been obtained for simulation of bed level changes in a straight alluvial channel under a steady flow discharge and simple assumption for sediment transport processes. The predicted results showed that for the simple case of 1D morphological problems considered in this study, artificial neural networks could provide a good performance. The calculated results showed that the ANN could perform well also for long term time series prediction. Moreover, it demonstrated that, a well-trained ANN model could be integrated in the hydromorphological model systems and could perform like conventional numerical operators. Further model developments are going on at the Institute of Hydraulic and Water Resources Engineering, Technische Universität München, to obtain a universal ANN-based approximator for morphological change in alluvial channels as well as to test and to develop a new concept for hydromorphological model using data driven methods.

REFERENCES

Grass, A.J. (1981): Sediment Transport by Waves and Currents, SERC London Cent. Mar. Technol., Report No: FL29.

Hornik K. (1989): Multilayer Feed-forward Networks are Universal Approximators. *Neural Networks*, 2, 359-66.

Hudson, J., Damgaard, J., Dodd, N., Chesher, T., Cooper, A., (2005): Numerical approaches for 1D morphodynamic modeling. *Coastal Engineering*, 52, 691–707.

Long, W.; Kirby, J. T.; Shao, Z. (2008): A numerical scheme for morphological bed level calculations. *Coastal Engineering*, 55, 167-180.

Marques de Sá J.P. (2001): Pattern Recognition. Concepts, Methods and Applications. Berlin, Heidelberg, New York: Springer-Verlag.

Penz, P. (2013). Contraction Scour Modeling using Artificial Neural Networks. MSc. Thesis, Technische Universität München.

Shahin, M.A.; Maier, H.R. & Jaksa, M.B. (2002). Predicting settlement of shallow foundations using neural networks. *Journal of Geotechnical & Geoenvironmental Engineering, ASCE*, 128(9), 785-793.

Van Rijn, L.C. (1993): Principles of Sediment Transport in Rivers, Estuaries and Coastal Seas, Aqua Publications.

Advances in Engineering Software 132 (2019) 18–28

Contents lists available at ScienceDirect

Advances in Engineering Software

journal homepage: www.elsevier.com/locate/advengsoft

Integration of artificial neural networks into TELEMAC-MASCARET system, new concepts for hydromorphodynamic modeling

Keivan Kaveh*, Minh Duc Bui, Peter Rutschmann

Institute of Hydraulic and Water Resources Engineering, Technische Universität München, Arcisstraße 21, D-80333 München, Germany

ARTICLE INFO

Keywords:
Artificial neural network
Sediment transport
Hydromorphological modeling

ABSTRACT

In this study, two new calculation schemes were proposed for hydromorphological changes in fluvial rivers, where artificial neural network (ANN) models have been integrated into a hydromorphological model system. For this purpose, the open-source finite-element system TELEMAC-MASCARET has been applied to simulate two complex hydro-morphological models including the evolution of a 3D isolated bump in a straight channel and the evolution of the bed in a 180° channel bend. The simulated results were used as input-data in ANN models to obtain ANN-based approximator for the new proposed schemes. The novelty of the proposed models is that they reduced the computation costs significantly in the prediction of both hydrodynamics variables and morphodynamics. To evaluate the prediction qualities of the proposed models, a comparative study has been carried out for these models by estimating several parameters that describe the errors associated with the model in terms of statistical measures of goodness-of-fit between the estimated bed change and TELEMAC-MASCARET simulation.

1. Introduction

Morphodynamic models of increasing complexity have been developed in the past 30 years which are now widely applied by the engineering community to predict the natural or anthropogenic bed evolution in rivers, estuaries and seas. Comprehensive morphodynamic modeling systems like ECOMSed [1], Mike-21 [2], Delft3D [3] and ROMS [4] generally include a flow module, a wave propagation module and a sediment transport module including bed-load and suspended load as well as bed level change. The processes of sediment transport and morphological evolution of the bed are determined by the properties of the fluid flow, which in turn are affected by the changes in the morphology of the bed that they induce. In the conventional hydro-morphological models the bed level changes are governed by the equation for conservation of sediment mass known as Exner's equation [5], where the bed load transport rate can be calculated based on several empirical functions. These equations have been developed based on the analysis of laboratory and field data using statistical methods such as the regression method, and there are drastic differences between them. At present there is no equation, which is valid for the most problems, so that the accuracy of computational sediment transport models remains a challenging question.

Further, the sediment conservation equation is physically a non-linear conservation equation for the bed level. Mathematically the most interesting feature of such equations is that they admit shock waves in their solution, discontinuities in the solution that can form even from smooth initial data [5]. Several numerical solution techniques have been developed for obtaining accurate and stable simulations of this shock behavior. In Hudson et al. [6] and Long et al. [7] several schemes using the artificial-viscosity and filtering processes as well as the so called shock capturing techniques were discussed for simulating bed level change with different accuracy and stability behaviors. Use of these schemes requires an estimate of phase speed of bed form, which is needed for approximating the flux functions and appreciating the numerical stability condition. In many instances, it is not very easy to estimate this parameter (e.g. when the bed level gradient approaches zero or changes its sign). Overestimation of phase speed could overly smooth the solution, while underestimation of phase speed may make the scheme unstable.

The technique of artificial neural network (ANN) attempts to mimic the function of the human brain and nervous system at a sub-symbolic level. ANN learns from data examples presented to them in order to capture the subtle functional relationships within the data. The majority of hydromorphological processes are highly nonlinear in nature and, in many cases, modeling these variables with conventional models may be limited by a poor understanding of the complex interactions that are involved in the process. In such cases, ANNs are often viewed as an appealing alternative, as they have the ability to extract a nonlinear

* Corresponding author.
E-mail addresses: keivan.kaveh@tum.de (K. Kaveh), bui@tum.de (M.D. Bui), peter.rutschmann@tum.de (P. Rutschmann).

https://doi.org/10.1016/j.advengsoft.2019.03.011
Received 11 February 2019; Received in revised form 12 March 2019; Accepted 30 March 2019

relationship from data without requiring an in depth knowledge of the physics occurring within the system.

The main objective of this paper is, therefore, to develop two new schemes for hydromorphodynamic modeling using ANN technique with the lowest computational costs. Applying the proposed schemes, the bed level changes are calculated directly from the defined flow without calculation of the bed load or suspended load. Therefore, they can solve the difficulties in bed-load measurement, as it only needs bed-level-change observation, which is easier. They are also able to fix the numerical instability of conventional methods in some cases. The prediction qualities of the designed network are studied by evaluating several statistical parameters that describe the errors associated with the model in terms of statistical measures of goodness-of-fit between the estimated bed changes obtained from different numerical models.

2. ANN approach

ANN is a broad term covering a large variety of network architectures. An ANN model consists of a number of artificial neurons variously known as processing elements or nodes. In general, three fundamentally different classes of network architectures may be identified as single layer feedforward, multi-layer feedforward, and recurrent networks. For a multi-layer feedforward network, which is the most common model, neurons are arranged in layers: an input layer, an output layer, and one or more intermediate or hidden layers. The net is formed by these layers of neurons and each neuron in a specific layer is connected to neurons in other layers via weighted connections. Neurons are defined as mathematical expressions that filter the signal through the net. From the connected neurons in the previous layer, an individual neuron receives its weighted inputs which are usually summed along with a bias unit. The bias unit is used to scale the input to a useful range in order to improve the convergence properties of the neural network. The result of this combined summation is passed through a transfer function so as to produce the output of the neuron. This output is then passed through weighted connections to neurons in the next layer, where the process is repeated. The weight vectors connecting the different nodes of the network are found by training normally based on the so-called error back-propagation method. During training the values of these parameters are varied so that the ANN output becomes similar to the measured output on a known data set [8,9]. A trained response is achieved by changing the connections' weights in the network according to an error minimization criterion. A validation process can be used during training in order to prevent overfitting. Once the network has been trained to simulate the best response to input data, the configuration of the network is fixed and a test process is conducted to evaluate the performance of the ANN as a predictive tool.

According to Shahin et al. [10], the structure and process for node *j* of an ANN model are illustrated in Fig. 1 More details about ANN approaches with these methods can be found in Haykin [8].

3. TELEMAC-MASCARET system

The open source TELEMAC-MASCARET was developed originally by the National Hydraulics and Environment Laboratory (LNHE) of the research and development directorate of the French Electricity Board (EDF) as a hydro-informatics system for free surface flows [11]. All modules of the system are based on unstructured grids and finite-element or finite volume algorithms. The model system includes 2D and 3D hydrodynamic modules (TELEMAC-2D and -3D), and a spectral wave propagation model (TOMAWA). The environment is extended by the two dimensional morphologic module SISYPHE for bed load and depth averaged suspended load and SEDI-3D for three dimensional suspended load. More detailed information about the system can be found on the website: http://www.opentelemac.org/.

TELEMAC-2D module solves the shallow water equations with several options for the horizontal dispersion terms (e.g. depth-averaged k–ε model, Elder model, and constant eddy viscosity models) and source terms (e.g. atmospheric pressure gradients, Coriolis force, etc.). The numerical discretization includes a choice of classical methods for the advection terms (e.g. characteristics, SUPG, distributive schemes…). The use of implicit schemes enables relaxation of the limitation on time steps (typically, values of a CFL-numbers up to 10 or 50 are acceptable). Recently, ideas stemming from finite volume techniques have been coupled with these implicit schemes to ensure monotonicity of depth and sediment concentrations, as well as mass conservation at machine accuracy. TELEMAC-3D solves the Reynolds-Averaged Navier–Stokes (RANS) equations in unstructured meshes obtained by a super- imposition of 2D meshes of triangles. The 3D model can be applied to capture the effect of vertical recirculation cells as well as stratification effects, assuming a hydrostatic or non-hydrostatic pressure distribution [12].

Sediment transport and bed change modules (SISYPHE) can be used to model complex morphodynamic processes for different flow conditions, sediment size classes and sediment transport modes. In SISYPHE, sediment transport processes are grouped as bed-load, suspended-load or total-load, with an extensive library of bed-load transport relations. A choice of different sediment transport formulae for bed-load or total-load is implemented. SISYPHE is applicable to non-cohesive sediments that can be uniform (single-sized) or non-uniform (multiple-sized), cohesive sediments (multi-layer consolidation models), as well as sand-mud mixtures. A number of physically-based processes are incorporated into SISYPHE, such as the influence of secondary currents to precisely capture the complex flow field induced by channel curvature, the effect of bed slope associated with the influence of gravity, bed roughness predictors, and areas of non-erodible bed, among others. SISYPHE can be coupled to the depth-averaged shallow water module TELEMAC-2D or to the three-dimensional Reynolds-averaged Navier–Stokes module TELEMAC-3D.

The sediment transport model relies on a complete description of the flow field, through internal coupling with the flow module. At each time step, the hydrodynamic model (TELEMAC) calculates the flow field and sends to the SISYPHE model the spatial distribution of the main hydrodynamic variables: water depth, flow velocity components, and bed shear stress. These sediment transport rates are calculated bed level change is used to account the effects of sediment transport on flow. The structure of such a coupled system is shown in Fig. 2.

Sediment transport rates in the modeling system are calculated with classical semi-empirical concepts, which involve the decomposition of sediment transport rates into bed-load and suspended load. The resulting bed evolution is then computed by solving the Exner's equation. The model is mainly applicable to non-cohesive sediment, composed of either uniform grains or multi-grains, characterized by their mean size and density.

The conventional method for performing hydro-morphodynamic simulations in rivers is to decouple the hydrodynamic and the morphodynamic modules. The decoupling approach is based on the rationale that the channel bed reacts at a much slower timescale than the flow. At implementation level, these modules communicate through a quasi-steady morphodynamic time-stepping mechanism: during flow computation, the bed level is assumed to be constant and during computation of the bed level, the flow and sediment transport quantities are assumed invariant to the bed level changes. The modules are linked together at the programming level.

All the simulation modules of the model system are written in FORTRAN 90, with no use of the specific language extensions in a given machine. When using a simulation module from the system, the user may have to program specific subroutines which are not in the code's standard release. In particular, that is made through a number of so-called user subroutines. These subroutines are written so that they can be modified, with the help of the guide for programming in the system. The procedure to be carried out in that case comprises the following steps of:

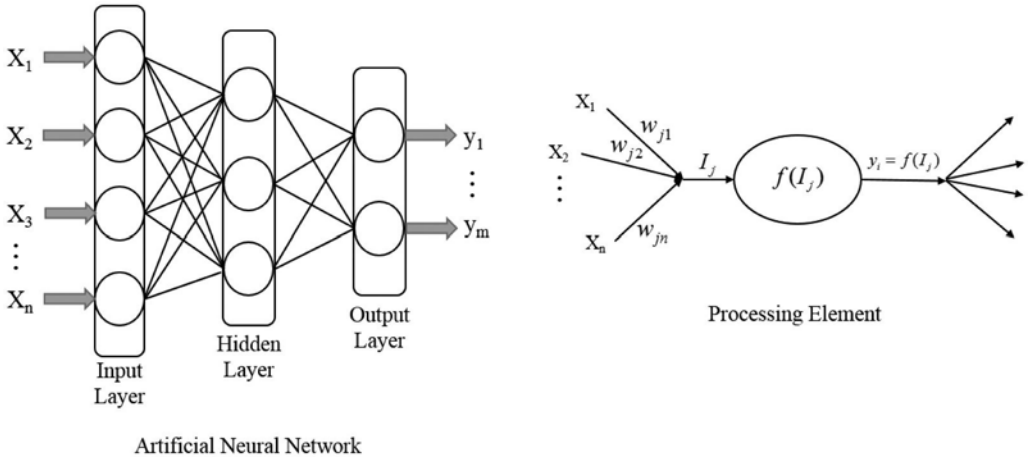

Fig. 1. Typical structure and operation of an ANN (I_j = level of node j; w_{ji} = connection weight between nodes j and i; x_i = input from node i; y_j = output of node j; and $f(I_j)$ = transfer function).

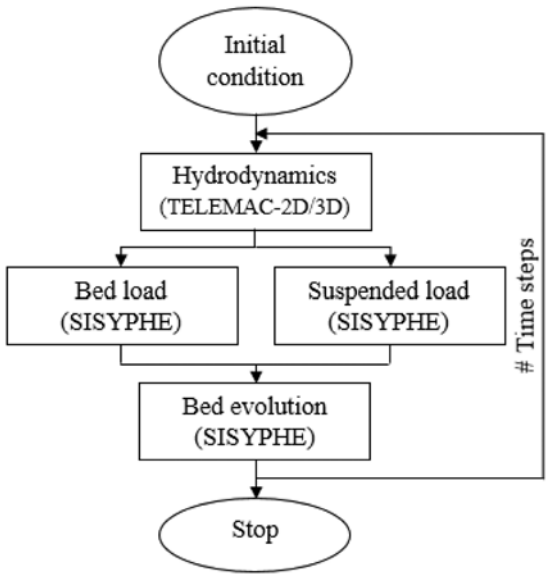

Fig. 2. Scheme of a conventional hydro-morphodynamic model system.

1. Recovering the standard version of the user subroutines provided with the system, and copying them into a file that will be the specific FORTRAN file of the given case,
2. Modifying the subroutines according to the model we wish to build,
3. Linking up the set of subroutines into a single FORTRAN file that will be compiled before the software start procedure.

During this programming phase, users may need to have access the various software variables. This is possible from any subroutines by using the structures of FORTRAN 90 gathered into a module type component.

4. New concept for hydromorphodynamic modeling

We propose two new schemes for the hydromorphodynamic modeling which are shown in Fig. 3. In the first scheme (Fig. 3a), the two ANN models are designed for hydrodynamic calculations. At each time step, the hydrodynamics variables (velocity field, water depth) are transferred into the morphodynamic model which is another ANN-based approximator. The bed elevation is updated and then sent back to the hydrodynamic model. Since the characteristic time scale of bed-evolution and bed load transport processes is normally much greater than that of fluid flow, it is assumed that changes in the bed elevation during one computational time step do not significantly influence the flow field. This assumption leads to the computationally attractive possibility of coupling flow and sediment computations in an iterative manner.

In the second scheme (Fig. 3b), our framework is TELEMAC-MASCARET system. According to this proposed scheme, the sediment transport model SISYPHE is replaced by an ANN model, which is coupled with either the 2D or 3D flow models. The time step of morphodynamic part (ANN-based approximator) can be much larger than the time step used in TELEMAC-2D/3D. For coupling TELEMAC-ANN, several subroutines in the TELEMAC-MASCARET system have to be modified.

One of the advantages of these proposed models is that the calculation of sediment transport rate and bed shear stress are not required and the prediction of bed level evolution is only based on the bed elevation and hydrodynamic characteristics. This reduces the computational costs of simulation.

Two morphological modules exist in the TELEMAC environment: SISYPHE and Sedi3D. The last named one is directly integrated into the 3D-hydrodynamic module and treats only suspended load for one-grain size problems. The module SISYPHE instead uses several structures to deal with fractional sediment transport and is used in this test case. One of the most important subroutines of SISYPHE is the bedload_solves_fe.f. This subroutine solves Exner equation to calculate the bed evolution.

After the training process, the weights and biases parameters of the configured network are adjusted so that an explicit equation for calculation of morphological bed level changes is obtained. This equation, which calculates the new bed level for each node every certain time step, will be used to modify subroutine bedload_solves_fe.f.

5. Test cases and data preparation

In this section, the open-source finite-element TELEMAC-MASCARET system is used to simulate the morphodynamic evolution in a channel. Two different test cases are considered for this part. Obtained results are then used as input data set for ANN training process.

5.1. Case-1: Transport of bed form in a straight channel

As the first case, a straight channel is considered in TELEMAC-3D modeling system with a length of 20 m and a finite amplitude perturbation of the bed level with a height of 0.3 m close to the center of the domain. The initial bathymetry is illustrated in Fig. 4. To build the

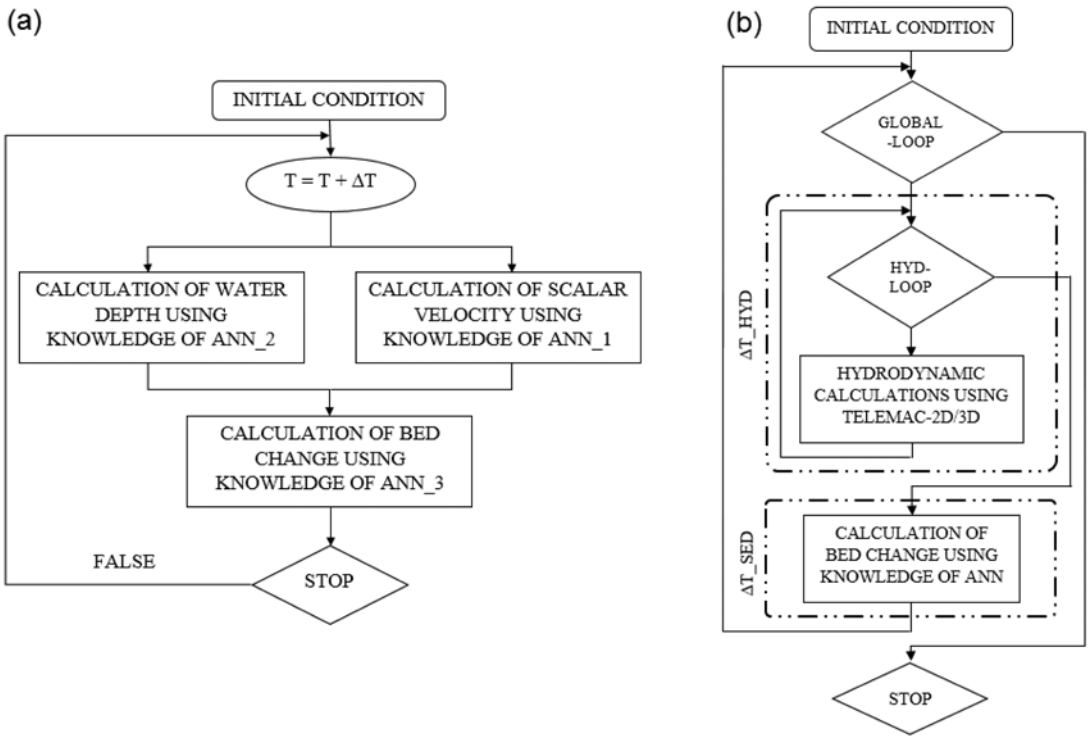

Fig. 3. Proposed hydrodynamic-morphologic modeling systems.

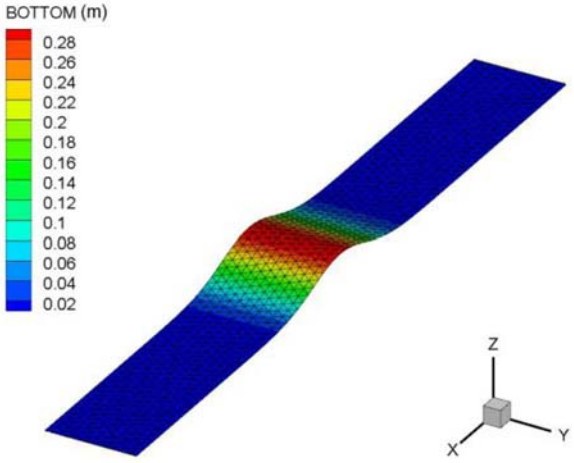

Fig. 4. Initial bathymetry of the first test case.

geometry, the mesh generator from the free licensed program BLUEKENUE is applied. It is developed by the Canadian Hydraulics Centre of the National Research Council. It can be used as a Pre- and Post-processor of TELEMAC. The mesh includes nodes and elements in 2D coordinates of x and y. However the bathymetry includes additional information of the elevations in z-direction. This can be done by interpolation of the mesh, which requires a point set consisting of x-, y- and z-coordinates. For the hump the elevation of points in z-direction are extracted from the Gaussian function. Finally, the mesh as in Fig. 4 shown is developed. The final geometry is then saved in a selafin file (.slf).

The hydrodynamic model is based on the 3D Reynolds-Averaged Navier–Stokes (RANS) equations in unstructured mesh grids. The prescribed flow rate and elevation are considered as inlet and outlet boundary condition, respectively. To start the simulation the definition of initial conditions is also required. By default, two options of constant water depth or constant elevation over all the domain are available. Here, a constant elevation of 3 m is applied as an initial condition. The turbulence components are calculated by the accurate standard k–ε model. The diffusion of velocity parameter for the 3D simulation must be given in horizontal and vertical directions. The value of $1e-6$ is considered for this part.

Another important parameter to be chosen for the TELEMAC simulation is the bed roughness or bed friction. The application of friction requires the definition of the friction law and its corresponding value in the steering file. The applied law in this model is the law of Nikuradse which uses a logarithmic velocity profile in z-direction. The friction coefficient for the bottom is 0.00015, whereas a high friction coefficient is considered for lateral solid boundaries (0.045) to get asymmetric movement of bed forms. As a result, during the simulation, the middle of the hump changes faster than channel sides, which makes the modeling more difficult for ANN.

The sediment transport model is calculated based on semi-empirical formulae, which includes bedload computation and bed evolution. Non-cohesive sediment with uniform grain size of 0.15 mm is used for sediment transport model. Suspended load is not considered in this model. Of the most important simulation parameters is the definition of the numerical solvers, schemes and related parameters. The most important parameter is the time step. A minor time step $\Delta t = 1$ s with repetition of 10,000 times is chosen. Further, an implication parameter is defined which corresponds to the discretization scheme. To get a more stable result, a full implicit scheme is applied.

After a successful simulation of the first test case using TELEMAC-3D modeling system, the obtained results can be used for networks training. These results consist of water depth, flow velocity components, and bed elevation at all spatial nodes and time steps. It is noteworthy that for the TELEMAC simulation discussed above a very small time step is chosen to satisfy stability conditions (e.g. $\Delta t = 1$ s), however for the ANN model, we use a large time step $\Delta t = 500$ s. Grid spacing is chosen to be $\Delta x = 0.1$ m.

Considering $0 \le t \le 10{,}000$ s and $0 \le x \le 20$ m and specified values for Δt, and Δx, we receive a data set, which is divided randomly into three training, validation and testing subsets, whereby the biggest

amount of data (70%) is added randomly to the training subset. The remaining data set samples are used for validating (15%) and testing the networks (15%). The training subset is used to design the weights. The validation subset is used additionally to monitor the accuracy of training, while training is ongoing. After each epoch, the validation subset acts as a barometer for determining when the accuracy of the multilayer perceptron is at an acceptable level. After the network is considered optimally trained, the test subset is used to verify its performance. Finally, three ANN models are considered to establish the proposed hydrodynamic-morphologic modeling system including water depth, scalar velocity, and bed level integrators.

5.2. Case-2: Flow and bed deformation in a curved channel

The mechanics of sediment transport in channel bends, frequently appearing in natural rivers, is much more complex than that in straight channels. Therefore, the second test case models the evolution of the bed in a 180° channel bend under unsteady-flow conditions with non-uniform sediment [13]. The unsteadiness of flow in this test case certainly has some effects on the structure of the flow field, thereby affecting the motion of sediment particles. The initial geometry of the test case is shown in Fig. 5.

The width of the channel is 1 m and the radius of curvature 4 m. At both ends of the channel, there is a straight reach of 11.5 m. Starting from a horizontal flat bed in the transverse direction with a longitudinal bed slope of 2%, a typical bank cross-section with a scour at the outer bank and deposition at the inner bank is formed without imposing any sediment discharge upstream. In the experiment, a layer of sand around 20 cm thick, with d50 of 1.0 mm is placed on the bed. The hydrodynamic model is based on the 2D Shallow Water Equations (SWE) in unstructured mesh grids. The base flow is set at 0.02 m^3/s, determined according to the condition of incipient motion for the sediment with d50 of 1.0 mm.

After the simulation of the second test case using TELEMAC-2D modeling system, the obtained results including flow velocity components, and bed elevation at all spatial nodes and time steps can be used for network training. For the TELEMAC simulation, a very small time step is chosen to satisfy stability conditions (e.g. $\Delta t = 0.1$ s), while this value for the ANN model is $\Delta t = 200$ s. Unlike the first scheme where we could use all information at structured grids, here we have to use the data exactly on unstructured grids which is generated by TELEMAC

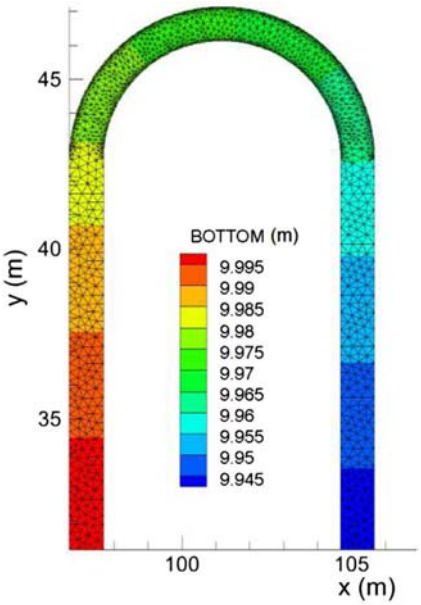

Fig. 5. Initial geometry of the second test case.

model. Considering $0 \le t \le 6000$ s and specified values for Δt, we receive a data set for training the network. Similarly, the data is divided randomly into three training (70%), validation (15%) and testing subsets (15%) (Fig. 6).

6. Design of ANN models

6.1. Model inputs

As mentioned before, all modules of the TELEMAC system are based on unstructured grids while for ANN training, using the first proposed scheme, all information are needed at structured grids. Thus, the interpolation technique is used to gain all required information at our desired grid points. Based on different numerical schemes used in [5–7] for calculation of morphological change in alluvial channels, the following combinations including different parameters at the time steps t and $t-1$ are considered as inputs of ANN models to predict the water depth, velocity and bed level change at the grid point (i, j) and at one time step ahead $t+1$. After a trial and error procedure, the best input combinations for each model is found as follows:

- For water depth and velocity integrators: bed elevation, water depth, and scalar velocity at grid points (i, j), $(i-1, j)$, $(i, j-1)$, $(i+1, j)$, and $(i, j+1)$ and at times $(t-1)$ and (t):

$$\vec{\mathbf{A}} = [Z^t_{b(i,j)}\ Z^t_{b(i-1,j)}\ Z^t_{b(i,j-1)}\ U^t_{(i,j)}\ U^t_{(i-1,j)}\ U^t_{(i,j-1)}\ H^t_{(i,j)}\ H^t_{(i-1,j)}\ H^t_{(i,j-1)}\ Z^{t-1}_{b(i,j)}\ Z^{t-1}_{b(i-1,j)}\ Z^{t-1}_{b(i,j-1)}\ U^{t-1}_{(i,j)}\ U^{t-1}_{(i-1,j)}\ U^{t-1}_{(i,j-1)}\ H^{t-1}_{(i,j)}\ H^{t-1}_{(i-1,j)}\ H^{t-1}_{(i,j-1)}],$$

- For bed level integrator: bed elevation and scalar velocity at grid points (i, j), $(i-1, j)$, $(i, j-1)$, $(i+1, j)$, and $(i, j+1)$ and at times $(t-1)$ and (t):

$$\vec{\mathbf{B}} = [Z^t_{b(i,j)}\ Z^t_{b(i-1,j)}\ Z^t_{b(i,j-1)}\ U^t_{(i,j)}\ U^t_{(i-1,j)}\ U^t_{(i,j-1)}\ Z^{t-1}_{b(i,j)}\ Z^{t-1}_{b(i-1,j)}\ Z^{t-1}_{b(i,j-1)}\ U^{t+1}_{(i,j)}\ U^{t+1}_{(i-1,j)}\ U^{t+1}_{(i,j-1)}],$$

Dissimilar to the first scheme, the networks training for the second scheme must be only completed based on unstructured mesh. The reason is that the updated bed level by the ANN should be sent back to the TELEMAC system for flow field calculations and TELEMAC needs the these values exactly on unstructured grids. In this case, the bed elevation and scalar velocity at each grid and its neighbor points are considered as the most important input parameters. Since the location of neighbor points around a node is irregular, another parameter must be introduced to represent the strength of each neighbor point. As a result, the area of each element around a node is considered as the other input parameter. Finally, after a trial and error procedure, the following input matrix including the mentioned parameters at the time steps t and $t-1$ are considered for ANN model to predict the bed level change at the grid point i and at one time step ahead:

$$\mathbf{C} = \begin{bmatrix} Z^t_1 & U^t_1 & Z^t_{11} & U^t_{11} & \cdots & Z^t_{1m} & U^t_{1m} & Z^{t-1}_1 & U^{t-1}_1 & Z^{t-1}_{11} & U^{t-1}_{11} & \cdots & Z^{t-1}_{1m} & U^{t-1}_{1m} & A_{11} & \cdots & A_{1m} \\ Z^t_2 & U^t_2 & Z^t_{21} & U^t_{21} & \cdots & Z^t_{2m} & U^t_{2m} & Z^{t-1}_2 & U^{t-1}_2 & Z^{t-1}_{21} & U^{t-1}_{21} & \cdots & Z^{t-1}_{2m} & U^{t-1}_{2m} & A_{21} & \cdots & A_{2m} \\ \vdots & \vdots & \vdots & \vdots & \vdots & \vdots & \vdots & \vdots & \vdots & \vdots & \vdots & \vdots & \vdots & \vdots & \vdots & \vdots & \vdots \\ Z^t_p & U^t_p & Z^t_{p1} & U^t_{p1} & \cdots & Z^t_{pm} & U^t_{pm} & Z^{t-1}_p & U^{t-1}_p & Z^{t-1}_{p1} & U^{t-1}_{p1} & \cdots & Z^{t-1}_{pm} & U^{t-1}_{pm} & A_{p1} & \cdots & A_{pm} \end{bmatrix}$$

where p is the maximum number of grid points, m is the maximum number of neighbor points around a node in entire domain, Z_i is bed elevation at grid point i, U_i is scalar velocity at grid point i, A_{ij} is the area of jth element around ith node, and Z_{ij} and U_{ij} are the bed elevation and scalar velocity of jth neighbor node around ith node, respectively. It should be noted that in the above matrix, the zero value would be

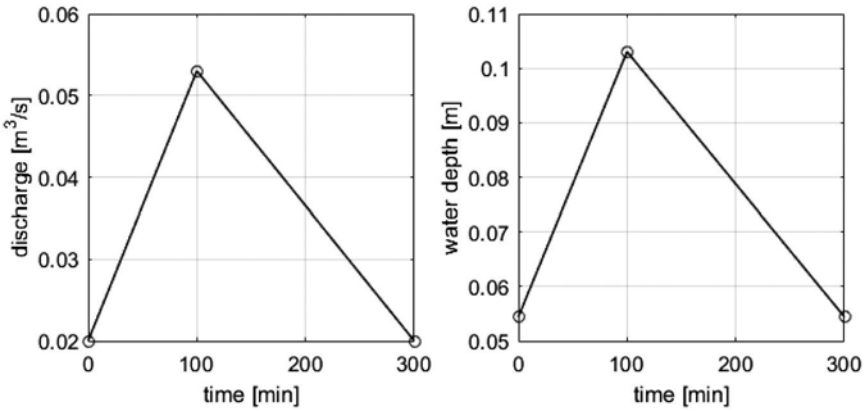

Fig. 6. Hydrograph used in the experiment and simulation.

Table 1
Statistical performance of the first proposed concept for modeling the bed change in a straight channel at different times.

Performance index	15,000 s	25,000 s
R	0.9876	0.9854
RMSE (m)	0.0119	0.0129
MAE (m)	0.0055	0.0064

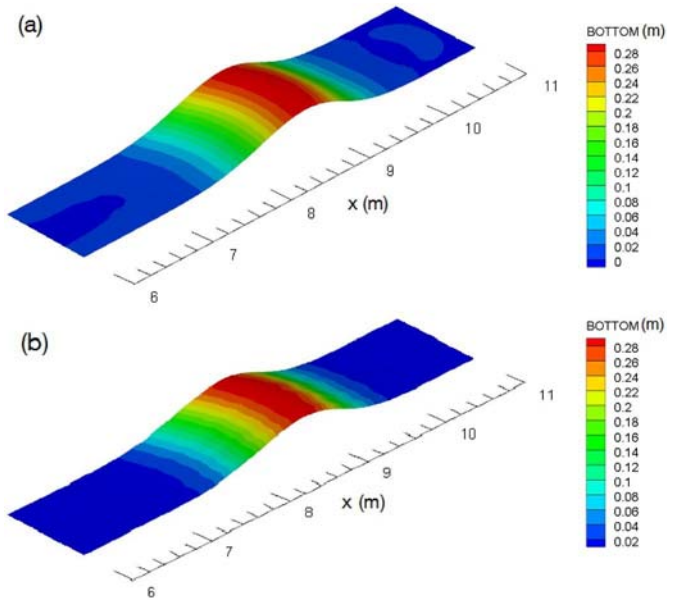

Fig. 7. Bed level simulation after 15,000 s; (a) ANN-based model, and (b) TELEMAC-3D.

assigned to Z_{ij}, U_{ij}, and A_{ij} if ith node has less neighbors than others.

6.2. Model development

As the optimal number of hidden layers and dependent nodes for the models is not known, a trial and error procedure needs to be applied to find the best network's structure for each model. For this purpose, the number of hidden layers and neurons were changed until the optimal architecture was determined based upon minimizing the difference among the neural network predicted values and the desired outputs. The training of the neural network models was stopped when either the acceptable level of error was achieved or the number of iterations exceeded a prescribed value. The neural network model configuration that minimized the MAE and RMSE and optimized the R was selected as

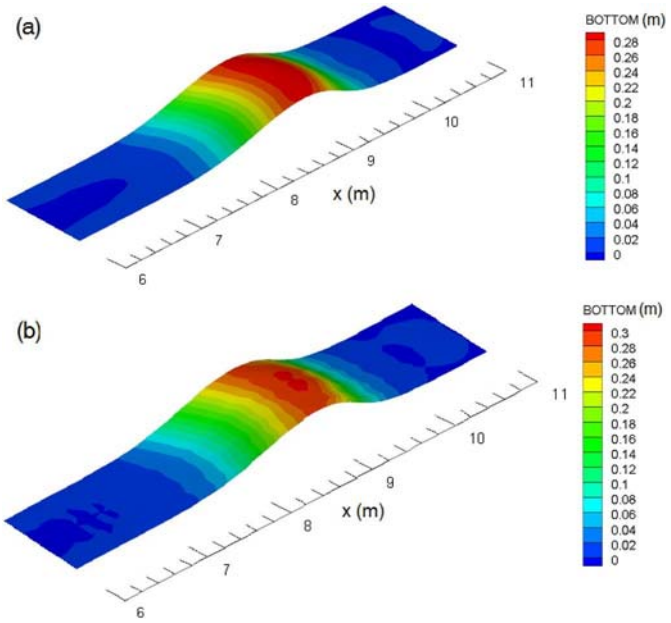

Fig. 8. Bed level simulation after 25,000 s; (a) ANN-based model, and (b) TELEMAC-3D.

the optimum and the whole analysis was repeated several times. After extensive trial and error processes, three optimal ANNs for velocity, water depth, and bed level change modeling were found. All models consist of only one hidden layer with ten neurons. The logistic sigmoid and linear transfer functions have been used for hidden and output layers, respectively. The Levenberg–Marquardt is applied to all models. Please refer to [5] for more detailed information about the procedure of the finding the best network's configuration.

After the training process, the weights and biases parameters of the configured networks are modified and get fixed, which represent the stored knowledge of the ANN models. These knowledge are stored in one input weight matrix IW1,1, one hidden layer weight matrix LW2,1, one bias vector b1, and one bias value b2 for each network. Finally, using the designed networks, we received the following equations for the normalized velocity, water depth, and bed level change calculations:

$$U_{(i,j)}^{t+1} = \mathbf{LW}_{2,1}^{u} \times logsig\left(\mathbf{IW}_{1,1}^{u} \times \mathbf{A}^{\mathrm{T}} + \vec{\mathbf{b}}_{1}^{u}\right) + b_{2}^{u}, \tag{1}$$

$$H_{(i,j)}^{t+1} = \mathbf{LW}_{2,1}^{h} \times logsig\left(\mathbf{IW}_{1,1}^{h} \times \mathbf{A}^{\mathrm{T}} + \vec{\mathbf{b}}_{1}^{h}\right) + b_{2}^{h}, \tag{2}$$

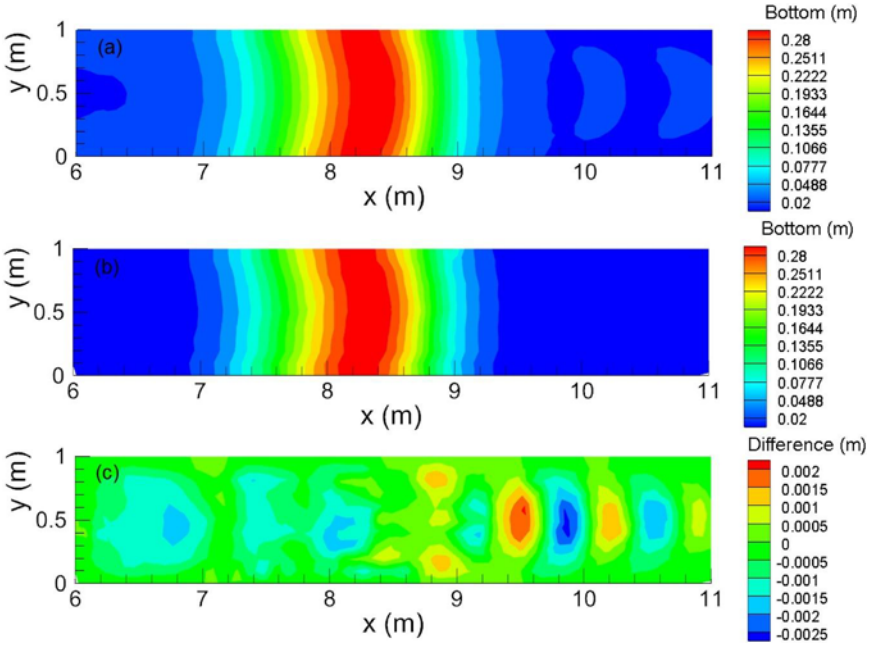

Fig. 9. 2D comparison of bed level simulation after 15,000 s; (a) TELEMAC-3D, and (b) ANN-based model, (c) Difference between two models.

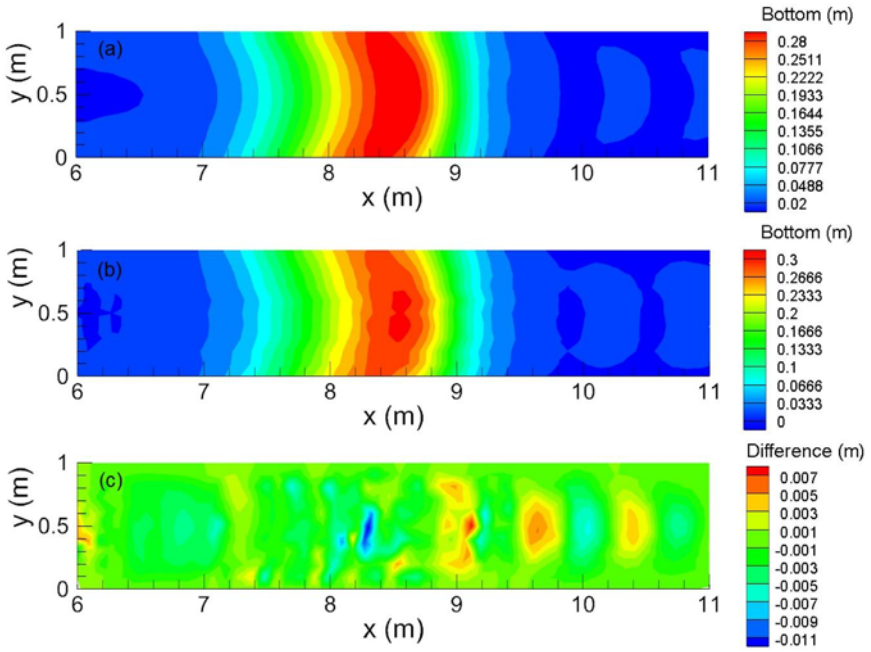

Fig. 10. 2D comparison of bed level simulation after 25,000 s; (a) TELEMAC-3D, and (b) ANN-based model, (c) Difference between two models.

Table 2
Statistical performance of the second proposed concept for modeling the bed change in a straight channel at different times.

Performance index	15,000 s	25,000 s
R	0.8938	0.9149
RMSE (m)	0.0266	0.0602
MAE (m)	0.0146	0.0384

$$Z_{b(i,j)}^{t+1} = \mathbf{LW}_{2,1}^{z} \times logsig\left(\mathbf{IW}_{1,1}^{z} \times \mathbf{B}^{\mathrm{T}} + \vec{\mathbf{b}}_{1}^{z}\right) + b_{2}^{z}, \tag{3}$$

where superscripts *u*, *h*, and *z* denote the corresponding ANN model (velocity, water depth and bed level integrator, respectively).

Finally, an ANN model is considered based on different input matrices to establish the proposed hydrodynamic-morphologic modeling system. The models consist of only one hidden layer with ten neurons. The logistic sigmoid and linear transfer functions have been used for hidden and output layers, respectively. The Levenberg–Marquardt is applied to all models. After a trial and error procedure, it is found that the input matrix arranged based on the node and element numbers is performing better.

The same procedure was carried out for the second scheme. Here, the only difference is that we have only one ANN model for calculation of the bed level changes and the hydrodynamic variables are calculated by TELEMAC system. It should be taken into consideration that the ANN model is trained by another input parameters which can be seen from matrix C. Finally, using the designed networks, the following

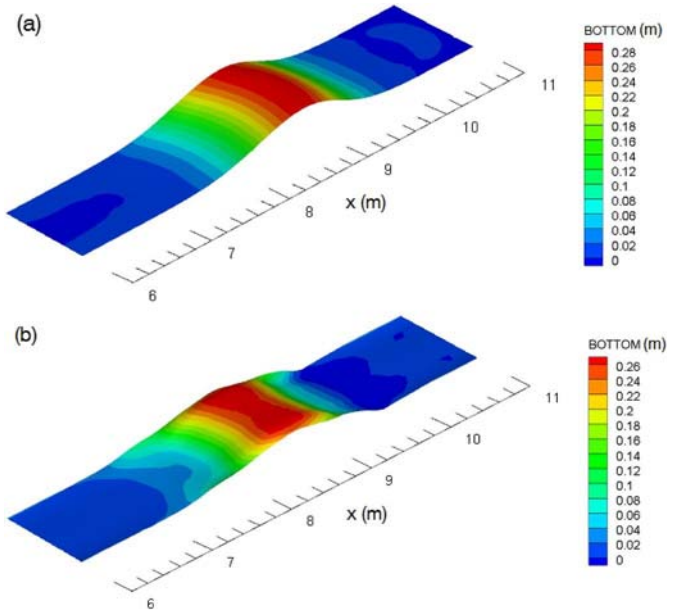

Fig. 11. Bed level simulation after 15,000 s; (a) TELEMAC-3D, and (b) TELEMAC-3D implementing ANN-based model.

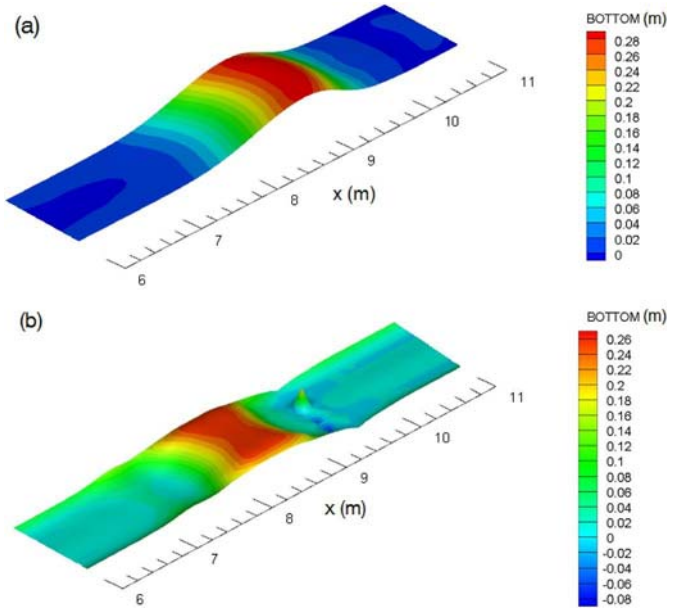

Fig. 12. Bed level simulation after 25,000 s; (a) TELEMAC-3D, and (b) TELEMAC-3D implementing ANN-based model.

equation for the normalized bed level change calculations is received:

$$Z_{b(i,j)}^{t+1} = \mathbf{LW}_{2,1}^{z} \times logsig\left(\mathbf{IW}_{1,1}^{z} \times \mathbf{C}^{\mathrm{T}} + \vec{\mathbf{b}}_{1}^{z}\right) + b_{2}^{z}, \tag{4}$$

where $\mathbf{IW_{1,1}}$ is the input weight matrix, $\mathbf{LW_{2,1}}$ is the hidden layer weight matrix, $\mathbf{b_1}$ is the bias vector, and b2 is the bias value which are obtained after a successful training process.

The Eq. (4) is used in the subroutine bedload_solves_fe.f to calculates the new bed level for each node at every time step. After modification of the subroutine, we have to recompile the code. Consequently the program can be ready to be launched with the user-defined functions in the subroutine.

7. Results and discussion

7.1. For test case-1

To assess the proficiency of the designed ANN models in the new proposed coupling model, the initial values at times $t = 0$ and 500 s are determined at every grid point explained above. The bed levels, velocity and water depth at one time step ahead $t = 1000$ s are updated using the ANN models. The procedure is repeated until the last time step is reached. Table 1 presents the statistical performances of the model based on a comparison between the predicted bed levels and simulation of TELEMAC-3D modeling system at different times. The results indicate that the designed ANN performs well the morphological change in the channel with high values of R as well as small values of RMSE and MAE. According to this table, the model performance reduces as time increases. As explained before, the reason is error accumulation problem, i.e. errors committed in the past are propagated into future predictions. This is more serious here as we have three ANNs instead of one.Figs. 7 and 8 show the simulation of TELEMAC and proposed hydrodynamic-morphologic modeling system after 15,000 and 25,000 s, respectively. In order to make a better comparison between the models and analyze our ANN-based scheme, 2D view of Figs. 8 and 9 on *xy*-plane are plotted in Figs. 9 and 10, respectively.

Now we analyze the capability of the second proposed concept and newly modified subroutine that implements the designed ANN model for prediction of bed level changes into the TELEMAC system. Using the initial values, the program can simulate the bed levels at every grid point i at one time step ahead. The minor time step of $\Delta t = 1$ s is chosen for hydrodynamic calculations while the coupling period with the morphologic module is $\Delta t = 500$ s. The bed level remains fixed during the hydrodynamic computation. After each 500 s, the results are sent to bed level change module and during the computation of the bed level the flow is invariant to the bed level changes. After updating the bed changes using the knowledge of ANN model, the results are sent back to the TELEMAC-3D for flow field calculations. The procedure is repeated until the last time step is reached.

The performance of the model is analyzed using statistical indicators such as Correlation Coefficient (R), Root Mean Square Error (RMSE) and Mean Absolute Error (MAE). Table 2 presents the accuracy of the proposed hydromorphodynamic model after 15,000 and 25,000 s. Figs. 11 and 12 show the simulation of the original TELEMAC-3D and the proposed modeling system after 15,000 and 25,000 s, respectively. A 2D comparison between the models are illustrated in Figs. 13 and 14, respectively.

According to Table 2, the proposed concept, which is integrating ANN model into TELEMAC system, performs poorly for the first test case. The statistical performance of the model indicates insufficient quality of results. The poor results can be also noticed from the figures. This might be due to the location of neighbor nodes as they play a crucial role in this concept.

7.2. For test case-2

To test the first proposed scheme using the second example, the initial values at time $t = 0$ and 200 s are defined at every grid point (i, j). Similar to the first test case, the velocity and water depth at one time step ahead $t = 400$ s are calculated using the ANN-based Eqs. (1) and (2). Using calculated values and applying the ANN-based Eq. (3) the bed change is calculated. The results are sent back for flow field calculations at the next time step. The procedure is repeated until the last time step is reached. Table 3 presents the statistical performance indices of the model based on a comparison between the predicted bed levels and simulation of the TELEMAC-2D modeling system at different times.

Fig. 15(a) and (b) plot the bed level simulated by the TELEMAC-2D model and the ANN-based model after 6000 s, respectively. The difference between two models is illustrated in Fig. 15(c) to make a

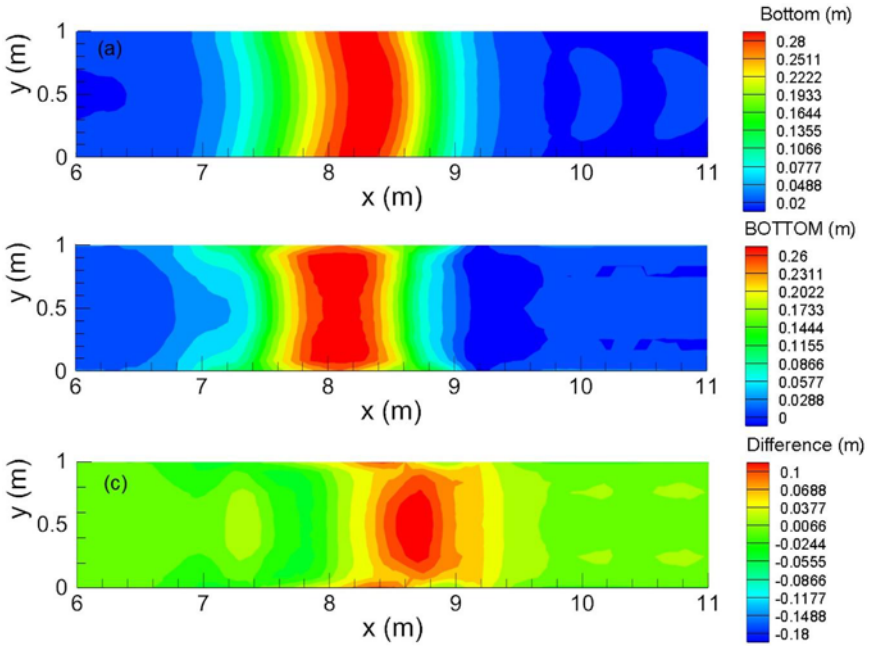

Fig. 13. 2D comparison of bed level simulation after 15,000 s; (a) TELEMAC-3D, (b) TELEMAC-3D implementing ANN-based model, and (c) Difference of models.

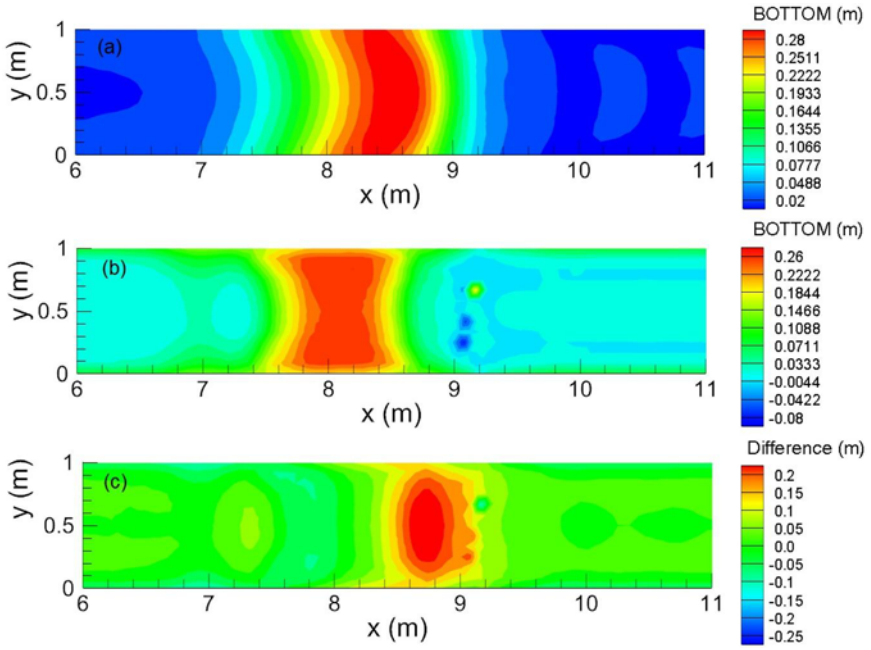

Fig. 14. 2D comparison of bed level simulation after 25,000 s; (a) TELEMAC-3D, (b) TELEMAC-3D implementing ANN-based model, and (c) Difference of models.

Table 3
Statistical performance of the first proposed concept for modeling the bed change in a channel curve at different times.

Performance index	6000 s	10,000 s	20,000 s
R	0.9999	0.9959	0.9865
RMSE (m)	0.0002	0.0016	0.0035
MAE (m)	0.0001	0.0011	0.0026

comparison between the models easier. As can be seen from this figure, the difference between the bed level calculations by two models is small which proves quality of the proposed model.

The long-term differences between the aforementioned models after 10,000 and 20,000 s simulations are illustrated in Fig. 16(a) and (b), respectively. According to Table 3, the R, RMSE, and MAE are in the range of 0.9999–0.9865, 0.0002–0.0035 m, and 0.0001–0.0026 m, respectively. These values and figures confirm good quality of results. It is noteworthy to mention that the simulation takes only few seconds by applying this new proposed concept while it would take the TELEMAC system few minutes.

Here we analyze the capability of the second proposed scheme for prediction of bed level changes in the new coupling model using the second test case. First, the initial values are defined at every grid point. The bed levels at one time step ahead are calculated using the explicit equation implemented in the modified subroutine. A minor time step for hydrodynamic calculations ($\Delta t_{hyd} = 0.1$ s) and a big time step for bed level changes simulation ($\Delta t_{sed} = 200$ s) are chosen. The bed level remains fixed during the hydrodynamic computation. After each

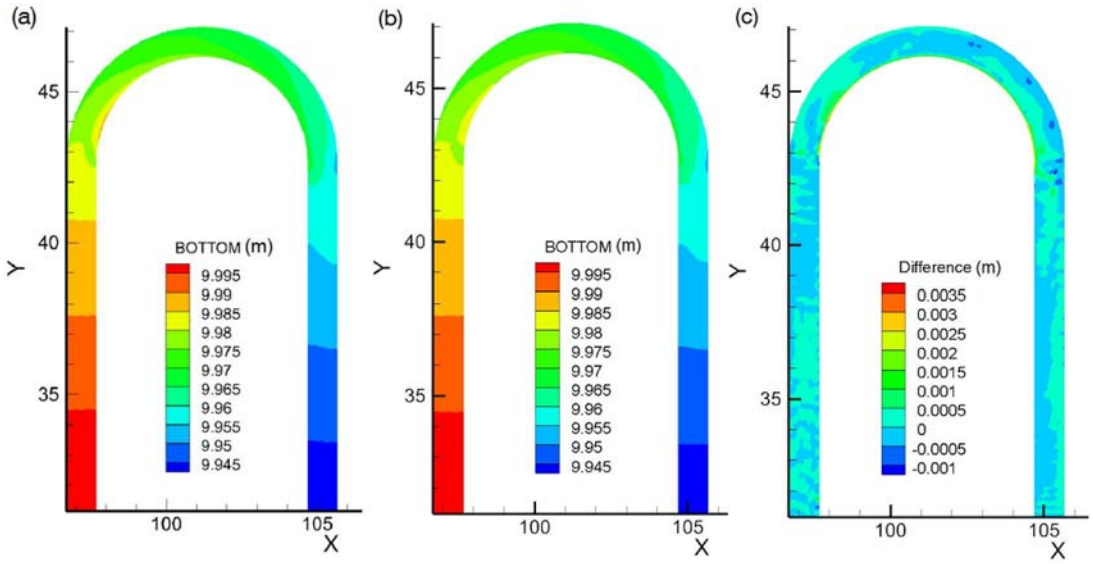

Fig. 15. Bed level simulation after 6000 s; (a) TELEMAC-2D, and (b) ANN-based model, (c) Difference between two models.

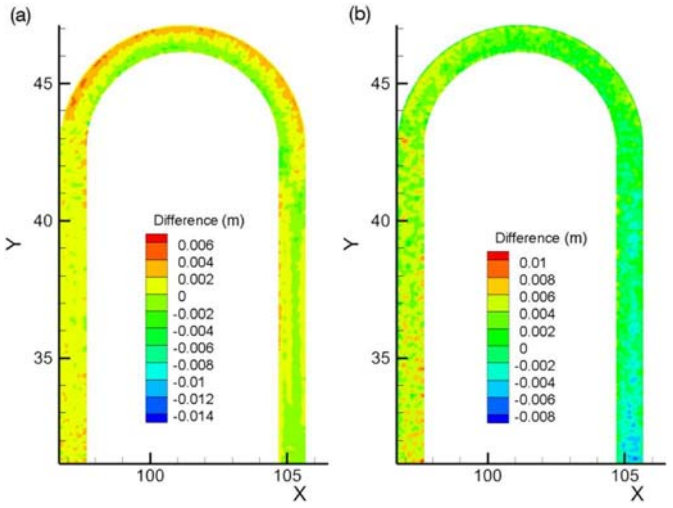

Fig. 16. Difference between two models; (a) After 10,000 s, (b) After 20,000 s.

Table 4
Statistical performance of the second proposed concept for modeling the bed change in a channel curve at different times.

Performance index	6000 s	10,000 s	20,000 s
R	0.9859	0.9821	0.9700
RMSE (m)	0.0020	0.0023	0.0030
MAE (m)	0.0011	0.0017	0.0023

200 (s), the results are sent to bed level change module and during the computation of the bed level the flow is invariant to the bed level changes.

The Table 4 shows the tabulation of the statistical performance of the proposed hydrodynamic-morphologic system implementing ANN into TELEMAC model after 6000, 10,000, and 20,000 s. The results confirm that there is a good agreement between the proposed scheme of hydrodynamic-morphologic system and the original TELEMAC modeling system.

Fig. 17(a)–(c) plot the difference between two models after 6000, 10,000 and 20,000 s. As can be seen from these figures, the difference between the bed level calculations by two models is almost zero except for the very small domain in the beginning and in the end of the curve. The predicted results show that the new proposed scheme could perform well for long-term time series prediction and ANN results could be integrated in the hydromorphological model systems.

8. Conclusions

Current research is focusing on developing new schemes of hydrodynamic-morphologic-model systems which integrate data-driven model, in particular Artificial Neural Networks, into hydromorphological models for fluvial channels. In the first scheme, 2 or 3 ANN models might be utilized for hydrodynamic calculations. At each time step, the hydrodynamic variables including velocity field and water depth were transferred into the morphodynamic model (ANN-based approximator), which then sent back the updated bed elevation to the hydrodynamic model. In the second scheme, the sediment transport model SISYPHE was replaced by an ANN model coupled with either the 2D or 3D flow models. The time step of morphodynamic part (ANN-based approximator) is much larger than the time step of TELEMAC-2D/3D and during the flow computation, the bed level is assumed constant. The main advantages of the proposed schemes are that there is no need for bed shear stress and sediment transport rate calculations. To test the efficiency and effectiveness of each proposed scheme, two different test cases were considered in this paper. The first test case included a straight channel with a finite amplitude perturbation of the bed level in the TELEMAC-3D modeling system. The evolution of the bed in a 180° channel bend under unsteady-flow conditions with uniform sediment was also considered as the second test case. The results showed that the model predictions of the first proposed scheme for both test cases agreed closely with the TELEMAC simulation. It was concluded from the results that the proposed scheme performed well for short and long-term time series predictions and would significantly reduce the computational time. The comparison of the prediction accuracies of the second proposed scheme and TELEMAC simulation indicated that the proposed model could sufficiently simulate and predict the morphological bed level changes for the second test case. However the second scheme did not perform as well for the first test case as compared to the first scheme. In general, it can be concluded that applying the schemes developed in this research would reduce the computational costs and simplify the computational procedure, as they did not require the shear stress and sediment transport rate calculations. It is also proved that these schemes could perform well for long-term time series prediction, even though the ANN models were not trained for that length of time.

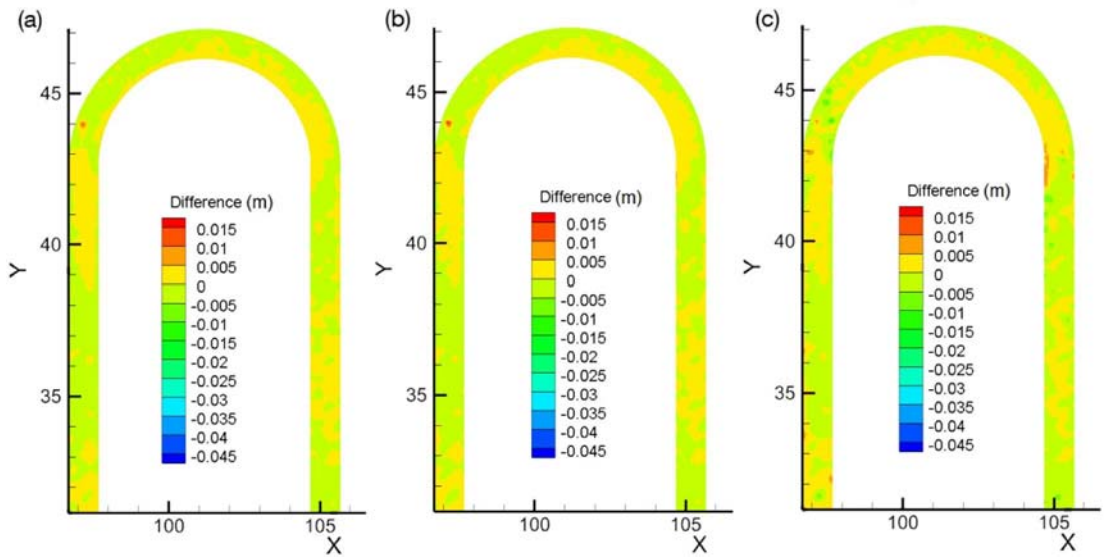

Fig. 17. Difference between original TELEMAC-2D and TELEMAC-2D implementing ANN based-model; (a) After 6000 s, (b) After 10,000 s, and (c) After 20,000 s.

Funding

This research was not funded by any foundation.

Conflicts of interest

The authors declare no potential conflict of interest.

CRediT authorship contribution statement

Keivan Kaveh: Conceptualization, Formal analysis, Methodology, Writing - original draft. **Minh Duc Bui:** Supervision, Writing - review & editing. **Peter Rutschmann:** Supervision, Writing - review & editing.

References

[1] Mahwah NJ. User's manual. USA: HydroQual, Inc.; 2002. p. 188. Version 1.3.
[2] Warren IR, Bach H. MIKE 21: a modelling system for estuaries, coastal waters and seas. Environ Softw 1992;7(4):229–40.
[3] Lesser GR, Roelvink JA, Van Kester JATM, Stelling GS. Development and validation of a three-dimensional morphological model. Coast Eng 2004;51(8):883–915.
[4] Warner JC, Sherwood CR, Signell RP, Harris CK, Arango HG. Development of a three-dimensional, regional, coupled wave, current, and sediment-transport model. Comput Geosci 2008;34(10):1284–306.
[5] Bui MD, Kaveh K, Rutschmann P. Integrating artificial neural networks into hydromorphological model for fluvial channels. Proc. of the 36th IAHR world congress. 2015.
[6] Hudson J, Damgaard J, Dodd N, Chesher T, Cooper A. Numerical approaches for 1D morphodynamic modeling. Coast Eng 2005;52(8):691–707.
[7] Long W, Kirby JT, Shao Z. A numerical scheme for morphological bed level calculations. Coast Eng 2008;55(2):167–80.
[8] Haykin S. Neural networks: a comprehensive foundation. Prentice Hall; 1999.
[9] Bhattacharya B, Price RK, Solomatine DP. Machine learning approach to modeling sediment transport. J Hydraul Eng 2007;133(4):440–50.
[10] Shahin MA, Maier HR, Jaksa MB. Predicting settlement of shallow foundations using neural networks. J Geotech Geoenviron Eng 2002;128(9):785–93. ASCE.
[11] Hervouet JM. Hydrodynamics of free surface flows: modelling with the finite element method. John Wiley & Sons; 2007.
[12] Villaret C, Hervouet JM, Kopmann R, Merkel U, Davies AG. Morphodynamic modeling using the Telemac finite-element system. Comput Geosci 2013;53:105–13.
[13] Yen CL, Lee KT. Bed topography and sediment sorting in channel bend with unsteady flow. J Hydraul Eng 1995;121(8):591–9.

3.3. Sedimenttransport in Kiessohlflüssen

Wie in Abschnitt 2.2 erwähnt, kann ein Mehrschichtmodell für fraktionierten Sediment zur Berechnung des Sedimenttransports und -sortierens sowie der Sohldeformation angewendet werden. Die meisten konventionellen Modelle gingen jedoch davon aus, dass die Porosität des Bettmaterials konstant ist, was für die Simulation des Sedimenttransports und der Bettvariation in Kiessohlflüssen nicht ausreicht.

Der folgende Artikel stellt ein neues numerisches Modell für Sohländerungen unter Berücksichtigung der Porositätsänderungen vor. Ein Modellkonzept für Austauschprozesse von Bettmaterial und Transportsediment wurde entwickelt, um die zeitlichen und räumlichen Änderungen von Korngrößenverteilung und Bettporosität zu ermitteln. Um die Verbesserung des neuen Konzepts zu verdeutlichen, wurden die simulierten Ergebnisse für einfache gerade Gerinnen mit Kiesbett mit den gemessenen Daten verglichen.

Darüber hinaus ist die Diskrete-Elemente-Methode (DEM) eine etablierte Methode u.a. in der Geotechnik zur Simulation von granularen Geomaterialien mit Kollisionen (Kozicki & Donzé, 2008). Drei Aspekte sind wichtig für DEM: die Repräsentation der Kontakte (weich vs. hart), die Repräsentation des Feststoffes und der Algorithmus für die Entdeckung und das Update der Kontakte (Cundall & Hart, 1992). DEM kann verschiedene verformbare oder nicht verformbare Objekte simulieren. Eine Beschreibung der realistischen Objekte bietet die Methode der Clusterbildung an. Innerhalb der Cluster können die Kontakte mit angemessener Rechenzeit berechnet werden (Jensen et al., 1999). In dem folgenden Artikel wird die Methode von DEM verwendet, um Infiltrationsprozesse zu modellieren und die Auswirkungen der relativen Größe des feinen Sediments zu dem Kies auf die Infiltrationstiefe zu bestätigen.

Das neue Modell wurde auf drei geraden Kanälen getestet. Die Analyse der berechneten Ergebnisse und der Vergleich mit den beobachteten Daten zeigen, dass das neue Modell den Sedimenttransport, die Sortierungsprozesse und die Sohlveränderung in Kiesbettflüssen erfolgreich simulieren kann.

- Bui, V.H.; M.D. Bui; P. Rutschmann (2019): “Advanced Numerical Modeling of Sediment Transport in Gravel-Bed Rivers”. Water. 11, 50. MDPI.

water

MDPI

Article

Advanced Numerical Modeling of Sediment Transport in Gravel-Bed Rivers

Van Hieu Bui [1,2,*], Minh Duc Bui [1] and Peter Rutschmann [1]

[1] Institute of Hydraulic and Water Resources Engineering, Technische Universität München, Arcisstrasse 21, D-80333 München, Germany; bui@tum.de (M.D.B.); peter.rutschmann@tum.de (P.R.)
[2] Faculty of Mechanical Engineering, Thuyloi University, 175 Tay Son, Dong Da, Hanoi 100000, Vietnam
* Correspondence: hieubv@tlu.edu.vn; Tel.: +49-152-134-15987

Received: 15 February 2019; Accepted: 13 March 2019; Published: 17 March 2019

Abstract: Understanding the alterations of gravel bed structures, sediment transport, and the effects on aquatic habitat play an essential role in eco-hydraulic and sediment transport management. In recent years, the evaluation of changes of void in bed materials has attracted more concern. However, analyzing the morphological changes and grain size distribution that are associated with the porosity variations in gravel-bed rivers are still challenging. This study develops a new model using a multi-layer's concept to simulate morphological changes and grain size distribution, taking into account the porosity variabilities in a gravel-bed river based on the mass conservation for each size fraction and the exchange of fine sediments between the surface and subsurface layers. The Discrete Element Method (DEM) is applied to model infiltration processes and to confirm the effects of the relative size of fine sediment to gravel on the infiltration depth. Further, the exchange rate and the bed porosity are estimated while using empirical formulae. The new model was tested on three straight channels. Analyzing the calculated results and comparing with the observed data show that the new model can successfully simulate sediment transport, grain sorting processes, and bed change in gravel-bed rivers.

Keywords: numerical modelling; bed porosity; grain sorting; gravel-bed rivers

1. Introduction

Sediment transport processes that are due to flowing water in gravel-bed rivers can be formed from bed load, suspended load, and movement inside the bed layer. More importantly, in the same hydraulics condition, the transport rate of coarse size fraction may be different from the rate of fine size fraction. These reasons lead to the distinct forms of gravel-bed rivers. Due to high-flow velocity, all of the finer particles may be eroded, leaving a layer of coarse particles. When the flow is unable to carry the coarse particles, then no more erosion occurs, which is known as an armoring process [1,2]. Inversely, under low-flow conditions, sediment transport can cause the extensive infiltration of fine sediment into void spaces in coarse bed material [3,4], which is also known as clogging or colmation [5,6] (see Figure 1).

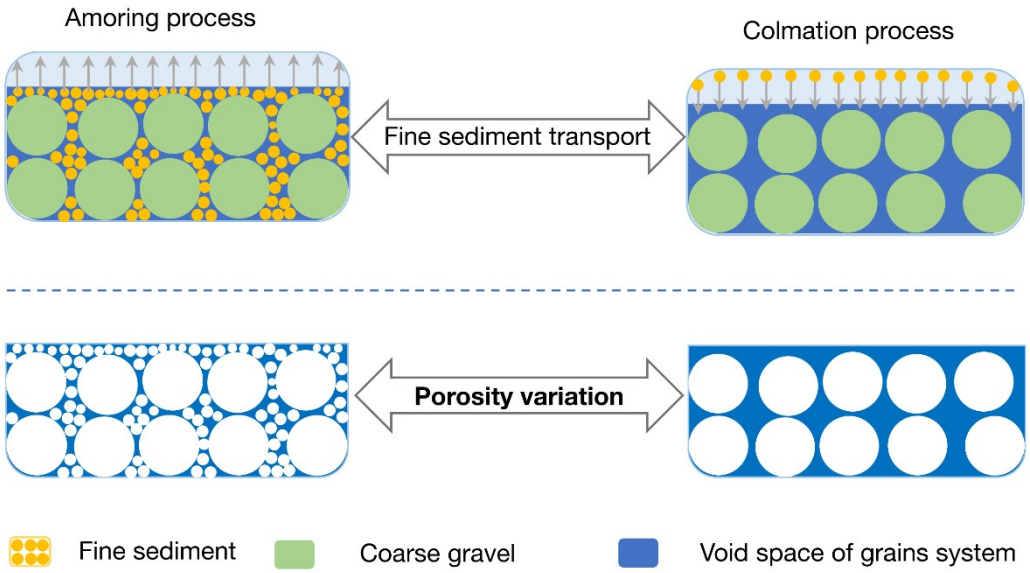

Figure 1. Porosity variation of grain system due to fine grain exchange.

The change in grain size distribution of coarse and fine sediment not only leads to the variation in bed profile, but it also mainly results in the change in bed porosity defined as a fraction of the volume of voids over the total volume of the gravel-bed river. According to [7,8], the porosity of sand-gravel mixtures can vary from about 0.10 to 0.50. For example, the measured porosity values in the Rhine River range from 0.06 to 0.48 [9].

The study of variation in porosity is vital for fluvial geomorphology assessment as well as in river ecosystem management. From a river management point of view, the amount of fine sediment stored in the void space of gravel-bed up to 22% [10] may be neglected during calculation by considering constant porosity. Furthermore, the porosity may exert strong influence on the rate of bed level changes [11,12]. The impact of void space of gravel-bed on habitats for fish and aquatic insects is essential, and particularly the importance of assessing the change in the void structure of the bed material has been pointed out strongly [13].

To model sediment transport processes as well as bed deformation, multi-layer models were applied for graded sediment transport. Despite the considerable variations of porosity, most of the conventional models assumed that the porosity of bed material is constant. Therefore, sediment transport in the form of infiltration into the void spaces of the coarse bed, or fine particles in sublayers and the entrainment of fine sediment into flow from the substrates, is not taken into account. This assumption can be inappropriate for simulating the sediment transport and bed variation in gravel-bed rivers. Toro-Escobar et al. [14] accounted for this process in terms of an appropriate transfer or exchange function at the interface between the surface layer and substrate. Based on the data from a large-scale experiment on the aggradation and the selective deposition of gravel, they proposed an empirical form for the transfer function, where material that is transferred to the substrate can be represented as a weighted average of bedload and surface material, with a bias toward bedload. Applying this function with the assumption of a constant porosity, Cui [15] developed a numerical model for sand entrainment/infiltration from/into the subsurface. The model was applied to study the dynamics of grain size distributions, including the fractions of sand in sediment deposits and on the channel bed surface. Further, Sulaiman et al. [16] proposed an approximated bed variation model while considering the change in bed porosity, where the thickness of each layer is assumed to be constant and equal. Furthermore, the exchange between bed material and the transported sediment only takes place on the surface layer, and sediment transport from an upper layer to the lower layer is neglected. These assumptions are improper in gravel-bed rivers, where finer sediment possibly drops into the subsurface layer.

To bridge above knowledge gap, in this paper we develop a numerical hydromorphological model that considers the bed porosity change and the exchange flux of fine sediment between two different bed layers. Further, the Discrete Element Method (DEM) is employed for modeling the infiltration processes. We test the new numerical model for three straight gravel-bed open channels. The calculated results are then compared with the observed data to verify the improved model.

2. Methodology

As usual, the structure of our proposed model consists of two modules: (1)—hydrodynamic module; and, (2)—sediment transport and bed variation module. In the hydrodynamic module, the backwater equation is employed for low Froude number conditions and the quasi normal flow assumption is applied for the high Froude number flow conditions. The friction slope is calculated with the Keulegan formulation, which is used for calculating the transport rate in the sediment transport and bed variation module. More details regarding the water flow equations can be found in the studies that were conducted by Cui and Parker [15,17–20]. The flow module interacts with sediment transport and bed variation module that is based on the mechanism of quasi-steady morphodynamic time-stepping, in which the interaction between the flow and bed profile is considered in two different times. More specifically, at each time step of the flow calculation, the bed level is considered to be constant, and the sediment transport is assumed not to effect the flow, whereas in the process of bed calculation, the flow is assumed to be invariant. Subsequently, the water depth, velocity, as well as the bed roughness are adjusted based on the results of the sediment transport and bed variation module. The calibrated roughness is used in the hydraulic module in the next time step. Since previous models contained some limitations, we developed a new sediment transport and bed variation module, which is presented in detail in the following sections.

In principle, the bed topography in a channel is related to the transport of both bed load and suspended load. In the case of a coarse-material bed, the influence of suspended load is negligible, whereas the bed load is predominant. Further, suspended sediment load is the fine material that moves through the channel in the water column. These materials are kept in suspension by the upward flux of turbulence that is generated at the bed of the channel. The upward currents must equal or exceed the particle fall-velocity for suspended sediment load to be sustained. In this paper, we assume the turbulent flow to be small, therefore we only consider bed load in sediment transport modelling.

The governing equations for flow, sediment transport, and bed variation are numerically solved while applying the finite volume method with the required initial and boundary conditions.

2.1. Sediment Transport and Bed Variation Module

The size-fraction method is applied to divide bed material into some size-fractions. Each fraction is characterized by an average grain size and volume percentage of occurrence in the bed material and presented these components as the probability of different group. Applying the so-called multi-layer concept, we divide the vertical bed structure into different layers. Figure 2 shows a diagram of this structure consisting of one active layer and several substrate layers. Sediment particles are continuously exchanged between the flow and the active layer. Generally, the sediments in this layer can be transported as bed load, suspended load, or infiltration. Furthermore, they can move between the active layer and sublayers, depending mostly on the bed porosity and grain size distribution, as it will be discussed below in Section 2.3. For example, sediments are exchanged between the active layer and substrates when the bed scours or fills, as well as when filtration occurs. As erosion occurs, the entrainment of sediment particles from the active layer and its ensuing downward displacement causes particles from substrate layers to be mixed with those in the active layer. On the contrary, the deposition of sediment particles on the bed leads to an upward displacement of the active layer and the initiation of new substrate layers. At high flow discharges, fine sediments in the top substrate (2) may also be attracted to the surface layer and entrained flow.

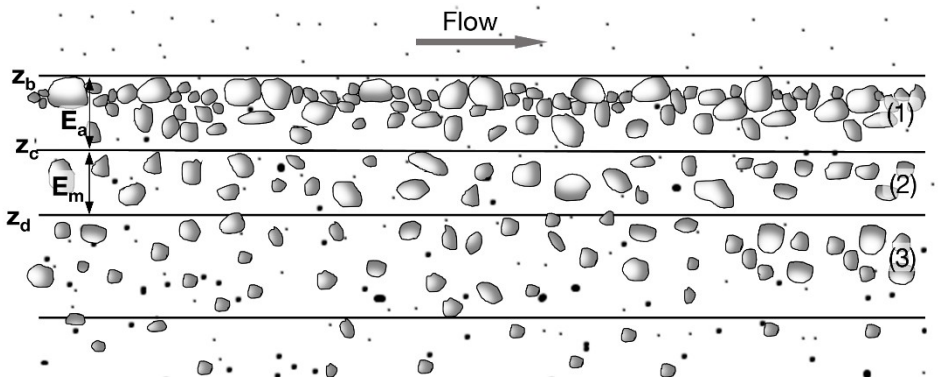

Figure 2. The structure diagram of the vertical cross-section is based on the multi-layers model. (1) = active layer; (2) and (3) = substrate layers; E_a and E_m = Active layer thickness and active-stratum layer thickness; z_b = bed elevation; z_c and z_d = substrate elevations.

Furthermore, the riverbed morphology in nature can be related to all three types of sediment transport that are mentioned above (bed load, suspended load, and infiltration of fine sediment). As mentioned above, when turbulent flow is week or the settling velocity of sediment particle is more significant than critical shear stress velocity, sediment particle only moves in the forms of bed load or infiltration. For the sake of simplicity of this paper, we assume that

- The horizontal surface is unchanged $z_d = 0$, so sediment sorting occurs only in the active layer (1) and the upmost sublayer (2); i.e., the bed consists of only two layers.
- The bed sediment is moving under two forms: infiltration or bed load.
- The flow and sediment transport are one-dimensional.

The change in the bed elevation is calculated using the law of continuity of bed sediment in the active layer:

$$\frac{\partial}{\partial t}\left[\int_0^{z_b}(1-p)dz\right] = -\frac{\partial q_b}{\partial x} \quad (1)$$

Where x = The coordinate axis along the flow direction; z = The coordinate axis along the vertical direction; t = time; p = p(x,z,t) = bed porosity; $q_b = q_b(x,t)$ = total specific volumetric bed load discharge. Its fraction $q_{b,j}$ is determined by experiment or semi-experiment when considering non-equilibrium bed load [21]. In this study, the fractional bed load rate is calculated while using the bed-load equation proposed by Wilcock and Crowe [22]. Further, Equation (1) can also be rewritten as:

$$\frac{\partial}{\partial t}\left[\int_0^{z_b-E_a}(1-p)dz + \int_{z_b-E_a}^{z_b}(1-p)dz\right] = -\frac{\partial q_b}{\partial x} \quad (2)$$

Applying the theorem of mean values and Leibniz integral rule for two finite integrals in the left-hand side of Equation (2) yields:

$$(1-p_s)\frac{\partial z_b}{\partial t} = -\frac{\partial q_b}{\partial x} + S_p S_p = \left[(z_b - E_a)\frac{\partial p_s}{\partial t} + E_a\frac{\partial p_a}{\partial t} + (p_a - p_s)\frac{\partial E_a}{\partial t}\right] \quad (3)$$

In which $p_a = p_a(x,t)$ = the average porosity of active layer; $p_s = p_s(x,t)$ = the average porosity of sublayer layer (Figure 3). If the porosity of layers is constant, the porosity source term $S_p = 0$ and Equation (3) becomes the Exner equation. Therefore, Equation (3) can be considered as the expansion of the Exner equation, when considering the variation of porosity in space and time.

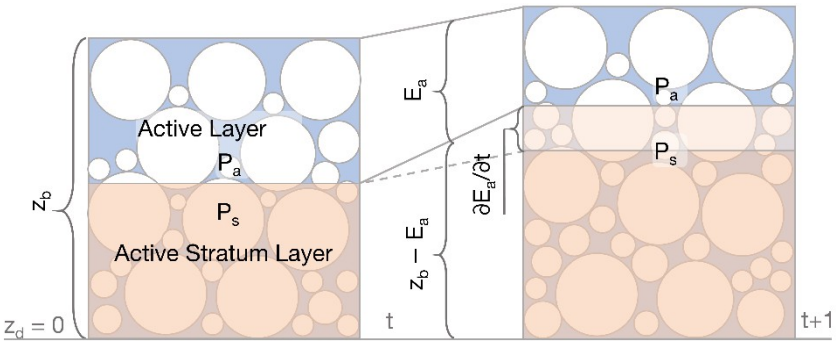

Figure 3. Bed level change due to porosity variation in different time steps.

Assuming that the grain sorting in an active layer only occurs under the flow interaction and exchange process between the active layer and the active stratum layer and while applying the mass conservation law in the active layer, we obtain the equation for the change of size fraction, as below:

$$\frac{\partial}{\partial t}\left[\int_{z_b-E_a}^{z_b}\beta_{a,j}(1-p_a)dz\right] = -\frac{\partial\left(\beta_{b,j}q_b\right)}{\partial x} + S_{F,j} \tag{4}$$

Equation (4) can be rewritten in the following form:

$$\frac{\partial\beta_{a,j}}{\partial t} = \frac{1}{E_a(1-p_a)}\left[\beta_{a,j}E_a\frac{\partial p_a}{\partial t} - \beta_{a,j}(1-p_a)\frac{\partial E_a}{\partial t} - \frac{\partial\left(\beta_{b,j}q_b\right)}{\partial x}\right] + \frac{S_{F,j}}{E_a(1-p_a)} \tag{5}$$

which $\beta_{a,j}$ = the size fraction of active layer; and, $\beta_{b,j}$ = the size fraction j of sediment transport in the form of bed load. The function $S_{F,j}$ expresses the exchange process of the active layer and sublayers of the size fraction j. Determining the $S_{F,j}$ value can be considered as the quantification of the bottom infiltration process and Section 2.2 provides a detailed description of this function.

Based on the mass conservation and assuming that the grain sorting of the active stratum layer is caused by the exchange process between the surface layer and subsurface one, we get the following equation for the size fraction change in the subsurface layer:

$$\frac{\partial\beta_{s,j}}{\partial t} = \frac{1}{(z_b-E_a)(1-p_s)}\left[\beta_{s,j}(z_b-E_a)\frac{\partial p_s}{\partial t} - \beta_{s,j}(1-p_s)\frac{\partial(z_b-E_a)}{\partial t}\right] - \frac{S_{F,j}}{(z_b-E_a)(1-p_s)} \tag{6}$$

In which $\beta_{s,j}$ is the size fraction j of sediment in the subsurface layer. As can be seen in Equations (3)–(6), the bed porosity variation and the sediment exchange between two neighbor bed layers are considered. Furthermore, the experimental studies show that the bed porosity depends on two main parameters: grain size distribution and compaction degree of bed material. Section 2.3 describes details regarding the determination of porosity.

2.2. Infiltration Process

The infiltration process is the movement of fine sediment, such as sand and silt, into void space in gravel-bed due to gravity. The infiltration process will stop when the sizes of these voids are small enough. Typically, bed sediments are divided into two different sizes: Fine sediment includes particles with a size less than 2 mm and coarse sediment with a particle size larger than 2 mm. The relative mean size of coarse sediment D_m and fine sediment d_m can be used to evaluate the depth of the infiltration process. For example, according to [23], if the ratio (D_m/d_m) of river bed less than 10, then fine sediment is almost impossible to infill through the void space of the gravel bed. If this ratio is between 10 and 30, then fine sediments will be deposited in the void space of the top gravel-bed layer and create a sand seal. If $30 < D_m/d_m < 70$, some fine sediments will be clogged at the void of the upper

layer, but they will not clearly create a sand seal. When the ratio D_m/d_m greater than 70, all of the fine sediment will settle down to the bottom of the gravel bed. These critical values may be changed when the bed material consists of almost uniform spherical particles for fine and coarse sediments. In other words, the infiltration process depends on the characteristic parameters of the bottom (including the size distribution as well as the shape of the sediment particles). Additionally, this process depends on the near bottom hydraulic conditions, i.e., near-bed flow water and flow through the void space of the gravel bed. Cui et al. [3] proposed a theoretical model, in which the fraction of fine sediment decreases exponentially along with the depth of the gravel bed. Wooster et al. [24] and Gibson et al. [25] also used this hypothesis with laboratory observation data to develop their models, in which the fine reduction sediment is determined as a function of gravel depth.

Based on the empirical equation of Toro-Escobar et al. [14], the following equation can be proposed to quantify the exchange between the active layer and active stratum layer for the fine fraction of size class j [26]:

$$S_{F,j} = \left[c\beta_{a,j} + (1-c)\beta_{b,j}\right]\left\{\frac{\partial q_b}{\partial x} + \frac{\partial}{\partial t}[E_a(1-p_a)]\right\} \quad (7)$$

where coefficient c can be considered as a parameter of the model. As can be seen in Equation (7), the function $S_{F,j}$ depends on sediment discharge of size class j, the time variation of bed porosity and active layer thickness. However, effects of sediments in the stratum layer was not yet considered in this equation.

Cundall and Strack initially proposed the Discrete Element Method (DEM) [27] to model the mechanical behavior of granular flows and to simulate the forces acting on each particle and its motion. Typically, a particle can be classified into two types of motion in DEM: translation and rotation. The momentum and energy of particles are exchanged during collisions with their neighbors or a boundary wall (contact forces), and particle-fluid interactions, as well as gravity. While applying Newton's second law of motion, we can determine the trajectory of each i-particle (including its acceleration, velocity, and position) from the following equations:

$$m_i \frac{d\vec{u}_i}{dt} = m_i \vec{g} + \sum_k \vec{f}_{i,k} + \vec{f}_{i,f} \quad (8)$$

$$I\frac{d\vec{\omega}_i}{dt} = \frac{d_i}{2}\sum_k \left(\vec{n}_{i,k} \times \vec{f}_{i,k}\right) \quad (9)$$

where m_i = the mass of a particle i; $\vec{u}_i$ = the velocity of a particle; $\vec{g}$ = gravity acceleration; $\vec{f}_{i,k}$ = interaction force between particle i and particle k (contact force); $\vec{f}_{i,f}$ = interaction force between the particle i and the fluid; I = moment of inertia; $\vec{\omega}_i$ = angular velocity; d_i = diameter of the grain i; $\vec{n}_{i,k}$ = directional contact = vector connecting the center of grains i and k.

We use a contact force model that is based on the principle of spring-dashpot, as well as the suggestions of Hertz–Mindlin [28]. The contact force is obtained from the force analysis method; the stiffness and damping factors are analyzed in two directions: orthogonal and tangent of the contact surface between the two grains:

$$f_{i,k}^{(n)} = k_i^{(n)}\delta_{i,k}^{(n)} + \alpha_i^{(n)}\Delta u_i^{(n)} \quad (10)$$

$$f_{i,k}^{(\tau)} = k_i^{(\tau)}\delta_{i,k}^{(\tau)} + \alpha_i^{(\tau)}\Delta u_i^{(\tau)} \quad (11)$$

(n) and (τ) are known as two components of contact force in a normal direction and tangential direction; k_i = stiffness of grain i; $\delta_{i,k}$ = The characteristic of the contact and displacement (also called the length of the springs in the two directions above); α_i = damping coefficient; and, Δu_i = relative velocity of grain at the moment of collision. Additionally, following Coulomb, the product of the coefficient of friction μ and the orthogonal force component determines the value of tangential friction. In the nonlinear contact force, the Hertz–Mindlin model, which is the tangential force component, will increase until

the ratio ($f^{(\tau)}/f^{(n)}$) reaching a value of μ, and it keeps the maximum value until the particles are no longer in contact with each other. A detail of the force models, as well as the method for determining the relevant coefficients, can be found in [28].

After calculating all of the forces acting on the sediment particles, as well as the velocity and the position of the particle at a previous time step, we can determine the velocity and position of grain at present step based on solving Equations (8) and (9). The grain size distribution, as well as the bed porosity for whole the domain, can be defined afterwards. As a result, we can also estimate the exchange rate of the fine fraction between different bed layers.

2.3. Porosity Estimation

Figure 4 shows a qualitative dependency between the bed porosity and fine size fraction, as well as their influence on the infiltration process (based on Church [29]). Additionally, the porosity of the gravel-bed is smallest when it is filled by fine sediment.

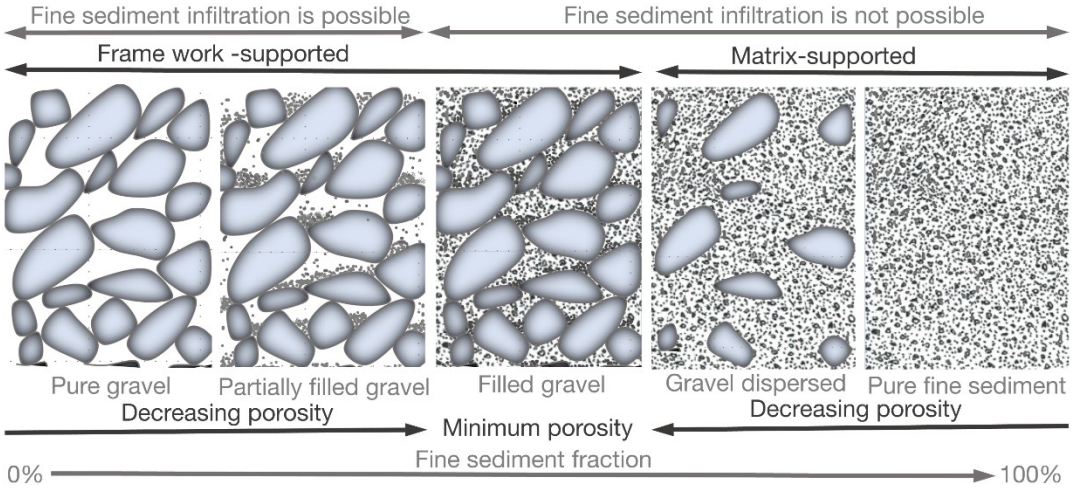

Figure 4. Schematic structure of bottom sediments as a function dependent on the magnitude of the fine component sediment.

Similarly to Bui et al. [30], we consider the volume of a unit bed sediment with a porosity p consisting of two types of sediment: coarse and fine, then the absolute volume (without porosity) of the bed sediment is $(1 - p)$. We assume that the ratio of fine particle size to coarse sediment is smaller than 0.154 (called as critical ratio) and fine particles do not affect the arrangement of coarse particles during the infiltration process.

Further, if the bed does not contain fine sediments, then the total volume of coarse sediment is $(1 - p^{(D)})$, where $p^{(D)}$ is porosity of coarse sediment. Correspondingly, the relative ratio of coarse sediment volume to the total volume of bed sediment is determined as:

$$f^{(D)} = \frac{1 - p^{(D)}}{1 - p} \tag{12}$$

While applying the same definition and similar symbols $p^{(d)}$ and $f^{(d)}$ for fine sediment, we have $f^{(d)} = (1 - f^{(D)})$ and obtained the correlation between porosity of bed and porosity of coarse sediment and the relative proportions of fine sediment, as follows:

$$p = \frac{p^{(D)} - f^{(d)}}{1 - f^{(d)}} \tag{13}$$

The minimum of bed porosity is ($p^{(D)} \times p^{(d)}$). Substituting this value into Equation (13), we obtain the relationship between the bottom porosity and the characteristics of fine sediment for this case, as follows:

$$p = \frac{p^{(d)} f^{(d)}}{1 - p^{(d)}\left(1 - f^{(d)}\right)} \tag{14}$$

Following Nunez-Gonzalez et al. [31], Equation (14) can be applied to calculate the porosity of the bed, with a predominance of the sand matrix (e.g., see right panel of Figure 4). Since Equations (13) and (14) have been obtained for the ideal gravel beds, their modifications that are based on measured data can be more suitable for different bed conditions. For example, Koltermann and Gorelick [32] proposed the following expression for calculating the bed porosity:

$$p = \begin{cases} p^{(D)} - \left(1 - p^{(d)}\right) f^{(d)} & \text{if} \quad f^{(d)} \le p^{(D)} \\ p^{(d)} f^{(d)} & \text{if} \quad f^{(d)} \ge p^{(D)} \end{cases} \tag{15}$$

The bed porosity reaches the minimum value p_{min} when the fraction of fine sediment is approximately equal to the porosity of the coarse sediment. Kamann et al. [33] has improved Equation (15) and then proposed the same expression to calculate the bed porosity:

$$p = \begin{cases} p^{(D)} - \left(\frac{p^{(D)} - p_{min}}{f^{(d)}_{min}}\right) f^{(d)} & \text{if} \quad f^{(d)} \le p^{(D)} \\ p^{(d)} + \left(\frac{p^{(d)} - p_{min}}{1 - f^{(d)}_{min}}\right)\left(f^{(d)} - 1\right) & \text{if} \quad f^{(d)} \ge p^{(D)} \end{cases} \tag{16}$$

where $f^{(d)}{}_{min}$ is a fine size fraction when the bed porosity reaches the minimum value.

Yu and Standish [34,35] developed a semi-analytical model for different grain sizes, which can be one of the best models in predicting the porosity of sand gravel mixtures [9]. The model is based on the assumptions that the grains are spherical sharp, no deformable, and uniform density, and random packing. Although these assumptions are not always valid for natural sediments, the model can be applied for natural sediments with angular grains [34].

We consider the mixture of n component with diameter $d_1 > d_2 > ... > d_j > \ldots > d_n$, initial specific volume $V_1, V_2, \ldots, V_j, \ldots, V_n$, and size fraction $\beta_1, \beta_2, \ldots, \beta_j, \ldots, \beta_n$.

For each component j, the parameters M_j and N_j are calculated using the critical size ratio (d/D = 0.154) and comparing with the other diameters.

$$M_j = \begin{cases} k & \text{if} \quad d_k \ge d_j/0.154 > d_{k+1} \\ 1 & \text{if} \quad d_j/0.154 > d_1 \end{cases} \tag{17}$$

$$N_j = \begin{cases} k & \text{if} \quad d_{k-1} \ge 0.154 d_j > d_k \\ n & \text{if} \quad d_j/0.154 < d_1 \end{cases} \tag{18}$$

The grain mixture is divided into partial specific volumes for each (d_j) grain based on M_j, N_j (see Figure 5). The middle zone is the controlling mixture of grain size jth (occupation), the first zone, and the last zone is presented filling mechanism. Particles in the first zone can fill in the structure component with diameter jth without disturbing in structure, and diameter jth is also filled in last zone structure.

$$V_j^T = f\left(V_j, \beta_j, d_j\right) \tag{19}$$

where: V_j^T is the specific volume of component jth with porosity p_j, which consists of three parts (Figure 5).

$$V_j^T = \left(V^S_{j,unmxg} + V^{MI}_{j,mix} + V^L_{j,unmxg}\right) \tag{20}$$

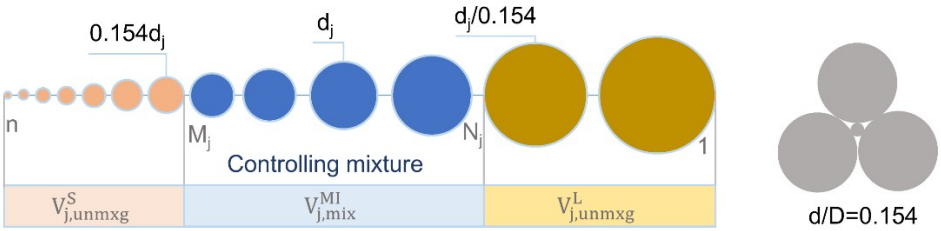

Figure 5. Classifying the mixture to partial specific volumes for diameter d_j.

$V^{MI}_{j,mix}$ presents the occupation mechanism (unmixing effect): change the skeleton of the controlling component. Because the partial specific of controlling mixture is the same as the specific volume when only these controlling components themselves form a packing mixture.

$$V^{MI}_{j,mix} = V_{j,mix} \sum_{i=Mj}^{Nj} \beta_i \tag{21}$$

$$V_{j,\,mix} = V_{j,0} + \frac{\sum_{h=Mj}^{Nj-1} \sum_{l=h+1}^{Nj} \delta_{hl} \beta_h \beta_l}{\left(\sum_{i=Mj}^{Nj} \beta_i\right)^2} + \frac{\sum_{h=Mj}^{Nj-1} \sum_{l=h+1}^{Nj} \gamma_{hl} \beta_h \beta_l (\beta_h - \beta_l)}{\left(\sum_{i=Mj}^{Nj} \beta_i\right)^3} \tag{22}$$

where $V_{j,0}$ is the initial specific volume; δ_{hl} and γ_{hl} are the empirical coefficients, which express the joint action of the mixture. $V^{S}_{j,ummxg}$ and $V^{L}_{j,unmxg}$ present the filling mechanism (Mixing effect). The semi empirical interaction functions f(j,i) and g(j,i) depend on the diameter and density of controlling mixture, which Yu and Standish modified [34]. The equations are slightly different from that by the previous equations. This is particularly true for spherical particles where the initial porosity is relatively low.

$$V^{L}_{j,unmxg} = \begin{cases} 0 & M_j = 1 \\ \sum_{i=1}^{M_j-1} [V_{i,mix} - (V_{i,mix} - 1) g(j,i)] \beta_i & M_j \geq 2 \end{cases} \tag{23}$$

$$V^{s}_{j,unmxg} = \begin{cases} 0 & N_j = n \\ \sum_{i=N_j+1}^{n} V_{i,mix} [1 - f(j,i)]\ \beta_i & N_j \leq n-1 \end{cases} \tag{24}$$

The overall specific volume of mixture (V) is obtained by the optimization and porosity of mixture (p) gained by simple equation

$$V = \max(V^T_1, V^T_2, V^T_3, \ldots, V^T_j, \ldots, V^T_n) \tag{25}$$

$$p = 1 - \frac{1}{V} \tag{26}$$

3. Results and Discussions

3.1. Infiltration of Fine Sediments into Gravel-Bed

The infiltration processes of fine sediment into gravel-bed are numerically tested with different sizes of particles. The tests are based on Gibson's experiment [25]. Numerical simulations are carried out for a flume with a width of 0.15 m and a length of 0.5 m. The flume is filled with a granular bed of spherical gravels having different diameters with the same specific weight (2700 kg/m^3). We refer to fine sediment as sand. The simulations are carried out for a bed with uniform sand and gravel (Case 1) and a graded sand-gravel-bed (Case 2). The sediment bed layer is 0.1 m thick with the following characteristics (Table 1):

- Case-1: uniform gravel size D = 10 mm and uniform sand with a size d defined from the following size ratios: Critical ratio for tetrahedral packing d/D = 0.154; One and halftime of the critical ratio for tetrahedral packing d/D = 0.231; and, Critical ratio for cubical packing d/D = 0.414.
- Case-2: Multi size fractions of sand and gravel bed: Sand with a mean diameter of d_m = 0.26 mm and standard deviation of $\sigma^{(d)}$ = 1.94; and, Gravel with a mean diameter of D_m = 7.1 mm and a standard deviation of $\sigma^{(D)}$ = 1.35.

Case 2 is similar to the experiment No.2 conducted by Gibson [25] with very slow water flow. Hence, the effects of water flow on infiltration and packing processes can be neglected in the numerical model.

Table 1. Parameters for numerical simulation.

Density of Sphere (kg/m^3)	Density of Water (kg/m^3)	Young's Modulus (Pa)	Poisson Ratio	Friction Between Grains	Coefficient of Restitution
2700	1000	5.0×10^6	0.45	0.5	0.4

A DEM model is implemented to test the influence of the size ratio of the fine to coarse sediment on the vertical distribution of the bed materials. We develop the DEM model that is based on the open source package LIGGGHTS [36]. In the model, we neglect the interaction between the flows and the particles, because of low flow velocity. For that, non-slip boundary flow condition is applied for the simulations. The force acting on the particle consists of the gravity, Archimedes, and contact forces.

In Case 1, during the first 20,000 time steps, the gravel-bed was generated by random packing with porosity $p^{(D)}$ = 0.454. The fine sediment was fed over the bed surface from the 20,000th step. The simulation process was stopped when the void space in the bed surface has been clogged or the bed has been fulfilled with fine sediments. Figure 6 presents the structure of the gravel-bed, as well as the vertical distribution of fine sediments with three different sizes at the end of simulation time. The simulated results are qualitatively comparable to the experimental results that were conducted by [37,38] for the idealized packing of the purely bimodal bed sediments. For the case d/D = 0.154 (Figure 6a), it can be observed that the fine sediments mostly filled into the void space and were then trapped there. However, while increasing the size ratio to d/D = 0.231, the fine sediment infiltrated into only a part of the void space (Figure 6b). Figure 6c shows the results for the case d/D = 0.414, where the initial void space was smaller than the diameters of fine sediment. The fine sediment was trapped in the bed surface and could not move down into the gravel bed. As expected, the calculated results confirm that the size ratio has a significant effect on the infiltration process, as well as the vertical distribution of the fine sediments.

Further simulations were carried out for Case 2, with a median grain size of the non-uniform fine sediments d_m = 0.26 mm and standard deviation $\sigma^{(d)}$ = 1.94. The gravel mixture has a median grain size of D_m = 7.1 mm and the end of simulation time $\sigma^{(D)}$ =1.35. Random packing during the first 41,000 time steps with porosity $p^{(D)}$ = 0.407 generated the gravel-bed. The infiltration process was stopped when the top gravel layer has been filled. Figure 7a shows the bed materials along the flume centerline at the end of the simulation, where the gradation of saturated gravels with percolated fines can be seen. Furthermore, as the pores on the surface layer were filled with fine sediment, fine particles could not infiltrate through this layer and saturate the subsurface pore space. Figure 7b compares the mean values of the simulated fine fractions along the depth, with the observations that were conducted by Gibson et al. [25].

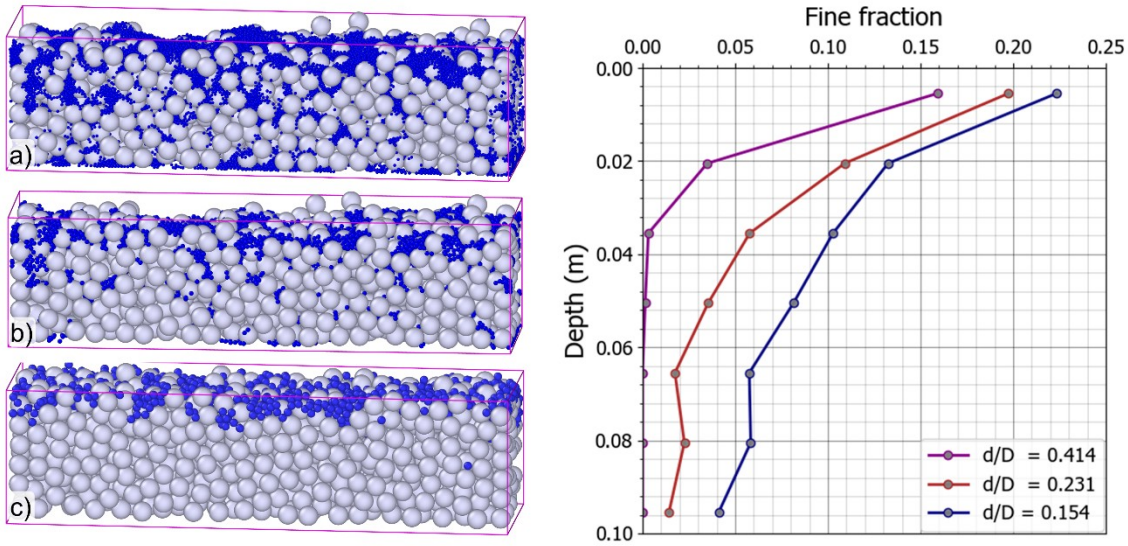

Figure 6. The structure of bed gravel and fine sediment distribution depends on the size ratio (d/D). **Left**: Fine sediments distribution at a cross-section along the channel at the final computational step with d/D = 0.154 (**a**), d/D = 0.231(**b**), and d/D = 0.414 (**c**); **Right**: Fine fraction variation in gravel depth with different size ratio.

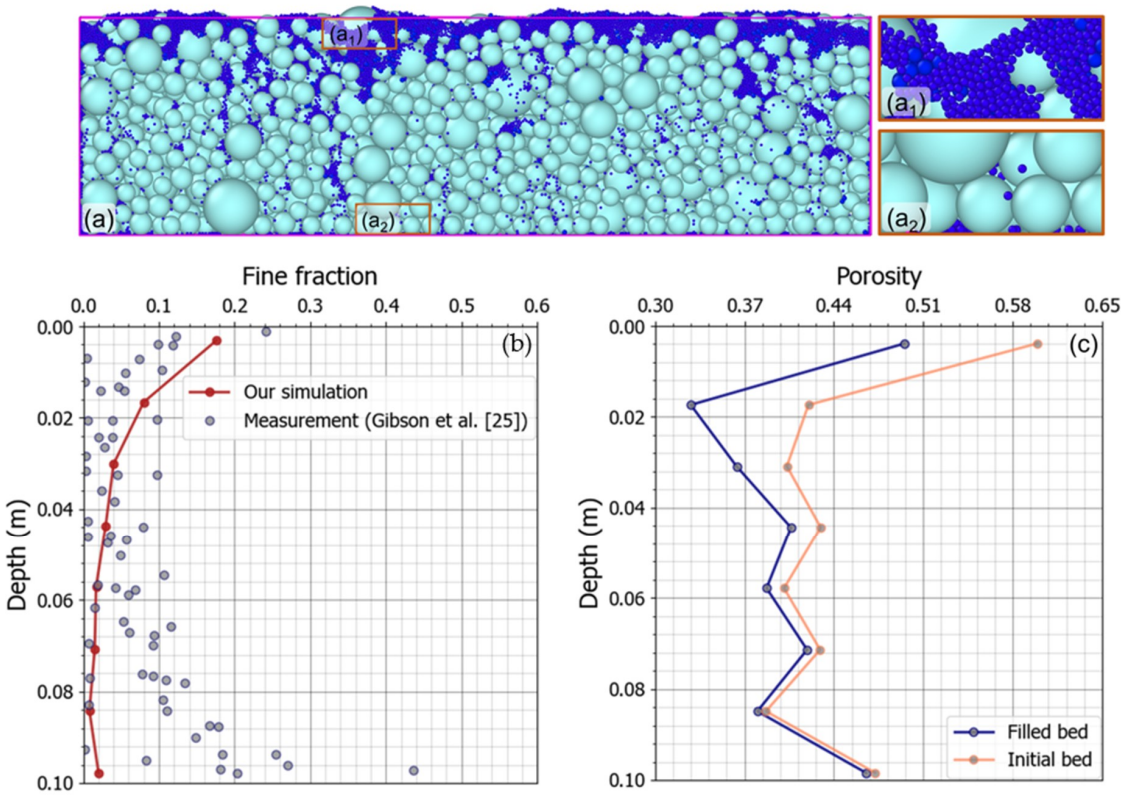

Figure 7. (**a**)—Structure of bed sediments at a cross-section along the channel at the final computational step (**b**)—Fine fraction distribution at the end of simulation; and, (**c**)—Bed porosity distribution along the depth at the beginning and the end of the computation time.

In the model, we used about 1150 coarse sediment particles for Case 1 and 3550 for Case 2. Depending on the grain size, three values of the number of the fine sediment particles (770, 6000, and 36,740) were implemented for Case 1. For Case 2, we used 113,770 fine particles. The computational

time that is required for Case 2 is about 4 h on a PC −3.9 GHz. The computational effort of study on large scale could be enormous and only completed successfully with extensive use of computer.

It needs to be emphasized that Gibson et al. [25] conducted the experiments in a large flume with a very low water velocity (no bed sediment transport), while due to high computational requirements, our DEM model only considered a small window (0.15 m wide and 0.5 m long) with quiescent water. It could be a reason of the differences between our results and measured data. However, it can be said that we obtained a qualitative good agreement with the experimental results. Figure 7c shows a variation of the calculated porosity along the depth at the beginning and the end of simulation time, which is correlated to the grain-size distribution.

3.2. Bed Form Movement and Porosity Variation

The simulation was conducted in a 500 m long straight channel with a rectangular cross section, a uniform specific water discharge of 23 $m^3/s/m$, a constant water elevation of 10 m long the channel, and the initial bed level defined, as follows:

$$z_b(x,0) = \begin{cases} \sin^2\left[\frac{\pi(x-200)}{100}\right] & 200 \le x \le 300 \\ 0 & \text{otherwise} \end{cases} \quad (27)$$

The bed mixture was sorted into two fractions (d_1 = 1 mm; d_2 = 7 mm), which was then used to compose a desired size gradation. The initial size fractions are ($\beta a_{,1}$ = 0.75 and $\beta a_{,2}$ = 0.25) in the active layer and ($\beta_{S,1}$ = 0.65 and $\beta_{S,2}$ = 0.35) in the stratum layer.

Figure 8 presents changes in bed characteristics over time. Figure 8a shows the bed elevation at different time steps, the dune moved forward with the water flow, and reduced its height. Especially, in the front of the dune, the gradient of sediment discharge is positive due to the increase in flow velocity, and this caused bed erosion. Inversely, sediment is deposited on the back of the dune, where the gradient of sediment discharge is negative. Figure 8c,d depict the size fraction of coarse and fine sediments along the channel. Since the fine sediment on the left side of the dune was eroded, transported by the increased water velocity, and deposited on the right side of dune due to the reduced water velocity. It led to an increasing in the coarse fraction on the left side of the dune and decreasing of the coarse fraction on the right side. An opposite picture was obtained for distibution of the fine fraction. Variation of the size fractions resulted in changing the bed porosity (Figure 8b). Porosity gets a minimal value of 0.2 on the right side of the dune at time 80,000 (s), where the coarse fraction is approximately 0.69 and the fine fraction about 0.31. Increasing the fine fraction from this value the bed porosity becomes larger. For the left side of the dune (coarse fraction > 0.73), growing the coarse fraction increases the bed porosity.

Figure 9 compares the new model with a conventional model (with a constant porosity). In the conventional model, a constant value of 0.25 for bed porosity was selected, while in the new model, it varied in a range from 0.21 to 0.28 due to size fraction change at the end of the calculation time. It can be seen that, due to the larger values of the calculated bed porosity on the left side of the dune, the predicted bed elevations were slightly higher than those that were obtained from the conventional model. An opposite picture can be seen on the right side of the dune. The new model provided a qualitatively good picture about the bed form movement and porosity variation in the channel.

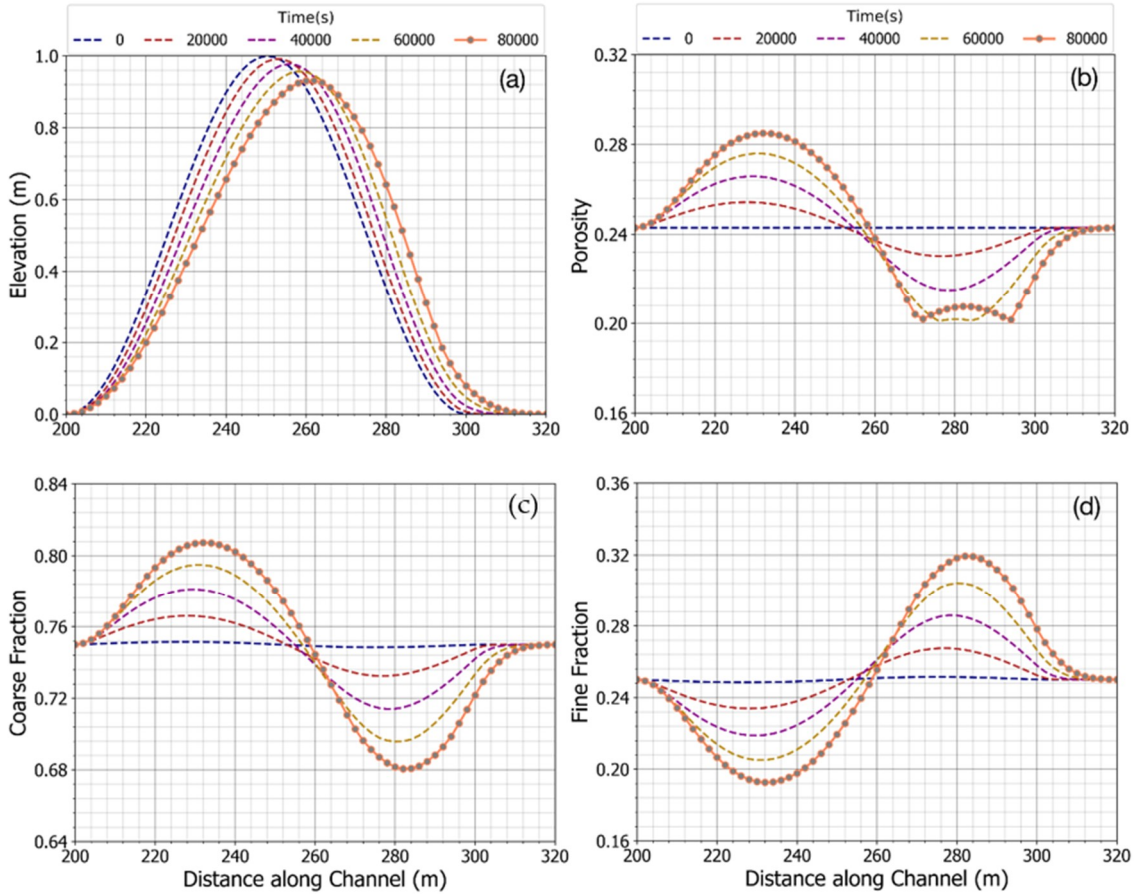

Figure 8. The performance of bed-porosity variation model in different times (**a**)—Bed elevation; (**b**)—Porosity of active-layer; (**c**)—Coarse size fraction of active-layer; and, (**d**)—Fine size fraction of active-layer.

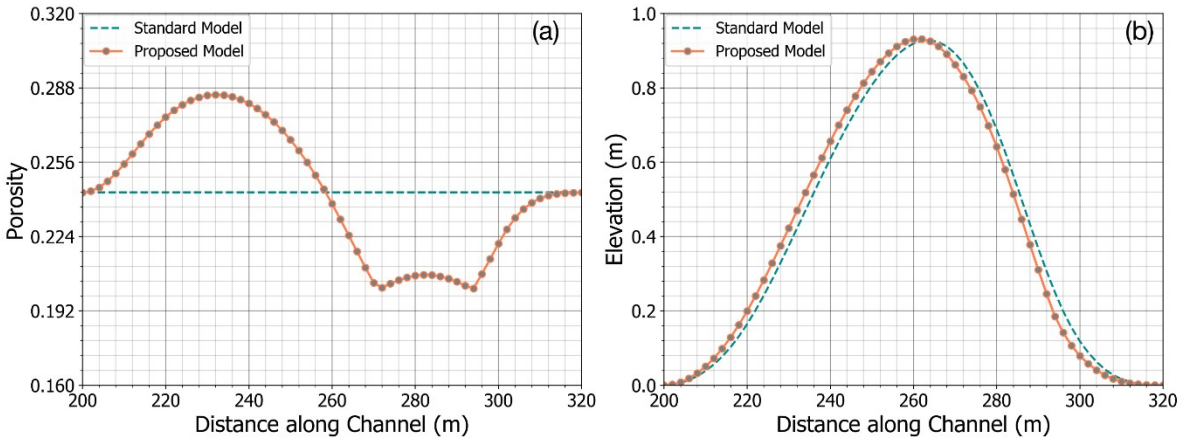

Figure 9. Comparison between the conventional model and the new model at the final time step (**a**)—Porosity of the active-layer; and, (**b**)—Bed elevation.

3.3. Sulaiman's Experiment

To identify the transformation processes of void structure in gravel bed, Sulaiman et al. [16] conducted experiments in a flume with a width of 0.40 m, a depth of 0.40 m, and a working length of 7.0 m (Figure 10). The slope of the flume was adjusted to 1/50. Water discharge was kept nearly constant for all of the runs and circulated. A sediment mixture was initially placed in the working section and then scraped flat. The thickness of the sediment layer was 5.3 cm. A weir with a height of

10 cm was placed at the end of the working section. The bed consisted of a coarse and fine fraction of sediments. The coarse fraction ranges from 4.75 mm to 26.5 mm in size with d_{50} = 15 mm, and the fine fraction ranges from 0.5 mm to 4.75 mm with d_0 = 2 mm. The sediments were mixed and then thoroughly homogenized. Experiments have been carried out for two situations. In Run-1, no sediment was supplied at the inlet; coarse sediment did not move actively, and only fine sediment was removed from the bed. In Run-2, an amount of the fine sediment fraction was continuously fed from the upstream of the flume, and these fine sediments could be deposited into the coarse bed or transported downstream. The condition of the riverbed at the end of Run-1 was used as an initial condition of Run-2. Cumulative time steps for Run-1 are 20, 65, 130, and 250 min and for Run-2 were 30, 50, 66, and 82 min. The total duration of Run-1 and Run-2 was 332 min. Table 2 summarizes the experimental conditions. Water depth h and velocity v are the initial average water depth and velocity in the uniform region. More details of the experiments description can be seen in [16].

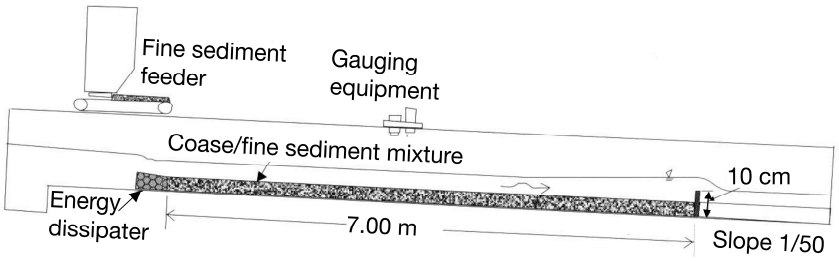

Figure 10. Schematic drawing of experimental channel and apparatus [16].

Table 2. Experimental conditions for two runs, where: q_w—water discharge; q_s—sediment discharge; Fr—Froude number; τ—non-dimensional bed shear stress [16].

Exp.	q_w (m^2/s)	$q_s \times 10^{-6}$ (m^2/s)	h (m)	v (m/s)	Fr	τ (Fine)	τ (Coarse)
Run-1	0.034	0	0.039	0.879	1.428	0.178	0.026
Run-2	0.034	31.8	0.045	0.754	1.133	0.203	0.030

Figure 11 shows the comparison of our results and Sulaiman's results for the erosion case (Run-1) and deposition case (Run-2) with regard to bed elevation, fine fraction, and porosity between, respectively. In Figure 11a, the results of our bed elevation with porosity variation are better than those in the constant models, because of the incorporation of porosity changes in our model. The erosion of the upstream part in our model is a good fit with the experimental result, while larger erosion of the upstream part of the constant model can be seen. The stored fine sediment in the pores of gravel-bed leaved the coarse layer increased the void space, but they did not contribute to lowering of the bed level. This result is consistent with the findings of [10]. Moreover, the storage capacity of the gravel-bed reached 30%, while fine sediment fraction was greater than the range of 31–37%. As a result, the bed elevation at the final step is lower than the initial elevation because of the erosion of fine sediment on the surface. Downstream, due to the bed load formula, the bed profile of our and Sulaiman's simulation are not good, which has not been developed for a mixture of two particle groups with very different grain sizes [39].

Figure 11b present bed elevation, fine fraction, and porosity to compare our results and Sulaiman's results for the deposition case (Run 2). The results of our bed elevation fit well when compared to the results that were derived from Sulaiman and constant models. However, the bed level differences in all models are small due to a hidden function in the bed load equation for fine sediment on the upper gravel-bed surface, and because bed shear stress is larger than the critical shear stress of most fine sediment. More detail about the comparison between the models can be seen in Table 3.

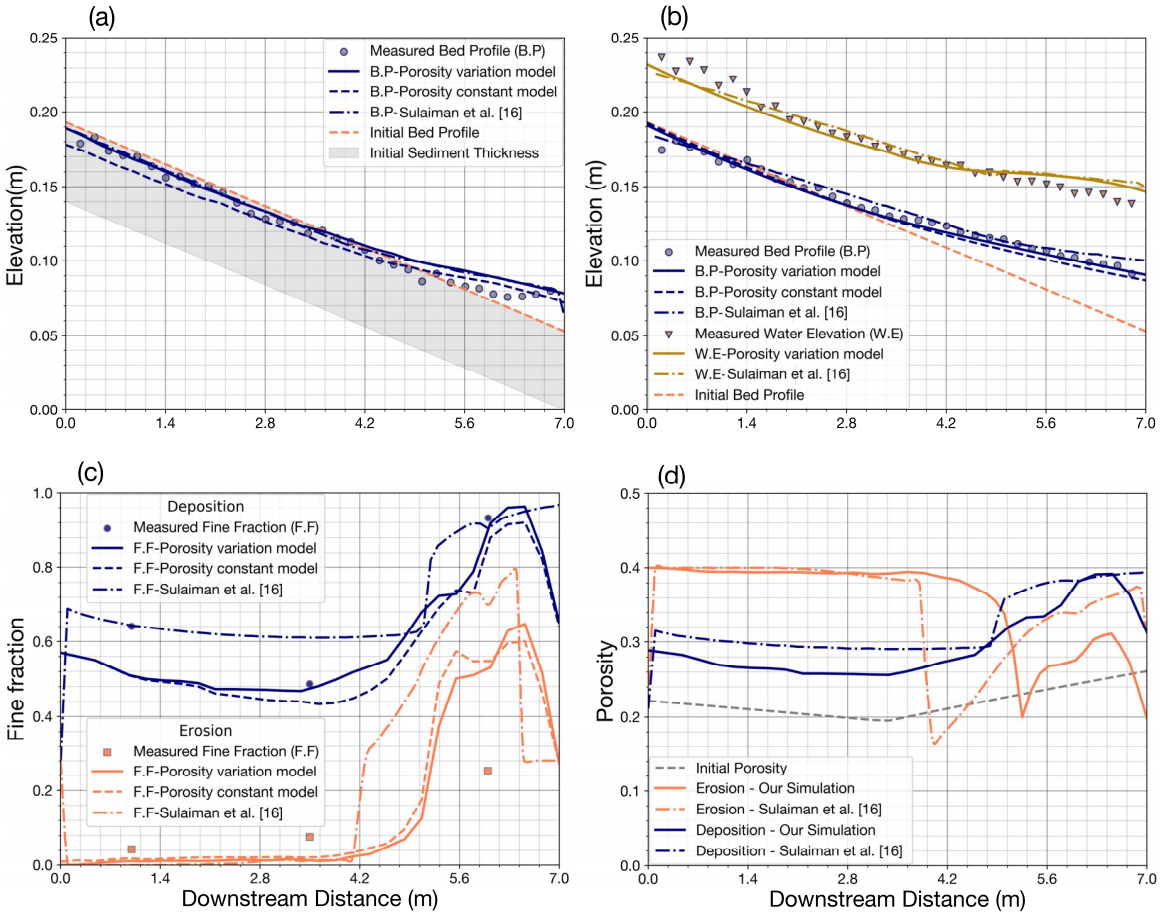

Figure 11. Bed variation for surface layer in comparison with observations from flume measurements [16]: (**a**) bed elevation—erosion case; (**b**) bed elevation—deposition case (**c**) Fine fraction variation in erosion and deposition cases; and, (**d**) Porosity variation in erosion and deposition cases.

Table 3. Statistical performances of bed variation model within surface layer.

	Erosion			**Deposition**		
	Variation	Constant	Sulaiman	Variation	Constant	Sulaiman
			Bed Elevation			
R	0.99510	0.99442	0.99412	0.99451	0.99538	0.99465
RMSE	0.00585	0.00631	0.00560	0.00347	0.00490	0.00414
MAE	0.00451	0.00546	0.00442	0.00275	0.00424	0.00343
			Fine Fraction			
R	0.98936	0.98953	0.99124	0.96269	0.98205	0.96953
RMSE	0.16423	0.17410	0.26149	0.07897	0.09265	0.07297
MAE	0.12371	0.12518	0.18397	0.05929	0.08579	0.05088

Grain size distribution (size fractions) due to sediment exchange in the bed surface layer was investigated for two cases, one for erosion and other for deposition. The calculated results were compared with the Sulaiman's and constant porosity models, as well as the observed data.

Figure 11c shows the fine fraction along the flume in these two cases. In the erosion case, fine sediment is removed from the bed material on the upstream part and it is deposited on the downstream part. The fine sediment fraction upstream is nearly zero and equal to 0.6 downstream (Figure 11c—coral color line). In the deposition case (navy color line), the supplied fine sediment completely filled the pore of the bed material increasing fine fraction to 0.6 upstream and 0.96 downstream. The results show that our model with variable porosity is slightly better than

the constant porosity model, because the fine fraction in our model tends to fluctuate widely when compared with those in the constant model. The results can be partly explained by considering the fine sediment that is stored in void spaces exchanged with sediment transport may lead to porosity changes. In Figure 11c—fine fraction for the deposition case—the results of Sulaiman are better than our results (navy color line), inversely our model performs better in the erosion case (coral color line). The slight difference in the fine fraction results between our porosity variation model and the Sulaiman porosity variation model and the minor variation in comparison with the porosity variation model and the constant model can also be seen in Table 3.

Figure 11d depicts the porosity due to sediment exchange on the surface layer in the cases of sediment erosion (coral color lines) and deposition (navy color lines). At the initial condition, the fine fraction upstream and downstream is from 37% to 22%, respectively, and the diameter ratio is d_{coarse}/d_{fine} = 7.5, the minimum porosity is equal to 0.195. At the end of the simulation, the fine sediment wholly filled in the void structure of gravel in the middle of the flume. In the erosion case, most of the fine particles are removed from gravel upstream (x = 4.2 m) and the porosity is reached the maximum value of 0.4. Afterward, the porosity decreased to a minimum value of 0.195 when the fine fraction increased from 0.22 to 0.30. In the deposition case, in contrast to the erosion case, the fine fraction is greater than 0.30, and the porosity is proportional to a fine fraction. The increase in porosity in the deposition case is less than that in the erosion case.

3.4. SAFL's Experiment

The SAFL (St. Anthony Falls Laboratory) downstream fining experiment is known as the most comprehensive set of experiments to date on gravel transport that have been performed at the St. Anthony Falls Laboratory in Minnesota by Parker and his co-workers [40–42]. The experiment was conducted in a 0.305-m wide and 50-m long flume with an initial concrete-bottom slope of 0.002 (Figure 12), a constant water discharge, and a constant sediment feed rate. The flume is ponded at its downstream reach by setting a constant water surface elevation at the downstream end, which drives channel aggradation and downstream fining. The relevant parameters for the run are given in Table 4. Seal et al. provide a full description of the experimental data [43].

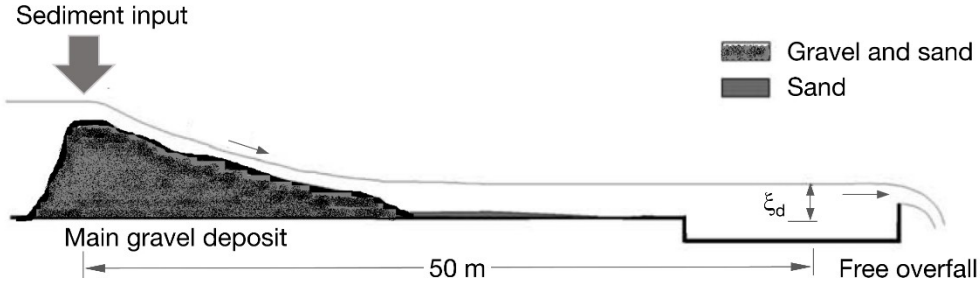

Figure 12. Flume set up for St. Anthony Falls Laboratory (SAFL) downstream fining experiments [15].

Table 4. Parameters for SAFL Downstream Fining Experiments; where: q_w—water discharge, q_s—sediment discharge, ξ_d—downstream water depth, S_0—flume slope, fs—sand fraction [15].

Exp.	q_w (m^2/s)	q_s (m^2/s)	ξ_d (m)	S_0 (%)	fs %	Time (h)
Run 1	0.163	2.37×10^{-4}	0.4	0.20	33	2, 8, 16.83

We simulated bed elevation, grain size distribution, and porosity in the surface layer and subsurface layer while considering the sediment exchange between these layers. A bed load equation that was developed by Wilcock & Crowe [22] was used to calculate sediment discharge for each size fraction. The thickness of the active layer is changing over time and space based on the multiplication of D_{90} and the coefficient of active layer thickness n_{active} = 2. The roughness height also varies over time and space, as defined by the product of D_{90} and roughness coefficient of n_k = 1.8.

Bed profile due to sediment transport and sediment exchange between the surface layer and subsurface layer is presented in Figure 13 for comparing with the experimental and simulation results of Cui et al. [15] (Figure 13a). The variable porosity model was also compared with our constant model (Figure 13b). It can be seen in Figure 13a,b that our results of bed profile that were obtained from both models agree well with the observations at 2 h (red line), 8 h (pink line), and 16.83 h (blue line) simulations. Since, in Cui's model, porosity was assumed as a constant of 0.3, we used this value for the initial condition in our simulations. The results in Figure 13a shows that our calculated bed profile has a higher correlation with the observations than Cui's bed profile, especially on the upstream part. The good agreement between our results and experiments suggests that the developed model with a constant porosity could be adequately satisfied for applying in this study case with low water discharge and week turbulent flow. Further, it can be seen in Figure 13b and Table 5 that the variable porosity model provides slightly better results than those in the constant porosity models. Generally, the bed profile that was obtained from the variable porosity model provides a slightly better agreement with the observation and lower values than those in the constant porosity model. This can be explained that porosity in the active layer and sub-layer tend to change in inverse directions. As a result, the total effect of porosity unsubstantially contributes to bed elevation. Figure 13c,d present the calculated fine fractions and bed porosities in the active and subsurface layers.

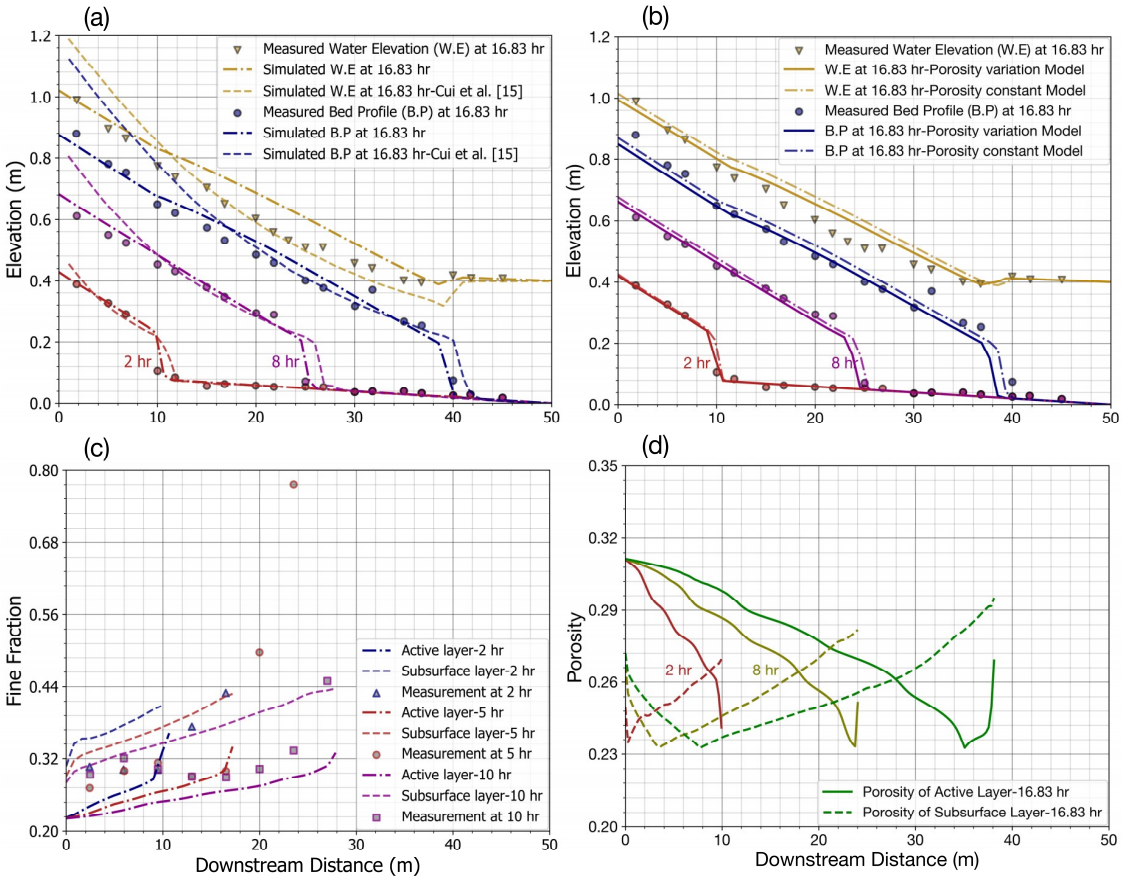

Figure 13. Simulated results in comparison with possible observations and Cui's study [15]: (**a**) bed and water elevations obtained from constant porosity model; (**b**) bed and water elevations obtained from both constant and variable porosity models; (**c**) Sand fraction obtained from variable porosity model; and, (**d**) Calculated porosity variation.

Table 5. Statistical performances of bed variation model in two layers.

	2 h			**8 h**			**16 h**		
	R	RMSE	MAE	R	RMSE	MAE	R	RMSE	MAE
Variation	0.987	0.019	0.010	0.998	0.016	0.013	0.989	0.033	0.027
Constant	0.980	0.023	0.011	0.996	0.024	0.018	0.988	0.034	0.032

Figure 13c shows the result of constant porosity model for the variation of the sand fraction in the surface layer and subsurface layer. The predicted results are compared with the results of the experiment and Cui simulations [15]. The simulated results of two layers for sand fraction variation are unable to be clearly compared with the result of one layer (total bed) of the Cui simulation and experiment. However, from the obtained results, we can realize that the trend of sand fraction variation in two-layer results is suitable with the variation of experimental results. The results of sand fraction variation that were obtained from the constant and variable porosity models will be compared with each other.

Figure 13c shows the fine fraction in the active layer and sublayer at 2 h, 5 h, and 10 h. Fine fraction, as calculated by the variable porosity model at different time experiments, is increased along with space (flume) and time. These results are suitable for the tendency of experiments with a lower value upstream and gradually increasing downstream. For example, the fine fraction is varied from 0.20 to 0.40 along the flume in the active layer and 0.30 to 0.44 in sublayer. The predicted results are also in line with the conclusions of previous studies [15,41]

Figure 13d shows the porosity change at different times of 2 h, 8 h, and 16.83 h for the active layer (solid line) and sub-layer (dash line). Porosity upstream on the surface layer is higher than those downstream, while porosity in the sub-layer tends to increase after reaching the minimum value of 0.24, which is correlated with the gravel fraction and fine fraction, is 0.69 and 0.31, respectively. The variation in porosity gravel-bed is significant, porosity in the active layer varies in range 0.24 to 0.31 and from 0.24 to 0.30 for sublayer.

The porosity of the active layer upstream is reaching its maximum value due to high velocity and gradually reducing because flow velocity decreased along the flume. However, a sudden reduction of velocity on the last part of downstream leads to a rapid increase in fine sediment. When a fine fraction is over the value of 0.31, then the porosity also rises from 0.24 to 0.27 in the active layer. In contrast to the active layer, porosity in sub-layer is not affected by flow velocity—high values of porosity on the upstream and downstream and reaching minimum value of 0.23, as described by the dash lines in Figure 13d.

4. Conclusions

A profound understanding of the phenomenon of natural sediment transport in the gravel-bed river is critical to river management and eco-hydraulics. Due to the complexity of the structure of the river bed and the mechanism of particles movements, most of conventional models simulate sediment transport and bed variation, but they are still limited by various assumptions. The proposed model in this study comes with bed porosity variability and takes the vertical fine sediment transport between multiple layers to assess bed elevation variations, disturbance, and grain sorting into account. In addition, we developed a new model for gravel-bed variation not only by adding a porosity to the Exner's equation but also by calculating size fraction on the surface layer and subsurface layer by taking into account the exchange rate of fine sediment, porosity variation in the multi-layer. Furthermore, the Discrete Element Method (DEM) was successfully applied to simulate infiltration processes of sediment particles into gravel-bed and effectively investigated the exchange of sediment between the surface layer and sub-layers, including grain size distribution and porosity changes. As a next step, the results that were obtained from the DEM model for different hydro-morphological conditions will be used with data-driven techniques (e.g., Artificial Neural Network) to improve the exchange rate function.

Our new bed variation model was verified by testing with the data from three cases, one numerical simulation, and two previous experiments. The results indicated that our model can be applied for simulating bed variations of both constant and variable porosity in gravel-bed rivers. The mode concept is testing and validated for other complicated flow conditions (2D and 3D) with bed-load and suspended-load transport. For this purpose, the new developed model is integrated into the TELEMAC-MASCARET system. Finally, the application of this model system will help stakeholders and managers to effectively maintain fine sediment that is stored in the river bed and to assess the effect of void spaces in gravel on living aquatic insects for eco-hydraulic management.

Author Contributions: V.H.B. designed the study, processed and analyzed the data, developed the models, interpreted the results and wrote the paper. The study has been carried out under the supervision of M.D.B. and P.R., who contributed to the model development stage with theoretical considerations and practical guidance, assisted in the interpretations and integration of the results and helped in preparation of this paper with proof reading and corrections.

Funding: This research was funded by the Vietnam International Education Development (VIED) Scholarship.

Acknowledgments: The contents of this paper are solely the liability of the authors and under no circumstances may be considered as a reflection of the position of the VIED Scholarship. The German Research Foundation (DFG) and the Technical University of Munich (TUM) supported this work in the framework of the Open Access Publishing Program. We much appreciate their help. Special thanks to TUM English Coaching Program for valuable supports and comments to improve this paper. We thank the editor and four anonymous reviewers for their constructive comments, which helped us to improve the manuscript.

Conflicts of Interest: The authors declare no potential conflict of interest.

References

1. Dietrich, W.E.; Kirchner, J.W.; Ikeda, H.; Iseya, F. Sediment supply and the development of the coarse surface layer in gravel-bedded rivers. *Nature* **1989**, *340*, 215. [CrossRef]
2. Wilcock, P.R.; DeTemple, B.T. Persistence of armor layers in gravel-bed streams. *Geophys. Res. Lett.* **2005**, *32*. [CrossRef]
3. Cui, Y.; Wooster, J.K.; Baker, P.F.; Dusterhoff, S.R.; Sklar, L.S.; Dietrich, W.E. Theory of fine sediment infiltration into immobile gravel bed. *J. Hydraul. Eng.-ASCE* **2008**, *134*, 1421–1429. [CrossRef]
4. Gibson, S.; Abraham, D.; Heath, R.; Schoellhamer, D. Bridging Process Threshold for Sediment Infiltrating into a Coarse Substrate. *J. Geotech. Geoenviron. Eng.* **2010**, *136*, 402–406. [CrossRef]
5. Schälchli, U. The clogging of coarse gravel river beds by fine sediment. *Hydrobiologia* **1992**, *235*, 189–197. [CrossRef]
6. Wu, F.-C.; Huang, H.-T. Hydraulic resistance induced by deposition of sediment in porous medium. *J. Hydraul. Eng.* **2000**, *126*, 547–551. [CrossRef]
7. Domenico, P.A.; Schwartz, F.W. *Physical and Chemical Hydrogeology*; Wiley: New York, NY, USA, 1998; Volume 506.
8. Selby, M.J.; Hodder, A.P.W. *Hillslope Materials and Processes*; Oxford University Press: Oxford, UK, 1993.
9. Frings, R.M.; Schuttrumpf, H.; Vollmer, S. Verification of porosity predictors for fluvial sand-gravel deposits. *Water Resour Res.* **2011**, 47. [CrossRef]
10. Frings, R.M.; Kleinhans, M.G.; Vollmer, S. Discriminating between pore-filling load and bed-structure load: A new porosity-based method, exemplified for the river Rhine. *Sedimentology* **2008**, *55*, 1571–1593. [CrossRef]
11. Verstraeten, G.; Poesen, J. Variability of dry sediment bulk density between and within retention ponds and its impact on the calculation of sediment yields. *Earth Surf. Process. Landf.* **2001**, *26*, 375–394. [CrossRef]
12. Wilcock, P.R. Two-fraction model of initial sediment motion in gravel-bed rivers. *Sciences* **1998**, *280*, 410–412. [CrossRef]
13. Gayraud, S.; Philippe, M. Influence of Bed-Sediment Features on the Interstitial Habitat Available for Macroinvertebrates in 15 French Streams. *Int. Rev. Hydrobiol.* **2003**, *88*, 77–93. [CrossRef]
14. Toro-Escobar, C.M.; Parker, G.; Paola, C. Transfer function for the deposition of poorly sorted gravel in response to streambed aggradation. *J. Hydraul. Res.* **1996**, *34*, 35–53. [CrossRef]
15. Cui, Y. The Unified Gravel-Sand (TUGS) Model: Simulating Sediment Transport and Gravel/Sand Grain Size Distributions in Gravel-Bedded Rivers. *Water Resour Res.* **2007**, *43*. [CrossRef]

16. Sulaiman, M.; Tsutsumi, D.; Fujita, M. Bed variation model considering porosity change in riverbed material. *J. Jpn. Soc. Eros. Control Eng.* **2007**, *60*, 11–18.
17. Parker, G. 1D Sediment Transport Morphodynamics with Applications to Rivers and Turbidity Currents. 2004. Available online: http://hydrolab.illinois.edu/people/parkerg/morphodynamics_e-book.htm (accessed on 14 January 2019).
18. Cui, Y.; Parker, G. A quasi-normal simulation of aggradation and downstream fining with shock fitting. *Int. J. Sediment Res.* **1997**, *12*, 68–82.
19. Chiu, Y.-J.; Lee, H.-Y.; Wang, T.-L.; Yu, J.; Lin, Y.-T.; Yuan, Y.J.W. Modeling Sediment Yields and Stream Stability Due to Sediment-Related Disaster in Shihmen Reservoir Watershed in Taiwan. *Water* **2019**, *11*, 332. [CrossRef]
20. Petti, M.; Bosa, S.; Pascolo, S.J.W. Lagoon sediment dynamics: A coupled model to study a medium-term silting of tidal channels. *Water* **2018**, *10*, 569. [CrossRef]
21. Bui, M.D.; Rutschmann, P. Numerical investigation of hydro-morphological changes due to training works in the Salzach River. In *River Flow 2012*; Taylor and Francis Group: London, UK, 2012; Volumes 1–2, pp. 589–594.
22. Wilcock, P.R.; Crowe, J.C. Surface-based transport model for mixed-size sediment. *J. Hydraul. Eng.* **2003**, *129*, 120–128. [CrossRef]
23. Leonardson, R. Exchange of Fine Sediments with Gravel Riverbeds. Ph.D. Thesis, University of California, Berkeley, CA, USA, 2010.
24. Wooster, J.K.; Dusterhoff, S.R.; Cui, Y.T.; Sklar, L.S.; Dietrich, W.E.; Malko, M. Sediment supply and relative size distribution effects on fine sediment infiltration into immobile gravels. *Water Resour. Res.* **2008**, *44*. [CrossRef]
25. Gibson, S.; Abraham, D.; Heath, R.; Schoellhamer, D. Vertical gradational variability of fines deposited in a gravel framework. *Sedimentology* **2009**, *56*, 661–676. [CrossRef]
26. Bui, M.D.; Rutschmann, P. Numerical modelling of non-equilibrium graded sediment transport in a curved open channel. *Comput. Geosci.* **2010**, *36*, 792–800. [CrossRef]
27. Cundall, P.A.; Strack, O.D. A discrete numerical model for granular assemblies. *Geotechnique* **1979**, *29*, 47–65. [CrossRef]
28. Johnson, K.L. *Contact Mechanics*; Cambridge University Press: Cambridge, UK, 1985.
29. Church, M. River bed gravels: Sampling and analysis. In *Sediment Transport in Gravel-Bed Rivers*; Wiley: Hoboken, NJ, USA, 1987; pp. 43–78.
30. Bui, M.D.; Bui, V.H.; Rutschmann, P. A new concept for modelling sediment transport in gravel bed rivers. In Proceedings of the 21st Vietnam Fluid Mechanics, Quynhon, Vietnam, 10–13 December 2018. (In Vietnamese)
31. Nunez-Gonzalez, F.; Martin-Vide, J.P.; Kleinhans, M.G. Porosity and size gradation of saturated gravel with percolated fines. *Sedimentology* **2016**, *63*, 1209–1232. [CrossRef]
32. Koltermann, C.E.; Gorelick, S.M. Fractional packing model for hydraulic conductivity derived from sediment mixtures. *Water Resour Res.* **1995**, *31*, 3283–3297. [CrossRef]
33. Kamann, P.J.; Ritzi, R.W.; Dominic, D.F.; Conrad, C.M. Porosity and permeability in sediment mixtures. *Groundwater* **2007**, *45*, 429–438. [CrossRef]
34. Yu, A.B.; Standish, N. Limitation of Proposed Mathematical-Models for the Porosity Estimation of Nonspherical Particle Mixtures. *Ind. Eng. Chem. Res.* **1993**, *32*, 2179–2182. [CrossRef]
35. Yu, A.B.; Standish, N. Estimation of the Porosity of Particle Mixtures by a Linear-Mixture Packing Model. *Ind. Eng. Chem. Res.* **1991**, *30*, 1372–1385. [CrossRef]
36. Zhang, H.; Makse, H. Jamming transition in emulsions and granular materials. *Phys. Rev. E.* **2005**, *72*, 011301. [CrossRef]
37. Kenney, T.; Chahal, R.; Chiu, E.; Ofoegbu, G.; Omange, G.; Ume, C. Controlling constriction sizes of granular filters. *Can. Geotech. J.* **1985**, *22*, 32–43. [CrossRef]
38. Indraratna, B.; Locke, M. Design methods for granular filters—Critical review. *Proc. Inst. Civ. Eng. -Geotech. Eng.* **1999**, *137*, 137–147. [CrossRef]
39. Sulaiman, M.; Tsutsumi, D.; Fujita, M. Porosity of sediment mixtures with different type of grain size distribution. *Annu. J. Hydraul. Eng.* **2007**, *51*, 133–138. [CrossRef]
40. Paola, C.; Parker, G.; Seal, R.; Sinha, S.K.; Southard, J.B.; Wilcock, P.R. Downstream fining by selective deposition in a laboratory flume. *Science* **1992**, *258*, 1757–1760. [CrossRef]

41. Toro-Escobar, C.M.; Paola, C.; Parker, G.; Wilcock, P.R.; Southard, J.B. Experiments on downstream fining of gravel. II: Wide and sandy runs. *J. Hydraul. Eng.* **2000**, *126*, 198–208. [CrossRef]
42. Seal, R.; Paola, C.; Parker, G.; Southard, J.B.; Wilcock, P.R. Experiments on downstream fining of gravel: I. Narrow-channel runs. *J. Hydraul. Eng.* **1997**, *123*, 874–884. [CrossRef]
43. Seal, R.; Parker, G.; Paola, C.; Mullenbach, B. *Laboratory Experiments on Downstream Fining of Gravel, Narrow Channel Runs 1 through 3: Supplemental Methods and Data*; External Memorandum M-239; St. Anthony Fall Anthony Falls Hydraulic Laboratory, University of Minnesota: Minneapolis, MN, USA, 1995.

4. DIVERSE ANWENDUNGEN

4.1. Sedimentmanagement bei Stauanlagen

Ein Flussdamm wird für die Erzeugung von elektrischer Energie, die Wasserversorgung und die Entwicklung der Landwirtschaft errichtet. Jedoch unterbricht die Dammkonstruktion die Längskontinuität des Fluss- und Sedimenttransports im Flusssystem. Vor dem Damm können große Teile der Geschiebe und Teil der Schwebstoffe abgelagert werden. Die schnelle Sedimentation des Stauraums verringert die Speicherkapazität. Um die Sedimentation des Speichers zu entfernen und zu reduzieren, werden verschiedene technische Ansätze entwickelt.

Da die grundsätzliche Verlandungsproblematik vor allem auf die stark reduzierten Fließgeschwindigkeiten im Stauraum zurückzuführen ist, wird i.d.R. versucht, mit Hilfe von Regelungsbauwerken (Buhnen, Längswerke, Kolkverbau, Schwellen, etc.) die lokale Strömung derart zu beeinflussen, dass lokal ein morphodynamischer Gleichgewichtszustand erzielt werden kann. Dabei nehmen die Bauwerke über die Veränderung der Strömung unmittelbar Einfluss auf die transportierte Geschiebefracht, die Sohltopografie und die Sohlrauheit.

Eine bewährte Methode um abgelagertes Material aus einem Stauraum herauszubekommen, ist die Anwendung von gesteuerten Spülvorgängen. Hierbei werden, für eine gewisse Zeit, Verschlüsse des absperrenden/aufstauenden Bauwerks geöffnet, was eine deutliche Steigerung der Fließgeschwindigkeit bewirkt. Werden die Spülvorgänge zeitlich mit einem Hochwasserereignis zusammengelegt, lässt sich Strömung noch weiter beschleunigen. Unter anderem wird das Spülen als der einzige wirtschaftliche Ansatz angesehen, um die Speicherkapazität des Reservoirs bei starker Ablagerung schnell wiederherzustellen.

Im Folgenden sind zwei Artikeln zusammengefasst:

1. Bui, M.D.; P. Rutschmann (2012): “Numerical investigation of hydro-morphological changes due to training works in the Salzach River”; Proc. of River-Flow-2012, San Jose, Costa Rica.
2. Bui, M.D.; P. Rutschmann (2013): “Assessment of Sedimentation and Flushing Efficiency for Kajbar Hydropower Project in the Nile River”; Proc. of the 35th IAHR World Congress, Chengdu, China.

Ziel beider Studien war es, numerischen Modelle zu entwickeln, die hydro-morphologische Veränderung prognostizieren und ingenieurtechnische Konzepte für Sedimentmanagement in Stauraum optimieren.

Numerical investigation of hydro-morphological changes due to training works in the Salzach River

M. D. Bui & P. Rutschmann
Institute of Hydraulic and Water Resources Engineering, Technische Universität München, Germany

ABSTRACT: This paper presents results of a 2D numerical model for long-term hydro-morphological simulation in a stretch of the Salzach River upstream of the hydroelectric power plant Hallein. The numerical model was calibrated using results of other models for the actual conditions and then applied for simulation of flow and sediment transport in the reach with alternative structures. The purpose of modeling study is to provide hydraulic and sediment parameters for structure design and evaluate the impact of various design alternatives on flow and sediment transport in the reach.

1 INTRODUCTION

The Salzach has its source at an altitude of 2,300m in the Kitzbüheler Alps. After flowing downhill for some 226km it converges with the River Inn near Braunau. The Salzach flows in a west-east direction from its headwater region down to Schwarzach, where it changes its course northwards. In the section from Bergheim to Braunau, the river marks the Austrian border with Germany. Man-made structures in the Salzach River and adjacent flood plain produced feedback on the hydro-morphological characteristics of the river regime. The Salzach has lost most of its former typical characteristics of a mountain river. Ever since the 15th century, human settlements and the construction of roads, railways and other infrastructure have required ongoing regulation measures. With the aim of protecting against floods, the Salzach's riverbed has gradually been straightened and its banks have been secured by massive hydraulic engineering structures. In the river stretch upstream of the hydroelectric power plant Hallein there is a dramatic problem with sediment deposition. Among the negative effects, the bed variation can be one of the possible causes of flood disasters along the river. Currently, the town Hallein is not protected against a 100-year flood sufficiently. Bed load aggradations upstream of the hydroelectric power plant Hallein deteriorate the danger of flooding. Some proposals focus on improving the bed load transport through the hydropower plant and the flood protection for Hallein. Beside the technical aspects regarding economy, engineers responsible for the design of such measures have to quantify the impact on river regime. Hydro-morphological investigations in the river reach are required in order to be able to choose an optimal solution for planners.

The depth-averaged model FAST2D using a finite-volume method with boundary-fitted grids has been developed and applied to simulate morphological processes in alluvial open channels. The numerical model consists of three basic modules: a hydrodynamic module describing the depth-averaged flow and the water surface elevation, a sediment transport module, and a sediment balance module providing the sedimentation and erosion rate and the bed level deformation. The secondary flow transport effects are taken into account by adjusting the dimensionless diffusivity coefficient in the depth-averaged version of the k-ε turbulence model. The numerical model has been developed, tested and validated previously by computing various flow situations in laboratory channels and natural rivers. This paper presents the results of the model for long-term hydro-morphological simulation in this river reach.

The purpose of modeling study presented in this paper is to provide hydraulic and sediment parameters for structure design and evaluate the impact of various design alternatives on flow and sediment transport in the reach. The numerical model is firstly calibrated using calculated results of other models for the actual conditions and then applies for simulation of flow and sediment transport in the reach with alternative structures.

2 MODEL SYSTEM

2.1 *Flow field*

In the model the velocity field and water surface elevation are calculated from the two-dimensional shallow water equations, including the effects of bottom friction and turbulence.

The bed shear stresses are determined by the quadratic friction law. The turbulent stress terms, which are usually important in rivers with complex geometry, are calculated with the aid of the depth-averaged k-ε turbulence model. In this model the dimensionless diffusivity is an adjustable empirical parameter which may be measured from dye-spreading experiments. The dispersion terms arise from splitting local quantities into depth-averaged values and deviations from these and then carrying out the depth-averaging of the equations. The physical meaning of the dispersion terms is similar to that of turbulent stresses as both represent gradients of the transport of momentum. It was pointed out in previous studies that the dispersion terms can be of greater significance in depth-averaged calculations when secondary flows are present. The importance of these terms and of the turbulent stresses may be quantitatively of the same order. In a 2D depth-averaged model the effects of the secondary motion can be accounted for indirectly by increasing the coefficient of exchange of momentum in the horizontal direction, i.e. the effective eddy viscosity. In the depth-averaged k-ε turbulence model used here this is achieved by increasing the dimensionless diffusivity coefficient e_*. The value of e_* is problem dependent and must in general be adjusted to the turbulent flow calculated (see Bui, 1998).

2.2 *Sediment transport and bed change*

In rivers with graded sediments, the transport rate of the coarse size-fractions may be different from the transport rate of the fine size-fractions and consequently the total transport rates of all grain sizes may differ. Depending on the hydraulic parameters, the incoming sediment distribution, and the bed composition, some particle sizes may be eroded, while others may be deposited or may be immovable. Consequently, several different processes may take place. For example, all the finer particles may be eroded, leaving a layer of coarser particles for which there is no carrying capacity and consequently no more erosion may occur. The bed is said to be armoured.

In order to account for these effects, the so-called size-fraction method can be used in a numerical morphological model. Here the bed material is divided into a number of size-fractions, each characterised by a certain diameter and by a volume percentage of occurrence in the bed material (probability). For graded bed material the sediment-transport rates depend on the bed-material composition, which itself depends on the history of erosion and deposition rates. Changes in the bed composition are not only restricted to a layer that is exposed to the flow, but a finer sub-layer also forms under the coarser surface layer. To reproduce these features, a multi-layer model is proposed, where the bed is divided into an active layer and several substrate layers. Sediment particles are continuously exchanged between flow and the active layer. They are exchanged between the active layer and substrate when the bed scours or fills. As erosion occurs, entrainment of sediment particles from the active layer and its ensuing downward displacement causes particles from substrate layers to be mixed with those in the active layer. On the contrary, deposition of sediment particles on the bed leads to an upward displacement of the active layer and the initiation of new substrate layers. Furthermore, in the processes of graded sediment movement, the coarser particles on the bed have a higher chance of exposure to the flow. The situation is reversed for the fine particles on the bed due to the fact that they are more likely to be sheltered by coarse particles. This effect (called hiding/exposure effect) results in a smaller critical bed shear stress for larger grains and a higher critical bed shear stress for smaller grains.

Most of the studies on graded sediment transport have been based on introducing some kind of correction factors to account for this effect and used these factors to modify the existing formulas of uniform sediment transport. In this paper the bed load capacity for a particular fraction is computed by using the theoretical bed load function of Meyer-Peter and Müller (1948) with some modifications by introducing different hiding/exposure factors, namely Egiazaroff (1965), Ashida and Michiue (1971), Karim et al. (1992), and Wu et al. (2000), accounting for the reduction or increase of the transport rate of a particular size fraction (see Bui, et al., 2006; and Wu, 2007):

$$Q_{b,j} = \beta_j 8 \left[\left(\frac{C}{C_{90}} \right)^{3/2} \zeta_{1j} \theta_j - \zeta_{2j} \theta_{cr} \right]^{3/2} \left(\Delta g d_j^{\,3} \right)^{-1/2} \qquad (1)$$

$$\theta_{cr} = 0.047$$

in which β_j = active-layer size fraction j; (ζ_{1j},ζ_{2j}) = hiding/exposure factors; C = Chézy value; C_{90} = grain related Chézy value; θ_j = fractional Shields parameter; θ_{cr} = critical Shields value; Δ = relative density; d_M = mean grain size of active-layer; and d_j = fractional grain size.

The bed-shear driven bed-load transport is in the direction of the bed shear stress and this coincides with the direction of the velocity near the bed.

Unfortunately, this direction is generally not always identical to that of the depth-average velocity, as assumed in some models. In the present model, the effects of non-equilibrium and bed slope on the bed-load transport are also taken into account (see Bui et al., 2004).

The active-layer can be reduced into finite elemental volumes of thickness E_m. The mass conservation for a size class j of particles in the active-layer volume is then:

$$(1-P)\frac{\partial(\beta_j E_m)}{\partial t} - (1-P)\frac{\partial Z_{b,j}}{\partial t} - S_{F,j} = 0 \qquad (2)$$

where P = porosity of the bed material; $(\partial Z_{b,j}/\partial t)$ = bed change due to the j-th fraction of sediment; $S_{F,j}$ = active-layer floor source term, which represents the exchange of sediment particles between the active-layer and the active-stratum control volumes.

The mass of a particular size class j in the active-stratum control volume changes only due to active-layer movement, i.e. due to exchange of material between the active-layer and active-stratum, while the active-stratum floor elevation remains unchanged. This is expressed by a mass conservation equation for a particular size class in the active-stratum control volume:

$$(1-P)\frac{\partial[\beta_{s,j}(Z_b - E_m)]}{\partial t} + S_{F,j} = 0 \qquad (3)$$

where $\beta_{s,j}$ = active-stratum size fraction j; Z_b = bed elevation. The active-layer thickness E_m is evaluated by an appropriate empirical concept of the depth of bed material which supplies material for bed load transport and suspended-sediment entrainment. Usually E_m is related to the flow and sediment conditions, as well as the instantaneous bed deformation. Throughout the last decades many new formulas to calculate E_m have been proposed. However, all were derived in a different way and no definition for E_m based on physical processes in this layer has been given. In the paper, E_m is assumed to be constant with time and position.

The bed deformation due to the j-th fraction of sediment $(\partial Z_{b,j}/\partial t)$ is calculated from the mass balance equation. The total bed change $(\partial Z_b/\partial t)$ is then determined by:

$$\frac{\partial Z_b}{\partial t} = -\frac{1}{(1-P)}\sum_{j=1}^{N}\left(\nabla.\vec{Q}_{b,j} + S_{E,j} - S_{D,j}\right) \qquad (4)$$

where $\vec{Q}_{b,i}$ = fractional bed load flux; $S_{E,j}$=fractional erosion rate; $S_{D,j}$=fractional deposition rate. These erosion and deposition rates are defined based on the equilibrium concentrations for suspended sediment near the bed and their depth averaged values.

2.3 *Numerical solution procedure*

The governing differential equations for 2D depth-averaged flow and sediment transport is written in common tensor notation in a curvilinear coordinate system and solved numerically with the computer code FAST2D.

In this code, the equations are discretized in the computational domain using the finite volume technique with a curvilinear non-orthogonal grid and a non-staggered variable arrangement. The central / upwind hybrid differencing scheme is employed in treating the convective and diffusive fluxes. In order to avoid checkerboard splitting for cell-centered arrangement, the momentum interpolation technique is used for evaluating cell face variables from centered quantities. The momentum equations coupled with transport equations for turbulence quantities are solved by an implicit finite volume procedure. The pressure or water depth, however, is not directly computed from the original continuity equation but with a pressure correction equation. For sediment transport calculation the finite volume procedure is also implemented. The bed level changes are computed using a predictor-corrector scheme. More details on the numerical solution can be obtained from Bui (1998).

3 MODEL SET UP

The investigated domain is 2.45km (Fig.1). For the discretization a curvilinear non-orthogonal grid with 70 points in the lateral and 380 points in the streamwise direction was used. The appropriately defined grid with smallest spacing between adjacent node points of 0.5m in the lateral and 1.0m in the streamwise direction accounts for regions of high gradients and conforms to the geometry of the island and the constructional measures.

For the morphological computation, as initial conditions, detailed information on the geometry and bed level in the area under consideration at an initial state and the roughness of the bed and also sediment properties (grain size distribution and bed porosity) in the whole area are required. In the study, the bottom elevation at the initial state at each grid point was interpolated from a DTM-data-set provided by the *hydro*consult GmbH.

Bed-sediment size distributions along this stretch are based on the measurements at several cross sections shown in Fig. 2 (Sackl, 2008). 10 grain classes (from very fine sand to very coarse gravel) with different average size-fractions are used in the numerical model as initial bed sediment mixture.

Figure 1: Calculation domain

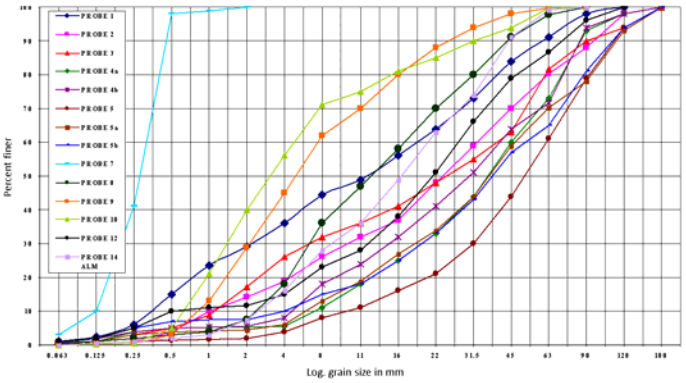

Figure 2: Measured distributions of bed grain sizes

As boundary condition upstream, an inflow hydrograph of discharges is specified, while at the downstream boundary a stage-discharge relationship is given. At the downstream boundary the zero-gradient condition is applied, while at the other boundaries the bed-load transport for equilibrium conditions is used.

4 CALCULATION RESULTS

The model was validated first by calculating the flow with a fixed bed. The results were compared with other models. As calibration parameters of the flow model, the bed roughness (k_{st}) and the dimensionless diffusivity coefficient (e_*) were adjusted until an acceptable agreement between our calculated results and that of others was obtained. The computations were carried out for a flooding event with constant discharge of 1690 m^3/s. The boundary conditions were defined as being constant with time. A fixed water elevation of 440.18 m above datum at the downstream boundary and an unchanged discharge at the upstream boundary of the computation domain were specified. Effects of constructional measures on the flow were taken into account by increasing k_{st} and e_* coefficients in these areas. The comparison of the predicted water levels at some cross sections along the river reach using the FAST2D and HYDRO_AS codes as well as data measurements in the physical model is shown exemplarily in Fig.3. A fairly good agreement between these predictions was obtained. The calibrated bed roughness factors according to Manning-Strickler were 20.0 $m^{1/3}/s$ (for bridge-pier and weir regions) and 28.0 $m^{1/3}/s$ (for the rest region). The calibrated dimensionless diffusivity coefficients wre 4.5 and 1.8 respectively.

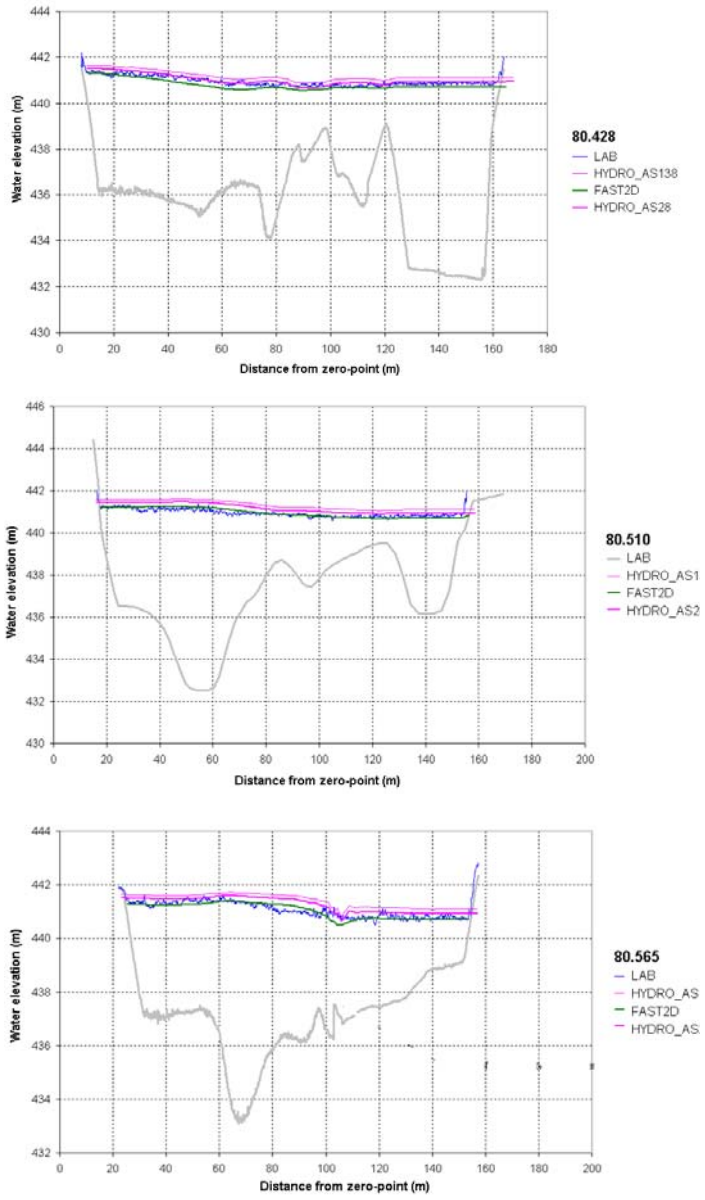

Figure 3: Water elevation at different cross sections

Observed data of the bed level at several cross sections at different times were used to calibrate the sediment transport calculations. The numerical morphological model was calibrated by comparing observed and computed results and adjusting the empirical coefficients appearing in the various empirical relations employed. Parameters influencing the transport processes the most are the hiding/expose factor and active-layer-thickness. The variation of these parameters needed numerous simulations to determine the best fitting parameter set.

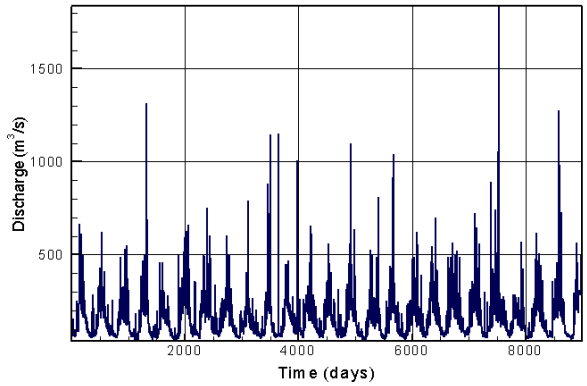

Figure 4: Time series of water discharge at the inlet

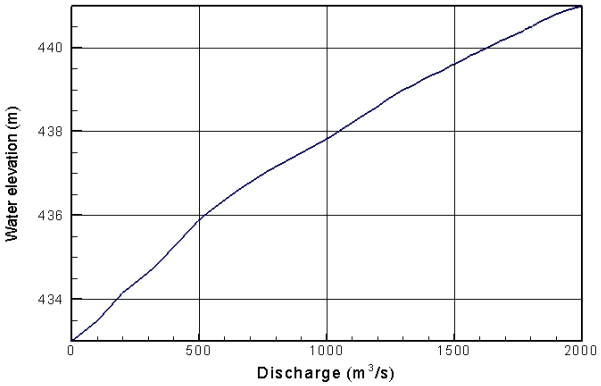

Figure 5: Rating curve at the outlet

Long-term morphological calculations were done for the time period 1981-2005 using different values of active-layer-thickness and different hiding/expose functions mentioned above. Figs. 4 and 5 show the time series of flow discharge and rating curve applied as hydraulic boundary conditions. By estimating the calculated results with a trial and error procedure, a value of E_m=5 cm for active-layer-thickness and Wu's hiding/exposure factor were chosen. Applying these model parameters, a satisfactory agreement between predicted bed changes and observations is achieved. Fig. 6 shows exemplarily bed elevation changes of cross sections 80.99 and 81.49 after 17 and 20 years.

Fig. 7 shows the bed change after 25 years simulation. Due to non-uniform sediment transport load rates, residual deposition and erosion occurred in the upper part of the study domain. The river constriction caused by bridge piers results in a general increase in the flow velocities beside it. In cross-stream and main-flow directions the calculated bed load changed consequently with the varying of flow velocities and bed shear stresses. Erosion occurred at channel constrictions followed by deposition just downstream. This was also observed in this river stretch especially under flood-flow conditions. Along the Small-Salzach, reducing water discharge resulted in the sedimentation at certain locations, especially at the entrance of this branch, and as a consequence may effect flood protection. In the lower part, water depth raised and flow velocity gradually reduced. As a result, more sediment was deposited. This points out also that the river reach continues to erode if no measures are performed.

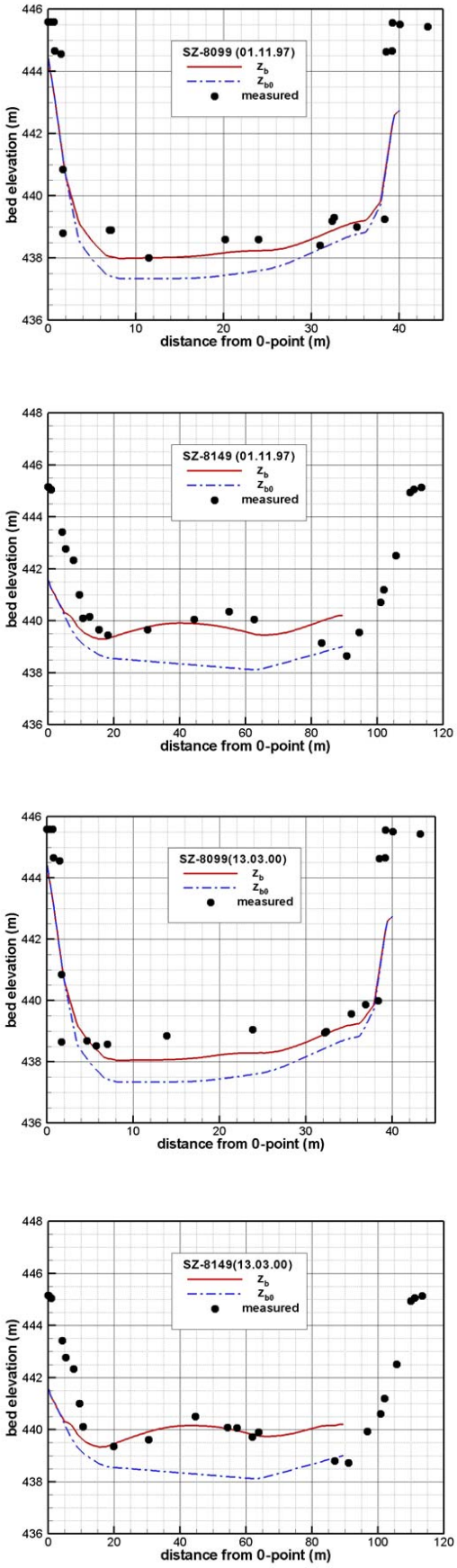

Figure 6: Bed elevations at different cross sections

One possible attempt to reduce deposition in the river reach is to raise the amount of sediment transported through the lower part by changing operating conditions and introducing some constructions in the reach and/ or to operate a sediment flushing facility.

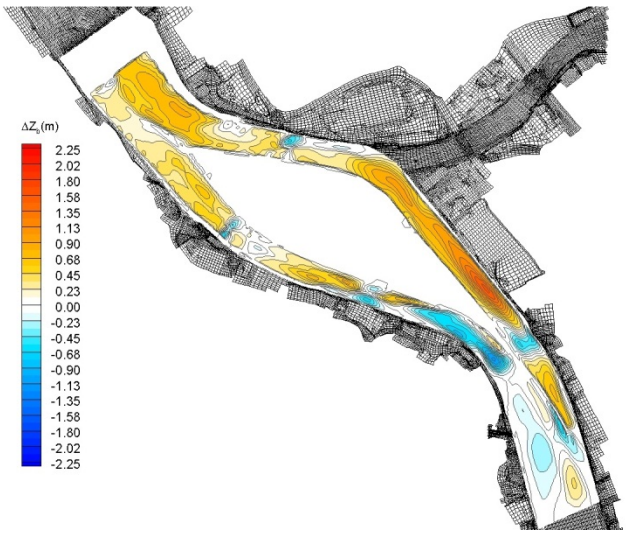

Figure 7: Calculated bed change for present river geometry

Using the calibrated model parameters mentioned above, further morphological calculations were done for several river geometries with proposed constructional measures. By introducing impermeable structures (within the river and/or at some locations along the banks of the lower part of the river reach) and lowering the bed elevation through the weirs, we can control the direction, velocity, or depth of flowing water. Fig. 8 presents the calculated bed deformation rates after 25 years simulation for three proposed projects. The effect of variations of the geometry is shown and compared in this figure illustrating that reduction of sediment deposition in the domain is possible. Variant number 3 provided the best solution to reduce long term sedimentation in the area by increasing the transport capacity of the lower reach and also of the Small-Salzach branch. In this case, the maximal deposited bed elevation value after 25 years simulation amounts to 0.72 m downstream and 0.25 m at the entrance of the Small-Salzach branch. the active-layer-thickness must be considered in the model calibration.

5 CONCLUSIONS

A 2D morphological model has been applied to simulate hydromorphological processes in the Salzach River. The secondary flow transport effects were taken into account by adjusting the dimensionless diffusivity coefficient in the depth-averaged version of the k-ε turbulence model. A multiple layer model was used to simulate bed composition changes. The influence of grain-size distribution on the bed-load, the bed development and consequently also the flow field was taken into account.

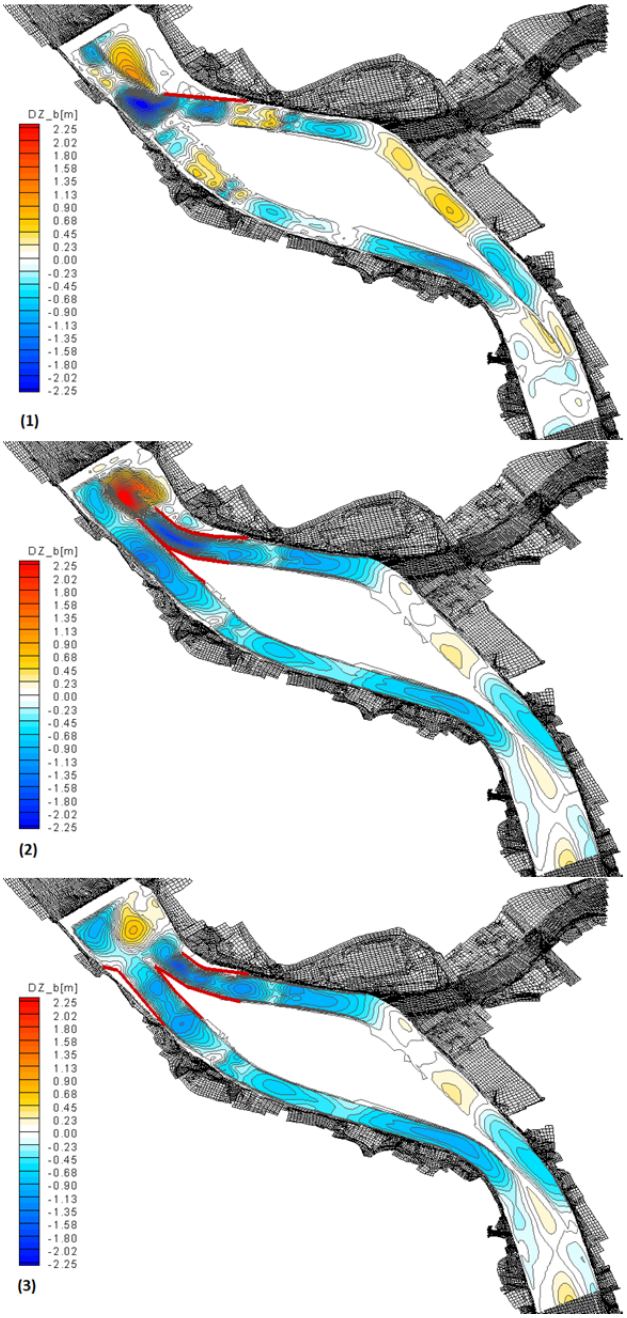

Figure 8: Calculated bed change for project river geometries

After calibration of some coefficients, the numerical model reproduced reasonably well the flow in a flood situation. The morphologic computational results reproduced expected trends in the river morphology. Different constructional measures and their long term effects on sediment transport and river morphology in the river reach were studied by means of numerical simulation. It can be shown that actions are essential to reduce the deposition processes which were evoked by

corrections of the river geometry with the construction of flow control measures in the lower part of the river reach. This possible solution can increase the sediment transport load through the hydropower plant and reduce the deposition in the river reach as well as simultaneously prevent the town from the danger of flooding.

ACKNOWLEDGEMENTS

The authors would like to express their gratitude to Prof. W. Rodi, Institute for Hydromechanics, University of Karlsruhe, for placing the FAST2D code at our disposal. The authors would like to thank Dr. B. Sackl, HydroConsult GmbH, Graz, for providing the data related to the model. The calculations have been carried out at the Institute of Water Engineering and Water Resources, Technische Universität München.

REFERENCES

Bui, M. D. 1998. Berechnung der Strömung und des Sedimenttransports in Flussläufen mit einem tiefengemittelten numerischen Verfahren. *Dissertation, Institut für Hydromechanik, Universität Karlsruhe.*

Bui, M. D., Wenka, T., Rodi, W. 2004. Numerical Modelling of Bed Deformation in Laboratory Channels. *Journal of Hydraulic Engineering, ASCE*, Vol.130, No.9.

Bui, M. D. & Rutschmann, P. 2006. A 3D Numerical Model of Graded Sediment Transport in Nonequilibrium Condition. *Proc. of the ICHE, Philadelphia.*

Meyer-Peter, E., Müller, R. 1948. Formulas for Bed-Load Transport. *IAHR, 2nd Meeting, Stockholm.*

Sackl, B. 2008. Geschiebehydraulische Untersuchung KW Sohlstufe Hallein bis KW Gamp km 80.34 bis 82.74, *Technischer Bericht 04.2008,* Hydroconsult GmBH, Graz.

Wu, W. 2007. *Computational River Dynamics.* Taylor & Francis.

Assessment of Sedimentation and Flushing Efficiency for Kajbar Hydropower Project in the Nile River

Minh Duc Bui
Research Coordinator, Institute of Hydraulic and Water Resources Engineering, TechnischeUniversitätMünchen,Arcisstr. 21, D-80333 München, Germany. Email: bui@tum.de

Peter Rutschmann
Professor, Institute of Hydraulic and Water Resources Engineering, TechnischeUniversitätMünchen,Arcisstr.21, D-80333 München, Germany. Email: rutschmann@tum.de

ABSTRACT: The Kajbar dam will be constructed on the Sudanese Nile River for production of electrical energy, water supply and development of agriculture. The dam construction will interrupt the longitudinal continuity of the flow and sediment transport in the river system. Upstream of the dam, most bed load and some parts of the suspended load sediment can be deposited. The rapid reservoir sedimentation decreases the storage capacity. In order to remove and reduce reservoir sedimentation, several technical approaches are developed. Among them, flushing is considered the only economic approach to swiftly restore the storage capacity of the reservoir with severe deposition.In this paper, a method of sediment management and hydro-morphological model for sediment transport and flushing in the reservoir is explained. Due to the scarcity of data for the model calibration, in the present study a reliable quantitative prediction of the morphological evolution cannot be achieved. However, based on experiences formerly gained from model validation and application, a qualitative estimation of bed change under different flow conditions in the reservoir is possible. The calculated results show that flushing can retrieve beneficial storage of the Kajbarreservoir.

KEY WORDS: Reservoir Sedimentation, Sediment Transport, Flushing, Hydro-Morphological Model, Nile River.

1 INTRODUCTION

The Nile River is formed by the confluence of the three main tributaries: White Nile, Blue Nile and Atbara River, and flows over 6,700km through ten African countries: Tanzania, Uganda, Rwanda, Burundi, Zaire, Eritrea, Kenya, Ethiopia, Sudan and Egypt. Most sediment carried by the water from the watersheds and received by the river in the wet season originates from the Ethiopian Plateau. The sediment mainly consists of fine sand, silt, and clay (Abdelsalamet al.,2008). The importance of the Nile has been recognized since biblical times. For centuries the river has been a lifeline for Sudan. On the Nile system, there are several dam reservoirs: two in Uganda, two in Ethiopia and a third under construction, five in Sudan, and two in Egypt. Further plans for new dams are under way. Most of them are built for multi-purpose e.g. irrigation, hydropower, water supply, flood control, navigation, fisheries, recreation, and environmental requirements.Due to the construction of a dam, the natural flow and sediment transport conditions of the river are significantly changed. Sediments are deposited in the reservoir, which reduce storage capacity, change the morphology of flooded areas, and pose risks of blockage of intake structures as well as sediment entrainment in hydropower schemes. Lack of sediment load affects the downstream river and its banks and accelerated erosions may occur. A reservoir is silted up more or less rapidly. In actual fact, reservoirs may completely be filled with sediments even within just a few years. Reservoir sedimentation reduces the value of or even nullifies the dam construction investment. The use for which a reservoir was built can be sustainable or represent a renewable source of energy only where sedimentation

is controlled by adequate management, for which suitable measures and operation schemes should be devised. A modern approach to the design of new hydropower project requires good understanding and accurate predictions of hydro-morphological processes inthe reservoir.

This paper presents an application of the numerical model for flow and sediment transport in a reach of the Nile River in Sudan, where the Kajbar dam will be constructed. A numerical model is applied for an area of about 7km×5km upstream of the dam. The main objective of the study is to estimate the long-term bed level changes due to reservoir impounding and to optimize sediment flushing scenarios with respect to reservoir capacity.

2 MODEL SYSTEM

In the study the FAST2D computer program system was used. The approach involves the following basic assumptions:

- The time scale of the bed change is much larger than the time scales of the flow and the sediment transport.
- The suspended sediment concentration is so small that the presence of sediment in the water has a negligible influence on the flow.

The computer code to calculate flow and sediment transport in alluvial channels was developed initially at the Institute for Hydromechanics, University of Karlsruhe. The model system consists of an unsteady hydrodynamic module with implementation of a moving boundary scheme, a sediment transport module and a bed-level-change module. The sediment transport module comprises semi-empirical models of suspended-load and non-equilibrium bed-load. The-bed-level change module is based on the mass-balance for sediment. The hydrodynamic module is based on the two-dimensional shallow water equations. The secondary flow transport effects are taken into account by adjusting the dimensionless diffusivity coefficient in the depth-averaged version of the k-ε turbulence model. A quasi-3D flow approach is used to simulate the effect of secondary flows due to channel geometry on bed-load transport. The former model assumed uniform bed material. In order to take into account the influence of grain size distribution of the bed-surface on the evolution of the bed topography and consequently also on the flow field, a sediment transport module has been presently developed at the Institute of Hydraulic and Water Resources Engineering, TechnischeUniversitätMünchen, for fractional sediment transport using a multiple layer model (Bui & Rutschmann, 2010). In this model, the bed is divided into an active layer and several substrate layers. The active layer and the first substrate layer (active stratum) constitute the so-called mixing layer. Sediment particles are continuously exchanged between flow and the active layer when the bed scours or fills. As erosion occurs, entrainment of sediment particles from the active layer and its ensuing downward displacement causes particles from substrate layers to be mixed with those in the active layer. On the contrary, deposition of sediment particles on the bed leads to an upward displacement of the active layer and the initiation of new substrate layers. Further, the bed material is divided into a number of size-fractions, each characterized by a certain diameter and by a volume percentage of occurrences in the bed material. The sediment-transport rates depend on the bed-material composition, which itself depends on the history of erosion and deposition rates. Changes in the bed composition are not only restricted to a layer that is to the material exposed to the flow, but that a finer sub-layer also forms under the coarser surface layer.

The governing differential equations for flow and sediment transport in a curvilinear coordinate system are written in common tensor notation form and solved numerically using a finite volume method with boundary-fitted grids. The central / upwind hybrid differencing scheme is employed in treating the convective and diffusive fluxes. In order to avoid checkerboard splitting for cell-centered arrangement, the momentum interpolation technique is used for evaluating cell face variables from centered quantities. The momentum equations coupled with transport equations for turbulence quantities are solved by an implicit finite volume procedure. The pressure or water depth, however, is not directly computed from the original continuity equation but with a pressure correction equation. More details on the numerical solution procedure can be obtained from Bui (1998) and Bui & Rutschmann (2010).

3 MODEL SETUP

A 3D-digital terrain model was created based on the raster dataset of 10m×10m and the cross

sections data. Accompanying structures (dam, power house, spillways and sluice gates)were also introduced in this 3D-digital terrain model.Based on the available data, an area about 7km×5km was chosen as study area for the 2D- numerical model tests. A mesh was generated with an average cell size of 10m×10m and of 5m×5m around the dam structures. The 3D-digital terrain model was used to define the bottom elevation at every grid points of the computation mesh (Fig. 1).

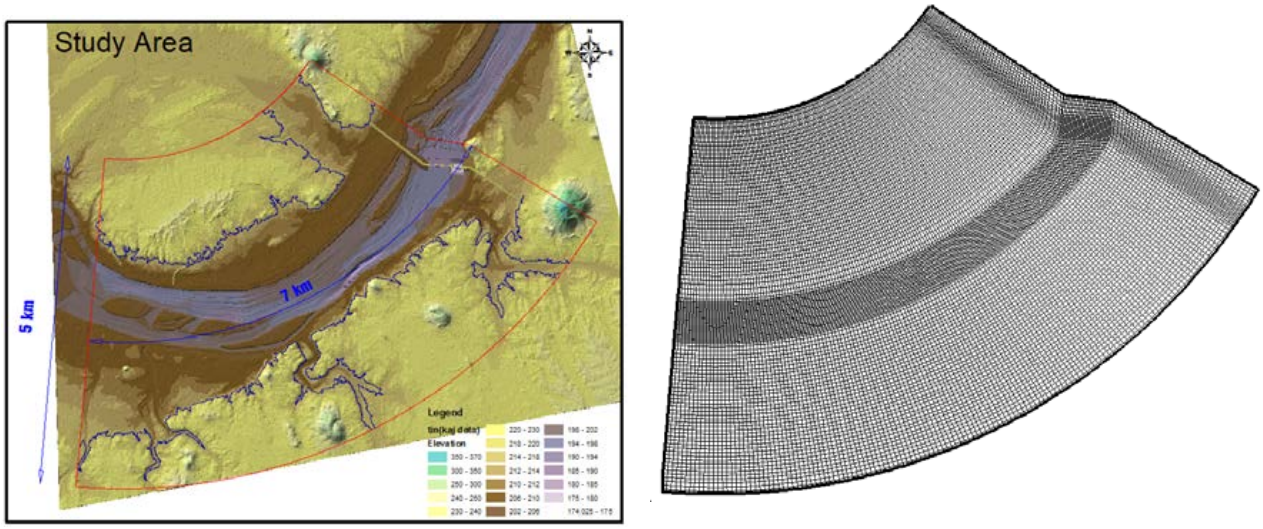

Figure 1 Computation domain and grid system

At the upstream boundary the discharges of flow and sediment transport are given while at the downstream boundary the water level is specified and Neumann boundary conditions with zero-gradient for sediment transport variables are applied.From the results of a 1D model we get the time variation curves of discharge and cross-sectional average of suspended sediment concentration at the inlet boundary of 2D model. Further, we assume that the concentration is uniform, the depth average velocity is proportional to the water depth, and the flow direction coincides with the main channel direction. At this boundary the bed load transport rates are estimated using Van Rijn's bed-load equation for equilibrium sediment transport.At the outlet boundary, the water level was related to the reservoir operation schemes. The flow rates passing theturbines (Q_{tb}) and spill ways as well as sluice gates (Q_{sg}) are defined based on the in-flow discharges (Q_{in}) as follows:

$$Q_{tb} = \min(Q_{in}, Q_{tb\_\max})$$
$$Q_{sg} = Q_{in} - Q_{tb}$$

where$Q_{tb_max}$is maximal flow discharge passing through the turbines. Based on these values of flow rates, the calculated mean velocities are then adjusted at the outlet boundary and re-calculated for the whole domain at every time steps.In case without flushing, the water level is keep constant as the Full Supply Level FSL= 216.5m. For flushing cases, the reservoir water level will be lowered at the flood season to the Drawdown Supply Level DSL= 210m (flushing scenarios no. 1 and no.2) or DSL= 213m (flushing scenario no. 3). At the same time the bed elevation in the spill ways domain will be drawdown with the same rate as the water level reduction (Fig. 2).Further, we assume no-bed-changes at this boundary and zero-gradient condition is applied for bed-load and suspended load. At the beginning of the simulation the active and passive layers have the same grain size distribution shown in Tab. 1.

Table 1 Initial bed sediment gradation

Sediment	1	2	3	4	5	6	7	8	9
Grain size (mm)	0.007	0.063	0.09	0.125	0.25	0.355	0.5	0.71	1.0
Fraction (%)	5.6	0.2	0.7	20	39.8	14.6	8.6	5	5.5

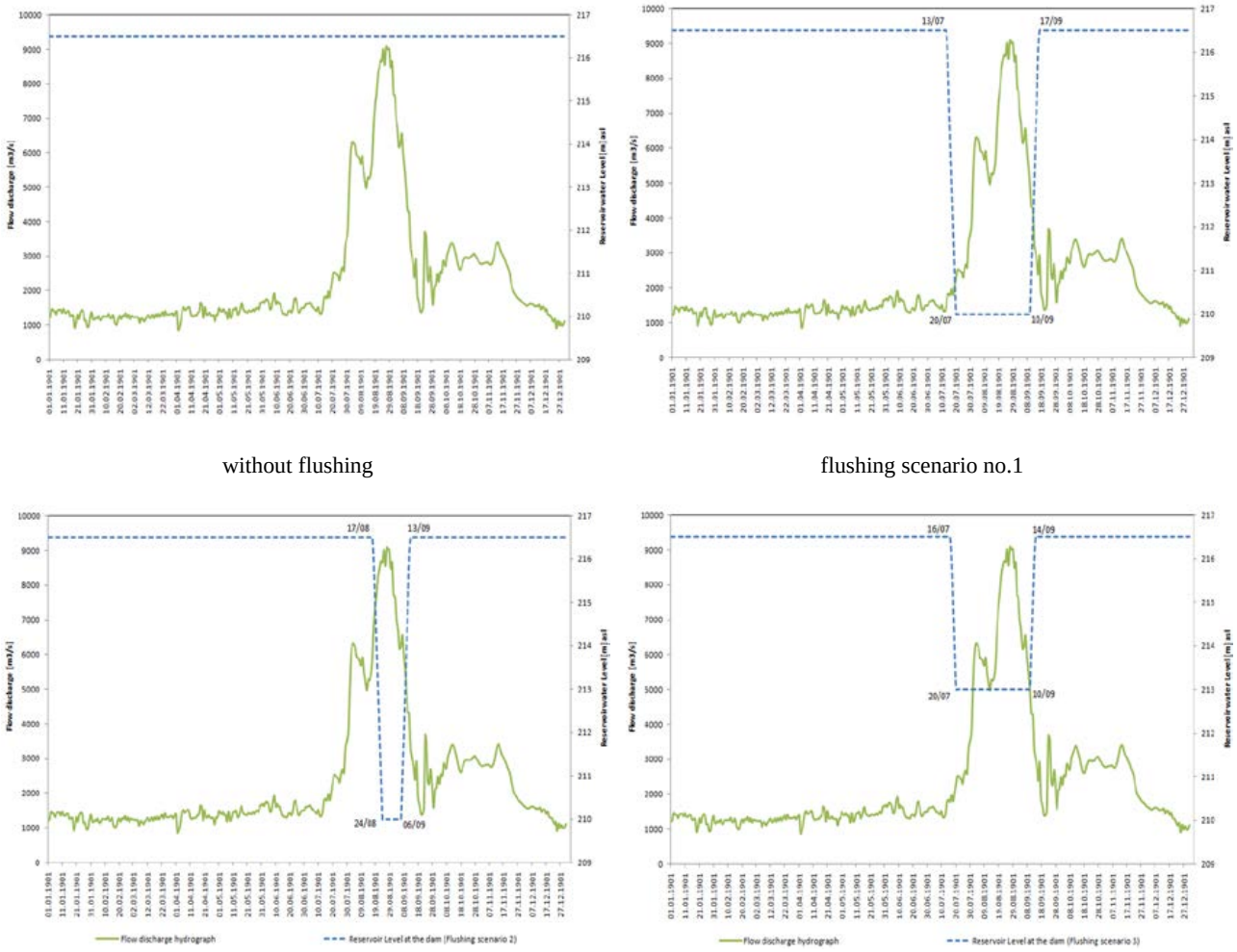

without flushing

flushing scenario no.1

flushing scenario no.2

flushing scenario no.3

Figure 2 Differentscenarios of dam operation

4 RESULTS AND DISCUSSION

Calculations have been done for the first scenario without flushing. The calculated results of depth averaged velocities at different discharges show that after entering into reservoir, flow shifts laterally to both sides of the main river but the water flow concentrates most in the river course and the left flood plain. Aside from the flow domain near the dam structure and in front of the sluice gates and power-house, a maximal depth averaged velocity of 0.76m/s at the highest water event was calculated in the left flood plain (Fig.3 – left). Bed level change(Fig. 3 - right) demonstrates the complex adjustments in channel morphology after 30 years. Deposition thickness at a cross section is by no means uniform across the channel width. Such complex adjustments in reservoir morphology directly affect the hydraulics of flow and sediment transport. It may therefore be stated that fluvial simulation in the reservoir domain near by the dam structures should be based on a 2D or 3D erodible boundary model instead of a 1D erodible bed one.Consider a slow-moving current that exerts a stress on the bed slightly larger than required to entrain sediment into suspension, producing a rate of sediment entrainment from the bed, which is less than the depositional rate. On the other hand, higher flow velocity can produce a rate of sediment entrainment from the bed, which is greater than the depositional rate. After 30 years simulation a maximal value of 2.65m for the bed change was obtained in the left flood plain close to the dam. It can be seen also a large amount of sediment has been deposited in the both sides of flood plains in front of the dam and in the right flood plain immediately after entering the reservoir domain. The amount of sediment deposition or removal within the investigation domain is the difference in total delivery from the cross section at the inlet to the other at the outlet boundary. For the investigated domain, the calculated amount of deposition

after 30 years amounts to 19.47 million tons.

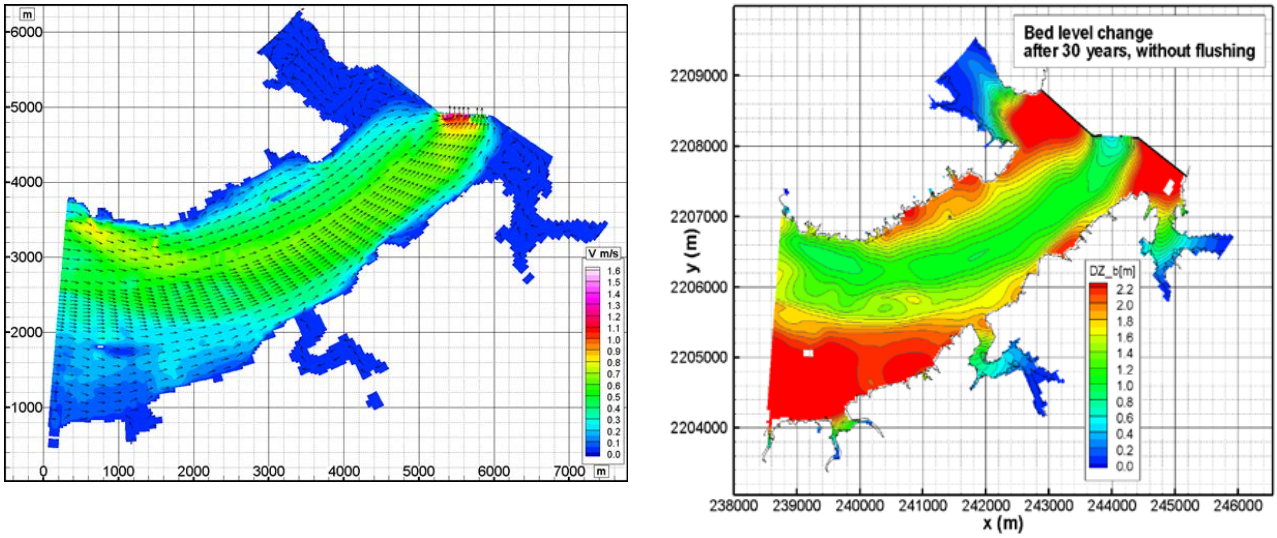

Figure 3 Mean velocity field at 8800m^3/s (left) and bed level change after 30 years without flushing (right)

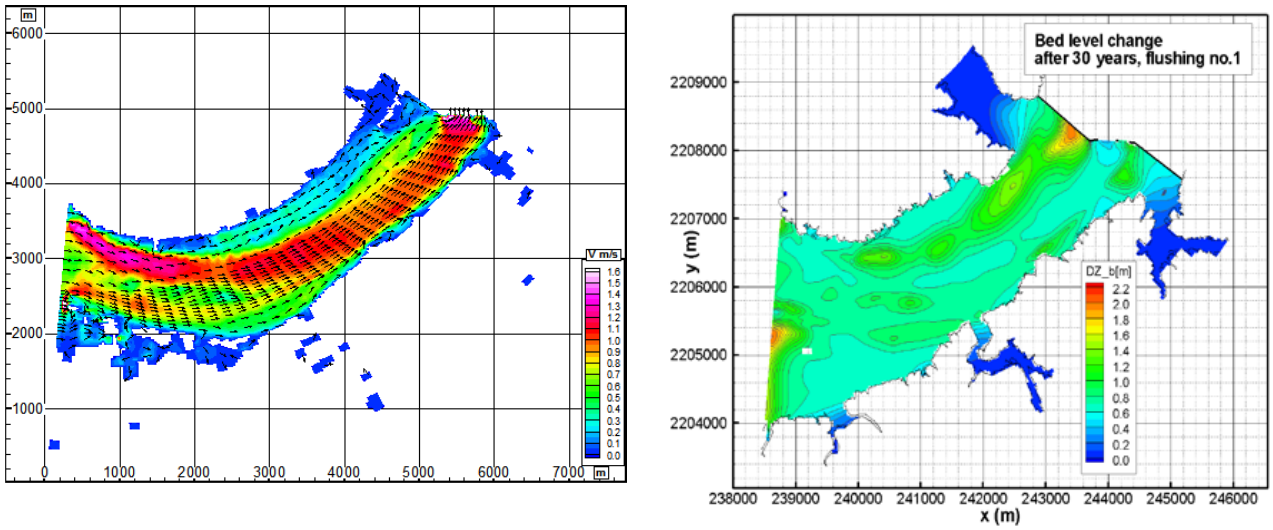

Figure 4 Mean velocity field at 8894m^3/s (left) and bed level change after 30 years for flushing scenario no.1 (right)

During the flood season, the flushing no.1 started as the flow discharge reached 1500m^3/s. The reservoir water level was fully drawn down from 216.5m to 210m in a period of 8 days. All gates then remained open for a period of 53 days to keep the reservoir water level at 210m. During 8 days at the end of the flood wave, the gates were closed to get the water level at 216.5m. The calculated result of depth averaged velocity at the highest-water discharge plotted in Fig. 4 (left) shows that strong riverine flow occurs along the length of the reservoir. Aside from the flow domain near the dam structure and in front of the sluice gates and power-house, a maximal depth averaged velocity of 1.55m/s at this high-water event was calculated in the left flood plain. Due to the complexity of the bed form and the channel, the distribution of mean velocity in the reservoir was relatively irregular, that affected on the sediment transport and also the bed level change in the studied domain.

Due to the high flow velocities, some previously deposited sediment was scoured. Since flushing also scours some previously deposited sediments so that sediment outflow exceeded inflow. Fig. 4 (right) shows the calculated spatial variation in bed elevations with flushing schema no.1. After 30 years simulation the maximal deposition thickness was calculated about 2.02m in the right flood plain and close to the river entrance. In the area locating in front of the left-side dam some sediments were trapped (with

a maximal deposition thickness of about 2.0m), the flushing operation could not arrest sediment accumulation also in this area. Generally, this flushing operation reduced reasonably sediment deposition within the reservoir. Following the 30 years of operation with the flushing scheme no.1 about 8.98 million tons of the deposited sediment had accumulated in the investigated domain (10.49 million tons less than for the case without flushing).

The flushing scheme no.2 started as the flow discharge reached 6500m^3/s. The reservoir water level was fully drawn down from 216.5m to 210m in a period of 8 days. All gates then remained open for a period of 14 days to keep the reservoir water level at 210m. During 8 days at the end of the flood wave, the gates were closed to get the water level at 216.5m. Fig. 5 (left) shows the predicted distributions of deposition layer thickness in the reservoir with flushing schema no.2. After 30 years simulation a maximal deposition thickness about 2.11m took place in the right flood plain and close to the river entrance. In the area locating in front of the left-side dam some sediments were always trapped (with a maximal deposition thickness of about 2.07m), the flushing operation could not arrest sediment accumulation also in this area. The flushing period was too short for removing a sufficient amount of sediment from the reservoir. After 30 years of operation with the flushing scheme no.2 about 14.55 million tons of the deposited sediment had accumulated in the investigated domain (4.92 million tons less than for the case without flushing).

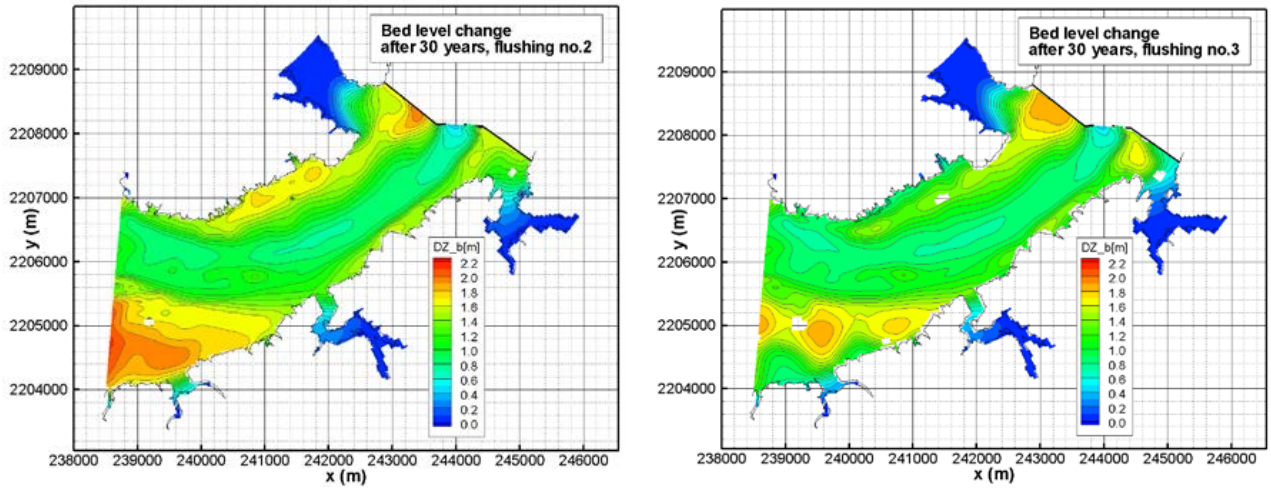

Figure 5 Bed level change after 30 years for flushing scenarios no.2 (left) and no.3 (right)

At the beginning of the high-flow season with a flow discharge larger than 2000m^3/s, the flushing schema no.3 started. The reservoir water level was fully drawn down from 216.5m to 213m in a period of 5 days. All gates then remained open for a period of 14 days to keep the reservoir water level at 213m. During 5 days at the end of the flood wave, the gates were closed to get the water level at 216.5m. The calculated result of depth averaged velocity at the highest-flow discharge shows that aside from the flow domain near the dam structure and in front of the sluice gates and power-house, the flow reached a maximal velocity of 1.05m/s in the left flood plain.Fig. 5 (right) shows the predicted layer thickness of deposited sediment in the reservoir with flushing schema no.3. After 30 years simulation a maximal deposition thickness about 1.89m was estimated at the region in the right flood plain and close to the river entrance. Also in this case, the flushing operation could not arrest sediment accumulation in the area locating in front of the left-side dam, wherea considered amount of sediment was trapped (with a maximal deposition thickness of about 1.87m). After 30 years of operation with the flushing scheme no.3 about 13.04 million tons of the deposited sediment had accumulated in the investigated domain (6.43 million tons less than for the case without flushing).

In the flood plain domains with moderate water flow velocity the amount of deposited sediment was large. In the areas with very low water flow velocities, the bed changes were very small due to the small concentration of suspended sediment. It seems to be quite different from the observations in the field. An available explanation here is: in the natural reservoir there may be other suspended sediment sources,

which enter the reservoir not through inlet boundary by river flows but from catchment area directly by surface water flows. It is too difficult to simulate these sources, so that they were not taken for account in the present numerical model.The calculated results also indicated that a minor deposited sediment rate and bed change was observed in the front of power-house-structures as the water velocity increased in this domain. A large difference in the bed level change after 30 years, by using four different reservoir operation schemes.

4 CONCLUSIONS

Sediment accumulation decreases the effective storage volume. Experiences have shown that reservoir sedimentation is neither an irreversible nor uncontrollable process. Various design, operational, and reconstruction strategies can be used to balance sediment inflow and outflow across impounded river reaches, thereby protecting a significant amount of useful storage sedimentation. One of the most important steps in the development of this technology is the refinement of generalized computer simulation techniques for analyzing sediment management problems in reservoir, and the testing of these techniques against field data from reservoirs where sediment management is being practiced.The numerical model can be used as a strategic evaluation tool for reservoir management. It can be applied to analyze various technical solutions to prevent sedimentation in the reservoir. Among others, predicting the time and duration of flushing for evacuating the sediments are important problems in reservoir operation. By undertaking flushing in the flood season, when most sediment enters the impoundment, deposition can be reduced after the flushing period. Based on the numerical simulations, the optimal timing of the opening of the bottom outlet and gates can also be determined to pass an important part of the sediment yield beyond the dam during floods.

The computer code FAST2D has been applied for detailed morphological simulations in an area about 7km×5km upstream of the Kajbar dam. The flow rates passing the spill ways, sluice gates and turbines based on the in-flow discharges were taken in the model into account. Long term simulated results can be summarized as follows:

- Reservoir sedimentation is closely related to hydraulic detention time, and sediment routing minimizes hydraulic detention time by lowering the reservoir level during those events that transport most sediments. The effectiveness of this strategy is enhanced because sediment concentrations tend to be highest during the rising limb of the hydrograph. Thus, the reservoir pool can be maintained at a low level to pass the flood and its associated heavy sediment concentration. This study demonstrates that sediment can be effectively flushed out of the reservoir by drawdown flushing during floods. With well-devised drawdown-discharge relations and operation rules, it is also feasible to reduce sediment accumulation in the reservoir over an extended operating period.
- The effectiveness of the different operation schemes on the reservoir sedimentation was studied. The flushing scenario no.1 provided the best results. Applying this flushing scheme during 30 years, the predicted amount of sediment deposited in the reservoir was around 8.98 million tons, as compared with 19.47 million tons estimated for the case without flushing. The maximal deposition around 2.0m was located close to the left side dam and in the right flood plain close to the river entrance.
- In all cases, only a minor deposited sediment rate and bed change was observed near power-house-structures. Since in this domain the water flow velocity increased, most sediment was effectively flushed out of these reservoirs, especially by drawdown flushing during floods. The maximal deposition thickness reached up to 2.65m in the left flood plain in front of the dam and in the right flood plain close to the reservoir entrance, after 30 years simulation.

Due to the scarcity of data for setting up as well as for calibrating the model, in the present study a reliable quantitative prediction of the morphological evolution cannot be ensured. However, based on experiences formerly gained from model validation and application, a qualitative estimation of bed change under different flow conditions in the reservoir is possible. In order to improve the quantitative predictions of the numerical model, further model verifications must be carried out by means detailed and accurate data. Namely, the field data of long-term observations of hydrodynamics, bed material distributions and sediment transport, as well as topographical changes must be observed and collected, as

soon as the hydropower project has been completed.

ACKNOWLEDGEMENT

The authors would like to express their gratitude to Prof. W.Rodi at the Institute for Hydromechanics, University of Karlsruhe,Germany, for placing the FAST2D code at our disposal.The authors also would like to thank Lahmeyer International (LI) and Dams Implementation Unit (DIU) for providing the data used in the model.

References

Abdelsalam, A. A. et al. (2008): “Sediment in the Nile River System ", UNESCO-IHP.

Bui, M.D. (1998): „Berechnung der Strömung und des Sedimenttransports in Flussläufen mit einem tiefengemittelten numerischen Verfahren“, Dissertation, Institut für Hydromechanik, Universität Karlsruhe.

Bui, M.D., and Rutschmann, P. (2010): "Numerical modelling of non-equilibrium graded sediment transport in a curved open channel"; Computers & Geosciences, Vol. 36, 792-800.

MDPIU(2007):“Water Level Fluctuations Downstream of Merowe Dam and Boundaries of the Reservoir”,. Design report, Merowe dam project Volume 2.

LI (2007): “Water Level Fluctuations Downstream of Merowe Dam and Boundaries of the Reservoir”, Merowe dam project, Volume 2.

Rutschmann, P., Bui, M.D., and EizeldinM. (2012): "Numerical Model Tests for morphological change and boundaries of reservoir”, KajbarHydropower Project, Final report.

4.2. Integratives Hochwassermodellsystem

Während in den meisten numerischen Hochwassermodellen lediglich Reinwasser-Abflüsse betrachtet wurden, sind an einigen Füssen aufgrund ihres alpinen Einzugsgebiets auch die Feststoffe in die Studie mit einzubeziehen. Dabei sind morphologische Fragestellungen zu bearbeiten wie z.B. die Mobilisierung und Ablagerung von Geschiebefrachten unmittelbar im Flusslauf, dies sowohl in ihrem örtlichen wie auch zeitlichen Auftreten oder die Sedimentablagerung nach Hochwasserereignissen in den Rückhalteräumen und Überflutungsflächen.

Im folgenden Paper wird ein hydromorphodynamisches Modell entwickelt und verwendet, um den morphodynamischen Einfluss auf Hochwassersimulation zu bewerten. Im Gegensatz zu dem integrativen Modell überschätzt das Standardmodell für klares Wasser mit Festsohle die Wasserhöhen, da es die signifikanten Änderungen in der Morphologie nicht berücksichtigen kann. Die Ergebnisse zeigen, dass das vorgeschlagene Modell die Überschwemmung in der Überschwemmungszone genauer darstellt und daher verwendet werden kann, um Entscheidungsträgern zuverlässigere Vorhersagen für eine verbesserte Hochwasserschutzstrategie zu liefern.

- Reisenbüchler, M.; M.D. Bui; D. Skublics; P. Rutschmann (2019): “An integrated approach for investigating the correlation between floods and river morphology: A case study of the Saalach River, Germany”. Science of the Total Environment. 647. Elsevier.

Science of the Total Environment 647 (2019) 814–826

Contents lists available at ScienceDirect

Science of the Total Environment

journal homepage: www.elsevier.com/locate/scitotenv

An integrated approach for investigating the correlation between floods and river morphology: A case study of the Saalach River, Germany

Markus Reisenbüchler [a,*], Minh Duc Bui [a], Daniel Skublics [b], Peter Rutschmann [a]

[a] Technical University of Munich, Arcisstrasse 21, 80333 Munich, Germany
[b] Wasserwirtschaftamt Rosenheim, Königstrasse 19, 83022 Rosenheim, Germany

HIGHLIGHTS

- Morphological developments and activities influence inundation.
- River engineering structures and straightening alter the morphology of the river.
- Stationary hydrodynamic models underestimate the flood risk.
- The developed integrative model represents flood events more accurate and realistic.

GRAPHICAL ABSTRACT

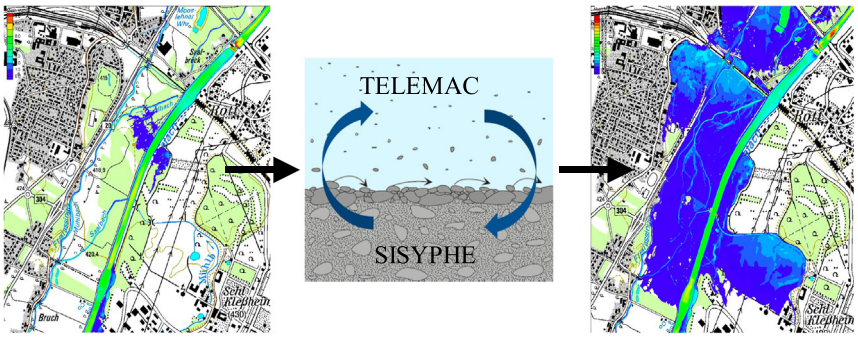

ARTICLE INFO

Article history:
Received 18 December 2017
Received in revised form 24 July 2018
Accepted 2 August 2018
Available online 04 August 2018

Keywords:
Saalach
Telemac
Sisyphe
Numerical modeling
Flood
Morphology

ABSTRACT

Man-made structures in the Saalach River have changed the hydromorphological characteristics of the river regime. In some river reaches, the Saalach has lost the high morphological versatility and high variation in sediment transport characteristic of a mountain river. Among the negative effects, an extreme flow discharge in combination with riverbed variation could be one of the possible causes of flood disasters along the river. For example, the heavy and long lasting rainfall in June 2013 led to a peak discharge of 1100 m^3/s, which was slightly above the 100-year flood return period, inundating a nearby city. However, the influence of the man-made structures on this flood event in this reach is unclear. In this study an integrative hydromorphological model is applied to evaluate this impact by a comparison with a standard clear water model with fixed bed. Moreover, a comparative analysis of a three-and two-dimensional flow model is performed to assess the models suitability representing the flow in this river stretch. The integrative model concept is based on the software TELEMAC-MASCARET, in an enhanced version for better representing graded sediment transport in rivers. In contrast to our integrative model, the standard clear water model with fixed bed overestimates the water elevations as it cannot take the significant changes in morphology into account. Results demonstrate that our proposed model more accurately represents the inundation in the floodplain and could thus be used to provide more reliable predictions to decision-makers for improved flood protection strategy.

1. Introduction

Flood events are frequent and often disastrous events worldwide. They are not usually directly linked to specific spatial conditions but can occur almost everywhere, triggered by long lasting or heavy rainfall

* Corresponding author.
E-mail address: markus.reisenbuechler@tum.de (M. Reisenbüchler).

https://doi.org/10.1016/j.scitotenv.2018.08.018
0048-9697/

or the combination of both (Bronstert, 2003). In 2013, middle Europe was affected once again by an extreme flood event. This caused losses of over €8 billion nationwide in Germany and can be classified as the most severe flood event in Germany for the last 60 years (Thieken et al., 2016). In order to mitigate the impact of future events, a lot of research and post-processing on this event has been done to understand the causes leading to the flooding (Blöschl et al., 2013; DKKV, 2015; LfU, 2014; Thieken et al., 2016). In the past, flood inundation maps were used to ascertain whether certain areas are likely to be affected by floods or not. In flood management, this is now extended by including a risk assessment based on the following considerations: overall hazard (e.g. flood magnitude, effect of climate change, etc.), spatial exposure (number of people affected and impact on infrastructure) and vulnerability (i.e. the sensitivity to a hazard). Röthlisberger et al. (2017) employed a spatial clustering approach identifying highly endangered regions. The Free State of Bavaria, Germany, implemented a similar approach, which was improved, adapted and extended after each flood event (StMUV, 2015). Many of these measures and suggested methodologies are based on the representation of flood events from numerical models. These models simulate the extension of 'design floods' and assess whether the floodplain and cities are at risk. In Germany, the design flood for river defense systems refers to a flood discharge with a return period of 100 years (LAWA, 2010a). Such models are commonly used to determine countermeasures, risk-maps and insurance premiums, and are therefore an important factor in the total flood risk management context (LAWA, 2010b; Thieken et al., 2016).

However, floods are not of course confined to clear water phenomena, and rivers are not stable over time. Different fields of research focus on the broader morphodynamic influence on flooding. Rickenmann et al. (2016) highlight the significant influence of sediment motion during flood events in alpine catchments and their damage potential. The profound influence of riverbed dynamics on flood events becomes even clearer when comparing the historic states of rivers with their present state, as Skublics et al. (2016) shows for the Danube River. Morphological activities can lead to an increase in the flood peak and to more severe situations. Guan et al. (2015) and Guan et al. (2016) confirmed this in experimental and real-world conditions using numerical hydromorphological modeling. Similarly, Carr et al. (2015) and Tu et al. (2017), analyzed the magnitude of flood inundation under changing morphological conditions using numerical models. In the framework of hydromorphological modeling, a morphological model is connected to a hydrodynamic one, using different coupling approaches (Duc et al., 2005; Nelson et al., 2016; Wu, 2004). In this procedure, the hydrodynamic model provides information on the flow, turbulence and shear stress, from which the morphological model calculates sediment transport rates, which in turn lead to erosion or deposition. However, the calculation of sediment transport rates commonly applies to several empirical formulae derived from regression or dimensional analyses of laboratory experiments as no formula sufficiently describes all processes (Meyer-Peter and Müller, 1948; van Rijn, 1984; Wilcock and Crowe, 2003; Wu, 2007). The variability of available formulas includes several adjustable parameters, representing the site-specific conditions and characteristics of sediments (e.g. a threshold of motion after Shields (1936)), which means they cannot be simply extrapolated from one river to another. In short, the complexity and heterogeneity of fluvial sediments and the difficulty of measuring them - for instance, bedload transport rates over time - makes the modeling process and defining reliable boundary conditions challenging (Habersack et al., 2017).

This brief survey of the literature makes clear that the representation of the effects of hydrodynamics and morphodynamics cannot be considered in isolation. However, the application of hydromorphodynamic models is not yet the standard for representing a flood event. It is evident that excluding morphological changes can lead to a false impression of the real situation when we examine the event in June 2013, which led to the 100-year flood in the Saalach River, located in southern Bavaria, Germany. In this river reach, several man-made structures might influence the flood wave propagation and produce feedback on the inundation. However, taking measurements during events is difficult and information is often only available after the event. In order to understand and represent the processes during the event, especially at man-made river structures, we developed a numerical hydromorphological model for a section of the Saalach. Such numerical models can extend the knowledge about the effects of man-made structures on flood events and morphology and contribute to sustainable river management. To demonstrate that a two-dimensional hydrodynamic model is able to accurately represent the flow situation even close to structures in the absence of detailed measurements, we performed a comparison with a three-dimensional flow model. Our model was then compared with a standard clear water model with a fixed bed for the same flood event to test the hypothesis that an integrative approach would provide more accurate and realistic results. For the simulations, we applied TELEMAC-MASCARET software, extended with a newly-developed morphological module, which provides stable and reliable results (Reisenbüchler et al., 2016). The present work serves to illustrate: (1) applicability of a two-dimensional flow model to this river stretch, (2) accurate representation and analysis of the processes during the 2013 flood event, and (3) remarks on possible measures for flood impact reduction taking morphological changes into account.

2. Study area

We studied the Saalach River, which is located in the southeastern part of Germany close to the Austrian border. All elevations in this study are therefore referenced to the German vertical elevation system in meters above sea level. The Saalach River has its source in the Austrian Alps at 1940 m, and after 103 km flows into the Salzach River at a level of 404 m, close to Salzburg in Austria. The river length is defined according to the German system, starting at $x = 0.0$ km at the confluence to the Salzach River, and increases towards to the river source in the Alps. The data used in this study was provided by the regional water agency, the Wasserwirtschaftsamt Traunstein (abbr.: WWA-TS) (WWA-TS, 2013). The study area is confined to the lower part of the Saalach River from $x = 20.6$ km to $x = 2.4$ km, Fig. 1. This section of the river forms the border between Bavaria (Germany) on the orographic left and the county of Salzburg (Austria) on the right bank. At the Siezenheim gauge at $x = 5.5$ km, the river still has the typical characteristics of an Alpine river with a high variation in discharge (statistical mean discharge MQ = 39.1 m^3/s; statistical mean flood discharge MHQ = 440.0 m^3/s and a statistical 100 year return period flood discharge HQ_{100} = 1093 m^3/s; from the time series 1976–2013) (BMLFUW, 2013) and rapid morphological activity (WWA-TS, 2016). However, the shape of the river has changed greatly over the last 200 years, (BVV, 2017). Based on the comparison of the estuary of the rivers Saalach and Salzach in their historical and current state, this change is shown in Fig. 2, which is representative of the entire river. The historical river had a winding and meandering shape, changing morphologically after every flood event. In 1820, in order to create a clear border and facilitate river management, regulation and straightening were performed along the national border (Schramm, 2012). Further benefits of this measure were the gain in land for agricultural use and the increase of flood protection due to higher flow velocities in a trapezoidal, straight channel. These higher velocities not only affect the flood wave propagation but also increase the shear stress acting on the bed and therefore the sediment transport capacity of the river. However, river training is not the only influencing factor. At the beginning of the 19th century, energy demand increased, particularly for the railway which connected the rural area around the city of Freilassing with the then urban center of Berchtesgaden. To this end, the hydropower plant (HPP) Saalach was constructed in Bad Reichenhall ($x = 20.6$ km), including the Kibling dam, in 1913 (Zitka, 1959), (Fig. 1). To counteract sedimentation of this reservoir, the accumulated gravel has

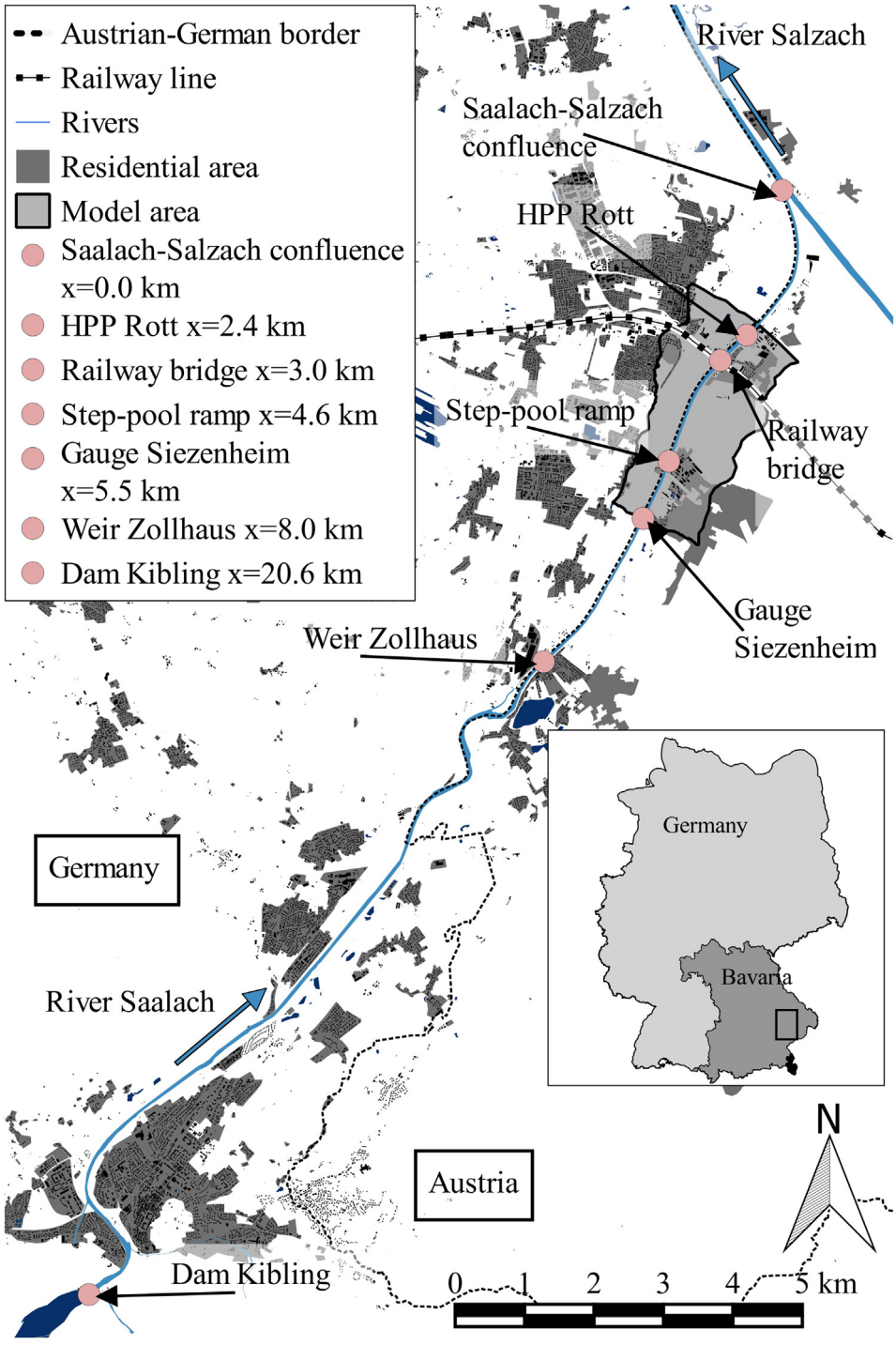

Fig. 1. Overview of the study area, highlighting relevant sites. Map after (OpenStreetMap contributors, 2018).

been excavated since 1940 and used for industrial purposes. Over time, further barriers have been constructed in the river for energy production and to improve timber rafting in the river, which has had a further negative impact on its morphology due to retention of sediment. Also important in the context of this study is the HPP Rott (x = 2.4 km, Fig. 1), constructed in 1940–1951 and rebuilt 100 m downstream in 2005 after exceeding its lifespan (WWA-TS, 2016; Zitka, 1959). One additional purpose of this HPP is to protect the foundations of the railway bridge (x = 3.0 km) located upstream at 413.8 m elevation. Sediment management by flushing and dredging is performed at the HPP Rott when aggregation of the riverbed elevation in the reservoir becomes too high. The combination of increased sediment transport capacity due to higher velocities resulting from the straightening of the river and the loss of supplied sediment from the source in the Saalach reservoir has led to a sediment deficit downstream, which has caused erosion and deepening of the riverbed. Analysis of cross-sections close to the confluence shows that 80 years after training the riverbed is around 4.50 m deeper than before (1920–1999). Fig. 3 shows cross-sectional profiles of the river close to the confluence at x = 0.6 km over several years. In order to prevent further deepening, sediment in the order of 50,000 m^3/a has been dredged from the reservoir head of the Kibling dam, transported by road and fed into the river downstream of the

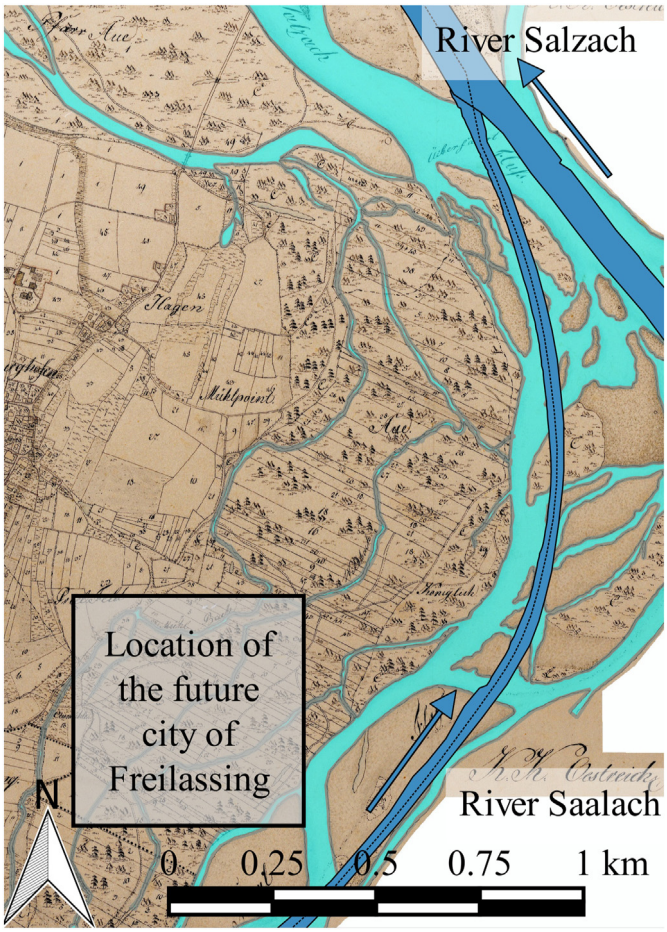

Fig. 2. Historical, meandering (cyan) and present, straight (blue) shape of the Saalach River at the confluence with the Salzach River, after (BVV, 2017). (For interpretation of the references to colour in this figure legend, the reader is referred to the web version of this article.)

dam since 1999 (WWA-TS, 2016). If there is a flood event, the supplied material is transported downstream along the river.

In addition, an open, step-pool ramp has been constructed in the river, situated at x = 4.6 km upstream of the HPP Rott reservoir in order to increase the stability of the river between the unregulated Zollhaus weir, x = 8.0 km, and the HPP Rott, x = 2.4 km, in 2005–06. Hengl (2014) and Stephan and Hengl (2010) showed that such embedded structures can provide morphological riverbed stability as they prevent erosion, but are at the same time ecologically friendly in the context of fish migration and sediment transport. A physical scale model of the step pool ramp was developed at the TU Wien, Austria, to test the stability of the construction, flood security, and sediment transport consistency. The structure consists of independent modular pools delimited by stone settings (Fig. 4). The final ramp design consists of eight stone barriers, with a crest at 416.10 m and the lowest point at 414.05 m. The inclination is 1:32, which results in a length of 65 m in total. Furthermore, the ramp is situated in an artificial lateral extension (original 35 m, now 52 m), which delivers ecological benefits (Gostner, 2005; Hengl et al., 2007). The purpose of this measure is to increase the riverbed upstream of the ramp by around one meter and to keep it stable at 415.50 m. This is necessary to protect the fine sediment layers below the riverbed surface from erosion. The aggregation and the flow over the fixed, stepped structure lower the energy potential of the river and therefore decrease the erosion potential. This ramp structure dissipates energy and thereby results in a mild slope in the upstream channel reach. Downstream, the ramp should have no effect on the river, as this section is already in the HPP Rott reservoir. However, some recently performed studies e.g. Beckers et al. (2015a) show that unexpected depositions occur in several sections of the Saalach River, which are counterproductive for flood protection.

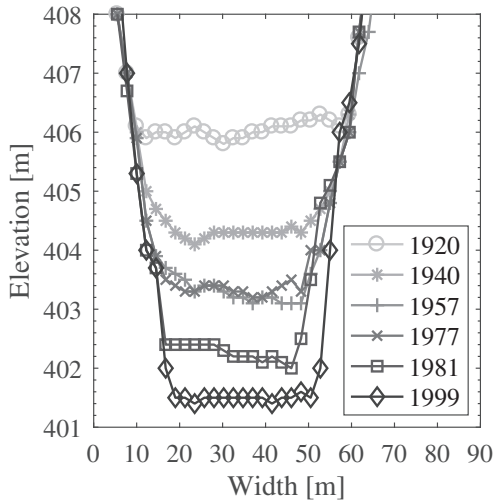

Fig. 3. Cross-sectional profiles of the Saalach riverbed for several years at x = 0.6 km.

3. Review of the 2013 flood event

Seasonal flood events induced by snow melting or short intense summer storms are typical for this region, (Ertl, 1940). However, in May and June 2013, almost continuous rainfall saturated the catchment area of the Saalach so that the subsequent heavier rain could not drain away, leading to extreme discharge into the river (Blöschl et al., 2013). This combination resulted in a flood event observed at the gauge Siezenheim (x = 5.3 km), named HQ_{2013}, which had a peak discharge of around Q = 1100 m^3/s, slightly higher than the statistical 100-year event. This caused extreme flooding on the Bavarian side of the floodplain, including the city of Freilassing, but did not affect the Austrian side of the river, where the city of Salzburg lies, thanks to the flood protection dam (Fig. 5). Analysis of the time series at the Siezenheim gauging station (1976–2014) shows that an event of this magnitude had never previously been observed (Eybl et al., 2013).

In addition to the unexpectedly high discharge, the extent of the inundation was not anticipated. It was assumed that the capacity of the channel would be approximately HQ_{100} and that a flood of this size would have a minimal impact on the region. However, the WWA-TS applied the measured discharges of the 2013 flood to a 2D-hydrodynamic model, HYDRO_AS-2D (Nujic, 2002), to a river bathymetry measured in March 2013. This reconstruction showed a severe inundation, close to the approximate extension of the actual flood (Fig. 5). Local residents' observations and photographs confirmed this scenario (WWA-TS, 2013). In a comparative study, WWA-TS applied the same hydrograph to their older model of river bathymetry measured in February 2002; this showed the flood passing through the region with only minor impact (Fig. 6).

The reason for the difference in the modeled inundations is due to spatial-temporal differences in the elevation of the riverbed. Fig. 7 shows average riverbed elevations along the channel over several years. While in the upper part from x = 8.0 km to x = 5.5 km only minor changes can be detected, in 2002 the lower part of the riverbed (grey line), from x = 5.5 km to x = 2.4 km, was significantly lower than in 2013 (black crossed line).

This comparison shows how sediment transport and morphological change over several years could affect the damage potential of flood events and ignoring these processes may lead to an underestimation of its magnitude.

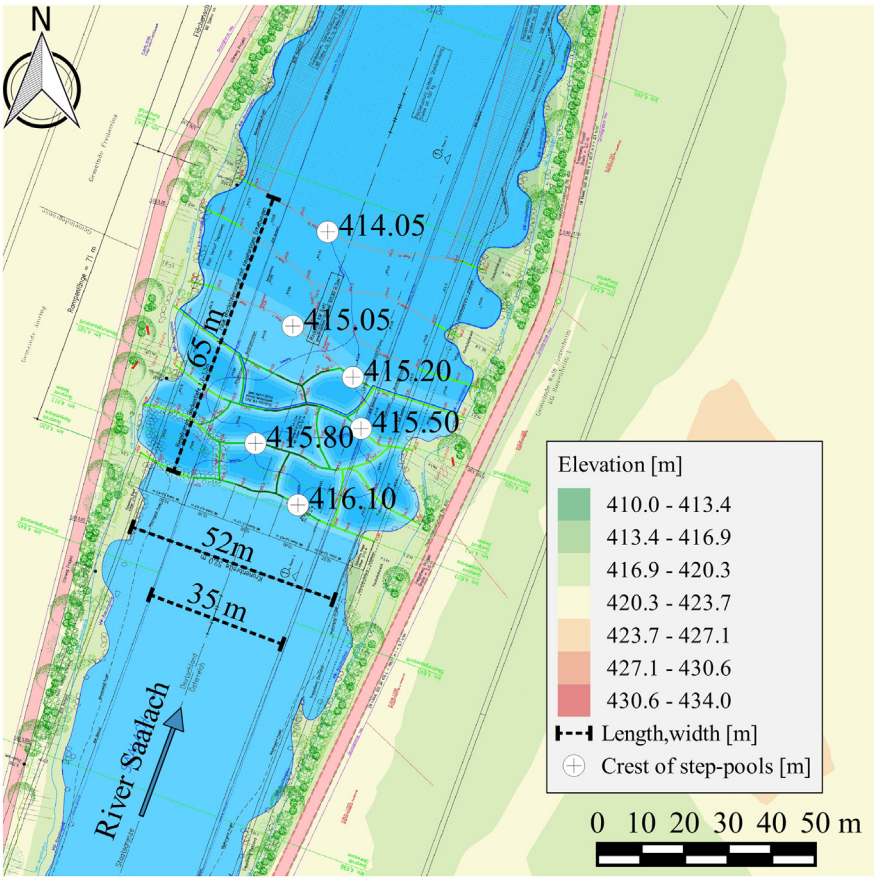

Fig. 4. Construction plan of the step-pool ramp at x = 4.6 km with scales and elevations, after (Gostner, 2005).

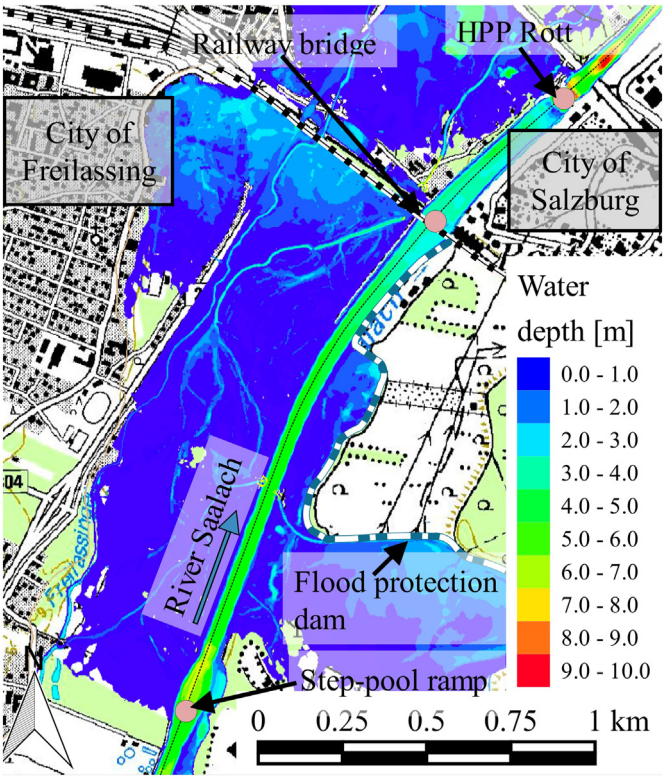

Fig. 5. Maximum simulated inundation, resulting from the 2013 flood hydrograph on a river bathymetry, which was measured in March 2013, after (WWA-TS, 2013).

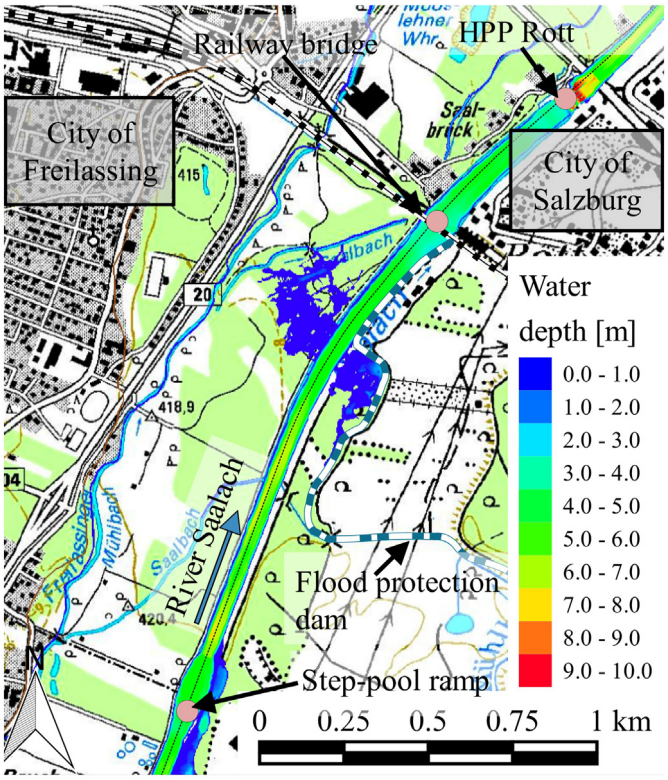

Fig. 6. Maximum simulated inundation, resulting from the 2013 flood hydrograph on an older river bathymetry, which was measured in February 2002, after (WWA-TS, 2013).

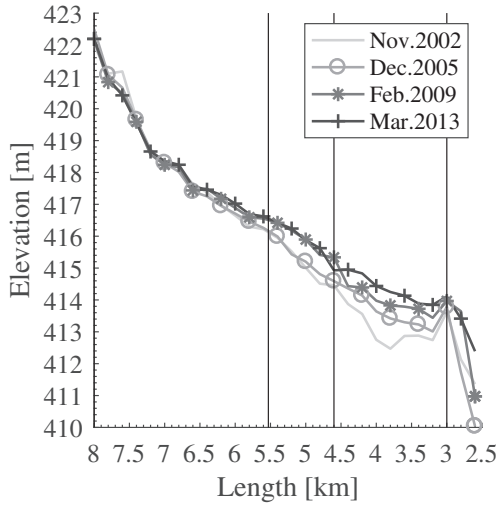

Fig. 7. Longitudinal section of mean riverbed elevations along the Saalach River for several years.

4. Methodology

In order to analyze the processes during this flood event in more detail, and to evaluate the influence of man-made structures, a numerical hydromorphological model was developed. In addition, a comparative analysis shows that a clear water model misrepresents this flood event. The model system TELEMAC-MASCARET is applied for the numerical modeling, including new code fragments to increase its numerical stability, accuracy, and the flexibility of the morphological module. The basics of the extensions and improvements are described in Reisenbüchler et al. (2016). The new model structure is here applied to our real-world scenario under heterogeneous and complex conditions. The applied methodology described below begins with the model generation, after which a clear water calibration with a fixed bed to determine the riverbed roughness is performed, followed by the selection of a suitable hydrodynamic model, and, finally, the application of the newly developed morphological codes to represent the flood event in 2013, which we treat as validation. This is followed by a further simulation, where the potential to mitigate the flood impact is discussed.

4.1. Hydrodynamic module

TELEMAC-MASCARET is an open source software package, capable of representing free surface flows with sediment transport. The suite consists of different modules, which can be coupled depending on the purpose.

TELEMAC3D (T3D) is the module for representing the Reynolds-Averaged-Navier-Stokes-Equations (RANS). The governing equations, in the non-hydrostatic version, are the following (Hervouet, 2007; Janin et al., 1992):

$$\frac{\partial U}{\partial x}+\frac{\partial V}{\partial y}+\frac{\partial W}{\partial z}=0 \tag{1}$$

$$\frac{\partial U}{\partial t}+U\frac{\partial U}{\partial x}+V\frac{\partial U}{\partial y}+W\frac{\partial U}{\partial z}=-\frac{1}{\rho}\frac{\partial p}{\partial x}+\nu\Delta U+F_x \tag{2}$$

$$\frac{\partial V}{\partial t}+U\frac{\partial V}{\partial x}+V\frac{\partial V}{\partial y}+W\frac{\partial V}{\partial z}=-\frac{1}{\rho}\frac{\partial p}{\partial y}+\nu\Delta V+F_y \tag{3}$$

$$\frac{\partial W}{\partial t}+U\frac{\partial W}{\partial x}+V\frac{\partial W}{\partial y}+W\frac{\partial W}{\partial z}=-\frac{1}{\rho}\frac{\partial p}{\partial z}+\nu\Delta W+F_z-g \tag{4}$$

where U, V, W = components of a three dimensional velocity vector $\vec{U}$ (m/s) in x, y (horizontal) and z (vertical) direction; t = time (s); ρ = density of fluid (kg/m^3); p = pressure (kg/ms^2); ν = coefficient of kinematic viscosity (m^2/s), F_x, F_y and F_z = source or sink terms in dynamic equations (m/s^2) representing forces such as Coriolis force or bottom friction, and g = gravitational acceleration (m/s^2). The three-dimensional model is applied worldwide though often in combination with high-performance-computing (HPC) due to the high computational effort (Hajivalie and Arabzadeh, 2017; Mattic, 2017; Moulinec et al., 2011; Ricci et al., 2015).

The module TELEMAC2D (T2D) consists of depth-averaged, two-dimensional Shallow-Water-Equations (SWEs). These equations normally fit well to free-surface river engineering problems, when the river width is significantly larger than the water depth. However, this approach is not suitable for modeling the flow over or around obstacles (e.g. bridge piers) (Hervouet, 2007). The 2D SWEs are used in the model in their conservative form as follows (Ata, 2017):

$$\frac{\partial h}{\partial t}+\ div\left(\vec{q}\right)=0 \tag{5}$$

$$\frac{\partial q_x}{\partial t}+\ div\left(q_x\vec{u}\right)=-gh\frac{\partial Z_S}{\partial x}+\ div\left(h\nu_e\vec{\nabla}u\right)+hF_x \tag{6}$$

$$\frac{\partial q_y}{\partial t}+\ div\left(q_y\vec{u}\right)=-gh\frac{\partial Z_S}{\partial y}+\ div\left(h\nu_e\vec{\nabla}v\right)+hF_y \tag{7}$$

where h = depth of water (m); $\vec{q}$ = vector of the scalar discharges q_x and q_y per unit length (m^2/s); u, v = depth averaged components of a two-dimensional velocity vector $\vec{u}$ (m/s) in x and y (horizontal) direction; g = gravitational acceleration (m/s^2); ν_e = diffusion coefficient, including dispersion and turbulence (m^2/s) and Z_S = free surface elevation (m). The software has been applied to many different fields of numerical modeling and research (e.g. (Capra et al., 2017; Chen et al., 2015; Sanyal, 2017; Stark et al., 2016; Vittecoq et al., 2017)).

4.2. Sediment transport and morphological module

The modeling package consists of an extra module for morphological issues, namely SISYPHE (SIS), which can be coupled to one of the above-mentioned hydrodynamic modules using a quasi-steady-state approach. Sediment transport is divided into suspended load and bed load. Furthermore, the module can represent multi-grain approaches such as hiding/exposure effects and riverbed armoring. The module is based on a mass-conservation equation - the Exner-Equation - to calculate the updating of the riverbed (Villaret et al., 2013). As only bedload is considered in this study, the Exner-Equation can be stated as follows:

$$(1-n)\frac{\partial Z_b}{\partial t}+\ \mathrm{div}\sum_i\vec{q}_{b,i}=S_b \tag{8}$$

where n = non cohesive bed porosity (−); Z_b = river bottom elevation (m); $\vec{q}_{b,i}$ = vector of bedload transport rate of fraction i per unit width (m^2/s) and S_b = local source for bottom elevation (m/s). Further information on the module can be found in Tassi and Villaret (2014).

The empirical, fractional bedload transport equation after Hunziker (1995) is applied in this study with the following structure:

$$|\ q_{b,i}\ |\ /\sqrt{(s-1)gd_{m,a}^3}=5f_i[\phi_i(\Theta_i-\Theta_{hunz})]^{1.5} \tag{9}$$

$$\Theta_{hunz}=\Theta_{\mathrm{crit}}\left(\frac{d_{m,s}}{d_{m,a}}\right)^{0.33} \tag{10}$$

$$\phi_i=\left(\frac{d_i}{d_{m,a}}\right)^{-\alpha} \tag{11}$$

where $|q_{b,i}|$ = magnitude of bedload transport rate of fraction i per unit width (m^2/s); s = specific density; g = gravitational acceleration (m/s^2); $d_{m,a}$ = mean diameter of surface bottom layer (m); f_i = availability of fraction i in the surface layer; ϕ_i = hiding/exposure factor of fraction i; Θ_i = dimensionless shear stress of fraction i; Θ_{hunz} = modification of the critical shear stress threshold Θ_{crit}; $d_{m,s}$ = mean diameter of subsurface bottom layer (m); d_i = diameter of grain class i (m) and α = correlation factor.

In applying the original morphological module for graded sediment transport, two main types of numerical instabilities and errors were observed. Firstly, for the numerical representation of sediment erosion to very thin layers, the sum of all sediment fractions was incomplete (i.e. <100%), which caused the simulation to abort. Secondly, cumulative errors occurred where simulations covered several days as the rounding error of the individual fractions was added up, which also led to termination. These errors are due to the implemented sediment layer concept, which updates the thickness and composition of the riverbed resulting from erosion and sedimentation. Similar errors are described by Dorfman et al. (2012). Reisenbüchler et al. (2016) developed an updated version of this module, which is applied in this study. These modifications are based on a vertical sediment layer concept, but in an implementation that follows Bui and Rutschmann (2010). Furthermore, this concept is extended by treating non-erodible regions in the domain differently, which are now represented by an additional, artificial grain class. This distinction provides a clear separation between movable and non-movable regions.

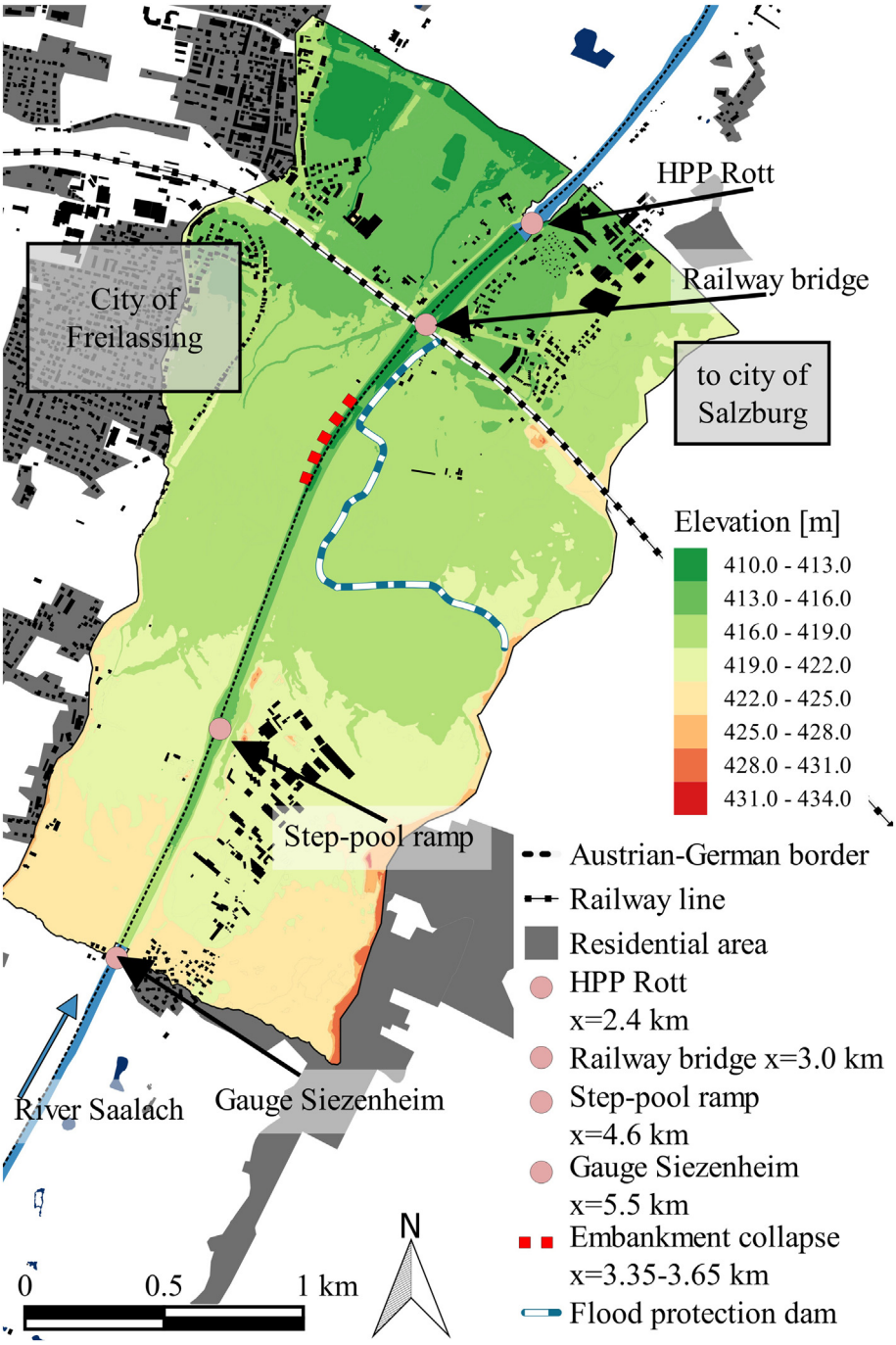

Fig. 8. Overview of the model area, including relevant sites. Map after (OpenStreetMap contributors, 2018).

Table 1
Definition of the developed geometrical and the applied numerical models.

Application	Date of the river bathymetry	Model designation	Applied numerical model
Calibration	Dec. 2005–Feb. 2006	M2006	T2D, T3D
Validation	Mar. 2013	M2013	T2D, T2DSIS
Scenario application	Mar. 2013 and maximum acceptable riverbed elevation at the HPP Rott	MSC	T2DSIS

4.3. Model setup

The modeled river reach is defined as a three-kilometer long section from the Siezenheim gauging station (x = 5.5 km) to the HPP Rott (x = 2.4 km) passing the step-pool ramp (x = 4.6 km) and a railway bridge, with an existing groundsill over the cross-section (x = 3.0 km), as shown in Fig. 8. At the Siezenheim gauging station, reliable measurements of the discharge in fifteen-minute time intervals have been available since 1985 (LfU, 2017). At the HPP Rott, information is available for the weir-operating-regulation, which defines the water elevation according to the discharge, as well as measurements during the latest flood events. The domain is discretized using a triangular unstructured grid with an average mesh size equal to 6.0 m along the river channel and a coarser mesh, with an average edge length of 10 m, to represent the floodplain. The heights of the geometry used for the floodplain are a digital elevation model, and interpolated cross-sectional measurements for the river, which were recorded every 200 m in distinct years (WWA-TS, 2013). In this study, several models are developed, whose specifications and applications are listed in Table 1.

The step-pool ramp, built in 2005–2006 was manually integrated in each model to represent its shape according to the construction plans (see Fig. 4). In total, the geometry consists of around 250,000 triangular elements and covers an area of 4.8 km^2. Data on the riverbed's granulometry are available from a previously performed drill-program in 1999, as well as from Beckers et al. (2015a); Beckers et al. (2016b); Beckers et al. (2015b). Based on this information, it can be assumed that the riverbed consists mostly of coarse gravel, which is discretized in eight different grain classes for modeling purposes. Furthermore, a vertical layering of the riverbed with a constant active layer thickness of $l_a = 0.14$ m thickness (=d_{max} of the sediment) and an active stratum with several additional substrate layers is defined, each up to three times the active layer. The characteristic mean diameter of the active layer is initially $d_{m,a} = 68$ mm and $d_{m,s} = 19$ mm for the substrate layers.

One pivotal issue in this framework is the correct representation of man-made structures in and along the river. Within the model area, there are several points to consider: the fixed embankments, the step-pool ramp with large stone settings (x = 4.6 km), the groundsill below the bridge (x = 3.0 km), and the intake structure in front of the hydropower plant (x = 2.4 km). These areas are considered as non-erodible in the context of sediment transport.

During the flood event of 2013, some parts of the fixed embankment structure collapsed. This not only lowered the elevation of the embankment, but supplied additional sediment material to the river. According to the WWA-TS, along x = 3.65 km to x = 3.35 km a volume of 21,000 m^3 bank materials was eroded (WWA-TS, 2013). The representation of such a sliding process cannot be captured by the applied morphological model directly. However, to include this aspect in the integrative modeling of the flood event in 2013, the following method is applied: the additional material is supplied in the river along this section via a temporal source during the high flood beginning at t = 47.75 h to t = 80.25 h. The collapsed embankments along the Bavarian side are lowered in our geometry of M2013 by up to 1 m to 416.7 m, according to the measurements after the event. By comparison, in a clear water model, it would not be possible to represent this additional material input.

5. Results and discussion

The TELEMAC-MASCARET system is capable of running in parallel mode using domain decomposition and MPI based codes, allowing us to decrease the computational time. The calibration, validation and scenario simulations have been carried out on a Linux-server with 64-cores at the Chair of Hydraulic and Water Resources Engineering, TUM.

5.1. Model calibration

During calibration, we determine if a 2D flow model represents the flow structures in the section of river analyzed or if a 3D model is necessary. Furthermore, we investigate whether available information on the riverbed roughness can be applied to our model, as this is the most important parameter for hydraulic simulations (Lane, 2014). Because the river has been straightened, the flow processes in the Saalach River are very regular; however, obstacles at the ramp, the groundsill, and the piers of the bridge may introduce some complex flow structures. Therefore, we simulated clear water first with T2D and T3D and then compared (fixed bed and no sediment transport). We selected a high flow event, as the desired model will be applied under these conditions. This comparison reveals the most accurate model taking into consideration computational effort. Models accuracy is evaluated using statistical goodness of fit (GOF) criteria. The GOF of the simulations is assessed by means of the coefficient of determination R^2, Nash-Sutcliffe-efficiency (NSE), the root mean square error (RMSE), and mean absolute error (MAE) (Moriasi et al., 2007). From an existing 2D model at the WWA-TS, roughness parameters are input in the models. The bed of the Saalach is a uniform Strickler roughness of k_{st} = 35 $m^{1/3}$ s^{-1}, representing coarse gravel material, and k_{st} = 25 $m^{1/3}$ s^{-1} at the fixed embankment. In the floodplain, Strickler values have been selected in line with the WWA-TS model, based on land use maps (meadows $k_{st} = 20$ $m^{1/3}$ s^{-1}; forest $k_{st} = 11$ $m^{1/3}$ s^{-1}; farmland $k_{st} = 24$ $m^{1/3}$ s^{-1}; residential area $k_{st} = 17$ $m^{1/3}$ s^{-1} and streets k_{st} = 40 $m^{1/3}$ s^{-1}) (WWA-TS, 2013). Furthermore, at modeled ramp, the roughness is adjusted according to the results of the technical report with $k_{st} = 20$ $m^{1/3}$ s^{-1} (Gostner, 2005). For T3D, nine vertical levels are defined to properly quantify the influence of vertical velocities.

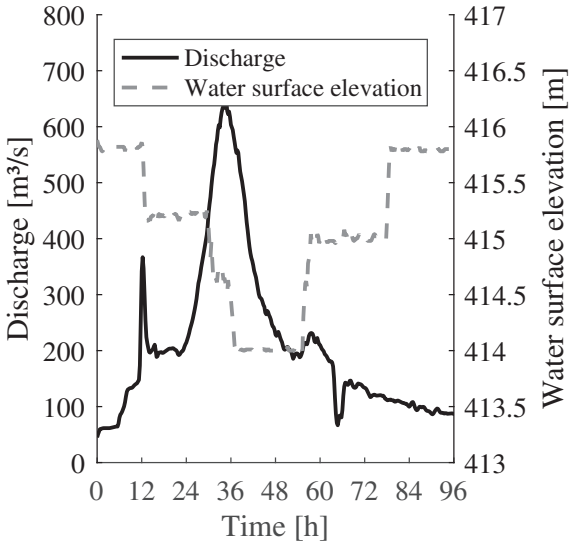

Fig. 9. Hydrodynamic boundary conditions for the calibration.

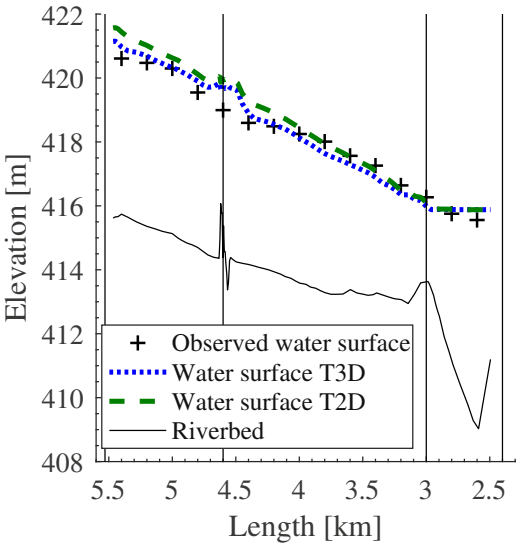

Fig. 10. Longitudinal section of observed and simulated water surfaces (T3D and T2D) and the riverbed elevation for the calibration.

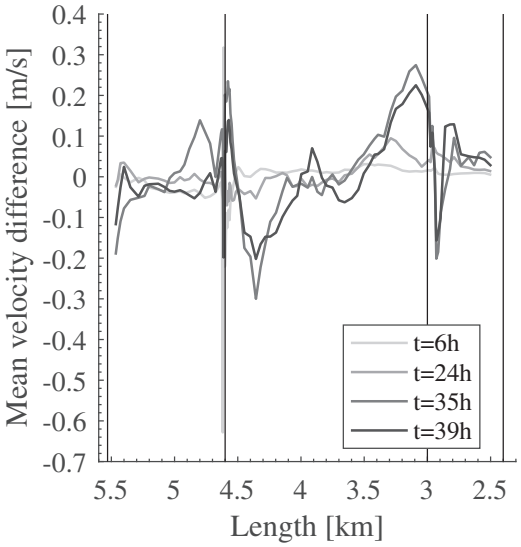

Fig. 11. Longitudinal section of mean velocity differences ($dv = \bar{v}_{T3D} - \bar{v}_{T2D}$) at different times t.

The number of vertical layers should be sufficiently high to represent 3D flow phenomena.

Water surface measurements along the river are used to quantify the accuracy of the simulations. In contrast to low or mean discharge situations, the information for flood events is often based on indirect measurements, performed after the event, e.g. derived from flood pathways or sediment lines at the embankment, and may include uncertainty.

Based on the available measurement data, an unsteady calibration scenario is run over a longer time frame, starting from a steady initial state with mean discharge conditions (Fig. 9). During calibration, we simulate the flood event in August 2006using the geometry M2006. The discharge increases from the mean flow and reaches the first peak ($Q = 350\ m^3/s$) at $t = 12$ h. At this point, the weirs at the HPP Rott are opened, leading to a drop in the water elevation. At $t = 24$ h, the flood wave increases to its final peak and at the hydropower plant the water elevation is lowered to 414.00 m (corresponding to the weir operating regulative). When the flood recedes, the reservoir is filled again by progressively closing the gates. During the flood event, no inundation of the floodplain occurs. We consider the morphological evolution during this flood event to be very low because the river is still dominated by the damming of the HPP Rott during the flood peak. Therefore, though some local sediment relocations may occur, the riverbed remains largely unchanged and thus allows a clear water model estimate of the roughness of the riverbed.

Fig. 10 provides the calculated distributions of water surface elevation using T2D and T3D and the observations, and Table 2 contains the corresponding statistical performance. The analysis demonstrates for this case that both models precisely predict the water surface elevation. The performance of the 2D model is only slightly lower than the 3D. In a visual comparison, the largest differences occur close to the location of the ramp, possibly because the flood event occurred half a year after the river bottom measurements were taken. In the intervening period, the area upstream of the ramp likely aggregates, so the transition from river to ramp is probably smoother than simulated. Errors in the observation are also possible, but cannot be quantified.

The differences betweenT2D and T3D, regarding the mean velocity, is evaluated in cross-sections at multiple, selected time steps. The flow velocities and the shear stresses derived from them are the driving force for sediment transport. If there are large velocity differences between the models, a different morphological development will occur. The selection of the time frames was made to capture all flow situations: the first time, $t = 6$ h, is selected at $Q = 80.02\ m^3/s$; the second right before the flood wave at $t = 24$ h; the third at the peak $t = 35$ h; and the last when the discharge is already decreasing at $t = 39$ h. Since velocity measurements were not conducted in this section of river, a comparison with the actual water velocity cannot be provided. Instead, the simulated mean velocities from T3D are set as reference values and compared with T2D. Fig. 11 provides absolute differences ($dv = \bar{v}_{T3D} - \bar{v}_{T2D}$) in the mean velocities at corresponding times along the river, and Table 3 shows the resulting error parameters, which also quantifies the difference between T2D and T3D.

During the 2006 flood event, velocity differences occur in a range between 0.35 and − 0.65 m/s. We found that the magnitude of the differences is roughly proportional to the discharge. At time $t = 6$ h, the discharge and the error display their minimum values representing identical velocities. The largest error appears at the peak discharge of around $Q = 650\ m^3/s$,; however, coefficients R^2 and NSE are still in the optimum range, and the RMSE and the MAE are very small, taking into account the high discharge and the absence of velocity measurements. The largest differences occur at the stone ramp (x = 4.6 km) since the structure introduces vertical velocities, whose influence can only be detected to a limited extent in a 2D model. A similar situation obtains at the groundsill of the railway bridge (x = 3.0 km), where the opening of the weirs causes something similar to a hydraulic jump.

Table 2
Performance criteria of the calibration for each applied numerical model.

Model	R^2	NSE	RMSE	MAE
	[−]	[−]	[m]	[m]
T2D	0.978	0.916	0.464	−0.293
T3D	0.976	0.961	0.317	−0.050

Table 3
Comparison of the simulated mean velocities using GOF criteria.

Time t	Discharge Q	R^2	NSE	RMSE	MAE
[h]	[m^3/s]	[−]	[−]	[m/s]	[m/s]
06:00	80.02	0.972	0.957	0.089	0.040
24:00	214.32	0.994	0.994	0.039	0.031
35:00	649.85	0.964	0.952	0.132	0.096
39:00	502.29	0.976	0.972	0.094	0.074

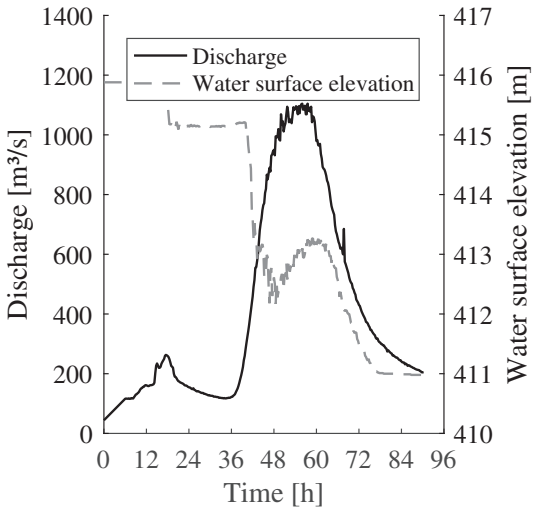

Fig. 12. Hydrodynamic boundary condition for the validation.

In summary, the comparison of the average velocity profiles of both flow models shows that, in the modeled river section, the T2D model is quite accurate, almost as precise as T3D. The good agreement between both models justify using T2D, as its computing time is about 12 times lower than that of T3D. As a result, the following hydromorphological simulations are performed with T2D.

5.2. Model validation

The representation of the processes during the 2013 flood event using the integrative model, T2D coupled with SIS, on the M2013 geometry, is carried out in this paper as the next step of model validation for accurate hydraulic calculation and as model calibration for hydromorphological calculation. The same bedload transport function is applied as Beckers et al. (2015a) use in their study, with the fractional bedload transport equation of Hunziker (1995), with a lowered critical Shields parameter of $\Theta_{crit} = 0.04$ for the beginning of sediment motion. With this adaptation, higher transport rates are modeled, which more realistically represents the characteristics of the Saalach River (Beckers et al., 2016a). A grain dependent roughness correction is applied to take into account granular changes in the riverbed. Here the quadratic grain dependent Nikuradse roughness is set in relation to the constant

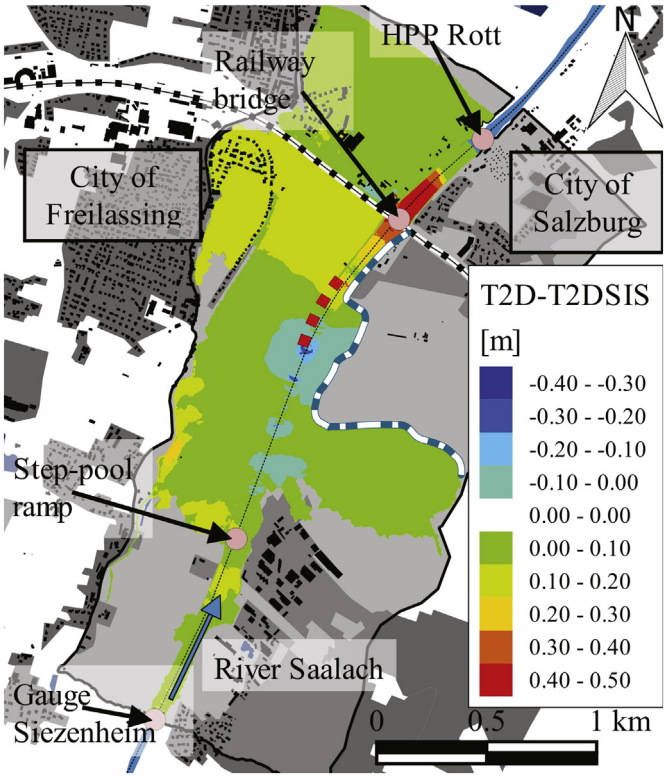

Fig. 14. Spatial differences of simulated maximum water surface elevation from clear water T2D and from integrative T2DSIS, on the geometry M2013. Map after (OpenStreetMap contributors, 2018).

quadratic bottom friction coefficient derived from the clear water simulation (Tassi and Villaret, 2014). This treatment directly affects the calculated bottom shear stress and therefore the sediment transport. In addition to the integrative approach including the morphology, a clear water simulation with T2D, excluding the morphology, is conducted for the flood event to highlight the importance of the integrative approach and identify any differences between both models.

The hydrodynamic boundary conditions are provided in Fig. 12, which shows the discharge at the inlet and water surface elevation at the outlet. Where an extraordinary discharge is indicated at $t = 12$ h, the weir is opened at the arrival of the first flood peak to decrease the

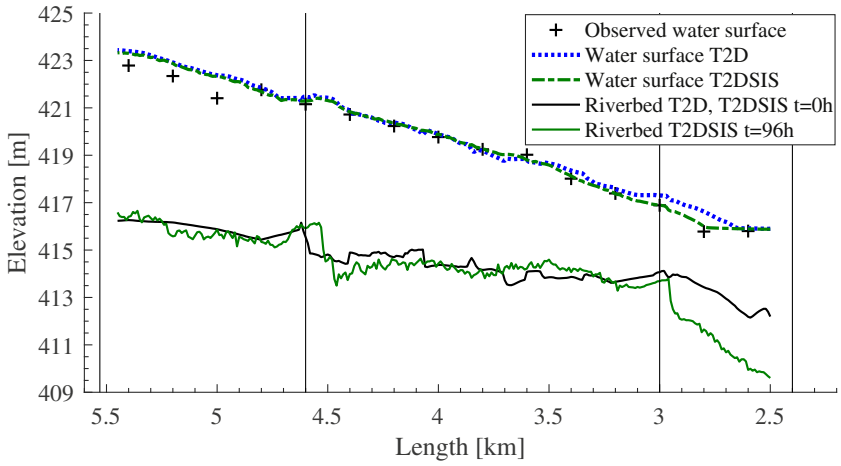

Fig. 13. Longitudinal section of the riverbed at $t = 0$ h (black) and at $t = 96$ h (green) and the maximum water surface from T2DSIS (green dashed) using the M2013 geometry; for comparison the maximum water surface from T2D (blue dashed) using the M2013 geometry at t = 0 h. (For interpretation of the references to colour in this figure legend, the reader is referred to the web version of this article.)

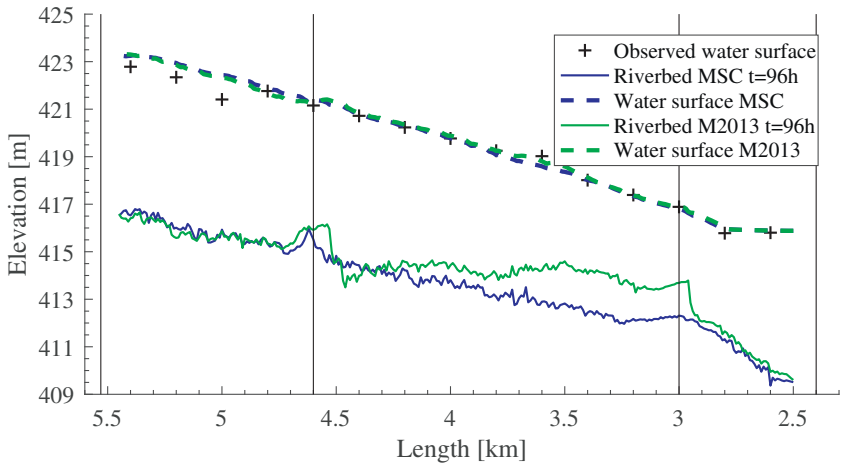

Fig. 15. Longitudinal section of the riverbed at t = 96 h (blue) and the maximum water surface (blue dashed) using the geometry MSC; for comparison the riverbed at t = 96 h (green) and the maximum water surface (green dashed) using the geometry M2013. (For interpretation of the references to colour in this figure legend, the reader is referred to the web version of this article.)

water elevation. At time t = 36 h, the weir is opened completely to provide the maximum discharge capacity in free-flow conditions. In this river, no bedload measurements are available, which would be necessary to define the sediment boundary condition. To overcome this limitation, a morphological equilibrium condition is defined at the inlet (Tassi and Villaret, 2014; Villaret et al., 2009). This boundary condition automatically delivers the bedload at the model inlet, defined by grain proportions and quantity, to keep the riverbed elevation at the inlet cross-section constant in time. An analysis of riverbed measurements from 2002 to 2013 validates this approach (Fig. 6). From 2002 to 2005 only very small changes can be identified in the upper reach x = 8 km to x = 6.0 km, but high variations are apparent in the reservoir in front of the HPP. As expected, the riverbed has risen in the section upstream of the ramp to x = 6.0 km since its construction in 2005–06. However, from 2009 to 2013, no further rising of the riverbed is apparent, and this sections seems to be in an equilibrium state. High morphological dynamics are visible only in the downstream section between the stone ramp x = 4.6 km and the groundsill x = 3.0 km.

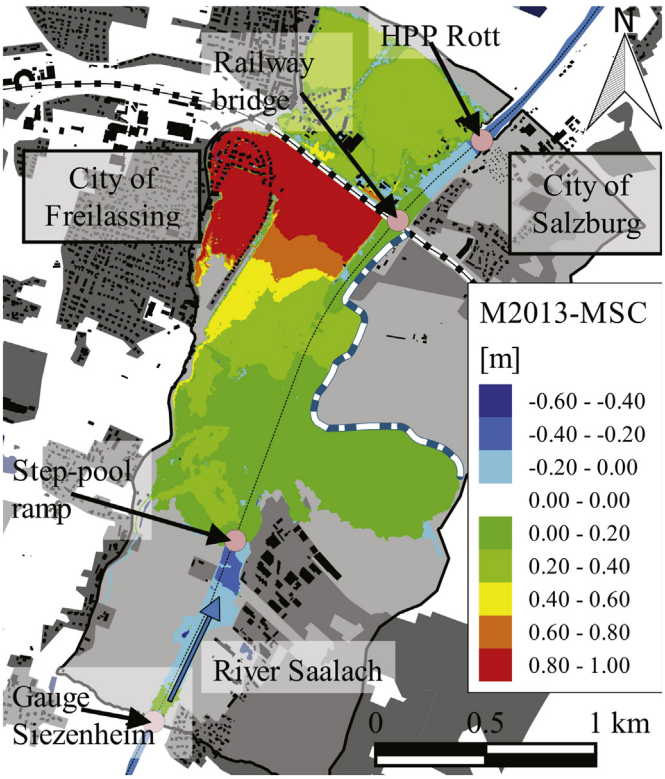

Fig. 16. Spatial differences of maximum water surface elevations using the T2DSIS model on the geometry M2013 and MSC. Map after (OpenStreetMap contributors, 2018).

Because no riverbed measurements were taken immediately after the 2013 event, the accuracy of the integrative model can only be assessed from the observed water surface elevation along the river. In Fig. 13, the longitudinal section of the modeled river is provided including the initial and final riverbed after the flood event and the maximum simulated water surface of the integrative model T2DSIS. The integrative model closely conforms to the measurements from the visual comparison as well as to the evaluation criteria (R^2 = 0.989, NSE = 0.979, RMSE = 0.325 m, MAE = 0.215 m). The morphological change during the flood event can be divided into three parts: one upstream of the ramp at x = 4.6 km, a second between the ramp and the groundsill at x = 3.0 km, and a third downstream of the groundsill. In the most upstream part x = 5.5 km to x = 4.6 km, only small bed changes occur, influenced by the equilibrium inlet boundary condition and the non-movable ramp structure. The step-pool ramp itself was filled with coarse sediment, a process that was also observed by the WWA-TS (WWA-TS, 2013). The second section between the ramp at x = 4.6 km and bridge x = 3.0 km, which is already part of the hydropower plant reservoir, was not significantly affected by flushing processes from the Rott HPP. The reason for this is the fixed ground structure at the bridge (x = 3.0 km) at 413.8 m, where a hydraulic jump breaks the flow. Only the third section, directly before the hydropower plant, shows greater morphological changes due to flushing. The WWA-TS and the operator of the HPP confirmed the simulated effects, which include partial flushing of the reservoir and aggregation at the ramp (WWA-TS, 2013).

Additionally, in Fig. 13 the maximum water surface elevations of the clear water model T2D are visible. The clear water model shows less agreement with the measurement according to the statistics (R^2 = 0.980, NSE = 0.961, RMSE = 0.439 m, MAE = 0.342 m), which is due to the differences in the region around the railway bridge at x = 3.0 km. Here the clear water model overestimates the water surface by up to 0.7 m because the reservoir flushing and the resulting higher channel capacity cannot be represented. The absence of sediment representation not only influences the modeling of water surface in the river but also the floodplain. Fig. 14 shows the absolute differences in the inundation between T2D and the coupled T2DSIS. T2D consequently

shows higher water surface elevations in the floodplain in a range of up to 0.20 m.

The results demonstrates that our integrative hydromorphological model is able to reproduce the measured water surface elevations more accurately than a clear water model, and at the same time provides a better understanding of the processes during the flood event.

5.3. Model application

We used the developed integrative model to analyze several technical measures designed to improve flood management in this region. The groundsill below the railway bridge was identified as a limiting factor for sediment transport during the 2013 flood event. Furthermore, the artificial extension at the step-pool ramp could have led to an accumulation of sediment close to the ramp and likely to a higher water surface elevation. We developed to study the impact of these structures, an additional geometry, called MSC. In this geometry, the non-erodible elevation below the bridge is defined 2 m lower at 411.85 m and the extension at the ramp is reduced by 17 m back to the original 35 m channel width. In addition, the riverbed elevation in the reservoir was adapted to represent the defined maximum allowed bed elevation. This adaptation is necessary to provide a statement that conforms to the legal regulations. For this scenario, the same hydro- and morphodynamic boundary conditions as for the validation scenario are applied (Fig. 12).

Fig. 15 shows that there is a difference in morphological development compared to the river section in original bed condition (M2013) and the modified one, MSC. The sedimentation of the ramp can be decreased even if this only has a very limited impact on the water surface at x = 4.6 km. Due to the reduction of the groundsill at x = 3.0 km, the riverbed in the whole reservoir is flushed out during the flood event and lower water elevations are reached. This has a further effect on the flood extension and the magnitude in the floodplain as can be seen in Fig. 16, which shows the differences in water surface between MSC and M2013. The depth of the simulated inundation in the city region of Freilassing is thereby decreased by up to 0.80 m, with an overall decrease of around 50% of the real flood event. The evaluated measures would help to design an efficient and suitable flood protection system for the city. For instance, future flood levees around the city could be lower if our proposed modifications were made to the river. This would reduce the construction costs of the planned measures drastically. On the other hand, if the levees are built at the planned height, our measures would ensure a higher level of security.

6. Conclusion

The TELEMAC-MASCARET modeling system incorporating our own developments for graded sediment transport was applied to simulate hydromorphodynamic processes in the lower Saalach River. The model reproduces the behavior of river flows for a high water condition using a 2D and a 3D model. Both models yield very accurate performance parameters. Applying a comparative analysis, we show that for this river section a computationally demanding 3D calculation does not provide more accurate results.

The 2D hydromorphodynamic model was successfully applied to the flood event of 2013 with the aim of improving process representation during the event and achieving accurate simulated high water surface elevations. As no real-time measurements of the riverbed or the transported material during the flood event were available, the morphological model is calibrated qualitatively based on process observations but not on real measurements. Furthermore, simulations were carried out for different scenarios to evaluate the effects of the step-pool ramp and potential improvements to the river for flood events. In addition, we demonstrated that lowering the groundsill below the railway bridge would significantly reduce water surface due to improved reservoir flush during flood events.

Moreover, this study shows that hydrodynamic flood inundation maps based on fixed riverbeds can lead to inaccurate estimates of the flood risk potential of a river. Only an integrative approach which includes the morphology and takes into account changes in the river structure is likely to ensure reliable inundation mapping for risk analysis. Water authorities should consider a bandwidth of possible riverbed elevations as benchmarks for inundation maps. We have also demonstrated the flood mitigation potential of riverbed flushing in a reservoir, which we recommend be analyzed further.

Acknowledgments

Data on the study site was provided by the Wasserwirtschaftsamt (Water Agency) in Traunstein, Germany. Their assistance is greatly appreciated. The first author would like to thank his colleagues at the Chair of Hydraulic and Water Resources Engineering at the Technical University of Munich for their helpful discussions. This research did not receive any specific funding from agencies in the public, commercial, or not-for-profit sectors.

References

Ata, R., 2017. Telemac2d User Manual. 7.2, EDF, online published. http://www.opentelemac.org/.

Beckers, F., Noack, M., Wieprecht, S., 2015a. Ergebnisse der Geschiebetransportmodellierung (GTM) im Unterlauf der Saalach. Publications of the Dept. of Hydraulic Engineering and Water Resources Management, Universität Stuttgart, online. http://www.iws.uni-stuttgart.de/publikationen/docs/Kurzfassung-Teilmodell%202.pdf.

Beckers, F., Sadid, N., Haun, S., Noack, M., Wieprecht, S., 2015b. Contribution of Numerical Modelling of Sediment Transport Processes in River Engineering: An Example of the River Saalach. IAHR World Congress 36, pp. 1–5. https://www.researchgate.net/publication/283666981_Contribution_of_numerical_modelling_of_sediment_transport_processes_in_river_engineering_an_example_of_the_river_Saalach.

Beckers, F., Noack, M., Wieprecht, S., 2016a. Geschiebetransportmodellierung (GTM) Salzach und Saalach - Teilmodel 2: Untere Saalach. Technical Report, Dept. of Hydraulic Engineering and Water Resources Management, Universität Stuttgart (unpublished).

Beckers, F., Noack, M., Wieprecht, S., 2016b. Reliability Analysis of a 2D Sediment Transport Model: An Example of the Lower River Salzach. Proceedings of the 13th International Symposium on River Sedimentation, pp. 147–152. https://www.researchgate.net/publication/308920158_Reliability_analysis_of_a_2D_sediment_transport_model_An_example_of_the_lower_river_Salzach.

Blöschl, G., Nester, T., Komma, J., Parajka, J., Perdigão, R.A.P., 2013. The June 2013 flood in the Upper Danube Basin, and comparisons with the 2002, 1954 and 1899 floods. Hydrol. Earth Syst. Sci. 17 (12), 5197–5212. https://doi.org/10.5194/hess-17-5197-2013.

BMLFUW, 2013. Hydrografisches Jahrbuch von Österreich 2013. 121. The Austrian Federal Ministry of Agriculture, Forestry, Environment and Water Management, Vienna, Austria. https://www.bmlfuw.gv.at/dam/jcr:bb100102-eac3-4b51-8d8d-f40b94e5d546/Jahrbuch_2013_Datenteil.pdf.

Bronstert, A., 2003. Floods and climate change: interactions and impacts. Risk Anal. 23 (3), 545–557. https://doi.org/10.1111/1539-6924.00335.

Bui, M.D., Rutschmann, P., 2010. Numerical modelling of non-equilibrium graded sediment transport in a curved open channel. Comput. Geosci. 36 (6), 792–800. https://doi.org/10.1016/j.cageo.2009.12.003.

BVV, 2017. Historical map of the River Saalach. Geoportal Bayern - BayernAtlas, Bayerische Vermessungs Verwaltung, online. https://v.bayern.de/bw8Gs, Accessed date: 12 November 2017.

Capra, H., Plichard, L., Bergé, J., Pella, H., Ovidio, M., McNeil, E., Lamouroux, N., 2017. Fish habitat selection in a large hydropeaking river: strong individual and temporal variations revealed by telemetry. Sci. Total Environ. 578, 109–120. https://doi.org/10.1016/j.scitotenv.2016.10.155.

Carr, K., Tu, T., Ercan, A., Kavvas, M., Nosacka, J., 2015. Two-dimensional Unsteady Flow Modeling of Flood Inundation in a Leveed Basin. World Environmental and Water Resources Congress 2015, pp. 1597–1606 https://doi.org/10.1061/9780784479162.156.

Chen, T., Joly, A., Pan, R., Ji, P., He, M., Chen, G., 2015. A methodology to analize the safety of a coastal nuclear power plant against the typhoon external flooding risks. J. Nucl. Radiochem. Sci. 3 (1), 7. https://doi.org/10.1115/1.4034974.

DKKV, 2015. Das Hochwasser im Juni 2013: Bewährungsprobe für das Hochwasserrisikomanagement in Deutschland. DKKV-Schriftenreihe 53, Deutsches Komitee Katastrophenvorsorge, Bonn, Germany. http://www.dkkv.org/fileadmin/user_upload/Veroeffentlichungen/Publikationen/DKKV_53_Hochwasser_Juni_2013.pdf

Dorfman, C., Harb, G., Zenz, G., 2012. Simulation of Hydrodynamic and Sediment Transport Processes – Two Austrian Case Studies. XIXth TELEMAC-MASCARET User Conference 2012, pp. 53–58. https://hdl.handle.net/20.500.11970/104215.

Duc, B.M., Bernhart, H.H., Kleemeier, H., 2005. Morphological numerical simulation of flood situations in the Danube River. Int. J. River Basin 3 (4), 283–293. https://doi.org/10.1080/15715124.2005.9635268.

Ertl, O., 1940. Der mittlere jährliche Gang des Wasserhaushalts der Saalach. Archiv für Wasserwirtschaft. 54. Reichsverband der Deutschen Wasserwirtschaft, Berlin.
Eybl, J., Godina, R., Lalk, P., Lorenz, P., Müller, G., Pavlik, H., Weilguni, V., Heilig, M., 2013. Hochwasser im Juni 2013–Die hydrographische Analyse. The Austrian Federal Ministry of Agriculture, Forestry, Environment and Water Management, Vienna, Austria. https://www.bmlfuw.gv.at/dam/jcr:c9a7d559-390a-4733-9888-acf8dc77a917/Hochwasser-VII3_Juni%202013-Hydrografie_1A_HP.pdf.
Gostner, R., 2005. Sohlrampe Saalach km 4,600 Bauentwurf/Einreichdetailprojekt. Technischer Bericht Ingenieurbüro Gostner und Aigner, Wals, Austria. http://geowasser.at/wp-content/referenzen/referenzdatenblaetter/WW_Seite3_Zeile7_Saalach-Sohlrampe_km_4-6.pdf.
Guan, M., Wright, N., Sleigh, A., 2015. Multiple effects of sediment transport and geomorphic processes within flood events: Modelling and understanding. Int. J. Sediment Res. 30 (4), 371–381. https://doi.org/10.1016/j.ijsrc.2014.12.001.
Guan, M., Carrivick, J.L., Wright, N.G., Sleigh, P.A., Staines, K.E.H., 2016. Quantifying the combined effects of multiple extreme floods on river channel geometry and on flood hazards. J. Hydrol. 538 (Supplement C), 256–268. https://doi.org/10.1016/j.jhydrol.2016.04.004.
Habersack, H., Kreisler, A., Rindler, R., Aigner, J., Seitz, H., Liedermann, M., Laronne, J.B., 2017. Integrated automatic and continuous bedload monitoring in gravel bed rivers. Geomorphology 291, 80–93. https://doi.org/10.1016/j.geomorph.2016.10.020.
Hajivalie, F., Arabzadeh, A., 2017. JAWRA Journal of the American Water Resources Association Science of the Total Environment. Int. J. Coast. Offshore Eng. 1 (1), 33–41. https://doi.org/10.18869/acadpub.ijcoe.1.1.33.
Hengl, M., 2014. Dimensionierung aufgelöster Rampen und praktische Erfahrungen. Forschung und Entwicklung zur Qualitätssicherung von Maßnahmen an Bundeswasserstraßen. Bundesantsalt für Gewässerkunde, Koblenz, Germany, pp. 119–123 https://doi.org/10.5675/BfG_Veranst_2015.1.
Hengl, M., Krouzecky, N., Baumer, A., Ulmer, B., 2007. Aufgelöste Rampe in der Saalach. Sohlrampe Saalach Fluss-km 4.6, Bundeswasserbauverwaltung, Salzburg, Austria. https://landversand.salzburg.gv.at/WebRoot/Store/Shops/Landversand/5252/A40F/7ED4/A3EA/16E9/4DEB/AE3E/2475/2043-20007-2007saalachrampe.pdf.
Hervouet, J.M., 2007. Hydrodynamics of Free Surface Flows: Modelling With the Finite Element Method. John Wiley and Sons, Chichester, England https://doi.org/10.1002/9780470319628.
Hunziker, R.P., 1995. Fraktionsweiser Geschiebetransport. 11037. Laboratory of Hydraulics, Hydrology and Glaciology (VAW), ETH Zürich, Zürich, Switzerland. https://doi.org/10.3929/ethz-a-001503776.
Janin, J.M., Lepeintre, F., Péchon, P., 1992. TELEMAC-3D: a finite element code to solve 3D free surface flow problems. In: Partridge, P.W. (Ed.), Computer Modelling of Seas and Coastal Regions. Springer Netherlands, Dordrecht, Netherlands, pp. 489–506 https://doi.org/10.1007/978-94-011-2878-0_36.
Lane, S.N., 2014. Acting, predicting and intervening in a socio-hydrological world. Hydrol. Earth Syst. Sci. 18 (3), 927–952. https://doi.org/10.5194/hess-18-927-2014.
LAWA, 2010a. Recommendation for the Establishment of Flood Risk Management Plans. 139. German Working Group on Water Issues of the Federal States and the Federal Government (LAWA), Dresden, Germany. http://www.lawa.de/documents/LAWA_HWRM-Plaene26032010_Text_Germany_ENG_337.pdf.
LAWA, 2010b. Recommendations for the Establishment of Flood Hazard Maps and Flood Risk Maps. 139. German Working Group on Water Issues of the Federal States and the Federal Government, Dresden, Germany. http://www.lawa.de/documents/LAWA_HWGK15062010_Text_Germany_ENG_f72_4d8.pdf.
LfU, 2014. Junihochwasser 2013. Wasserwirtschaftlicher Bericht, Bavarian Environment Agency Augsburg, Germany. https://media.hnd.bayern.de/berichte/Junihochwasser2013_2014-02-26_2.pdf.
LfU, 2017. Hochwassernachrichtendienst. http://www.hnd.bayern.de/pegel/inn/siezenheim-18643505/statistik.
Mattic, O., 2017. Telemac3d user manual. 7.2, EDF. online published. http://www.opentelemac.org/.
Meyer-Peter, E., Müller, R., 1948. Formulas for Bed-load Transport. Proc., Proceedings of the International Association for Hydraulic Research, IAHR pp. 39–64.
Moriasi, D.N., Arnold, J.G., Van Liew, M.W., Bingner, R.L., Harmel, R.D., Veith, T.L., 2007. Model evaluation guidelines for systematic quantification of accuracy in watershed simulations. Trans. Am. Soc. Agric. Eng. 50 (3), 885–900. https://doi.org/10.13031/2013.23153.
Moulinec, C., Denis, C., Pham, C.T., Rougé, D., Hervouet, J.M., Razafindrakoto, E., Barber, R.W., Emerson, D.R., Gu, X.J., 2011. TELEMAC: an efficient hydrodynamics suite for massively parallel architectures. Comput. Fluids 51 (1), 30–34. https://doi.org/10.1016/j.compfluid.2011.07.003.
Nelson, J.M., McDonald, R.R., Shimizu, Y., Kimura, I., Nabi, M., Asahi, K., 2016. Modelling flow, sediment transport and morphodynamics in rivers. In: Kondolf, G.M., Piegay, H. (Eds.), Tools in Fluvial Geomorphology. John Wiley & Sons, Ltd., pp. 412–455 https://doi.org/10.1002/9781118648551.ch18.
Nujic, M., 2002. Hydro_As-2d - Ein zweidimensionales Strömungsmodell für die wasserwirtschaftliche Praxis, Benutzerhandbuch (User Manual).
OpenStreetMap contributors, 2018. MapData. online:. https://www.openstreetmap.org.
Reisenbüchler, M., Bui, M.D., Rutschmann, P., 2016. Implementation of a new layer-subroutine for fractional sediment transport in Sisype. In: Bourban, S. (Ed.), Proceedings of the XXIIIrd Telemac-Mascaret User Conference. HR Wallingford Ltd, Wallingford, England , pp. 215–220. http://www.opentelemac.org/images/clubu/2016/XXIII-TELEMAC-MASCARET-user-conference-2017.pdf.
Ricci, S., Piacentini, A., Weaver, A., Ata, R., Goutal, N., Lollino, M.A.G., 2015. Variational data assimilation with telemac. Proof of concept for model state correction on the berre lagoon 3D-model. In: Guzzetti, F., Culshaw, M., Bobrowsky, P., Luino, F. (Eds.), Engineering Geology for Society and Territory. Springer, Cham, Germany, pp. 633–637 https://doi.org/10.1007/978-3-319-09048-1_123.
Rickenmann, D., Badoux, A., Hunzinger, L., 2016. Significance of sediment transport processes during piedmont floods: the 2005 flood events in Switzerland. Earth Surf. Process. Landf. 41 (2), 224–230. https://doi.org/10.1002/esp.3835.
van Rijn, L.C., 1984. Sediment transport, part III: bed forms and alluvial roughness. J. Hydraul. Eng. 110 (12), 1733–1754. https://doi.org/10.1061/(ASCE)0733-9429(1984)110:12(1733).
Röthlisberger, V., Zischg, A.P., Keiler, M., 2017. Identifying spatial clusters of flood exposure to support decision making in risk management. Sci. Total Environ. 598 (Supplement C), 593–603. https://doi.org/10.1016/j.scitotenv.2017.03.216.
Sanyal, J., 2017. Uncertainty in levee heights and its effect on the spatial pattern of flood hazard in a floodplain. Hydrol. Sci. J. 62 (9), 1483–1498. https://doi.org/10.1080/02626667.2017.1334887.
Schramm, J.-M., 2012. Geologische Folgewirkung einer “nassen Grenze” – Zum kausalen Zusammenhang zwischen Napoleons Kriegen und technisch geologischen Problemen im Salzburger Stadtbereich. In: Angetter, D., Hubmann, B., Seidl, J. (Eds.), Berichte der Geologischen Bundesanstalt. Verlag der Geologischen Bundesanstalt (GBA), Vienna, Austria , pp. 344–374. http://www.zobodat.at/pdf/BerichteGeolBundesanstalt_96_0037-0044.pdf.
Shields, A., 1936. Application of Similarity Principles and Turbulence Research to Bed-load Movement. 167. Hydrodynamics Laboratory California Institute of Technology, Pasadena. https://authors.library.caltech.edu/25992/1/Sheilds.pdf.
Skublics, D., Blöschl, G., Rutschmann, P., 2016. Effect of river training on flood retention of the Bavarian Danube. J. Hydrol. Hydromech. 64 (4), 349–356. https://doi.org/10.1515/johh-2016-0035.
Stark, J., Plancke, Y., Ides, S., Meire, P., Temmerman, S., 2016. Coastal flood protection by a combined nature-based and engineering approach: Modeling the effects of marsh geometry and surrounding dikes. Estuar. Coast. Shelf Sci. 175, 34–45. https://doi.org/10.1016/j.ecss.2016.03.027.
Stephan, U., Hengl, M., 2010. Physical and numerical modelling of sediment transport in river Salzach. In: Dittrich, A., Koll, K., Aberle, J., Geisenhainer, P. (Eds.), River Flow 2010. Federal Waterways Engineering and Resarch Institute, Karlsruhe, Germany , pp. 1259–1265. https://hdl.handle.net/20.500.11970/99777.
StMUV, 2015. Hochwasserrisikomanagement-Plan für den bayerischen Anteil der Flussgebietseinheit Donau. Bavarian State Ministry of the Environment and Consumer Protection, Munich, Germany https://www.lfu.bayern.de/wasser/hopla_donau/doc/hwrmp_donau_endversion.pdf.
Tassi, P., Villaret, C., 2014. Sisyphe user's manual. 6.3, EDF, online published. http://www.opentelemac.org/.
Thieken, A.H., Kienzler, S., Kreibich, H., Kuhlicke, C., Kunz, M., Mühr, B., Müller, M., Otto, A., Petrow, T., Pisi, S., Schröter, K., 2016. Review of the flood risk management system in Germany after the major flood in 2013. Ecol. Soc. 21 (2), 12. https://doi.org/10.5751/ES-08547-210251.
Tu, T.B., Carr, K.J., Ercan, A., Trinh, T., Kavvas, M.L., Nosacka, J., 2017. Assessment of the effects of multiple extreme floods on flow and transport processes under competing flood protection and environmental management strategies. Sci. Total Environ. 607-608, 613–622. https://doi.org/10.1016/j.scitotenv.2017.06.271.
Villaret, C., Hervouet, J., Huybrechts, N., Van, L., Davies, A., 2009. In: Villaret, C., et al. (Eds.), Effect of bed friction on morphodynamic modelling: application to the central part of the Gironde estuary. CRC Press, Proceedings of the River, Coastal and Estuarine Morphodynamics Conference, pp. 890–899.
Villaret, C., Hervouet, J.-M., Kopmann, R., Merkel, U., Davies, A.G., 2013. Morphodynamic modeling using the Telemac finite-element system. Comput. Geosci. 53, 105–113. https://doi.org/10.1016/j.cageo.2011.10.004.
Vittecoq, M., Gauduin, H., Oudart, T., Bertrand, O., Roche, B., Guillemain, M., Boutron, O., 2017. Modeling the spread of avian influenza viruses in aquatic reservoirs: a novel hydrodynamic approach applied to the Rhône delta (southern France). Sci. Total Environ. 595, 787–800. https://doi.org/10.1016/j.scitotenv.2017.03.165.
Wilcock, P.R., Crowe, J.C., 2003. Surface-based transport model for mixed-size sediment. J. Hydraul. Eng. 129 (2), 120–128. https://doi.org/10.1061/(ASCE)0733-9429(2003)129:2(120).
Wu, W., 2004. Depth-averaged two-dimensional numerical modeling of unsteady flow and nonuniform sediment transport in open channels. J. Hydraul. Eng. 130 (10), 1013–1024. https://doi.org/10.1061/(ASCE)0733-9429(2004)130:10(1013).
Wu, W., 2007. Computational River Dynamics. Taylor & Francis, London.
WWA-TS, 2013. In: Heinz, R., Prokoph, R., Skublics, D. (Eds.), Dataset for the Analysis of the Saalach Flood in 2013.
WWA-TS, 2016. Umsetzungskonzepte für die Flusswasserkörper 1-F652 Saalach mit Saalachstausee bis unterhalb Piding und 1-F653 Saalach von unterhalb Piding bis Mündung in die Salzach. EG-Wasserrahmenrichtlinie, Wasserwirtschaftsamt Traunstein, Traunstein, Germany http://www.wwa-ts.bayern.de/fluesse_seen/massnahmen/wrrl_saalach/doc/wrrl_saalach.pdf.
Zitka, H.-R., 1959. Die wirtschaftlichen Veränderungen im bayerischen Raum zwischen Inn und Salzach. Schriften des Instituts für Kultur-und Solzialfoschung e. 6. Edmund Gans Verlag, Munich, Germany.

4.3. Flussökologisches Modellsystem

Morphologische Veränderung in Flüssen kann eine potenzielle Gefährdungsquelle für den ökologischen Zustand der Gewässer darstellen. Wesentliche Risiken entstehen durch die direkte Wirkung auf benthische Organismen, die das Sediment als Nahrungs- bzw. Fortpflanzungshabitat nutzen. Als Beispiel sei hier genannt, dass der Eintrag von Feinsedimenten aus verschiedensten Quellen vor allem für kieslaichende Fischarten, wie Nase, Barbe, Nerfling, Äsche und Bachforelle, einen erheblichen Gefährdungsfaktor darstellen kann. Durch das Zusetzen des Lückensystems im Gewässergrund wird die natürliche Fortpflanzung erheblich gestört, weil die abgelegten Eier von der Sauerstoffversorgung abgeschnitten werden und letztendlich absterben.

Im Folgenden sind zwei Artikeln zusammengefasst:

1. Bui, M.D.; P. Rutschmann (2015c): „Anwendung eines numerischen Modellsystems zur Bewertung von Geschiebehaushalt und Äsche-Laichhabitaten des Hochrheins“. Wasserwirtschaft. Vol. 105, Nr. 7-8. Springer.
2. Yao, W.; M.D. Bui; P. Rutschmann (2018): “Development of eco-hydraulic model for assessing fish habitat and population status in freshwater ecosystems”. Ecohydrology. Vol. 11, Issue 5. Wiley.

In Studie [1] wird ein Computermodellsystem zur Simulation und Bewertung der hydromorphologischen Prozesse und der Fischhabitateignungen sowie deren Verbesserungspotenziale im Hochrhein vorgestellt. In Artikel [2] wird ein Öko-Hydraulikmodell entwickelt, mit dem hydromorphodynamische Prozesse, das Fischhabitat und die Fischpopulation simuliert werden können. Das Modell wurde in der Aare in der Schweiz implementiert. Die Auswirkungen der Hydromorphodynamik auf das Habitat und die Fischpopulation wurden diskutiert. Die beiden entwickelten Modellsysteme bieten die Möglichkeit, negative Aspekte eines Projekts umzugestalten, zu erneuern und zu minimieren sowie die Möglichkeit zu erhöhen, ein hohes Maß an ökologischer Integrität zu erreichen.

Minh Duc Bui und Peter Rutschmann

Anwendung eines numerischen Modellsystems zur Bewertung von Geschiebehaushalt und Äsche-Laichhabitaten des Hochrheins

Ein mehrdimensionales Computermodellsystem zur Simulation und Bewertung der hydromorphologischen Prozesse und der Fischhabitateignungen sowie deren Verbesserungspotenziale in großen Flüssen wird vorgestellt. Das Werkzeug zeigt die Möglichkeiten moderner Programme auf und illustriert deren Einsatz sowie Vorteile für entsprechende Untersuchungen am Beispiel des Hochrheins. Die Ergebnisse zeigen, dass mit solchen Werkzeugen geplante Flussbaumaßnahmen auf deren Erfolg und Kosteneffizienz untersucht werden können und dass Sohlen- und Habitatänderungen im Fluss nicht aus Sicht einer „Mittelwertsoptik" gesehen und beurteilt werden dürfen, sondern dass in den entsprechenden Prozessen eine hohe Dynamik stattfindet und zu berücksichtigen ist.

1 Einleitung

Die Hochrheinstrecke zwischen Bodensee und Rhein kann in zwei Abschnitte unterteilt werden: In einen oberen, vom Bodensee bis zur Mündung der voralpinen Thur bei Andelfingen, und in einen unteren Abschnitt bis zur Landesgrenze bei Basel. Während im oberen Abschnitt keine großen Geschiebeumlagerungen zu erwarten sind, fanden im unteren Abschnitt früher große Umlagerungen statt. Ab 1900 wurden im Rhein allerdings elf Staustufen gebaut, so dass heute nur noch vier frei fließende Flussstrecken existieren, innerhalb derer die hydromorphologischen Prozesse durch den Kraftwerksbau kaum beeinflusst sind. Die übrigen Strecken sind entweder Stauhaltungen oder Ausleitungsstrecken. Dies in Verbindung mit der zunehmenden Verbauung der Zuflüsse und Ufer führt zu einer Unterbrechung des Fließgewässerkontinuums und zu einer weitgehenden Unterbindung der natürlichen, dynamischen Prozesse mit vielschichtigen Auswirkungen auf die Hydromorphologie und die Fischfauna. So hat beispielsweise der Gesamtfang von Äschen im Hochrhein seit den 90er-Jahren drastisch abgenommen [1], [4].

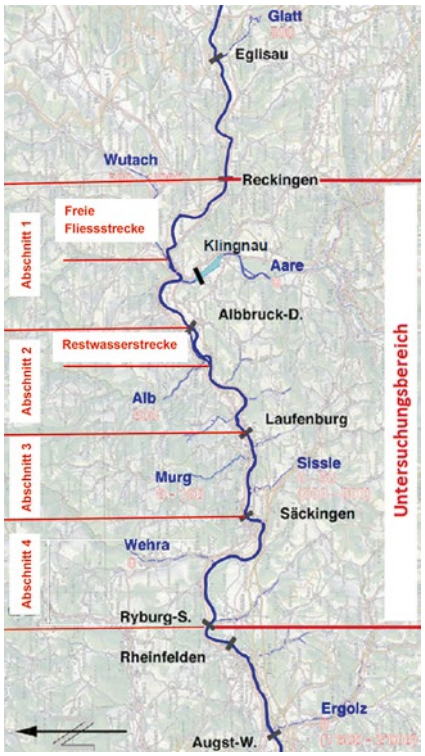

Bild 1: Untersuchungsgebiet für die Modellierungen (Quelle: [6])

Da der Hochrhein in den kommenden Jahren wieder vermehrt für das Geschiebe durchgängig gemacht werden soll, wurde durch das schweizerische Bundesamt für Energie und das baden-württembergische Regierungspräsidium in Freiburg eine Arbeitsgemeinschaft mit einer Studie beauftragt, an der neben zwei privaten Auftragnehmern (Flussbau AG, WFN – Wasser Fisch Natur) auch die TU München mit Geschiebe- und Fischhabitat-Berechnungen beteiligt war. Der Lehrstuhl für Wasserbau und Wasserwirtschaft der TU München hat eine mehrdimensionale Modellierung des rund 50 km langen Bereichs zwischen Reckingen und Ryburg-Schwörstadt durchgeführt (**Bild 1**). Dabei wird u. a. eine Reaktivierung des Geschiebetransports und damit eine Verbesserung der Habitat-Bedingungen für die gefährdete Äsche angestrebt. Als Aktivierungsmaßnahmen für das Geschiebe wurden Stauabsenkungen während Hochwasser, aber auch Geschiebezugaben stromabwärts von Wasserkraftanlagen untersucht. Ebenfalls wurden Untersuchungen durchgeführt, inwiefern die Habitat-Bedingungen für Äschen durch Geschiebezugaben unterschiedlicher Volumina sowie mit selektiver und optimierter

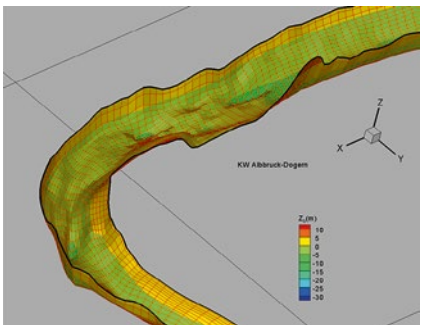

Bild 2: Exemplarisches Gitternetz (Quelle: [6])

Kornverteilungskurve verbessert werden können. Die erzielten Berechnungsergebnisse zeigen die Dynamik in Stauräumen während eines Hochwassers sowohl in Bezug auf die Geschiebebewegungen als auch auf die Habitat-Änderungen auf.

2 Das Programsystem FAST

Die Untersuchungen wurden mit dem Programm FAST (Flow Analysis Simulation Tool) durchgeführt, einem Werkzeug, das an der Universität Karlsruhe entstand [2] und in den letzten zehn Jahren an den Universitäten Innsbruck und München kontinuierlich weiterentwickelt wurde. Die Modellstruktur des Codes besteht aus mehreren Modulen. Das erste berechnet die Wassergeschwindigkeiten, die Sohlenschubspannungen und die turbulenten Schubspannungen. Das zweite dient der Berechnung des Geschiebe- und Schwebstofftransports sowie der Gesamttransportrate. In Abhängigkeit des Gesamttransports wird abschließend die Sohlenveränderung im dritten Modul berechnet. Das vierte Modul berücksichtigt die hydromorphologischen Resultate und ermittelt unter Beachtung der präferierten Bedingungen einer bestimmten Fischspezies die Habitat-Eignung in Bezug auf diese Art.

2.1 Hydromorphologische Berechnung

Den Simulationen der Strömung liegen die 2-D-Flachwassergleichungen zugrunde, die allerdings analytisch so verbessert werden, dass ein quasi 3-D-Strömungsfeld resultiert. Neben einer vertikalen, logarithmischen Geschwindigkeitsverteilung können auch 3-D-Sekundärströmungen berechnet werden, indem Dispersionsterme aus den vertikalen Ungleichförmigkeiten der Strömung im entsprechend angepassten, tiefengemittelten k-ε-Turbulenzmodell Berücksichtigung finden.

Der sich im lokalen Gleichgewicht mit der Strömung befindliche Geschiebetransport kann alternativ mit unterschiedlichen Transportformeln ermittelt werden. Hier wird eine Beziehung verwendet, die den Geschiebetransport unter Ungleichgewichtsbedingungen durch die Lösung einer semi-empirischen Bilanzgleichung berücksichtigt. Durch Anwendung eines quasi 3-D-Strömungsmodells wird im Sedimenttransportmodul der Einfluss der Sohlenneigung und der Gerinnekrümmung auf die Größe sowie die Richtung des Geschiebetransports berücksichtigt. Zur Berechnung des Schwebstofftransports wird die tiefengemittelte Advektions-Diffusionsgleichung eingesetzt. Die Transportberechnungen werden in Abhängigkeit der im hydrodynamischen Modul berechneten Strömungsverhältnisse durchgeführt. Das Modell zur Berechnung der Geschiebefracht arbeitet mit dem Konzept aktiver und inaktiver Sohlenschichten. Zwei Prozesse werden simuliert: (1) Die Durchmischung zwischen Sohlenmaterial und dem Flüssigkeits-Geschiebe-Gemisch durch die Bewegung der Flüssigkeit und (2) die Durchmischung zwischen aktiver und inaktiver Schicht durch die Bewegung der Sohlenoberfläche.

Die Sohlenveränderung kann als Summe aller Änderungsraten je Kornfraktion angegeben werden. Die Änderungsrate der Anteile jeder Fraktion basiert auf der Massenbilanz für das Sediment. In Gerinnen mit fraktionierten Sohlenmaterialien sind die großen Körner übermäßig dem Strömungsangriff ausgesetzt. Die kleinen Körner sind im Strömungsschatten der großen Körner, weshalb ihre Transportkapazität verringert wird. Zur Berücksichtigung dieser Effekte führt man in dem mathematischen Modell den sog. Hiding/Exposure-Faktor ein, wodurch der kritische Shields-Parameter oder die Geschiebefracht modifiziert wird. Es existieren verschiedene, empirische Formeln für den Hiding/Exposure-Faktor. In der Arbeit wird die von Wu et al. [2] modifizierte Meyer-Peter-&-Müller-Formel benutzt. Die Sortierungsprozesse oder Kornanteilveränderungen in der Deck- und Unterschicht können durch die Massenerhaltungsgleichung beschrieben werden.

Die partiellen Differentialgleichungen für Strömung und Sedimenttransport in einem krummlinigen Koordinatensystem werden in allgemeiner Tensornotation aufgestellt. Die numerische Lösung dieser Erhaltungsgleichungen erfolgt mit der Finiten-Volumen-Methode. Zur Erfassung komplexer Gebietsberandungen werden randangepasste, numerische Gitter aus weitgehend beliebig geformten Viereckelementen verwendet. Für die Flachwasser-Gleichungen wird ein Verfahren einge-

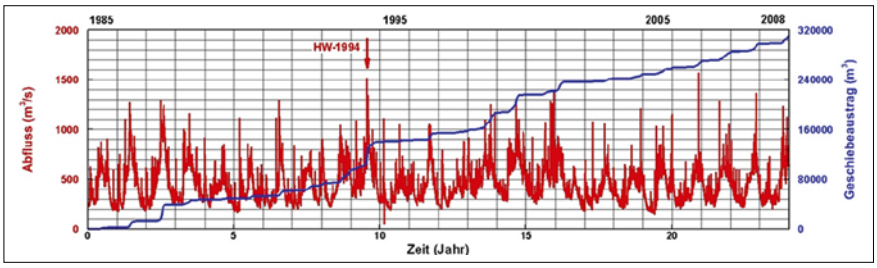

Bild 3: Zeitlicher Verlauf des Geschiebeaustrags aus der Stauhaltung zwischen KW Reckingen und KW Albbruck-Dogern (Quelle: [6])

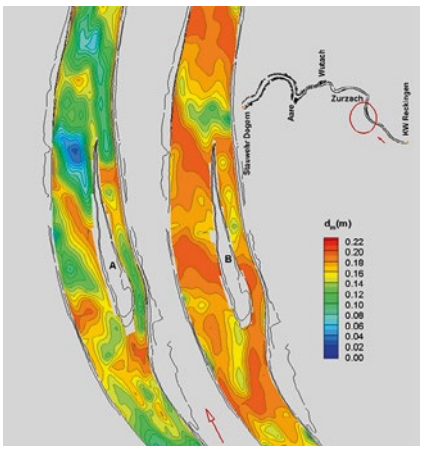

Bild 4: Mittlere Korndurchmesser der Deckschicht (dm) vor (A) und nach (B) dem Hochwasser 1994 (Quelle: Bui und Rutschmann)

Bild 5: Prozentualer Flächenanteil der für den Äsche-Laich geeigneten Flächen in der freien Fließstrecke vor und nach dem Hochwasser 1994 (Quelle: Bui und Rutschmann)

setzt, das die direkte Lösung der Kontinuitätsgleichung und die Technik des Druckkorrekturalgorithmus kombiniert. Die zeitabhängigen Terme in den Erhaltungsgleichungen des hydrodynamischen Moduls sowie des Sedimenttransportmoduls werden mit einem impliziten Verfahren erster Ordnung in der Zeit approximiert. Mit Ausnahme der Sohlenveränderung- bzw. Kornsortierungsgleichung und der Gleichung für Ungleichgewichts-Geschiebetransport haben sämtliche Erhaltungsgleichungen die gleiche Struktur. Die daraus resultierenden Matrizen sind schwach besetzt und haben überwiegend Bandstruktur, so dass sie sehr effizient z. B. mit dem Thomas-Algorithmus gelöst werden können. Eine detaillierte Herleitung der Gleichungen und deren numerische Lösungsverfahren können Bui [2] und Bui et al. [3] entnommen werden.

2.2 Fischhabitat

Die meisten neueren Fischhabitat-Modelle benutzen die Fließgeschwindigkeit, die Wassertiefe, das Sohlensubstrat und teilweise die Wassertemperatur zur Charakterisierung der Eignung. Der Maßstab für die Habitat-Qualität einer räumlichen Einheit ist der Habitat-Eignungsindex (Habitat Suitability Index, HSI). Dieser Index hat einen Wert von 0 bis 1, mit 0 für ein ungeeignetes Habitat und 1 für ein optimal geeignetes Habitat.

Als Kenngrößen zur Quantifizierung der Habitat-Qualität werden der hydraulische Habitat-Eignungsindex (Hydraulic Habitat Suitability Index, HHS) und zur Quantifizierung des Habitat-Angebots die gewichtete nutzbare Fläche (Weighted Usable Area, WUA) verwendet. Die WUA wird berechnet durch die Multiplikation aller Einzelflächen (A_i) mit ihrer Eignung (HSI_i) und nachfolgender Aufsummierung. Durch Teilen dieses integralen Habitat-Angebots WUA durch die benetzte Fläche erhält man den HHS. Dieser beschreibt demnach das Habitat-Angebot als prozentualen Wert und eliminiert so den Einfluss der mit dem Abfluss veränderlichen benetzten Fläche.

Daten bezüglich der Präferenzen bzw. Anforderungen einer Fischart können je nach Modellierungsmethode in unterschiedlicher Form berücksichtigt werden. Die üblichste Methode ist die Anwendung der sogenannten Präferenzkurve. Für jede Rechenzelle eines Flussstreckenmodells werden partielle Eignungsindices (Suitability Indices, SI) für eine Fischart berech-

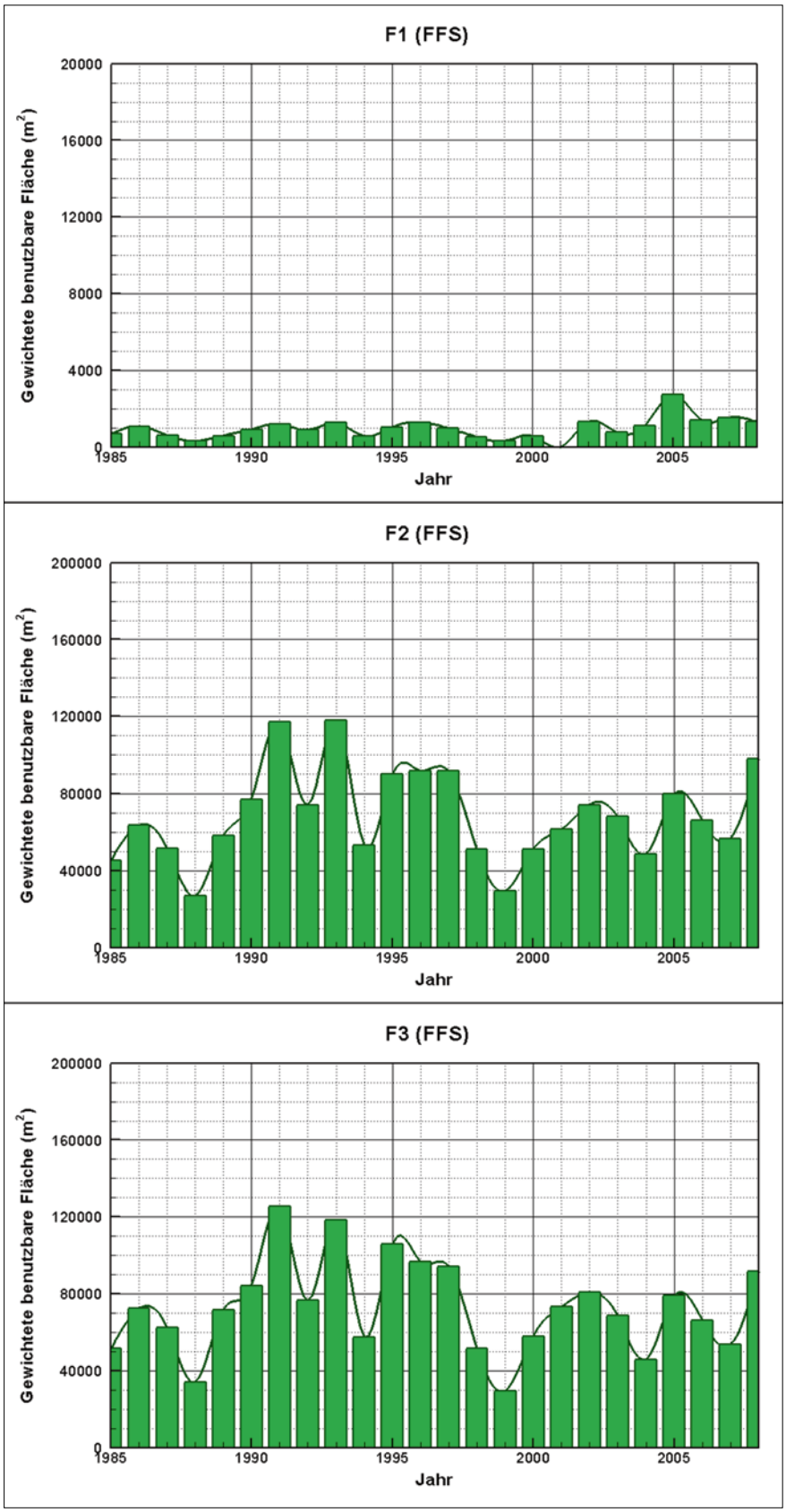

Bild 6: Zeitlicher Verlauf der gewichteten, benutzbaren Fläche in der freien Fließstrecke während der Laichzeit; im mittleren Bild (F2) werden oberhalb der Stauwurzel 10 000 m³ Geschiebe zugegeben, im unteren Bild (F3) die doppelte Menge von 20 000 m³; oben (F1) das Referenzbild ohne Zugaben (Quelle: [6])

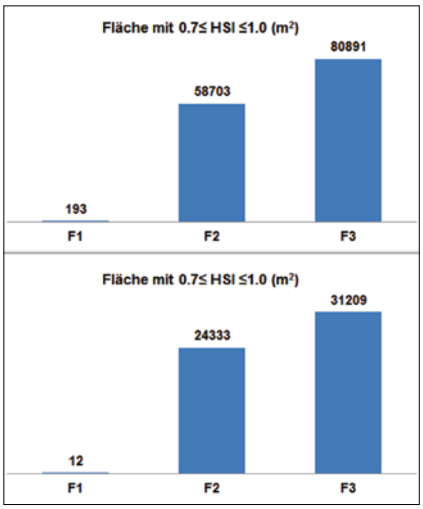

Bild 7: Mittlere Werte der Eignungsfläche im „sehr guten" Bereich für den Äsche-Laich in der ganzen Flussstrecke (oben) und in der freien Fließstrecke (unten) nach 24 Jahren (Quelle: [6])

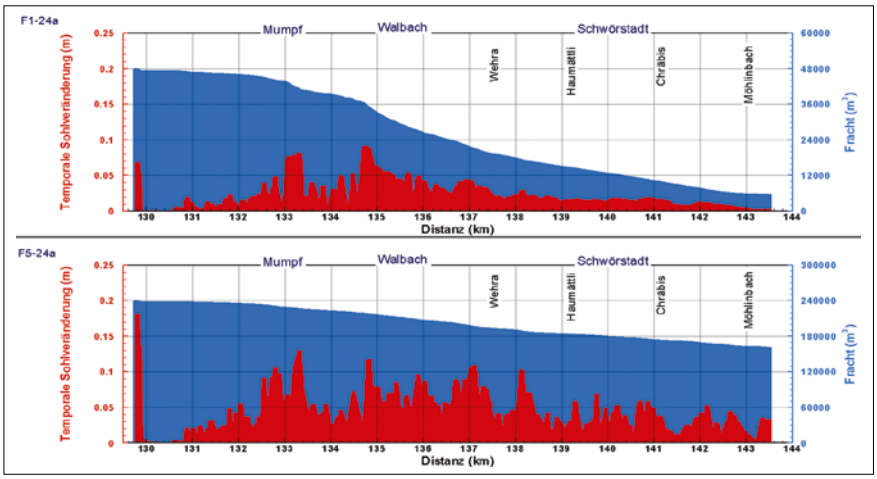

Bild 8: Querschnittgemittelte temporale Sohlenveränderung und Geschiebefracht für Fall F1 (heutiger Betriebszustand mit einem Geschiebeeintrag von 2 000 m³/a; oben) und Fall F5 (5-fache Vergrößerung der Geschiebezugaberaten am Einströmrand und Stauzielabsenkungen von 3,0 m gegenüber Normalstau bei Hochwasser; unten) nach 24 Jahren in der Flussstrecke zwischen KW Säckingen und KW Ryburg-Schwörstadt (Quelle: [6])

net, die anhand von univarianten Präferenzkurven in Relation zu Wassertiefe, Fließgeschwindigkeit und Substrattypen berechnet werden. Der Habitat-Eignungsindex einer Rechenzelle (HSI_i) kann mit unterschiedlichen Mittelungsverfahren ermittelt werden. In der Arbeit wird dafür der arithmetische Mittelwert aller Eignungsindices (SI_d, SI_v und SI_s) in Bezug auf Wassertiefe, Geschwindigkeit und Substrat verwendet. Diese Eignungsindices werden von den Präferenzkurven bestimmt. Die Auswahl der Präferenzkurven hat eine große Auswirkung auf die Ergebnisse. Präferenzkurven, die unter ähnlichen Konditionstypen und auf der Grundlage von großen Datenmengen ermittelt werden, liefern die genauesten Ergebnisse.

3 Modellerstellung

Im Untersuchungsgebiet befinden sich vier Stauhaltungen, die je mit einem quasi 3-D-Modell getrennt berechnet werden. Zur Generierung des Rechengitters und der topographischen Gegebenheiten im Gebiet werden die von der Firma Trenkel AG gelieferten digitalen Geländedaten (vermessene Flusssohle von 1992) verwendet. Dabei wird je ein randangepasstes Berechnungsgitter verwendet (**Bild 2**). Die gewählte Diskretisierung berücksichtigt die Staustufe zwischen KW Ryburg-Schwörstadt und KW Säckingen mit 614 x 26 Gitterpunkten, die Staustufe zwischen KW Säckingen und KW Laufenburg mit 356 x 32 Gitterpunkten, die Staustufe zwischen KW Laufenburg und KW Albbruck-Dogern mit 646 x 26 Gitterpunkten und die Staustufe zwischen KW Albbruck-Dogern und KW Reckingen mit 630 x 28 Gitterpunkten. Zusätzlich wird das Gitter mit unterschiedlichen Materialindices versehen, damit verschiedene Rauheits- bzw. Turbulenzaustauschzonen für den Rechenbereich verwendet werden können.

Als Anfangsbedingung für das Strömungsfeld wird ein stationärer Strömungszustand, der die numerische Vorhersage eines stationären Strömungsproblems bei Niederwasser ist, verwendet. Die vorhandene, gemessene bzw. interpolierte Kornverteilung wird für das ganze Gebiet verwendet.

Der Abfluss wird am oberen Modellrand vorgegeben. Die Geschwindigkeitsverteilung über den Querschnitt kann näherungsweise der Verteilung der Wassertiefen angepasst werden. Die Schwebstofffracht wurde unter Verwendung einer Schwebstofffunktion in Rheinfelden berechnet [6] und als Randbedingung festgelegt. Dabei wird der Geschiebeeintrag an diesem Rand und in einigen vorgeschlagenen Bereichen angegeben. Am Ausstromrand wird der Wasserspiegel spezifiziert. Mit der Annahme, dass für diesen Rand annähernd gleichförmige Strömungs- und Sedimenttransportverhältnisse gelten, werden die Gradienten der verbleibenden Strömungs- und Sedimentgrößen orthogonal zum Rand zu Null gesetzt. Der Wasser-Land-Rand ist in Flüssen bei Gleichheit der Wasser- und Bodenhöhe erreicht, der vom Wasserstand in dem Gebiet abhängt.

Für die Habitat-Simulationen interessieren die Bedingungen für Äschen in der Laichzeit zwischen März und April. Die Präferenzkurven des Äsche-Laichs werden von einer früheren Studie von Holzer et al. [5] übernommen, welche die allgemeinen Eignungskriterien für die Äsche in der Aare entwickelten. Die Präferenz der Wassertiefen reicht von 20 bis 279 cm, wobei der am stärksten bevorzugte Bereich zwischen 60 und 200 cm liegt. Die Präferenz der mittleren Fließgeschwindigkeit reicht von 0 bis 70 cm/s, wobei der genutzte Bereich nur zwischen 2 und 50 cm/s liegt. Die sich daraus ergebende Präferenz reicht von 10 bis 60 cm/s und besitzt den am stärksten bevorzugten Bereich in der Klasse von 20 bis 30 cm/s. Auf den Laichplätzen kommen ausschließlich Anteile von Feinkies, Mittelkies und Grobkies vor. Der bevorzugte Bereich liegt in den Klassen, in denen der Hauptanteil Mittelkies dominiert.

4 Modellergebnisse

Unter Verwendung der hydrologischen und sedimentologischen Randbedingungen der Jahre 1985 bis 2008 (für die Flussstrecke zwischen KW Reckingen und KW Säckingen) und der Jahre 1980 bis 2003 (für die Stauhaltung zwischen KW Säckingen und KW Ryburg-Schwörstadt) wurden Berechnungen der Sohlendynamik, basierend auf Stundenwerten, und

Prognosen der Habitatqualität für den Äschelaich durchgeführt. Dabei wurden neben dem Ist-Zustand auch Szenarien mit unterschiedlichen Geschiebezugaben und Stauzielabsenkungen im Hochwasserfall berücksichtigt.

4.1 Effekt des Hochwassers

Bild 3 zeigt die vermessene Ganglinie über 24 Jahre und die berechneten bzw. prognostizierten Feststofffrachten aus dem Stauraum zwischen KW Reckingen und KW Albbruck-Dogern. Dabei ist zu beachten, dass die Geschiebefracht (blaue Kurve) starke Sprünge aufweist. So ist beispielsweise deutlich ersichtlich, dass während des Hochwassers von 1994 etwa die 2,5-fache Menge einer durchschnittlichen Jahresfracht an Geschiebe transportiert wurde. Zunächst erstaunt diese Feststellung vielleicht nicht so sehr. Gefühlsmäßig ist sich jeder bewusst, dass während eines Hochwassers sehr viel mehr Feststoffe transportiert werden. Allerdings sollte man nicht nur in Werten von Volumina denken, sondern auch die zeitliche und qualitative Veränderung der Sohle während eines Hochwassers im Auge behalten. Eine 2,5-fache Jahresfracht an Feststofftransport kann massive Veränderungen der Höhenlage einer Sohle und damit der Hochwassersicherheit nach sich ziehen. Im Falle von Erosion in einer Fließstrecke kann sich die Kapazität eines Gerinnes erhöhen, im Falle von Anlandungen kann aber auch eine Kapazitätsminderung und damit eine Verschärfung der Hochwassersituation eintreten. Es war ein wichtiger Punkt der Untersuchungen, auch die maximalen Wasserspiegel bei veränderter Sohle zu überprüfen, um eine Verschärfung der Hochwassergefahr auszuschließen.

Genauso wie zeitliche Veränderungen der Sohlenlage für die Hochwassersicherheit zu beachten sind, ist auch die qualitative Veränderung der Zusammensetzung der Sohle für eine Habitat-Modellierung von großer Wichtigkeit. **Bild 4** zeigt diese Veränderungen ebenfalls am Beispiel des Hochwassers von 1994 auf. Man kann in gewissen Bereichen praktisch eine Verdoppelung der mittleren Korndurchmesser der Sohle feststellen. Während das gröbere Sohlenmaterial einen geringeren Einfluss auf die Wasserspiegel bei gegebenem Abfluss hat (erhöhte Sohlenrauigkeit), so kann der Einfluss auf das Laichen der Fische sehr große Auswirkungen, zum Guten wie zum Schlechten je nach Fischart und Präferenz, haben. **Bild 5** zeigt den Anteil sehr guter (grün) und geeigneter (gelb) Flächen für das Laichen von Äschen. Obschon die Bedingungen im Stauraum vor allem wegen der hohen Wassertiefe und der geringen Geschwindigkeiten insgesamt schlecht sind, kann mindestens eine relative Verbesserung in der freien Fließstrecke um den Faktor 2 erreicht werden. Schaut man nun auch bei der Habitat-Eignung etwas genauer hin, so sieht man, dass die Habitat-Bedingungen natürlich ebenfalls großen zeitlichen Schwankungen unterworfen sind.

4.2 Effekt der Geschiebezugabe

Bild 6 zeigt exemplarisch die Eignung für den Äsche-Laich in der freien Fließstrecke, wobei neben dem Referenzfall ohne Geschiebezugabe, die beiden Fälle mit einer Zugabe von 10 000 m³/a bzw. 20 000 m³/a dargestellt sind. Die Graphiken zeigen nicht nur, dass eine große, relative Verbesserung der Habitat-Bedingungen durch Zugaben erreicht wird, sondern auch dass die Bedingungen starken jährlichen Schwankungen unterworfen sind. Mit einer Geschiebezugabe erweisen sich die Jahre 1991 und 1993 als die beste Zeit für den Äsche-Laich in der Flusstrecke. Wie aus den **Bildern 6** und **7** ersichtlich ist, kann die Habitat-Qualität für den Äsche-Laich durch eine Vergrößerung des Geschiebeeintrags verbessert werden. Trotzdem kann die Habitat-Verbesserung durch eine doppelte Volumenzugabe an Geschiebe nicht ebenfalls verdoppelt werden.

4.3 Effekt von Stauzielabsenkungen

Die berechneten Ergebnisse für die Stauhaltung zwischen KW Säckingen und KW Ryburg-Schwörstadt haben gezeigt, dass

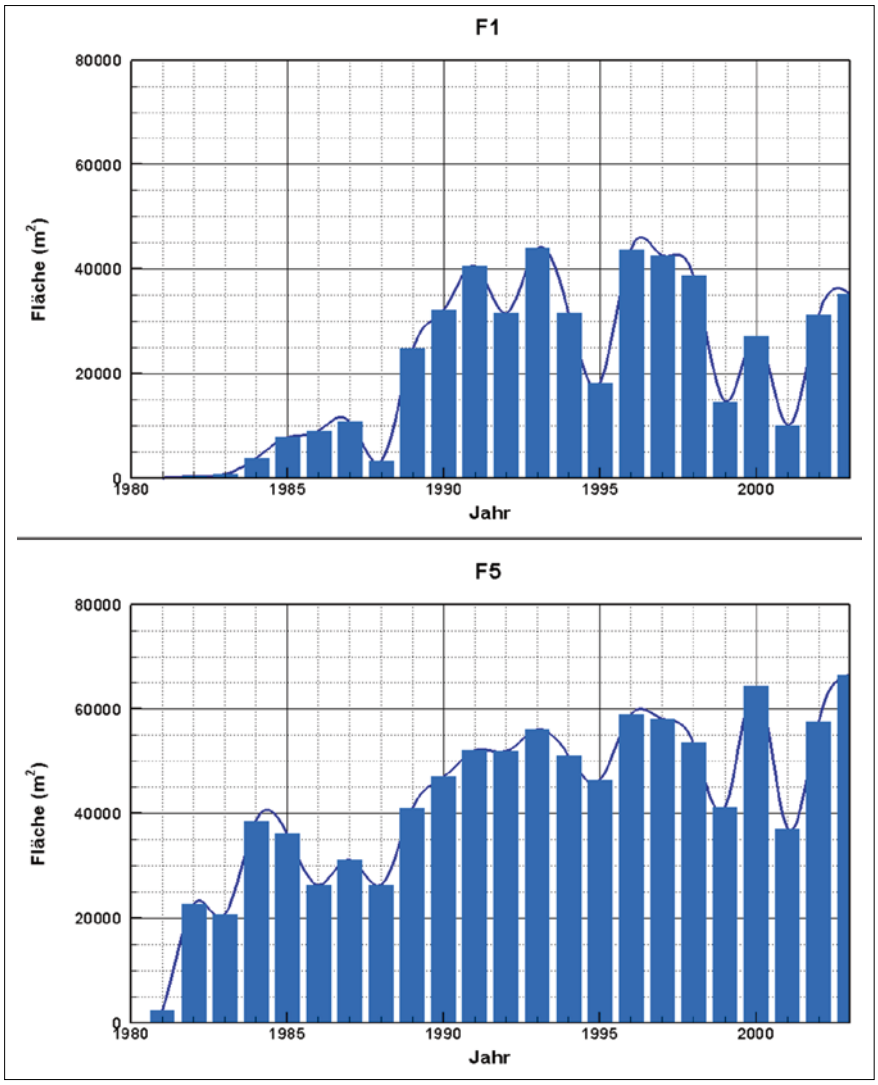

Bild 9: Zeitlicher Verlauf der Eignungsfläche im „sehr guten" Bereich in der ganzen Flussstrecke während der Laichzeit in der Flussstrecke zwischen KW Säckingen und KW Ryburg-Schwörstadt (Quelle: [6])

sich die Geschiebeumlagerung durch eine höhere Geschiebezugabe verstärkt (**Bild 8**).

Der Einflussbereich der Stauhaltung ist wegen der hohen Fließtiefen in jedem Fall ein wenig geeignetes Habitat für den Äsche-Laich. Aber mit einer geeigneten Wahl der Zugabemenge bzw. deren Kornverteilung kann die Habitat-Qualität für den Äsche-Laich in den Fließstrecken gezielt verbessert werden (**Bild 9**). Selbst wenn durch gezielte Geschiebezugaben das Sohlensubstrat flächig verbessert werden kann, so sind die sehr guten Laichplätze trotzdem nur in den flachen Uferbereichen zu erwarten.

5 Folgerungen

Die Untersuchungen am Hochrhein zeigen auf, dass die Habitat-Eignung eines Flusses stark durch dessen hydrologische und sedimentologische Dynamik geprägt wird. Deswegen können sich Maßnahmen, welche diese Dynamik unterstützen, positiv auf die Reproduktion von Fischen auswirken. Insbesondere zeigte sich, dass durch eine Staulegung im Hochwasserfall und durch die Zugabe von Geschiebe die Habitate für Äschen in der freien Fließstrecke sehr positiv beeinflusst werden können. Ebenso kann gezeigt werden, dass mit dem hier dargestellten, numerischen Werkzeug eine diesbezügliche Kosten-/Nutzen-Analyse vorgenommen werden kann. So ist klar ersichtlich, dass eine doppelte Zugabemenge an Geschiebe und damit eine Verdoppelung der Kosten nicht auch eine Verdoppelung der sehr gut geeigneten Laichhabitate zur Folge hat.

Es ist erstaunlich, dass in die Renaturierung von Flüssen hohe Finanzmittel fließen, ohne dass normalerweise eine Kosten-/Nutzen-Abschätzung mit z. B. geeigneten, numerischen Werkzeugen stattfindet. Dies erstaunt insbesondere deshalb, da ein Monitoring zwar die aussagekräftigeren Resultate erbringen kann, dies allerdings mit einem hohen Kostenaufwand und erst nach etlichen Jahren, nach denen sich ein erneutes Gleichgewicht der Fischpopulationen eingestellt hat.

Minh Duc Bui and Peter Rutschmann

Application of a Numerical Model System to Evaluate Sediment Transport and Spawning Habitats for European Graylings in the High Rhine

The paper presents a complex multidimensional computer modelling system to investigate hydromorphological processes and fish habitat suitability as well as optimization potentials for large rivers. The software tool illustrates the possibilities of modern computer programs and their advantages using the High Rhine investigation as a study case. The results show that by applying these advanced tools the success and cost-effectiveness of the planned hydraulic and river engineering measures can be investigated and rated. Especially, the hydromorphological and habitat changes in the river should not be seen with "mean performance optics", but rather as processes with high spatial and temporal dynamics.

Минх Дук Буи и Петер Ручманн

Применение цифровой системы моделирования для оценки донных отложений и мест нереста хариуса на Верхнем Рейне

Представлена многомерная система компьютерного моделирования для моделирования и оценки гидроморфологических процессов на крупных реках и пригодности мест для обитания рыб, а также возможности улучшения ситуации. Система демонстрирует возможности современных программ – на примере Верхнего Рейна показывается ее применение и преимущества при проведении соответствующих исследований. Результаты показывают, что при использовании таких систем запланированные строительные мероприятия на реках могут быть изучены на предмет их успеха и эффективности затрат; при этом изменения русла и речной среды обитания могут быть рассмотрены и оценены не только с точки зрения «средних значений», но и на предмет наличия и учета высокой динамики соответствующих процессов.

6 Danksagung

Die Autoren bedanken sich bei den Auftraggebern der Hochrheinstudie (Bundesamt für Energie Bern, Regierungspräsidium Freiburg i. Br.) und der PGG-Hochrhein. Ein namentlicher Dank gebührt den Herren Abegg (Flussbau AG), Kirchhofer (WFN), Hohl (BFE), Gläser (Regierungspräsidium Freiburg), Dr. Marti (Kanton Zürich), Dr. Bloesch (Aqua Viva), Dr. Fust (Energiedienst Holding AG) und Müller (Axpo AG). Die Autoren möchten sich bei Herrn Professor W. Rodi vom Institut für Hydromechanik der Universität Karlsruhe bedanken, dass sie mit seiner Zustimmung den FAST-Code weiterentwickeln und für die Hochrhein-Studie einsetzen durften.

Autoren

Dr.-Ing. Minh Duc Bui
Prof. Dr. Peter Rutschmann
Lehrstuhl für Wasserbau und Wasserwirtschaft
Technische Universität München
Arcisstr. 21, 80333 München
bui@tum.de
rutschmann@tum.de

Literatur

[1] AQUARIUS (Hrsg.): Kraftwerk Ryburg-Schwörstadt: Erneuerung der Konzession Umweltverträglichkeitsbericht. Fachbericht C.5.2; Beitrag zur Reaktivierung des Geschiebehaushaltes im Hochrhein, 2007 (unveröffentlicht).

[2] Bui, M. D.: Berechnung der Strömung und des Sedimenttransports in Flüssen mit einem tiefengemittelten numerischen Verfahren., Institut für Hydromechanik, Universität Karlsruhe, 1998 (Dissertation).

[3] Bui, M. D.; Rutschmann, P.: Numerical modelling of non-equilibrium graded sediment transport in a curved open channel. In: Computers & Geosciences 36 (2010), S. 792-800.

[4] Friedl, C.: Fischfangrückgang und schweizerischen Fließgewässern. BUWAL, 1999.

[5] Holzer, G., Müller, M.; Peter, A.,; Schneider M.: Fischereiliches Gutachten über die Aarebaggerung in Thun. Forschungsbericht EAWAG, 2002.

[6] Rutschmann, P.; Bui, M. D.; Abdelaziz, S.: Hydromorphologische Berechnungen und Fischhabitatmodellierung für den Hochrheinabschnitt zwischen KW Reckingen und KW Ryburg – Schwörstadt. Fachbericht zum „Masterplan – Massnahmen zur Geschiebe-reaktivierung im Hochrhein", Lehrstuhl für Wasserbau und Wasserwirtschaft, TU München, 2013.

[7] Wu, W.: Computational River Dynamics. Taylor & Francis, 2007.

Received: 7 September 2017 | Revised: 1 January 2018 | Accepted: 27 February 2018

DOI: 10.1002/eco.1961

RESEARCH ARTICLE

WILEY

Development of eco-hydraulic model for assessing fish habitat and population status in freshwater ecosystems

Weiwei Yao[1,2] | Minh Duc Bui[2] | Peter Rutschmann[2]

[1] Key Laboratory of Environmental Remediation, Institute of Geographic Sciences and Natural Resources Research, China Academy of Sciences, Beijing 100101, China

[2] Institute of Hydraulic and Water Resources Engineering, Technical University Munich, Munich, Germany

Correspondence
Weiwei Yao, Key Laboratory of Environmental Remediation, Institute of Geographic Sciences and Natural Resources Research, China Academy of Sciences, Beijing 100101, China.
Email: weiweiyao@igsnrr.ac.cn

Funding information
CAS, Grant/Award Number: Y6V60222YZ; National Key R&D Program of China, Grant/Award Number: 2016YFC0502004; CCA, Grant/Award Number: (2017.07)

Abstract

An eco-hydraulic model is described, namely, "WW-Eco-tools." The model is composed of hydro-morpho-dynamic, habitat, and population models. Fish habitat suitability models assess habitat quality, based on abiotic parameters, namely, flow velocity, depth, and substratum data. These are all derived from a hydro-morpho-dynamic model. The relationships between parameters and habitat features are represented as suitability index curves (SI curves) or fuzzy rules. To dynamically simulate fish species, two different population models are developed. The first is converted from a logistic population concept. Its model parameters are related to time-dependent fish habitat conditions, namely, weighted usable areas and an overall suitability index. The second model is based on a matrix population concept, with numbers as the only state vector. Age-specific fecundities and survival rates depend on the habitat qualities defined in the matrix population model. The eco-hydraulic model provides very promising results, highlighting the fundamental role of temporal variability of hydro-morphological parameters in structuring habitat and populations of fish species. Using this software to anticipate water management changes, simulated population trends can help decision-makers optimize management measures.

KEYWORDS

eco-hydraulic model, freshwater ecosystems, habitat model, hydro-morpho-dynamic model, population model, WW-Eco-tools

1 | INTRODUCTION

Eco-hydraulics predicts river ecosystem behaviour based on knowledge of physical variables coupled with biological requirements. It investigates the effects of physical variables on aquatic habitat and organism community structure of a river ecosystem (Tonina & Jorde, 2013). Eco-hydraulics requires advanced numerical models, as well as ecological theories, to provide accurate results for management of rivers and aquatic organisms (Lancaster & Downes, 2010a; Rice, Little, Wood, Moir, & Vericat, 2010). Researchers gain better knowledge to fulfil both hydraulic engineering and ecological requirements, based on an eco-hydraulic model (Wang, Lee, & Xu, 2013; Tonina & Jorde, 2013). Interdisciplinary knowhow assists hydraulic engineers, geomorphologists, river managers, ecologists, biologists, and researchers. They can develop more effective approaches to handling river infrastructure, such as predicting aquatic species number and fish density fluctuations (Gamito, 1998; Lancaster & Downes, 2010b; Yao, Chen, & He, 2018). Balancing ecological systems and citizen requirements calls for innovative and effective solutions, which ensure that the needs of both aquatic species and people are met.

A hydro-morpho-dynamic model is rooted in eco-hydraulic models, and it focuses on flow properties and prediction of fluvial morphodynamics used in eco-hydraulics. In particular, it focuses on flow velocity, depth, and substrate distribution modelling and its application to river ecosystems (Guan & Liang, 2017; Xia, Cao, Pender, & Borthwick, 2017). There are many models and numerical codes, which can satisfy the hydro-morpho-dynamic simulation requirement. The models or numerical codes named FaSTMECH, River2D, FAST2D, CCHE2D, OPENTELEMAC, SRH-2D, Hydro-2D, MIKE, Delft3D, Flow3D, and OpenFOAM can applied in hydro-morpo-dynamic

simulation (Steffler, 2002; Tonina & Jorde, 2013; Yao, 2016). In eco-hydraulics, 2D hydraulic modelling is currently an efficient approach, and it is suggested that 2D modelling can be sufficient for the majority of eco-hydraulics applications.

Habitat modelling has been a critical component of eco-hydraulic models. The first example of eco-hydraulic modelling was a habitat model, developed in the 1970s by the United States Fish and Wildlife Service (Tomsic, Granata, Murphy, & Livchak, 2007; USFWS, 1980). In the 1980s, Bovee (1982) developed a habitat model and applied it in river management based on physical variables including depth, velocity, and substrates. Later, the physical habitat simulation (PHABSIM), in-stream flow requirements (CASiMiR), MesoHABSIM, River2D, EVHA, and HABSCORE models were developed and applied to assess stream habitat features (Alfredsen & Killingtveit, 1996; Bovee, 1982, 1986; Ginot, 1995; Jorde & Bratrich, 2000; Parasiewicz, 2001). More recently, "Software for Assisted Habitat Modelling" has been used in analysing endangered species and invasive species in many case studies (Armstrong, Kemp, Kennedy, Ladle, & Milner, 2003; Bovee, Waddle, Talbert, Hatten, & Batt, 2008; Mouton, Schneider, Depestele, Goethals, & De Pauw, 2007; Nagaya et al., 2008; Steffler, 2002; Stohlgren et al., 2010; Talbert & Talbert, 2012; Zhou, Zhao, Song, Bi, & Zhang, 2014).

Population modelling is also a critical component of eco-hydraulic models, which studies population dynamics to obtain a better understanding of population ecology and fish species management. Many studies recommend population models as effective tools for evaluating fish population protection, particularly for endangered fish species protection (Coggins & Walters, 2009; Gouraud, Sabaton, & Capra, 2004; Hess, 1996; Ibrahim, Preuss, Schaeffer, & Hommen, 2014; Korman, Yard, Walters, & Coggins, 2009; Morris & Doak, 2002). One example is the "individual-based model," which can describe population traits with a distribution and can explicitly represent individual performance and local interactions (Deangelis & Gross, 1992; Grimm, 1999; Hall et al., 2006). Other population models include the CVI watershed tool (Rashleigh et al., 2004), in-stream model (Harvey, Jackson, & Lamberson, 2009), Salmon model (Bartholow, 1996; Bartholow, Laake, Stalnaker, & Williamson, 1993), logistic population model (Gamito, 1998; Li, Wang, & Su, 2011; Shepherd & Stojkov, 2007; Tsoularis & Wallace, 2002), and matrix population model (Caswell, 2001; Yao, Kumar, & Rutschmann, 2014; Yao, Rutschmann, & Bamal, 2014). In addition, another population model simulates the cumulative barrier and passage effects of main-stream hydropower dams on migratory fish population in the Lower Mekong Basin (Burnhill, 2009). Further models include those of Naghibi and Lence (2012), Korman et al. (2012), and Ibrahim et al. (2014). Among these models, the most robust population models are logistic and matrix population models.

Ecohydraulic studies also provide the opportunities to recast, innovate, and minimize negative aspects of a project and increase the possibility of achieving a high level of ecological integrity. However, to the best of the authors' knowledge, there is no software or numerical codes to simultaneously simulate hydro-morpho-dynamic processes, habitat quality distributions, and population status. Thus, we aim to present the concept of an eco-hydraulic model, describing an eco-hydraulic model for a river system. The eco-hydraulic model is composed of hydro-morpho-dynamic, habitat, and population models, which are used to assess the habitat and population status of the Aare River ecosystems. The first version of the model is named WW-Eco-tools. In the following section, the eco-hydraulic model framework will be described, followed by an application of the framework in a case study using WW-Eco-tools applied to the Aare River, Switzerland.

2 | MATERIALS AND METHODS

2.1 | Model overview

The eco-hydraulic model comprised a hydro-morpho-dynamic model, habitat model, and population model. Riverine morpho-dynamic processes, fish hydraulic habitat, population changes, and density distributions were simulated. The eco-hydraulic model could use the SI curve habitat model and fuzzy logic habitat model to calculate the habitat value and do the habitat sensitivity analysis. The eco-hydraulic model used a logistic population model and matrix population model to simulate the total fish number and fish number in each life stage. The objective of the 2D eco-hydraulic model is to represent dynamic behaviour of river ecosystems. In a 2D eco-hydraulic model, the hydro-morpho-dynamic model responds to external forces such as hydrological variations, riverbed deformation over time, and other hydrodynamic effects. The habitat models can mainly be divided into two types, namely, SI curve habitat models and fuzzy logic habitat models. The logistic and matrix population models are also described in this section. The concept of the eco-hydraulic model is shown in Figure 1, and sequences of the eco-hydraulic model are shown in Figure 2. In the eco-hydraulic model, all parameters can be simultaneously simulated.

2.2 | Hydro-morpho-dynamic model

The calculation of flow and sediment transport is one of the most important tasks in river engineering and river ecosystem assessment (Wu, 2008). The hydro-morpho-dynamic model is aimed at identifying both hydrodynamic and morpho-dynamic issues in riverine regions. The hydrodynamics is based on the 2D shallow water equation, which includes the continuity equation and two momentum equations. In the shallow water equation, the Reynolds stress and

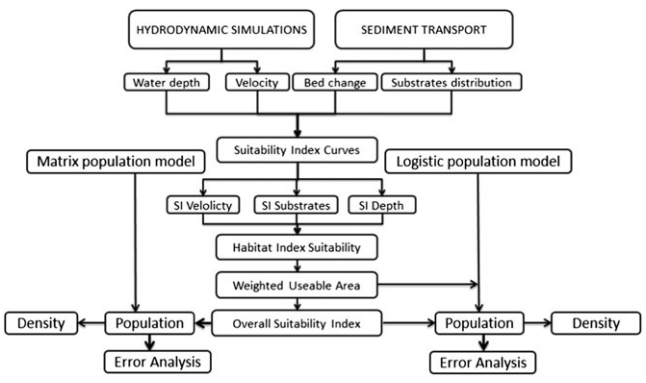

FIGURE 1 The flowchart of the eco-hydraulic model

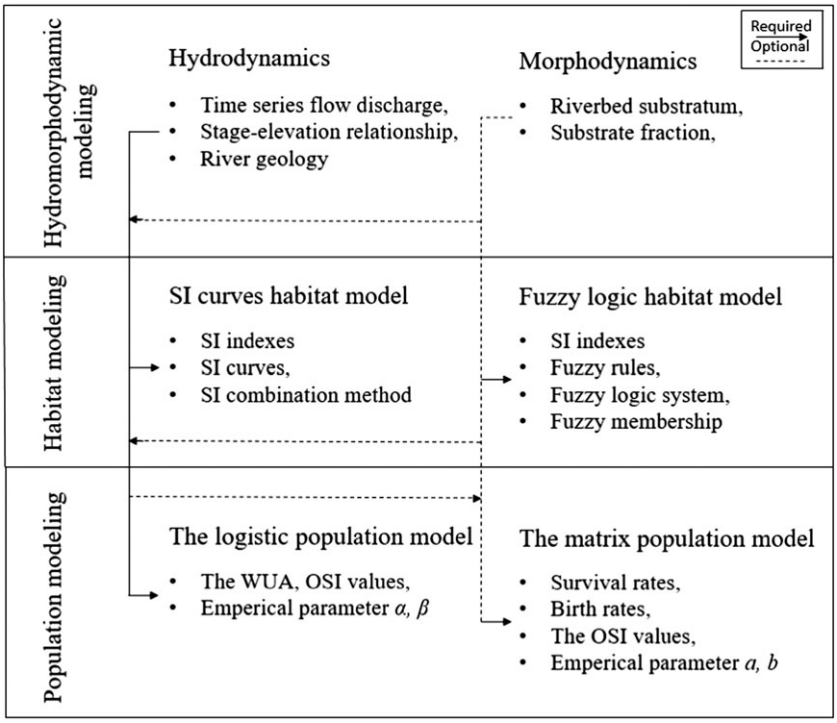

FIGURE 2 Detailed input, output, and sequences for the eco-hydraulic model. WUA = weighted usable areas; OSI = overall suitability index

river bed shear stress are included. The Reynolds stress is calculated with a turbulence model, such as the *k*-ε and *k*-ω turbulence models. The river bed shear stress can be calculated, based on an empirical formula such as the Chezy, Strickler, Manning, or Nikuradse friction laws (Yao, 2016).

The morpho-dynamic processes are based on sediment transport, which is the transport of sediment particles by flowing water, as either bed-load or suspended load. This transport depends on the size of the bed material particles and the flow conditions (Van Rijn, 1984). The morpho-dynamics is mainly focused on calculating bed-load, suspended load, riverbed deformation, and riverbed grain size distribution, such as main grain size diameters and grain size fractions. The bed-load can be calculated based on one of numerous semiempirical formula, such as Meyer-Peter Müller, Einstein-Brown, Engelund Hansen, Van Rijn, or Hunziker equations (Meyer-Peter & Müller, 1948; Einstein, 1942; Brown, 1950; Engelund & Hansen, 1967; Van Rijn, 1984; Van Rijn, 1993; Hunziker, 1995; Ackers & White, 1973; Brunner, 2005; Nielsen, 1992). The choice of the bed-load formula depends on the suitability range of these formulae. The suspended load concentration is obtained by integrating the 3D sediment transport equation over the suspended zone. There are several empirical formulae for calculating suspended load concentration, such as Zyserman and Fredsøe (1994) and Van Rijn (1984). A brief description of the hydro-morpho-dynamic model used in this eco-hydraulic model can be found in Appendix A.

2.3 | Habitat model

In the WW-Eco-tools software, the habitat model can be divided into SI curves and fuzzy logic habitat model, according to the habitat model types. Both SI curves and fuzzy logic habitat are included in WW-Eco-tools. The two basic components of the SI curves habitat model are the SI values and the habitat suitability index (HSI) values. The SI values are derived from hydrodynamic and corresponding habitat suitability criteria. SI curves are mainly based on the literature, professional judgement, lab studies, or field observations of the frequency distribution for the habitat variables. HSI values mainly depend on combined functions of SI values. There are four functions of HSI combinations, including:

$$\text{O1} \quad HSI_{i,t} = (SI_1 \times SI_2 \times SI_3 \ldots SI_n)^{1/n}, \tag{1}$$

$$\text{O2} \quad HSI_{i,t} = \frac{(SI_1 + SI_2 + SI_3 + \ldots + SI_n)}{n}, \tag{2}$$

$$\text{O3} \quad HSI_{i,t} = (SI_1 \times SI_2 \times SI_3 \ldots SI_n), \tag{3}$$

$$\text{O4} \quad HSI_{i,t} = \text{Min}(SI_1, SI_2, SI_3, \ldots SI_n), \tag{4}$$

where SI_1, SI_2, and SI_n are the related suitability indices obtained from the fish SI curves. The graphs of HSI range from 0 to 1 for the species (0 is indicating the most unsuitable conditions, and 1 is representing the optimal condition). A case study of the habitat suitability criteria and the structure of habitat suitability based on SI curves are shown in Figure 3. These are from a literature review and field observation (Nykänen & Huusko, 2004; Nykänen, Huusko, & Mäki-Petäys, 2001; Sempeski & Gaudin, 1995).

The fuzzy logic habitat models use physical and biological parameters, through the application of an expert knowledge rule system. The structure of fuzzy logic habitat models is based on the fuzzy logic system. A fuzzy logic system is defined as the nonlinear mapping of an input data set to a scalar output data set. In fuzzy logic habitat models, the linguistic values such as "low," "moderate," and "high" were assigned to the input variables (flow velocity, depth, and riverbed

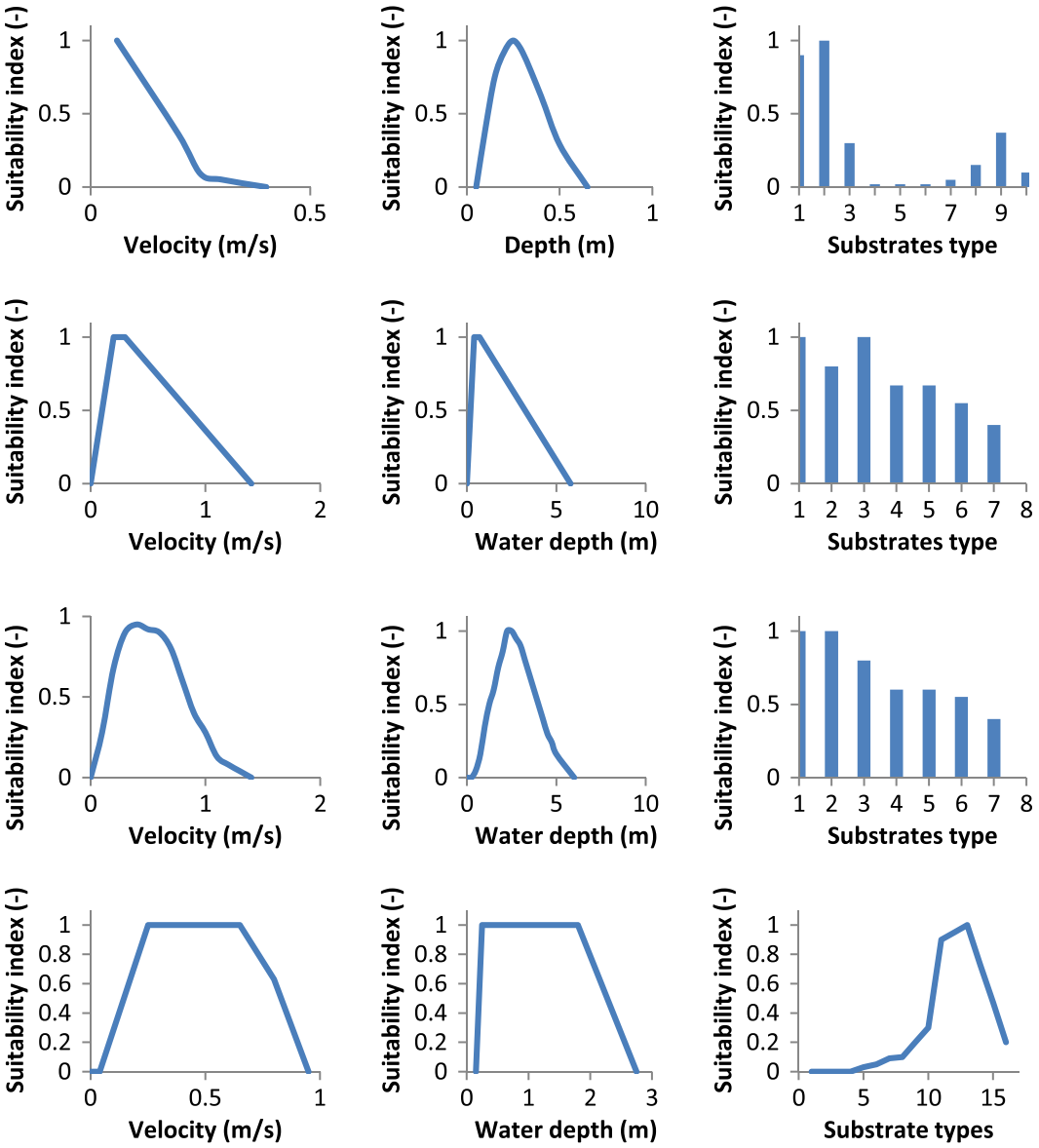

FIGURE 3 Fry, juvenile, adult, and spawning (from top to bottom) European grayling SI curves for velocity, water depth, and substrate types

substrates) and the output variable (HSI). These linguistic values were defined by fuzzy rules, a membership function of particular fuzzy rules, and indicate the degree to which an element belongs to this fuzzy set. The membership values range from 0 to 1 (Mouton, De Baets, & Goethals, 2009, 2011). For the fuzzy logic habitat model, there are several steps, namely: input selection, output selection, and membership definition for input and output along with fuzzy rule definition, based on input and output. Figures 4–6 illustrate the fuzzy logic habitat model.

There are two more parameters of importance that should also be calculated during the habitat modelling process. These are the weighted usable areas (WUA) and the overall suitability index (OSI).

$$WUA = \sum_{i=1}^{M} A_i HSI_i, \tag{5}$$

where A_i is the horizontal surface of mesh cell i (m^2), HSI_i is the HSI of mesh cell i, and M the number of meshes in the studied river stretch. The OSI is defined as the ratio of the weighted usable area and the total computational domain area in the horizontal plane:

$$OSI = \frac{\sum_{i=1}^{M} A_i HSI_i}{\sum_{i=1}^{M} A_i}. \tag{6}$$

2.4 | Logistic and matrix population model

Population models allow a better understanding of how complex processes, responsible for growth or decay of populations, along with interactions. Modelling dynamic interactions in nature can provide a manageable way for understanding how population numbers change over time. Ecological population modelling is concerned with the population size, age distribution, and density variations. Ecological population modelling is affected by the physical environment and the individuals of their species. In WW-eco-tools, the logistic population and matrix population models are included and also used in the case study.

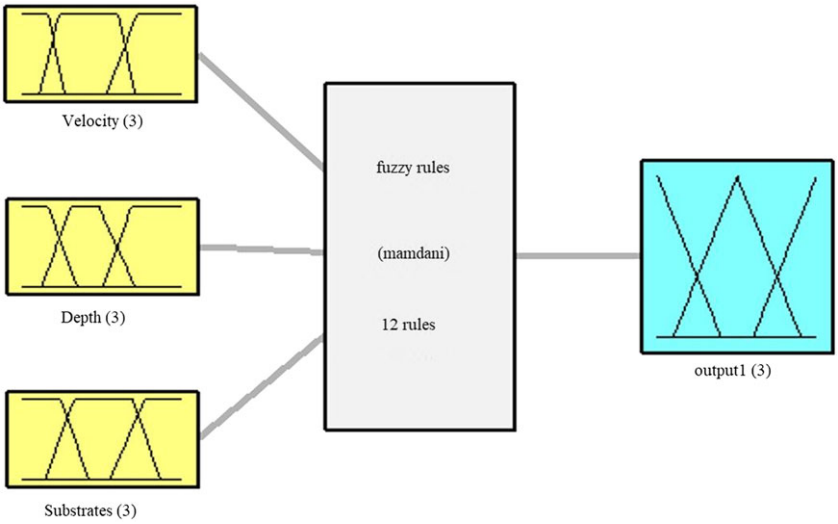

FIGURE 4 The fuzzy logic based habitat model

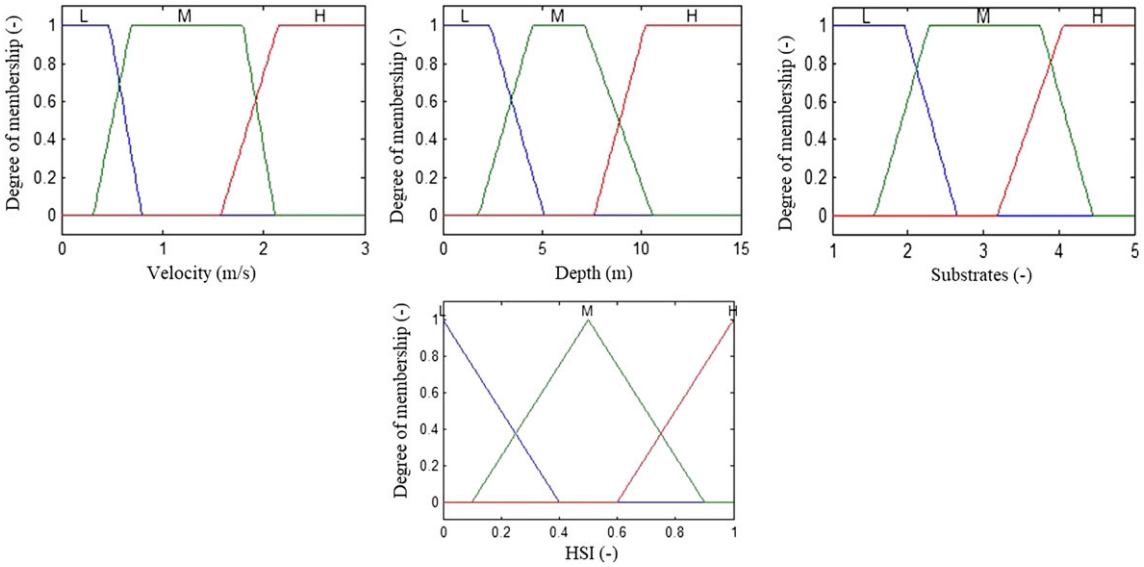

FIGURE 5 Membership functions for the input variables (velocity, water depth, and substrate) and the output variable habitat suitability index (HSI)

The logistic population model includes the growth rate and fish numbers that the river habitat can support. In this model application, WUA and OSI obtained from the habitat model, based on spawning SI curves, are used to represent the maximum number and growth rate, respectively. The logistic function is used to represent changes of fish population number. The population numbers calculated by the logistic model are shown in Equation 7, and a detailed description of the logistic population model used in this eco-hydraulic model can be found in Appendix B (Fox Jr & William, 1970; Russ & Alcala, 2004; Shepherd & Stojkov, 2007).

$$P_{t+\Delta t}^{F}=\frac{\beta\times WUA_{t+\Delta t}^{F}\times {P_t}^{F}\times e^{\alpha\times\left(OSI_{t+\Delta t}^{F}-OSI_{t}^{F}\right)}}{\beta\times WUA_{t+\Delta t}^{F}+P_{t}^{F}\times\left(e^{\alpha\times\left(OSI_{t+\Delta t}^{F}-OSI_{t}^{F}\right)}-1\right)}, \tag{7}$$

where ${P_t}^{F}$ and ${P^{t+\Delta t}}_{F}$ are population numbers at time t and $t + \Delta t$ for fish species F, respectively; α and β are model empirical parameters (–); $WUA_{t+\Delta t}^{F}$ is the weighted usable areas at time $t + \Delta t$ for fish species F (m^2); OSI_{t}^{F} and $OSI_{t+\Delta t}^{F}$ are overall suitability indices at time t and $t + \Delta t$ for fish species F, respectively (–).

The matrix population model (Equation 8), also named "age structure population" model, is developed from the classic matrix population model (Caswell, 2001; Aziz-Alaoui, 2002). The classic matrix is one of the most well-known ways to describe changes of population. In the classic matrix population model, population is divided into groups based on age classes. At each time step, the population is represented by a vector with an element for each age class. The classic matrix model is a square matrix with the same number of rows and columns as the population vector. The birth rate and survival rate are included in the square matrix. The OSI is also inserted into the birth rate and survival rate. The detailed parameter setting and the sensitivity analysis in model application can be found in Appendix C.

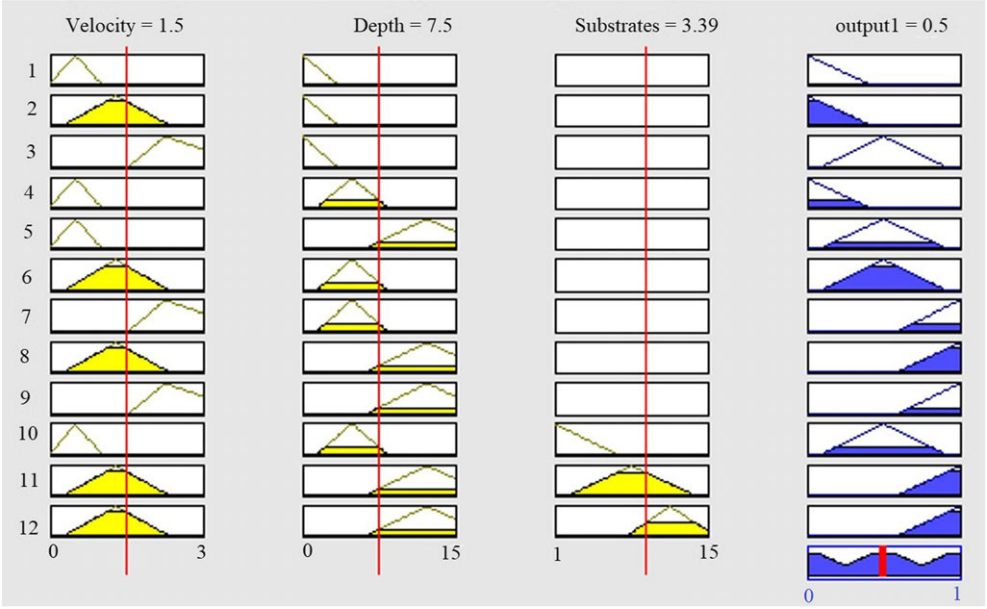

FIGURE 6 Fuzzy rule settings illustration

$$\begin{bmatrix} N_{1,t+\Delta t} \\ N_{2,t+\Delta t} \\ \dots \\ N_{i,t+\Delta t} \\ \dots \\ N_{j,t+\Delta t} \\ \dots \\ N_{n-1,t+\Delta t} \\ N_{n,t+\Delta t} \end{bmatrix} = \begin{bmatrix} F_{1,t} & F_{2,t} & \dots & F_{i,t} & \dots & F_{j,t} & \dots & F_{n-1,t} & F_{n,t} \\ S_{1,t} & 0 & \dots & 0 & \dots & 0 & \dots & 0 & 0 \\ \dots & \dots & \dots & \dots & \dots & \dots & \dots & \dots & \dots \\ 0 & 0 & \dots & S_{i-1,t} & \dots & 0 & \dots & 0 & 0 \\ \dots & \dots & \dots & \dots & \dots & \dots & \dots & \dots & \dots \\ 0 & 0 & \dots & 0 & \dots & S_{j-1,t} & \dots & 0 & 0 \\ \dots & \dots & \dots & \dots & \dots & \dots & \dots & \dots & \dots \\ 0 & 0 & \dots & 0 & \dots & 0 & \dots & 0 & 0 \\ 0 & 0 & \dots & 0 & \dots & 0 & \dots & S_{n-1,t} & S_{n,t} \end{bmatrix} \times \begin{bmatrix} N_{1,t} \\ N_{2,t} \\ \dots \\ N_{i,t} \\ \dots \\ N_{j,t} \\ \dots \\ N_{n-1,t} \\ N_{n,t} \end{bmatrix}, \tag{8}$$

with

$$\begin{aligned} F_{i,t} &= f_{i,t} \times \left(1 + \frac{e^{(OSI_{i,t}-a)} - e^{-(OSI_{i,t}-a)}}{e^{(OSI_{i,t}-a)} + e^{-(OSI_{i,t}-a)}}\right); \; S_{i,t} \\ &= s_{i,t} \times \left(1 + \frac{e^{(OSI_{i,t}-b)} - e^{-(OSI_{i,t}-b)}}{e^{(OSI_{i,t}-b)} + e^{-(OSI_{i,t}-b)}}\right), \end{aligned} \tag{9}$$

where $N_{i,\,t}$ is fish number at time t for fish stage i (−); $S_{i,\,t}$ is model survival rate at time t (−); $F_{i,\,t}$ is birth rate of for spawning fish at time t (−); $f_{i,\,t}$ is the basic birth rate at time t for the stage i (−); $s_{i,\,t}$ is the basic survival rate at time t for the stage of i (−); a and b are the empirical parameters for spawning fish and other life stages of fish. Its shows that when the OSI values are bigger than a and b, the fish population number will show an increasing trend. When the OSI values are smaller than a and b, then the fish population number will show a decreasing trend.

The population density $P^F_{i,t}$ in mesh cell i at time t is defined as:

$$P^F_{i,t} = \frac{A_{i,t} \times HSI^F_{i,t} \times P^F_t}{WUA^F_t}, \tag{10}$$

where $A_{i,t}$ is the horizontal surface of mesh cell i (m^2); $HSI_{i,t}$ is the HSI of mesh cell i (−); $P_t{}^F$ is population numbers at time t for fish species F; and $P^F_{i,t}$ is the population density (fish number in per mesh cell).

2.5 | Model setup and model calibration

The WW-Eco-tools setup requires model choices. Here, in the hydro-morpho-dynamic model, SI curves habitat model, logistic population model, and matrix population model are chosen. WW-Eco-tools uses the Visual Studio and Matlab interface. All models in the modelling system are coupled based on unstructured grids at the computational program level. In the WW-Eco-tools software, the hydro-morpho-dynamic model is solved by an open source software TELEMAC, with a new subroutine developed by the authors. The numerical codes of habitat and the population models are those developed by the authors. The software named Tecplot, Blue Kenue, and ParaView can be used to view the prediction results. The more detailed model setup and calibration can be found in Yao (2016).

3 | RESULTS

3.1 | The eco-hydraulic model application

The Aare River can be used to demonstrate the WW-Eco-tools framework. The specific site is located where the Aare River flows out of Lake Thun, 30 km south of Bern. The Aare River is a tributary of the High Rhine and the longest river, which rises and ends entirely within Switzerland. The river drains an area of 2,490 km^2. It rises in the Aare Glacier of the Bernese Alps in canton Bern, below the Finsteraarhorn and west of the Grimsel Pass, in the south-central part of Switzerland (Mouton et al., 2007). The river stretch used in this case study is a 1.35-km-long river stretch. The whole computational domain is subdivided into 5,403 mesh cells and 9,619 nodes (Figure 7). The European grayling is chosen as the target fish species and divided into nine life stages. The WUA and OSI values, based on spawning SI curves, are used in the logistic population model. The OSI values based on fry, juvenile, adult, and spawning SI curves are used in the matrix population model. For the European grayling, the first year is defined

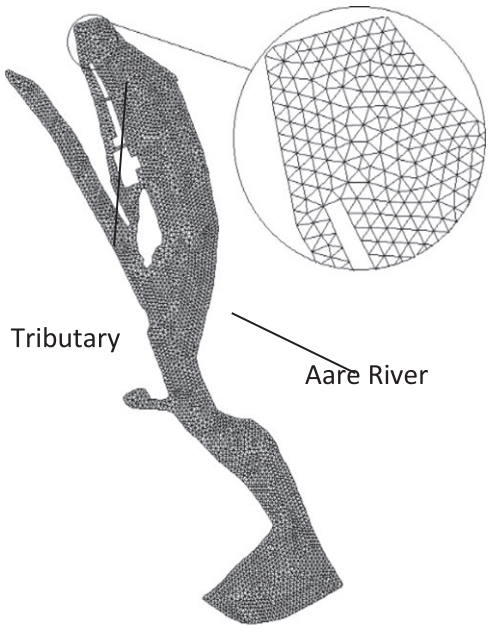

FIGURE 7 The generated mesh for computational river stretch

as the fry life stage; the second year is defined as the juvenile life stage, and the third to ninth is defined as the adult life stage; the spawning life stage is defined as the third to ninth year of the spawning season (April & May). The WW-Eco-tools case study interface is shown in Figure 8.

3.2 | Habitat quality simulation

Figure 9 shows the HSI distributions in O1, O2, O3, and O4. Based on O1 in 1970, more specifically, the HSI distributions showed that most of the unsuitable HSI values occurred in a tributary of the Aare River, outlet, and midlength of the river stretch. The regions with high water depths had low SI values for water depth. For O1, the HSI values for the rest of the domain resulted in a value of approximately 0.5. In 1980, the HSI distributions for O1 were similar to those in 1970, for the majority of areas, except some small regions with very high HSI values scattered along the river stretch. In 1990, the HSI distribution had the same trend as the HSI distribution in 1980 for O1, O2, O3, and O4, except that the HSI values improved near the regions with the highest water depths. At the end of the simulation period in 2000, regions with high HSI values were very small, for all four computational options. High HSI value regions were located in the regions near the outlet and scattered along the axis of the river. For O2, the HSI quality was better than for O1; HSI values for the main river ranged from 0.3 to 0.7, and the HSI values in the river tributary were nearly 0.1. Habitat quality for O3 and O4 was worse than the habitat quality for O1 and O2, with low HSI values distributed along the whole river stretch. Figure 9 also indicates that the HSI distribution, based on O2, produced better habitat quality results than the habitat quality at O1, O3, and O4. The worst HSI distribution was displayed by O3 and O4.

WUA and OSI values showed a slightly increased trend from 1970 to 1980 and then remained stable (Figure 10). More

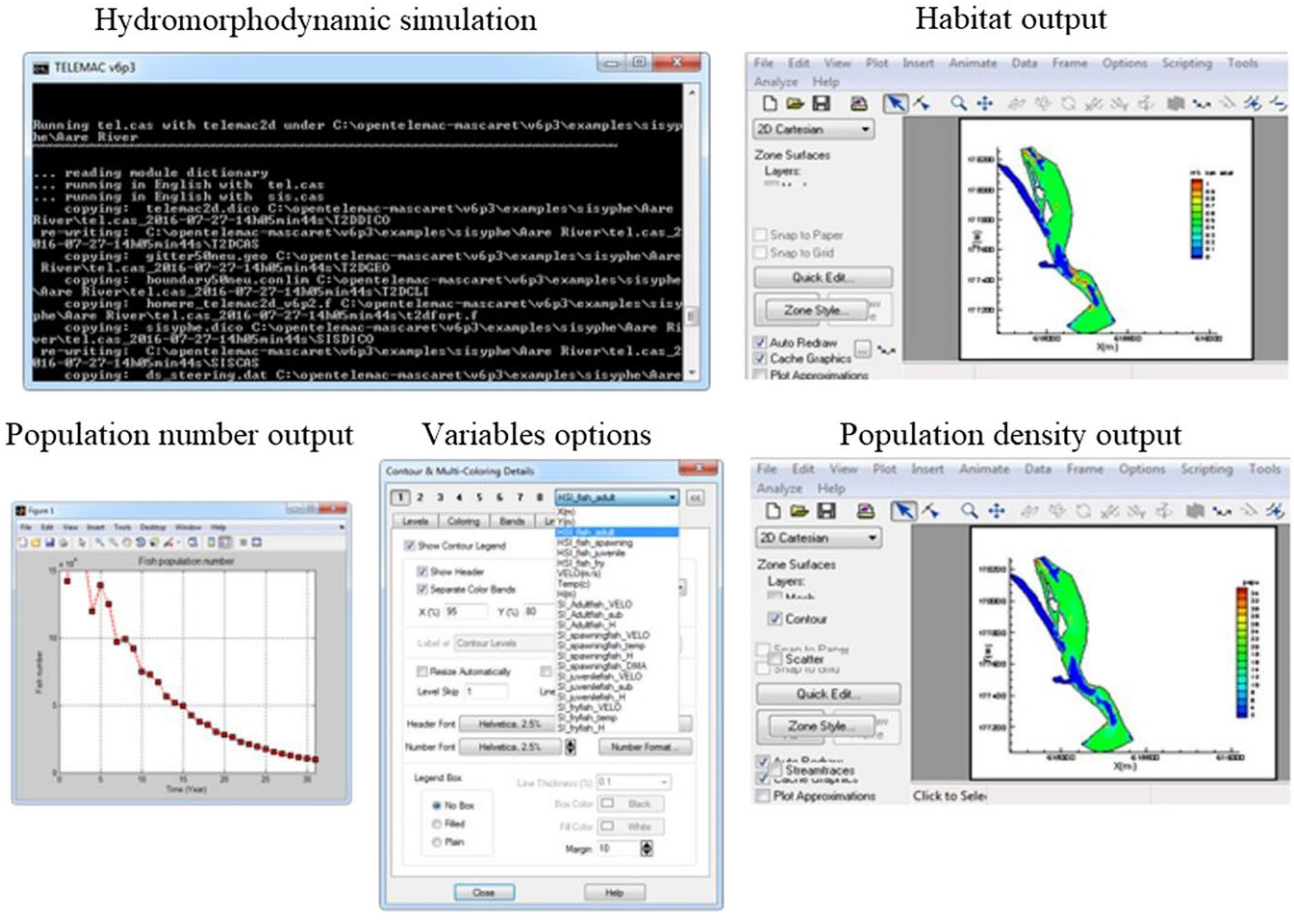

FIGURE 8 Sample use of the eco-hydraulic model

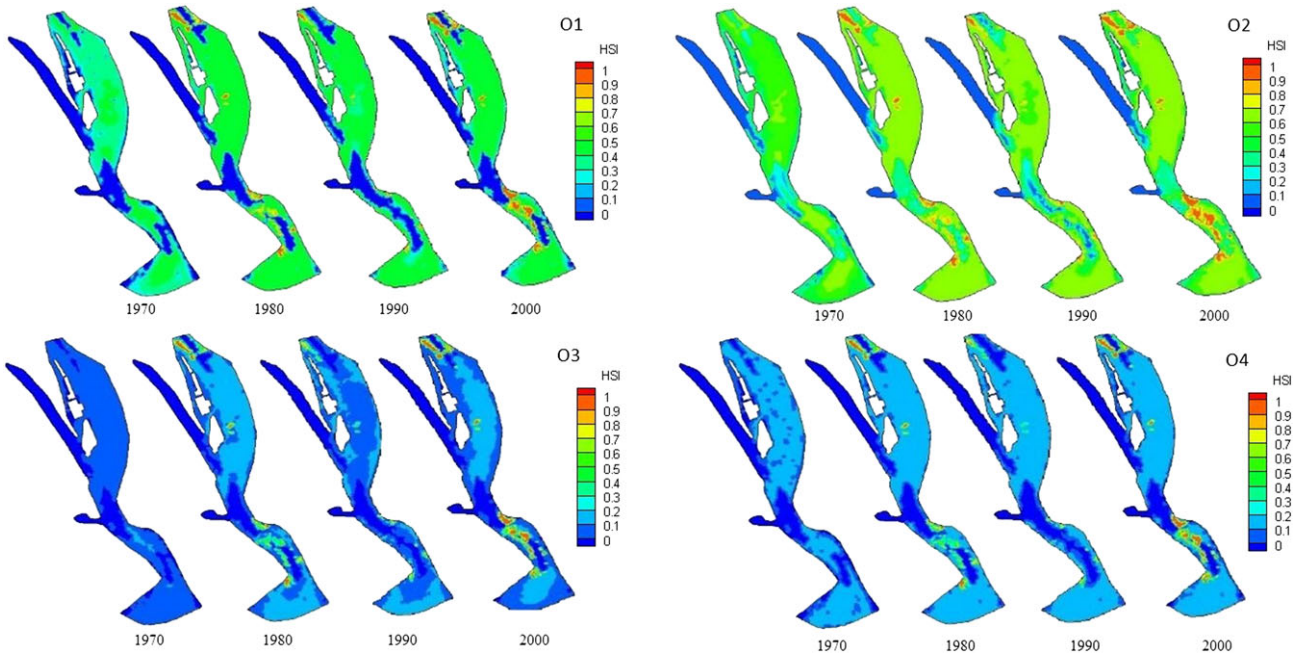

FIGURE 9 Simulated European grayling habitat suitability index (HSI) distribution in 1970, 1980, 1990, and 2000, using four different computational options

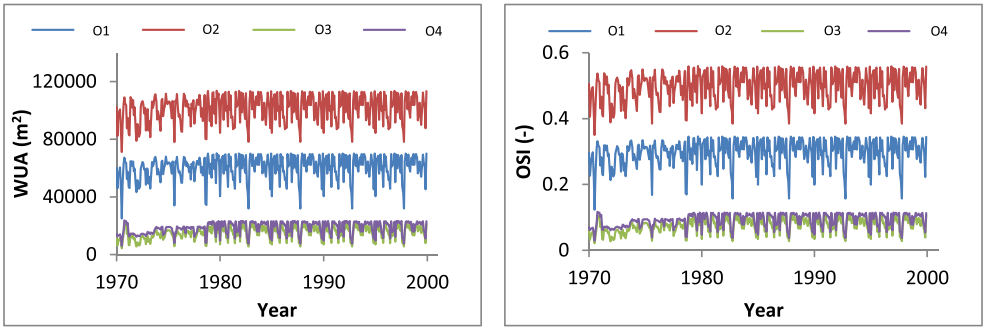

FIGURE 10 The European grayling weighted usable areas (WUA) and overall suitability index (OSI) distribution from 1970 to 2000, for O1, O2, O3, and O4

specifically, in Scenario E2, the WUA values for O1 mainly ranged from 4.7×10^4 to 7.0×10^4 m^2, and the corresponding OSI values ranged from 0.23 to 0.34. For O2, the WUA values changed between 1.1×10^5 and 8.0×10^4 m^2, and the corresponding OSI values changed between 0.44 and 0.55. The WUA and OSI values for O3 and O4 had the same trend. The WUA values fluctuated between 1.2×10^4 and 2.3×10^4 m^2 for O3 and O4, whereas OSI values changed between 0.047 and 0.1 for O3 and O4. The WUA and OSI value differences for O3 and O4 were much higher than the values for O1 and O2.

3.3 | Population number analysis

Applying the logistic population model, the simulated fluctuation of European grayling fish number is shown in Figure 11. It was recognized that the simulated European grayling fish number agreed well with the surveyed fish number in O1, O2, O3, and O4. The numerical model results also indicated that there were relatively large fluctuations in fish numbers from 1970 to 2000 in O1 and O2. Fluctuations of simulated fish number for O3 and O4 were insignificant, when compared with the O1 and O2. For O1, O2, O3, and O4, the simulated fish numbers decreased from 1.4×10^5 in 1970 to the level of 2.5×10^4 in 2000. It can be seen that the simulated number of European grayling showed reasonable agreement with the fish numbers caught for O1, O2, O3, and O4.

Applying the matrix population model, European grayling numbers for all life stages were simulated (Figure 12). Total simulated fish numbers had good agreement with the measured fish data in O1, O2, O3, and O4. Although the first life stage's fish population numbers showed an increasing trend from 1970 to 1972 for O1, O2, O3, and O4, then the first life stage's fish population numbers decreased dramatically from 1972 to 2000 for O1, O2, O3, and O4. In contrast to the first life stage's fish numbers, the other fish life stages showed a decreasing trend during the simulation periods. The fish numbers in the first life stage represented a large proportion of the whole population numbers during the simulated periods (Figure 13).

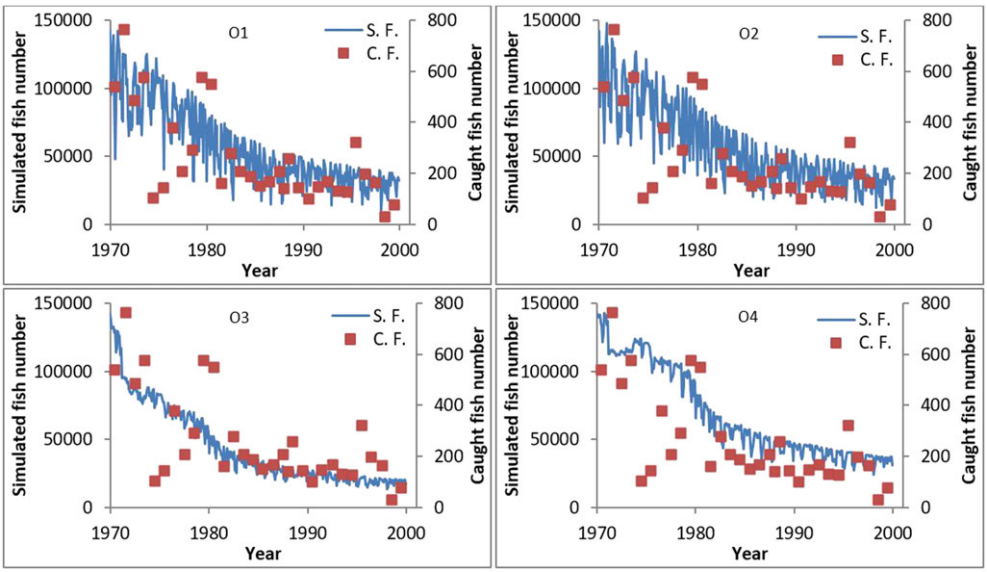

FIGURE 11 The European grayling simulated numbers based on the logistic population model

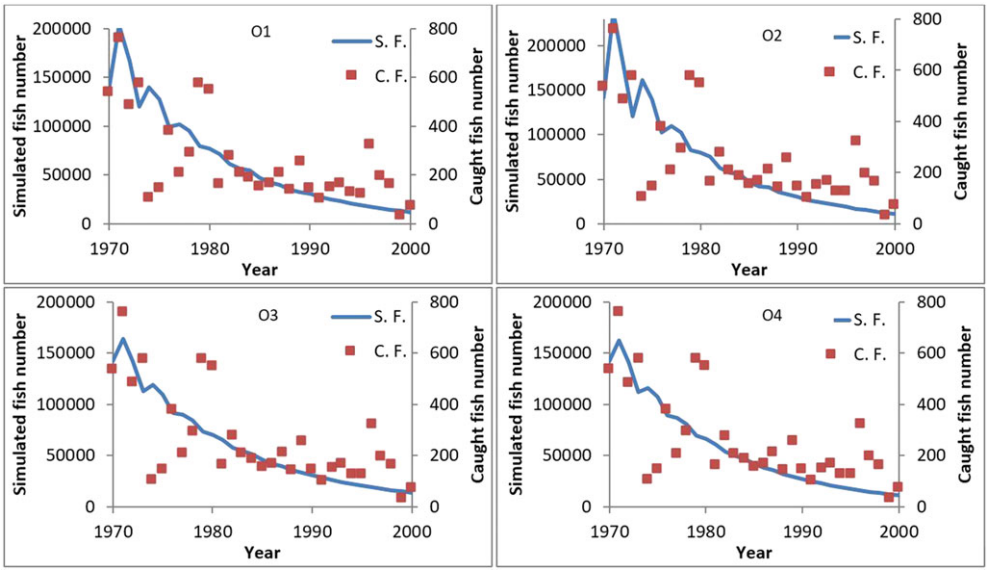

FIGURE 12 The simulated European grayling numbers based on the matrix population model

3.4 | Population density analysis

Based on the logistic population model, the European grayling density distribution was calculated, and the results are shown in Figure 14. The fish population density distribution showed similar trends for O1, O2, O3, and O4. In O1, the maximum fish density value was shown to be 55 fish per mesh cell in 1970s, and the maximum fish density decreased to 35 fish per mesh cell in 1980. Notably, the maximum fish density value in 1990 was similar to 1980, and the fish density distribution trend in 2000 was very similar to the distribution trend in 1990. In O2, the fish density distribution showed similar trends at all times, with the maximum values of 50, 30, 30, and 20 fish per mesh cell for 1970, 1980, 1990, and 2000, respectively. Additionally, similar distribution trends in fish populations in most years were observed in O3 and O4, and the maximum fish density values in O4 was higher than the values in O3.

Simulated results of European grayling density distributions are shown in Figure 15, based on the matrix population model. For O1, the high fish density values occurred mainly on the river bank areas, with a maximum value of 100 fish per mesh cell in 1970. However, the maximum fish density value decreased to 30 fish per mesh in 1980, to 20 fish per mesh in 1990, and dropped to nearly 0 fish per mesh in 2000. For O2, the fish density distribution is more even distributed, except in areas along the river tributary. The maximum fish density values were 60, 15, 10, and 8 fish per mesh cell in 1970, 1980, 1990, and 2000, respectively. For O3 and O4, the fish density distribution was mainly concentrated along the river bank and the downstream regions.

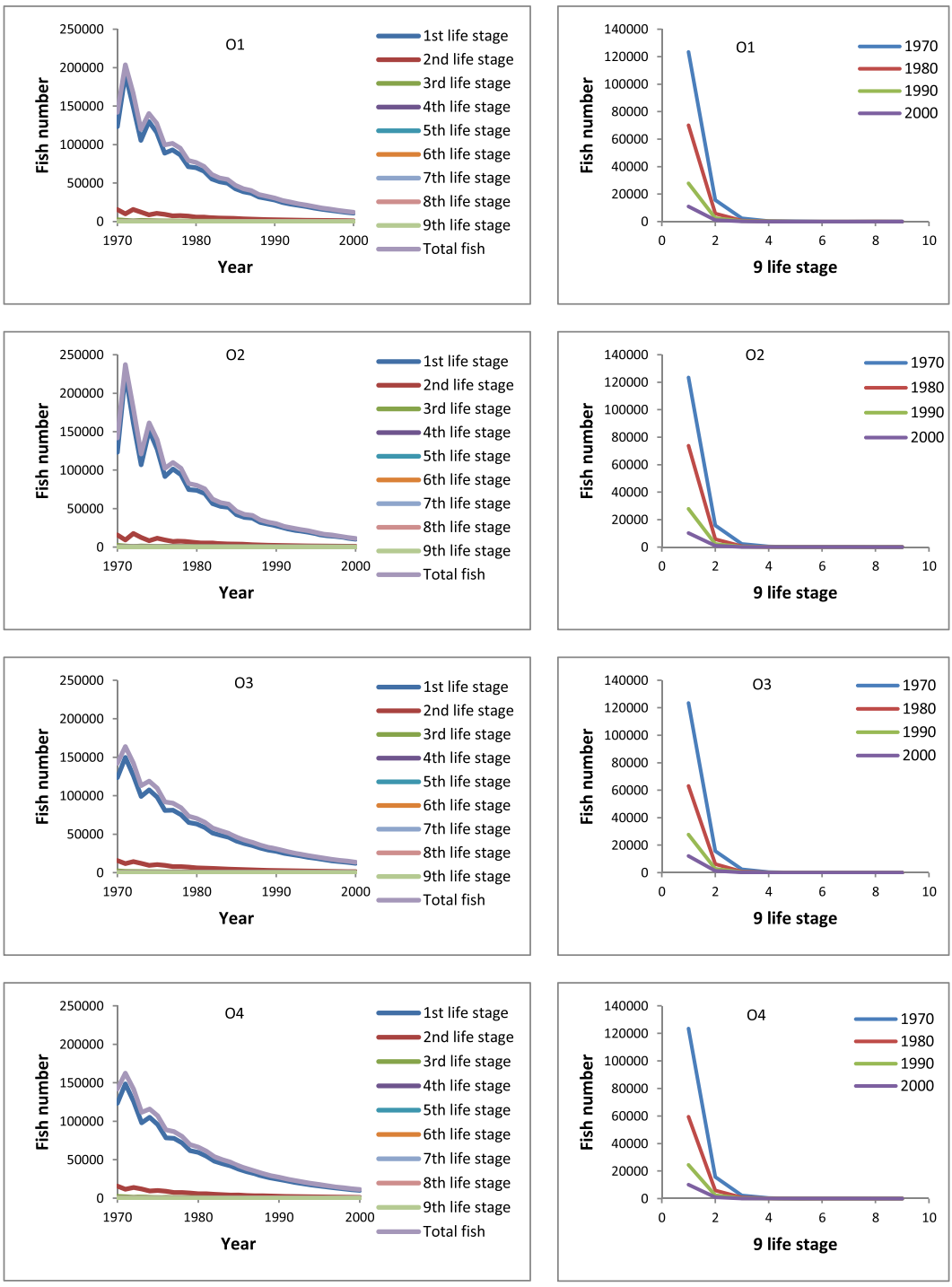

FIGURE 13 The European grayling population numbers and age structure based on the matrix population model

4 | DISCUSSION

4.1 | Evaluation of WW-Eco-tools suitability for operational eco-hydraulic analysis

The WW-Eco-tools is very important for eco-hydraulic system analysis. They highlight the fundamental role of temporal variability of hydro-morphological parameters in fish habitat distribution and in structuring populations of fish species. Using the software developed in this study, simulating population trends in anticipation of any changes in water management mode can provide decision-makers with useful information to optimize their management measures (Yao, 2016).

The WW-Eco-tools results are the most direct measure of hydro-morpho-dynamic aspects in rivers, eco-hydraulic variations in the computational domain, and eco-hydraulic fluctuations over time. The results of hydro-morpho-dynamic and total fish number data are easily calibrated with monitoring data. The WW-Eco-tools prediction results are visual and tend to draw maximum attention by software users. The visual results of the computation domain provide statistical analysis used to further process results, with the spatial simulation results being the most advanced output of WW-Eco-tools.

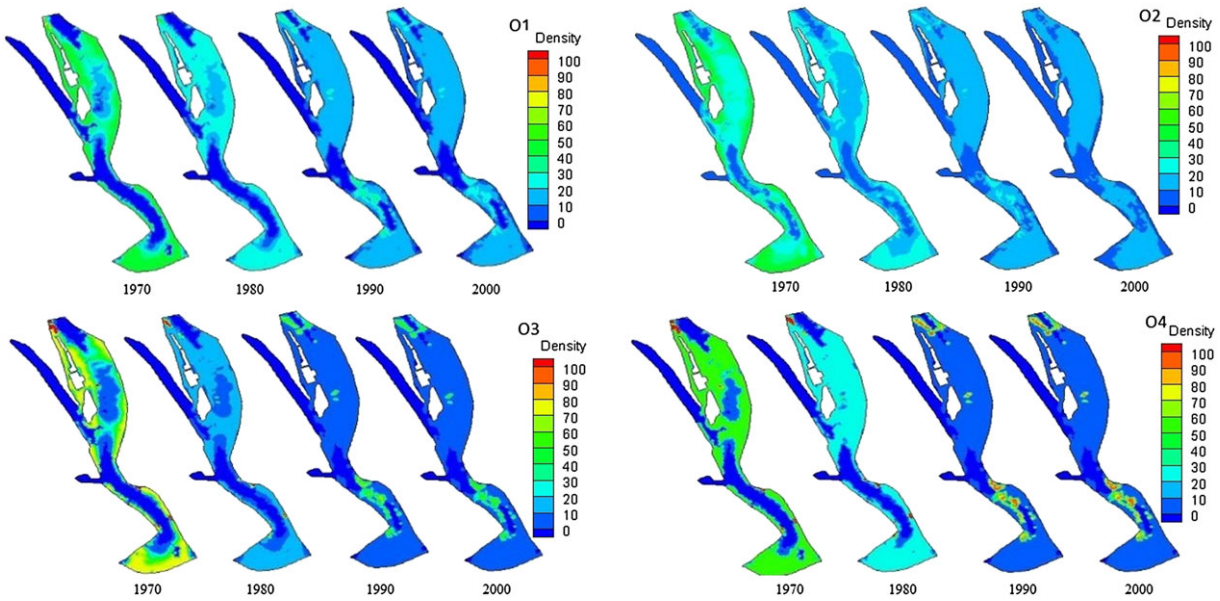

FIGURE 14 The European grayling population density fluctuation for O1, O2, O3, and O4 based on the logistic population model

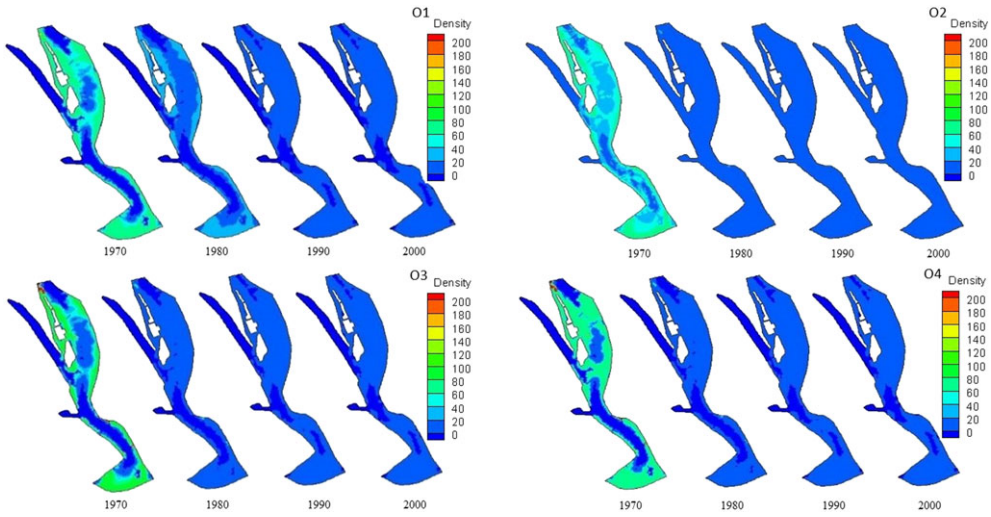

FIGURE 15 The European grayling population density fluctuation for O1, O2, O3, and O4 based on the matrix population model

Applications of WW-Eco-tools mainly focus on aquatic habitat and population status prediction in rivers, reservoirs, or lakes. Within this domain, the software is capable of testing population dynamics of selected fish species, effects of dam construction in a selected river, and the efficiency of fish stocking strategies (Yao, 2016). WW-Eco-tools allows investigation of model performance, via comparisons with surveyed data and sensitivity analyses of the model parameters (Yao & Rutschmann, 2015; Yao, 2016).

The WW-Eco-tools can be used in tandem with other models. For example, in this model application, the developed fish habitat suitability and fish population models were incorporated into an open source hydro-morpho-dynamic software, named TELEMAC (Hervouet, 2000). The WW-Eco-tools can be also incorporated into many other hydro-morpho-dynamic software or tools, such as FAST2D, Flow3D, OpenFOAM, and CCHE2D (Jasak, Jemcov, & Tukovic, 2007; Jia & Wang, 2001; Papanicolaou, Elhakeem, Krallis, Prakash, & Edinger, 2008; Roussel, Geiker, Dufour, Thrane, & Szabo, 2007). Through these settings, the WW-Eco-tools aligns with other engineering software such as an eco-hydraulic component of linked modelling systems.

4.2 | The opportunities and challenges of the eco-hydraulic model

The hydro-morpho-dynamic model has been widely used in river engineering and fluvial geomorphology for describing the river hydrodynamics and hydromorphology (Abad, Buscaglia, & Garcia, 2008; Wu, 2008; Zhang et al., 2016). The hydro-morpho-dynamic model's accuracy has been intensively tested by researchers and efficiency in both cost and time could be guaranteed (Wu, 2008). In addition, the habitat model has shifted from narrow studies that concentrate on a single approach to a diversity of methods. Habitat models that link fish species SI curves to physical conditions in rivers have become a very effective tool to assess the river habitat qualities (Parasiewicz, 2001; Yao et al., 2017; Yao, Chen, Zhong, Zhang, & Fan, 2017; Yi, Sun,

Zhang, & Yang, 2016). The different HSI combinations, as well as the four functions of HSI combinations, have been tested and verified by EAWAG (2002). The population model included in the eco-hydraulic model has become at the forefront and could obtain a better understanding of the complex interactions and processes of population ecology. The population model could also provide a quantitative approach for river management and could suggest indicators for river ecosystem health (Richter, Mathews, Harrison, & Wigington, 2003; Yao, 2016). Although the link between habitat and population models has been challenged, researchers found that the population models were highly connected with the habitat model, and the population models could also be evolved from habitat modelling (Katopodis, 2012). Thus, an eco-hydraulic model would have and continue to make significant contributions to high levels of ecological integrity and sustainable acceptance.

4.3 | The eco-hydraulic model future development

The WW-Eco-tools is not well suited for habitat quality classification. For example, it is unlikely to identify the proportion of HSI values bigger than a specific value (e.g., 0.7) or the proportion of HSI values smaller than a specific value (e.g. 0.3). In addition, it is difficult to calibrate fish numbers at a specific life stage, due to it being almost impossible to measure the specific age of surveyed fish vastly and effectively. This is also due to the surveyed fish data mainly focusing on fish length measurement. Another limitation of the eco-hydraulic model is that the population density is difficult to test and validate. It is also worth noting that an additional constraint is needed to insure the function of birth rate term in the matrix population model is in the range 0 to 1.

Work has begun on software updating to address model weaknesses, by enabling users to determine the habitat quality classes, such as ideal habitat, middle habitat, and unsuitable habitat proportions. Another feature of software updating is converting the matrix population model into a fish length distribution model. Through the model conversion, it is possible to relate the length of a fish to its age. As surveyed fish data mainly focuses on fish length measurement, a length–age relationship is more meaningful. Therefore, to compare modelling results with observations, the matrix population model should be converted into a fish length distribution model. We also tried to test the other adjustment factor functions in the matrix population model, which could fully guaranteed that all birth rate terms range from 0 to 1, without any qualifying conditions.

5 | CONCLUSIONS

This paper describes a 2D eco-hydraulic model (WW-Eco-tools) that can simulate hydro-morpho-dynamic features, habitat quality, population number, and population density status. This eco-hydraulic model has been implemented in the Aare River, Switzerland. The impact of the hydro-morpho-dynamic, four habitat computational options, and two population models are discussed. This model is particularly interesting because it has to account for a complex eco-hydraulic model including hydro-morpho-dynamic, habitat, and population models.

It is worth noting that WW-Eco-tools is specific to the Aare River and European grayling, but this eco-hydraulic model can easily be adapted to other river stretches, both natural rivers and rivers separated by hydraulic structures. Overall, the developed WW-Eco-tools has paved the way for paradigm shifts in engineering designs, habitat quality assessments, habitat restorations, dam construction effects, fish population management, maintenance of water resource, and aquatic resources infrastructure projects. The WW-Eco-tools also provides opportunities to recast, innovate, and minimize negative aspects of a project and increase the possibility to achieve a high level of ecological integrity.

ACKNOWLEDGEMENTS

This paper reflects my research time in the Technical University Munich, Germany. The work forms part of Weiwei Yao's PhD work and publication of this paper financially supported by National Key R&D Program of China (2016YFC0502004), CCA (2017.07), and CAS (Y6V60222YZ). The author gives thanks for the valuable comments from Prof Wolfgang Kinzelback in ETH Zurich and Prof Yuansheng Chen in the Chinese Academic of Science. We also thank Martin Parkes' help in handling the grammar issues.

CONFLICT OF INTEREST

No potential conflict of interest was reported by the authors.

ORCID

Weiwei Yao http://orcid.org/0000-0003-1050-9188

REFERENCES

Abad, J. D., Buscaglia, G. C., & Garcia, M. H. (2008). 2D stream hydrodynamic, sediment transport and bed morphology model for engineering applications. *Hydrological Processes*, *22*(10), 1443–1459.

Ackers, P., & White, W. R. (1973). Sediment transport: New approach and analysis. *Journal of the Hydraulics Division, American Society of Civil Engineers*, *99*(HY 11), 2040–2060.

Alfredsen, K., & Killingtveit, A. (1996). The habitat modelling framework: A tool for creating habitat analysis programs. In *Proceedings of the second international symposium on habitat hydraulics* (Vol. B) (pp. 215–227). Quebec City, Canada.

Armstrong, J. D., Kemp, P. S., Kennedy, G. J. A., Ladle, M., & Milner, N. J. (2003). Habitat requirements of Atlantic salmon and brown trout in rivers and streams. *Fisheries Research*, *62*(2), 143–170.

Aziz-Alaoui, M. A. (2002). Study of a Leslie–Gower-type tritrophic population model. *Chaos, Solutions & Fractals*, *14*(8), 1275–1293.

Bartholow, J. M. (1996). Sensitivity of a salmon population model to alternative formulations and initial conditions. *Ecological Modeling*, *88*(1–3), 215–226.

Bartholow, J. M., Laake, J. L., Stalnaker, C. B., & Williamson, S. (1993). A salmonid population model with emphasis on habitat limitations. *Rivers*, *4*, 265–279.

Bovee, K. D. (1982). A guide to stream habitat analysis using the in-stream flow incremental methodology. In-stream Flow Information Paper No. 12 US Fish and Wildlife Service, Fort Collins, Colorado 248 pp.

Bovee, K. D. (1986). Development and evaluation of habitat suitability criteria for use in the in-stream flow incremental methodology. In-stream flow information paper no. 21, US Fish and Wildlife Service Biological Report, 86 (7) Washington, DC.

Bovee, K. D., Waddle, T. J., Talbert, C., Hatten, J. R., & Batt, T. R. (2008). Development and application of a decision support system for water

management investigations in the upper Yakima River, Washington. US Geological Survey.

Brown, C. B. (1950). Sediment transport. In H. Rouse (Ed.), *Engineering hydraulics, Ch. 12*. Wiley.

Brunner, G. W., & Stanford, G. (2005). Sediment transport modeling in HEC RAS. Impacts of Global Climate Change. 1–12.

Burnhill, T. J. (2009). *Modeling the cumulative barrier and passage effects of main-stream hydropower dams on migratory fish populations in the Lower Mekong Basin*. Mekong River Commission.

Caswell, H. (2001). *Matrix population models*. Washington DC: John Wiley & Sons, Ltd.

Coggins, L. G., & Walters, C. J. (2009) Abundance trend and status of the Little Colorado River population of humpback chub: An update considering data from 1989-2008. U.S. Geological Survey Open-File Report 2009–1075, 18p.

Deangelis, D. L., & Gross, L. J. (1992). *Which individual-based approach is most appropriate for a given problem? Individual-based models and approaches in ecology*. (pp. 67–87). New York, NY: Routledge, Chapman, and Hall.

EAWAG (Swiss Federal Institute for Environmental Science and Technology) (2002). *Fischereiliches Gutachten uber die Aarebaggerung in Thun*. (p.201). Kastanienbaum, Switzerland: Forschungsanstalt des ETH-Bereichs. (in German)

Einstein, H. A. (1942). *Formulae for transportation of bed-load, trans* (Vol. 107). (pp. 561–577). Washington DC: ASCE.

Engelund, F., & Hansen, E. (1967). *A monograph on sediment transport in alluvial streams*. Copenhagen, Denmark: Teknisk Forlag.

Fox Jr, W., & William, W. (1970). An exponential surplus-yield model for optimizing exploited fish population. *Transactions of the American Fisheries Society*, *99*(1), 80–88.

Gamito, S. (1998). Growth models and their use in ecological modelling: An application to a fish population. *Ecological Modelling*, *113*(1), 83–94.

Ginot, V. (1995). EVHA, a Windows software for fish habitat assessment in streams. In *Bulletin Francais de la Peche et de la Pisciculture (France)*. Lyon: Division Biologie des Ecosystemes Aquatiques, Laboratoire d'Hydroecologie Quantitative.

Gouraud, V., Sabaton, C., & Capra, H. (2004). Role of habitat variability in trout population dynamics: Application of a dynamic population model to three French rivers. *Hydroécologie Appliquée*, *14*, 221–244.

Grimm, V. (1999). Ten years of individual-based modeling in ecology: What have we learned and what could we learn in the future? *Ecological modeling*, *115*(2), 129–148.

Guan, M., & Liang, Q. (2017). A two-dimensional hydro-morphological model for river hydraulics and morphology with vegetation. *Environmental Modelling & Software*, *88*, 10–21.

Hall, A. J., McConnell, B. J., Rowles, T. K., Aguilar, A., Borrell, A., Schwacke, L., & Wells, R. S. (2006). Individual-based model framework to assess population consequences of polychlorinated biphenyl exposure in bottle-nose dolphins. *Environmental Health Perspectives*, *114*, 60.

Harvey, B. C., Jackson, S. K., & Lamberson, R. H. (2009). In-stream: The individual-based stream trout research and environmental assessment model. (Vol. 218). US Department of Agriculture, Forest Service, Pacific Southwest Research Station.

Hervouet, J.-M. (2000). TELEMAC modelling system: An overview. *Hydrological Processes*, *14*(13), 2209–2210.

Hess, G. R. (1996). Linking extinction to connectivity and habitat destruction in meta-population models. *American Naturalist*, *148*, 226–236.

Hunziker, R. P. (1995). Fraktionsweiser Geschuebetransport, Ph.D. thesis, Mitteeilungen Nr 138 deer Versuchanstalt fur Wasserbau, Hydrologie und Glaziologie, ETH Zurich, Switzerland.

Ibrahim, L., Preuss, T. G., Schaeffer, A., & Hommen, U. (2014). A contribution to the identification of representative vulnerable fish species for pesticide risk assessment in Europe—A comparison of population resilience using matrix models. *Ecological Modeling*, *280*, 65–75.

Jasak, H., Jemcov, A., & Tukovic, Z. (2007). OpenFOAM: A C++ library for complex physics simulations. In *International workshop on coupled methods in numerical dynamics* (Vol. 1000). Croatia: IUC Dubrovnik.

Jia, Y., & Wang, S. S. (2001). CCHE2D: Two-dimensional hydrodynamic and sediment transport model for unsteady open channel flows over loose bed. Technical Rep. No. NCCHE-TR-2001-1, University of Mississippi, Oxford.

Jorde, K., & Bratrich, C. (2000). Ecological evaluation of in-stream flow regulations based on temporal and spatial variability of bottom shear stress and hydraulic habitat quality. In *Eco-hydraulics, 2nd International Symposium on Habitat Hydraulics*. Quebec City, Canada.

Katopodis, C. C. (2012). Ecohydraulic approaches in aquatic ecosystem: Integration of ecological and hydraulic aspects of fish habitat connectivity and suitability. *Ecological Engineering*, *48*, 1–7.

Korman, J., Martell, S. J., Walters, C. J., Makinster, A. S., Coggins, L. G., Yard, M. D., & Persons, W. R. (2012). Estimating recruitment dynamics and movement of Rainbow trout (Oncorhynchus mykiss) in the Colorado River in Grand Canyon using an integrated assessment model. *Canadian Journal of Fisheries and Aquatic Sciences*, *69*(11), 1827–1849.

Korman, J., Yard, M., Walters, C., & Coggins, L. G. (2009). Effects of fish size, habitat, flow, and density on capture probabilities of age-0 Rainbow trout estimated from electro-fishing at discrete sites in a large river. *Transactions of the American Fisheries Society*, *138*(1), 58–75.

Lancaster, J., & Downes, B. J. (2010a). Linking the hydraulic world of individual organisms to ecological processes: Putting ecology into eco-hydraulics. *River Research and Applications*, *26*(4), 385–403.

Lancaster, J., & Downes, B. J. (2010b). Eco-hydraulics needs to embrace ecology and sound science, and to avoid mathematical artefacts. *River Research and Applications*, *26*(7), 921–929.

Li, W., Wang, K., & Su, H. (2011). Optimal harvesting policy for stochastic logistic population model. *Applied Mathematics and Computation*, *218*(1), 157–162.

Meyer-Peter, E., & Müller, R. (1948). Formulas for bed-load transport. In Proceedings of the 2nd meeting of the International Association for Hydraulic Structures Research: 39–64.

Morris, W. F., & Doak, D. F. (2002). *Quantitative conservation biology: The theory and practice of population viability analysis*. Sunderland, USA: Sinauer Associates.

Mouton, A. M., De Baets, B., & Goethals, P. L. (2009). Knowledge-based versus data-driven fuzzy habitat suitability models for river management. *Environmental Modelling & Software*, *24*(8), 982–982.

Mouton, A. M., Alcaraz-Hernández, J. D., De Baets, B., Goethals, P. L., & Martínez-Capel, F. (2011). Data-driven fuzzy habitat suitability models for brown trout in Spanish Mediterranean rivers. *Environmental Modelling & Software*, *26*(5), 615–622.

Mouton, A. M., Schneider, M., Depestele, J., Goethals, P. L., & De Pauw, N. (2007). Fish habitat modelling as a tool for river management. *Ecological Engineering*, *29*(3), 305–315.

Nagaya, T., Shiraishi, Y., Onitsuka, K., Higashino, M., Takami, T., Otsuka, N., … Ozeki, H. (2008). Evaluation of suitable hydraulic conditions for spawning of Ayu with horizontal 2D numerical simulation and PHABSIM. *Ecological Modelling*, *215*(1), 133–143.

Naghibi, A., & Lence, B. (2012). Assessing impacts of high flow events on fish population: Evaluation of risk-based performance measures. *Ecological Modelling*, *240*, 16–28.

Nielsen, P. (1992). *Coastal bottom boundary layers and sediment transport* (Vol. 4). Singapore: World Scientific.

Nykänen, M., & Huusko, A. (2004). Transferability of habitat preference criteria for larval European grayling (Thymallus thymallus). *Canadian Journal of Fisheries and Aquatic Sciences*, *61*(2), 185–192.

Nykänen, M., Huusko, A., & Mäki-Petäys, A. (2001). Seasonal changes in the habitat use and movements of adult European grayling in a large subarctic river. *Journal of Fish Biology*, *58*(2), 506–519.

Papanicolaou, A. T. N., Elhakeem, M., Krallis, G., Prakash, S., & Edinger, J. (2008). Sediment transport modeling review—Current and future developments. *Journal of Hydraulic Engineering*, *134*(1), 1–14.

Parasiewicz, P. (2001). MesoHABSIM: A concept for application of instream flow models in river restoration planning. *Fisheries*, *26*(9), 6–13.

Rashleigh, B., Barber, M. C., Cyterski, M. J., Johnston, J. M., Parmar, R., & Moham-oud, Y. (2004). Population models for stream fish response to habitat and hydrologic alteration: The CVI Watershed Tool. Research Triangle Park (NC): USEPA. EPA/600/R-04/190.

Rice, S. P., Little, S., Wood, P. J., Moir, H. J., & Vericat, D. (2010). The relative contributions of ecology and hydraulics to eco-hydraulics. *River Research and Applications*, *26*(4), 363–366.

Richter, B. D., Mathews, R., Harrison, D. L., & Wigington, R. (2003). Ecologically sustainable water management: Managing river flows for ecological integrity. *Ecological Applications*, *13*(1), 206–224.

Robson, D. S., & Chapman, D. G. (1961). Catch curves and mortality rates. *Transactions of the American Fisheries Society*, *90*(2), 181–189.

Roussel, N., Geiker, M. R., Dufour, F., Thrane, L. N., & Szabo, P. (2007). Computational modeling of concrete flow: General overview. *Cement and Concrete Research*, *37*(9), 1298–1307.

Russ, G. R., & Alcala, A. C. (2004). Marine reserves: Long-term protection is required for full recovery of predatory fish population. *Oecologia*, *138*(4), 622–627.

Sempeski, P., & Gaudin, P. (1995). Habitat selection by grayling-II. Preliminary results on larval and juvenile daytime habitats. *Journal of Fish Biology*, *47*(2), 345–349.

Shepherd, J. J., & Stojkov, L. (2007). The logistic population model with slowly varying carrying capacity. *ANZIAM Journal*, *47*, C492–C506.

Steffler, P., & Blackburn, J. (2002). *River2D two-dimensional depth averaged model of river hydrodynamics and fish habitat. Introduction to depth averaged modeling and user's manual*. (p. P120). Canada: University of Albert.

Stohlgren, T. J., Ma, P., Kumar, S., Rocca, M., Morisette, J. T., Jarnevich, C. S., & Benson, N. (2010). Ensemble habitat mapping of invasive plant species. *Risk Analysis*, *30*(2), 224–235.

Talbert, C. B., & Talbert, M. K. (2012). *User manual for SAHM package for VisTrails*. Fort Collins, CO: US Geological Survey, Fort Collins Science Center. 72 p.

Tomsic, C. A., Granata, T. C., Murphy, R. P., & Livchak, C. J. (2007). Using a coupled eco-hydro-dynamic model to predict habitat for target species following dam removal. *Ecological Engineering*, *30*(3), 215–230.

Tonina, D., & Jorde, K. (2013). Hydraulic modelling approaches for ecohydraulic studies: 3D, 2D, 1D and non-numerical models. In *Ecohydraulics: An integrated approach* (pp. 31–74). NYC: John Wiley & Sons, Ltd.

Tsoularis, A., & Wallace, J. (2002). Analysis of logistic growth models. *Mathematical Biosciences*, *179*(1), 21–55.

USFWS (U.S. Fish and Wildlife Service) (1980). Habitat as a basis for environmental assessment. USFWS, Report 101 ESM, Fort Collins, CO.

Van Rijn, L. C. (1984). Sediment transport, part I: Bed load transport. *Journal of Hydraulic Engineering*, *110*(10), 1431–1456.

Van Rijn, L. C. (1993). *Principles of sediment transport in rivers, estuaries and coastal seas* (Vol. 1006). Amsterdam: Aqua publications.

Wang, Z., Lee, J. H., & Xu, M. (2013). Eco-hydraulics and eco-sedimentation studies in China. *Journal of Hydraulic Research*, *51*(1), 19–32.

Wu, W. (2008). *Computational river dynamics*. London: CRC Press.

Xia, C., Cao, Z., Pender, G., & Borthwick, A. (2017). Numerical algorithms for solving shallow water hydro-sediment-morphodynamic equations. *Engineering Computations*, *34*(8), 2836–2861.

Yao, W. (2016) Application of eco-hydraulic model on hydraulic and water resources engineering (ISSN 1437-3513; ISBN 978-3-943683-11-0).

Yao, W., Chen, Y., & He, X. (2018). Glen Canyon Dam operation effects on rainbow trout habitat and population status. *Polish Journal of Environmental Study*. https://doi.org/10.15244/pjoes/74366

Yao, W., Liu, H., Chen, Y., Zhang, W., Zhong, Y., Fan, H., … Bamal, S. (2017). Simulating spawning and juvenile rainbow trout (Oncorhynchus mykiss) habitat in Colorado River based on high-flow effects. *Water*, *9*(2), 150.

Yao, W., & Rutschmann, P. (2015). Three high flow experiment releases from Glen Canyon Dam on rainbow trout and flannel-mouth sucker habitat in Colorado River. *Ecological Engineering*, *75*, 278–290.

Yao, W., Rutschmann, P., & Bamal, S. (2014). Modeling of river velocity, temperature, bed deformation and its effects on rainbow trout (Oncorhynchus mykiss) habitat in Lees Ferry, Colorado River. *International Journal of Environmental Research.*, *8*(4), 887–896.

Yao, W. W., Chen, Y., Zhong, Y., Zhang, W., & Fan, H. (2017). Habitat models for assessing river ecosystems and their application to the development of river restoration strategies. *Journal of Freshwater Ecology*, *32*(1), 601–617.

Yao, W. W., Kumar, V., & Rutschmann, P. (2014). *Simulating dam effects on river deformation and rainbow trout (Oncorhynchus mykiss) population number*. (pp. 2477–2483). New York, NY, USA: CRC press.

Yi, Y., Sun, J., Zhang, S., & Yang, Z. (2016). Assessment of Chinese sturgeon habitat suitability in the Yangtze River (China): Comparison of generalized additive model, data-driven fuzzy logic model, and preference curve model. *Journal of Hydrology*, *536*, 447–456.

Zhang, M. L., Xu, Y. Y., Yang, Q. I. A. O., Jiang, H. Z., Zhang, Z. Z., & Zhang, G. S. (2016). Numerical simulation of flow and bed morphology in the case of dam break floods with vegetation effect. *Journal of Hydrodynamics, Series B*, *28*(1), 23–32.

Zhou, J., Zhao, Y., Song, L., Bi, S., & Zhang, H. (2014). Assessing the effect of the Three Gorges reservoir impoundment on spawning habitat suitability of Chinese sturgeon (Acipenser sinensis) in Yangtze River, China. *Ecological Informatics*, *20*, 33–46.

Zyserman, J. A., & Fredsøe, J. (1994). Data analysis of bed concentration of suspended sediment. *Journal of Hydraulic Engineering*, *120*(9), 1021–1042.

How to cite this article: Yao W, Bui MD, Rutschmann P. Development of eco-hydraulic model for assessing fish habitat and population status in freshwater ecosystems. *Ecohydrology*. 2018;e1961. https://doi.org/10.1002/eco.1961

APPENDIX A

DESCRIPTION OF THE HYDRO-MORPHODYNAMIC MODEL

2D shallow water equations

The continuity equation is written as

$$\frac{\partial h}{\partial t} + u\frac{\partial h}{\partial x} + v\frac{\partial h}{\partial y} = 0, \tag{A.1}$$

and the two horizontal momentum equations for the x and y components.

$$\frac{\partial u}{\partial t} + u\frac{\partial u}{\partial x} + v\frac{\partial u}{\partial y} = -g\frac{\partial \eta}{\partial x} + \frac{1}{h}\left(\frac{\partial h\tau_{xx}}{\partial x} + \frac{\partial h\tau_{xy}}{\partial y}\right) - \frac{\tau_{bx}}{\rho h} + f_{Cor}v, \tag{A.2}$$

$$\frac{\partial v}{\partial t} + u\frac{\partial v}{\partial x} + v\frac{\partial v}{\partial y} = -g\frac{\partial \eta}{\partial y} + \frac{1}{h}\left(\frac{\partial h\tau_{yx}}{\partial x} + \frac{\partial h\tau_{yy}}{\partial y}\right) - \frac{\tau_{by}}{\rho h} - f_{Cor}u, \tag{A.3}$$

where u and v are depth integrated velocity components in x and y directions, respectively (m/s); t is time (s); g is gravitational acceleration

(m/s^2); η is the water surface elevation (m); ρ is the density of water (kg/m^3); h is the water depth (m); f_{cor} is the Coriolis parameter (this number is related to the earth's rotation, for most cases, $f_{Cor} = 0$); τ_{xx}, τ_{xy}, τ_{yx}, and τ_{yy} are depth integrated Reynolds stresses (1/ms); and τ_{bx} and τ_{by} are shear stresses on the bed and flow interface (1/ms).

The bed shear stresses τ_{bx} and τ_{by} can be calculated based on the following equations:

$$\tau_{bx} = \rho_w c_f u \left(u^2 + v^2\right)^{1/2}, \tag{A.4}$$

$$\tau_{by} = \rho_w c_f v \left(u^2 + v^2\right)^{1/2}, \tag{A.5}$$

where ρ_w is the water density (kg/m^3); C_f is the bottom friction, which is calculated based on an empirical formula (−).

For the 2D hydrodynamic model, τ_{xx}, τ_{xy}, τ_{yx}, and τ_{yy} are depth integrated Reynolds stresses. They are also called depth averaged turbulence shear stresses, which are calculated with the following equations:

$$\tau_{xx} = 2v_t \frac{\partial u}{\partial x}; \tau_{xy} = \tau_{yx} = v_t \left(\frac{\partial u}{\partial y} + \frac{\partial v}{\partial x}\right); \tau_{yy} = 2v_t \frac{\partial v}{\partial y}, \tag{A.6}$$

where v_t is the eddy viscosity (m^2/s); v_t is composed of two parts: turbulence viscosity v_{tt} and water viscosity v_w.

The general bed-load transport equation for the Meyer-Peter and Muller function is represented by

$$Q_b = \begin{cases} 0 & \theta' \le 0.47 \\ \alpha\left(\theta' - \theta_c\right)^{3/2} & \theta' > 0.47 \end{cases}, \tag{A.7}$$

with

$$\theta' = \frac{\mu\tau_0}{(\rho_s - \rho_w) g D_{50}}; \quad \theta_c = 0.047, \tag{A.8}$$

where θ' is the shields number (−); α is Meyer Peter Muller (MPM) parameter (−); ρ_s is sediment density (kg/m^3).

The suspended load transport is calculated by the following equation:

$$\frac{\partial(Ch)}{\partial t} + \frac{\partial(Chu)}{\partial x} + \frac{\partial(Chv)}{\partial y} = \frac{\partial}{\partial x}\left(\varepsilon_t h \frac{\partial C}{\partial x}\right) + \frac{\partial}{\partial y}\left(\varepsilon_t h \frac{\partial C}{\partial y}\right) + E - D, \tag{A.9}$$

$$\text{with } \varepsilon_t = \frac{v_t}{\sigma_t} \text{ and } E - D = w_s(C_{eq} - C_{ref}), \tag{A.10}$$

where C is the suspended sediment concentration (kg/m^3); h is water depth (m); D is the deposition rate (kg/m^2s), and E is the suspension rate (kg/m^2s); $(E - D)$ is the net exchange of sediment between suspended load and bed-load layer; σ_t is Schmidt number, also called Prantl number (0.6); ε_t is turbulence diffusivity scalar (m^2/s); v_t is the turbulence viscosity (m^2/s); C_{eq} is suspended load concentration at reference level under equilibrium conditions (kg/m^3); C_{ref} is suspended load concentration at reference level (kg/m^3).

To calculate the bed evolution affected by bed-load and suspended load, the Exner equation needs to be solved.

$$(1-p)\frac{\partial Z_f}{\partial t} + \frac{\partial Q_s}{\partial x} + \frac{\partial Q_s}{\partial y} + (E-D)_{Z=Zref} = 0 \tag{A.11}$$

where p is the noncohesive bed porosity (−); Z_f is the bottom elevation (m); Q_s is the solid volume transport (bed-load) per unit width (kg/ms); $(E - D)_{Z = Zref}$ is the net exchange of sediment between suspended load and bed-load layer at the reference level (kg/m^2s).

APPENDIX B

DESCRIPTION OF THE POPULATION MODEL

The logistic population model:

$$\frac{dP}{dt} = rP\left(1 - \frac{P}{K}\right). \tag{B.1}$$

Integrating the differential equation, first multiple by K on both sides:

$$\frac{KdP}{dt} = rP(K-P), \tag{B.2}$$

$$\frac{KdP}{P(K-P)} = rdt, \tag{B.3}$$

$$dP\left(\frac{1}{P} + \frac{1}{K-P}\right) = rdt, \tag{B.4}$$

$$\frac{dP}{P} + \frac{dP}{K-P} = rdt. \tag{B.5}$$

Do the integration on both sides:

$$\int \frac{dP}{P} + \int \frac{dP}{K-P} = \int rdt. \tag{B.6}$$

Due to

$$\int \frac{dP}{P} = LnP + C_1; \int \frac{dP}{K-P} = -Ln(K-P) + C_2. \tag{B.7}$$

The left side of Equation B.6 becomes

$$LnP - Ln(K-P) + C_3 = rt + C_4; \; C_3 = C_1 + C_2, \tag{B.8}$$

$$Ln\frac{P}{K-P} = rt + C_5; \; C_5 = C_3 + C_4, \tag{B.9}$$

$$e^{rt+C_5} = \frac{P}{K-P}, \tag{B.10}$$

$$P = Ke^{rt+C_5} - Pe^{rt+C_5}, \tag{B.11}$$

$$P = \frac{Ke^{rt+C_5}}{1+e^{rt+C_5}} = \frac{K}{1+Ce^{-rt}}; \; C = e^{-C_5}. \tag{B.12}$$

Set $t = 0$, $p = Nt$, then

$$C = \frac{K - N_t}{N_t}. \tag{B.13}$$

Introduce it into Equation B.12:

$$P = \frac{K}{1 + \left(\frac{K - N_t}{N_t}\right)e^{-rt}} = \frac{KN_t e^{rt}}{K + N_t(e^{rt} - 1)}. \quad \text{(B.14)}$$

In order to combine habitat model with the population model, K is replaced by $\beta \times WUA$; rt is replaced by $\alpha \times (OSI_{t+\ t} - OSI_t)$, then the Equation B.14 becomes as follows and the logistic population model with solution:

$$P^{t+\Delta t} = \frac{\beta \times WUA_{t+\Delta t} \times P_t \times e^{\alpha \times (OSI_{t+\ \Delta t} - OSI_t)}}{\beta \times WUA_{t+\Delta t} + P_t \times (e^{\alpha \times (OSI_{t+\ \Delta t} - OSI_t)} - 1)}. \quad \text{(B.15)}$$

The empirical parameters α and β based on four computational options (O1, O2, O3, and O4) for European grayling in Aare River were as follows:

$$\alpha_1 = 8, \alpha_2 = 8, \ \alpha_3 = 7, \alpha_4 = 7, \ \ \beta_1 = 7, \ \beta_2 = 3, \ \beta_3 = 15, \ \beta_4 = 15. \quad \text{(B.16)}$$

APPENDIX C

THE MATRIX POPULATION MODEL

The matrix population model is developed from the classic matrix population model. The birth rate and the survival rate are included in a square matrix. The OSI is also inserted into the birth rate and survival rate.

$$\begin{bmatrix} N_{1,t+\Delta t} \\ N_{2,t+\Delta t} \\ \dots \\ N_{i,t+\Delta t} \\ \dots \\ N_{j,t+\Delta t} \\ \dots \\ N_{n-1,t+\Delta t} \\ N_{n,t+\Delta t} \end{bmatrix} = \begin{bmatrix} F_{1,t} & F_{2,t} & \dots & F_{i,t} & \dots & F_{j,t} & \dots & F_{n-1,t} & F_{n,t} \\ S_{1,t} & 0 & \dots & 0 & \dots & 0 & \dots & 0 & 0 \\ \dots & \dots & \dots & \dots & \dots & \dots & \dots & \dots & \dots \\ 0 & 0 & \dots & S_{i-1,t} & \dots & 0 & \dots & 0 & 0 \\ \dots & \dots & \dots & \dots & \dots & \dots & \dots & \dots & \dots \\ 0 & 0 & \dots & 0 & \dots & S_{j-1,t} & \dots & 0 & 0 \\ \dots & \dots & \dots & \dots & \dots & \dots & \dots & \dots & \dots \\ 0 & 0 & \dots & 0 & \dots & 0 & \dots & 0 & 0 \\ 0 & 0 & \dots & 0 & \dots & 0 & \dots & S_{n-1,t} & S_{n,t} \end{bmatrix} \times \begin{bmatrix} N_{1,t} \\ N_{2,t} \\ \dots \\ N_{i,t} \\ \dots \\ N_{j,t} \\ \dots \\ N_{n-1,t} \\ N_{n,t} \end{bmatrix}, \quad \text{(C.1)}$$

with adjust factor

$$F_{i,t} = f_i \times \left(1 + \frac{e^{(OSI_{i,t}-a)} - e^{-(OSI_{i,t}-a)}}{e^{(OSI_{i,t}-a)} + e^{-(OSI_{i,t}-a)}}\right); \quad S_{i,t} = s_i \times \left(1 + \frac{e^{(OSI_{i,t}-b)} - e^{-(OSI_{i,t}-b)}}{e^{(OSI_{i,t}-b)} + e^{-(OSI_{i,t}-b)}}\right), \quad \text{(C.2)}$$

where $N_{i,\,t}$ is fish number at time t for fish stage i (−); $S_{i,\,t}$ is model survival rate at time t (−); $F_{i,\,t}$ is birth rate of for spawning fish at time t (−); f_i is the basic birth rate for the stage i (−); s_i is the basic survival rate the stage of i (−); a and b are the empirical parameters of matrix population model based on four computational options (O1, O2, O3, and O4) for European grayling in Aare River were as follows:

$$a_1 = 0.4, a_2 = 0.6, a_3 = 0.3, a_4 = 0.3, b_1 = 0.4, b_2 = 0.6, b_3 = 0.3, b_4 = 0.3 \quad \text{(C.3)}$$

For the European grayling in Aare River, the first year was defined as fry life stage; the second year was defined as juvenile life stage, and the third to ninth was defined as adult life stage; the spawning life stage was defined as the third to ninth year at spawning season (April & May). The OSI_i definition show as follows:

The basic survival rate was defined through the method of Robson and Chapman (1961). For the basic birth rate determination, the f_1 and f_2 is equal to 0 due to the fish has not reach to spawning age. Starting from third life stage and the ninth life stage, the logarithm growth curves were applied to determine the basic birth rate based on trial calculation and matrix iteration. The all birth rate terms could be determined until all life stage of the basic matrix model were become stable. The solution of survival rate (s_i) and birth rate (f_i) of the European grayling for the matrix population model were as follows:

$$f_1 = 0, f_2 = 0, f_3 = 29, f_4 = 37, f_5 = 46, f_6 = 47, f_7 = 48, f_8 = 48, f_9 = 48, \quad \text{(C.4a)}$$

TABLE C1 European grayling life stage definition

Fish life stage	1	2	3	4	5	6	7	8	9
OSI life stage	Larval	Juvenile	Adult	Adult	Adult	Adult	Adult	Adult	Adult
OSI life stage at spawning season	-	-	Spawning	Spawning	Spawning	Spawning	Spawning	Spawning	Spawning

Note. OSI = overall suitability index.

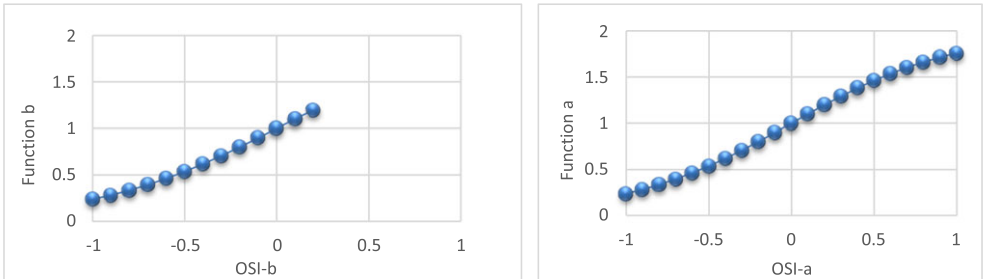

FIGURE C1 The sensitivity analysis of birth rate term and $F_{i,t}$ and survival rate term $S_{i,t}$

$$s_1 = 0.127, s_2 = 0.146, s_3 = 0.171, s_4 = 0.206, s_5 = 0.259, s_6 = 0.350, s_7 = 0.537, s_8 = 0.838, s_9 = 0.0001. \quad \text{(C.4b)}$$

In the matrix population model, due to the $S_{i,t}$ need to be guaranteed in the range of 0 to 1, the range of the Function $b\frac{e^{(OSI_{i,t}-b)}-e^{-(OSI_{i,t}-b)}}{e^{(OSI_{i,t}-b)}+e^{-(OSI_{i,t}-b)}}$ is between −1 and 0.2 in this model application. The range of Function $a\frac{e^{(OSI_{i,t}-a)}-e^{-(OSI_{i,t}-a)}}{e^{(OSI_{i,t}-a)}+e^{-(OSI_{i,t}-a)}}$ for the birth rate term $F_{i,t,}$ is between −1 and 1. The sensitivity analysis of the birth rate term $F_{i,t}$ and survival rate term $S_{i,t}$ were down and the results show as follows:

5. SCHLUSSBETRACHTUNG

Probleme im Zusammenhang mit der Hydromorphodynamik in Flüssen sind in den meisten wasserbaulichen und wasserwirtschaftlichen Projekten von enormer Bedeutung und erfordern die Gestaltung von Maßnahmen unter Berücksichtigung von Sedimenttransportproblemen bereits in sehr frühen Phasen der Projektentwicklung. Es müssen auch angemessene Betriebsregelungen für ein nachhaltiges Sedimentmanagement sowohl in kurz- als auch in langfristiger Perspektive entwickelt werden. Aufgrund der Komplexität und Dynamik der hydromorphologischen Vorgänge in Flüssen spielt die numerische Modellierung in diesem Gebiet eine immer wichtigere Rolle. Obwohl der Sedimenttransport seit fast zweihundert Jahren untersucht wird, gibt es aber noch viele Wissenslücken, besonders bei dem fraktionierten Sedimenttransport. Während die Navier-Stokes- und Kontinuitätsgleichungen eine allgemein anerkannte mathematische Beschreibung der Strömung darstellen, gibt es kein vergleichbares Modell für die vollständige Wechselwirkung zwischen Strömung, Sedimenttransport und Flusssohländerung. Daher bleibt der Sedimenttransport auch heute ein herausforderndes Forschungsthema, weil eine einheitliche Beschreibung der Prozesse noch erreicht werden soll. Dabei sind sowohl neue experimentelle Ansätze als auch fortgeschrittene numerische Modelle erforderlich. Ersteres bietet neue Einblicke in grundlegende Prozesse, während letzteres, die Ergebnisse für reale Anwendungen zu skalieren, ermöglicht.

Diese Studie hat zu verschiedenen Erkenntnissen geführt und auch Potentiale für die zukünftige Modellentwicklung des fraktionierten Sedimenttransportes sichtbar gemacht. Nachfolgend werden zuerst die Erkenntnisse formuliert und anschließend in einem Ausblick Möglichkeiten für die künftigen Forschungen aufgezeigt.

5.1. Schlussfolgerung aus dem Istzustand der Modelle

Wie oben gezeigt, haben die Modellkonzepte zur Beschreibung des Sedimenttransports auch einen stark empirischen Charakter. Im Allgemeinen wurden diese Formeln und die darin enthaltenen Parameter in Labor- oder Feldversuchen unter bestimmten Bedingungen entwickelt. Darüber hinaus wurden sie meistens von einer sehr beschränkten Datenbasis hergeleitet. Deshalb kann bei der Anwendung einer Formel nur dann mit zuverlässigen Ergebnissen gerechnet werden, wenn die Bedingungen im zu untersuchenden Problem jenen bei der Formelerstellung zumindest ähneln. Die Verschiedenartigkeit vieler Labordaten und der Mangel an Felddaten schränken die Formelanwendung ein und führen dazu, dass nur wenige originale Formeln allgemein akzeptiert bzw. als direkt brauchbar für praktische Anwendung eingestuft werden. Um den komplexen Transportmechanismus des Sedimentes in natürlichen Fließgewässern mit Mischsohle wenigstens qualitativ richtig zu beschreiben, sind Mehrkorn- und Mehrschichtansätze unabdingbar. Darüber hinaus kann in numerischen Modellen angenommen werden, dass die herkömmlichen Sedimenttransportformeln in einem räumlich

und zeitlich begrenzten Rahmen gültig sind. In Modellen wird dann der Sedimenttransport mit Korrekturparametern modifiziert oder/und mit zusätzlichen Ansätzen modelliert, um die anderen Effekten zu erfassen. Deshalb können numerischen Modelle die realen Naturprozesse der Flussmorphologie nur über mathematische Näherungsbeziehungen mit den oft starken Vereinfachungen nachbilden. Da die Modelle zahlreiche Parameter enthalten, die nur geschätzt werden können, sind Sensitivitätsanalyse und Modellkalibrierung sowie Modellvalidierung erforderlich für die Modellanwendung.

Zusätzlich zu den Schwierigkeiten, die zugrundeliegende Physik zu erfassen, sind numerische Modelle durch unvollständige Informationen über die Anfangs- und Randbedingungen sowie Modellparameter begrenzt. Selbst mit einem perfekten Modell können Unsicherheiten dieser Informationen zu einem Anwachsen von Prognosefehlern führen und daher die Fähigkeit eines numerischen morphodynamischen Modells beeinträchtigen. Um zuverlässige Vorhersagen über die langfristige morphodynamische Entwicklung zu erhalten, müssen sowohl die Anfangsbedingungen bei Modellerstellung als auch die Modellparameter und die dazugehörigen Randbedingungen bei Modellkalibrierung gut geschätzt werden.

Erosions- und Sedimentationsvorgänge wechseln sich einander in einem Fließgewässer ständig ab und charakterisieren den Geschiebehaushalt des Gewässers. Wie im Kapitel 2 gezeigt, spielt sich der Geschiebetransport in den sohlennahen Bereichen ab. Daher ist er einer der wichtigsten Faktoren bei der Ausformung der Flusssohle. Im Folgenden diskutieren wir über die konzeptionellen Probleme der Geschiebeberechnungen und über die praktischen Probleme der Verwendung von numerischen Modellen sowie über ihre möglichen Lösungen.

5.1.1. Geschiebetransportberechnung

Wie in Abschnitt 2.2 gezeigt, wird in den konventionellen Transportansätzen für Sedimentmischungen die Gesamtgeschieberate als die Summe der einzelnen Transportraten der unterschiedenen Fraktionen verstanden. Die Geschieberate pro Fraktion wird dann wiederum mit den für den uniformen Sedimenttransport empirisch entwickelten Konzepten beschrieben, in denen die antreibende Kraft für den Sedimenttransport die Sohlenschubspannung ist. Dabei kann sich eine Kornfraktion nur bewegen, wenn die Sohlenschubspannung einen Grenzwert der kritischen Sohlenschubspannung überschreitet. Des Weiteren wird die Energie, die das Wasser auf den Boden überträgt, nicht in vollem Umfang als Antriebsenergie für den Sedimenttransport genutzt, da die auf dem Boden vorhandenen Sohlformen einen Teil der Wasserenergie verbrauchen, ohne dass dies zum Sedimenttransport beiträgt. Der Einfluss der Sohlformen äußert sich in dem sog. Sohlform-Faktor. Dieser Sohlform-Faktor reduziert die Sohlenschubspannung auf eine effektive Sohlenschubspannung für den Transport. Außerdem kann grobes Korn den Kräften der Wasserbewegungen mehr ausgesetzt werden als feines Korn. Die kleineren Körner verbergen sich gleichsam hinter den größeren. Um diesen Effekt berechnen zu können, wird je nach Zusammenstellung der Fraktionen der Transport pro Fraktion mit dem sogenannten Hiding-Exposure-Faktor korrigiert. Die gegenseitige Wechselwirkung zwischen den Körner äußert sich in diesem Korrektur-Faktor.

Jedoch muss erkannt werden, dass Geschiebetransportformeln nur bedingt gültig sind, und nur in Kombination mit den adäquaten Modellen für Sohlschubspannung, Sohlform-Faktor und Hiding-Exposure-Faktor. Es sei angemerkt, dass Fehler in diesen Modellen zu einer großen Unsicherheit der berechneten Geschieberaten führen können. Variationen in den Prognosen verschiedener Geschiebetransportmodellen entstehen vor allem durch Unterschiede in der Methode der Schubspannungsberechnung und der Behandlung des kritischen Shields-Parameters für die diversen Sedimentfraktionen. Bei der Anwendung in einem anderen Flussgebiet muss man sich darüber im Klaren sein und im Hinblick auf die zu kalibrierenden Größen eine vernünftige Wahl treffen. Für die praktische Anwendung ist daher immer Sorgfalt erforderlich. Darüber hinaus treten bei den diversen Formeln doch beträchtliche Abweichungen von den Messwerten auf, deshalb wird vorgeschlagen, Naturmessungen vorzunehmen, um damit die Datenbasis für eine sinnvolle Formelauswahl zu besitzen und Daten für die Verifikation der Formeln zur Verfügung zu haben (ÖWAV, 2011).

Geschiebeansätze sind global in zwei Gruppen zu unterteilen, nämlich stochastische und deterministische Modelle. Es hängt davon ab, wie die effektive Sohlschubspannung bestimmt wird. Beispielsweise kommt in einem stochastischen Modell der Charakter des Geschiebetransportes in einer Wahrscheinlichkeitsverteilung der auf die Sohle wirkenden Schubspannungen zum Ausdruck, um vor allem den Effekt von turbulenten Bewegungen dicht oberhalb der Sohle auszudrücken.

Kritische Sohlschubspannung

Das Grundprinzip zum Transportbeginn basiert auf der Gleichgewichtsvorstellung, dass die Kraftwirkung durch den Strömungswiderstand eines Kornes bzw. der Sohle ausgeglichen wird. Ein Korn verbleibt in Ruhe, solange ein Kräfte- bzw. Momentengleichgewicht unter der Wirkung der treibenden und haltenden Kräfte möglich ist. Es gerät in Bewegung, wenn Korn und Unterlage so beschaffen sind, dass sich die für ein Gleichgewicht mit den treibenden Kräften erforderliche haltende Kraft nicht mehr einstellen kann. Die Grenze zwischen stabilem und instabilem Zustand des Korns, die als kritischer Zustand oder Grenzzustand bezeichnet wird und die den Bewegungsbeginn des Korns kennzeichnet, wird somit durch die hydrodynamische Bedingung einerseits und die Beschaffenheit von Korn und Unterlage andererseits bestimmt.

Obwohl die Kräftebilanz an einem Einzelkorn physikalisch eindeutig formuliert werden kann, ist die Frage nach dem Transportbeginn einer Mischsohle nicht leicht zu beantworten. Jedes Korn an der Sohle hat normalweiser unterschiedliche Eigenschaften: Durchmesser, Form und Dichte sind innerhalb einer gewissen Bandbreite variabel. Daraus folgt, dass auch die Lagerungsbedingungen von Korn zu Korn verschieden sind: sie ragen mehr oder weniger weit aus der Sohle heraus und sind auf unterschiedliche Art zwischen den umgebenden Auflagerkörnern eingebettet. Die Definition des Transportbeginns ist schwierig, weil sowohl die auslösenden hydrodynamischen Kräfte, die von Turbulenzströmung induziert werden, als

auch die Größen, die die Korn- bzw. Sohleneigenschaften bestimmen, nur statistisch erfasst werden können. Aus der Variabilität der wirkenden Kräfte und Größen folgt, dass die Körner der Sohle nicht gleichzeitig in Bewegung geraten. Auch bei kleinsten Strömungsbeanspruchungen können sich immer einzelne kleine Körner der Sohle bewegen.

In der Regel ist das Experiment im Labor unabdingbare Voraussetzung für die Untersuchung der wesentlichen Zusammenhänge des Sedimenttransportes. So entstanden die Beziehungen für den Transportbeginn meist durch systematische Laborversuche unter kontrollier- und wiederholbaren Bedingungen. Die exakte Bestimmung des Zeitpunktes für den Transportbeginn ist dabei immer noch von der Subjektivität des Beobachters im Labor abhängig (Vollmers, 1998). Der kritische Zustand, ab dem sich ein maßgeblicher Teil der Sohle in Bewegung setzt, wird von verschiedenen Autoren unterschiedlich definiert. Im Folgenden werden ein paar Definitionen des Transportbeginns exemplarisch aufgeführt.

- Shields (1936) bestimmte die kritische Schubspannung des Bewegungsbeginns durch Extrapolation von gemessenen Geschiebetransportraten und den zugehörigen Schubspannungswerten in Richtung des verschwindenden Geschiebetransportes.
- Meyer-Peter & Müller (1948) definierten visuell den Transportbeginn, indem die hydraulische Belastung kontinuierlich gesteigert wird, bis das Einsetzen der Bewegung auf einer Referenzfläche beobachtet werden kann.
- Vanoni (1964) hat versucht, den Zustand des Bewegungsbeginns anhand der Beobachtung eines kleinen Sohlenausschnitts und Zählung der sog. Aufbrüche (bursts) pro Zeiteinheit zu klassifizieren. Er definierte vier Kriterien für den Sedimenttransportbeginn nämlich vernachlässigbare, geringe, kritische und allgemeine Bewegung. Jeder Zustand kann den Bewegungsbeginn darstellen, obwohl die Unterschiede in der maximalen Strömungsgeschwindigkeit zwischen der minimalen und der maximalen Anzahl der Aufbrüche pro Sekunde sehr groß sind. Diese Kriterien können als das Bewegungsrisiko definiert werden (Zanke, 1990).
- Neil und Yalin (1969) legten den Schwellenwert bei einer gewissen Anzahl Partikel, die sich pro Einheitsfläche bewegen, fest.
- Graf und Pazis (1977) nahmen an, dass keine kritischen Bedingungen beim Bewegungsbeginn existieren, sondern nur eine schwache Kornbewegung bei Erosion.
- Nach Hrissanthou, et al. (1995) lässt sich die Grenze zwischen Ruhe und Bewegung nicht eindeutig festlegen. Es ist daher zweckmäßig, den Bewegungsbeginn nicht mit einem exakten Zahlenwert zu beschreiben, sondern jeweils einen Bereich anzugeben, in dem die Startbedingungen möglich sind.

Die praktische Bedeutung des Transportbeginns führte zu einer Vielzahl von Arbeiten, die entsprechenden Kriterien enthalten. Obwohl der kritische Zustand unterschiedlich von verschiedenen Autoren definiert ist, kann er sich tatsächlich auf eine sehr geringe Sediment-

transportrate beziehen. Grundlagen für eine detailliertere Analyse des Transportbeginns sind in z.B. Zanke (2001), Luckner (2002), Bezzola (2002) und Dey (2014) zu finden. Eine Formulierung für den Bewegungsbeginn unter Berücksichtigung des turbulenzinduzierten vertikalen Druckgradienten und der Lagerungsbedingungen des Korns ist in Vollmer & Kleinhans (2007) beschrieben.

Diverse Methoden zur Bestimmung des Transportbeginns bei unterschiedlichen morphologischen Randbedingungen werden z.B. in Chien & Wan (1999) oder in Dey (2014) angeführt. Grundsätzlich lassen sich für den Bewegungsbeginn zwei Betrachtungsmöglichkeiten unterscheiden, nämlich auf Grundlage eines deterministischen Modelles oder einer stochastischen Methode. Unter anderem wurden Ansätze der Sohlschubspannungen häufig in numerischen Modellen verwendet.

Deterministische Betrachtung

In deterministischen Modellen bildet die effektive Schubspannung einen Grenzwert für den Geschiebetransport, wobei der Fraktionstransport Null ist, wenn die Schubspannungsgröße unter diesen Wert kommt. Da bei der Sedimentbewegung viele Einflussfaktoren zusammenwirken, ist die Quantifizierung des Einflusses dieser Faktoren teilweise nicht eindeutig geklärt. Manche Autoren (z.B. Shields, 1936; Meyer-Peter & Müller, 1948; Parker, 1990) vernachlässigen die Lift-, andere (z.B. Einstein, 1950; Van Rijn, 1984; Dittrich, 1998; Zanke, 2001; Luckner, 2002; Dey, 2003; Luckner & Zanke, 2007; Jang et al., 2011) die Schleppkraft. Zusätzlich zu diesen Unsicherheiten in der Modellvorstellung variiert der Strömungsangriff auf die Körner zeitlich und räumlich. Außerdem beeinflussen die Korneigenschaften sowie die Lagerungsbedingungen des Korns den Beginn der Sedimentbewegung.

Die ursprüngliche Arbeit von Shields (1936) bestand darin, den Bewegungsbeginn gleichförmigen Sohlmaterials für beliebige Sedimentdichten bzw. -größen, unterschiedliche Flüssigkeiten und Strömungsbedingungen in schwach geneigten Gerinnen experimentell zu ermitteln. Er fasste gemessene kritische Zustände des Bewegungsbeginns in dimensionsloser Darstellung zusammen, wobei zwei dimensionslose Größen, welche als Shields-Parameter θ (auch dimensionslose Sohlschubspannung genannt) und Partikel-Reynolds-Zahl bezeichnet werden, verwendet wurden. Shields (1936) selbst gab die Grenzen $\theta = 0.03$ für den Zustand der absoluten Ruhe, d.h. kein Korn ist in Bewegung, und $\theta_c = 0.06$ für den Bewegungsbeginn der Kiessohle an. Mit der Empfehlung von Meyer-Peter & Müller (1948) erhält man $\theta_c = 0.047$ für die kritische Sohlenschubspannung im hydraulisch rauen Bereich.

Jedoch kann aus Beobachtungen gefolgert werden, dass auch bei Schubspannungen unterhalb derjenigen nach Shields berechneten noch geringer Transport stattfindet. Die Untersuchungen von Paintal (1971), Taylor & Vanoni (1972), Unsöld (1984) und Schöberl (1990) haben gezeigt, dass auch unterhalb der Shields-Kurve noch systematische Zusammenhänge zwischen Sohlenschubspannung und Transportrate zu erkennen sind. Hieraus kann ge-

schlossen werden, dass die kritischen Schubspannungen der Shields-Kurve äußerstenfalls mit geringen Kornbewegungen verknüpft sind, aber nicht den Ruhestand charakterisieren (Dittrich, 1998). Die Untersuchungen von Zanke (2001) haben auch gezeigt, dass die Grenzschubspannung nach Shields für den absoluten Bewegungsbeginn demnach etwas zu hoch liegt. Dies kann u.a. durch die Vernachlässigung der Liftkraft oder der stochastischen Eigenschaft des Transportbeginns bedingt sein. Er hat einen analytischen Ansatz entwickelt, der es ermöglicht, den Bewegungsbeginn allein durch den Winkel der inneren Reibung und die Turbulenz zu beschreiben. Aufgrund seines Konzeptes wird bei einer turbulenzfreien Strömung die bewegungsauslösende Sohlschubspannung eines Partikels allein durch den Reibungswinkel des Sedimentes bestimmt. Die dimensionslose kritische Sohlschubspannung ist definiert durch das Verhältnis der Schubkraft (oder Schleppkraft) parallel zur Sohle und der Gewichtkraft der oberen Sedimentschicht, auf die die Sohlschubspannung wirkt. Bei einer turbulenten Strömung treten Druckschwankungen und die daraus resultierenden Liftkräfte an den Partikeln auf. Wird der Bewegungsbeginn der Sedimente durch den zeitlichen Mittelwert der dimensionslosen Schubspannung ausgedrückt, ist die wirklich bewegungsauslösende Schubspannung immer stärker als die mittlere kritische Sohlschubspannung.

Stochastische Betrachtung

Die Unsicherheit der deterministischen Ansätze liegt daran, dass bei der genauen Feststellung der kritischen Größen nur von den Mittelwerten von Strömungsangriff und Kornwiderstand ausgegangen wird. Die deterministischen Modelle sind somit Schwellenwertfunktionen, bei denen in der Natur (bedingt durch die verschiedenen Sedimentzusammensetzungen sowie die Turbulenzbewegungen) keine scharfe Trennung in dieser Form existieren. Aufbauend auf dieser Erkenntnis hat Einstein (1950) dieses Phänomen mittels eines stochastischen Ansatzes abgebildet. Er leitete Wahrscheinlichkeitsverteilungen für die angreifende Sohlschubspannung und für den Erosionswiderstand am einzelnen Korn her, um den Bewegungsbeginn zu beschreiben.

Des Weiteren entwickelte Grass (1970) ein Modell für den Bewegungsbeginn, wobei die von den deterministischen Modellen verwendeten Mittelwerte der momentanen antreibenden Größen (z.B. Geschwindigkeiten bzw. Schubspannungen) und der momentanen Widerstände (kritische Größen), die zur Destabilisierung einzelner Körner notwendig sind, durch zwei voneinander unabhängige Wahrscheinlichkeitsverteilungsfunktionen (WVF) ersetzt wurden. Diese WVF charakterisieren die vorhandene Strömung bzw. das vorhandene Sediment mit gegebener Korngröße und -form sowie -lagerung. Der Grad ihrer Überlappung kann ein Maß für die mögliche Sedimentbewegung präsentieren. Zanke (1990) führte den Begriff des Bewegungsrisikos ein und berücksichtigte damit die Schwierigkeit der Erfassung des Übergangszustands von Ruhe zu Bewegung. Der Bewegungsbeginn lässt sich durch das Bewegungsrisiko umfassender angeben. Das Diagramm von Shields wurde modifiziert mit Angabe dieses Bewegungsrisikos. Kleinhans & Van Rijn (2002) haben in ihrem Modell die Sohlschubspannung als eine stochastische Größe aufgefasst.

Allgemein können die stochastischen Ansätze bessere Ergebnisse als vergleichbare deterministische Ansätze ergeben, wobei die Geschieberate bei niedrigen Schubspannungen zu berücksichtigen ist. Jedoch liefern die stochastischen Ansätze keine besseren Ergebnisse als einfacher aufgebaute Ansätze und sind zumeist sehr komplex formuliert. Eine weitere umfassende Übersicht über zahlreiche spätere Forschungsergebnisse zu dem Bewegungsbeginn und kritischen Shields-Parameter bzw. den kritischen Schubspannungen kann z.B. der Studie von Buffington & Montgomery (1997) oder von Dey (2014) entnommen werden.

Sohlform-Faktor

Sohlformen sind eigentlich eine Folge des Sedimenttransports. Je nach Sohlform wird Energie des fließenden Wassers zerstört, die dann für den Transport des Sediments nicht mehr zur Verfügung steht. Auf diese Weise besteht eine starke Wechselwirkung zwischen den Sohlformen einerseits und dem Sedimenttransport andererseits.

Die meisten Geschiebeansätze teilen die gesamte Sohlschubspannung in zwei Komponente auf: ein Anteil, die sog. effektive Sohlschubspannung, wirkt direkt auf die Körner ein; der andere Anteil wird durch Druckunterschiede um die Sohlform auf die Sohle übertragen. Des Weiteren wird beim Geschiebetransport davon ausgegangen, dass vor allem die effektive Sohlschubspannung von Bedeutung ist. Basierend auf diesem Konzept können wir die Hypothese der Hysterese im Sedimenttransport folgendermaßen erklären: Da die Entwicklung der Sohlformen bei Zunahme der Schubspannung hinterherlaufend ist, erreichen sie in der steigenden Phase der Hochwasserwelle ihre maximale Höhe noch nicht und daher ist der Energieverbrauch durch die Sohlformen noch nicht allzu groß. Der Anteil der effektiven Schubspannung ist dann groß. In der sinkenden Phase der Hochwasserwelle sind die Flussbettformen stark entwickelt und verbrauchen viel Energie. Die kornbezogene Schubspannung ist dann kleiner. Dies hat zur Folge, dass der Sedimenttransport bei demselben Abfluss in der steigenden Phase größer sein kann als in der sinkenden Phase.

Als Folge der Sohlformen tritt eine vertikale Sortierung auf. Das Sohlenmaterial ist relativ feiner in den Dünenspitzen und relativ gröber in den Dünenmulden sowie in der Sohltiefe. Diese vertikale Sortierung beeinflusst ihrerseits wieder den Geschiebetransport. Dies ist vor allem nach dem Passieren des Höhepunktes einer Hochwasserwelle wichtig. Die Schubspannungen nehmen dann ab und die groben Körner haben die Neigung, sich in den tieferen Mulden der Dünenbildungen abzusetzen. Bei abnehmenden Schubspannungen bleibt nicht genügend Energie übrig, um das grobe Sediment in den tiefen Mulden aufzunehmen. Auf diese Weise entsteht eine allmähliche Verfeinerung der Transportschicht, mit einem relativ zunehmenden Sedimenttransport als Folge, weil die feinen Körnungen sich leichter transportieren lassen als die groben Körner. Die Untersuchung in Bezug auf vertikale Sortierung in Situationen, wo es zu Dünenbildung kommt, befindet sich noch in einer Phase theoretischer Konzepte (z.B. Blom et al., 2003).

Die Entwicklung von Sohlformen und die dazugehörigen Sedimenttransportprozesse werden jedoch immer noch nicht vollständig erfasst. Für die praktische Anwendung müssen wir noch stets Zuflucht in stark empirischen Ansätze suchen, mit allen hiermit verbundenen Modellbegrenzungen (z.B. Meyer-Peter & Müller, 1948; Van Rijn, 1993).

Hiding-Exposure-Faktor

Die sogenannte Hiding-Exposure (HE) Erscheinung ist eine wichtige Ursache dafür, dass ein Korn aus einer Mischung einen abweichenden Transport hat, verglichen mit seinem Transport aus einem uniformen Material unter denselben Randbedingungen. Die Bedeutung der HE-Effekte bei der Kontrolle der Mobilität einer Sedimentmischung wurde zuerst in der Arbeit von Einstein (1950) beschrieben. Er berücksichtigte den HE-Faktor durch eine Ausgleichsfunktion, die allerdings im sog. Strömungsintensitätsparameter (oder dimensionslose Transportrate) enthalten war. Jedoch wurde eine genaue Berechnungsformel dieser Ausgleichsfunktion nicht angegeben.

Egiazaroff (1965) hat eine Ausgleichsfunktion vorgeschlagen. Er ging davon aus, dass der kritische Shields-Parameter bei jeder Kornfraktion von dem Verhältnis des Fraktionsdurchmessers und mittleren Korndurchmessers in der Oberschicht abhängig ist. Er hat eine Ausgleichsfunktion vorgeschlagen. Gessler (1965) untersuchte den Geschiebebeginn bei Sand-Kies-Mischungen. Eine wichtige Beobachtung von ihm war, dass sowohl in der stabilen Deckschicht als auch im transportierten Sohlmaterial immer alle Fraktionen enthalten sind. Seine Ausgleichsfunktion korrigiert die überschüssige bzw. effektive dimensionslose Schubspannung einer Fraktion. Die Effektivität der HE-Funktionen wurde von Profitt & Sutherland (1983) gezeigt, die herausgefunden haben, dass ihr Einsatz die Größenverteilung des transportierten Sediments verbessert. Hunziker (1995) zog daraus die Schlussfolgerung, dass der Schwellenwert für alle Fraktionen der gleichen kritischen Schubspannung entsprechen muss. Deswegen empfiehlt sich, die effektive Schubspannung mit der Ausgleichsfunktion zu korrigieren. Diese Gleichmobilitätshypothese kann als $\beta_{bk} = \beta_{sk}$ ausgedrückt werden, wobei β_{bk} und β_{sk} jeweils die Gewichtsanteile der k-Kornfraktion in der Geschiebeschicht und der Sohlmischung repräsentieren. Eine Konsequenz der Gleichmobilität ist, dass die gesamte Geschiebetransportrate durch einen einzigen vertretenden Korndurchmesser berechnet werden kann. Allerdings haben die anderen Arbeiten gezeigt, dass für niedrige und mittlere Sohlschubspannungen dies nicht der Fall ist. Genauer zeigte Wilcock (1992), dass in diesem kritischen Bereich von Schubspannungen (was maßgebend in vielen Kiessohlflüssen ist) die Änderungen der relativen Mobilität sowohl von der Korngröße als auch von der Schubspannung in einer komplexen Art und Weise abhängen. Eines der wichtigsten Ergebnisse ist, dass ein Zustand des Teiltransports vorhanden ist (Wilcock & McArdell, 1993), in dem ein Anteil von einigen Kornfraktionen auf der Sohloberfläche bei einer gegebenen Schubspannung (d.h. $\beta_{bk} \neq \beta_{sk}$) unbeweglich bleiben. Offensichtlich bedeutet dies, dass es Unterschiede in der Mobilität innerhalb der Kornfraktionen gibt und diese Variation das Verhalten der Sedimentmischung signifikant beeinflusst. Wu et al. (2000a) verwendeten eine stochastische Ausgleichs-

funktion. Dabei korrelierten sie die Wahrscheinlichkeit der Abschattungs- und Depositionseffekte mit dem Korndurchmesser. Diverse Ausgleichsfunktionen für HE-Faktor, die empirisch unter eine Anzahl von verschiedenen experimentellen und reellen Konditionen ermittelt wurden, sind in u.a. Sutherland (1991) und Wu (2007) zu finden. Im Allgemeinen wurden diese Funktionen dazu benutzt, die kritischen Bedingungen oder Geschieberaten numerisch anzupassen. Jedoch versuchen diese Funktionen nicht, individuelle physikalische Prozesse zu simulieren, die durch die Interaktion zwischen verschiedene Kornfraktionen verursacht werden. Zudem erfordert die erfolgreiche Anwendung der Funktionen normalerweise Vorwissen über das Ergebnis, sodass eine passende Funktion ausgewählt werden kann.

5.1.2. Modellerstellung

Bei den numerischen Simulationen des fraktionierten Sedimenttransports bestehen noch zahlreiche Wissenslücken, die die erfolgreiche Modellanwendung einschränken. Deshalb muss beim Modelleinsatz eine große Anzahl von Entscheidungen getroffen werden. Wie oben erwähnt, haben Modellkonzepte einen stark empirischen Charakter und die eingebrachte Empirie basiert häufig auf Laborversuchen oder auf sehr spezifischen Felddaten, man muss sich deshalb vor der Studie dieser Konzepteinschränkungen bewusst sein, um erfolgreich modellieren zu können.

Für die Aussagefähigkeit des verwendeten Modells ist gleichermaßen entscheidend, wie repräsentativ die maßgeblichen hydromorphologischen Prozesse, Charakteristika des Untersuchungsgebietes und Randbedingungen mit ausreichender Genauigkeit abgebildet werden. Theoretisch kann ein feines 3D Modellsystem bessere Ergebnisse liefern als die anderen Modelle. Je höher die Dimension des gewählten numerischen Modellsystems ist, desto größer sind der Datenbedarf, der Bearbeitungsaufwand und die Ansprüche an die Vorerfahrung des Modellverwenders. Modellverfeinerungen bedingen nicht nur einen erheblichen rechentechnischen Mehraufwand, sondern führen auch zum Problem der messtechnischen Unbestimmbarkeit von Parametern und damit zur Problematik der nur vagen und eigentlich nicht mehr zuverlässig ableitbaren Vorgabewerte. Damit werden in die Modelle Unsicherheitsfaktoren eingetragen, welche die erreichbare Aussagegüte verschleiern. Grundsätzlich soll die Verfeinerung und Leistungsfähigkeit des verwendeten Modells mit der Datensituation im Studiengebiet und der Modellerfahrung in Balance stehen.

Morphologische Anfangsbedingungen

Morphologische Modelle für den fraktionierten Sedimenttransport stellen hohe Anforderungen an die detaillierte Sohlenschematisierung. Pro Gitterzelle muss eine komplette Fraktionsverteilung für jede Bodenschicht angegeben werden. In Deutschland ist die gebräuchliche Einteilung der Sedimentfraktionen durch die DIN 4022 bestimmt. Im Allgemeinen stehen solche detaillierten Informationen für ein ganzes Untersuchungsgebiet nicht zur Verfügung und müssen hinsichtlich der verfügbaren Kornverteilungskurven in der Längs- und Querrichtung sowie in der Tiefe geschätzt werden. Morphologische Berechnungen werden zuerst mit

dieser geschätzten Fraktionsverteilung unter einem mittleren Abfluss durchgeführt. Die erhaltenen Ergebnisse werden als Anfangsbedingung für weitere Simulation verwendet.

Für das feine Bodenmaterial spielt die Dünenbildung jedoch sehr wohl eine Rolle und beeinflusst in starkem Maße den vertikalen Sedimentaustausch. Die Größe der Sohlform hängt dabei unmittelbar von der Abflussgröße des Abflusses ab und kann mit einer empirischen Formel abgeschätzt werden. Häufig wird angenommen, dass die Dicke der Aktivschicht etwa der Hälfte der Dünenhöhe entspricht und mit der Zeit variiert. Im Allgemeinen tritt bei grobem Bodenmaterial mit einer starken Gradierung keine oder nur sehr geringe Dünenbildung auf. In diesem Fall kann man sich für eine konstante Dicke der Aktivschicht entscheiden, indem sie beispielsweise auf einer charakteristischen Korngröße des Sohlmaterials basiert. Da viele der existierenden Dünenhöhenmodelle auf Experimenten mit uniformem Sediment basieren und die Bildung von Sohlformen noch nicht in ausreichendem Maße erfasst ist, ist es wünschenswert, in diesen Situationen unter Umständen auch Messungen der Sohlformen zur Verfügung zu haben. Ferner ist es zu empfehlen, die Empfindlichkeit der verschiedenen Vorgehensweisen im Modell zu testen.

In fraktionierten morphologischen Modellen muss man sich entscheiden, ob man die Mächtigkeit der Aktivschicht im Laufe der Zeit als konstant oder variabel voraussetzt. Es ist wichtig zu berücksichtigen, dass die Aktivschichtdicke Einfluss auf die berechnete morphologische Veränderung hat. Beispielsweise erfolgen Kornsortierungsprozesse in einer dünnen Aktivschicht relativ schnell im Vergleich zur Kornsortierung in einer mächtigeren Aktivschicht. Daher wird eine gering mächtige Aktivschicht im Fall von Erosion eher abpflästern und somit die Erosion schneller zum Stillstand bringen als eine mächtige Aktivschicht. In Abschnitt 2.3.2 sind verschiedene Formeln für die Dicke der Aktivschicht zu finden.

Des Weiteren wird die Sohle in eine Reihe von Unterschichten aufgeteilt. Die Anzahl der Bodenschichten hängt davon ab, ob die Sohlenzusammensetzung eine starke Schichtung in der Tiefe aufweist. Je größer die Anzahl der Unterschichten ist, umso mehr Informationen müssen in das morphologische Modell eingegeben werden. Es ist zu empfehlen, eine Dicke für die Unterschichten zu wählen, die kleiner ist als die Dicke der Aktivschicht.

Darüber hinaus müssen erodierbare Sohlbereiche von nichterodierbaren und damit transportunwirksamen Bereichen abgetrennt werden. Die nichterodierbaren Bereiche können oberflächlich oder in tieferen Schichten anstehen und müssen als morphologisch maßgebliche Anfangsbedingungen bereits in den Eingangsdaten berücksichtigt werden.

Morphologische Randbedingungen

Gemäß Abschnitt 2.4 ist je nach spezifischer Problemstellung eine Vielzahl von Randbedingungen zu berücksichtigen. Alle diese Angaben müssen für den vorgesehenen Rechenzeitraum festgelegt werden.

Am Einströmrand des Modells werden das zeitliche Sohlenniveau und die zeitliche Sedimenttransportrate als morphologische Randbedingung angegebenn, wobei die Sohlzusammensetzung, die Größe und die Zusammensetzung des hereinkommenden Sedimenttransports pro Kornfraktion zu definieren sind. Die definierte Kornzusammensetzung an der Einströmgrenze muss also sorgfältig ausgewählt werden. Es wird aber zur Bedingung gemacht, dass hierüber genügend Informationen bekannt sind. Dieser Aspekt stellt bei Untersuchungen des fraktionierten Sedimenttransports grundsätzlich eine große Herausforderung dar, da hier im Einzelfall keine direkte Messung für alle Parameter durchgeführt werden kann. Für die Bestimmung des gesamten Schwebstofftransports sind schon teilweise Messdaten verfügbar. Messdaten des Geschiebetransports liegen jedoch nur selten vor. Eine mögliche Lösung wäre: Anstatt der direkten Eingabe der gemessenen Werte wird die Sedimenttransportrate näherungsweise über die Transportkapazitätsbeziehungen bestimmt. Daher müssen die morphologischen Randbedingungen auch bei der Modellkalibrierung berücksichtigt werden. Um sogenannte Randbedingungseffekte im Interessensgebiet zu vermeiden, ist in der Praxis das gewählte Modellgebiet größer als das Untersuchungsgebiet.

Je nachdem, ob im Untersuchungsgebiet örtliche Geschiebeentnahmen oder -zugaben stattfinden, werden die zeitabhängigen Geschiebeentnahmen mengenmäßig definiert. Bei Geschiebezugaben ist neben der Menge auch noch die Angabe der Kornverteilung erforderlich.

5.1.3. Sensitivitätsanalyse

Die Sensitivitätsanalyse ist eine mathematische Methode, die die Variabilität einzelner Modellparameter mit der Variabilität der Ausgangsgröße des Modells in Zusammenhang bringt. Das Ziel des Verfahrens ist, Modellparameter einzeln zu variieren und den Einfluss auf die Ausganggröße qualitativ und quantitativ zu untersuchen. Durch die Sensitivitätsanalyse können demnach besonders sensitive Modellparamater identifiziert werden, die den größten Einfluss auf die Unsicherheit der Ausgangsgröße haben. Ebenfalls kann die Sensitivitätsanalyse helfen, die weniger einflussreichen Parameter zu identifizieren und gegebenenfalls auszuschließen, um bei der Modellentwicklung den Rechenaufwand zu minimieren. Alle Parameter, die bei kleinen Variationen zu großen Veränderungen in den Ergebnissen führen, sind bei der Kalibrierung besondere Aufmerksamkeit zu schenken. So kann man rascher eine einfache und gute Modellkalibrierung erzielen. Sensitivitätsanalyse ist besonders für Bereiche wichtig, in denen keine Messdaten zur Modellkalibrierung vorliegen oder die Messdaten oft ungenügend bzw. sehr unsicher sind.

Sensitivitätsanalysen können in zwei Gruppen klassifiziert werden: lokale und globale Sensitivitätsanalysen. Man spricht auch von deterministischen und stochastischen Methoden.

- Bei der lokalen oder deterministischen Sensitivitätsanalyse untersucht man die Veränderung der Ausgangsgrößen eines Modells bei der gleichzeitigen Variation einer einzelnen

Eingangsgröße, während die restlichen Eingangsgrößen konstant gehalten werden. Wiederholt man dieses Vorgehen für jeden einzelnen Modellparameter, so kann die jeweilige spezifische Sensitivität in Form von Korrelationskoeffizienten bestimmt werden. Diese lokalen Bewertungsmaße sollen deshalb nur im Falle eines linearen Zusammenhangs zwischen Eingangs- und Ausgangsgrößen verwendet werden.

- Anders als bei den lokalen Methoden werden in den globalen oder stochastischen Sensitivitätsanalysen alle Modellparameter gleichzeitig verändert und es wird der gesamte Werteraum der Eingangs- und Ausgangsgrößen in Betracht gezogen. Die Streuung jedes einzelnen Parameters kann durch verschiedene Verteilungsfunktionen charakterisiert werden. Mittels eines stochastischen Verfahrens lassen sich beliebig viele unterschiedliche Parametersätze testen und einzelne Parameter miteinander vergleichen. Außerdem können die Sensitivitätsindices von Sobol als die zugehörigen globalen Sensitivitätsmaße verwendet werden, um Interaktionen zwischen einzelnen Parametern zu berücksichtigen und zu quantifizieren bzw. um den Einfluss der Veränderung der Eingangsgrößen auf die Streuung der Ausgangsgrößen im gesamten nichtlinearen Werteraum zu betrachten.

Eine Kombination lokaler und globaler Verfahren ist die Screening-Methode, die hauptsächlich zur Reduzierung des Rechenaufwands in globalen Verfahren benutzt wird. Bei dieser Methode werden die Parameter mit geringem Einfluss auf die Ausgangsgröße auf einem konstanten Wert gehalten und die restlichen Parameter gemäß ihren Verteilungsfunktionen variiert. Eine solche Methode ist in u.a. Morris (2004) zu finden.

Da die Umsetzung der lokalen Sensitivitätsanalyse recht einfach ist und sie einen ersten Überblick über die Sensitivität einzelner Eingangsgrößen bietet, wird diese Methode trotz einiger Nachteile häufig in hydromorphologischen Modellen verwendet. Obwohl die globale Sensitivitätsanalyse einen deutlich größeren Rechenaufwand erfordert, wird empfohlen, die Parameterinteraktionen in einem numerischen Modell zu berücksichtigen (Saltelli et al., 2000).

5.1.4. Modellkalibrierung und -validierung

An dieser Stelle erscheint es sinnvoll nochmals zu betonen, dass viele Sedimenttransportparameter in der Regel nicht direkt messbar sind. Sie können daher nur über ihre Wirkungen auf die simulierte Realität durch eine optimale Anpassung von Simulationsergebnissen an Beobachtungsdaten approximativ bestimmt werden. Dieser Prozess wird Parameteridentifikation oder Modellkalibrierung genannt und stellt eine inverse Aufgabe dar, die die Ursache der Wirkungen bestimmt. Zu ihrer Lösung werden Optimierungsverfahren eingesetzt.

Die Modellkalibrierung ist ein grundlegender Bestandteil der Entwicklung eines morphodynamischen Modells. Als Grundlage sollen unbedingt Messdaten bzw. aus diesen Daten abgeleitete Werte verwendet werden. In der Kalibrierung wird die erste Schätzung der Modellerstellung überprüft und dann durch Vergleich mit Messdaten verbessert. Mit der Kalibrierung müssen die Modellparameter für das Untersuchungsgebiet abgestimmt werden.

Aus den bisherigen Ausführungen wird deutlich, dass das betrachtete inverse Problem inkorrekt ist. Das heißt, Existenz, Eindeutigkeit und Stabilität der Lösung können nicht garantiert werden. Ursache sind der Verlust an Informationen über die wahrgenommene Realität während des Prozesses der Modellierung sowie der Mangel an Informationen und deren Fehlerhaftigkeit bei der Erfassung der Messdaten zur Parameteridentifikation.

Neben den Informationen zur geometrischen Entwicklung sollen auch die anderen Datenvergleiche zwischen Messung und Rechnung für die Modellkalibrierung genutzt werden z.B. Geschiebetriebbeginn und Geschiebetransportraten sowie Korngrößen an Geschiebemessstellen; Schwebstoffkonzentrationen und Korngrößenverteilungen an Schwebstoffmessstellen; Sieblinien in Sedimentationsbereichen; Sieblinien von Deckschichten; Sedimentaustrag am unteren Modellrand.

Während der Kalibrierung wird die Abweichung zwischen Modellergebnissen und Messdaten minimiert. In der Regel erfolgt die Kalibrierung auf der Basis von „Versuch und Irrtum“. Das heißt, Modellrechnungen werden durchgeführt und ihre Ergebnisse werden mit den vorhandenen Messdaten verglichen. Aus Sensitivitätsanalysen lernt man, wie die Modellparameter zu verändern sind, um eine bessere Übereinstimmung zwischen den Ergebnissen und Messdaten zu haben. Falls Probleme bei der Anpassung der Modellparameter auftreten, sollte man überprüfen, ob das gewählte Modellsystem für die Nachbildung der gegebenen physikalischen Prozesse geeignet ist und ob eine globale oder stochastische Sensitivitätsanalyse für alle Modellparameter benötigt wird. Da in der Regel Eingangsdaten mit Messunsicherheiten behaftet sind, können Fehler in einzelnen Messdaten auch eine Ursache sein. Mit der Kalibrierung ist es möglich, Ungenauigkeiten der Eingangsdaten zu erkennen.

Es ist wichtig zu berücksichtigen, dass das Sedimenttransportmodell von einem hydrodynamischen Modell angetrieben wird und dass hochgradig nichtlineare Beziehungen zwischen Sohlschubspannung, Turbulenz, Sedimentmobilisierung, -transport und -ablagerung bestehen. Jede Einschränkung bei der hydrodynamischen Kalibrierung könnte sich erheblich auf das Sedimentmodell auswirken. Es ist daher von entscheidender Bedeutung, die bestmögliche hydrodynamische Kalibrierung zu erzielen.

Der herkömmliche Ansatz ist die manuelle Kalibrierung oder Anpassung des Modells anhand von Beobachtungsdaten. In den letzten Jahren wurden jedoch mit zunehmenden Rechenkapazitäten viele neue, häufig komplexe, automatisierte Algorithmen zur Parameteroptimierung entwickelt. Einige Methoden basieren auf der Bestimmung eines einzigen besten Parametersatzes, wie z.B. die Downhill-Simplex-Optimierung von Hill et al. (2003); der genetische Algorithmus von Knaapen & Hulscher (2003) und der hybride genetische Algorithmus von Ruessink (2005a). Nebenbei wurden auch probabilistische Ansätze verwendet, wie das Bayesian Generalized Likelihood Uncertainty Estimation (GLUE) von Beven & Binley (1992) und von Ruessink (2005b, 2006). Die probabilistischen Methoden basieren auf dem Prinzip, dass es keinen einzigen besten Parametersatz gibt. Stattdessen werden die Parameter als Wahr-

scheinlichkeitsvariablen behandelt, wobei jedem Parametersatz ein Wahrscheinlichkeitswert zugewiesen wird. Die Eignung eines bestimmten Ansatzes hängt von Faktoren wie Modellkomplexität, Verfügbarkeit von Beobachtungsdaten, Rechenressourcen und Anwenderkompetenz ab.

Grundsätzlich liefert die Anwendung eines kalibrierten Modells mit Datensätzen, die bei der Kalibrierung nicht verwendet wurden, eine Möglichkeit zur Bewertung der Modellzuverlässigkeit. Ein Modell kann als konsistent eingeschätzt werden, wenn die zusätzlichen Datensätze, die nach Möglichkeit unterschiedliche hydromorphologische Bedingungen beinhalten sollten, realistisch vom Modell abgebildet werden können. Bei dem Vorgang, bei dem die Berechnungen mit den kalibrierten Modellparametern durchgeführt werden und die Differenzen zwischen den Berechnungsergebnissen und den Messdaten anschließend dargestellt werden, spricht man von Modellvalidierung. Die Abweichungen zu den Messdaten aus der Validierung sollten nicht wesentlich größer sein als jene aus der Kalibrierung. Zeigen sich unerwartet große Abweichungen, sollte man die Plausibilität der Daten aus dem Validierungsdatensatz überprüfen oder die Kalibrierung nochmals verbessern. Falls eine zufrieden stellende Validierung des Modells nicht möglich ist, muss entweder die Aussagekraft des Modells eingeschränkt werden, oder es ist ein besser geeignetes Modell zu wählen.

5.2. Ausblick über die Zukunft der hydromorphologischen Modellierung

Sedimenttransport in der Mischsohle ist ein äußerst komplexes Thema, wobei die Wechselwirkung zwischen Wasserbewegung und Körner sowie der Körner untereinander in ihrem vollen Umfang noch lange nicht erfasst wird. Es kann gesagt werden, dass die damalige Einschätzung von Albert Einstein, der seinem Sohn Hans-Albert geraten hat, sich ein einfacheres Dissertationsthema zu suchen, durchaus berechtigt und auch aus heutiger Sicht immer noch zutreffend ist.

Für die Zukunft ergeben sich eine Reihe von Herausforderungen an die Modelleure. Die hydromorphologischen numerischen Modelle müssen im Hinblick auf Prozesse vervollständigt werden und in den Stand gesetzt werden, über längere Zeiträume in größeren Gebieten integriert werden zu können. Dazu ist die Ankopplung hydromorphologischer Modelle an die hydrologischen Modelle erforderlich und auch der Einsatz von Hochleistungscomputern (HPC) in Kombination mit speziell angepasster Software unverzichtbar. Erste Ansätze dieser Art werden in verschiedenen Forschungsprojekten am Lehrstuhl für Wasserbau und Wasserwirtschaft der Technischen Universität München (TUM) verfolgt.

5.2.1. Verfeinerung der Sedimenttransportansätze

Wie in Kapitel 2 gezeigt, wird oft in konventionellen Modellen die Strömungsberechnung mittels einer der klassischen Methoden vorgenommen, und die morphologische Berechnung als

gekoppeltes Problem unter Zuhilfenahme verschiedener empirischen Formeln für den Sedimenttransport numerisch gelöst. Die Strömungsberechnung, beispielsweise mittels eines numerischen Verfahrens und mithilfe geeigneter Turbulenzansätze, ist erprobt und effizient, so dass keine Alternativen zu suchen wären. Der Schwachpunkt des gängigen Vorgehens liegt in der Darstellung des Geschiebetransports und der Austauschprozesse in einem klassischen Kontinuumsansatz, da in einem solchen die Physik der Prozesse nicht enthalten sein kann. Jedoch gibt es eine große Anzahl von Beziehungen, die die zugrundeliegenden Prozesse aber höchstens teilweise in einem physikalischen Sinne korrekt abbilden. Beispiele sind Austauschprozesse zwischen den Schichten, die von wesentlicher Bedeutung für das Modell des fraktionierten Sedimenttransportes sind. Da sie nicht explizit dargestellt werden können, bleibt nur die Möglichkeit einer indirekten Darstellung. Man nennt diese Technik „Parametrisierung". Diese Parameterisierungen, wie oben erwähnt, sind in ihrer funktionalen Form in der Regel physikalisch motiviert. Jedoch werden diverse numerische Konstanten nach empirischen Befunden und günstiger Wirkung beim Einsatz in den gängigen numerischen Modellen fixiert. Praktisch alle Sedimenttransportmodelle enthalten solche Parameterungen, deren Existenz für den Puristen jedoch unbefriedigend ist.

Eine besser quantitative Prognose der hydromorphologischen Entwicklung in Flüssen ist nur möglich, wenn Modelle zum Einsatz kommen, die alle wichtigen Prozesse nachbilden. Deshalb liegen die besonderen Herausforderungen an die Modelleure in der Zukunft darin, die fehlende Prozesse in Modelle zu integrieren sowie die vorhandenen, vereinfachten Modellansätze zu verbessern.

Die Entwicklung der Sedimenttransportformeln kann durch die Anwendung von hochaufgelösten numerischen Simulationen und ANN Modellen verbessert werden. Es ist wichtig, dass diese Simulationen möglichst nahe an der Wirklichkeit sind und sowohl die Wasser- als auch die Sedimentphase korrekt abbilden. Die Transportformel kann man sich dann sowohl als einen algebraischen Ausdruck, als auch als ein ANN Modell vorstellen, das durch die hochaufgelösten, numerischen Simulationen trainiert wird. Ein solches Vorgehen verschiebt den Rechenaufwand in eine Vorphase, um anschließend bei den eigentlichen Simulationen recht schnelle Antworten zu liefern. Ebenfalls klar ist, dass dieser Weg nur für den Bereich der sog. Trainingsrechenläufe sinnvolle Resultate liefern wird. Hierzu ergeben sich zwei folgende möglichen Wege:

- Die Anwendung eines CFD-DEM-Modellsystems, wobei die Phasenbewegung von diskreten Partikeln durch die Diskrete-Elemente-Methode (DEM) mit Hilfe der Newtonschen Bewegungsgesetze ermittelt wird. Die Wasserströmung kann mathematisch durch die Navier-Stokes-Gleichungen beschrieben werden, die mit der traditionellen Computational Fluid Dynamics (CFD) gelöst werden können. Die Wechselwirkungen zwischen der Strömung und dem Sedimenttransport lassen sich nach dem dritten Newtonschen Gesetz modellieren. Das hier geschilderte Vorgehen hätte den Vorteil, dass die vorhandenen, konventionellen Programme und die unbestreitbaren Vorteile einer klassischen Strömungssi-

mulation (z.B. DNS und LES) mit dem gesamten, vorhandenen und großen Erfahrungsschatz beibehalten werden könnte.

- Die Verwendung eines alternativen, numerischen Verfahrens, das in der Lage ist, sowohl die Strömung als auch die Sedimentphase in voller Komplexität und Prozessgenauigkeit abzubilden. Die größten Chancen dafür sind in einem Smoothed Particle Hydrodynamics (SPH) Ansatz, einem Multiphase Particle in Cell (MPPIC) Ansatz, oder einem Cellular Automation (CA) Ansatz zu sehen. Diese Methoden erlauben die Modellierung beider Phasen mit dem gleichen Simulationsansatz und scheinen das Potential zu haben, sowohl die Strömung inklusive der Turbulenzen als auch eine fraktionierte Geschiebephase mit allen Kollisionseffekten unter Erhalt von Masse, Impuls und Energie korrekt zu simulieren. Mit der SPH-Methode können im Gegensatz zu klassischen CFD-Methoden auch hochdynamische Fluidbewegungen mit freien Oberflächen und mehreren Phasen simuliert werden. Die Methode ist besonders geeignet für hochdynamischen Strömungsprozesse. Hier stoßen herkömmliche CFD Modelle schnell an ihre Grenzen und SPH bietet eine attraktive Alternative.

Partikelsimulationen ermöglichen eine äußerst detaillierte Beobachtung dynamischer hydromorphologischer Vorgänge. Jedoch hängt die Qualität der Ergebnisse wie bei den meisten anderen Simulationsmethoden vom Grad der Diskretisierung ab. Eine hohe Ergebnisgüte macht somit ebenfalls die Berücksichtigung einer großen Anzahl von Partikeln erforderlich. Wenn große Simulationen unvermeidlich sind, um eine vorgegebene Simulationsaufgabe zu lösen, stoßen auch moderne Workstations leicht an ihre Grenzen, v.a. wenn die verwendete Software die Rechenleistung nicht optimal nutzt. Allerdings kann das Problem durch den Einsatz von hochleistungsfähigen Supercomputern relativiert werden (Maruzewski et al., 2010; Herault et al., 2010).

MacVicar et al. (2006) verwendeten ein stochastisches Partikel-Modell, das die Sohlevolution in kiesführenden Gewässern simulieren kann. Die Strömungsgeschwindigkeit infolge der Turbulenz wird mit einer Gauß-Verteilung simuliert. Die Partikel werden in drei Größen eingeteilt. Die Bewegung der Partikel wird allerdings nicht direkt mit der Strömung gekoppelt, sondern durch die Partikelgröße mit der Strömungsgeschwindigkeit nach vorgegebenen Algorithmen berechnet. Narteau et al. (2009) haben ein Modell für die Sanddünenevolution. Das Modell besteht aus zwei gekoppelten Modulen: einem CA Modul für das Sediment und einem „Lattice Gas Cellular Automation“ (LGCA) Modul für das Fluid. Der Sedimenttransport wird durch die Interaktionen der benachbarten Partikel und einen zeitabhängigen stochastischen Prozess im CA Modul geregelt. Die Strömung und die Sohlschubspannung werden durch das LGCA-Modul simuliert. Im Vergleich zu den auf den Navier-Stokes-Gleichungen basierenden Methoden stellt LGCA eine länger etablierte, alternative Methode dar. Die wellenartige Sohlformdynamik unterliegt einer linearen Stabilität. Ausbaufähig ist dieser Ansatz hinsichtlich der Turbulenz, der Erweiterung des Bewegungsmechanismus sowie der Kornsortierung und Sohlabpflasterung. Die numerische Simulation liefert eindrucksvolle Ergebnisse der Sohldynamik. Bialik et al. (2011) erweiterten das Partikel-Modell von Niño & García (1994, 1996)

und berücksichtigten dabei die Basset-Kräfte mit der Approximationsmethode von Bombardelli et al. (2008), die Turbulenz in der Sohlennähe mit der Spektra-Methode von Nikora & Goring (2000) und die Partikel-Partikel-Interaktionen mit der Monte-Carlo-Methode.

Im Kontext einer makroskaligen Rechnung kann das Geschiebe mit Partikelmethoden physikalisch korrekt modelliert werden. Um die Partikel-Partikel-Interaktion und Partikel-Strömung-Interaktion besser zu berücksichtigen, sind verschiedene Ansätze zu entwickeln. Deshalb ist für jeden Anwendungsfall eine Kalibrierung notwendig.

5.2.2. Großskalige numerische Modelle

Um komplexe hydromorphologische Prozesse mit den konventionellen numerischen Modellen zu beschreiben, wird in der Regel ein komplexes mehrdimensionales Rechenmodell sowohl für die Strömung als auch den Sedimenttransport benötigt. Für meist großskalige Gebiete mit ausreichender Gitterauslösung müssen rechenintensive Gleichungen gelöst werden. Um solche Simulationen effizient und in vertretbarer Zeit durchzuführen, ist es notwendig, die numerischen Verfahren des Computercodes zu optimieren und auch entsprechend die Rechenleistung von Computern zu vergrößern.

Vor allem bieten moderne Workstations von Generation zu Generation zunehmend mehr Rechenkerne (Cores). Um diese Multicoresysteme ausnutzen zu können, ist es notwendig, die Berechnungen auf verschieden Ebenen zu parallelisieren. Die Idee hier ist, dass man die Ausführungszeit einer Aufgabe eines Programms dadurch reduziert, dass mehrere Berechnungen auf verschiedenen Prozessorkernen gleichzeitig zur Ausführung gelangen und durch koordinierte Zusammenarbeit die gewünschten Aufgaben erledigen. Anders gesagt, teilt man eine Aufgabe in kleinere Teilaufgaben, die dann von verschiedenen Prozessorkernen erledigt werden. Die Bearbeitung von Teilaufgaben ist möglicherweise nicht vollkommen unabhängig voneinander, sondern kann durch Daten und Kontrollabhängigkeiten miteinander gekoppelt sein. Der Grund dafür ist, dass manche Teilaufgaben nicht ausgeführt werden, bevor andere Teilaufgaben alle benötigten Daten oder Informationen bereitgestellt haben. Deswegen wird für die korrekte Abarbeitung einer Aufgabe die Ausführung von Kommunikationsanweisungen notwendig. Durch diese Anweisungen warten alle beteiligten Prozessorkernen aufeinander, um miteinander Informationen auszutauschen. Die Ausführungszeit einer Aufgabe setzt sich aus der Rechenzeit jedes beteiligten Prozessorkerns und der Zeit für den Informationsaustausch unter diesen Prozessorkernen zusammen. Um eine optimale parallele Laufzeit zu bekommen, sollte eine möglichst gleichmäßige Lastverteilung auf die Prozessorkerne angestrebt werden, sodass ein Lastgleichgewicht entsteht. Was hier auch beachtet werden sollte ist, dass der Informationsaustausch zwischen den Prozessorkernen so gering wie möglich gehalten werden sollte, damit die Prozessorkerne nicht lange aufeinander warten müssen.

Des Weiteren können große Untersuchungsgebiete oft nicht im Arbeitsspeicher eines einzelnen Rechners gehalten werden, weshalb sie in verschiedene Teilgebiete zerlegt werden, in denen alle Variablen auf den einzelnen Rechnern in jedem Rechenschritt parallel berechnet

werden. Am Ende werden die Ergebnisse zusammengeführt und der Rechenschritt abgeschlossen. Diese gängige Technik ist auch bekannt als das Domain Decomposition Verfahren. Aufgrund der Datenabhängigkeit aus der Diskretisierung und der hieraus resultierenden regelmäßigen Kommunikation zwischen den Rändern der Teilgebiete ist der Einsatz von modernen Rechnern mit schnellen Netzwerken notwendig. Daraus kann man schließen das Parallelität in der Zukunft eines der zentralen Themen der hydromorphologischen numerischen Modelle spielen wird.

Moderne Grafikkarte besitzt eine große Anzahl Kerne in der Grafikprozessoreinheit (GPU, Graphics Processing Unit), die völlig unabhängig voneinander Berechnungen durchführen können. Darüber hinaus sind GPUs auf massive Parallelisierung ausgelegt, sie können deshalb eine enorme Rechenleistung erbringen und bei vielen parallel ausführbaren und rechenintensiven Aufgaben sogar die Hochleistungs-CPUs in den Schatten stellen. GPU-Computing (oder GPGPU, General Purpose Computation on Graphics Processing Unit) bezeichnet die Verwendung von GPUs für wissenschaftliche, technische oder wirtschaftliche Simulationen. Durch die hohe Verfügbarkeit und den geringen Preis hat die Verbreitung von GPU-Computing in den letzten Jahren rasant zugenommen. Durch bessere Hardware und ausgereifte Softwarebibliotheken haben sich GPUs für die numerische mathematische Problemlösung durch massiv-parallele Rechenwerke etabliert. Auch im Bereich der hydromorphologischen numerischen Modellierung ist GPU-Computing für Ingenieure und Wissenschaftler nicht mehr wegzudenken.

Weiterhin werden die Fragestellungen an den Wasserbau und die Wasserwirtschaft immer größer und umfangreicher. Als Beispiel, es hat sich bei den vergangenen Hochwasserereignissen gezeigt, dass die Berechnungsergebnisse der auf einer statischen Sohle basierenden Modelle strenggenommen nur für den im Modell vorgegebenen Sohlzustand zutreffen. Bei entsprechender Veränderung der Flusssohle kann es zu erheblichen Veränderungen der Wasserspiegellage kommen, die ohne weiterführende Untersuchungen äußerst schwer zu quantifizieren sind. Da sich die Flusssohle beim Hochwasser sehr stark verändern kann, kann die Annahme einer statischen Flusssohle zur Unterschätzung der Hochwassergefahren führen. Darüber hinaus haben die Untersuchungen am Lehrstuhl für Wasserbau und Wasserwirtschaft der TUM auch gezeigt, dass eine zwar einfache aber gut kalibrierte Niederschlags-/Abflussberechnung durch eine komplexe, hydrodynamische Abbildung der Prozesse des Gerinnes nicht verbessert werden kann. Ein Grund dafür ist, dass die Übergabe des Abflusses aus der Fläche in Bezug auf Menge und zeitliche Verteilung fehlerhaft ist. Eine hydrologisch-hydromorphodynamische Kopplung mit hoher Prozessauflösung auf den HPC Systemen stellt deshalb die Grundvoraussetzungen dar, um das Abflussgeschehen und die morphologische Entwicklung realitätsnäher erfassen bzw. zukünftige Planungen von Hochwasserschutzmaßnahmen ganzheitlich angehen zu können.

LITERATURVERZEICHNIS

Almedeij, J.H. (2002): „Bedload transport in gravel-bed streams under a wide range of Shields stresses“, PhD Diss., Faculty of the Virginia Polytechnic Institute and State University

Armanini, A. (1995): Non-uniform sediment transport: dynamics of the active layer, Journal of Hydraulic Research, 33.

Armanini, A.; Di Silvio, G. (1988): ”A one-dimensional model for the transport of a sediment mixture in non-equilibirum conditions”, Journal of Hydraulic Research , 26(3).

Arnold, U.; Höttges, J.; Rouve, G. (1989): Turbulence and Mixing Mechanisms in Compound Open Channel Flow. Proc. Of the 23th IAHR Congress, Ottawa, Canada.

ASCE (1982): “Relationships between morphology of small streams and sediment yields”, Journal of Hydraulics Division, 108(HY11).

Ateeq-Ur-Rehman, S.; Bui, M.D.; Rutschmann, P. (2018): “Variability and Trend Detection in the Sediment Load of the Upper Indus River”, Water, 10, 16, MDPI.

Azmathullah, H.M.; Chang, C.K.; Ghani, A.A.; Ariffin, J.; Zakaria, N.A; Hasan, Z.A. (2009): “An ANFIS-based approach for predicting the bed load for moderately sized rivers”, J. Hydro-envir. Research, 3.

Bagnold, R. (1956): “The flow of cohesionless grains in fluids”, Philosophical transactions of the Royal Society of London, Series A, 249.

Batchelor, G. (1967): An Introduction to Fluid Dynamics. Cambridge University Press.

Bauer, W. (1998): Berechnung turbulenter Strömungen mit starken Stromlinienkrümmungen beziehungsweise mit Rotation. Dissertation, FG Gasturbinen und Flugantriebstechnik, TU Darmstadt.

Beffa, C.J. (1994): Praktische Lösung der tiefengemittelten Flachwassergleichungen. Mitteilung der VAW, Nr. 133, ETH, Zürich.

Bennett, J.P.; Nordin, C.F. (1977): “Simulation of sediment transport and armouring”, Hydrological Sciences Bulletin, 22(4), 555-569.

Beven, K.; Binley, A. (1992): “The future of distributed models: model calibration and uncertainty prediction”, Hydrol. Proc. 6.

Beyer, W.; Banscher, E. (1975): „Zur Kolmation der Gewässerbetten bei der Uferfiltratgewinnung", Zeitung der angewandten Geologie, 21 (12), 565 – 570.

Bezzola, G.R. (2002): Fliesswiderstand und Sohlenstabilität natürlicher Gerinne unter besonderer Berücksichtigung des Einflusses der relativen Überdeckung. Mitteilung der VAW, Nr. 173, ETH, Zürich.

Bialik, R. (2011): "Particle-particle collision in Lagrangian modelling of saltating grains", Journal of Hydraulic Engineering , 49(1).

Blom, A. (2008): "Different approaches to handling vertical and streamwise sorting in modeling river morphodynamics", Water Resources Research, Vol. 44.

Blom, A.; Ribberink, J.; de Vriend, H. (2003): "Vertical sorting in bed forms: Flume experiments with a natural and a trimodal sediment mixture", Water Resources Research , 39 (2).

Blom, A.; Ribberink, J. S.; Parker, G. (2008): "Vertical sorting and the morphodynamics of bed form–dominated rivers: A sorting evolution model", Journal of Geophysical Research, 113.

Borah, D.K.; Alonso, C.V.; Prasad, S.N. (1982): "Routing Graded Sediments in Streams: Formulations", J. Hydr. Div., 108(HY 12).

Buffington, J.M.; Montgomery, D.R. (1997): "A systematic analysis of eight decades of incipient motion studies, with special reference to gravel-bedded rivers", Water Resources Research, 33.

Bui, M.D.; Huber, D.; K. Kaveh, K.; da Silva, A.M.F.; Rutschmann, P. (2016): "Application of artificial neural networks for river regime", Proc. of River-Flow-2016, Saint Louis, USA.

Bui, M.D.; Kaveh, K.; Penz, P.; Rutschmann, P. (2015a): "Contraction scour estimation using data-driven methods", Journal of Applied Water Engineering and Research, 3(2).

Bui, M.D.; Kaveh, K.; Rutschmann, P. (2015b): "Integrating artificial neural networks into hydromorphological model for fluvial channels", Proceedings of the 36th IAHR World Congress, The Hague, The Netherlands.

Bui, M.D.; Rutschmann, P. (2015c): „Anwendung eines numerischen Modellsystems zur Bewertung von Geschiebehaushalt und Äsche-Laichhabitaten des Hochrheins", Wasserwirtschaft, 105(7-8).

Bui, M.D.; Rutschmann, P. (2013): “Assessment of Sedimentation and Flushing Efficiency for Kajbar Hydropower Project in the Nile River”; Proc. of the 35th IAHR World Congress, Chengdu, China.

Bui, M.D.; Rutschmann, P. (2012): “Numerical investigation of hydro-morphological changes due to training works in the Salzach River”; Proc. of River-Flow-2012, San Jose, Costa Rica.

Bui, M.D.; Rutschmann, P. (2010): “Numerical modelling of non-equilibrium graded sediment transport in a curved open channel”, Computers and Geosciences , 36.

Bui, M.D.; Eizel-Din, M.; Rutschmann, P. (2009): “Simulation of morphological changes due to flooding in the Inn River”; Proceedings of the 33rd IAHR World Congress, Vancouver, Canada.

Bui, M.D.; Rodi, W. (2008): “Numerical Simulation of Contraction Scour in an Open Laboratory Channel”; Journal of Hydraulic Engineering, ASCE, 134(4).

Bui, M.D.; Rodi, W. (2006): “Dreidimensionales Modell zur Berechnung des Sedimenttransports bei Ungleichgewicht in Flüssen“; Bericht No.828, Institut für Hydromechanik, Universität Karlsruhe.

Bui, M.D.; Wenka, Th.; Rodi, W. (2004): “Numerical Modelling of Bed Deformation in Laboratory Channels”; Journal of Hydraulic Engineering, ASCE, 130(9).

Bui, M.D. (1998): „Berechnung der Strömung und des Sedimenttransports in Flussläufen mit einem tiefengemittelten numerischen Verfahren“, Dissertation, Institut für Hydromechanik, Universität Karlsruhe.

Bui, V.H.; Bui, M.D.; Rutschmann, P. (2019): “Advanced Numerical Modeling of Sediment Transport in Gravel-Bed Rivers”, Water, 11, 50, MDPI.

Celik, I.; Rodi, W. (1984): “Computation of Oscillatory Turbulent Flows in Open Chanels”, Energy Sources Technology Conference, New Orleans, Louisiana, USA.

Chien, N.; Wan, Z. (1999): “Mechanics of Sediment Transport”, ASCE Press.

Cundall, P.A.; Hart, R. (1992): “Numerical modeling of discontinua”, J. of Eng. Comput., 9.

Dey, S. (2003): “Threshold of sediment motion on combined transverse and longitudinal sloping beds“, Journal of Hydraulic Research, 41(4).

Dey, S. (2014): Fluvial Hydrodynamics - Hydrodynamic and Sediment Transport Phenomena; Springer Heidelberg.

Dinehart, R.L. (1992): “Evolution of coarse-gravel bedforms, field measurements at flood stage”, Water Resources Research, 28(10): 2667-2689.

Dittrich, A. (1998): „Wechselwirkung Morphologie/Strömung naturnaher Fliessgewässer“, Heft 198, Mitteilung des Institutes für Wasserwirtschaft und Kulturtechnik der Universität Karlsruhe.

Elder, J.W. (1959): The dispersion of marked fluid in turbulent shear flow. Journal of Fluid Mechanics, 5.

Egiazaroff, I. (1965): “Calculation of non-uniform sediment concentrations”, Journal of Hydraulic Engineering , Vol. 91.

Einstein, H. (1950): “The bed-load function for sediment transportation in open channel flows”, (Bd. No. 1026), US Department of Agriculture.

Engelund, F.; Fredsoe , J. (1976): “A sediment transport model for straight alluvial channels”, Nordic Hydrology , 7.

Flokstra, C. (1977): “The Closure Problem for Depth-Average Two Dimensional Flow”, Waterloopkundig Laboratorium, Delf Hydraulics Laboratory, Publication No.190.

Fröhlich, J. (2006): Large-Eddy Simulation Turbulenter Strömungen. Wiesbaden, Teubner Verlag.

Galdi, G. (1994): “An Introduction to the Mathematical Theory of the Navier–Stokes Equations, I: Linearized Steady Problems”, vol. 38 of Springer Tracts in Natural Philosophy. Springer.

Geldner, P. (1982): „Ein strömungsmechanischer Ansatz zur Bestimmung der Selbstdichtung in natürlichen Gewässern“, Wasserwirtschaft, 72 (9), 311 – 317.

Gessler, J. (1965): „Der Geschiebebeginn bei Mischungen untersucht an natürlichen Abpflästerungserscheinungen in Kanälen“, Mitteilung Nr. 69, Versuchsanstalt für Wasserbau und Erdbau der ETH Zürich.

Gill, A. (1995): „Modellierung der Verbrennung in einem Schichtlade – Motor unter Verwendung detaillierter chemischer Reaktionsmechanismen“. Dissertation, Universität Stuttgart.

Graf, W.H.; Pazis, G.C. (1977): “Les phenomenes de deposition et d’erosion dans un canal alluvionnaire”, Journal de Recherches Hydrauliques, 15(2).

Grass, A. J. (1970): “Initial instability of fine sand”, Journal of Hydraulics Division, ASCE, 96(3).

Gray, J.M.N.T.; Shearer, M.; Thornton, A.R. (2006): “Time-dependent solutions for particlesize segregation in shallow granular avalanches”, Proceedings of the Royal Society A: Mathematical, Physical and Engineering Science, 462 (2067), 947 – 972.

Henderson, F.M. (1966): Open Chanel Flow. Macmillan Publishing Co., New York.

Hérault, A.; Bilotta, G.; Dalrymple, R.A. (2010): “SPH on GPU with CUDA”, Journal of Hydraulic Research, 48, Extra Issue.

Hill, D.C.; Jones S.E.; Prandle, D. (2003): “Derivation of sediment resuspension rates from acoustic backscatter time-series in tidal waters”, Continental Shelf Res., 23.

Hinterberger, C. (2004): "Dreidimensionale und tiefengemittelte Large–Eddy–Simulation von Flachwasserströmungen", Dissertation, Institut für Hydromechanik, Universität Karlsruhe..

Hirano, M. (1971): “River bed degradation with armouring”, Trans. Jpn. Soc. Civ. Eng. , 3.

Holly, F.M. and Odgaard, A.J. (1992): “Sediment transport modelling in the upper Rhine River, Assessment of modelling opportunities”, Limited distribution report, Iowa institute of hydraulic research, University of Iowa.

Höttges, J. (1992): „Zur Methode der numerischen Simulation von Stoffausbreitungsvorgängen in Fließsgewässern“, Mitteilung, Institut für Wasserbau und Wasserwirtschaft, Rheinisch-Westfällische Technische Hochschule Aachen, Band 86.

Hrissanthou, V.; Vollmers, H.J.; Hartmann, S. (1995): „Beginn des Feststofftransports - Eine zusamenfassende Betrachtung“, Mitteilungen 54, Institut für Wasserwesen, Universität der Bundeswehr München.

Hunziker, R. (1995): „Fraktionsweiser Geschiebetransport“, Mitteilung 138, Versuchsanstalt für Wasserbau, Hydrologie und Glaziologie der ETH Zürich.

Jain, S.K. (2008): “Development of Integrated Discharge and Sediment Rating Relation Using a Compound Neural Network”, Journal of Hydraulic Engineering, 13 (3).

Jang, J.H. ; Ho, H.Y. ; Yen, C.I. (2011): “Effects of Lifting Force on Bed Topography and Bed-

Surface Sediment Size in Channel Bend", Journal of Hydraulic Engineering, 137(9).

Jensen, R.P.; Bosscher, P.J.; Plesha, M.E.; Edil, T.B. (1999): "DEM simulation of granular media – structure interface: effects of surface roughness and particle shape", International Journal for Numerical and Analytical Methods in Geomechanics, 23.

Jin, Y.C; Steffler, P.M. (1993): "Predicting Flow in Curved Open Channels by Depth-Averaged Method", Journal of Hydraulic Engineering, 119(1).

Kaveh, K.; Bui, M.D.; Rutschmann, P. (2019): "Integration of Artificial Neural Networks into TELEMAC-MASCARET system, new concepts for hydromorphodynamic modeling", Advances in Engineering Software, 132.

Kaveh, K.; Bui, M. D.; Rutschmann, P. (2017): "A comparative study of three different learning algorithms applied to ANFIS for predicting daily suspended sediment concentration", International Journal of Sediment Research, 32(3).

Kleinhans, M., Van Rijn, L. (2002): "Stochastic prediction of sediment transport in sand-gravel bed rivers", Journal of Hydraulic Engineering , 128.

Knaapen, M.A.F.; Hulscher, S.J.M.H. (2003): "Use of a genetic algorithm to improve prediction of alternate bar dynamics", Water Resources Res. 39: 1231.

Koll, K. (2002): „Feststofftransport und Geschwindigkeitsverteilung in Raugerinnen", Dissertation, Universität Karlsruhe, Fakultät für Bauingenieur- und Vermessungswesen.

Lin, B.N. (1984): "Current study of unsteady transport of sediment in China", Proc. Japan-China Bilateral Seminar on River Hydraulics and Engineering Experiences, July, Tokyo-Kyoto-Saporo, Japan.

Little, W.C.; Mayer, P.G. (1976): "Stability of channel beds by armouring". Journal of the Hydraulic Division, ASCE, 102 (HY11).

Luckner, T. (2002): "Zum Bewegungsbeginn von Sedimenten", Dissertation, TU-Darmstadt, Institut für Wasserbau und Wasserwirtschaft.

Luckner, T.; Zanke, U. (2007): "An analytical solution for calculating the initiation of motion", International Journal of Sediment Research, 2282).

MacVicar, B.; Parrott, L.; Roy, A. (2006): "A two-dimensional discrete particle model of gravel bed rive systems", Journal of Geophysical Research , 111.

Maruzewski, P.; Le Touzé, D.; Oger, G.; Avellan, F. (2010): “SPH high-performance computing simulations of rigid solids impacting the free-surface of water”, Journal of Hydraulic Research, 48, Extra Issue.

Meyer-Peter, E.; Müller, R. (1948): “Formulas for bed-load transport”, Proc. of IHAR , Stockholm.

Mitchener, H.; Torfs, H. (1996): “Erosion of mud/sand mixtures”. Coastal Eng., 29 (1/2).

Moin, P.; Kim, J. (1982): “Numerical investigation of turbulent channel flow”, J. Fluid Mech., 118, 341–377.

Morris, M. (2004): “IMPACT: Investigation of Extreme Flood Processes and Uncertainty”. Risk and Uncertainty (WP5) - Technical Report Wallingford, UK. Contract No. EVG1-CT-2001-00037.

Nagy, H.M.; Watanabe, K.A.N.D.; Hirano, M. (2002): “Prediction of sedimentload concentration in rivers using artificial neural network model”, Journal of Hydraulic Engineering, 128 (6).

Narteau, C.; Zhang, D.; Rozier, O.; Claudin, P. (2009): ”Setting the length and time scales of a cellular automaton dune model from the analysis of superimposed bed forms”, Journal of Geophysical Research, 114.

Neill, C.R.; Yalin, M.S. (1969): “Quantitative Definition of Beginning of Bed Movement”, Journal of the Hydraulics Division, ASCE, Vol. 95(HY1).

Nikora, V.; Goring, D. (2000): “Flow turbulence over fixed and weakly mobile gravel beds”, Journal of Hydraulic Engineering, 126(9).

Niño, Y.; García , M. (1996): „Experiments on particle-turbulence interactions in the near-wall region of an open channel flow: implications for sedimen transport”, J. Fluid Mech., 326.

Niño, Y.; García , M. (1994): ”Gravel saltation II: Modeling”, Water Resources Research, 30(6).

Niño, Y.; García , M.; Ayala, L. (1994): ”Gravel saltation I: Experiments”, Water Resources Research, 30(6).

ÖWAV (2011): “Fließgewässermodellierung – Arbeitsbehelf Feststofftransport und Gewässermorphologie“.

Odgaard, A.J; Bergs M.A. (1988): “Flow Processes in a Curved Alluvial Channel”, Water Resources Research, 24(1).

Paintal, A. (1971): “A stochastic model of bedload transport”, J. of Hydraulic Research, 9(4).

Park, I.; Jain, S. (1987): ”Numerical Simulation of Degradation of Alluvial Channel Beds”, J. Hydraul. Eng., 113(7).

Parker, G. (1990): “Surface-based bedload transport relation for gravel rivers”, Journal of Hydraulic Research , 28(4).

Parker, G. (1991a): “Selective sorting and abrasion of river gravel, I: Theory”, J. Hydraulic Eng., 117.

Parker, G. (1991b): “Selective sorting and abrasion of river gravel, II: Applications”, J. Hydraul. Eng., 117.

Parker, G.; Klingeman, P. (1982): “On why gravel bed stremas are paved”, Water Resources Research , 18 (5).

Parker, G.; Paola, C.; Leclair, S. (2000): “Probabilistic Exner Sediment continuity Equations for mixtures with no active layer”, Journal of Hydraulic Engineering, 126(11).

Powell, D. M. (1998): “Patterns and processes of sediment sorting in gravel-bed rivers”, Progress in Physical Geography, 22(1).

Prandl, L. (1965): Führer durch die Strömungslehre. 6. Auflage, Friedr. Vieweg & Sohn, Braunschweig.

Profitt, G.; Sutherland, A. (1983): “Transport of non-uniform sediments”, Journal of Hydraulic Research , 21(1).

Reisenbüchler, M.; Bui, M.D.; Skublics, D.; Rutschmann, P. (2019): “An integrated approach for investigating the correlation between floods and river morphology: A case study of the Saalach River, Germany”, Science of the Total Environment, 647.

Ribberink, J.S. (1987): Mathematical modelling of one-dimensional morphological changes in rivers with non-uniform sediment, Ph.D. thesis, Delft University.

Rodi, W. (1993): Turbulence models and their applications in hydraulics. IAHR Monograph. 3rd Ed. Balkema, Rotterdam, The Netherlands.

Rodi, W.; Constantinescu, G.; Stoesser, T. (2013): Large Eddy Simulation in Hydraulics. IAHR Monograph. CRC Press.

Ruessink, B.G. (2005a): „Calibration of nearshore process models – application of a hybrid genetic algorithm“, J. Hydroinform., 7.

Ruessink, B.G. (2005b): „Predictive uncertainity of a nearshore bed evolution model“, Cont. Shelf Res., 25.

Ruessink, B.G. (2006): „A Bayesian estimation of parameter-induced uncertainty in a nearshore alongshore current model“, J. Hydroinform., 7.

Saltelli, A.; Tarantola, S.; Campolongo, F. (2000): “Sensitivity analysis as an ingredient of modeling”, Statistical Science, 15.

Schälchli, U. (1993): Die Kolmation von Fließgewässersohlen: Prozesse und Berechnungsgrundlagen. Versuchsanstalt für Wasserbau, Hydrologie und Glaziologie der Eidgenössischen Technischen Hochschule Zürich, Mitteilungen 124.

Schlichting, H.; Gersten, K. (2006): Grenzschicht–Theorie, Springer.

Schöberl, F. (1981): „Abpflasterungs- und Selbststabilisierungsvermögen erodierter Gerinne“. Österreichische Wasserwirtschaft, Jg. 33, Heft 7/8.

Shields, A. (1936): „Anwendung der Ähnlichkeitsmechanik und der Turbulenzforschung auf die Geschiebebewegung“, Heft 26, Mitteilung der Preussischen Versuchsanstalt für Wasserbau und Schiffbau, Berlin.

Spasojevic, M.; Holly, F. (1994): “Three-dimensional numerical simulation of mobile-bed hydrodynamics”, Contract Report HL-94-2. Waterways Experiment Station, U. S. Army Corps Engineer, Vicksburg, Mississipi.

Struiksma, N. (1999): Mathematical modelling of bedload transport over non-erodible layers. Proceedings IAHR Symp. River Coastal and Estuarine Morphodynamics, Genova, 1.

Sutherland, A.J. (1991): “Hiding functions to predict self armouring”, Proc. Grain sorting seminar, Ascona, Switzerland.

Taylor, B.D.; Vanoni, V.A. (1972): "Temperature effects in low-transport, flat-bed flows". ASCE, Journal of Hydraulics Division, 98(HY8).

Temam, R. (1995): Navier–Stokes Equations and Nonlinear Functional Analysis, vol. 66 of

CBMS–NSF Regional Conference Series in Applied Mathematics. 2nd Ed. Philadelphia: SIAM.

Uhlmann, M. (2000): Generation of initial fields for channel flow investigation. Tech. rep., Potsdam Institute for Climate Impact Research, Potsdam.

Unsöld, G. (1984): "Der Transportbeginn feinstkörnigen rolligen Sohlenmaterials in gleichförmigen turbulenten Strömungen: Eine experimentelle Oberprüfung und Erweiterung der SHIELDS-Funktion". Reports Sonderforschungsbereich 95: Wechselwirkung Meer-Meeresboden, Heft Nr. 70, Universität Kiel , Kiel.

Van Rijn, L.C. (1984): “Sediment transport. Part I: Bed-load transport”, Journal of Hydraulic Engineering, 110(10).

Van Rijn, L.C. (1987): “Mathematical Modelling of Morphological Processes in the Case of Suspended Sediment Transport”, Delft Hydraulics Communication, No.382.

Van Rijn, L.C. (1993): Principles of Sediment Transport in Rivers, Estuaries and Coastal Seas. Aqua Publications.

Vanoni, V.A. (1964): „Measurements of critical shear stress for entraining fine sediments in a boundary layer, California Institute of Technology, Report No. KH-R-7, Pasadena, USA.

Venditti, J.G.; Dietrich, W.E.; Nelson, P.A.; Wydzga, M.A.; Fadde, J.; Sklar, L. (2010): “Mobilization of coarse surface layers in gravel-bedded rivers by finer gravel bed load”, Water Resources Research, 46, W07506, 1 – 10.

Vogel, K.; van Niekerk, A.; Slingerland, R.; Bridge, J. (1992): ”Routing of Heterogeneous Sediments over Movable Bed: Model Verification”, J. Hydraul. Eng., 118(2).

Vollmer, S.; Kleinhans, M. (2007): “Predicting incipient motion, including the effect of turbulent pressure fluctuations in the bed”, Water Resources Research, 43.

Wathen, S.J.; Ferguson, R.I.; Hoey, T.B.; Werritty A. (1995): “Unequal mobility of gravel and sand in weakly bimodal river sediments”, Water Resources Research, 31 (8), 2087-2096.

Whiting, P. J. (1996): “Sediment sorting over bed topography,” Advances in Fluvial Dynamics and Stratigraphy, Carling, P. A., and M. R. Dawson, eds., John Wiley & Sons, 203-228.

Wilcock, P.R. (1992): “Experimental investigation of the effect of mixture properties on transport dynamics”, in Dynamics of Gravel-bed Rivers, edited by P. Billi, R. D. Hey, C. R. Thorne, and P. Tacconi, John Wiley, New York.

Wilcock, P.R. (1993): “Critical shear stress of natural sediments”, Journal of Hydraulic Engineering, 19 (4), 491-505.

Wilcock, P.R.; McArdell, B.W. (1993): “Surface-based fractional transport rates: Mobilization thresholds and partial transport of a sand-gravel sediment”, Water Resour. Res., 29.

Wilcock, P.R. (1997): “The components of fractional transport rate”, Water Resources Research, 33 (1).

Wilcock, P.R.; Barta, A.F.; Shea, C.C.; Kondolf, G.M.; Matthews, W.V.G.; Pitlick, J.C. (1996): “Observations of flow and sediment entrainment on a large gravel-bed river”, Water Resources Research, 32(9).

Williams, F.A. (1985): Combustion Theory. Benjamin/Cummings Publishing Company, Menlo Park, CA.

Wong, M., Parker, G., DeVries, P., Brown, T. M., and Burges, S. J. (2007): “Experiments on dispersion of tracer stones under lower-regime plane-bed equilibrium bed load transport”, Water Resour. Res., 43.

Wu, W. (2007). Computational River Dynamics. Taylor & Francis, London.

Wu, W.; Wang, S.S.Y.; Jia, Y, (2000). “Non uniform sediment transport in alluvial rivers”, J. of Hydr. Res., 38(6).

Yalin, M.S. (1985): “On the determination of ripple geometry”, J. Hydr. Eng., ASCE, 111(8):1148–1155

Yao, W.; Bui, M.D.; Rutschmann, P. (2018): “Development of eco-hydraulic model for assessing fish habitat and population status in freshwater ecosystems”, Ecohydrology, 11(5).

Zanke, U. (1990): „Der Beginn der Sedimentbewegung als Wahrscheinlichkeitsproblem“, Wasser & Boden, 42(1).

Zanke, U. (2001): „Zum Einfluss der Turbulenz auf den Beginn der Sedimentbewegung“, Mitteilungen des Instituts für Wasserbau und Wasserwirtschaft der TU Darmstadt, Heft 120.

Zanke, U. (2013): Hydraulik für den Wasserbau. Springer Vieweg.